

# Electroweak and Higgs Measurements Using Tau Final States with the LHCb Detector

by Philip Ilten



UNIVERSITY COLLEGE DUBLIN

School of Physics

This thesis is submitted to University College Dublin in fulfilment of the requirements for the degree of Doctor of Philosophy.

|                 |                     |
|-----------------|---------------------|
| Head of School: | Prof. Pádraig Dunne |
| Supervisor:     | Dr. Ronan McNulty   |
| Submitted:      | September, 2013     |
| Examined:       | November, 2013      |

*Viva Voce* Panel

|                    |                        |
|--------------------|------------------------|
| Chairperson:       | Prof. Pádraig Dunne    |
| Internal Examiner: | Prof. Martin Grünewald |
| External Examiner: | Prof. Eilam Gross      |

*I, Philip Ilten, hereby certify that the submitted work is my own work, was completed while registered as a candidate for the degree of Doctor of Philosophy at University College Dublin, and I have not obtained a degree elsewhere on the basis of the research presented in the submitted work.*

This thesis is licensed under the Creative Commons Attribution 3.0 license. The contents of this thesis, in full or in part, can be copied, distributed, transmitted, or remixed if the material is attributed to the author.



© 2013 by Philip Ilten

# Contents

|  |           |
|--|-----------|
| <i>Abstract</i>                                    | <b>iv</b> |
| <i>Authorship</i>                                  | <b>v</b>  |
| <i>Acknowledgements</i>                            | <b>vi</b> |
| <b>1. Introduction</b>                             | <b>1</b>  |
| <b>2. Theory</b>                                   | <b>3</b>  |
| 2.1. Standard Model . . . . .                      | 3         |
| 2.1.1. Scattering Matrix . . . . .                 | 5         |
| 2.1.2. Lagrangians . . . . .                       | 11        |
| 2.1.3. Experimental Observables . . . . .          | 22        |
| 2.1.4. Alternatives and Extensions . . . . .       | 29        |
| 2.2. Monte Carlo Techniques . . . . .              | 34        |
| 2.2.1. Parton Showers . . . . .                    | 37        |
| 2.2.2. Hadronisation . . . . .                     | 40        |
| 2.2.3. Particle Decays . . . . .                   | 42        |
| <b>3. Tau Leptons</b>                              | <b>48</b> |
| 3.1. Tau Lepton Production . . . . .               | 49        |
| 3.1.1. Electroweak Production . . . . .            | 49        |
| 3.1.2. Higgs Boson Production . . . . .            | 51        |
| 3.1.3. Other Production . . . . .                  | 54        |
| 3.1.4. Initial and Final State Radiation . . . . . | 55        |
| 3.2. Tau Lepton Decays . . . . .                   | 55        |
| 3.2.1. Two-Body Decays . . . . .                   | 57        |
| 3.2.2. Three-Body Decays . . . . .                 | 57        |
| 3.2.3. Four-Body Decays . . . . .                  | 61        |
| 3.2.4. Five-Body Decays . . . . .                  | 75        |
| 3.2.5. Six-Body Decays . . . . .                   | 80        |
| 3.3. Implementation . . . . .                      | 85        |
| 3.3.1. Tau Decays . . . . .                        | 86        |
| 3.3.2. Matrix Elements . . . . .                   | 88        |
| 3.3.3. Validation . . . . .                        | 90        |

|  |            |
|--|------------|
| <b>4. Experimental Setup</b>                             | <b>92</b>  |
| 4.1. Large Hadron Collider . . . . .                     | 92         |
| 4.1.1. Layout . . . . .                                  | 94         |
| 4.1.2. Injection Chain . . . . .                         | 95         |
| 4.2. LHC Beauty Detector . . . . .                       | 96         |
| 4.2.1. Tracking . . . . .                                | 97         |
| 4.2.2. Particle Identification . . . . .                 | 102        |
| 4.3. LHCb Event Reconstruction . . . . .                 | 107        |
| 4.3.1. Tracking Information . . . . .                    | 108        |
| 4.3.2. Calorimeter Information . . . . .                 | 109        |
| 4.3.3. Triggers . . . . .                                | 111        |
| 4.3.4. Luminosity Determination . . . . .                | 112        |
| <b>5. Z Boson Cross-Section</b>                          | <b>115</b> |
| 5.1. Analysis . . . . .                                  | 117        |
| 5.1.1. Particle Identification . . . . .                 | 120        |
| 5.1.2. Event Selection . . . . .                         | 123        |
| 5.1.3. Background Estimation . . . . .                   | 132        |
| 5.2. Cross-Section . . . . .                             | 137        |
| 5.2.1. Reconstruction Efficiency . . . . .               | 138        |
| 5.2.2. Selection Efficiency . . . . .                    | 149        |
| 5.2.3. Acceptance and Branching Fractions . . . . .      | 151        |
| 5.3. Results . . . . .                                   | 152        |
| <b>6. Higgs Boson Limits</b>                             | <b>157</b> |
| 6.1. Higgs Phenomenology . . . . .                       | 158        |
| 6.1.1. Branching Fractions . . . . .                     | 159        |
| 6.1.2. Cross-Sections . . . . .                          | 164        |
| 6.2. Event Model . . . . .                               | 167        |
| 6.2.1. Simulation . . . . .                              | 167        |
| 6.2.2. Event Yields . . . . .                            | 168        |
| 6.2.3. Mass Distributions . . . . .                      | 170        |
| 6.3. Statistical Methods . . . . .                       | 171        |
| 6.3.1. Hypothesis Testing . . . . .                      | 173        |
| 6.3.2. Likelihoods, Medians, and Uncertainties . . . . . | 180        |
| 6.4. Results . . . . .                                   | 183        |
| 6.4.1. Validation . . . . .                              | 184        |
| 6.4.2. Final Limits . . . . .                            | 187        |
| <b>7. Conclusion</b>                                     | <b>192</b> |
| <b>Bibliography</b>                                      | <b>194</b> |

|   |            |
|---|------------|
| <b>Appendices</b>                                     | <b>210</b> |
| <b>A. Theory</b>                                      | <b>211</b> |
| A.1. Notation . . . . .                               | 211        |
| A.2. Electroweak Lagrangian . . . . .                 | 212        |
| A.3. Higgs Lagrangian . . . . .                       | 213        |
| <b>B. Tau Leptons</b>                                 | <b>214</b> |
| <b>C. Z Boson</b>                                     | <b>216</b> |
| C.1. Distributions . . . . .                          | 216        |
| C.2. Efficiencies . . . . .                           | 216        |
| C.3. Combined Fit . . . . .                           | 228        |
| <b>D. Higgs Boson</b>                                 | <b>231</b> |
| D.1. Higgs Phenomenology . . . . .                    | 231        |
| D.1.1. MSSM Higgs Boson Masses . . . . .              | 231        |
| D.1.2. SM Branching Fraction Calculations . . . . .   | 232        |
| D.1.3. MSSM Branching Fraction Calculations . . . . . | 233        |
| D.1.4. SM Cross-Section Calculations . . . . .        | 233        |
| D.1.5. MSSM Cross-Section Calculations . . . . .      | 235        |
| D.2. Acceptances and Efficiencies . . . . .           | 236        |
| D.3. Statistical Methods . . . . .                    | 240        |
| D.3.1. Asimov Dataset . . . . .                       | 240        |
| D.3.2. Marginalisation . . . . .                      | 243        |

# Abstract

Spin correlations for  $\tau$  lepton decays are included in the PYTHIA 8 event generation software with a framework which can be expanded to include the decays of particles other than the  $\tau$  lepton. The spin correlations for the decays of  $\tau$  leptons produced from electroweak and Higgs bosons are calculated. Decays of the  $\tau$  lepton using sophisticated resonance models are included in PYTHIA 8 for all channels with experimentally observed branching fractions greater than 0.04%. The mass distributions for the decay products of these channels calculated with PYTHIA 8 are validated against the equivalent distributions from the HERWIG++ and TAUOLA event generators. The technical implementation of the  $\tau$  lepton spin correlations and decays in PYTHIA 8 is described.

A measurement of the inclusive  $Z \rightarrow \tau\tau$  cross-section using  $1.0 \text{ fb}^{-1}$  of data from  $pp$  collisions at  $\sqrt{s} = 7 \text{ TeV}$  collected with the LHCb detector is presented. Reconstructed final states containing two muons, a muon and an electron, a muon and a charged hadron, or an electron and a charged hadron are selected as  $Z \rightarrow \tau\tau$  candidates. The cross-section for  $Z$  bosons with a mass between 60 and 120 GeV decaying into  $\tau$  leptons with pseudo-rapidities between 2.0 and 4.5 and transverse momenta greater than 20 GeV is measured to be  $72.3 \pm 3.5 \pm 2.9 \pm 2.5 \text{ pb}$ . The first uncertainty is statistical, the second uncertainty is systematic, and the third is due to the integrated luminosity uncertainty. The  $Z \rightarrow \tau\tau$  to  $Z \rightarrow \mu\mu$  cross-section ratio is found to be  $0.94 \pm 0.09$  and the  $Z \rightarrow \tau\tau$  to  $Z \rightarrow ee$  cross-section ratio is found to be  $0.95 \pm 0.07$ . The uncertainty on these ratios is the combined statistical, systematic, and luminosity uncertainties.

Limits on the production of neutral Higgs bosons decaying into  $\tau$  lepton pairs with pseudo-rapidities between 2.0 and 4.5 are set at a 95% confidence level using the same LHCb dataset. A model independent upper limit on the production of neutral Higgs bosons decaying into  $\tau$  leptons is set and ranges between 8.6 pb for a Higgs boson mass of 90 GeV to 0.7 pb for a Higgs boson mass of 250 GeV. This limit is compared to the expected standard model cross-section. An upper limit on  $\tan\beta$  in the  $m_{A^0}$  and  $\tan\beta$  plane is set for the  $m_{h^0}^{\text{max}}$  scenario of the minimal supersymmetric model and varies from 34 for a  $\mathcal{CP}$ -odd Higgs boson mass of 90 GeV to 70 for a  $\mathcal{CP}$ -odd Higgs boson mass of 140 GeV.

# Authorship

I undertook the work presented in this thesis as a member of the LHCb collaboration at CERN, sharing responsibility with the rest of the collaboration for the collection and integrity of the data used in this thesis. The analysis of Chap. 5 was performed independently by me and then combined with that of another University College Dublin student [1] in order to produce a paper [2] whose results I have shown at conference [3]. The analysis of Chap. 6 is my own and extends the results of Chap. 5 to a search for the Higgs boson. I wrote the paper [4] and presented the results at conference [5]. The theoretical work in Chap. 3 was undertaken at the University of Lund, under the supervision of Prof. Torbjörn Sjöstrand, and was presented at the *12th International Workshop on Tau Physics* [6] with proceedings to appear in Ref. [7].

# Acknowledgements

This thesis would not have been possible without the support from a set of extraordinary people.

I would first like to acknowledge my supervisor, Ronan McNulty. His scientific integrity and rigour are unparalleled and his work speaks volumes, but his dedication to education, whether of his PhD students, undergraduates, or the general public, is uncompromising. He allowed me free reign with my ideas, but always made sure I understood the practicalities of the situation as well. He supported me in every step of my PhD, even if this meant sending me to Sweden for a semester.

My time in Sweden was an incredible opportunity which I owe entirely to Torbjörn Sjöstrand, my supervisor away from home. Not only is he an outstanding physicist, he is also one of the kindest people I have had the pleasure of meeting. Despite his busy schedule of teaching, theoretical research, and developing PYTHIA, Torbjörn took the time to make me feel at home in Lund. I owe a debt of gratitude to Torbjörn, MCNet, and everyone in Lund. Thank you for the experience.

My PhD would not have been possible without funding from the UCD physics department, Science Foundation Ireland, and MCNet through Marie Curie grant MRTN-CT-2006-035606. I sincerely hope that these funding sources will be able to continue to support particle physics research in the future, especially in Ireland.

Joining a collaboration, especially one as large as LHCb is never easy, but I had the support of some amazing colleagues in the electroweak, exotica, and Monte Carlo groups. I am especially indebted to Tara Shears, Roger Barlow, and Gloria Corti.

The UCD particle physics group also provided me with critical support over my four years at UCD. Thank you Steve, Simone, James, Dermot, Ronan (Wallace), Wenchao, Zoltan, Francesco, Shane, and Sara. I would like to especially thank Simone Bifani who always had the answer I needed, and gently notified me when the cluster was not working. I cannot thank Steve Farry enough. His patience in dealing with me is nearly unrivalled (except for my wife), and despite his attempts to fool people with his knowledge of football, he is a particle physicist at heart. He is a true scholar and a gentleman.

I would like to also thank everyone else in the UCD physics department who has helped me through the years. Thank you Marian, Bairbre, and John for making the physics department not just a loose affiliation of students and teachers but a real community. Thank you Pádraig and Lorraine for guiding the school over the years and supporting my research, and thank you Peter for trusting me to tutor your classes.

To all my friends at UCD over the years, thank you. The karate club kept me sane and fit, and was my home away from home. There is nothing like some light sparring to take your mind



off particle physics. Thanks to the CASL and Settlers of Catan crews, my Thursday evenings were always enjoyable. I also am indebted to Dominic's group for letting me drop by and chat.

As for my housemates, past and present, I could not ask for better. Majella, thank you for the wine, food, and stories. I always I could come home looking forward to a (usually) good story and an interesting conversation. Noel and Eibhlin, thank you for the hikes, dives, and barbeques; they shall continue!

To all my friends I have not yet mentioned, thanks for helping me become the person I am today. I would like to especially thank John Wuestneck, Andrew Hulke, and the Core: Matt, Mary, Sarah, and Dan. Everyone who made it out to my and Éadaoin's wedding, thank you. To all my Irish friends, thank you for welcoming me with open arms. Of course I cannot neglect  $Z\Psi$  and especially the  $AG$ s,  $\tau\kappa\phi$ . Coblenz, thank you for the statistics discussions, they were very illuminating, and Akil, thank you for understanding why the eagles could not just fly into Mordor.

Of course, I would not have reached this point without incredible teachers over the years. I would especially like to thank Markus for sending me off to Ireland, Tim Corcoran for teaching me to love science, and John Rubel for helping me truly understand the scientific method.

Finally, I would like to thank my family immediate and extended. Mom, Dad, Jen, and Nathan, I would be nothing without you. Karen and Adam, thank you for joining the Ilten family, I cherish your love and support. Zoe and Henry, thanks for remembering who crazy uncle Phil is! Peter and Caitriona, thank you for unconditionally accepting me into your family. I am proud to be your son-in-law. Dónal, Andrew, Deirdre, and Dónal, thank you for all the good times, past, present and future. Éadaoin, there are so many things I should thank you for that I will just thank you for being my better half.

Thank you.

*To Éadaoin Ilten, my wife and the love of my life.*

# 1. Introduction

The natural world is complex, and humankind attempts to understand this complexity through the search for the underlying laws by which nature is governed. This search takes many forms, but at the forefront is particle physics, which endeavours to describe the mechanisms whereby the fundamental constituents of nature interact. The predictive power of particle physics spans from the early formation of the universe to the structure of the proton, yet remains incomplete.

The theoretical framework for the standard model (SM) of particle physics is relativistic quantum field theory where fundamental particles, thought to be the indivisible constituents of matter, are represented as the quanta of relativistic fields. The quantum nature of the SM dictates that its predictions are not certainties but rather probabilities: the probabilities for particles to interact through collisions or the probabilities for particles to decay. Many of these probabilities can be directly calculated with the SM to produce theoretical predictions which can be confirmed or rejected with experiment. A review of the SM and how these calculations are made is provided in Chap. 2 of this thesis.

Within the SM the interactions of the fundamental particles are through the electromagnetic, weak, and strong forces. These forces are carried through fundamental particles which are labelled bosons. By the symmetry of the theory, these bosons are expected to be massless. However, the two carriers of the weak force, the  $W$  and  $Z$  bosons, are massive. To rectify this in the SM, an additional field, the Higgs field, is introduced. This field can be used not only to generate the masses of the  $W$  and  $Z$  bosons, but also the masses for all remaining fundamental particles with non-zero mass. The Higgs field also has an associated particle, the Higgs boson, with a mass not fixed by theory and whose interaction strength with other particles is proportional to their mass.

A particle with a mass near 125 GeV has been discovered [8, 9] which exhibits many of the properties of the expected Higgs boson from the SM. To verify this particle is indeed consistent with the SM Higgs boson, its decay probabilities must be fully measured. An SM Higgs boson with a mass of 125 GeV is expected to decay into a pair of  $\tau$  leptons in approximately 6% of all its decays. The  $\tau$  lepton is the heaviest of the charged leptons, fundamental particles which interact through only the electromagnetic and weak forces, and can decay into a large variety of complex final states that can be experimentally detected. Consequently, to measure the probability of the Higgs boson decaying into  $\tau$  lepton pairs, the decays of the  $\tau$  lepton must first be theoretically understood.

In Chap. 3, all  $\tau$  lepton decays with a probability greater than 0.04% are implemented using a variety of theoretical models in the open-source software PYTHIA 8 [10, 11, 12], which performs theoretical calculations by simulating events where particles interact and decay. The type of

particle producing the  $\tau$  lepton influences its intrinsic spin. This spin in turn influences the kinematics of the  $\tau$  lepton decay products. To ensure the kinematics of the  $\tau$  lepton decays are properly modelled, full spin correlations are also included in the decay models of the  $\tau$  lepton in Chap. 3.

The probabilities of particle interactions and decays are experimentally measured by using accelerators where particles are collided together at high energies within particle detectors. The detectors measure the passage of particles produced from the collision, and the output from the detector is processed using specialised software which reconstructs the particles from the collision. The reconstructed particles can then be used to determine the interactions and decays occurring within the collision and measure the probabilities predicted by the SM.

The Large Hadron Collider (LHC) is a particle accelerator which collides two protons head-on, each with an energy of 3.5 TeV. The Large Hadron Collider Beauty detector (LHCb) is built around one of the four LHC collision points and measures the production of particles along the forward direction of the beam. The LHCb detector is designed to detect  $B$ -mesons, composite particles whose decays might help explain the observed asymmetry between matter and anti-matter in the universe. In Chap. 4 the LHC and LHCb are described, as well as the techniques used to reconstruct particles passing through the LHCb detector.

The detector characteristics which allow LHCb to identify  $B$ -mesons are also well suited for the identification and reconstruction of  $\tau$  lepton decays. Consequently, LHCb can be used to search for the production of Higgs bosons decaying into  $\tau$  lepton pairs. However, these Higgs boson events are expected to be rare, and cannot be easily separated from events where a  $\tau$  lepton pair is produced from a  $Z$  boson decay. In Chap. 5 the cross-section, or probability per particle flux and time, is measured for the production of  $Z$  bosons which decay into  $\tau$  lepton pairs within LHCb. This cross-section can be used to refine current knowledge of the proton structure. Additionally, the  $Z$  boson is expected to decay with equal probability into the three types of charged leptons: electrons, muons, and  $\tau$  leptons. This prediction is tested by comparing the  $Z \rightarrow \tau\tau$  cross-section to the cross-sections of  $Z$  bosons decaying into muon and electron pairs.

An excess in the  $Z \rightarrow \tau\tau$  cross-section might indicate the presence of the Higgs boson or some other new physics contaminating the number of observed events of Chap. 5. In Chap. 6 a statistical analysis is performed to determine upper limits on the cross-section for the production of Higgs bosons decaying into  $\tau$  leptons within LHCb that is consistent with the number of observed events. This limit is compared to the cross-section expected from the SM, as well as from the alternative minimal supersymmetric model (MSSM). A conclusion summarising all the results from Chap. 3, Chap. 5, and Chap. 6 of this thesis is provided in Chap. 7.

## 2. Theory

A review is given in this chapter which provides the necessary theoretical framework for this thesis. The chapter is split into two sections, Sects. 2.1 and 2.2. In Sect. 2.1, an overview of the standard model of particle physics is given. This includes an introduction to the perturbative methods used to calculate experimental observables, the underlying Lagrangian densities used in these perturbative calculations, and the experimental observables themselves. Additionally, an outline of alternatives and extensions to the standard model is given. The results from this section are used in Chap. 3 to model  $\tau$  lepton decays, in Chap. 5 to calculate the  $pp \rightarrow Z \rightarrow \tau\tau$  cross-section, and in Chap. 6 to place limits on Higgs boson production. In Sect. 2.2 numerical analysis techniques used to calculate the experimental observables introduced in Sect. 2.1 are presented. These include the methods necessary for the modelling of  $\tau$  lepton decays in Chap. 3, as well as the simulation of background and signal events for Chaps. 5 and 6.

### 2.1. Standard Model

The standard model (SM) of particle physics [13, 14] describes the interactions between all the experimentally observed particles of Fig. 2.1 through the electromagnetic, weak, and strong forces, but not gravity. In Fig. 2.1 the symbol, electromagnetic charge quantum number, spin quantum number, and mass for each particle is given. The particles are grouped by their spin quantum numbers into fermions, half-integer spin particles, and bosons, integer spin particles. The fermions are the constituents of matter and are further grouped into quarks, particles which interact through all three forces, and leptons, particles which interact through only the electromagnetic and weak forces. Both quarks and leptons have a spin quantum number of  $1/2$ .

Each quark has a colour charge quantum number of either red, blue, or green. The up ( $u$ ), charm ( $c$ ), and top quarks ( $t$ ) all have an electromagnetic charge quantum number of  $+2/3$  while the down ( $d$ ), strange ( $s$ ), and bottom ( $b$ ) quarks have an electromagnetic charge quantum number of  $-1/3$ . Each quark type also has a corresponding anti-quark type which carries an anti-colour of anti-red, anti-blue, or anti-green, and the opposite sign electromagnetic charge. The quarks are grouped into three generations of up/down, charm/strange, and top/bottom. While a quark can interact with another quark outside its generation, this type of behaviour is suppressed in the SM by the Cabibbo-Kobayashi-Maskawa (CKM) matrix which relates the mass and flavour eigenstates of the quarks. The quarks listed in Fig. 2.1 are mass eigenstates with well defined masses, but because all the quarks except the massive top quark have only been observed in bound states, their masses have not been directly measured experimentally.

The leptons are grouped into charged leptons which have an electromagnetic charge quantum

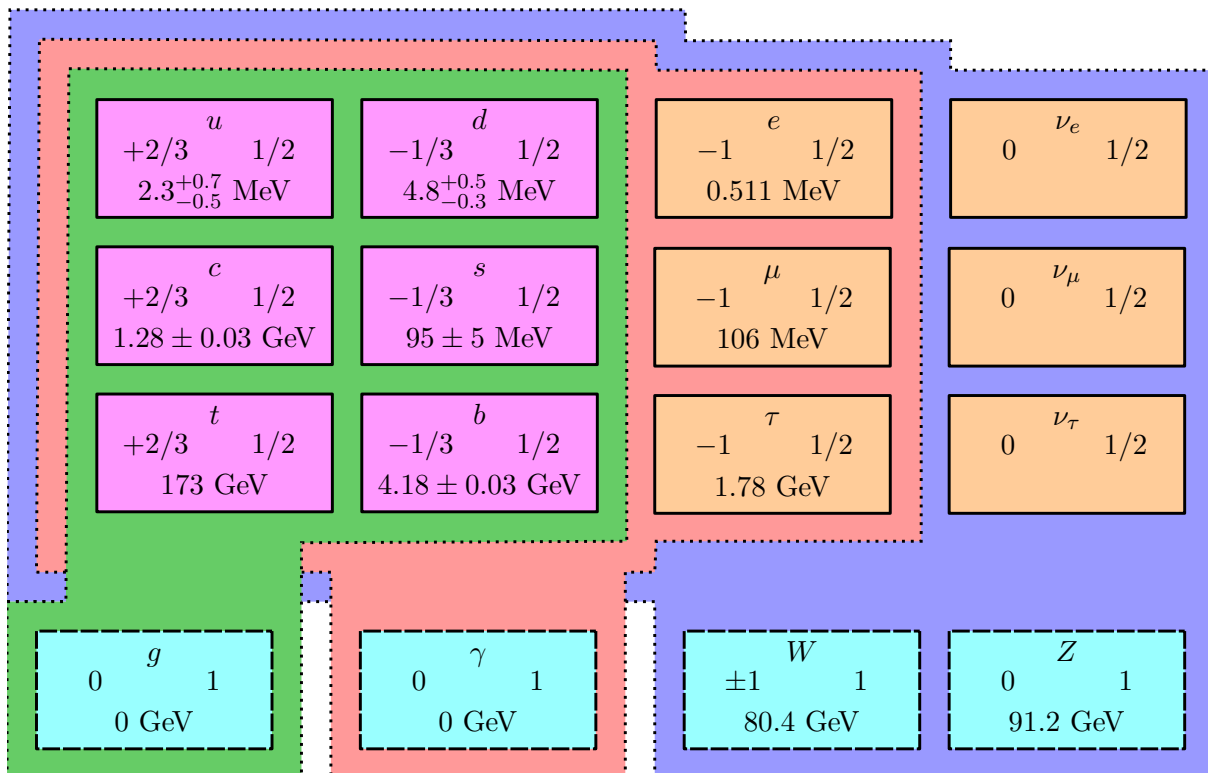


**Figure 2.1.:** The SM particles: the spin-1/2 fermions (solid boxes) divided into quarks (magenta) and leptons (orange), and the spin-1 gauge bosons (dashes and cyan). The spin-0 Higgs boson has not been included. The fermions are within dotted lines representing their interactions with the strong (green), electromagnetic (red), and weak (blue) forces, with the force mediating bosons included in the grouping. The top line for each particle is its symbol, the left middle its electromagnetic charge, the right middle its spin, and the bottom its mass. The masses are reported up to an uncertainty on three significant digits and are taken from Ref. [15]. No masses are given for the neutrinos as they are not mass eigenstates.

number of  $-1$ , and neutrinos with an electromagnetic charge quantum number of  $0$ . There are three flavours of charged lepton, the electron ( $e$ ), the muon ( $\mu$ ), and the  $\tau$  lepton ( $\tau$ ), each grouped with a neutrino of the same flavour, the electron ( $\nu_e$ ), muon ( $\nu_\mu$ ), and  $\tau$  lepton ( $\nu_\tau$ ) neutrinos. Each charged lepton has an anti-lepton partner with anti-flavour and an electromagnetic charge of  $+1$ , while each neutrino has an anti-neutrino partner with anti-flavour. Within the SM, lepton flavour is approximately conserved with the exception of oscillations of the neutrinos between their flavour eigenstates. The charged leptons of Fig. 2.1 are mass eigenstates with well defined masses, while the neutrinos are flavour eigenstates. The neutrinos are also known to have mass eigenstates  $\nu_1$ ,  $\nu_2$ , and  $\nu_3$ , but only the mass differences between these states have been measured.

In the SM there are four gauge bosons with a spin quantum number of  $1$ . The gluon ( $g$ ) is the massless mediator of the strong force and carries one of eight colour/anti-colour charge quantum number combinations. The photon ( $\gamma$ ) is the massless mediator of the electromagnetic force, while the  $W$  and  $Z$  bosons are the massive mediators of the weak force. The gluons only interact with fermions with colour charge, photons only interact with fermions with non-zero electromagnetic charge, and the weak bosons interact with all the fundamental fermions. The

gauge bosons can also interact amongst themselves, with the details of these interactions given in Sect. 2.1.2. The  $W$  and  $Z$  bosons acquire their masses through the Higgs mechanism which requires the presence of at least one spin-0 boson, the Higgs boson ( $H$ ). Recently, a Higgs-like boson has been observed [8, 9], but further measurements to fully understand its nature are needed.

The SM requires 18 experimentally measured parameters, excluding the parameters for the neutrino sector which are not yet sufficiently understood. One possible representation for these 18 parameters is the 9 masses of the fundamental fermions with the neutrino masses excluded, 3 angles and 1 phase describing the mixing of the quark generations with the CKM matrix, 2 couplings and 1 mixing angle describing the strengths of the three forces, and 1 vacuum expectation value and 1 mass describing the Higgs sector. A comprehensive review of most experimental measurements to date of these parameters, as well as world averages and theoretical reviews can be found in Ref. [15].

The mathematical framework describing the interactions between the fundamental particles of the SM is a relativistic quantum field theory (QFT), where particles are associated with continuous physical fields that are invariant under the Poincaré group. In Sect. 2.1.1 the scattering matrix, which is used to calculate observables of the SM, is introduced. The Lagrangian densities used to construct scattering matrices for the SM are then provided in Sect. 2.1.2, as well as the underlying gauge symmetries used to build them. In Sect. 2.1.3 the experimental observables that can be calculated from the scattering matrix are presented, as well as issues arising from these calculations. Finally, in Sect. 2.1.4, alternative models and extensions to the SM are explored. All these sections are intended to provide a broad overview of how QFT is used with the SM to produce observable predictions, and is not intended as a rigorous treatment of QFT; indeed most of the subtleties behind QFT are omitted from these sections. However, many excellent QFT textbooks exist, including Refs. [16], [17], [18], and [19] which are used as references for these sections.

### 2.1.1. Scattering Matrix

In a typical high energy particle physics experiment a set of initial particles is collided and the momentum and energy of the resultant final particles are then measured. The experiment is repeated a large number of times and the probability of observing a specific final state of particles, given an initial state, is measured. The initial particles are separated by a large length-scale, as are the final particles, and only during the collision do the length-scales between the particles become sufficiently small for the particles to interact. Consequently, both the initial and final particles are considered as free states and so using the standard Dirac notation of Ref. [20] the probability of observing a final state  $|B\rangle$  after the interaction of an initial state  $|A\rangle$  is,

$$\left| {}_{+\infty}\langle B | A \rangle_{-\infty} \right|^2 = \left| {}_{+\infty}\langle b_1 \dots b_m | a_1 \dots a_n \rangle_{-\infty} \right|^2 \quad (2.1)$$

where  $|A\rangle$  and  $\langle B|$  consist of  $n$  fully specified free particles  $a_1$  through  $a_n$  and  $m$  free particles  $b_1$  through  $b_m$ , respectively. Here the initial state is at a time in the far past,  $t = -\infty$ , while the

final state is at a time in the far future,  $t = +\infty$ , as the time-scale of the particle interactions is very small.

To calculate Eq. 2.1 either  $|A\rangle$  must be evolved to  $t = +\infty$  or  $\langle B|$  to  $t = -\infty$ . The scattering-matrix  $S$  is defined such that,

$$|\Psi\rangle_{+\infty} = S^\dagger |\Psi\rangle_{-\infty}, \quad S^\dagger S = 1 \quad (2.2)$$

for the state  $|\Psi\rangle_t$  at time  $t$  and so the probability of Eq. 2.1 becomes,

$$\left| {}_{+\infty}\langle B | A \rangle_{-\infty} \right|^2 = \left| {}_{-\infty}\langle B | S | A \rangle_{-\infty} \right|^2 \quad (2.3)$$

where the final state is now also at  $t = -\infty$ . The scattering-matrix can be divided into a non-interacting and interacting term such that the probability amplitude can be written as,

$$\begin{aligned} {}_{-\infty}\langle B | S | A \rangle_{-\infty} &= {}_{-\infty}\langle B | A \rangle_{-\infty} + i(2\pi)^4 \delta \left( \sum_i^n q_{a_i} - \sum_j^m q_{b_j} \right) \\ &\mathcal{M}_{A \rightarrow B} \prod_i^n \frac{1}{\sqrt{2E_{a_i} \mathcal{V}}} \prod_j^m \frac{1}{\sqrt{2E_{b_j} \mathcal{V}}} \end{aligned} \quad (2.4)$$

where the first term is one if the final state is the same as the initial, and zero otherwise, and the second term describes the interactions between the initial particles. The delta-function in the second term imposes conservation of energy and momenta,  $q$ , between the initial and final particles, while the matrix element  $\mathcal{M}$  provides the interactions between the initial particles for the production of the given final state. The normalisation is given by the two products over  $i$  and  $j$ , where  $\mathcal{V}$  is the unit volume for the particles with the particle energy  $E$  included, as the term  $\mathcal{V}E$  is Lorentz invariant.

In the following two sections, the time-dependent perturbation and functional integration methods for calculating Eq. 2.1 will be outlined. This is followed by the formulation of the Feynman rules used to build  $\mathcal{M}$ , which can be derived from either the time-dependent perturbation method or functional integration method.

### Time-dependent Perturbation Theory

From the definition of Eq. 2.2 the scattering-matrix can be interpreted as a time-evolution operator  $U(t, t_0)$  where  $t_0 = -\infty$  and  $t = +\infty$  or  $U(+\infty, -\infty)$ . Consequently, the calculation of the time-evolution operator will yield the scattering-matrix. The Schrödinger picture wavefunction  $|\Psi_S\rangle_{t_0}$  for a state at time  $t_0$  can be evolved to an arbitrary time  $t$  by,

$$|\Psi_S\rangle_t = U_S(t, t_0) |\Psi_S\rangle_{t_0} \quad (2.5)$$

where  $U_S(t, t_0)$  is the Schrödinger picture time-evolution operator with the conditions  $U_S(t_0, t_0) = 1$  and  $U^\dagger(t, t_0)U(t, t_0) = 1$ . Given a time-dependent Hamiltonian in the Schrödinger picture  $H_S(t)$ ,



the Schrödinger equation of Ref. [21] applied to  $|\Psi_S\rangle_t$  is,

$$i\frac{\partial U_S(t, t_0)}{\partial t} |\Psi_S\rangle_{t_0} = H_S(t)U_S(t, t_0) |\Psi_S\rangle_{t_0} \quad (2.6)$$

but since  $|\Psi_S\rangle_{t_0}$  is constant then  $U_S(t, t_0)$  must fulfil,

$$\frac{\partial U_S(t, t_0)}{\partial t} = -iH_S(t)U_S(t, t_0) \quad (2.7)$$

which, when  $H_S$  is time-independent, results in the solution,

$$U_S(t, t_0) = e^{-iH_S(t-t_0)} \quad (2.8)$$

where  $H_S(t - t_0)$  is the product of  $H_S$  and  $t - t_0$ , and not  $H_S$  evaluated at time  $t - t_0$ .

When  $H_S(t)$  can be split into,

$$H_S(t) = H_{S0} + H_{S1}(t) \quad (2.9)$$

where  $H_{S0}$  is a Schrödinger picture time-independent Hamiltonian without interaction terms and  $H_{S1}(t)$  is a Schrödinger picture time-dependent Hamiltonian with interaction terms, working in the Dirac picture rather than the Schrödinger picture is oftentimes more convenient. In the Dirac picture, both the states and observables are time-dependent, unlike the Schrödinger picture where only the states are time-dependent. The transformations,

$$|\Psi_D\rangle_t = e^{iH_{S0}t} |\Psi_S\rangle_t, \quad O_D(t) = e^{iH_{S0}t} O_S(t) e^{-iH_{S0}t} \quad (2.10)$$

take the state  $|\Psi_S\rangle_t$  and the operator  $O_S(t)$  from the Schrödinger picture to the Dirac picture. Using Eq. 2.5 once, and the transformation of Eq. 2.10 twice, the state  $|\Psi_D\rangle_t$  can be written as,

$$|\Psi_D\rangle_t = e^{iH_{S0}t} U_S(t, t_0) |\Psi_S\rangle_{t_0} = e^{iH_{S0}t} U_S(t, t_0) e^{-iH_{S0}t_0} |\Psi_D\rangle_{t_0} \quad (2.11)$$

and so,

$$U_D(t, t_0) = e^{iH_{S0}t} U_S(t, t_0) e^{-iH_{S0}t_0} \quad (2.12)$$

is the Dirac time-evolution operator which takes the state  $|\Psi_D\rangle_{t_0}$  to the state  $|\Psi_D\rangle_t$ .

The derivative of the Dirac time-evolution operator is,

$$\begin{aligned} \frac{\partial U_D(t, t_0)}{\partial t} &= e^{iH_{S0}t} \left( \frac{\partial U_S(t, t_0)}{\partial t} \right) e^{-iH_{S0}t_0} + iH_{S0} e^{iH_{S0}t} U_S(t, t_0) e^{-iH_{S0}t_0} \\ &= -i \left( e^{iH_{S0}t} H_{S1}(t) e^{-iH_{S0}t} \right) \left( e^{iH_{S0}t} U_S(t, t_0) e^{-iH_{S0}t_0} \right) \\ &= -iH_{D1}(t) U_D(t, t_0) \end{aligned} \quad (2.13)$$

where Eqs. 2.7 and 2.9 are used in the second line and Eqs. 2.10, and 2.12 in the third. Here,  $H_{D1}(t)$  is the interaction Hamiltonian in the Dirac picture. Equation 2.13 was first proposed in a covariant formulation of quantum electrodynamics by Tomonaga in Ref. [22] and Schwinger in Ref. [23].

The power series method for solving differential equations of Ref. [24] can be used to solve Eq. 2.13 for  $U_D(t, t_0)$ ,

$$U_D(t, t_0) = 1 + \sum_n^{\infty} \left( (-i)^n \int_{t_0}^t \dots \int_{t_0}^{t_{n-1}} H_{D1}(t'_1) \dots H_{D1}(t'_n) dt'_n \dots dt'_1 \right) \quad (2.14)$$

where the power series has been expanded about the Dirac picture interaction Hamiltonian  $H_{D1}(t)$ , beginning with  $n = 1$ . The scattering-matrix in the Dirac picture can then be found by setting  $t_0 = -\infty$  and  $t = +\infty$ ,

$$S_D = 1 + \sum_n^{\infty} \left( \frac{(-i)^n}{n!} \int_{-\infty}^{+\infty} \dots \int_{-\infty}^{+\infty} T \{ H_{D1}(t_1) \dots H_{D1}(t_n) \} dt_n \dots dt_1 \right) \quad (2.15)$$

where the integration has been simplified by applying the time-ordering operator  $T$  to the operators  $H_{D1}(t)$  such that  $t_n > t_{n+1}$ . This expansion is the Dyson series of Ref. [25] which can be used in conjunction with the contractions of Wick's theorem from Ref. [26] to calculate the probability of Eq. 2.1 in the Dirac picture.

### Functional Integration

An alternative, yet equivalent method to using the time-perturbation derived scattering-matrix of Eq. 2.15 to determine the probability of Eq. 2.1, is the method of functional integration first introduced by Dirac in Ref. [27] and more fully realised by Feynman in Ref. [28]. The method of functional integration provides several advantages to the time-perturbation method: a clear graphical interpretation via Feynman diagrams, a general method to determine Feynman rules for complex interactions, a non-perturbative calculation of Eq. 2.1, and a manifestly Poincaré invariant formalism. However, the mathematical derivation of the functional integration formalism is more involved than time-perturbation theory, and so only a short overview is given here.

In the Schrödinger picture the probability of Eq. 2.1 can be calculated using the probability amplitude,

$${}_{t_B} \langle B_S | U_S(t_B, t_A) | A_S \rangle_{t_A} \quad (2.16)$$

where  $U_S(t, t_0)$  is the Schrödinger picture time-evolution operator given by the solution of Eq. 2.7. The time between  $t_A$  and  $t_B$  can be broken down into  $n + 1$  elements of time  $\varepsilon$ , and given a complete set of  $n$  coordinate-space states  $X_i$ ,

$$\int |X_i\rangle_t {}_t \langle X_i| dX_i = 1 \quad (2.17)$$

such that the probability amplitude of Eq. 2.18 can be written as,

$${}_{t_B}\langle B_S | U_S(t_B, t_A) | A_S \rangle_{t_A} = \int \dots \int {}_{t_B}\langle B_S | U_S(t_B, t_B - \varepsilon) | X_n \rangle_{t_B - \varepsilon} \dots \int {}_{t_A + \varepsilon}\langle X_1 | U_S(t_A + \varepsilon, t_A) | A_S \rangle_{t_A} dX_1 \dots dX_n \quad (2.18)$$

which can be thought of as the probability amplitude of  $|A_S\rangle$  transitioning through the intermediate states  $|X_i\rangle$  to the state  $\langle B_S|$ . In Ref. [28] Feynman showed that this can be written as,

$${}_{t_B}\langle B_S | U_S(t_B, t_A) | A_S \rangle_{t_A} = \int \dots \int e^{\int_{t_A}^{t_B} \int \mathcal{L} d\vec{x} dt} \mathcal{D}X_1 \dots \mathcal{D}X_n \quad (2.19)$$

where  $\mathcal{D}X_i$  indicates the functional integral over the path  $X_i$ . Here  $\vec{x}$  is a space three-vector and  $\mathcal{L}$  is the Lagrangian density, which following the convention of Ref. [18], will be labelled as just the Lagrangian. The result of Eq. 2.19 can be interpreted as  $n$  paths contributing equally to the probability amplitude of Eq. 2.18, but each with a phase given by the classical action for that path.

### Feynman Rules

The paths of the functional integration method can be graphically depicted by Feynman diagrams where each diagram represents a component matrix element of the total matrix element  $\mathcal{M}$  introduced in Eq. 2.4. The total matrix element is then the sum of the component matrix elements. Each component matrix element also corresponds to a term from the Dyson series of Eq. 2.15 after applying Wick contractions. Example Feynman diagrams are given in Fig. 2.2 where each line represents a fully specified particle, which for the SM corresponds to a given momentum and energy, electromagnetic charge, colour charge, and spin. The diagrams proceed from left to right, with the time axis given along the  $x$ -axis and the spacial axis along the  $y$ -axis. Consequently, the leftmost lines correspond to the initial state particles, and all remaining lines reaching the edge of the diagram are final state particles. Every Feynman diagram consists of the following three components which are derived from the Lagrangian describing the free particles and their interactions.

vertices: The junction of  $n$  lines corresponds to an interaction between the  $n$  particles represented by the lines. Each vertex is given by an interaction term from the Lagrangian, where the fields contained in the term dictate the lines of the vertex and the remainder of the term yields the vertex factor. The vertex factors are translated into momentum-space from the Lagrangian, where each  $i\partial_\mu$  is replaced with a  $p_\mu$ . The incoming electromagnetic charge, colour charge, energy, and momentum are conserved in the corresponding outgoing quantities of the vertex.

propagators: All internal lines connecting two vertices are propagators, or virtual particles through which the scattering process proceeds. Each propagator is given by the product of  $i$  and the inverse of the free field equation without the field term for that propagator

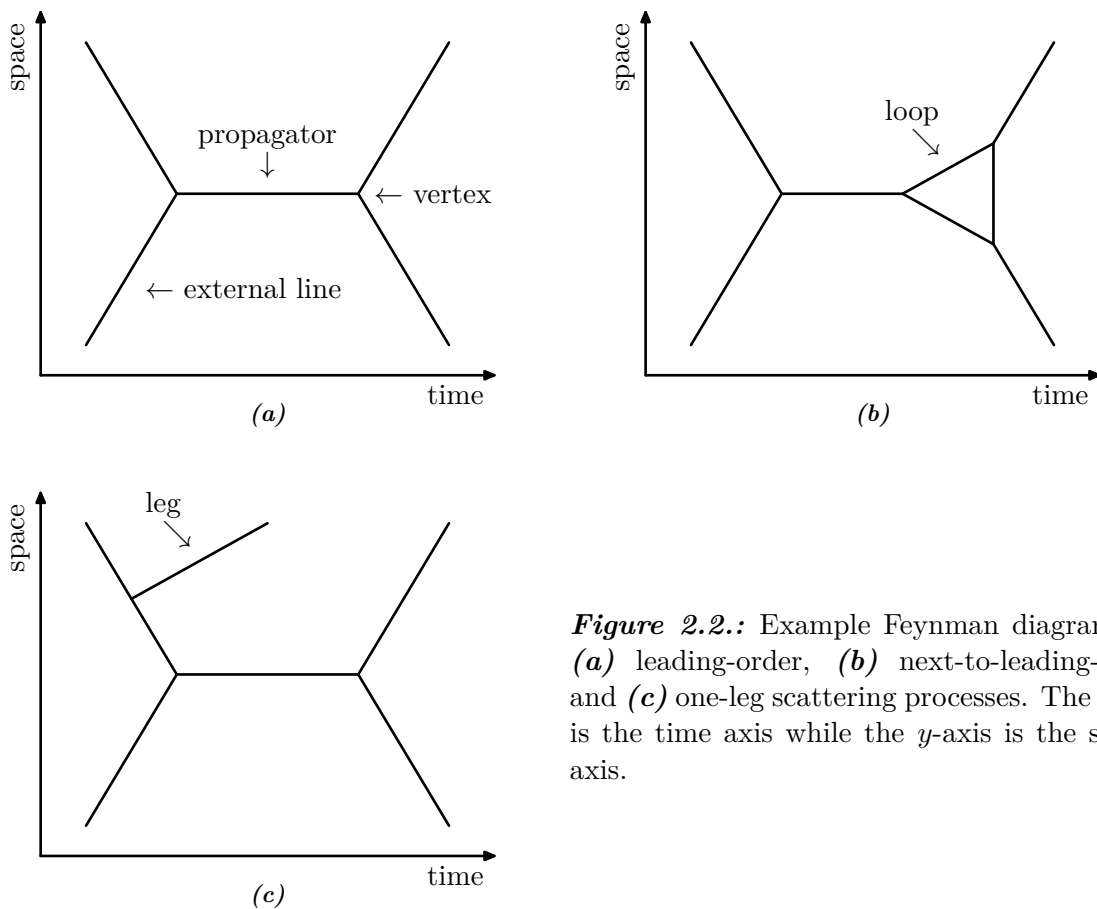


**Figure 2.2.:** Example Feynman diagrams for (a) leading-order, (b) next-to-leading-order, and (c) one-leg scattering processes. The  $x$ -axis is the time axis while the  $y$ -axis is the spacial axis.

type, derived from the corresponding free Lagrangian. Again, the propagator is translated into momentum-space.

external lines: All external lines correspond to real initial and final state particles that can be observed. These lines represent the scalar or vector pre-factors to the plane-wave solutions of the free field equation for the field of the corresponding particle type.

The component matrix element for a Feynman diagram is then the product of the ordered external lines, internal lines, and vertex factors. In the diagram of Fig. 2.2(a), a two-to-two scattering process occurs, for which a minimum of two vertices is necessary. Any diagrams with the minimum number of vertices are the leading-order terms of the total matrix element, while diagrams containing the next-to-minimum number of vertices, such as the diagram of Fig. 2.2(b), are the next-to-leading order terms of the total matrix element. If an additional final state line is added to a diagram, like the two-to-three scattering process of Fig. 2.2(c), the diagram is typically categorised as a one-leg diagram. The  $n$ -leg terminology is used when explicitly calculating hard radiation from the initial or final state with the matrix element. Any diagram without internal loops, *i.e.* Figs. 2.2(a) and 2.2(c), are tree-level diagrams, while a diagram with  $n$  loops is an  $n$ -loop level diagram, like the one-loop level diagram of Fig. 2.2(b).

### 2.1.2. Lagrangians

In order to derive the Feynman rules introduced in Sect. 2.1.1 and calculate the matrix elements for a given theory, the Lagrangian must be known. Beginning with the Lagrangians for the free fields of the theory provides the rules for both the propagators and external lines. The Euler-Lagrange equation is given for a field  $\phi$  by,

$$\partial_\mu \left( \frac{\partial \mathcal{L}}{\partial (\partial_\mu \phi)} \right) - \frac{\partial \mathcal{L}}{\partial \phi} = 0 \quad (2.20)$$

and is applied to the free Lagrangians to determine the equations of motion for the free fields, which can then be translated to propagators. The solutions to the equations of motion produce the rules for the external lines. Within the SM, three fundamental particle types of spin-0, spin-1/2, and spin-1 have been observed, corresponding to scalar, spinor, and vector fields. Consequently, the free Lagrangians for these fields provide the propagators and external lines for the SM.

In this section, first the free Lagrangians for the SM particles are introduced, as well as their corresponding propagators and external line factors. A summary of these Feynman rules are provided in Table 2.1. Next, local gauge invariances of the free Lagrangian for fermions is imposed, producing the full SM Lagrangian,

$$\mathcal{L}_{\text{SM}} = \mathcal{L}_{\text{QCD}} + \mathcal{L}_{\text{EWK}} + \mathcal{L}_{\text{MHM}} \quad (2.21)$$

consisting of the quantum chromodynamics (QCD), electroweak (EWK), and minimal Higgs mechanism (MHM) Lagrangians. From these Lagrangians the vertex rules for the SM are provided.

#### Free Fields

The free Lagrangian for spin-0 fields is given by the Klein-Gordon equation,

$$\mathcal{L}_{\text{spin-0}} = \frac{1}{2} \left( \partial_\mu \phi \partial^\mu \phi - m^2 \phi^\dagger \phi \right) \quad (2.22)$$

where  $m$  is the mass of the particle corresponding to the scalar field  $\phi$ . Applying Eq. 2.20 results in the equation of motion,

$$\left( \partial_\mu \partial^\mu + m^2 \right) \phi = 0 \quad (2.23)$$

for scalar fields. Using the prescription of Sect. 2.1.1 the scalar propagator is,

$$\frac{i}{q^2 - m^2} \quad (2.24)$$

where  $q$  is the four-momentum of the particle. Since the solution to Eq. 2.23 is just a plane-wave, the external line for a scalar is 1.

The free Lagrangian for spin-1/2 fields can be found from the Dirac equation of Ref. [29],

$$\mathcal{L}_{\text{spin-1/2}} = i\bar{\psi}\gamma^\mu\partial_\mu\psi - m\bar{\psi}\psi \quad (2.25)$$

for a spinor field  $\psi$  and adjoint spinor field  $\bar{\psi}$ , where  $\gamma^\mu$  are the Dirac matrices. The equation of motion for the field is then

$$(i\gamma^\mu\partial_\mu - m)\psi = 0 \quad (2.26)$$

which produces

$$\frac{i}{\gamma^\mu q_\mu - m} \quad (2.27)$$

as the propagator for a spin-1/2 particle. The external lines for spin-1/2 particles are given by the spinors  $u(q, \lambda)$  for particles and the anti-spinors  $v(q, \lambda)$  for anti-particles, where  $\lambda$  is the helicity  $\pm 1$  and  $q$  is the momentum four-vector. For the purposes of calculating the helicity matrix elements necessary for Chap. 3, these spinors are defined using the conventions of Ref. [30].

In the Weyl basis the two vectors,

$$\kappa(q, \lambda) = \begin{cases} \frac{1}{2(\vec{q}^2 + |\vec{q}|q_z)} \begin{pmatrix} iq_y - q_x \\ |\vec{q}| + q_z \end{pmatrix} & \text{for } \lambda = +1, \begin{pmatrix} 0 \\ 1 \end{pmatrix} & \text{as } q_z \rightarrow -|\vec{q}| \\ \frac{1}{2(\vec{q}^2 + |\vec{q}|q_z)} \begin{pmatrix} |\vec{q}| + q_z \\ iq_y + q_x \end{pmatrix} & \text{for } \lambda = -1, \begin{pmatrix} -1 \\ 0 \end{pmatrix} & \text{as } q_z \rightarrow -|\vec{q}| \end{cases} \quad (2.28)$$

are eigenvectors to the helicity operator,

$$\frac{\sigma_j q^j}{|\vec{q}|} \kappa(q, \lambda) = \lambda \kappa(q, \lambda) \quad (2.29)$$

where  $\sigma_i$  are the Pauli matrices,

$$\sigma_0 = \begin{pmatrix} 1 & 0 \\ 0 & 1 \end{pmatrix}, \quad \sigma_1 = \begin{pmatrix} 0 & 1 \\ 1 & 0 \end{pmatrix}, \quad \sigma_2 = \begin{pmatrix} 0 & -i \\ i & 0 \end{pmatrix}, \quad \sigma_3 = \begin{pmatrix} 1 & 0 \\ 0 & -1 \end{pmatrix} \quad (2.30)$$

and the index  $j$  indicates the spatial components of  $q$ :  $x$ ,  $y$ , and  $z$ . The spinors and anti-spinors can then be written as,

$$u(q, \lambda) = \begin{pmatrix} \kappa(q, \lambda)\sqrt{E - \lambda|\vec{q}|} \\ \kappa(q, \lambda)\sqrt{E + \lambda|\vec{q}|} \end{pmatrix}, \quad v(q, \lambda) = \begin{pmatrix} -\lambda\kappa(q, -\lambda)\sqrt{E + \lambda|\vec{q}|} \\ \lambda\kappa(q, -\lambda)\sqrt{E - \lambda|\vec{q}|} \end{pmatrix} \quad (2.31)$$

where  $E$  is the energy component of  $q$ . These solutions of Eq. 2.26 provide the Feynman rules

**Table 2.1.:** A summary of the Feynman rules for the particles of the SM, excluding vertices but including the symbols used when drawing the Feynman diagrams.

|                    | propagator   | incoming line                        | outgoing line                        | equ. | symbols                              |
|--------------------|--|--------------------------------------|--------------------------------------|------|--------------------------------------|
| spin-0             | $\frac{i}{q^2-m^2}$  | 1                                    | 1                                    |      | ---- $H$                             |
| spin-1/2           | $\frac{i}{\gamma^\mu q_\mu - m}$                             | $u(q, \lambda), \bar{v}(q, \lambda)$ | $\bar{u}(q, \lambda), v(q, \lambda)$ | 2.31 | $\longrightarrow$ $f$                |
| spin-1 ( $m = 0$ ) | $\frac{-ig_{\mu\nu}}{q^2}$                                   | $\varepsilon(q, \lambda)$            | $\varepsilon^\dagger(q, \lambda)$    | 2.38 | $\sim$ $\gamma$<br>$\text{oooo}$ $g$ |
| spin-1 ( $m > 0$ ) | $\frac{-i(g_{\mu\nu} - \frac{q_\mu q_\nu}{m^2})}{q^2 - m^2}$ | $\varepsilon(q, \lambda)$            | $\varepsilon^\dagger(q, \lambda)$    | 2.38 | ---- $W/Z$                           |

for spin-1/2 external lines and require the Dirac matrices to be defined as,

$$\gamma^0 = \begin{pmatrix} 0 & 1 \\ 1 & 0 \end{pmatrix}, \quad \gamma^i = \begin{pmatrix} 0 & \sigma_i \\ -\sigma_i & 0 \end{pmatrix}, \quad \gamma^5 = \begin{pmatrix} -1 & 0 \\ 0 & 1 \end{pmatrix} \quad (2.32)$$

where the bar of a spinor or anti-spinor is given by  $\bar{u} = u^\dagger \gamma^0$  if  $u^\dagger$  is the Hermitian adjoint of  $u$ .

The free Lagrangian for spin-1 fields can be found from the Proca equation, resulting in,

$$\mathcal{L}_{\text{spin-1}} = (\partial^\mu \omega^\nu - \partial^\nu \omega^\mu) (\partial_\mu \omega_\nu - \partial_\nu \omega_\mu) - \frac{m^2}{2} \omega^\nu \omega_\nu \quad (2.33)$$

for a vector field  $\omega^\mu$ . Applying Eq. 2.20 yields the equation of motion,

$$\partial_\mu (\partial^\mu \omega^\nu - \partial^\nu \omega^\mu) - m^2 \omega^\nu = 0 \quad (2.34)$$

which provides the propagator,

$$\frac{-i}{q^2 - m^2} \left( g_{\mu\nu} - \frac{q_\mu q_\nu}{m^2} \right) \quad (2.35)$$

for massive spin-1 particles. If the mass term from Eq. 2.33 is removed, *i.e.* a massless spin-1 particle like the photon or gluon, and the Lorentz condition  $\partial_\mu \omega^\mu = 0$  is imposed, then the equation of motion becomes,

$$\partial^2 \omega^\nu = 0 \quad (2.36)$$

which yields the propagator,

$$\frac{-ig_{\mu\nu}}{q^2} \quad (2.37)$$

for massless spin-1 particles.

The external lines for spin-1 particles are given by the polarisation vectors  $\varepsilon^\mu$  which satisfy Eq. 2.34. Again, to calculate the helicity matrix elements necessary for Chap. 3 the conventions of Ref. [31] which are consistent with the conventions of Ref. [30] are used. The helicity polarisation vectors are defined as,

$$\varepsilon(q, \lambda) = \begin{cases} \lambda \begin{pmatrix} 0 \\ \frac{q_x q_z}{|\vec{q}| q_T} - \frac{i q_y}{q_T} \\ \frac{q_y q_z}{|\vec{q}| q_T} + \frac{i q_x}{q_T} \\ -\frac{q_T}{|\vec{q}|} \end{pmatrix} & \text{for } \lambda = \pm 1, \lambda \begin{pmatrix} 0 \\ q_z \\ 0 \\ 0 \end{pmatrix} \text{ as } q_T \rightarrow 0 \\ \frac{1}{m|\vec{q}|} \begin{pmatrix} \vec{q}^2 \\ E q_x \\ E q_y \\ E q_z \end{pmatrix} & \text{for } \lambda = 0 \text{ and } m > 0 \end{cases} \quad (2.38)$$

where there is no  $\lambda = 0$  polarisation state for massless spin-1 particles and  $q_T = \sqrt{q_x^2 + q_y^2}$ .

A summary of the Feynman rules derived from the free Lagrangians are given in Table 2.1 for the spin-0, spin-1/2, and spin-1 particles of the SM. The only spin-0 SM particle is the Higgs boson, while both leptons and quarks are the spin-1/2 SM particles, and photons, gluons,  $W$  bosons, and  $Z$  bosons are the SM spin-1 particles. Free Lagrangians for particles with spins not given in Table 2.1 can be built using the Bargmann-Wigner equations of Ref. [32], but are not currently necessary in the SM.

### Quantum Chromodynamics

A method for generating Lagrangians invariant under non-Abelian local gauge theory was first proposed in Ref. [33] by Yang and Mills, laying the groundwork for both QCD and unified electroweak theory. Yang-Mills theory was then applied to QCD in Ref. [34] requiring the free fields for quarks to be invariant under local  $SU(3)$  gauge transformations, leading to the conservation of three colour charge quantum numbers. Direct evidence for three colour charges has been observed by measuring the ratio of hadron production to muon pair-production in electron-positron collisions, which should be approximately 11/3 at off resonance centre-of-mass energies below the  $t$ -quark mass. Reference [35] provides this measurement made using the experiments on LEP. Further measurements testing the underlying group structure of QCD have also been made by LEP experiments and reported in Ref. [36], with results consistent with the SM and  $SU(3)$  theory. Because quarks of different colours with the same flavour are identical except for colour, the three quark colour fields can be written as a colour triplet,

$$q_f = \begin{pmatrix} q_{f_r} \\ q_{f_b} \\ q_{f_g} \end{pmatrix} \quad (2.39)$$



where  $f$  is one of the six flavours of the quark, and  $r$ ,  $b$ , and  $g$  are the colour charges. Substituting  $q_f$  for  $\psi$  into the free Lagrangian for a spin-1/2 particle, Eq. 2.25, results in the free Lagrangian for the quark fields.

This Lagrangian is invariant under global  $U(3)$  transformations of the field,

$$Uq_f = e^{i\theta} e^{i\theta_a \lambda^a} q_f \quad (2.40)$$

where the first exponential is a  $U(1)$  transformation and the second exponential is an  $SU(3)$  transformation. The  $U(1)$  transformation is given by a phase  $\theta$  while the  $SU(3)$  transformation is given by eight phases  $\theta_a$  and Gell-Mann matrices  $\lambda^a$ . The Gell-Mann matrices are,

$$\begin{aligned} \lambda^1 &= \begin{pmatrix} 0 & 1 & 0 \\ 1 & 0 & 0 \\ 0 & 0 & 0 \end{pmatrix}, & \lambda^2 &= \begin{pmatrix} 0 & -i & 0 \\ i & 0 & 0 \\ 0 & 0 & 0 \end{pmatrix}, & \lambda^3 &= \begin{pmatrix} 1 & 0 & 0 \\ 0 & -1 & 0 \\ 0 & 0 & 0 \end{pmatrix}, \\ \lambda^4 &= \begin{pmatrix} 0 & 0 & 1 \\ 0 & 0 & 0 \\ 1 & 0 & 0 \end{pmatrix}, & \lambda^5 &= \begin{pmatrix} 0 & 0 & -i \\ 0 & 0 & 0 \\ i & 0 & 0 \end{pmatrix}, & \lambda^6 &= \begin{pmatrix} 0 & 0 & 0 \\ 0 & 0 & 1 \\ 0 & 1 & 0 \end{pmatrix}, \\ \lambda^7 &= \begin{pmatrix} 0 & 0 & 0 \\ 0 & 0 & -i \\ 0 & i & 0 \end{pmatrix}, & \lambda^8 &= \frac{1}{\sqrt{3}} \begin{pmatrix} 1 & 0 & 0 \\ 0 & 1 & 0 \\ 0 & 0 & -2 \end{pmatrix} \end{aligned} \quad (2.41)$$

where their commutation relations are,

$$[\lambda^a, \lambda^b] = i2f^{abc} \lambda^c \quad (2.42)$$

and  $f^{abc}$  are the 512 anti-symmetric  $SU(3)$  structure constants.

Requiring that the free Lagrangian for the quark fields remains invariant under a local  $SU(3)$  transformation,  $e^{i\theta_a(x)\lambda^a}$ , necessitates the introduction of eight vector fields  $G^\mu$ , corresponding to the eight gluons of the SM, by replacing  $\partial_\mu$  in Eq. 2.25 with,

$$D_\mu = \left( \partial_\mu + \frac{ig_s}{2} \lambda_a G_\mu^a \right) \quad (2.43)$$

the QCD covariant derivative. Including the free Lagrangian for the gluon fields, given by Eq. 2.33 without the mass term, results in the Lagrangian,

$$\begin{aligned} \mathcal{L}_{\text{QCD}} &= \underbrace{-\frac{1}{2} (\partial^\mu G_a^\nu - \partial^\nu G_a^\mu) (\partial_\mu G_\nu^a - \partial_\nu G_\mu^a)}_{\text{Eqs. 2.37, 2.38}} \underbrace{-\frac{ig_s}{2} \bar{q}_i^f \gamma^\mu \lambda_{ij}^a q_f^j G_\mu^a}_{\text{Fig. 2.3(a)}} \\ &\quad \underbrace{-ig_s f^{abc} (\partial^\mu G_a^\nu - \partial^\nu G_a^\mu) G_\mu^b G_\nu^c}_{\text{Fig. 2.3(b)}} \underbrace{-\frac{i}{4} g_s^2 f^{abc} f^{adc} G_\mu^b G_\nu^c G_\mu^d G_\nu^e}_{\text{Fig. 2.3(c)}} \end{aligned} \quad (2.44)$$

for QCD, where the Feynman diagram for each interaction term is given in Fig. 2.3. The first term is the gluon propagator, the second term is a coupling of the gluon with two quarks, the third term a coupling of three quarks, and the fourth term a coupling of four quarks. Here,  $g_s$  is the strong coupling constant. In Eq. 2.44 the free Lagrangian for the quark fields has been explicitly omitted, as this Lagrangian will be included in the electroweak Lagrangian for all fermions. However, when this term is included, the QCD Lagrangian is invariant under local  $SU(3)$  gauge transformations.

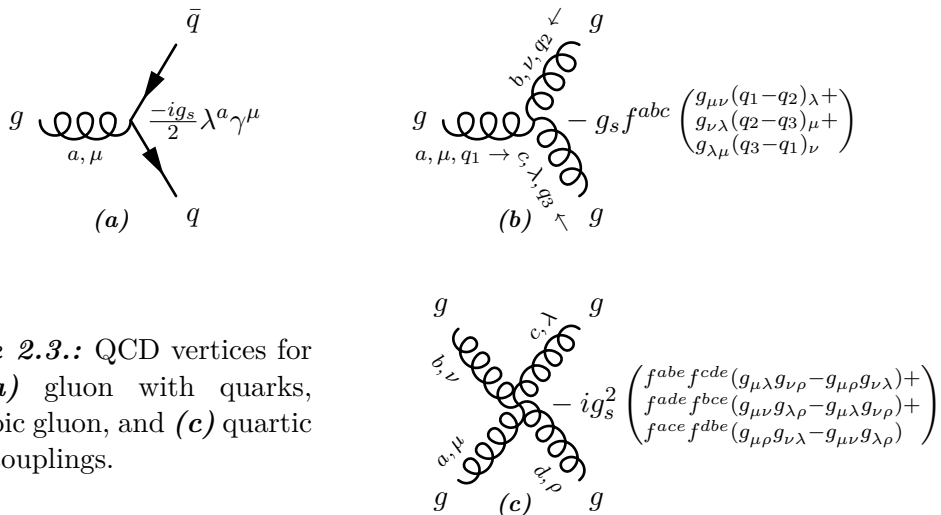


**Figure 2.3.:** QCD vertices for the (a) gluon with quarks, (b) cubic gluon, and (c) quartic gluon couplings.

Because the  $SU(3)$  colour group is non-Abelian, *i.e.* the Gell-Mann matrices of Eq. 2.41 do not commute, as evidenced by non-zero structure constants  $f^{abc}$  in Eq. 2.42, cubic and quartic self-interacting gluon terms are introduced into the Lagrangian. These terms in conjunction with the number of quark flavours,  $N_f$ , and colour charges,  $N_c$ , dictate the range of the force. If  $2N_f - 11N_c$  is greater than 0 the strong force increases at small length-scales, otherwise the strong force decreases at small length-scales [37]. The number of quark flavours in the SM is 6 and the number of colours 3, and so the strong force decreases at small length-scales or high energies. This phenomena, or asymptotic freedom, was first proposed in Refs. [38] and [39] and allows for the perturbative calculation of interactions involving the strong force at high energies using the methods of Sect. 2.1.1. Conversely, at large length-scales and low energies the strong force becomes large, resulting in the confinement of quarks in colourless states, *i.e.* hadrons. While confinement has been observed both in experiment and in lattice QCD calculations, see Ref. [40], no theoretical proof accepted by the particle physics community has yet been made, primarily due to the non-perturbative nature of this energy regime.

### Electroweak Theory

A unification of the electromagnetic and weak forces was first proposed by Glashow in Ref. [41], where the masses of the fermions and gauge bosons are neglected, and a local  $U(2)$  gauge invariance is required. The quark and lepton fields can be decomposed into left-handed and

right-handed components via the chirality operators,

$$\psi_L = \frac{1 - \gamma^5}{2}\psi, \quad \psi_R = \frac{1 + \gamma^5}{2}\psi \quad (2.45)$$

where  $\psi_L$  indicates a left-handed field and  $\psi_R$  a right-handed field. These two types of fields are assigned a weak isospin quantum number  $T$ , which is  $1/2$  for left-handed fields and  $0$  for right-handed fields. The third component of isospin,  $T_3$ , is  $+1/2$  for the left-handed neutrino and  $u$ -type quark fields, and  $-1/2$  for the charged leptons and  $d$ -type quark fields. Both the left-handed and right-handed fields are also assigned a weak hypercharge quantum number,  $Y$ .

The left-handed fields can be combined into weak isospin doublets,

$$t_f = \begin{pmatrix} \nu_f \\ \ell_f \end{pmatrix}_L, \quad \begin{pmatrix} u_f \\ d'_f \end{pmatrix}_L \quad (2.46)$$

each consisting of a  $T_3 = +1/2$  and  $T_3 = -1/2$  left-handed field. Here, the left-handed fields  $\nu_f$  and  $u_f$  correspond to neutrinos and  $u$ -type quarks of generation  $f$  and  $T_3 = +1/2$ , while the left-handed fields  $\ell_f$  and  $d'_f$  correspond to charged leptons and weak eigenstate  $d$ -type quarks of generation  $f$  and  $T_3 = -1/2$ .

The field  $d'_f$  is not an observable mass eigenstate, but rather a flavour eigenstate that is a superposition of the mass eigenstates  $d_f$ . The quark flavour eigenstates are related to their mass eigenstates by the Cabibbo-Kobayashi-Maskawa (CKM) matrix  $V$  of Ref. [42],

$$\begin{pmatrix} d' \\ s' \\ b' \end{pmatrix} = \begin{pmatrix} c_{12}c_{13} & s_{12}c_{13} & s_{13}e^{-i\delta} \\ -s_{12}c_{23} - c_{12}s_{23}s_{13}e^{i\delta} & c_{12}c_{23} - s_{12}s_{23}s_{13}e^{i\delta} & s_{23}c_{13} \\ s_{12}s_{23} - c_{12}c_{23}s_{13}e^{i\delta} & -c_{12}s_{23} - s_{12}c_{23}s_{13}e^{i\delta} & c_{23}c_{13} \end{pmatrix} \begin{pmatrix} d \\ s \\ b \end{pmatrix} \quad (2.47)$$

where  $V$  is fully specified by the experimentally determined mixing angles  $\theta_{12}$ ,  $\theta_{13}$ , and  $\theta_{23}$ , and the  $\mathcal{CP}$ -violating phase angle  $\delta$ . Here,  $c_{ij}$  indicates  $\cos \theta_{ij}$  and  $s_{ij}$  indicates  $\sin \theta_{ij}$ .

Unlike the left-handed fields, the right-handed fields have a weak isospin of zero and must be written as weak hypercharge singlets,

$$y_f = (\ell_f)_R, \quad (u_f)_R, \quad (d_f)_R \quad (2.48)$$

where the neutrinos have been assumed to be massless and only left-handed. Evidence for neutrino oscillations, see *e.g.* Ref. [43], indicates the neutrinos must have mass with eigenstates  $\nu_1$ ,  $\nu_2$ , and  $\nu_3$ , but indirect measurements constrain the sum of these three masses with an upper limit of approximately  $0.5$  eV [15]. In this thesis the neutrinos are assumed to be massless, but the SM can be extended to include either Majorana or Dirac mass terms for the neutrinos [44].

Substituting the weak isospin doublets  $t_f$  of Eq. 2.46 and weak hypercharge singlets  $y_f$  of Eq. 2.48 into the free Lagrangian of Eq. 2.25 for a spin-1/2 field  $\psi$ , without the mass term, provides the free Lagrangians for  $t_f$  and  $y_f$ . The weak isospin doublet Lagrangian is invariant

under global  $U(2)$  transformations of the field,

$$Ut_f = e^{i\theta} e^{\frac{i}{2}\theta_j \sigma^j} t_f \quad (2.49)$$

where the first exponential is a  $U(1)$  transformation with phase  $\theta$ , and the second exponential is a  $SU(2)$  transformation with three phases  $\theta_j$  and the Pauli matrices  $\sigma^j$  of Eq. 2.30. The weak hypercharge singlet Lagrangian is also invariant under,

$$Uy_f = e^{i\theta} y_f \quad (2.50)$$

or global  $U(1)$  transformations of the fields  $y_f$ . Requiring the free Lagrangians to be invariant under local transformations of these types with  $\theta(x)$  and  $\theta_i(x)$  necessitates the replacement of  $\partial_\mu$  with the covariant derivative,

$$D_\mu = \left( \partial_\mu + \frac{ig_1 Y_f}{2} B_\mu + ig_2 |T_{3f}| \sigma_i W_\mu^i \right) \quad (2.51)$$

for the free Lagrangians of  $y_f$  and  $t_f$ , where  $Y_f$  is the weak hypercharge for fermion  $f$ . Here, one vector field  $B_\mu$  and three vector fields  $W_\mu^i$  with gauge coupling strengths  $g_1$  and  $g_2$ , respectively, have been introduced. These four fields can be transformed to physical fields by,

$$\begin{pmatrix} W_\mu^+ \\ W_\mu^- \\ Z_\mu \\ A_\mu \end{pmatrix} = \begin{pmatrix} \frac{1}{\sqrt{2}} & \frac{i}{\sqrt{2}} & 0 & 0 \\ \frac{1}{\sqrt{2}} & \frac{-i}{\sqrt{2}} & 0 & 0 \\ 0 & 0 & \cos \theta_w & -\sin \theta_w \\ 0 & 0 & \sin \theta_w & \cos \theta_w \end{pmatrix} \begin{pmatrix} W_\mu^1 \\ W_\mu^2 \\ W_\mu^3 \\ B_\mu \end{pmatrix} \quad (2.52)$$

where  $A_\mu$  is the field for a photon,  $W_\mu^\pm$  for  $W$  bosons, and  $Z_\mu$  for  $Z$  bosons, and the couplings are related by  $g_1 = g_e/\cos \theta_w$  and  $g_2 = g_w = g_e/\sin \theta_w$ . The fermion charge can be written as,

$$Q = T_3 + Y/2 \quad (2.53)$$

in terms of the third component of weak isospin  $T_3$  and the weak hypercharge  $Y$ .

Introducing the covariant derivatives of Eq. 2.51 into the free Lagrangians for  $y_f$  and  $t_f$ , the Lagrangian for unified electroweak theory  $\mathcal{L}_{\text{EWK}}$  can then be written, and is supplied in Eq. A.4 of App. A.2 due to its length. However, the vertex factors from the interactions of the electroweak Lagrangian, used in Chap. 3, are given in Fig. 2.4. The vector and axial couplings of the fermions with the  $Z$  boson are given in Table 2.2.

| fermion                    | $v$                               | $a$ |
|----------------------------|-----------------------------------|-----|
| $\nu_e, \nu_\mu, \nu_\tau$ | 1                                 | 1   |
| $e, \mu, \tau$             | $\sin^2 \theta_w - 1$             | -1  |
| $u, c, t$                  | $1 - \frac{8}{3} \sin^2 \theta_w$ | 1   |
| $d, s, b$                  | $\frac{4}{3} \sin^2 \theta_w - 1$ | -1  |

**Table 2.2.:** Vector and axial couplings of the fermions with the  $Z$  boson used in the vertex of Fig. 2.4(b).

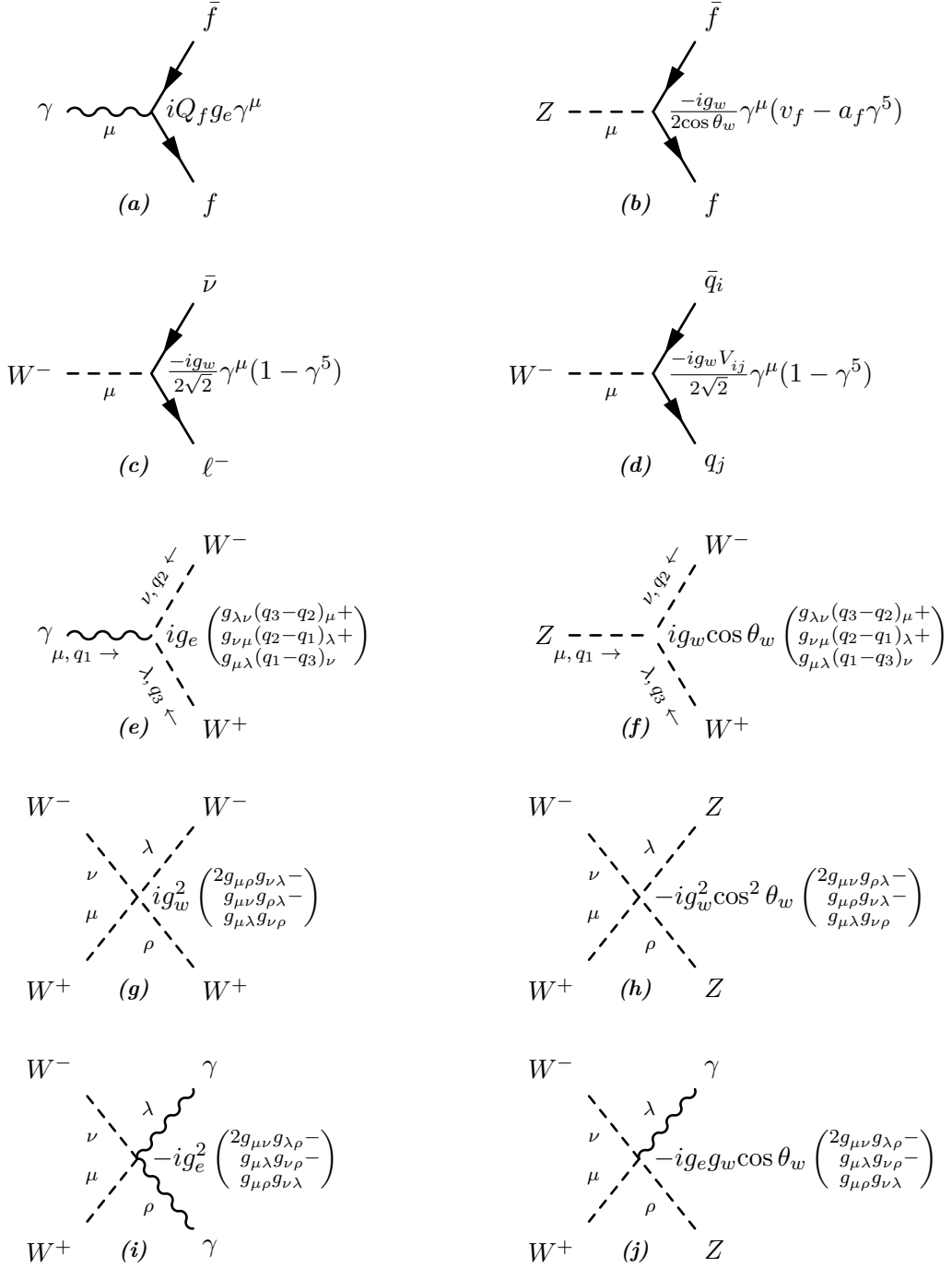


**Figure 2.4.:** Electroweak vertices for the (a)–(d) gauge bosons with fermions, (e)–(f) cubic gauge boson, and (g)–(j) quartic gauge boson couplings.

### Higgs Mechanism

The local  $U(2)$  gauge symmetry of unified electroweak theory is broken with the introduction of mass terms for the fermions and bosons. However, Weinberg and Salam in Refs. [13] and [14] introduced mass terms into the electroweak Lagrangian via the Higgs mechanism of Refs. [45], [46], and [47], which allows for spontaneous symmetry breaking of electroweak theory. Consider a scalar weak isospin doublet with,

$$h = \begin{pmatrix} h_+ \\ h_0 \end{pmatrix} = \frac{1}{\sqrt{2}} \begin{pmatrix} h_3 + ih_4 \\ h_1 + ih_2 \end{pmatrix} \quad (2.54)$$

which is made up of four real scalar fields  $h_1$  through  $h_4$  that can be written in terms of two complex scalar fields  $h_+$  and  $h_0$ . Let both complex scalar fields  $h_+$  and  $h_0$  have hypercharge +1. Then using Eq. 2.53, the upper field has charge +1 while the lower field has charge 0, hence the + and 0 subscript notation. The free Lagrangian for this doublet is then given by substituting  $h$  for  $\phi$  into Eq. 2.22 and changing  $\partial_\mu$  to the covariant derivative  $D_\mu$  given by Eq. 2.51. Furthermore, let the mass term  $m^2\phi^\dagger\phi/2$  be replaced with the potential,

$$V = \mu^2\phi^\dagger\phi + \lambda(\phi^\dagger\phi)^2 \quad (2.55)$$

where  $\mu^2$  and  $\lambda$  are free real parameters. This potential as a function of the norm of the scalar field is plotted in Fig. 2.5. Here, the potential is given for the four possible sign combinations of the parameters  $\mu^2$  and  $\lambda$ . As can be seen, for a stable potential  $\lambda$  must be greater than zero, and for a non-zero potential minimum,  $\mu^2$  must be less than zero.

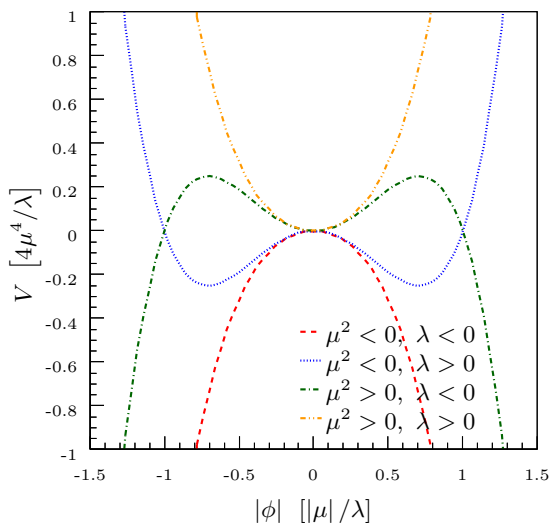


**Figure 2.5.:** The potential  $V$  of Eq. 2.55 as a function of the complex scalar field  $\phi$ . The units on  $V$  are in terms of  $4\mu^4/\lambda$  while the units on  $|\phi|$  are given in terms of  $|\mu|/\lambda$ .

This choice of signs for the parameters  $\mu^2$  and  $\lambda$  results in the minimum potential,

$$V_0 = -\frac{4\mu^4}{\lambda} = -\frac{\lambda v^4}{4} \quad (2.56)$$

for the complex scalar field doublet of Eq. 2.54 at,

$$|h| = \sqrt{\frac{-\mu^2}{\lambda}} = \frac{v}{\sqrt{2}} \quad (2.57)$$

where  $v = \sqrt{-\mu^2/\lambda}$  is the vacuum expectation value for the ground state of  $h$ . The symmetry of the potential can then be spontaneously broken by choosing the unitary gauge,  $h_2 = h_3 = h_4 = 0$ , where  $h_1$  is the only non-zero field. Equation 2.54 can then be written as,

$$h = \frac{1}{\sqrt{2}} \begin{pmatrix} 0 \\ v + H \end{pmatrix} \quad (2.58)$$

where  $h_1$  has been expanded as the neutral scalar field  $H$  about the vacuum expectation value  $v$ .

The Lagrangian density of the Higgs field  $h$ , using the unitary gauge, results in the terms,

$$-\frac{v^2 g_w^2}{4} W_\mu^+ W^{-\mu}, \quad -\frac{v^2 g_w^2}{8 \cos^2 \theta_w} Z_\mu Z^\mu, \quad -\frac{\lambda v^2}{2} H H \quad (2.59)$$

where the first two terms are from introducing the covariant derivative of Eq. 2.51 and the last term is from the potential of Eq. 2.55. These terms, however, are just mass terms for the  $W$ ,  $Z$ , and Higgs bosons where,

$$m_W = \frac{v g_w}{2}, \quad m_Z = \frac{v g_w}{2 \cos \theta_w}, \quad m_H = v \sqrt{\lambda} \quad (2.60)$$

gives their masses in terms of  $g_w$ ,  $\cos \theta_w$ , and  $v$ . Notice that before requiring the unitary gauge the Higgs doublet  $h$ , as well as the massless fields  $W_\mu^i$  and  $B_\mu$ , constitute twelve free fields as the four scalar fields of  $h$  take on only one polarisation state, while the massless vector fields  $W_\mu^i$  and  $B_\mu$  take on two polarisation states each. After choosing the unitary gauge there are still twelve fields; three scalar fields have been eliminated but three of the massless vector fields now are massive, taking on an additional polarisation state each.

The vacuum expectation value  $v$  can be measured from the decays of muons assuming a four-point Fermi function, and so the masses of both the  $W$  and  $Z$  bosons are fully predicted, whereas the mass of the Higgs boson remains a free variable which must be measured experimentally. Yukawa couplings of the Higgs boson with the fundamental fermions of the form  $-m_f^2 \bar{\psi}_f \psi_f$  can also be added to the Higgs Lagrangian without breaking the underlying symmetry and provide mass terms for the fermions [48]. Note that all of these masses are also free parameters, and must be measured experimentally. The full Higgs Lagrangian  $\mathcal{L}_{\text{MHM}}$  is extensive, like the electroweak Lagrangian, and consequently is also supplied in Eq. A.5 of App. A.3. However, the vertices for the interaction terms, used in Chap. 3, are provided in Fig. 2.6. Further details on Higgs boson phenomenology are explored in Chap. 6.

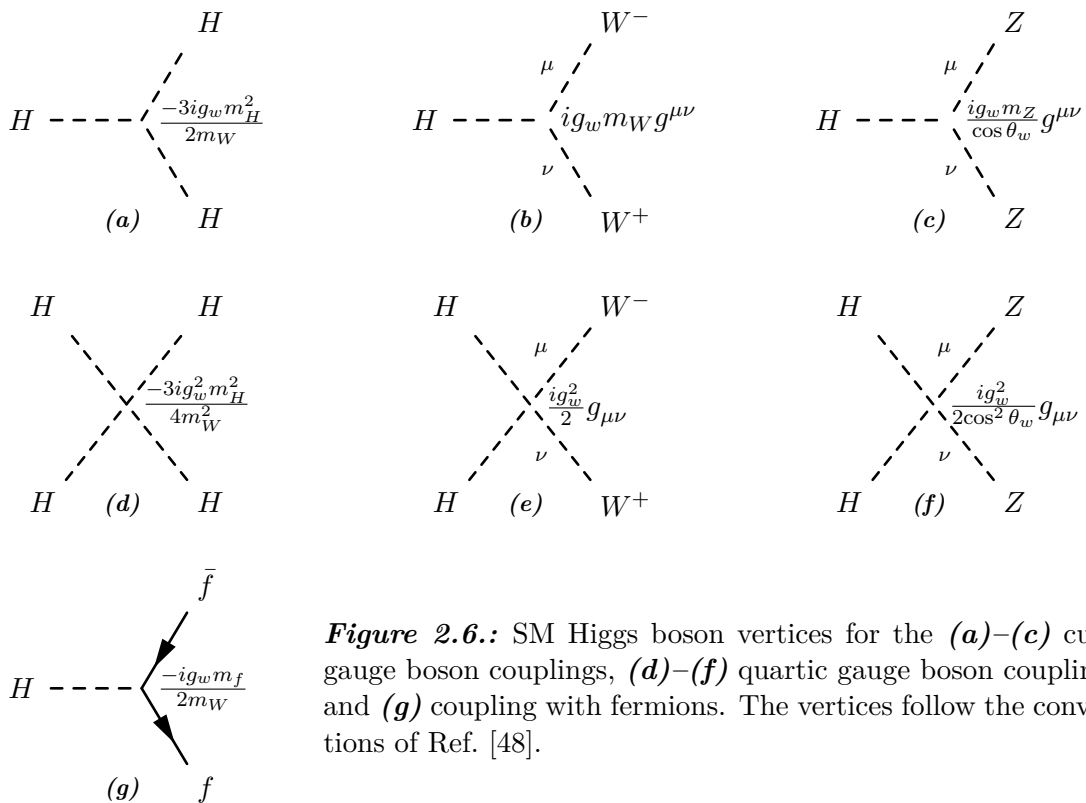


**Figure 2.6.:** SM Higgs boson vertices for the (a)–(c) cubic gauge boson couplings, (d)–(f) quartic gauge boson couplings, and (g) coupling with fermions. The vertices follow the conventions of Ref. [48].

### 2.1.3. Experimental Observables

The theory of Sects. 2.1.1 and 2.1.2 provides a method for calculating the probability of observing a free initial state transitioning into a free final state. Consequently, to test the theory, these probabilities must be related to viable experimental measurements. Colliding single particles and observing the outcome is experimentally challenging, and so oftentimes bunches of particles are collided and the result is measured. In this type of experiment, the cross-sections, either for all possible momentum configurations of a specific final state or differentially with respect to some experimental observable, are measured. From these measurements more complex analyses can be applied to extract measurements of the theory.

Within this section the cross-section is defined, as well as the decay widths for particles. The technical difficulties in calculating the perturbative scattering-matrix used for higher order predictions of cross-sections and decay widths are then introduced, as well as an overview on the methods used to overcome these difficulties. Finally, a procedure for calculating cross-sections from bound states such as the proton is given.

### Cross-sections and Decay Widths

In experimental particle physics either the scattering of two particles or the decay of a single particle is typically measured. Both of these measurements can be theoretically described using the probability from Eq. 2.1. From Eq. 2.4 the differential probability, with respect to the momenta of the outgoing particles, for observing a transition from the initial state  $|A\rangle$  to a



different final state  $|B\rangle$  per unit time  $\mathcal{T}$ , is given by,

$$\begin{aligned} d\mathcal{W}_{A\rightarrow B} &= \frac{|\langle B|S|A\rangle|_{-\infty}^2}{\mathcal{T}} \prod_i^m \frac{\mathcal{V}}{(2\pi)^3} d\vec{q} \\ &= \frac{\mathcal{V}^{1-n}}{(2\pi)^{3m-4}} \delta\left(\sum_i^n q_{a_i} - \sum_j^m q_{b_j}\right) |\mathcal{M}_{A\rightarrow B}|^2 \prod_i^n \frac{1}{2E_{a_i}} \prod_j^m \frac{d\vec{q}_{b_j}}{2E_{b_j}} \end{aligned} \quad (2.61)$$

where the square of the delta-function yields  $\delta(q)^2 = \mathcal{V}\mathcal{T}\delta(q)$ . Integrating over all final state momenta provides,

$$\mathcal{W}_{A\rightarrow B} = \frac{\mathcal{V}^{1-n}}{(2\pi)^{3m-4}} \prod_i^n \frac{1}{2E_{a_i}} \int \dots \int \delta\left(\sum_i^n q_{a_i} - \sum_j^m q_{b_j}\right) |\mathcal{M}_{A\rightarrow B}|^2 \prod_j^m \frac{d\vec{q}_{b_j}}{2E_{b_j}} \quad (2.62)$$

or the transition probability per unit time.

The cross-section can then be defined as,

$$\sigma_{A\rightarrow B} = \frac{\mathcal{W}_{A\rightarrow B}}{\mathcal{F}} \quad (2.63)$$

which is the transition probability per unit time over the particle flux  $\mathcal{F}$ . Consider observing the process of two initial state particles  $a_1$  and  $a_2$  scattering into  $m$  final state particles  $b_j$  in the centre-of-mass frame  $\vec{q}_{a_1} = -\vec{q}_{a_2}$ . The particle flux is given by,

$$\mathcal{F} = \frac{|\vec{v}_{a_1} - \vec{v}_{a_2}|}{\mathcal{V}} = (E_{a_1} + E_{a_2}) \frac{|\vec{q}_{a_1}|}{\mathcal{V}E_{a_1}E_{a_2}} = \sqrt{(q_{a_1}q_{a_2})^2 - (m_{a_1}m_{a_2})^2} \frac{1}{\mathcal{V}E_{a_1}E_{a_2}} \quad (2.64)$$

and so the cross-section for this two-to- $m$  process is,

$$\begin{aligned} \sigma_{a_1a_2\rightarrow B} &= \frac{1}{\mathcal{S}4(2\pi)^{3m-4} \sqrt{(q_{a_1}q_{a_2})^2 - (m_{a_1}m_{a_2})^2}} \\ &\quad \int \dots \int \delta\left(q_{a_1} + q_{a_2} - \sum_j^m q_{b_j}\right) |\mathcal{M}_{a_1a_2\rightarrow B}|^2 \prod_j^m \frac{d\vec{q}_{b_j}}{2E_{b_j}} \end{aligned} \quad (2.65)$$

where  $\mathcal{S}$  is the number of sets of identical particle types in the final state. Both the normalisation and integral of the cross-section are Lorentz invariant, and so the cross-section itself must also be Lorentz invariant. The cross-section has units of area which are typically given in barns where  $1 \text{ b} = 10^{-28} \text{ m}^2$ .

In a typical scattering experiment the cross-section for a specific two-to- $m$  scattering process, given by Eq. 2.65, is determined by

$$\sigma_{a_1a_2\rightarrow B} = \frac{N}{\mathcal{L}} \quad (2.66)$$

where  $N$  is the number of scattering events observed, and  $\mathcal{L}$  is the integrated luminosity for the experiment. The luminosity is defined as the number of particles per unit area and time, so the integrated luminosity is the number of particles per unit area. The luminosity can be written

as,

$$\frac{\partial \mathcal{L}}{\partial t} = \rho |\vec{v}_{a_1} - \vec{v}_{a_2}| = \frac{N |\vec{v}_{a_1} - \vec{v}_{a_2}|}{\mathcal{V}} = N \mathcal{F} \quad (2.67)$$

where  $\rho$  is the particle density.

Following a similar process to the cross-section formula determination, the decay width or decay rate for a particle  $a_1$  decaying into  $m$  particles  $b_j$  can be written as,

$$\Gamma_{a_1 \rightarrow B} = \frac{1}{2E_{a_1} (2\pi)^{3m-4}} \int \dots \int \delta \left( q_{a_1} - \sum_j^m q_{b_j} \right) |\mathcal{M}_{a_1 \rightarrow B}|^2 \prod_j^m \frac{d\vec{q}_{b_j}}{2E_{b_j}} \quad (2.68)$$

which is not Lorentz invariant. Typically, the decay width is defined in the rest frame of the decaying particle and so  $E_{a_1} = m_{a_1}$ . Conceptually, the decay width is not consistent with the definition of the scattering matrix because an unstable particle cannot be a free state, but the optical theorem, see *e.g.* Ref. [18], validates the relation of Eq. 2.68. Decay widths are usually given in units of eV and are related directly to the mean lifetime of the particle by  $1/\Gamma$ . Consequently, decay widths can be experimentally determined by measuring the mean lifetimes of particles at rest.

### Renormalisation

One of the issues in comparing theory and experiment is determining theoretical predictions to the same level of precision as the experimental results. Because predictions such as cross-sections must be calculated perturbatively, the precision of the theoretical prediction is dependent not only on the order at which it was calculated, but also on the rate of convergence of the perturbation series. Consider the example from Ref. [37] for the  $t$ -channel electron-muon scattering cross-section calculated at leading order using only the diagram of Fig. 2.7(a) and at next-to-leading order using both the diagram of Fig. 2.7(a) and of Fig. 2.7(b).

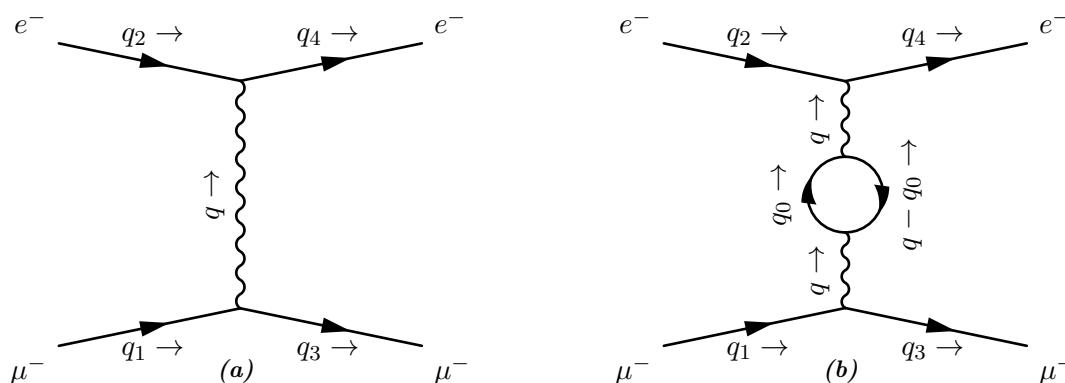


**Figure 2.7.:** Feynman diagrams for  $t$ -channel muon-electron scattering at (a) leading-order, and (b) next-to-leading-order with one electron loop, corresponding to vacuum polarisation.

The matrix element for the leading-order calculation can be determined by applying the

Feynman rules of Table 2.1 and the interaction vertex of Fig. 2.4(a) to Fig. 2.7(a), resulting in,

$$\mathcal{M}_{\mu e \rightarrow \mu e}^{\text{LO}} = -g_e^2 (\bar{u}(q_3, \lambda_3) \gamma^\mu u(q_1, \lambda_1)) \frac{g_{\mu\nu}}{q^2} (\bar{u}(q_4, \lambda_4) \gamma^\nu u(q_2, \lambda_2)) \quad (2.69)$$

which is finite. Consequently, when Eq. 2.69 is used in Eq. 2.65, the resulting cross-section is finite. The matrix element from the next-to-leading order diagram of Fig. 2.7(b) is given by,

$$\mathcal{M}_{\mu e \rightarrow \mu e}^{\text{NLO}} = -g_e^2 (\bar{u}(q_3, \lambda_3) \gamma^\mu u(q_1, \lambda_1)) \mathcal{I}_{\mu\nu} (\bar{u}(q_4, \lambda_4) \gamma^\nu u(q_2, \lambda_2)) \quad (2.70)$$

$$\mathcal{I}_{\mu\nu} = \frac{ig_e^2}{q^4} \int \frac{\text{Tr} \left( \gamma_\mu (\not{q}_0 + m_e) \gamma_\nu (\not{q}_0 - \not{q} + m_e) \right)}{(2\pi)^4 (q_0^2 - m_e^2) ((q_0 - q)^2 - m_e^2)} dq_0$$

where the integral  $\mathcal{I}_{\mu\nu}$  is due to the internal loop and  $\not{q} \equiv q^\mu \gamma_\mu$  is Dirac slash notation. The trace, Tr, in the integral arises from applying Casimir's trick [49] to sum over all spin states of the internal loop. This matrix element is not finite; the integral  $\mathcal{I}_{\mu\nu}$  between the two fermion lines diverges and approaches  $\ln |q_0|$  as  $|q_0|$  approaches infinity. Consequently, a cross-section calculated with this matrix element included is also not finite. This type of divergence, when the momentum approaches infinity, is an ultraviolet divergence, as opposed to an infrared divergence which occurs when the momentum approaches zero.

The divergent integral of Eq. 2.70 can be rewritten, or regularised, in such a way that it diverges for only a single cut-off parameter  $\Lambda$  as,

$$\mathcal{I}_{\mu\nu} = -g_{\mu\nu} q^2 \frac{g_e^2}{12\pi^2} \left( \ln \left( \frac{\Lambda^2}{m_e^2} \right) - \mathcal{R} \left( \frac{-q^2}{m_e^2} \right) \right) \quad (2.71)$$

where,

$$\mathcal{R}(x) = \frac{4}{x} - \frac{5}{3} + \frac{2(x-2)}{x} \sqrt{\frac{x+4}{x}} \tanh^{-1} \sqrt{\frac{x}{x+4}} \quad (2.72)$$

is finite for the limits of  $x$  approaching both zero and infinity. For further details, see Ref. [37]. The infinite cut-off term can then be absorbed into a renormalised coupling constant,

$$g_r^2 \equiv g_e^2 \left( 1 - \frac{g_e^2}{12\pi^2} \ln \left( \frac{\Lambda^2}{m_e^2} \right) \right), \quad g_r^2(q) \equiv g_r^2 \left( 1 - \frac{g_r^2}{12\pi^2} \mathcal{R} \left( \frac{-q^2}{m_e^2} \right) \right) \quad (2.73)$$

so the matrix element of the sum of the leading-order and next-to-leading-order terms can be written as,

$$\mathcal{M}_{\mu e \rightarrow \mu e} = -g_r^2(q) (\bar{u}(q_3, \lambda_3) \gamma^\mu u(q_1, \lambda_1)) \frac{g_{\mu\nu}}{q^2} (\bar{u}(q_4, \lambda_4) \gamma^\nu u(q_2, \lambda_2)) \quad (2.74)$$

where the divergence has been absorbed by the renormalised momentum dependent coupling. This renormalised coupling is the experimentally measured coupling.

Any Lagrangian where the infinities from higher-order diagrams can be absorbed into constants of the Lagrangian, *i.e.* masses and couplings, is renormalisable. In Ref. [50] t'Hooft and Veltman demonstrated that all gauge theories are renormalisable using the process of di-

dimensional regularisation. This is a method by which integrals similar to that of Eq. 2.70 can be rewritten in terms of a single cut-off parameter. Since the Lagrangian of the SM is an  $SU(3)_C \otimes SU(2)_T \otimes U(1)_Y$  gauge theory, the Lagrangian for the SM is fully renormalisable, and the ultraviolet divergences are absorbed in the masses and couplings of the SM Lagrangian. The minimal subtraction (MS) scheme for renormalisation was proposed by t'Hooft in Ref. [51] and Weinberg in Ref. [52] from which emerged the modified minimal subtraction ( $\overline{\text{MS}}$ ) scheme. This renormalisation scheme is currently used for most SM calculations.

One of the consequences of renormalisation is the running of the couplings as a function of momentum. Oftentimes the couplings  $g_e$  and  $g_s$  with the Weinberg angle  $\theta_w$ , are expressed as [53],

$$\begin{aligned}\alpha_1 &= \left(\frac{5}{3}\right) \frac{g_e^2}{(4\pi)\cos^2\theta_w}, & \alpha_1^{-1}(m_Z) &= 58.9 \pm 0.3 \\ \alpha_2 &= \frac{g_e^2}{(4\pi)\sin^2\theta_w}, & \alpha_2^{-1}(m_Z) &= 29.7 \pm 0.2 \\ \alpha_3 &= \frac{g_s^2}{4\pi}, & \alpha_3^{-1}(m_Z) &= 8.47 \pm 0.5\end{aligned}\tag{2.75}$$

where the factor of  $5/3$  for  $\alpha_1$  is a normalisation from the  $SU(5)$  unification theory of Ref. [54] and the numerical values are from Ref. [55].

Performing renormalisation at the one-loop level, like that of Eq. 2.73, results in the renormalised couplings fulfilling the differential equation,

$$\frac{\partial\alpha_i^{-1}}{\partial\ln\left(\frac{Q}{Q_0}\right)} = \frac{-b_i}{2\pi}, \quad b_i = \left(\frac{41}{10}, \quad \frac{-19}{6}, \quad -7\right)\tag{2.76}$$

where  $Q$  is the renormalisation group scale and the values  $b_i$  arise from the SM Lagrangian [56]. Solving this for  $\alpha_i^{-1}$  results in the relation,

$$\alpha_i^{-1}(Q) = \alpha_i^{-1}(Q_0) - \frac{b_i}{2\pi} \ln\left(\frac{Q}{Q_0}\right)\tag{2.77}$$

for the running of the couplings, which is plotted in Fig. 2.8 using the  $\alpha_i^{-1}(m_Z)$  from Eq. 2.75. From this figure the confinement and asymptotic freedom properties of QCD are apparent. At low  $Q$  the QCD coupling  $g_s$  increases, while for high  $Q$  it decreases. As  $Q$  becomes smaller, perturbative QCD calculations begin to no longer converge, and at around  $Q = 1$  GeV perturbative QCD fails completely.

## Factorisation

In the formulation of the scattering matrix from Sect. 2.1.1, the initial and final states are assumed to be free states. When colliding bound states, such as two protons at the LHC, or a proton and an anti-proton at the Tevatron, the initial states are no longer free, and so a method

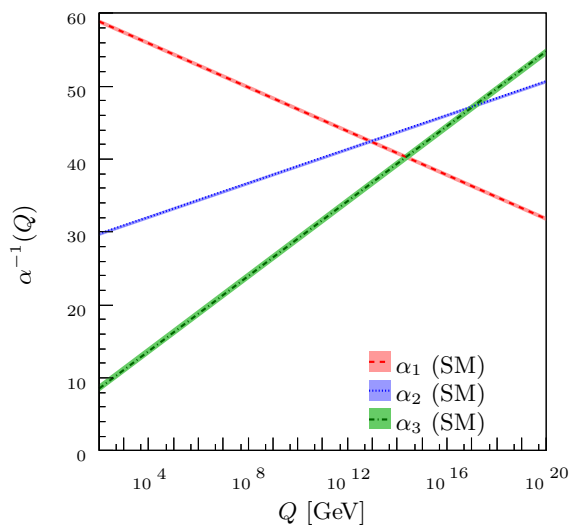


**Figure 2.8.:** Running of the couplings  $\alpha_i^{-1}(Q)$  given by Eqs. 2.76 and 2.77. The couplings are run upwards from their experimental values at  $m_Z \approx 10^2$  GeV from Eq. 2.75.

is needed to theoretically calculate cross-sections for these processes. Consider scattering an electron off a proton at low energies. Here, the proton is resolved as a point charge and the scattering of the electron can be treated classically. However, at higher energies the electron begins to probe the inner structure of the proton and will scatter off partons such as the valence  $u$ -quarks and  $d$ -quarks. At higher energies yet, the electron will be able to resolve even more structure of the proton, including gluons and sea quarks such as anti-quarks and heavy-flavour quarks.

The cross-section for an electron scattering off a quark can be calculated using Eq. 2.65, but the momentum of both the electron and quark is needed. Consequently, if the fractional momentum of the proton carried by the quark is known, then the cross-section for an electron scattering off a quark within the proton can be calculated. Similarly, if two protons are collided, and the momentum fractions of the two interacting partons of the protons are known, then the cross-section can again be calculated with Eq. 2.65. The factorisation theorem generalises this concept; the cross-section for two colliding bound states  $a_1$  and  $a_2$  with interacting partons  $p_1$  and  $p_2$  producing a final state  $B$  which can be written as,

$$\sigma_{a_1 a_2 \rightarrow B} = \int \int f_{a_1}(x_{p_1}, Q^2, p_1) f_{a_2}(x_{p_2}, Q^2, p_2) \sigma_{p_1 p_2 \rightarrow B} dx_{p_1} dx_{p_2} \quad (2.78)$$

where  $f_{a_i}(x_{p_i}, Q^2, p_i)$  is the parton distribution function (PDF) at the energy scale  $Q^2$  for parton type  $p_i$  of the bound state  $a_i$ , and  $\sigma_{p_1 p_2 \rightarrow B}$  is the partonic cross-section which can be calculated with Eq. 2.65.

The PDF, at leading-order for a given bound state, is the joint probability density function for finding a parton of type  $p_i$  with a longitudinal momentum fraction  $x_{p_i}$ . Since the parton cannot have a momentum larger than the momentum of the bound state, the momentum fraction  $x_{p_i}$  must range between 0 and 1. The PDF evaluated for a given parton type  $p_i$  as a function of momentum fraction  $x_{p_i}$  is typically notated as  $f(x_{p_i}, Q^2, p_i)$ . Because the PDF is a probability density function, the  $f$  for a given parton type, integrated over  $x$ , is the probability of observing

that parton type in the bound state. Consequently, the sum of the integrated  $f$  over all parton types is unity. The PDFs for bound states must be determined from fits of experimental data, and are energy scale dependent. In Fig. 2.9(a) the  $f$ , with uncertainties, for  $u$ -quarks,  $d$ -quarks, their corresponding anti-quarks, and gluons are given for an energy scale of  $Q^2 = 100 \text{ GeV}^2$  using the MSTW08 leading-order proton PDF set of Ref. [57]. For low momentum fractions the gluon dominates the structure of the proton, while at very high momentum fractions, the valence  $u$ -quark dominates. At this energy scale, gluons carry approximately 46% of the proton momentum while  $u$ -quarks carry 26% and  $d$ -quarks carry 12%.

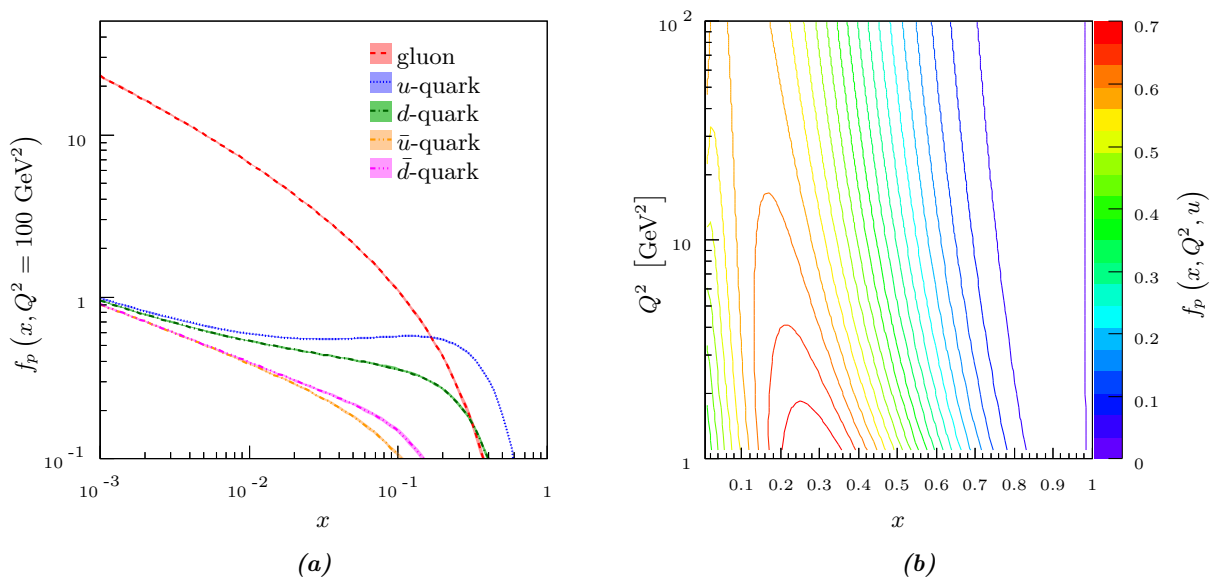


**Figure 2.9.:** (a) The  $f$  as a function of momentum fraction  $x$  for the  $u$ -quark,  $d$ -quark,  $\bar{u}$ -quark,  $\bar{d}$ -quark, and gluon partons of the leading-order MSTW08 proton PDF set at an energy scale of  $Q^2 = 100 \text{ GeV}^2$ . (b) The  $f$  for the  $u$ -quark parton of the proton as a function of momentum fraction  $x$  and energy scale  $Q^2$ .

The PDFs, just like the couplings of Eq. 2.77, are both energy scale dependent and renormalisation scheme dependent. The Dokschitzner Gribov-Lipatov Altarelli-Parisi (DGLAP) equation of Refs. [58], [59], and [60] is an analogue to Eq. 2.77, evolving the PDF measured at some energy scale  $Q_0^2$  to the energy scale  $Q^2$ . The  $f$  for the partons of a hadron must satisfy,

$$Q^2 \frac{\partial}{\partial(Q^2)} \begin{pmatrix} f(x, Q^2, q_i) \\ f(x, Q^2, g) \end{pmatrix} = \frac{\alpha_s(Q^2)}{2\pi} \sum_j \int_x^1 \frac{1}{x'} \begin{pmatrix} \mathcal{P}_{q_i q_j}(\frac{x}{x'}, \alpha_s(Q^2)) & \mathcal{P}_{q_i g}(\frac{x}{x'}, \alpha_s(Q^2)) \\ \mathcal{P}_{g q_j}(\frac{x}{x'}, \alpha_s(Q^2)) & \mathcal{P}_{g g}(\frac{x}{x'}, \alpha_s(Q^2)) \end{pmatrix} \begin{pmatrix} f(x', Q^2, q_j) \\ f(x', Q^2, g) \end{pmatrix} dx' \quad (2.79)$$

where  $q_i$  is a quark of flavour  $i$  and  $g$  is a gluon. The splitting functions  $\mathcal{P}_{p_i p_j}$  encode the splitting of a parton into two additional partons via the QCD vertices of either Fig. 2.3(a) or Fig. 2.3(b). These splitting functions are also used for the evolution of parton showers, and are described at leading order in Sect. 2.2.1 where  $\mathcal{P}_{q_i q_j}$  is zero unless the flavour of  $q_i$  and  $q_j$  are the same. For further details on these splitting functions as well as a derivation of Eq. 2.79,

see Ref. [61]. In Fig. 2.9(b) the  $f$  for the  $u$ -quark parton of the proton is given as a function of momentum transfer  $x$  and energy scale  $Q^2$  as evolved with the DGLAP equation. Generally, at lower energy scales the  $u$ -quark partons carry a larger fraction of the proton momentum than at higher energies. For example, the  $u$ -quarks carry 38% of the proton momentum at  $Q^2 = 1 \text{ GeV}^2$  and only 26% at  $Q^2 = 100 \text{ GeV}^2$ .

#### 2.1.4. Alternatives and Extensions

While the SM provides predictions which have been experimentally validated to better than 1%, there remain a variety of outstanding issues, both experimental and theoretical. The following list is by no means exhaustive, but is intended to provide a general overview of some of the issues currently confronting the particle physics community.

gravity: Currently, the SM does not account for gravity, as the gravitational forces acting on particles at the scattering energies of most particle physics experiments is nearly forty times weaker than the electroweak or strong forces. In the development of the Lagrangians in Sect. 2.1.2, only special relativity was accounted for, and not general relativity. Introducing fields for gravity into the SM Lagrangian results in a non-renormalisable theory and so the question of how to incorporate gravity into the SM remains.

unification: In the SM the electromagnetic and weak forces are unified into the electroweak force via a  $SU(2)_T \otimes U(1)_Y$  gauge symmetry. Is it possible to unify the strong force with the electroweak force, and possibly gravity as well? In a unified theory the couplings  $\alpha_i$  of Eq. 2.75 would converge at some grand unified theory (GUT) scale. As can be seen for the SM in Fig. 2.8, this is not the case, but if the forces do unify, the GUT scale is expected to be on the order of  $\approx 10^{16} \text{ GeV}$ .

parameters: There are 18 parameters within the SM which must be experimentally determined, excluding the neutrino sector, which introduces an additional 7 parameters. For a fundamental theory, one might assume only a single parameter must be experimentally determined, or even better, no parameters. Furthermore, within the SM the observed mass of the Higgs boson is the result of large cancellations from renormalisation and requires fine-tuning, which many theorists think is unnatural and is indicative of a more fundamental theory.

dark matter: Measurements of the rotational velocities of galaxies as a function of the galactic radius do not match the expected velocities determined from the visible mass of the galaxies, see *e.g.* Ref. [62]. This discrepancy implies the presence of a new type of weakly interacting massive particles (WIMP) not accounted for within the SM.

anti-matter: According to the standard cosmological big-bang theory of Ref. [63] both matter and anti-matter should have been created in equal parts during the early formation of the universe. However, precision observations of the cosmic microwave background from Ref. [64] indicate that the universe is primarily made of matter. Currently, the LHCb

collaboration is exploring aspects as to why this matter/anti-matter asymmetry in the universe exists. Additionally, the AMS experiment of Ref. [65] is searching for cosmic sources of anti-matter.

neutrinos: As stated in Sect. 2.1.2, the observation of neutrino oscillations implies neutrinos have mass. However, the details on how massive neutrinos should be incorporated into the SM have not yet been fully determined by experiment. For a review of current neutrino experiment results see Ref. [66].

Higgs boson: The details of the Higgs mechanism introduced in Sect. 2.1.2 have not yet been fully confirmed by experiment. However, the observation of a Higgs-like boson by the ATLAS [8] and CMS [9] collaborations with a mass of approximately 125 GeV are the beginnings of detailed measurements of the Higgs mechanism. Furthermore, this thesis investigates the forward production of Higgs bosons within LHCb.

Within the remainder of this section the supersymmetry extension to the SM is presented, where in Chap. 6 parts of this theory are tested. Alternative models such as  $SU(5)$  [54],  $SO(10)$  [67], technicolour [68], and string theory [69] have also been proposed, but are not discussed here.

### Supersymmetry

Consider a diagram with an internal fermion loop similar to the diagram of Fig. 2.7(b), but replacing the photon mediator with the neutral SM Higgs boson. This loop also produces a divergent integral, that is no longer proportional to  $g_e^2$  as in the case of the photon with the vertex of Fig. 2.4(a), but rather is proportional to the mass of the fermion squared, given by the vertex factor of Fig. 2.6(g). Consequently, the divergence from this one-loop correction is now absorbed in the renormalised Higgs boson mass of the form,

$$m_r^2 = m_H^2 - \frac{g_f^2}{8\pi^2} \left( \Lambda^2 + 3m_f^2 \ln \left( \frac{\Lambda^2}{m_f^2} \right) - 2m_f^2 + \frac{m^4}{\Lambda^2 + m_f^2} \right) \quad (2.80)$$

where  $m_H$  is the bare Higgs boson mass,  $m_f$  is the mass of the fermion,  $g_f$  is the coupling of the fermion to the Higgs boson, and  $\Lambda$  is some cut-off parameter. Notice that this renormalisation contains a quadratically divergent term,  $\Lambda^2$ , unlike the renormalised coupling  $g_r$  of Eq. 2.73 which is only logarithmically divergent. The measured value of the Higgs vacuum expectation value  $v$  requires the renormalised Higgs boson mass to be near 100 GeV which is consistent with the Higgs-like boson observed by ATLAS and CMS. Consequently, if the cut-off parameter is on the order of the Planck scale, where  $\Lambda \approx 10^{19}$  GeV and effects from quantum gravity become significant, then the bare mass must also be on the same order and a cancellation of at least 17 digits must occur to produce the renormalised Higgs boson mass. This problem is known as the naturalness or fine-tuning problem.

Massive scalars which couple to the Higgs boson, such as the self-coupling of Fig. 2.6(a), also



contribute to the renormalised Higgs boson mass at the one-loop level,

$$m_r^2 = m_H^2 + \frac{g_\phi^2}{16\pi^2} \left( \Lambda^2 - m_\phi^2 \ln \left( \frac{\Lambda^2}{m_\phi^2} \right) \right) \quad (2.81)$$

where  $g_\phi$  is the coupling of the scalar with the Higgs boson and  $m_\phi$  is the mass of the scalar. These contributions also contain a quadratically divergent term, but with the opposite sign to the term from the fermion, and so the quadratic divergences of the renormalised Higgs boson mass could be cancelled if there is a symmetry between fermions and bosons. This type of symmetry is a supersymmetry (SUSY) and was introduced by Wess and Zumino in Ref. [70] where the translations,

$$\delta\phi = 2\bar{\epsilon}\psi, \quad \delta\psi = -i\gamma^\mu\epsilon(\partial_\mu\phi) \quad (2.82)$$

mix scalar fields  $\phi$  with spinor fields  $\psi$ , and  $\delta$  and  $\epsilon$  describe the transformations [37]. A Lagrangian invariant under this translation can be constructed by combining the spin-0 Lagrangian of Eq. 2.22 with the spin-1/2 Lagrangian of Eq. 2.25, where both fields correspond to particles with the same mass.

A supersymmetric Lagrangian is built by requiring a fermionic or bosonic superpartner for every particle of the SM and combining them into supermultiplets which preserve the gauge groups of the SM. For every fermion/boson pair the number of bosonic degrees of freedom must equal the number of fermionic degrees of freedom. For each spin-1/2 fermion of the SM, a complex scalar field or sfermion must be introduced. The sfermion partners to leptons are sleptons, while the sfermion partners to quarks are squarks. The gauge bosons give rise to gaugino fermionic superpartners: gluinos, winos, zinos, photinos, and higgsinos. This however, is only an introduction to some of the creative naming conventions of SUSY models. None of the plethora of new particles introduced by SUSY has been experimentally observed, and this requires that SUSY is also a broken symmetry, similar to electroweak symmetry. Methods for breaking SUSY are not explored here, but an excellent introduction is given in Ref. [56].

The minimal supersymmetric model (MSSM) is the SUSY model with the simplest Higgs sector: a two Higgs doublet model consisting of a weak isospin doublet with hypercharge +1 and two complex fields, and a weak isospin doublet with hypercharge -1, also with two complex fields. The two doublets, analogous to the single SM doublet of Eq. 2.54, are typically written as,

$$h_u = \begin{pmatrix} h_u^+ \\ h_u^0 \end{pmatrix}, \quad h_d = \begin{pmatrix} h_d^0 \\ h_d^- \end{pmatrix}, \quad (2.83)$$

where  $h_u$  has hypercharge +1 and  $h_d$  has hypercharge -1. Just as a potential was introduced for the SM Higgs doublet with Eq. 2.55, the potential,

$$V = (|\mu|^2 + m_{h_u}^2) (h_u^{0\dagger}h_u^0 + h_u^{+\dagger}h_u^+) + (|\mu|^2 + m_{h_d}^2) (h_d^{0\dagger}h_d^0 + h_d^{-\dagger}h_d^-) + m_{h_{ud}}^2 (h_u^+h_d^- - h_u^0h_d^0 + h_u^{+\dagger}h_d^{-\dagger} - h_u^{0\dagger}h_d^{0\dagger}) \quad (2.84)$$

$$\begin{aligned}
& + \frac{(g_1^2 + g_2^2)}{8} \left( h_u^{0\dagger} h_u^0 + h_u^{+\dagger} h_u^+ - h_d^{0\dagger} h_d^0 - h_d^{-\dagger} h_d^- \right)^2 \\
& + \frac{g_2}{2} \left( h_u^+ h_d^{0\dagger} + h_u^0 h_d^{-\dagger} \right)^\dagger \left( h_u^+ h_d^{0\dagger} + h_u^0 h_d^{-\dagger} \right)
\end{aligned}$$

must be introduced for the MSSM Higgs Lagrangian [48, 56]. Here,  $\mu$  is the Higgs mixing parameter and  $m_{h_u}$ ,  $m_{h_u}$ , and  $m_{h_{ud}}$  are additional constants which can be related to more physical constants. The field  $h_u^0$  has a vacuum expectation value of  $v_u$  while the field  $h_d^0$  has a vacuum expectation value of  $v_d$ . These two vacuum expectation values are specified by,

$$v_u^2 + v_d^2 = \frac{2m_Z^2}{(g_1^2 + g_2^2)} \quad (2.85)$$

and so only the ratio of the two is unknown, which is normally written as  $\tan \beta \equiv v_u/v_d$ .

The eight real fields of the two doublets can be written as mass eigenstates by the relations,

$$\begin{aligned}
\begin{pmatrix} h_u^0 \\ h_d^0 \end{pmatrix} &= \begin{pmatrix} v_u \\ v_d \end{pmatrix} + \frac{1}{\sqrt{2}} \begin{pmatrix} \cos \alpha & \sin \alpha \\ -\sin \alpha & \cos \alpha \end{pmatrix} \begin{pmatrix} h^0 \\ H^0 \end{pmatrix} + \frac{i}{\sqrt{2}} \begin{pmatrix} \sin \beta & \cos \beta \\ -\cos \beta & \sin \beta \end{pmatrix} \begin{pmatrix} \phi^0 \\ A^0 \end{pmatrix} \\
\begin{pmatrix} h_u^+ \\ h_d^{-\dagger} \end{pmatrix} &= \begin{pmatrix} \sin \beta & \cos \beta \\ -\cos \beta & \sin \beta \end{pmatrix} \begin{pmatrix} \phi^+ \\ H^+ \end{pmatrix}
\end{aligned} \quad (2.86)$$

for the neutral and charged mass eigenstates, assuming  $v_u$  and  $v_d$  minimise the tree-level potential. At tree-level the  $h^0$  is a light  $\mathcal{CP}$ -even Higgs boson, the  $H^0$  a heavy  $\mathcal{CP}$ -even Higgs boson, and the  $A^0$  a  $\mathcal{CP}$ -odd Higgs boson. There are two real charged Higgs bosons where  $H^{+\dagger} = H^-$  and two charged Goldstone bosons,  $\phi^{+\dagger} = \phi^-$ , which are absorbed into the longitudinal polarisations of the  $W$  bosons with an appropriate gauge transformation. Similarly,  $\phi^0$  is a neutral Goldstone boson which is absorbed into the longitudinal polarisation of the  $Z$  boson with the proper transformation. The masses are related via both  $\beta$  and the Higgs boson mass mixing angle  $\alpha$  which is given by the relations,

$$\frac{\sin 2\alpha}{\sin 2\beta} = \frac{-m_{H^0}^2 - m_{h^0}^2}{m_{H^0}^2 - m_{h^0}^2}, \quad \tan 2\alpha = \frac{m_{A^0}^2 + m_Z^2}{m_{A^0}^2 - m_Z^2} \quad (2.87)$$

in terms of  $\beta$ , the masses of the neutral mass eigenstates, and the mass of the  $Z$  boson.

The parameters of the potential given by Eq. 2.84 can then be related by the equations,

$$\begin{aligned}
m_{h_u}^2 &= m_{A^0}^2 \cos^2 \beta + \frac{m_Z^2}{2} \cos 2\beta - |\mu|^2 \\
m_{h_d}^2 &= m_{A^0}^2 \sin^2 \beta + \frac{m_Z^2}{2} \cos 2\beta - |\mu|^2 \\
m_{h_{ud}}^2 &= \frac{m_{A^0}^2}{2} \sin 2\beta
\end{aligned} \quad (2.88)$$

where typically the free parameters are taken as  $\tan \beta$ ,  $m_{A^0}$ , and  $|\mu|^2$ . The masses of the remaining Higgs bosons can also be specified in terms of these parameters, and is done so in the

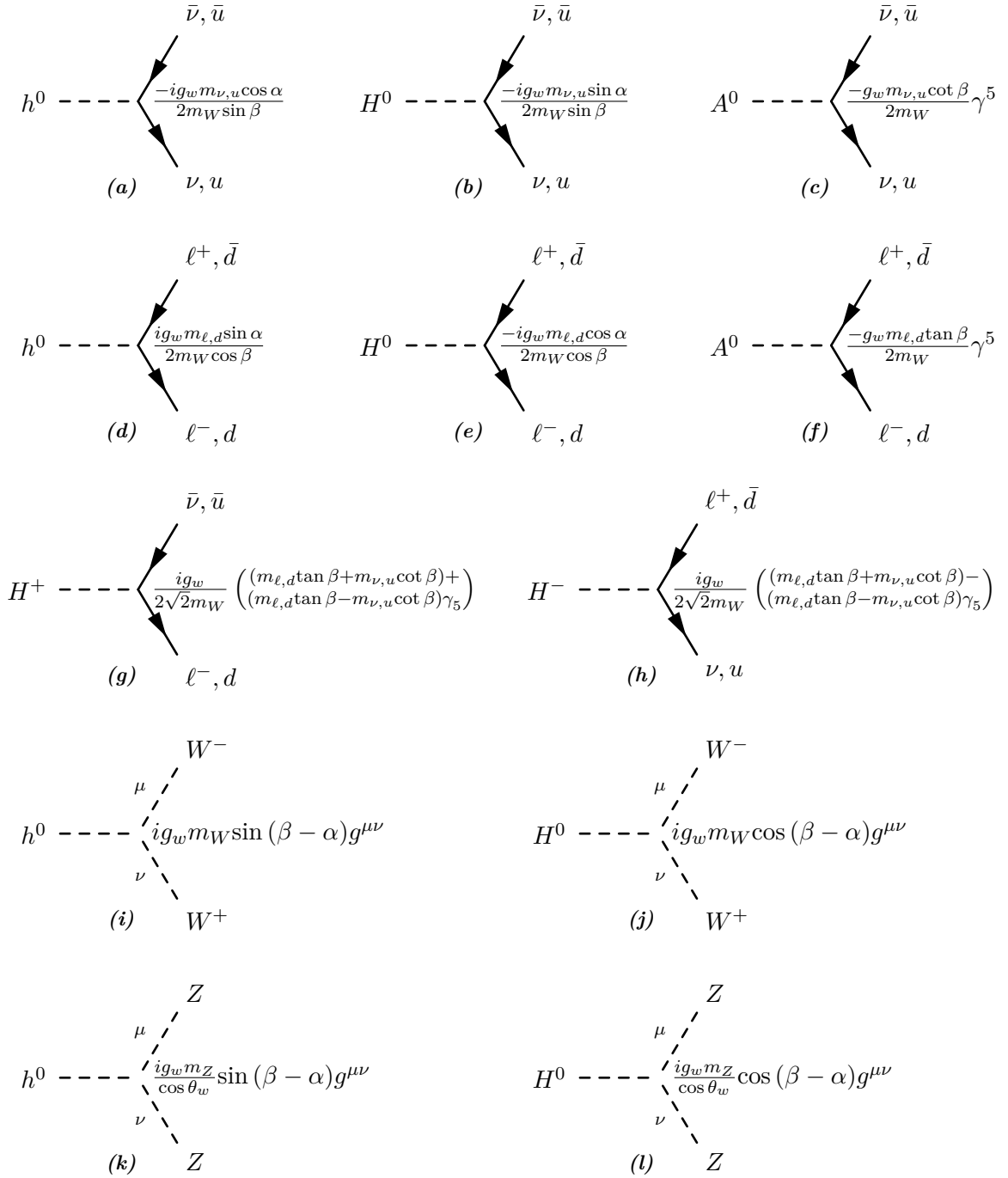


**Figure 2.10.:** Neutral MSSM Higgs boson couplings with (a)–(c)  $u$ -type fermions ( $u, c, t, \nu$ ) and (d)–(f)  $d$ -type fermions ( $d, s, b, \ell$ ). (g)–(h) Charged Higgs boson couplings with fermions. (i)–(l) Couplings of the neutral MSSM Higgs bosons with two gauge bosons. The vertices follow the conventions of Ref. [48].

MSSM Higgs boson phenomenology presented in Chap. 6. Vertices for the MSSM Higgs bosons coupling with  $u$ -type and  $d$ -type fermions as well as for the neutral Higgs bosons coupling with  $W$  and  $Z$  bosons pairs are given in Fig. 2.10. Note that the  $\mathcal{CP}$ -odd Higgs boson does not have  $W$  and  $Z$  boson pair couplings. These couplings are used in Chap. 3 when determining the spin correlations for  $\tau$  leptons produced from MSSM Higgs bosons, and in Chap. 6 for the MSSM Higgs boson phenomenology used to produce Higgs boson limits.

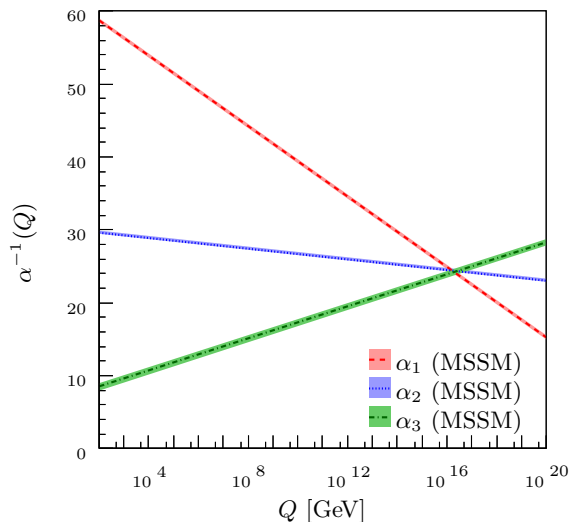


**Figure 2.11.:** Running of the couplings  $\alpha_i^{-1}(Q)$  given by Eqs. 2.76 and 2.77, using the MSSM coefficients of Eq. 2.89. The couplings are run upwards from their experimental values at  $m_Z \approx 10^2$  GeV from Eq. 2.75.

The MSSM, and SUSY in general, could resolve some of the current issues with the SM. Because SUSY maintains the gauge symmetries of the SM, it can also be unified with  $SU(5)$  theory. When this is done for the MSSM, the coefficients  $b_i$  for the couplings  $\alpha_i$  of Eq. 2.77 at the one-loop level become,

$$b_i = \left( \frac{33}{5}, 1, -3 \right) \quad (2.89)$$

which results in the forces unifying at an energy of  $\approx 2 \times 10^{16}$  GeV, as shown in Fig. 2.11. Additionally, the introduction of the superpartners provides the possibility of weakly interacting massive particles which could be dark matter candidates. Finally, the introduction of these superpartners stabilises the observable mass of the Higgs bosons, and solves the fine-tuning problem. However, the addition of superpartners requires even more model parameters than the SM, with a minimum of 124 parameters required for the MSSM, nearly five times the number of the SM [15]. Currently, no experiments have observed any evidence for SUSY, and with results from the LHC, SUSY is rapidly being excluded as a viable theory.

## 2.2. Monte Carlo Techniques

The groundwork for performing perturbative calculations of experimental observables such as the cross-section of Eq. 2.65 and the decay width of Eq. 2.68 has been laid in Sect. 2.1 for both the SM and the Higgs boson sector of the MSSM. However calculating these observables can be non-

trivial and sometimes impossible using only perturbative methods, and so advanced numerical methods, many of which rely on random sampling, must be employed. These numerical methods are often broadly classified as Monte Carlo. Within this section the general usage of Monte Carlo within high energy particle physics will be introduced with an emphasis given to the techniques required in Chap. 3.

Calculating a two-to- $n$  cross section or the width of an  $n$ -body decay requires a  $3n - 4$  dimensional integral over the momentum three-vectors of the  $n$  final particles, not including integration over quantum numbers such as helicity, flavour, or colour. One of the most robust methods to numerically perform large multi-dimensional integrals is Monte Carlo integration. In the simplest form of Monte Carlo integration for an  $n$ -dimensional integral,  $N$  random points are uniformly selected from some  $n$ -dimensional volume bounded by the limits of the integral, and the integrand is evaluated for each point. The running average of the integrand is computed, and the integral is then the product of the sampling volume and the average integrand.

The precision of Monte Carlo integration converges on the order of  $N^{-1/2}$ , where  $N$  is the number of integration points, and is not dependent upon the dimensionality of the integral. Comparatively, if the desired precision for a one-dimensional integral using quadrature methods is obtained with  $N$  points, then roughly  $N^n$  sampling points will be needed to maintain the same precision for an  $n$ -dimensional integral. Monte Carlo integration also can be terminated whenever a sufficient precision is reached and does not require complicated boundary conditions, unlike quadrature methods which require pre-determined boundaries and sampling points, and cannot be prematurely terminated [71].

Because particle scattering events are truly random by nature, Monte Carlo integration also has the advantage that each sampling point is a simulated scattering event, where the final state particles are fully specified. The correct distribution of random events, according to theory, can then be obtained by using the accept-and-reject method. An additional uniform random number is selected for each point; if this number is less than ratio of the integrand at that point over the maximum possible integrand, the event is accepted, otherwise it is rejected and another point is chosen. Consequently, the accepted sampling points from Monte Carlo integration can be passed directly through material simulations of experimental detectors. These simulations can then be used to estimate detector effects which are necessary for detector design and calibration, as well as for many physics analyses. Within the experimental high energy particle physics community, the term Monte Carlo is often synonymous with detector simulation.

Monte Carlo techniques are also well suited for extending the perturbative calculations of Sect. 2.1.1 to non-perturbative regimes, primarily for QCD. Specifically, Monte Carlo can handle infrared and collinear divergences in the radiation of massless particles, such as gluons and photons, as well provide models to combine quarks and gluons into hadrons. These techniques are known as parton showering and hadronisation respectively. Additionally, Monte Carlo can provide methods for calculating the soft QCD interactions of the underlying events from hadron collisions like those at the LHC.

General purpose Monte Carlo generators are programs that combine all of the techniques outlined above, and more, into a single coherent generation of particle physics events. A variety of

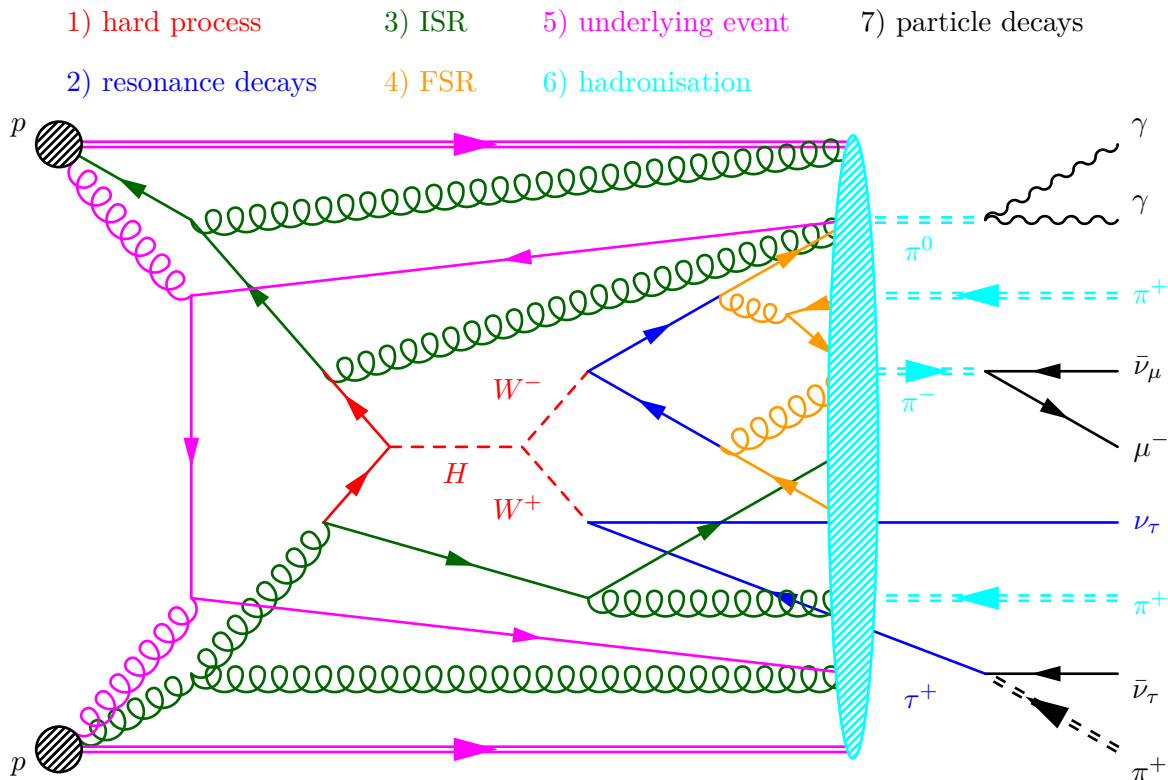


**Figure 2.12.:** Schematic of an example proton-proton to SM Higgs boson event produced by a general purpose Monte Carlo generator such as PYTHIA . The process begins with a  $q\bar{q} \rightarrow H \rightarrow WW$  hard process and then proceeds with resonance decays, FSR, ISR, the underlying event, hadronisation, and finally, particle decays.

generators are publicly available, each with advantages and disadvantages, but the three primary general purpose generators are PYTHIA 8 [10, 11, 12], HERWIG++ [72, 73], and SHERPA [74, 75]. A schematic of an example event produced by a general purpose Monte Carlo generator is provided in Fig. 2.12. This schematic is a simplification of the process, but attempts to provide all the salient features. The event generation begins with the calculation of the hard process by performing Monte Carlo integration of the cross-section formula of Eq. 2.65, where the matrix element is built from the elements of Sect. 2.1.2. In this example, the hard process is the production of an SM Higgs boson from a quark pair decaying into two  $W$  bosons.

Next, resonance decays are performed, again using perturbative QFT and Monte Carlo integration. Resonance decays occur on a time-scale shorter than the hadronisation of quarks and gluons, and are primarily decays of  $W$ ,  $Z$ , or Higgs bosons, or  $t$ -quarks. In Fig. 2.12, the  $W^-$  from the hard process decays into a quark pair, and the  $W^+$  into a  $\tau$  lepton and neutrino. After the hard process and resonance decays are simulated, the initial and final state quarks and gluons are dressed with parton showers which probabilistically simulate the radiation of gluons and quarks as determined by perturbative theory. The parton shower on the final state particles is labelled final state radiation (FSR) and the shower on the initial state particles is initial state radiation (ISR). Here, FSR is only performed on the decay products of the  $W^-$  as the  $W^+$  has not decayed to quarks or gluons. At this point electromagnetic final state radiation may also be

added, but is not included in Fig. 2.12.

In hadron-hadron collisions, interactions besides just the hard process will also occur between the partons of the hadrons and are categorised as underlying event. These interactions are typically via soft QCD and are simulated in Monte Carlo generators using non-perturbative models which must be tuned to data. Both FSR and ISR must also be applied to the underlying event, although they have not been included in Fig. 2.12. Following this, the partons from the resonance decays, parton showers, and underlying event are combined into bound hadrons using phenomenological models. This process is typically called hadronisation but is sometimes referred to as fragmentation. In the final step of the event, all unstable particles are decayed, using either perturbative QFT or models determined using non-perturbative theories. In Chap. 3 sophisticated models for the decays of  $\tau$  leptons are implemented in PYTHIA 8.

In the remainder of this section further details are given on parton showers in Sect. 2.2.1, hadronisation in Sect. 2.2.2, and particle decays in Sect. 2.2.3. The particle decay techniques are further used in Chap. 3 for the modelling of  $\tau$  lepton decays. For an excellent overview on all aspects of Monte Carlo event generation see Ref. [76], while for more specifics on the QCD aspects of parton showering and hadronisation see Ref. [61].

### 2.2.1. Parton Showers

Following the example of Refs. [76] and [61], consider the leading-order tree-level production of a quark pair from electron-positron annihilation as shown in Fig. 2.13(a). The cross-section for this diagram,  $\sigma_{e^+e^- \rightarrow q\bar{q}}$ , is finite and can be calculated using Eq. 2.65, Table 2.1, and the vertices of Figs. 2.4(a) and 2.4(b). However, because of confinement, the quarks of Fig. 2.13(a) must somehow interact through the strong force to produce stable hadrons which are then experimentally observable. The idea behind the parton shower is to evolve the quarks of Fig. 2.13(a) from the energy scale at which they are produced, using perturbative QCD, to the non-perturbative QCD regime where hadronisation can then be applied to create bound final states.

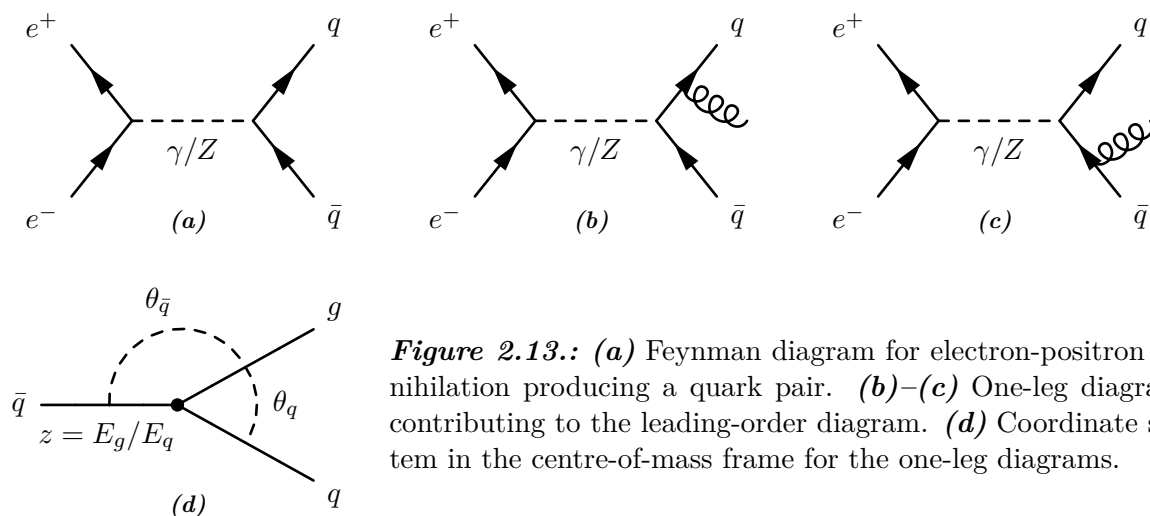


**Figure 2.13.:** (a) Feynman diagram for electron-positron annihilation producing a quark pair. (b)–(c) One-leg diagrams contributing to the leading-order diagram. (d) Coordinate system in the centre-of-mass frame for the one-leg diagrams.

In Fig. 2.13(a) the quarks can interact through the strong force via either a real or virtual

emission of a gluon. The real gluon emission results in an additional leg added on to the tree-level diagram in the two configurations of Figs. 2.13(b) and 2.13(c). The differential cross-section for the sum of the three diagrams from Figs. 2.13(a) through 2.13(c) can be approximated as,

$$d\sigma_{e^+e^- \rightarrow q\bar{q}g} \approx \sigma_{e^+e^- \rightarrow q\bar{q}} \left( \frac{2 d\cos\theta_q}{\sin^2\theta_q} \right) \left( \frac{\alpha_s}{2\pi} \right) \left( \frac{N_c^2 - 1}{2N_c} \right) \left( \frac{1 + (1-z)^2}{z} \right) dz \quad (2.90)$$

where the coordinates are summarised in Fig. 2.13(d) and only the divergent terms are included but with full interference. Here,  $z$  is the fractional energy of the gluon with respect to the quark energy  $E_g/E_q$ ,  $\theta_q$  is the opening angle between the quark and gluon in the centre-of-mass frame, and  $N_c = 3$  is the number of colour charges. This differential cross-section diverges for three limits of the phase-space: when  $z$  approaches zero, when  $\theta_q$  approaches zero, and when  $\theta_q$  approaches  $\pi$ .

The first divergence is an infrared divergence where the energy of the emitted gluon is much less than that of the emitting quark,  $E_g \ll E_q$  and the divergence does not depend on  $\theta_q$ . Consequently, this divergence can be attributed to the interference between the two diagrams of Figs. 2.13(b) and 2.13(c). The second divergence occurs when a gluon is emitted in the same direction as the quark, while the third divergence occurs when a gluon is emitted in the same direction as the anti-quark. Both of these emissions are collinear divergences which can be interpreted as independent emissions of the gluon by either the quark or the anti-quark and so Eq. 2.90 can be factorised as,

$$d\sigma_{e^+e^- \rightarrow q\bar{q}g} \approx \sigma_{e^+e^- \rightarrow q\bar{q}} \sum_i \left( \left( \frac{d\theta_{p_i}^2}{\theta_{p_i}^2} \right) \left( \frac{\alpha_s}{2\pi} \right) \left( \frac{N_c^2 - 1}{2N_c} \right) \left( \frac{1 + (1-z)^2}{z} \right) dz \right) \quad (2.91)$$

where  $\theta_{p_i}$  is the opening angle between parton  $p_i$  and the gluon. Here the summation is over the two partons, the quark and the anti-quark. Note that this cross-section only accounts for the collinear divergences.

The relation of Eq. 2.91 can be generalised to any scattering process resulting in final state quarks or gluons as,

$$d\sigma_{A \rightarrow Bb_j} \approx \sigma_{A \rightarrow B} \sum_i \left( \left( \frac{d\theta_{b_i}^2}{\theta_{b_i}^2} \right) \mathcal{P}_{b_j b_i}(z, \alpha_s) dz \right) \quad (2.92)$$

where  $b_i$  are the final state partons of  $B$  with flavour  $i$  which can emit a parton of flavour  $j$ . The splitting functions  $\mathcal{P}_{b_j b_i}$  are the same splitting functions used for the DGLAP evolution of Eq. 2.79 and are given by,

$$\begin{aligned} \mathcal{P}_{gq}(z, \alpha_s) &= \left( \frac{\alpha_s}{2\pi} \right) \left( \frac{N_c^2 - 1}{2N_c} \right) \left( \frac{1 + (1-z)^2}{z} \right) & (q \rightarrow gq) \\ \mathcal{P}_{gg}(z, \alpha_s) &= \left( \frac{\alpha_s}{2\pi} \right) (2N_c) \left( \frac{1-z}{z} + \frac{z}{1-z} + z(1-z) \right) & (g \rightarrow gg) \\ \mathcal{P}_{q\bar{q}}(z, \alpha_s) &= \left( \frac{\alpha_s}{2\pi} \right) \left( \frac{1}{2} \right) (z^2 + (1-z)^2) & (g \rightarrow q\bar{q}) \end{aligned} \quad (2.93)$$



$$\mathcal{P}_{qq}(z, \alpha_s) = \left(\frac{\alpha_s}{2\pi}\right) \left(\frac{N_c^2 - 1}{2N_c}\right) \left(\frac{1+z^2}{1-z}\right) \quad (q \rightarrow qg)$$

in their helicity-averaged form [60]. See Ref. [61] for their helicity-dependent form,  $\mathcal{P}_{b_j b_i}(z, \phi, \alpha_s)$ , where  $\phi$  is the azimuthal angle of the splitting and the helicity dependent  $\mathcal{P}_{gq}$  can be found by  $\mathcal{P}_{gq}(1-z, \phi, \alpha_s)$ . The splitting functions of Eq. 2.93 correspond to the splitting process given in brackets after each function.

### Final State Showers

The term  $\theta^2$  of Eq. 2.92 can be replaced by the virtuality  $q^2$ , where  $q$  is the momentum of the parton being split. Because the splitting parton is from some hard process,  $q^2$  must be less than some maximum virtuality  $Q^2$  given by the hard process scale. Additionally there is some virtuality scale  $Q_0^2$  where the emission of a parton cannot be physically resolved from the emitting parton, typically on the order of 1 GeV<sup>2</sup>. The probability of a parton not emitting between the virtualities  $q_1^2$  and  $q_2^2$  is given by a Sudakov form factor,

$$\Delta_{ij}(q_1^2, q_2^2) = \exp\left(-\int_{q_2^2}^{q_1^2} \frac{1}{q^2} \int_{Q_0^2/q^2}^{1-Q_0^2/q^2} \mathcal{P}_{ji}(z, \alpha_s) dz dq^2\right) \quad (2.94)$$

where the probability of not emitting a resolvable parton is then  $\Delta_{ij}(Q^2, Q_0^2)$ .

A final state parton shower (FSR) is performed by uniformly picking a random number  $r$  between 0 and 1, and solving  $\Delta_{ij}(Q^2, q^2) = r$  for  $q^2$ . If  $q^2$  is above  $Q_0^2$  an emission is generated at the scale  $q^2$ , otherwise the shower is terminated. This process is iteratively applied until the condition  $q^2 < Q_0^2$  is met and terminates the process for each showerable parton. The parton shower includes not only the effect of tree-level diagrams with unresolvable collinear emissions, but also the effect of one-loop diagrams, as a non-emission can either be an unresolvable parton or a virtual emission. A large number of issues regarding final state parton showers have not been addressed here, including soft gluon emission, and further details can be found in Ref. [76].

### Initial State Showers

Just as final state partons are expected to radiate, initial state partons leading up to the hard process are also expected to radiate. Consequently, a process similar to the final state shower could be applied to determine these emissions, and ultimately, the partons used in the hard process. Using the same prescription as forward evolution for final state showers, partons could be randomly selected using the incoming PDFs of the hadrons and evolved downwards until the parton shower is terminated with the condition  $q^2 < Q_0^2$  for each branch. However, this would result in a large number of events generated where the partons after showering would not be suitable for use in the hard process of choice, *e.g.*  $W$ ,  $Z$ , or Higgs boson production. A more efficient method is to choose the partons of the hard process first using  $x_{a_1} x_{a_2} Q^2 \approx s$  where  $x_{a_1}$  and  $x_{a_2}$  are the longitudinal momentum fractions of the two incoming partons,  $Q^2$  is the

centre-of-mass energy of the hard process, and  $s$  is the centre-of-mass energy of the two colliding hadrons. The emissions are then evolved backward, starting with a large  $Q^2$  and small  $x$ , and move towards a smaller  $q^2$  and larger  $x$  [77, 78].

The Sudakov form factor of Eq. 2.94 must be modified for backwards evolution by,

$$\Delta_{ij}(q_1^2, q_2^2, x) = \exp \left( - \int_{q_2^2}^{q_1^2} \frac{1}{q^2} \int_{Q_0^2/q^2}^{1-Q_0^2/q^2} \mathcal{P}_{ij}(z, \alpha_s) \left( \frac{x}{zx} \right) \left( \frac{f(x/z, q^2, j)}{f(x, q^2, i)} \right) dz dq^2 \right) \quad (2.95)$$

where  $f(x, q^2, i)$  is the parton distribution function from Sect. 2.1.3 for parton  $i$  at momentum transfer  $x$  and energy scale  $q^2$ . The initial state parton shower (ISR) is then performed by picking a uniform random number  $r$  between 0 and 1 and solving  $\Delta_{ij}(Q^2, q^2, x) = r$  for  $q^2$ , where  $x$  is the momentum transfer for the parton from the hard process being showered. If  $q^2$  is above the cut-off  $Q_0^2$  then an emission is generated, and the process is iteratively continued, just as is done for a final state parton shower. Now, however, the momentum fraction  $x$  must be recalculated for each step in the parton shower at the new lower  $q^2$ . By this process, the partons are evolved backwards to a low energy scale with high momentum transfer. Further details on how final and initial state parton showers are matched with the hard process can be found in Ref. [76].

### 2.2.2. Hadronisation

Hadronisation is the process by which coloured quarks and gluons from the initial and final state showers are combined to produce colourless hadrons which are then either decayed or observable in the final state. The hadronisation step of a general purpose Monte Carlo generator involves all quarks and gluons from the event, including particles from the underlying event and beam remnants, which are not discussed here. Because of QCD confinement, hadronisation must be performed via phenomenological models, although these models are based on behaviour observed in non-perturbative QCD such as lattice QCD. Currently two major hadronisation models are used in general purpose Monte Carlo generators, the Lund string fragmentation model of Ref. [79] and the cluster model of Ref. [80]. The PYTHIA 8 event generator uses the string model, while HERWIG++ and SHERPA use the cluster model. Early versions of both models were originally introduced in Ref. [81] but hadronisation studies did not begin in earnest until an iterative process for jet production was outlined in Ref. [82]. Note that in many of these papers the terms hadronisation and fragmentation are used interchangeably, although occasionally fragmentation is used to denote both parton showers and hadronisation.

#### String Model

The string model is based on the linear confinement of quarks at large distances observed from lattice QCD results; for a study of three quark systems see *e.g.* Ref. [83]. These results have shown that the potential for a static multi-quark system can be modelled with the sum of a

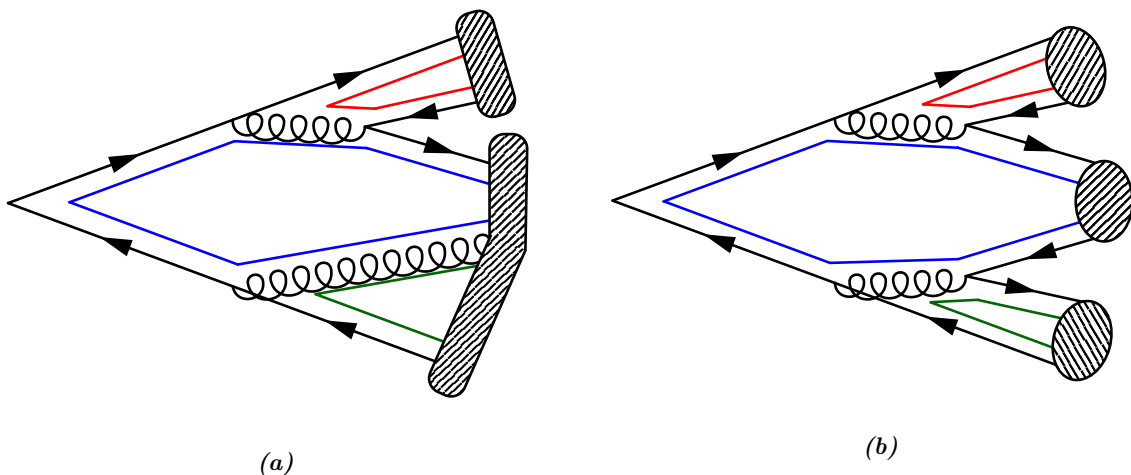


**Figure 2.14.:** Schematic of the final state parton shower from Fig. 2.12 with (a) string hadronisation and (b) cluster hadronisation models applied. For the string model the lower gluon creates a kink in the string, while for the cluster model, the gluon is forced to split. The coloured lines indicate the colour flow of the event.

linear and Coulomb potential,

$$V \approx \kappa r - \frac{4\alpha_s}{3r} \quad (2.96)$$

where the linear potential is thought to arise from the self-interaction of the gluon. Here,  $r$  is the distance between the quarks and  $\kappa$  is the string constant. The Coulomb potential is only significant at small distances, and in the string hadronisation model, is neglected, as it is expected only to affect the properties of the hadrons and not their production distribution. In the string model, quark/anti-quark pairs are connected via colour flux tubes or strings where the potential arising from the string is the linear portion of the potential,  $V = \kappa r$ . Here, the string constant  $\kappa$  is estimated to have an energy per unit length of approximately  $0.2 \text{ GeV}^2$  from experimental measurements of hadron masses [10].

After the hard process, parton shower, and underlying event steps of a general purpose Monte Carlo generator, the quarks, anti-quarks, and gluons are divided into colour singlets dictated by the colour flow of the event, assuming the large  $N_c$  limit. In this limit, a unique colour is introduced for each QCD splitting within the event. For simplicity, consider a colour singlet consisting of a quark and anti-quark,  $q_0\bar{q}_0$ , and connected by a colour string. As the two partons separate from each other, the potential increases linearly until the string splits into another quark/anti-quark pair,  $q_1\bar{q}_1$ , as dictated by a fragmentation function. This split produces two new colour singlets,  $q_0\bar{q}_1$  and  $q_1\bar{q}_0$ , each connected by their own colour string. The process can be then iterated until the invariant masses of the colour singlets are small enough to form mesons. A system which splits  $n$  times will produce  $n + 1$  final state mesons,  $q_0\bar{q}_1$  through  $q_n\bar{q}_0$ . Baryons can also be produced in the string model by the creation of di-quark/anti-di-quark pairs in addition to the creation of just quark/anti-quark pairs, although the popcorn models of Refs. [84] and [85] are more commonly used to handle baryon production.

Gluons are incorporated into the string model by attaching them to colour strings between quark/anti-quark pairs. This produces kinks in the strings that influence the kinematics of the string splittings. With the inclusion of gluons in the string model, only a few parameters are required to produce the final state kinematics of the hadrons, and these kinematics are well matched by experimental observation, including the string effect first observed by the JADE experiment in Ref. [86]. However, a large number of parameters are required to describe the flavours of the quark/anti-quark pairs produced in the string splittings, and so the flavour composition of the final state hadrons is not predictive and oftentimes does not match well with experimental observation. An example schematic of the string model applied to the final state parton shower of Fig. 2.12 is given in Fig. 2.14(a).

### Cluster Model

The cluster model is based on the property of pre-confinement from Ref. [87], where the colour singlet combinations of partons, or clusters, have an invariant mass distribution that does not depend upon the scale of the hard process,  $Q^2$ , but rather is only dependent on the QCD scale and the parton shower cut-off scale  $Q_0^2$ . The large  $N_c$  limit is used to determine the colour flow of the partons and form the colour singlet clusters of quarks where the gluons carry colour/anti-colour lines and the quarks and anti-quarks carry either colour or anti-colour. In the cluster hadronisation model, the clusters are formed by forcing all gluons to split into quark/anti-quark pairs which enhances the  $g \rightarrow q\bar{q}$  splitting of Eq. 2.93. Some measurements of jet profiles, such as Ref. [88], indicate that perhaps this gluon splitting enhancement is experimentally supported.

After the clusters are formed from the final parton colour singlets, they are decayed via a series of two-body decays until stable final state hadrons are reached. The kinematics of the hadrons from the simple cluster hadronisation model do not match experiment well, and require a variety of additional phenomenological mechanisms and parameters to be introduced. However, the flavour composition of the final state hadrons is controlled by only a few parameters, and produces a flavour spectrum that provides a better match to experiment than the string hadronisation model. An example schematic of the cluster model applied to the final state parton shower of Fig. 2.12 is given in Fig. 2.14(b).

### 2.2.3. Particle Decays

After hadronisation, a set of colourless final state particles have been produced, but these particles themselves might still decay. For example, a pion produced from the hadronisation process might decay into a muon and neutrino, or a muon produced from the hard process might decay into an electron or neutrino. These decays can then be continued until stable particles terminate the decay chain. However, in typical high energy particle physics experiments the particles produced are travelling near the speed of light, so particles that would quickly decay in their own rest frame, such as muons, are considered stable in the laboratory frame. Consequently, most general purpose Monte Carlo generators provide a variety of options for when particles should be decayed. By default, all particles with a mean lifetime times the speed of light  $c\tau$

less than 1 m are decayed by PYTHIA 8, and all other particles are set as stable. With this default behaviour, particles such as the  $\tau$  lepton and neutral pion are decayed, while particles such as the muon and charged pion are not. For full detector simulation, the final state particles after decays by the Monte Carlo generator are passed to the simulation software, where material interactions are then modelled.

In the simplest form of particle decays, a list of available decay channels is supplied for each particle. Each decay channel specifies the decay products of the channel, as well as the relative decay width for the channel with respect to the total decay width of the particle, *i.e.* the branching fraction for that channel. Typically the branching fractions for the decay channels are set from experimental observation and are not calculated from theory, unlike for resonance decays, which must be calculated for the invariant mass of the resonance. The decay channel for the particle is randomly selected from the available decay channels, weighted by their branching fractions. The  $n$ -body decay of the particle is then performed, where the decay products are kinematically distributed according to isotropic phase-space.

If the matrix element for the decay is known from either perturbative theory or some phenomenological model, a more realistic distribution of the kinematics for the decay products can be produced by weighting the decays by the matrix element for the decay channel. Additionally, if the kinematics of the decay are influenced by helicity correlations from the hard process, further weighting can be applied. In the remainder of this section, the method used for determining isotropic phase-space for  $n$ -body decays used in Chap. 3, as well as the helicity correlation algorithm used in Chap. 3 are described.

### Phase-Space

One of the requirements of any decay algorithm is the ability to distribute an  $n$ -body decay with isotropic phase-space, *i.e.* the kinematic distribution of the decay products assuming the decay matrix element,  $\mathcal{M}$ , is unity. For decays involving only massless decay products, the random momenta and boosts (RAMBO) algorithm of Ref. [89] is completely efficient. The RAMBO approach randomly generates the momenta for the  $n$  decay products and then rescales their invariant mass to match the decaying particle mass. However, this rescaling is not possible for massive decay products, and so the RAMBO approach is not suitable for  $\tau$  leptons. Instead, the phase-space generator for  $\tau$  lepton decays implemented in PYTHIA 8 is based on the  $m$ -generator algorithm of Ref. [90].

The principle behind the  $m$ -generator algorithm is that two-body phase-space can be distributed in the rest frame of the decaying particle by uniformly sampling  $\phi$  and  $\cos\theta$  where  $\phi$  and  $\theta$  are the azimuthal and polar angles of the decay products. Consequently, an  $n$ -body decay can be written as a series of intermediate  $n - 1$  two-body decays, where each two-body decay is performed in the rest frame of the decaying intermediate particle.

The phase-space element for a two-body decay, using Eq. 2.68, is given by,

$$d\Phi_2(q_0, q_1, q_2) = \left( \frac{1}{(2\pi)^2 2^2} \right) \delta(q_0 - q_1 - q_2) \frac{d\vec{q}_1}{E_1} \frac{d\vec{q}_2}{E_2} \quad (2.97)$$

where  $q_0$ ,  $q_1$ , and  $q_2$  are the momentum four-vectors for the decay particle and its two decay products, and  $E_1$  and  $E_2$  are the energies of the two decay products. In a similar fashion the three-body phase-space element can be written as,

$$d\Phi_3(q_0, q_1, q_2, q_3) = \left( \frac{1}{(2\pi)^5 2^3} \right) \delta(q_0 - q_1 - q_2 - q_3) \frac{d\vec{q}_1}{E_1} \frac{d\vec{q}_2}{E_2} \frac{d\vec{q}_3}{E_3} \quad (2.98)$$

where  $q_3$  is the momentum four-vector for the third decay product. An intermediate decay product with momentum  $q_{12} = q_1 + q_2$  can be introduced and the three-body phase-space element can be rewritten as,

$$\begin{aligned} d\Phi_3(q_0, q_1, q_2, q_3) &= \left( \frac{1}{(2\pi)^5 2^3} \right) \delta(q_0 - q_1 - q_2 - q_3) \frac{d\vec{q}_1}{E_1} \frac{d\vec{q}_2}{E_2} \frac{d\vec{q}_3}{E_3} \\ &\quad \delta(q_{12} - q_1 - q_2) \delta(q_{12}^2 - m_{12}^2) dq_{12} dm_{12}^2 \\ &= \left( \frac{2}{\pi} \right) d\Phi_2(q_0, q_{12}, q_3) m_{12} dm_{12} d\Phi_2(q_{12}, q_1, q_2) \end{aligned} \quad (2.99)$$

where in the second step, the three-body phase-space element has been expressed in terms of the two-body decay  $p_0 \rightarrow p_{12}p_3$ , the two-body decay  $p_{12} \rightarrow p_1p_2$ , and the intermediate mass  $m_{12}^2$ . Here  $p_i$  indicates particle  $i$ . The process can then be recursively applied to  $n$ -body phase-space,

$$\begin{aligned} d\Phi_n(q_0, \dots, q_n) &= \left( \frac{2}{\pi} \right)^{n-2} d\Phi_2(q_0, q_{1\dots n-1}, q_n) m_{1\dots n-1} dm_{1\dots n-1} \\ &\quad \dots d\Phi_2(q_{123}, q_{12}, q_3) m_{12} dm_{12} d\Phi_2(q_{12}, q_1, q_2) \end{aligned} \quad (2.100)$$

where  $n - 1$  two-body decays are performed with  $n - 2$  intermediate decay products.

The two-body phase-space element of Eq. 2.97 can be rewritten in terms of invariant masses,

$$d\Phi_2(m_0^2, m_1^2, m_2^2) = \left( \frac{1}{(2\pi)^2 2^2} \right) \frac{\sqrt{\mathcal{K}(m_0^2, m_1^2, m_2^2)}}{2m_0^2} d\Omega_0 \quad (2.101)$$

using the centre-of-mass frame of the two-body decay where  $d\Omega_0$  is the solid angle element for the rest frame of the decaying particle  $p_0$  and,

$$\mathcal{K}(m_0^2, m_1^2, m_2^2) = (m_0^2 - m_1^2 - m_2^2)^2 - 4m_1^2 m_2^2 \quad (2.102)$$

is the Källén triangle function. The  $n$ -body phase-space element of Eq. 2.100 then becomes,

$$\begin{aligned} d\Phi_n(m_0^2, \dots, m_n^2) &= \left( \frac{1}{m_0 2^{4n-2} \pi^{3n-4}} \right) \frac{\sqrt{\mathcal{K}(m_0^2, m_{1\dots n-1}^2, m_n^2)}}{m_0} dm_{1\dots n-1} d\Omega_0 \\ &\quad \dots \frac{\sqrt{\mathcal{K}(m_{123}^2, m_{12}^2, m_3^2)}}{m_{123}} dm_{12} d\Omega_{123} \\ &\quad \frac{\sqrt{\mathcal{K}(m_{12}^2, m_1^2, m_2^2)}}{m_{12}} d\Omega_{12} \end{aligned} \quad (2.103)$$

which is differential in terms of the solid angle elements  $d\Omega$  and the intermediate invariant mass elements  $dm$ .

The relationship of Eq. 2.103 can then be translated into a Monte Carlo algorithm for an  $n$ -body decay where first the intermediate masses are randomly sampled, and then the solid angles. To sample the intermediate masses, select  $n - 2$  random numbers  $r_1$  to  $r_{n-2}$  and order them so that  $r_i < r_{i+1}$ . The  $n - 2$  intermediate masses  $m_{12}$  through  $m_{1\dots n-1}$  can then be generated by,

$$m_{1\dots i} = \sum_j^i m_j + r_{i-1} \Delta m, \quad \Delta m = m_0 - \sum_j^n m_j \quad (2.104)$$

where all summation indices begin at 1 and  $i$  runs between 2 and  $n - 1$ . This set of intermediate masses then covers the intermediate mass space with a weight,

$$\mathcal{J} = \frac{\sqrt{\mathcal{K}(m_0^2, m_{1\dots n-1}^2, m_n^2)}}{m_0} \dots \frac{\sqrt{\mathcal{K}(m_{123}^2, m_{12}^2, m_3^2)}}{m_{123}} \frac{\sqrt{\mathcal{K}(m_{12}^2, m_1^2, m_2^2)}}{m_{12}} \quad (2.105)$$

which is proportional to the integrand of Eq. 2.103. The invariant masses can then be randomly sampled by using the accept-and-reject method where an additional uniform random number  $r_0$  between 0 and 1 is selected, and if  $r_0$  is less than  $\mathcal{J}/\mathcal{J}_{\max}$ , the masses are accepted. Here,  $\mathcal{J}_{\max}$  is the maximum  $\mathcal{J}$  which can be determined empirically.

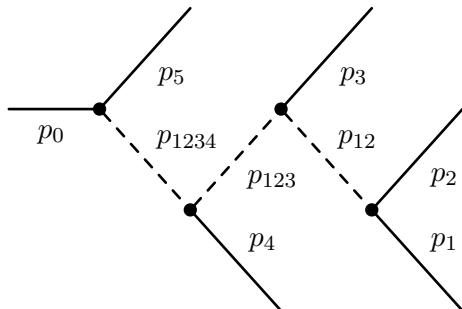


**Figure 2.15.:** Example of the  $m$ -generator algorithm for a five-body decay where the particle  $p_0$  decays into its products  $p_1$  through  $p_5$  via the intermediate particles  $p_{1234}$ ,  $p_{123}$ , and  $p_{12}$  indicated by the dashed lines. Each vertex represents a two-body decay and the solid lines represent the real particles.

After the intermediate masses have been sampled, the individual two-body decays can then be performed. The decay  $p_0 \rightarrow p_{1\dots n-1} p_n$  is first performed, in the rest frame of  $p_0$ . This is done by uniformly sampling  $\phi$  between 0 and  $2\pi$  and  $\cos \theta$  between  $-1$  and  $1$ . The momenta for  $q_{1\dots n-1}$  and  $n$  are then fully determined by these two angles. Next the decay,  $p_{1\dots n-1} \rightarrow p_{1\dots n-2} p_{n-1}$  is performed in the rest frame of  $p_{1\dots n-1}$  using the same method for sampling  $\phi$  and  $\cos \theta$ . The decay products are then boosted back into the rest frame of  $p_0$ . This process continues until all  $n - 1$  two-body decays have been performed. A schematic of the process for a five-body decay is shown in Fig. 2.15, where each solid line indicates either the decaying particle  $p_0$  or one of its decay products, and each dashed line indicates an intermediate particle. Each vertex represents a two-body decay.

### Helicity Correlations

Using the  $m$ -generator algorithm of Eqs. 2.104 and 2.105, an  $n$ -body isotropic decay can be performed. Furthermore, the decay matrix element for the decay,  $\mathcal{M}$ , can be calculated and used to weight the isotropic decays. However, this does not take into account helicity correlations between the decays of particles within the event. This is of particular importance for  $\tau$  lepton decays where the helicities of the  $\tau$  leptons play an important role in their decays. The helicity correlation algorithm implemented in PYTHIA 8 for the  $\tau$  lepton decays of Chap. 3, is described here and is based on the algorithm expanded by Richardson in Ref. [91] and proposed in its original form by Collins and Knowles in Refs. [92] and [93].

First, the momenta of the two-to- $n$  hard process is calculated using the matrix element weight,

$$\mathcal{W} = \rho_{1\kappa_1\kappa'_1}\rho_{2\kappa_2\kappa'_2}\mathcal{M}_{\kappa_1\kappa_2\lambda_1\dots\lambda_n}\mathcal{M}_{\kappa'_1\kappa'_2\lambda'_1\dots\lambda'_n}^\dagger \prod_i^n D_{i\lambda_i\lambda'_i} \quad (2.106)$$

where  $\kappa_i$  is the helicity of incoming particle  $p_i$ ,  $\lambda_i$  is the helicity of outgoing particle  $p_i$ ,  $\rho_i$  is the helicity density matrix for the incoming particle  $p_i$ ,  $\mathcal{M}$  is the helicity matrix element for the hard process, and  $D_i$  is the decay matrix for the outgoing particle  $p_i$ . Here, repeated indices are summed over and the product of  $D_i$  is over all  $n$  outgoing particles. The helicity density matrix for a two helicity state incoming particle is given by,

$$\rho_{\kappa\kappa'} = \begin{pmatrix} \frac{1}{2}(1 + \mathcal{P}_z) & 0 \\ 0 & \frac{1}{2}(1 - \mathcal{P}_z) \end{pmatrix} \quad (2.107)$$

where  $\mathcal{P}_z$  is the longitudinal polarisation of the incoming particle with respect to the beam axis. The decay matrices  $D_i$  for the outgoing particles begin as the identity matrix.

After the hard process is generated, one of the outgoing particles  $p_j$  is chosen, and its helicity density matrix  $\rho_j$  is calculated by,

$$\rho_{j\lambda_j\lambda'_j} = \rho_{1\kappa_1\kappa'_1}\rho_{2\kappa_2\kappa'_2}\mathcal{M}_{\kappa_1\kappa_2;\lambda_1\dots\lambda_n}\mathcal{M}_{\kappa'_1\kappa'_2;\lambda'_1\dots\lambda'_n}^\dagger \prod_{i \neq j}^n D_{i\lambda_i\lambda'_i} \quad (2.108)$$

and normalised,  $\rho_j = \rho_j / \text{Tr}(\rho_j)$ , such that its trace is one. An  $m$ -body decay channel for particle  $p_j$  is selected, and then  $p_j$  is decayed according to the matrix element weight,

$$\mathcal{W} = \rho_{j\lambda_0\lambda'_0}\mathcal{M}_{\lambda_0\lambda_1\dots\lambda_m}\mathcal{M}_{\lambda'_0\lambda'_1\dots\lambda'_m}^\dagger \prod_k^m D_{k\lambda_k\lambda'_k} \quad (2.109)$$

where  $\mathcal{M}$  is now the helicity matrix element for the decay of  $p_j$ ,  $\lambda_0$  is the helicity of  $p_j$ , and  $\lambda_k$  is the helicity of decay product  $p_k$ . Given that the decay channel of  $p_j$  is an  $m$ -body decay, the product of  $D_k$  runs from 1 to  $m$ .

After decaying  $p_j$ , one of its  $m$  outgoing particles  $p_l$  is picked at random and the helicity



density matrix for this particle is calculated by,

$$\rho_{l\lambda_l\lambda'_l} = \rho_{j\lambda_0\lambda'_0} \mathcal{M}_{\lambda_0;\lambda_1\dots\lambda_m} \mathcal{M}_{\lambda'_0;\lambda'_1\dots\lambda'_m}^\dagger \prod_{k \neq l}^m D_{k\lambda_k\lambda'_k} \quad (2.110)$$

and then normalised such that the trace of the helicity density matrix is one. Here  $\mathcal{M}$  is still the helicity matrix element for the decay of  $p_j$  and  $D_k$  is the decay matrix for outgoing particle  $p_k$  from the decay of  $p_j$ . The process of selecting a particle from the decay, calculating the helicity density matrix using Eq. 2.110, and then decaying the particle using the weight of Eq. 2.109, continues until a particle is reached where all the decay products are stable. Up until this point, all decay matrices  $D$  have been initialised as the identity matrix. Assuming that all the decay products  $p_k$  of particle  $p_j$  have either already been decayed or are stable, the decay matrix for  $p_j$  is then updated by,

$$D_{j\lambda_0\lambda'_0} = \mathcal{M}_{\lambda_0;\lambda_1\dots\lambda_m} \mathcal{M}_{\lambda'_0;\lambda'_1\dots\lambda'_m}^\dagger \prod_k^m D_{k\lambda_k\lambda'_k} \quad (2.111)$$

which must be normalised such that the trace of  $D_j$  is one.

After the end of a decay chain is reached, a new undecayed particle from the decay prior to the terminating decay is randomly selected. If this particle is from the hard process, Eq. 2.108 is used to calculate its helicity density matrix, otherwise Eq. 2.110 is used. Note that at this point, the decay matrices  $D$  used in the calculation of the helicity density matrix are no longer necessarily identity matrices, and for particles that have already been decayed, are given by Eq. 2.111. The process of performing decays using the weight of Eq. 2.109 until reaching a terminating decay with only stable particles, tracing backwards and calculating the decay matrix of the prior decay with Eq. 2.111, and then moving forward again, is continued until all particles in the event have been decayed.

### 3. Tau Leptons

The  $\tau$  lepton, unlike the lighter muon and electron, can decay both leptonically and hadronically. Consequently, the  $\tau$  lepton provides an important bridge between electroweak and QCD theory. Additionally, the low mass of the  $\tau$  lepton with respect to the energy regime of perturbative QCD places the hadronic decay of the  $\tau$  lepton at the border of non-perturbative and perturbative regimes, allowing  $\tau$  lepton decays to be modelled through a variety of theories including both lattice QCD and chiral perturbation theory [94, 95].

While the hadronic decay of the  $\tau$  lepton is important for low energy QCD,  $\tau$  lepton decays are also important for both direct and indirect Higgs boson searches. Within the SM, the minimal Higgs mechanism of Sect. 2.1.2 predicts a branching fraction of  $\approx 10\%$  for the Higgs boson decaying into a  $\tau$  lepton pair within the mass window of 115 to 140 GeV. For large portions of parameter space in the MSSM, the neutral Higgs bosons are predicted to have a branching fraction to  $\tau$  lepton pairs of  $\approx 10\%$  and the charged Higgs boson can decay almost exclusively to a  $\tau$  lepton and  $\tau$  lepton neutrino [96]. Further Higgs boson phenomenology is explored in Chap. 6.

Because of the role the  $\tau$  lepton plays in new physics searches, it is important that current Monte Carlo event generators handle the decay of the  $\tau$  lepton using the best possible models. The phase-space distribution of the  $\tau$  lepton decay products can be heavily influenced by the polarisation of the  $\tau$  lepton, and so it is also important to ensure that proper spin correlations between the  $\tau$  leptons and their decay products are modelled. Currently, the HERWIG++ [72, 73] event generator incorporates  $\tau$  lepton decays with full correlation effects [97] while the SHERPA [74, 75] event generator incorporates approximate correlation effects [98]. The  $\tau$  lepton specific event generator TAUOLA performs only  $\tau$  lepton decays but provides approximate correlation effects for a variety of  $\tau$  lepton decays and can be interfaced with many current event generators [99].

For PYTHIA 6 and previous versions of PYTHIA 8 (at or below 8.145), leptonic  $\tau$  lepton decays were distributed by the standard vector-axial matrix element while hadronic decays were distributed by phase-space weighted by a factor of  $2E_{\nu_\tau}/m_\tau(3 - 2E_{\nu_\tau})$ , where  $E_{\nu_\tau}$  is the energy of the neutrino in the rest frame of the  $\tau$  lepton [10]. No polarisation information in the decays of the  $\tau$  lepton are included in PYTHIA 6. In this chapter the implementation of well modelled matrix elements with full spin correlations using the algorithm of Sect. 2.2.3 for  $\tau$  lepton decays in PYTHIA 8 is described.

The spin correlation algorithm does not implement the full recursion of the algorithm of Sect. 2.2.3, as this is not necessary for  $\tau$  lepton decays, and assumes that the  $\tau$  leptons are produced directly from the hard process of the event. The isotropic phase-space of the  $\tau$  lepton

decays is distributed using an implementation of the  $m$ -generator outlined in Sect. 2.2.3. The matrix elements used in both the helicity correlation algorithm and decay calculations are built from the Feynman rules of Table 2.1 and the vertices from Figs. 2.3, 2.4, 2.6, and 2.10.

In Sect. 3.1 the  $\tau$  lepton production matrix elements available in PYTHIA 8 are outlined and in Sect. 3.2 the matrix elements used for  $\tau$  lepton decays are documented. Finally, in Sect. 3.3 the implementation of  $\tau$  lepton decays within PYTHIA 8 is summarised.

### 3.1. Tau Lepton Production

In PYTHIA 8 the hard process is already calculated using helicity averaged matrix elements and so the first step of using Eq. 2.106 from the spin correlation algorithm of Sect. 2.2.3 is not necessary. However, the helicity matrix element of the hard process is still needed to calculate the helicity density matrices of the outgoing  $\tau$  leptons from the hard process in Eq. 2.108. For the case of  $\tau$  lepton production from particles that are not spin zero, such as  $Z \rightarrow \tau\tau$ , the full information of the hard process is required, whereas for  $\tau$  leptons produced from spin zero particles, such as Higgs bosons, the incoming particles of the hard process are not required. In either case it is important that the helicity matrix elements match the helicity averaged matrix elements used in the hard process machinery of PYTHIA 8.

Most helicity matrix elements which produce  $\tau$  leptons within PYTHIA 8 have been implemented and fall into three broad categories which are presented here. In Sect. 3.1.1 the available electroweak matrix elements are outlined, while in Sect. 3.1.2 the Higgs boson matrix elements are presented, and in Sect. 3.1.3 approximated helicity matrix elements from other mechanisms such as  $B$ -hadron decays, where the production of the  $\tau$  lepton is not a hard process, are considered. Additionally, the method used for handling initial state and final state radiation in the calculation of the hard process helicity matrix elements is outlined in Sect. 3.1.4.

#### 3.1.1. Electroweak Production

A  $\tau$  lepton can be produced from a hard electroweak process in PYTHIA 8 through either a Drell-Yan process or a  $W$  boson. For these two hard processes the momenta and types of the incoming particles must be known to fully calculate the helicity matrix element and ensure the correct polarisation of the outgoing  $\tau$  leptons. The helicity matrix element for Drell-Yan fermion production mediated by an excited photon is given by,

$$\mathcal{M}_\gamma = \frac{g_e^2 Q_0 Q_2}{s} (\bar{v}_1 \gamma_\mu u_0) (\bar{u}_3 \gamma^\mu v_2) \quad (3.1)$$

using the vertex of Fig. 2.4(a) and the spinors of Eq. 2.31 where  $s$  is the mass of the propagator squared,  $p_0$  and  $p_1$  are the incoming fermions,  $p_2$  and  $p_3$  are the outgoing fermions, and  $Q_i$  is the charge of particle  $p_i$ . Here the numerical subscripts indicate the corresponding particle to which the quantity belongs, *i.e.*  $\bar{v}_1$  is the anti-spinor for  $p_1$ . Additionally, the explicit dependence of the spinors on momentum and helicity are omitted for brevity. This convention is maintained throughout the chapter.

The Drell-Yan process can also be mediated by a  $Z$  boson for which the helicity matrix element is given by the vertex of Fig. 2.4(b),

$$\mathcal{M}_Z = \frac{g_e^2}{16\cos\theta_w^2\sin\theta_w^2\left(s - m_Z^2 + i\frac{\Gamma_Z}{m_Z}\right)} \left( \bar{v}_1\gamma^\mu(v_0 - a_0\gamma^5)u_0 \right) \left( g_{\mu\nu} - \frac{q_\mu q_\nu}{m_Z^2} \right) \left( \bar{u}_3\gamma^\nu(v_2 - a_2\gamma^5)v_2 \right) \quad (3.2)$$

where  $a_i$  and  $v_i$  are the axial and vector couplings of fermion  $p_i$  to the  $Z$  boson given in Table 2.2. When both incoming fermions are oriented along the  $z$ -axis and their helicities are equal,  $\lambda_0 = \lambda_1$ , the full matrix element is zero. This simplification is used for numerical speed.

In PYTHIA 8 it is possible to produce  $\tau$  leptons from a Drell-Yan hard process with either the excited photon matrix element or the  $Z$  boson matrix element, or full interference through both the excited photon and  $Z$  boson matrix elements. When full interference is requested the helicity matrix element for the process is,

$$\mathcal{M}_{\text{DY}} = \mathcal{M}_\gamma + \mathcal{M}_Z \quad (3.3)$$

where the simplification for the  $Z$  boson matrix element is still made when the incoming fermions are oriented along the  $z$ -axis and  $\lambda_0 = \lambda_1$ .

The matrix element for fermions produced from a  $W$  boson created in the hard process is given by,

$$\mathcal{M}_W \propto (\bar{v}_1\gamma_\mu(1 - \gamma_5)u_0)(\bar{u}_3\gamma^\mu(1 - \gamma_5)v_2) \quad (3.4)$$

where the  $s$ -channel has been assumed. Here  $p_0$  and  $p_1$  are the incoming particles and  $p_2$  and  $p_3$  are the outgoing fermions. Because  $\mathcal{M}_W$  is not combined with any other matrix elements for interference effects, unlike the  $\gamma$  and  $Z$  matrix elements, the additional factors of proportionality from the  $SU(2)$  gauge coupling have been omitted for numerical simplicity.

The effects of helicity correlations in  $\tau$  leptons from the electroweak matrix elements outlined above are most readily observed in the rest frame of the decaying electroweak boson where the  $\tau$  lepton decays into a  $\tau$  lepton neutrino and a charged pion. In this frame the number of events,  $N$ , is proportional to,

$$N \propto 1 + 2\mathcal{P}_\tau \left( \frac{2E_{\pi^-}}{\sqrt{s}} - \frac{1}{2} \right) \quad (3.5)$$

where  $E_{\pi^-}$  is the energy of the charged pion in the rest frame of the electroweak boson,  $\sqrt{s}$  is the interaction energy, and  $\mathcal{P}_\tau$  is the average polarisation of the  $\tau$  leptons produced from this type of event. For on-shell  $W$  boson production the average  $\tau$  lepton polarisation should be  $\mathcal{P}_\tau \approx -1$ , while the average  $\tau$  lepton polarisation from an on-shell  $Z$  boson depends upon the type of incoming fermions, but for proton-proton collisions is  $\mathcal{P}_\tau \approx -0.15$ . For the case of the photon, the average  $\tau$  lepton polarisation is zero.

In Fig. 3.1 the energy of the charged pion, in the rest frame of the intermediate electroweak

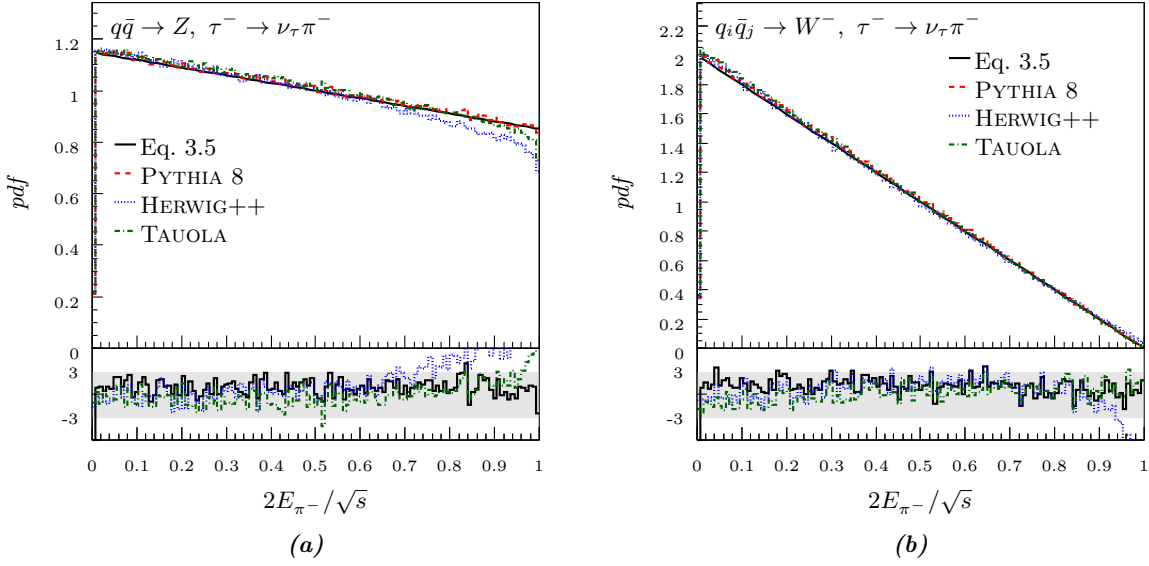


**Figure 3.1.:** Comparisons of the fractional energy of a charged pion from a  $\tau$  lepton decay in the rest frame of the electroweak boson producing the  $\tau$  lepton. The distributions are sensitive to the average  $\tau$  lepton polarisations and are given for PYTHIA 8, HERWIG++, and TAUOLA with  $\tau$  lepton production from a (a)  $Z$  boson hard process and a (b)  $W$  boson hard process.

boson, is plotted for both a  $Z$  boson hard process and  $W$  boson hard process. For the  $Z$  boson hard process the  $Z$  is produced with all photon interference turned off. All plots within this chapter, unless specified otherwise, are generated from proton-proton simulations at  $\sqrt{s} = 14$  TeV, although this does not affect most distributions. A total of  $10^6$  events are generated for each sample. Additionally, the lower subplot of each figure provides the difference divided by the statistical uncertainty between the PYTHIA 8 result and any other generator distributions or analytic functions in the plot. The grey band indicates a difference range within three standard deviations. As can be seen, PYTHIA 8 agrees well with both HERWIG++ and TAUOLA. Additionally, PYTHIA 8 matches the expected distribution of Eq. 3.5, assuming  $\mathcal{P}_\tau = -0.15$  for Fig. 3.1(a) and  $\mathcal{P}_\tau = -1$  for Fig. 3.1(b).

### 3.1.2. Higgs Boson Production

Because Higgs bosons, either SM or beyond, are spin zero, the production of the Higgs boson does not influence the decay correlation of the  $\tau$  leptons, and only the vertex factor for the Higgs boson coupling with the two fermions is needed. For  $\mathcal{CP}$ -even Higgs bosons the Higgs boson is predicted by the SM and MSSM as a scalar and so the helicity matrix element is proportional to,

$$\mathcal{M}_{\mathcal{CP}\text{-even}} \propto \left( \frac{ig_w m_2}{2m_W} \right) \bar{u}_3 F_{\phi^0 p_2 p_3} v_2 \quad (3.6)$$

for a neutral Higgs boson coupling with two fermions, where  $g_w$  is the  $SU(2)$  gauge coupling,  $m_2$  is the mass of one of the outgoing fermions, and  $F_{\phi^0 p_2 p_3}$  is the vector coupling of the Higgs

to the outgoing fermions  $p_1$  and  $p_2$  where  $p_0$  is the incoming Higgs boson. Within PYTHIA 8 these couplings are not included in the calculation of the helicity matrix element for numerical simplicity and speed but are given for the SM Higgs boson,  $H$ , in the vertex of Fig. 2.6(g) and for the MSSM light Higgs boson,  $h^0$ , and heavy Higgs boson,  $H^0$ , in the vertices of Figs. 2.10(a) and 2.10(b) for  $u$ -type fermions and Figs. 2.10(d) and 2.10(e) for  $d$ -type fermions.

For the  $\mathcal{CP}$ -odd MSSM Higgs boson the vertex factor for the coupling of the Higgs boson to fermions is proportional to,

$$\mathcal{M}_{\mathcal{CP}\text{-odd}} \propto - \left( \frac{g_w m_2}{2m_W} \right) \bar{u}_3 F_{\phi^0 p_2 p_3} \gamma^5 v_2 \quad (3.7)$$

where the coupling constant  $F_{\phi^0 p_2 p_3}$  is given in the vertices of Figs. 2.10(c) and 2.10(f) for the MSSM  $\mathcal{CP}$ -odd Higgs boson,  $A^0$ . The vertex factors of Figs. 2.10(g) and 2.10(h) for the charged Higgs boson,  $H^\pm$ , gives the matrix element,

$$\mathcal{M}_{H^\pm} \propto \left( \frac{ig_w}{2\sqrt{2}m_W} \right) \bar{u}_3 \left( (m_2 \tan \beta + m_3 \cot \beta) \pm (m_2 \tan \beta - m_3 \cot \beta) \gamma^5 \right) v_2 \quad (3.8)$$

where  $p_1$  is a  $d$ -type fermion and  $p_2$  is a  $u$ -type fermion. Note the change in sign between the vector and axial portions of the vertex depend upon the charge of the Higgs boson.

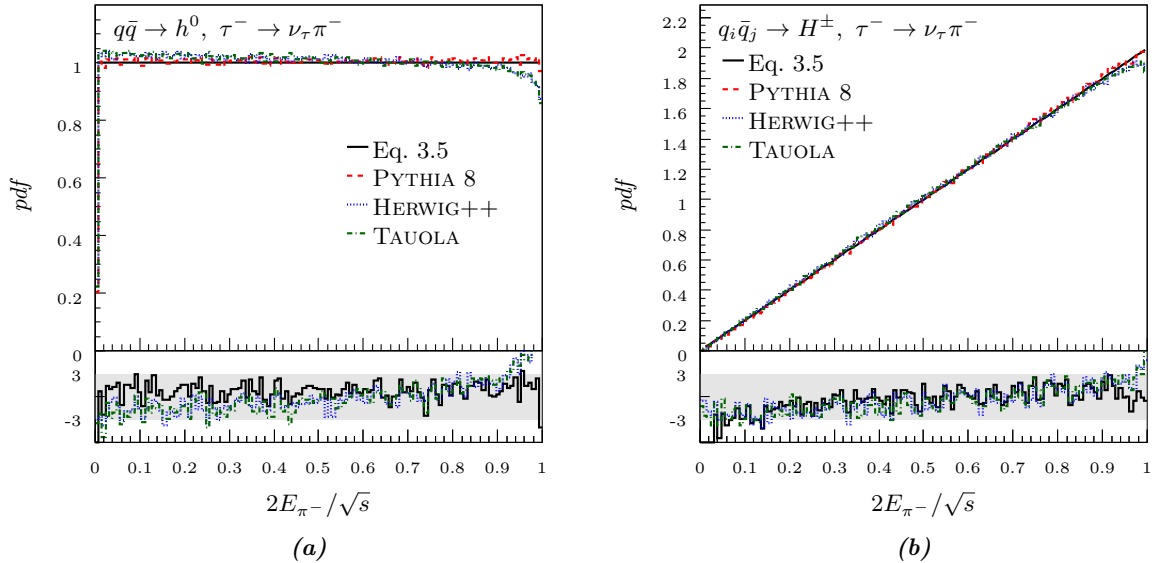


**Figure 3.2.:** The same distributions as Fig. 3.1 but for  $\tau$  lepton production from a (a)  $\mathcal{CP}$ -even light Higgs boson hard process and a (b) charged Higgs boson hard process.

Because the Higgs bosons are spin zero, the equivalent distributions of Fig. 3.1 yield flat distributions, shown in Fig. 3.2(a) where  $\mathcal{P}_\tau = 0$  is used for Eq. 3.5. However,  $\tau$  leptons produced from the charged MSSM Higgs boson have an average polarisation of  $\mathcal{P}_\tau \approx +1$  as shown in Fig. 3.2(b) where Eq. 3.5 is plotted for  $\mathcal{P}_\tau = +1$ . As can be seen, there is good agreement between PYTHIA 8, HERWIG++, TAUOLA, and the expected distribution of Eq. 3.5 in both of these plots.

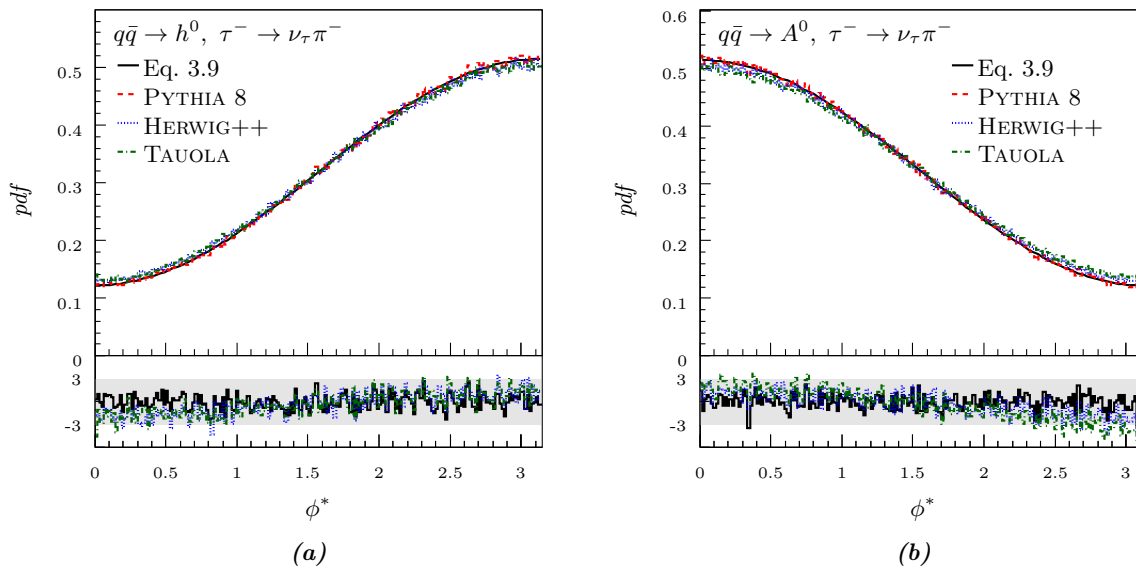
The  $\mathcal{CP}$ -even Higgs boson of Eq. 3.6 and the  $\mathcal{CP}$ -odd Higgs boson of Eq. 3.7 produce a correlation in the polarisation of  $\tau$  leptons that can be seen by plotting the acoplanarity angle  $\phi^*$  between the two pions from  $\tau$  lepton decays into a  $\tau$  lepton neutrino and single charged pion [100]. The acoplanarity angle is defined as the azimuthal angle between the two decay planes of the  $\tau$  lepton in the rest frame of the Higgs boson and can be written as,

$$\phi^* = \text{acos}(\vec{n}_2 \cdot \vec{n}_3) \quad (3.9)$$

where the vector  $\vec{n}_i$  is given by,

$$\vec{n}_i = \frac{\vec{q}_i \times \vec{q}_1}{|\vec{q}_i \times \vec{q}_1|} \quad (3.10)$$

and  $q_0$  is the  $\tau^+$  three-momentum,  $q_1$  is the  $\tau^-$  three-momentum,  $q_2$  is the  $\pi^+$  three-momentum, and  $q_3$  is the  $\pi^-$  three-momentum [101].



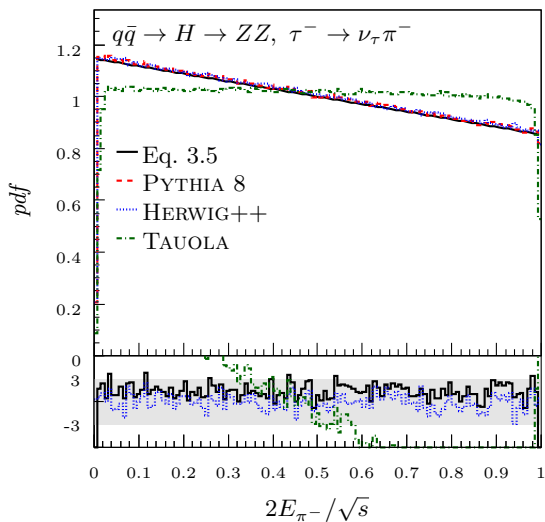
**Figure 3.3.:** Comparisons of the acoplanarity angle,  $\phi^*$ , defined in Eq. 3.9 for  $\tau$  leptons produced from a (a)  $\mathcal{CP}$ -even Higgs boson and a (b)  $\mathcal{CP}$ -odd Higgs boson where the  $\tau$  lepton decays through the  $\tau^- \rightarrow \nu_\tau \pi^-$  channel.

Figure 3.3 provides distributions of the acoplanarity angle for the  $\mathcal{CP}$ -even Higgs boson in Fig. 3.3(a) and  $\mathcal{CP}$ -odd Higgs boson in Fig. 3.3(b), where the Higgs bosons are decaying into  $\tau$  lepton pairs which are further decaying into final states with a  $\tau$  lepton neutrino and charged pion. The number of events,  $N$ , is proportional to,

$$N \propto 1 \pm \frac{\pi^2}{16} \cos \phi^* \quad (3.11)$$

for the  $\mathcal{CP}$ -even and  $\mathcal{CP}$ -odd Higgs bosons respectively [100]. All three generators match the theoretically expected distribution of Eq. 3.9 well.

Higgs bosons can also decay into  $Z$  boson and  $W$  boson pairs which then subsequently de-



**Figure 3.4.:** Distribution of  $2E_{\pi^-}/\sqrt{s}$  from  $\tau^- \rightarrow \nu_\tau \pi^-$  decays where the  $\tau$  lepton is produced from a  $H \rightarrow ZZ$  hard process. The subplot compares the difference divided by uncertainty between the PYTHIA 8 distribution and the HERWIG++, TAUOLA, and Eq. 3.5 distributions.

decay into final states with  $\tau$  leptons. These decays are treated in PYTHIA 8 by assuming the electroweak bosons produced from the Higgs boson are unpolarised and so the matrix element,

$$\mathcal{M}_{ZZ} \propto \varepsilon_{0\mu} \left( \bar{u}_3 \gamma^\mu (v_2 - a_2 \gamma^5) v_2 \right) \quad (3.12)$$

is used for  $\tau$  leptons produced from a  $Z$  boson where  $\varepsilon_0$  is the polarisation vector of the  $Z$  boson given by Eq. 2.38 and  $p_1$  and  $p_2$  are the two  $\tau$  leptons. The analytic distribution of Eq. 3.5 also applies for  $\tau$  leptons produced with this mechanism, where  $\mathcal{P}_\tau \approx -0.15$ . In Fig. 3.4 the distribution of  $2E_{\pi^-}/\sqrt{s}$  for  $\tau$  leptons produced from a Higgs boson decaying into a  $Z$  boson pair hard process, where the  $\tau$  leptons decay via  $\tau^- \rightarrow \nu_\tau \pi^-$ , is given. Both PYTHIA 8 and HERWIG++ model this correctly, while TAUOLA does not, as compared to Eq. 3.5 using  $\mathcal{P}_\tau = -0.15$ . For  $\tau$  leptons produced from  $\phi \rightarrow WW$ , the polarisation of the  $\tau$  lepton is assumed to be  $\mathcal{P}_\tau = -1$ , as the  $W$  boson will have a mass much larger than the  $\tau$  lepton, and so no specialised matrix element is needed.

### 3.1.3. Other Production

Within PYTHIA 8,  $\tau$  leptons can also be produced from a variety of decays which are not the hard process or do not match the electroweak or Higgs boson hard processes of Sects. 3.1.1 and 3.1.2. A special case is top quark production and decay, which is considered as a hard process and is handled using the  $W$  boson helicity matrix element of Eq. 3.4 as the top quark, bottom quark,  $\tau$  lepton, and  $\tau$  lepton neutrino from the process are all well defined within the PYTHIA 8 event record.

For the case of  $\tau$  leptons produced from  $D$  or  $B$ -mesons, however, the constituent quarks are not recorded in the PYTHIA 8 event record, and it is necessary to approximate the incoming particles of the  $W$  helicity matrix element. When the meson decays into another meson plus a  $\tau$  lepton and  $\tau$  lepton neutrino, the incoming quark momentum is approximated as the momentum of the decaying meson, while the momentum of the outgoing quark is approximated



as the incoming meson momentum less the  $\tau$  lepton and  $\tau$  lepton neutrino momentum. The properties of the incoming and outgoing quarks are set to that of a  $b$ -quark. For the decay of a  $D$  or  $B$ -meson to only a  $\tau$  lepton and  $\tau$  lepton neutrino, the two incoming quark momenta are approximated as half the momentum of the decaying meson.

For the production of  $\tau$  leptons from virtual photons, the excited photon matrix element of Eq. 3.1 is used. The incoming fermions are set as  $d$ -quarks and the momenta for each quark is set as half the momentum of the virtual photon. For this decay there are two  $\tau$  leptons produced, and so full correlations between the decays of the two  $\tau$  leptons are calculated.

For any process where the production of the  $\tau$  lepton is unknown or does not match the scenarios described above, the  $\tau$  lepton is assumed to be uncorrelated, and the helicity density of the  $\tau$  lepton is set as a normalised identity matrix, *i.e.* the two on-diagonal elements are one half and the off-diagonal elements are zero.

### 3.1.4. Initial and Final State Radiation

Both initial state and final state radiation can effect the helicity density matrix for  $\tau$  leptons and can be handled through a variety of methods. The most complete solution would be to treat each radiation as a decay and perform the full correlation algorithm of Sect. 2.2.3. This method, however, is not possible to implement for initial state radiation in PYTHIA 8 without significant changes.

Because the helicity density matrices for the hard processes are used only for the calculation of  $\tau$  lepton helicity density matrices, it is possible to approximate the incoming and outgoing particles using particles before or after initial and final state radiation have been applied without a significant change in the calculation of the helicity density matrices. Within PYTHIA 8 the incoming particles used in the helicity density matrices for the hard process are taken before initial state radiation is applied, and the outgoing particles are taken after final state radiation has been applied.

## 3.2. Tau Lepton Decays

The  $\tau$  lepton can decay through a large variety of channels, and so while an attempt has been made to implement as many channels as possible in PYTHIA 8, some very rare and high multiplicity channels are missing, and modelled using only isotropic phase-space. Currently, all known  $\tau$  lepton decays with a branching fraction greater than 0.04% are implemented with fully modelled helicity matrix elements. Additionally, the implementation of the helicity matrix elements within the PYTHIA 8 code is intended to be both transparent and easily extensible so the implementation of new channels in the future, or the modification of old channels, is possible. Many of the hadronic currents presented in this section are based on the hadronic currents implemented in HERWIG++ [97] and TAUOLA [99].

The  $\tau$  lepton decays through a weak interaction and so all  $\tau$  lepton decays take the form of  $p_0 \rightarrow p_1 + p_2 \dots + p_n$  where  $p_0$  is a  $\tau$  lepton,  $p_1$  is a  $\tau$  lepton neutrino, and  $p_2$  through  $p_n$  are the remaining leptonic or hadronic children of the decay. The matrix element for the  $\tau$  lepton

decay can be written as,

$$\mathcal{M} = \frac{g_w^2}{8m_W^2} L_\mu J^\mu \quad (3.13)$$

where  $L_\mu$  is the leptonic current of the  $\tau$  lepton and  $\tau$  lepton neutrino fermion line and  $J^\mu$  is the hadronic current. Here the propagator for the  $W$  has been approximated as  $1/m_W^2$  as  $m_\tau \ll m_W$  and  $g_w$  is the  $SU(2)$  gauge coupling. The leptonic current is given by,

$$L_\mu = \bar{u}_1 \gamma_\mu (1 - \gamma^5) u_0 \quad (3.14)$$

where  $\bar{u}_1$  is the spinor for the outgoing  $\tau$  lepton neutrino and  $u_0$  is the spinor for the decaying  $\tau$  lepton.

In many of the hadronic currents for the  $\tau$  lepton decays of this section, Breit-Wigner distributions are used to model hadronic resonances. The fixed width Breit-Wigner used is,

$$BW(s, m, \Gamma) = \frac{im\Gamma - m^2}{s - m^2 + im\Gamma} \quad (3.15)$$

while the  $s$ -wave Breit-Wigner,

$$BW_s(m_0, m_1, s, m, \Gamma) = \frac{m^2}{m^2 - s - \left(\frac{i\Gamma m^2}{\sqrt{s}}\right) \left(\frac{g(m_0, m_1, s)}{g(m_0, m_1, m^2)}\right)} \quad (3.16)$$

is used for spin-0 systems, the  $p$ -wave Breit Wigner,

$$BW_p(m_0, m_1, s, m, \Gamma) = \frac{m^2}{m^2 - s - \left(\frac{i\Gamma m^2}{\sqrt{s}}\right) \left(\frac{g(m_0, m_1, s)}{g(m_0, m_1, m^2)}\right)^3} \quad (3.17)$$

is used for spin-1 systems, and the  $d$ -wave Breit Wigner,

$$BW_d(m_0, m_1, s, m, \Gamma) = \frac{m^2}{m^2 - s - \left(\frac{i\Gamma m^2}{\sqrt{s}}\right) \left(\frac{g(m_0, m_1, s)}{g(m_0, m_1, m^2)}\right)^5} \quad (3.18)$$

is used for spin-2 systems where,

$$g(m_0, m_1, s) = \frac{\sqrt{(s - (m_0 + m_1)^2)(s - (m_0 - m_1)^2)}}{2\sqrt{s}} \quad (3.19)$$

and  $m_0$  and  $m_1$  are the masses of the particles from the resonance decay while  $s$  is the square of the centre-of-mass energy of the resonance. Here,  $m$  is the on-shell mass of the resonance and  $\Gamma$  is the width of the resonance. For some decay matrix elements more sophisticated running widths for the Breit-Wigners are necessary, but these running widths are explicitly defined for each hadronic current as required.

In this section the implemented  $\tau$  lepton decay channels are described and grouped by the multiplicity of the decay. The helicity matrix elements for each channel are given by Eq. 3.13

and so only the hadronic current  $J^\mu$  is given for each channel. The hadronic current is given only to a constant of proportionality, as the branching fractions of the  $\tau$  lepton are given *a priori* within PYTHIA 8 and not calculated from the helicity matrix elements.

For each channel the  $\tau$  lepton is designated by  $p_0$ , the  $\tau$  lepton neutrino as  $p_1$ , and the remaining particles of the decay as  $p_i$ , where the order is specified. The four-momentum of each particle is denoted by  $q_i$ , and the mass by  $m_i$ . Plots comparing the important invariant mass distributions for each decay channel are given. When possible, results from PYTHIA 8, HERWIG++, and TAUOLA are plotted. In some cases where the specific decay channel is not available in TAUOLA, the TAUOLA distribution has been omitted.

### 3.2.1. Two-Body Decays

The  $\tau$  lepton has only two known decay channels available with two decay products,  $\tau^- \rightarrow \nu_\tau \pi^-$  and  $\tau^- \rightarrow \nu_\tau K^-$ , both of which are decays to a pseudoscalar meson. The hadronic current for the decay is given by [102],

$$J^\mu = f_2 q_2^\mu \quad (3.20)$$

where  $f_2$  is given by  $130.41 \pm 0.20$  MeV for the charged pion channel and  $156.1 \pm 0.85$  MeV for the charged kaon channel [15]. The maximum helicity averaged matrix element amplitude for this channel is given by,

$$\langle |\mathcal{M}|^2 \rangle_{\max} = \frac{g_W^4}{16m_W^4} m_0^2 (m_0^2 - m_2^2) \quad (3.21)$$

where  $g_w$  is the  $SU(2)$  gauge coupling and  $m_W$  the mass of the  $W$  boson.

### 3.2.2. Three-Body Decays

The  $\tau$  lepton can decay through a variety of three-body channels, and currently, three models have been implemented in PYTHIA 8 for three-body decays. These models are for  $\tau$  lepton decays into a  $\tau$  lepton neutrino and two leptons via a leptonic current, a neutrino and two mesons via a vector current, and a neutrino and two mesons via a vector and scalar current.

#### Three Leptons

The three lepton current for the decays  $\tau^- \rightarrow \nu_\tau e^- \bar{\nu}_e$  and  $\tau^- \rightarrow \nu_\tau \mu^- \bar{\nu}_\mu$  is given by,

$$J^\mu = \bar{u}_2 \gamma^\mu (1 - \gamma^5) v_3 \quad (3.22)$$

where  $p_2$  is the charged lepton and  $p_3$  is the corresponding neutrino. The maximum helicity average matrix element amplitude is,

$$\langle |\mathcal{M}|^2 \rangle_{\max} = \frac{g_W^4}{4m_W^4} (m_0^2 - m_2^2)^2 \quad (3.23)$$

where the masses of the neutrinos are assumed to be zero and  $m_2$  is the mass of the outgoing electron or muon.

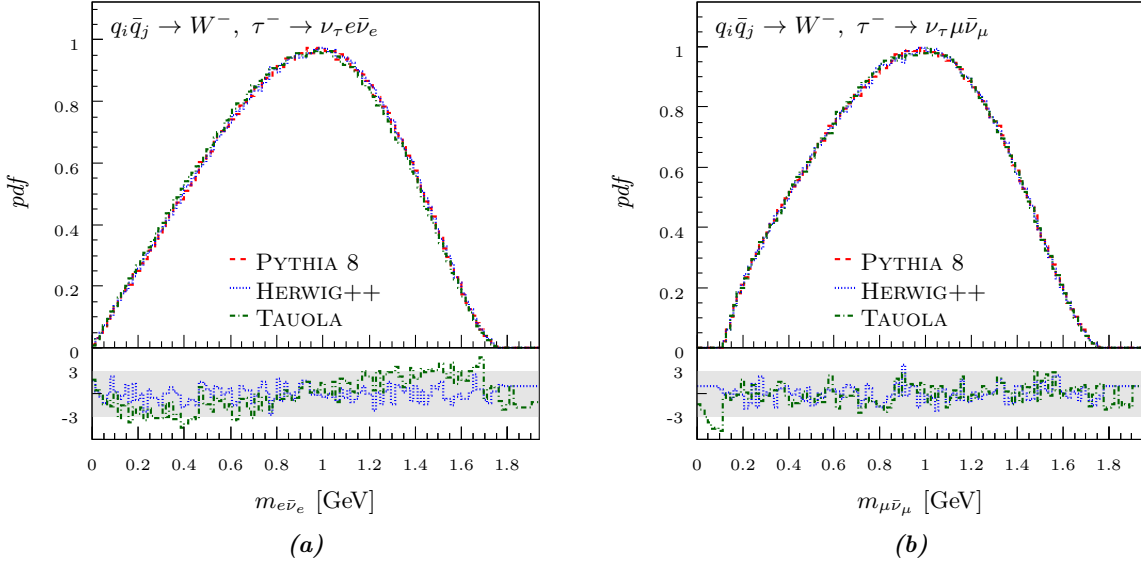


**Figure 3.5.:** Distributions of the combined  $p_2$  and  $p_3$  invariant mass,  $m_{23}$  for (a)  $\tau^- \rightarrow \nu_\tau e^- \bar{\nu}_e$  and (b)  $\tau^- \rightarrow \nu_\tau \mu^- \bar{\nu}_\mu$  decays.

Figure 3.5 gives the invariant mass distributions for the lepton and anti-lepton neutrino system,  $m_{23}$ , for PYTHIA 8, HERWIG++, and TAUOLA. As expected, there is good agreement between the three generators.

### Two Mesons Via a Vector Current

The  $\tau$  lepton can decay into two mesons via a vector meson resonance for the  $\tau^- \rightarrow \nu_\tau \pi^0 \pi^-$ ,  $\tau^- \rightarrow \nu_\tau K^0 K^-$ , and  $\tau^- \rightarrow \nu_\tau \eta K^-$  channels. The hadronic current for these decays is given by the Kühn and Santamaria model [103],

$$J^\mu \propto \left( (q_3 - q_2)^\mu - \frac{s_1}{s_2} (q_2 + q_3)^\mu \right) \sum_i w_{vi} BW_p(m_2, m_3, s_2, m_{vi}, \Gamma_{vi}) \quad (3.24)$$

where  $s_1$  is given by  $(q_3 - q_2)_\mu (q_2 + q_3)^\mu$ ,  $s_2$  is given by  $(q_2 + q_3)_\mu (q_2 + q_3)^\mu$ ,  $w_{vi}$  are complex weights for the vector resonances,  $BW_p$  is the  $p$ -wave Breit-Wigner of Eq. 3.17,  $m_{vi}$  are the on-shell masses of the vector resonances, and  $\Gamma_{vi}$  are the on-shell widths of the vector resonances. The  $\tau^- \rightarrow \nu_\tau \pi^0 \pi^-$  and  $\tau^- \rightarrow \nu_\tau K^0 K^-$  channels proceed through  $\rho$  resonances, while the  $\tau^- \rightarrow \eta K^-$  channel proceeds through  $K^*$  resonances. Because the  $\rho$  resonances are dominated by the  $\pi^0 \pi^-$  decay, the masses used in calculating the  $p$ -wave Breit-Wigner are set at  $m_2 = m_{\pi^0}$  and  $m_3 = m_{\pi^-}$ . For the  $K^*$  resonances, the  $\pi^- \bar{K}^0$  channel dominates and so the masses used in calculating the  $p$ -wave Breit-Wigner are set at  $m_2 = m_{\pi^-}$  and  $m_3 = m_{K^0}$ . The  $\tau^- \rightarrow \nu_\tau \pi^- \bar{K}^0$  channel is not modelled using the hadronic current of Eq. 3.24, but rather through the model of Finkemeier and Mirkes in Ref. [104], where a scalar meson resonance is included. The hadronic current for this model is given in the following section by Eq. 3.26.

**Table 3.1.:** Parameters used for the  $\tau$  lepton decay into two mesons via a vector meson resonance.

| resonance    | $m$ [GeV] | $\Gamma$ [GeV] | $\phi$ | $A$   |
|--------------|-----------|----------------|--------|-------|
| $\rho(770)$  | 0.7746    | 0.149          | 0      | 1     |
| $\rho(1450)$ | 1.408     | 0.502          | $\pi$  | 0.167 |
| $\rho(1700)$ | 1.7       | 0.235          | 0      | 0.050 |
| $K^*(892)$   | 0.8921    | 0.0513         | 0      | 1     |
| $K^*(1680)$  | 1.7       | 0.235          | $\pi$  | 0.038 |

The parameters used for the hadronic current of Eq. 3.24 are given in Table 3.1 and are the same as those used in HERWIG++ which are based on the fits of CLEO [105]. The complex weights for the vector resonances are calculated from the phases,  $\phi_{vi}$ , and amplitudes,  $A_{vi}$ , as a position vector in the complex plane.

$$w_i = A_i (\cos \phi_i + i \sin \phi_i) \quad (3.25)$$

Three  $\rho$  resonances are used,  $\rho(770)$ ,  $\rho(1450)$ , and  $\rho(1700)$  while only two  $K^*$  resonances are used,  $K^*(892)$  and  $K^*(1680)$ .

Plots comparing the hadronic invariant masses of the  $\pi^0\pi^-$ ,  $K^0K^-$ , and  $\eta K^-$  for the three decay channels modelled with Eq. 3.24 are given in Figure Fig. 3.6. For both the  $\pi^0\pi^-$  and  $K^0K^-$  there is good agreement between PYTHIA 8 and HERWIG++ while the vector resonance is slightly sharper in TAUOLA for the  $K^0K^-$  invariant mass. The  $\tau^- \rightarrow \nu_\tau \eta K^-$  decay channel is not available in TAUOLA, but the  $\eta K^-$  invariant mass distributions generated by HERWIG++ and PYTHIA 8 match well.

### Two Mesons Via Vector and Scalar Current

For the rare decays  $\tau^- \rightarrow \nu_\tau \pi^- \bar{K}^0$  and  $\tau^- \rightarrow \nu_\tau \pi^0 K^-$ , the  $\tau$  lepton decay can proceed through both vector and scalar meson resonances. These channels have been modelled by Finkemeier and Mirkes in Ref. [104] with the hadronic current,

$$\begin{aligned}
J^\mu \propto & \frac{c_v}{\sum_i w_{vi}} \left( (q_3 - q_2)^\mu \sum_i w_{vi} BW_p(m_2, m_3, s_2, m_{vi}, \Gamma_{vi}) \right. \\
& \left. - s_1 (q_2 + q_3)^\mu \sum_i \frac{w_{vi} BW_p(m_2, m_3, s_2, m_{vi}, \Gamma_{vi})}{m_{vi}^2} \right) \\
& + \frac{c_s}{\sum_j w_{sj}} (q_2 + q_3)^\mu \sum_j w_{sj} BW_s(m_2, m_3, s_2, m_{sj}, \Gamma_{sj})
\end{aligned} \quad (3.26)$$

where  $c_v$  and  $c_s$  are the couplings to the vector and scalar resonances,  $w_{vi}$  and  $w_{sj}$  are the complex vector and scalar weights,  $m_{vi}$  and  $m_{sj}$  are the on-shell resonance masses, and  $\Gamma_{vi}$  and  $\Gamma_{sj}$  are the on-shell resonance widths. The energies  $s_1$  and  $s_2$  are the same as for the vector resonance current of Eq. 3.24. Again, the complex weights are calculated from a phase,  $\phi$ , and amplitude,  $A$ , using Eq. 3.25. The propagator for the vector resonances is modelled using a  $p$ -

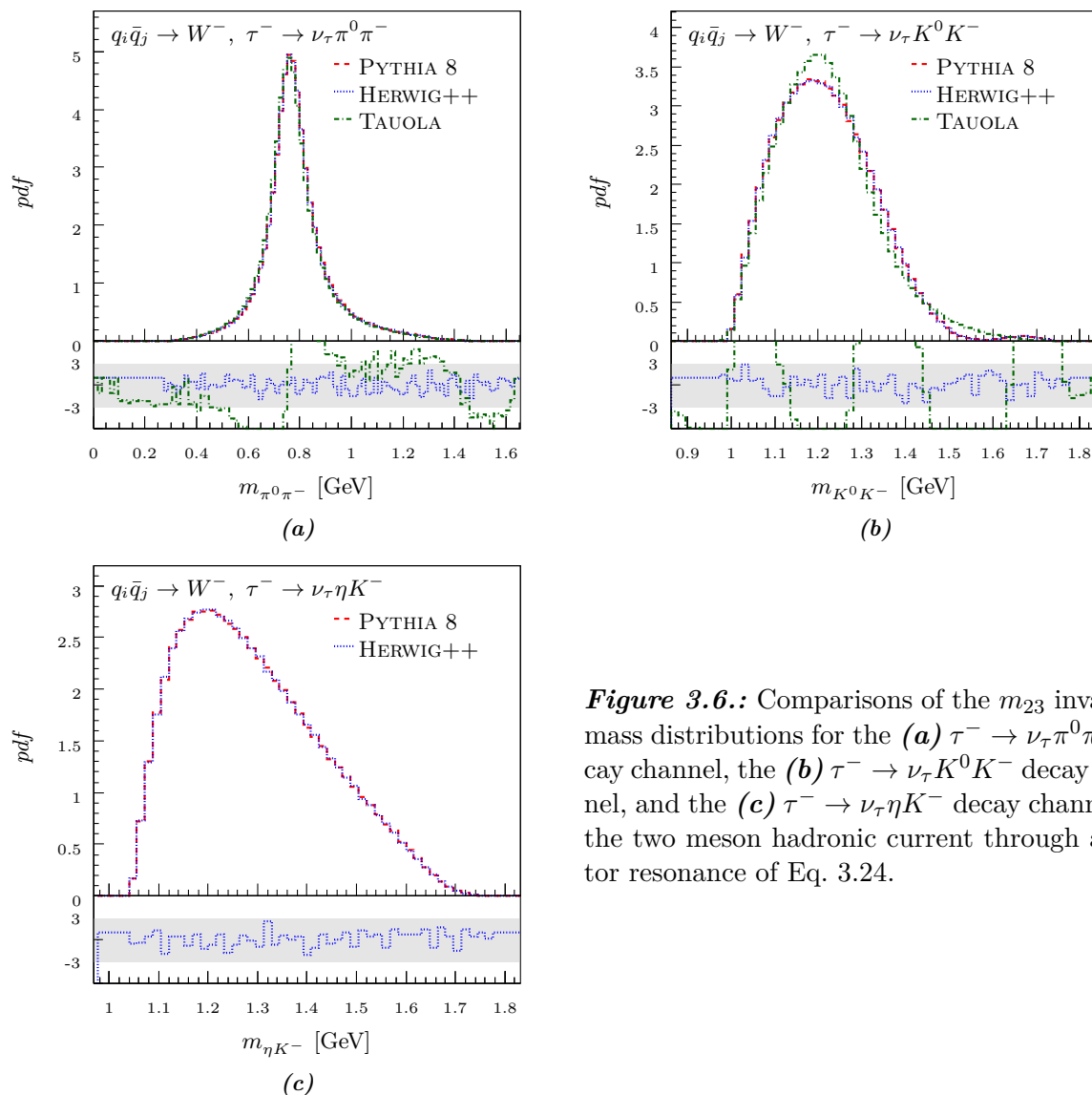


**Figure 3.6.:** Comparisons of the  $m_{23}$  invariant mass distributions for the (a)  $\tau^- \rightarrow \nu_\tau \pi^0 \pi^-$  decay channel, the (b)  $\tau^- \rightarrow \nu_\tau K^0 K^-$  decay channel, and the (c)  $\tau^- \rightarrow \nu_\tau \eta K^-$  decay channel for the two meson hadronic current through a vector resonance of Eq. 3.24.

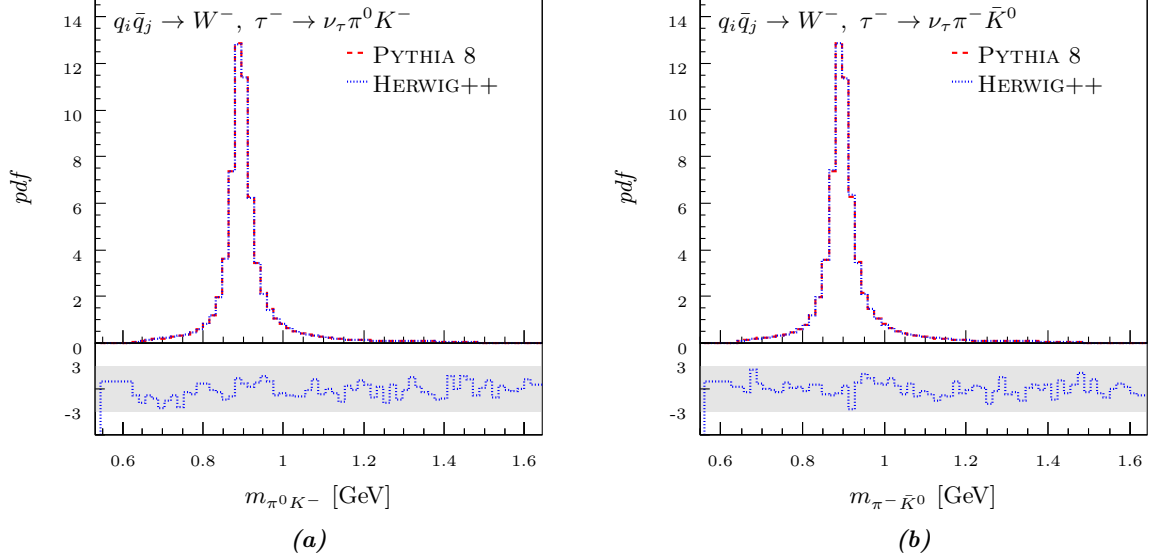
wave Breit-Wigner, given by Eq. 3.17, while the propagator for the scalar resonances is modelled using an  $s$ -wave Breit-Wigner, given by Eq. 3.16.

Table 3.2 gives the parameters used in PYTHIA 8 for the hadronic current of Eq. 3.26. The vector resonances proceed through a  $K^*(892)$  and a  $K^*(1410)$  while the scalar resonance proceeds through only a  $K_0^*(800)$ . Both the  $\tau^- \rightarrow \nu_\tau \pi^0 K^-$  and  $\tau^- \rightarrow \nu_\tau \pi^- K^0$  channels proceed through all three resonances. The vector resonance coupling is  $c_v = 1$  and the scalar resonance coupling is  $c_s = 0.465$ . These parameters match those used in HERWIG++ and are taken from the fits of Belle in Ref. [106].

Figure 3.7 provides the comparison plots between PYTHIA 8 and HERWIG++ for  $\tau^- \rightarrow \nu_\tau \pi^0 K^-$  and  $\tau^- \rightarrow \nu_\tau \pi^- K^0$  decays. The  $m_{\pi^0 K^-}$  and  $m_{\pi^- K^0}$  distributions are similar, and the distributions from PYTHIA 8 and HERWIG++ agree well for both decay channels.

**Table 3.2.:** Parameters used for the  $\tau$  lepton decay into two mesons via both vector and scalar meson resonances.

| resonance    | $m$ [GeV] | $\Gamma$ [GeV] | $\phi$ | $A$   |
|--------------|-----------|----------------|--------|-------|
| $K^*(892)$   | 0.89547   | 0.04619        | 0      | 1     |
| $K^*(1410)$  | 1.414     | 0.232          | 1.4399 | 0.075 |
| $K_0^*(800)$ | 0.878     | 0.499          | 0      | 1     |

**Figure 3.7.:** Distributions of the  $m_{23}$  invariant mass for the (a)  $\tau^- \rightarrow \nu_\tau \pi^0 K^-$  decay channel and the (b)  $\tau^- \rightarrow \nu_\tau \pi^- K^0$  decay channel for the two meson hadronic current via vector and scalar resonances using Eq. 3.26.

### 3.2.3. Four-Body Decays

Currently four models are implemented in PYTHIA 8, which provide four-body decays of the  $\tau$  lepton into three mesons for a total of twelve  $\tau$  lepton decay channels. The first hadronic current is used specifically for final states with three pions, while the second two hadronic currents are generalised currents which can be used for final states with both pions and kaons. The final four-body hadronic current includes an explicit photon for the  $\pi^0 \pi^-$  channel. The general hadronic current is given by,

$$J^\mu \propto \left( g^{\mu\nu} - \frac{q^\mu q^\nu}{s_1} \right) \left( (F_3 - F_2)q_2 + (F_1 - F_3)q_3 + (F_2 - F_1)q_4 \right)^\mu + F_4 q^\mu + iF_5 \epsilon^\mu(q_2, q_3, q_4) \quad (3.27)$$

from Ref. [107], where  $F_i$  are form factors specific to the model,  $\epsilon$  is the permutation operator, and  $q$  is  $q_2 + q_2 + q_3$ , where  $q_2$ ,  $q_3$ , and  $q_4$  are the four-momenta of the three mesons. The centre-of-mass energies are defined as,

$$s_1 = (q_2 + q_3 + q_4)^\mu (q_2 + q_3 + q_4)_\mu \quad (3.28)$$

$$\begin{aligned}
s_2 &= (q_3 + q_4)^\mu (q_3 + q_4)_\mu \\
s_3 &= (q_2 + q_4)^\mu (q_2 + q_4)_\mu \\
s_4 &= (q_2 + q_3)^\mu (q_2 + q_3)_\mu
\end{aligned}$$

where  $s_1$  gives the centre-of-mass energy for the three meson system, while  $s_2$ ,  $s_3$ , and  $s_4$  provide the centre-of-mass energies for the combinations of meson pairs.

### CLEO Current

The  $\pi^0\pi^0\pi^-$  and  $\pi^-\pi^-\pi^+$  decay channels are modelled using the current from the CLEO collaboration fit of Ref. [108] which first proceed through an  $a_1$  resonance, and then an additional scalar or tensor resonance. Both the  $\pi^0\pi^0\pi^-$  and  $\pi^-\pi^-\pi^+$  decay channels can proceed through scalar  $f_0$ , tensor  $f_2$ , or scalar  $\sigma$  resonances. The  $F_4$  and  $F_5$  form factors for the CLEO current are zero, and so only the first three form factors need to be specified.

The form factor  $F_1^-$  for the  $\pi^-\pi^-\pi^+$  channel is given by,

$$\begin{aligned}
F_1^- &= BW_{a_1}(s_1) \sum_i \left( -w_{\rho_i}^p BW_p(m_3, m_4, s_2, m_{\rho_i}, \Gamma_{\rho_i}) \right. \\
&\quad \left. - \frac{w_{\rho_i}^d}{3} BW_p(m_2, m_4, s_3, m_{\rho_i}, \Gamma_{\rho_i})(s_2 - s_4) \right) \\
&\quad \left. - \frac{2}{3} \left( w_\sigma BW_s(m_2, m_4, s_3, m_\sigma, \Gamma_\sigma) + w_{f_0} BW_s(m_2, m_4, s_3, m_{f_0}, \Gamma_{f_0}) \right) \right) \\
&\quad + w_{f_2} \left( \frac{s_4 - s_3}{2} BW_d(m_3, m_4, s_2, m_{f_2}, \Gamma_{f_2}) \right. \\
&\quad \left. - \frac{1}{18s_3} (4m_2^2 - s_3)(s_1 + s_2 - m_2^2) BW_d(m_2, m_4, s_3, m_{f_2}, \Gamma_{f_2}) \right)
\end{aligned} \tag{3.29}$$

while the first form factor for the  $\pi^0\pi^0\pi^-$  channel is given by,

$$\begin{aligned}
F_1^0 &= BW_{a_1}(s_1) \sum_i \left( w_{\rho_i}^p BW_p(m_3, m_4, s_2, m_{\rho_i}, \Gamma_{\rho_i}) \right. \\
&\quad \left. - \frac{w_{\rho_i}^d}{3} BW_p(m_2, m_4, s_3, m_{\rho_i}, \Gamma_{\rho_i})(s_4 - s_2 - m_4^2 - m_2^2) \right) \\
&\quad + \frac{2}{3} \left( w_\sigma BW_s(m_2, m_3, s_4, m_\sigma, \Gamma_\sigma) + w_{f_0} BW_s(m_2, m_3, s_4, m_{f_0}, \Gamma_{f_0}) \right) \\
&\quad + \frac{w_{f_2}}{18s_4} (s_1 - m_4^2 + s_4)(4m_2^2 - s_4) BW_d(m_2, m_3, s_4, m_{f_2}, \Gamma_{f_2})
\end{aligned} \tag{3.30}$$

where  $w_{\rho_i}^p$  are the complex couplings of the  $p$ -wave  $\rho$  resonances to the  $a_1$ ,  $w_{\rho_i}^d$  are the  $d$ -wave  $\rho$  couplings,  $w_{f_0}$  is the  $f_0$  coupling,  $w_{f_2}$  is the  $f_2$  coupling, and  $w_\sigma$  is the  $\sigma$  coupling.



The second form factor,  $F_2$ , is given by,

$$\begin{aligned}
F_2^- = & BW_{a_1}(s_1) \sum_i \left( w_{\rho_i}^p BW_p(m_2, m_4, s_3, m_{\rho_i}, \Gamma_{\rho_i}) \right. \\
& \left. - \frac{w_{\rho_i}^d}{3} BW_p(m_3, m_4, s_2, m_{\rho_i}, \Gamma_{\rho_i})(s_3 - s_4) \right) \\
& - \frac{2}{3} \left( w_{\sigma} BW_s(m_3, m_4, s_2, m_{\sigma}, \Gamma_{\sigma}) + w_{f_0} BW_s(m_3, m_4, s_2, m_{f_0}, \Gamma_{f_0}) \right) \\
& + w_{f_2} \left( \frac{s_4 - s_2}{2} BW_d(m_2, m_4, s_3, m_{f_2}, \Gamma_{f_2}) \right. \\
& \left. - \frac{1}{18s_2} (4m_2^2 - s_2)(s_1 + s_2 - m_2^2) BW_d(m_3, m_4, s_2, m_{f_2}, \Gamma_{f_2}) \right)
\end{aligned} \tag{3.31}$$

for the  $\pi^- \pi^- \pi^+$  channel while,

$$\begin{aligned}
F_2^0 = & BW_{a_1}(s_1) \sum_i \left( -\frac{w_{\rho_i}^p}{3} BW_p(m_2, m_4, s_3, m_{\rho_i}, \Gamma_{\rho_i}) \right. \\
& \left. - w_{\rho_i}^d BW_p(m_3, m_4, s_2, m_{\rho_i}, \Gamma_{\rho_i})(s_4 - s_3 - m_4^2 - m_3^2) \right) \\
& + \frac{2}{3} \left( w_{\sigma} BW_s(m_2, m_3, s_4, m_{\sigma}, \Gamma_{\sigma}) + w_{f_0} BW_s(m_2, m_3, s_4, m_{f_0}, \Gamma_{f_0}) \right) \\
& + \frac{w_{f_2}}{18s_4} (s_1 - m_4^2 + s_4)(4m_2^2 - s_4) BW_d(m_2, m_3, s_4, m_{f_2}, \Gamma_{f_2})
\end{aligned} \tag{3.32}$$

is the second form factor for the  $\pi^0 \pi^0 \pi^-$  channel.

The third form factor is given by,

$$\begin{aligned}
F_3^- = & BW_{a_1}(s_1) \sum_i -w_{\rho_i}^d \left( \frac{1}{3} (s_3 - s_4) BW_p(m_2, m_4, s_2, m_{\rho_i}, \Gamma_{\rho_i}) \right. \\
& \left. - \frac{1}{3} (s_2 - s_4) BW_p(m_2, m_4, s_3, m_{\rho_i}, \Gamma_{\rho_i}) \right) \\
& - \frac{2}{3} \left( w_{\sigma} BW_s(m_3, m_4, s_2, m_{\sigma}, \Gamma_{\sigma}) + w_{f_0} BW_s(m_3, m_4, s_2, m_{f_0}, \Gamma_{f_0}) \right) \\
& + \frac{2}{3} \left( w_{\sigma} BW_s(m_2, m_4, s_3, m_{\sigma}, \Gamma_{\sigma}) + w_{f_0} BW_s(m_2, m_4, s_3, m_{f_0}, \Gamma_{f_0}) \right) \\
& + w_{f_2} \left( -\frac{1}{18s_2} (4m_2^2 - s_2)(s_1 + s_2 - m_2^2) BW_d(m_3, m_4, s_2, m_{f_2}, \Gamma_{f_2}) \right. \\
& \left. + \frac{1}{18s_3} (4m_2^2 - s_3)(s_1 + s_3 - m_2^2) BW_d(m_2, m_4, s_3, m_{f_2}, \Gamma_{f_2}) \right)
\end{aligned} \tag{3.33}$$

**Table 3.3.:** Parameters for the  $\rho$  resonances used by the  $\tau$  lepton decay into three pions.

| resonance    | $m$ [GeV] | $\Gamma$ GeV | $\phi_p$ | $A_p$ | $\phi_d$  | $A_d$                |
|--------------|-----------|--------------|----------|-------|-----------|----------------------|
| $\rho(770)$  | 0.7743    | 0.1491       | 0        | 1     | -0.471239 | $3.7 \times 10^{-7}$ |
| $\rho(1450)$ | 1.37      | 0.386        | 3.11018  | 0.12  | 1.66504   | $8.7 \times 10^{-7}$ |
| $\rho(1700)$ | 1.72      | 0.25         | 0        | 0     | 0         | 0                    |

**Table 3.4.:** Parameters used by the three pion  $\tau$  lepton decay channels for the secondary  $f_0$ ,  $f_2$ , and  $\sigma$  resonances.

| resonance   | $m$ [GeV] | $\Gamma$ [GeV] | $\phi$   | $A$                  |
|-------------|-----------|----------------|----------|----------------------|
| $f_0(980)$  | 1.186     | 0.350          | -1.69646 | 0.77                 |
| $f_2(1270)$ | 1.275     | 0.185          | 1.75929  | $7.1 \times 10^{-7}$ |
| $\sigma$    | 0.86      | 0.88           | 0.722466 | 2.1                  |

for the  $\pi^-\pi^-\pi^+$  channel and,

$$\begin{aligned}
F_3^0 = & BW_{a_1}(s_1) \sum_i w_{\rho_i}^d \left( -\frac{1}{3}(s_4 - s_3 - m_4^2 + m_3^2) \right. \\
& BW_p(m_3, m_4, s_2, m_{\rho_i}, \Gamma_{\rho_i}) \\
& \left. + \frac{1}{3}(s_4 - s_2 - m_4^2 + m_2^2) BW_p(m_2, m_4, s_3, m_{\rho_i}, \Gamma_{\rho_i}) \right) \\
& - \frac{w_{f_2}}{2}(s_2 - s_3) BW_d(m_2, m_3, s_4, m_{f_2}, \Gamma_{f_2})
\end{aligned} \tag{3.34}$$

for the  $\pi^0\pi^0\pi^-$  channel.

All the complex couplings are calculated from a phase and amplitude using Eq. 3.25. The on-shell widths and masses along with the phases and couplings used in PYTHIA 8 for the  $\rho$  resonances are given in Table 3.3, while the scalar  $f_0$  and *sigma*, and tensor  $f_2$  parameters are given in Table 3.4. Both sets of parameters are based on the fits performed by the CLEO collaboration [108].

The Breit-Wigners used in the form factors  $F_1$ ,  $F_2$ , and  $F_3$  are given by the  $s$ ,  $p$ , and  $d$ -wave Breit-Wigners of Eqs. 3.16, 3.17, and 3.18. The Breit-Wigner for the  $a_1$  is given by,

$$BW_{a_1}(s) = \frac{m_{a_1}^2}{m_{a_1}^2 - s - \Gamma_{a_1}(s)} \tag{3.35}$$

where  $m_{a_1}$  is the on-shell mass of the  $a_1$ . The running width  $\Gamma_{a_1}(s)$  is the weighted sum of the three partial widths  $\Gamma_{\pi^0\pi^0\pi^-}(s)$ ,  $\Gamma_{\pi^-\pi^-\pi^+}(s)$ , and the  $s$ -wave contribution  $\Gamma_{KK^*}(s)$ ,

$$\Gamma_{a_1}(s) = w_\pi(\Gamma_{\pi^0\pi^0\pi^-}(s) + \Gamma_{\pi^-\pi^-\pi^+}(s)) + w_K\Gamma_{KK^*}(s) \tag{3.36}$$

where  $w_\pi$  and  $w_K$  are the pion and kaon weights given in Table 3.6, and  $\Gamma_{\pi^0\pi^0\pi^-}(s)$ ,  $\Gamma_{\pi^-\pi^-\pi^+}(s)$ , and  $\Gamma_{KK^*}(s)$  are piece-wise fitted functions given in Table 3.5 with the parameters given in

**Table 3.5.:** Functions used to fit the partial widths of the running  $a_1$  width used in the hadronic current for the decay of the  $\tau$  lepton into three pions.

| $\Gamma_{\text{partial}}$  | limits $[\text{GeV}^2]$                     | $\Gamma(s)$ [GeV]   |
|----------------------------|---|---|
| $\Gamma_{\pi^-\pi^-\pi^+}$ | $0 \leq s < m_{3\pi^-}$                     | 0   |
|                            | $m_{3\pi^-} \leq s < m_{\rho\pi^0}$         | $P_0(s - m_{3\pi^-})^3 (1 - P_1(s - m_{3\pi^-}) + P_2(s - m_{3\pi^-})^2)$                     |
|                            | $m_{\rho\pi^0} \leq s$                      | $P_0 + P_1s + P_2s^2 + P_3s^3 + P_4s^4$   |
| $\Gamma_{\pi^0\pi^0\pi^-}$ | $0 \leq s < m_{2\pi^0\pi^-}$                | 0   |
|                            | $m_{2\pi^0\pi^-} \leq s \leq m_{\rho\pi^0}$ | $P_0(s - m_{2\pi^0\pi^-})^3$<br>$(1 - P_1(s - m_{2\pi^0\pi^-}) + P_2(s - m_{2\pi^0\pi^-})^2)$ |
|                            | $m_{\rho\pi^0} \leq s$                      | $P_0 + P_1s + P_2s^2 + P_3s^3 + P_4s^4$   |
| $\Gamma_{KK^*}$            | $0 \leq s < m_{KK^*}$                       | 0   |
|                            | $m_{KK^*} \leq s$                           | $\sqrt{(s - (m_K + m_{K^*})^2)(s - (m_K - m_{K^*})^2)}/(2s)$                                  |

| parameter         | value                                   |
|-------------------|---|
| $w_\pi$           | $0.2384^2/1.0252088$                    |
| $w_K$             | 4.7621                                  |
| $m_{3\pi^-}$      | $(m_{\pi^-} + m_{\pi^-} + m_{\pi^+})^2$ |
| $m_{2\pi^0\pi^-}$ | $(m_{\pi^0} + m_{\pi^0} + m_{\pi^-})^2$ |
| $m_{\rho\pi^0}$   | $(m_\rho + m_{\pi^0})^2$                |
| $m_{KK^*}$        | $(m_K + m_{K^*})^2$                     |

**Table 3.6.:** Parameters used for the  $a_1$  Breit-Wigner and running width of Eq. 3.36 and Table 3.5 for the three pion hadronic current of the  $\tau$  lepton.

Tables 3.6 and 3.7.

Figure 3.8 gives the  $\pi^0\pi^-$  and  $\pi^-\pi^+$  invariant mass distributions for the  $\pi^-\pi^-\pi^+$  and  $\pi^0\pi^0\pi^-$  decay channels. There is good general agreement between HERWIG++ and PYTHIA 8 for the  $\pi^-\pi^-\pi^+$  channel but a sizable discrepancy for the  $\pi^0\pi^0\pi^-$  channel due to a difference in the implementation of the second form factor,  $F_2^0$ , of Eq. 3.32. Additional differences between the two distributions for both decay channels arise from the choice of parameters used.

**Table 3.7.:** Parameters used in the  $a_1$  running partial width fits of Table 3.5 for the three pion hadronic current.

| $\Gamma_{\text{partial}}$  | limits                                      | parameters      |                  |                 |
|----------------------------|---|-----------------|------------------|-----------------|
| $\Gamma_{\pi^-\pi^-\pi^+}$ | $m_{3\pi^-} \leq s < m_{\rho\pi^0}$         | $P_0 = 5.8090$  | $P_1 = 3.0098$   | $P_2 = 4.5792$  |
|                            | $m_{\rho\pi^0} \leq s$                      | $P_0 = -13.914$ | $P_1 = 27.69$    | $P_2 = -13.393$ |
|                            |   | $P_3 = 3.1924$  | $P_4 = -0.10487$ |                 |
| $\Gamma_{\pi^0\pi^0\pi^-}$ | $m_{2\pi^0\pi^-} \leq s \leq m_{\rho\pi^0}$ | $P_0 = 6.28450$ | $P_1 = 2.9595$   | $P_2 = 4.3355$  |
|                            | $m_{\rho\pi^0} \leq s$                      | $P_0 = -15.411$ | $P_1 = 32.088$   | $P_2 = -17.666$ |
|                            |   | $P_3 = 4.9355$  | $P_4 = -0.37498$ |                 |

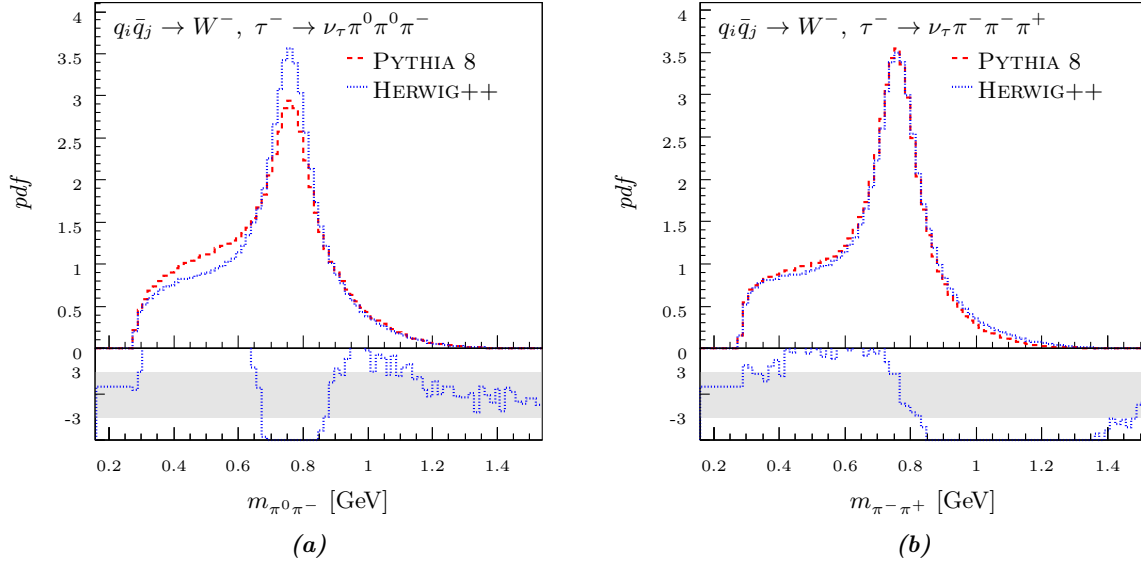


**Figure 3.8.:** Comparisons of the  $m_{23}$  invariant mass distributions for the (a)  $\pi^0\pi^0\pi^-$  decay channel and the (b)  $\pi^-\pi^-\pi^+$  decay channel for the three pion hadronic current.

### Three Mesons with Kaons

The model of Ref. [109] by Finkemeier and Mirkes is implemented in PYTHIA 8 to provide  $K^-\pi^-K^+$ ,  $K^0\pi^-\bar{K}^0$ ,  $K_S^0\pi^-K_S^0$ ,  $K_L^0\pi^-K_L^0$ ,  $K_S^0\pi^-K_L^0$ ,  $K^-\pi^0K^0$ ,  $\pi^0\pi^0K^-$ ,  $K^-\pi^-\pi^+$ , and  $\pi^-\bar{K}^0\pi^0$  decays for the  $\tau$  lepton. For this model the  $F_1$ ,  $F_2$ , and  $F_4$  form factors are non-zero, while the  $F_3$  and  $F_5$  form factors are zero. The form factors for this model are given in Table 3.9 for  $F_1$ , Table 3.9 for  $F_2$ , and Table 3.11 for  $F_4$ . These form factors use the weighted sums of the intermediate resonances,

$$t(s, \vec{m}, \vec{\Gamma}, \vec{w}) = \frac{1}{\sum_i w_i} w_i BW(s, m_i, \Gamma_i) \quad (3.37)$$

$$t_p(m_0, m_1, s, \vec{m}, \vec{\Gamma}, \vec{w}) = \frac{1}{\sum_i w_i} w_i BW_p(m_0, m_1, s, m_i, \Gamma_i)$$

where  $\vec{m}$  is a vector of the resonance masses,  $\vec{\Gamma}$  are their widths, and  $\vec{w}$  are their real weights. The lengths of these three vectors are the same, and correspond to the number of resonances being modelled. Here,  $t$  is a sum of fixed width Breit-Wigners, given by Eq. 3.15 and  $t_p$  is the sum of  $p$ -wave Breit-Wigners, given by Eq. 3.17.

The channels containing a single pion can proceed through an initial  $a_1$  resonance, similar to the three pion channels modelled with the CLEO current. The Breit-Wigner for the  $a_1$  is now defined as,

$$BW_{a_1}(s) = \frac{m_{a_1}^2}{m_{a_1}^2 - s - im_{a_1}\Gamma_{a_1} \frac{g_{a_1}(s)}{g_{a_1}(m_{a_1}^2)}} \quad (3.38)$$

**Table 3.8.:** Vectors of masses, widths, and real weights for the resonances used in the form factors of Tables 3.9 through 3.11 for  $\tau$  lepton decays into three mesons where one or more of the mesons are kaons.

| resonances | $\vec{m}$ [GeV]         | $\vec{\Gamma}$ [GeV]    | $\vec{w}$                            |
|------------|-------------------------|-------------------------|--------------------------------------|
| $\rho_a$   | $(0.773, 1.370)$        | $(0.145, 0.510)$        | $(1, -\frac{29}{200})$               |
| $\rho_v$   | $(0.773, 1.500, 1.750)$ | $(0.145, 0.220, 0.120)$ | $(1, -\frac{13}{52}, -\frac{1}{26})$ |
| $K^*_a$    | $(0.892, 1.412)$        | $(0.050, 0.227)$        | $(1, -\frac{27}{200})$               |
| $K^*_v$    | $(0.892, 1.412, 1.714)$ | $(0.050, 0.227, 0.323)$ | $(1, -\frac{13}{52}, -\frac{1}{26})$ |
| $K_{1a}$   | $(1.402, 1.270)$        | $(0.174, 0.090)$        | $(1, \frac{33}{100})$                |
| $K_{1b}$   | $(1.270)$               | $(0.090)$               | $(1)$                                |
| $\omega$   | $(0.782, 1.020)$        | $(0.00843, 0.0443)$     | $(1, \frac{1}{20})$                  |

where,

$$g_{a_1}(s) = \begin{cases} 0 & \text{if } s < (3m_{\pi^-})^2 \\ 4.1(s - 9m_{\pi^-}^2)^3(1 - 3.3(s - 9m_{\pi^-}^2) & \text{else if } s < (m_\rho + m_{\pi^-})^2 \\ + 5.8(s - 9m_{\pi^-}^2)^2 & \\ s(1.623 + \frac{10.38}{s} - \frac{9.32}{s^2} + \frac{0.65}{s^3}) & \text{else} \end{cases} \quad (3.39)$$

is an  $a_1$  phase-space factor as given in Ref. [103]. The channels with a single pion can also proceed through initial  $\rho$  resonances which are modelled with  $p$ -wave Breit-Wigners. The channels containing two pions proceed through either initial  $K_1$  resonances modelled with fixed width Breit-Wigners or  $K^*$  resonances modelled with  $p$ -wave Breit-Wigners.

All the channels with a single pion can proceed through secondary  $K^*$  or  $\rho$  resonances, except the  $K_S^0\pi^-K_S^0$  and  $K_L^0\pi^-K_L^0$  channels which can only proceed through secondary  $K^*$  resonances. Additionally, the  $K^-\pi^-K^+$ ,  $K^0\pi^-\bar{K}^0$ , and  $K_S^0\pi^-K_L^0$  channels can proceed via secondary  $\omega$  resonances. The channels with two pions can proceed through secondary  $K^*$  resonances, and the  $K^-\pi^-\pi^+$  and  $\pi^-\bar{K}^0\pi^0$  can proceed through additional secondary  $\rho$  resonances.

The  $m_{23}$  distributions for the five channels modelled with this current containing a single pion are given in Fig. 3.9 while the distributions for the three channels containing two pions are given in Fig. 3.10. For all single pion channels, the PYTHIA 8 and HERWIG++ distributions match well. However, the TAUOLA distributions, particularly in the  $K^0\pi^-\bar{K}^0$  and  $K^-\pi^0K^0$  channels, do not match. This is expected, as the TAUOLA implementation for these channels uses an older model, which among other differences, does not include the  $K^*(1410)$  resonance. This older model is used for general three meson decays and is introduced in the following section. A similar level of agreement between the PYTHIA 8 and HERWIG++ distributions for the two pion channels can also be seen, with the same expected discrepancies with the TAUOLA distributions.

**Table 3.9.:** The  $F_1$  form factors for the three mesons with kaons decay model given for the relevant  $\tau$  lepton decay channels.

| channel                     | $F_1$  |
|-----------------------------|--|
| $K^- \pi^- K^+$             | $-\frac{1}{6}BW_{a_1}(s_1)t_p(m_{\pi^-}, m_{K^0}, s_2, \vec{m}_{K^*a}, \vec{\Gamma}_{K^*a}, \vec{w}_{K^*a})$   |
| $K^0 \pi^- \bar{K}^0$       | $-\frac{1}{6}BW_{a_1}(s_1)t_p(m_{\pi^-}, m_{K^0}, s_2, \vec{m}_{K^*a}, \vec{\Gamma}_{K^*a}, \vec{w}_{K^*a})$   |
| $K_{S/L}^0 \pi^- K_{S/L}^0$ | $\frac{1}{6}BW_{a_1}(s_1)(t_p(m_{\pi^-}, m_{K^0}, s_2, \vec{m}_{K^*a}, \vec{\Gamma}_{K^*a}, \vec{w}_{K^*a}) - t_p(m_{\pi^-}, m_{K^0}, s_4, \vec{m}_{K^*a}, \vec{\Gamma}_{K^*a}, \vec{w}_{K^*a}))$  |
| $K_S^0 \pi^- K_L^0$         | $-\frac{1}{6}BW_{a_1}(s_1)(t_p(m_{\pi^-}, m_{K^0}, s_2, \vec{m}_{K^*a}, \vec{\Gamma}_{K^*a}, \vec{w}_{K^*a}) - t_p(m_{\pi^-}, m_{K^0}, s_4, \vec{m}_{K^*a}, \vec{\Gamma}_{K^*a}, \vec{w}_{K^*a}))$   |
| $K^- \pi^0 K^0$             | $-\frac{1}{6}BW_{a_1}(s_1)(t_p(m_{\pi^-}, m_{K^0}, s_2, \vec{m}_{K^*a}, \vec{\Gamma}_{K^*a}, \vec{w}_{K^*a}) - t_p(m_{\pi^-}, m_{K^0}, s_4, \vec{m}_{K^*a}, \vec{\Gamma}_{K^*a}, \vec{w}_{K^*a}))$   |
| $\pi^0 \pi^0 K^-$           | $-\frac{1}{3}t(s_1, \vec{m}_{K_{1a}}, \vec{\Gamma}_{K_{1a}}, \vec{w}_{K_{1a}})t_p(m_{\pi^-}, m_{K^0}, s_2, \vec{m}_{K^*a}, \vec{\Gamma}_{K^*a}, \vec{w}_{K^*a})$   |
| $K^- \pi^- \pi^+$           | $-\frac{1}{3}t(s_1, \vec{m}_{K_{1b}}, \vec{\Gamma}_{K_{1b}}, \vec{w}_{K_{1b}})t_p(m_{\pi^-}, m_{\pi^-}, s_2, \vec{m}_{\rho_a}, \vec{\Gamma}_{\rho_a}, \vec{w}_{\rho_a})$   |
| $\pi^- \bar{K}^0 \pi^0$     | $-\frac{1}{3}t(s_1, \vec{m}_{K_{1a}}, \vec{\Gamma}_{K_{1a}}, \vec{w}_{K_{1a}})(t_p(m_{\pi^-}, m_{K^0}, s_2, \vec{m}_{K^*a}, \vec{\Gamma}_{K^*a}, \vec{w}_{K^*a}) - t_p(m_{\pi^-}, m_{K^0}, s_4, \vec{m}_{K^*a}, \vec{\Gamma}_{K^*a}, \vec{w}_{K^*a}))$ |

**Table 3.10.:** The  $F_2$  form factors for the three mesons with kaons decay model given for the relevant  $\tau$  lepton decay channels.

| channel                     | $F_2$   |
|-----------------------------|---|
| $K^- \pi^- K^+$             | $\frac{1}{6}BW_{a_1}(s_1)t_p(m_{\pi^-}, m_{\pi^-}, s_3, \vec{m}_{\rho_a}, \vec{\Gamma}_{\rho_a}, \vec{w}_{\rho_a})$   |
| $K^0 \pi^- \bar{K}^0$       | $\frac{1}{6}BW_{a_1}(s_1)t_p(m_{\pi^-}, m_{\pi^-}, s_3, \vec{m}_{\rho_a}, \vec{\Gamma}_{\rho_a}, \vec{w}_{\rho_a})$   |
| $K_{S/L}^0 \pi^- K_{S/L}^0$ | $\frac{1}{6}BW_{a_1}(s_1)(t_p(m_{\pi^-}, m_{K^0}, s_4, \vec{m}_{K^*a}, \vec{\Gamma}_{K^*a}, \vec{w}_{K^*a}))$   |
| $K_S^0 \pi^- K_L^0$         | $\frac{1}{6}BW_{a_1}(s_1)(2t_p(m_{\pi^-}, m_{\pi^-}, s_3, \vec{m}_{\rho_a}, \vec{\Gamma}_{\rho_a}, \vec{w}_{\rho_a}) + t_p(m_{\pi^-}, m_{K^0}, s_4, \vec{m}_{K^*a}, \vec{\Gamma}_{K^*a}, \vec{w}_{K^*a}))$  |
| $K^- \pi^0 K^0$             | $\frac{1}{6}BW_{a_1}(s_1)(2t_p(m_{\pi^-}, m_{\pi^-}, s_3, \vec{m}_{\rho_a}, \vec{\Gamma}_{\rho_a}, \vec{w}_{\rho_a}) + t_p(m_{\pi^-}, m_{K^0}, s_4, \vec{m}_{K^*a}, \vec{\Gamma}_{K^*a}, \vec{w}_{K^*a}))$  |
| $\pi^0 \pi^0 K^-$           | $\frac{1}{3}t(s_1, \vec{m}_{K_{1a}}, \vec{\Gamma}_{K_{1a}}, \vec{w}_{K_{1a}})t_p(m_{\pi^-}, m_{K^0}, s_3, \vec{m}_{K^*a}, \vec{\Gamma}_{K^*a}, \vec{w}_{K^*a})$   |
| $K^- \pi^- \pi^+$           | $\frac{1}{3}t(s_1, \vec{m}_{K_{1a}}, \vec{\Gamma}_{K_{1a}}, \vec{w}_{K_{1a}})t_p(m_{\pi^-}, m_{K^0}, s_3, \vec{m}_{K^*a}, \vec{\Gamma}_{K^*a}, \vec{w}_{K^*a})$   |
| $\pi^- \bar{K}^0 \pi^0$     | $\frac{2}{3}t(s_1, \vec{m}_{K_{1b}}, \vec{\Gamma}_{K_{1b}}, \vec{w}_{K_{1b}})t_p(m_{\pi^-}, m_{\pi^-}, s_3, \vec{m}_{\rho_a}, \vec{\Gamma}_{\rho_a}, \vec{w}_{\rho_a}) + \frac{1}{3}t(s_1, \vec{m}_{K_{1a}}, \vec{\Gamma}_{K_{1a}}, \vec{w}_{K_{1a}})t_p(m_{\pi^-}, m_{K^0}, s_4, \vec{m}_{K^*a}, \vec{\Gamma}_{K^*a}, \vec{w}_{K^*a})$ |

**Table 3.11.:** The  $F_4$  form factors for the three mesons with kaons decay model given for the relevant  $\tau$  lepton decay channels.

| channel                     | $F_4$  |
|-----------------------------|--|
| $K^- \pi^- K^+$             | $\frac{\sqrt{2}-1}{8\pi^2 w_\pi^2} t_p(m_{\pi^-}, m_{\pi^-}, s_1, \vec{m}_{\rho_v}, \vec{\Gamma}_{\rho_v}, \vec{w}_{\rho_v}) (\sqrt{2}t(s_3, \vec{m}_\omega, \vec{\Gamma}_\omega, \vec{w}_\omega) + t_p(m_{\pi^-}, m_{K^0}, s_2, \vec{m}_{K^*_a}, \vec{\Gamma}_{K^*_a}, \vec{w}_{K^*_a}))$   |
| $K^0 \pi^- \bar{K}^0$       | $\frac{1-\sqrt{2}}{8\pi^2 w_\pi^2} t_p(m_{\pi^-}, m_{\pi^-}, s_1, \vec{m}_{\rho_v}, \vec{\Gamma}_{\rho_v}, \vec{w}_{\rho_v}) (\sqrt{2}t(s_3, \vec{m}_\omega, \vec{\Gamma}_\omega, \vec{w}_\omega) + t_p(m_{\pi^-}, m_{K^0}, s_2, \vec{m}_{K^*_a}, \vec{\Gamma}_{K^*_a}, \vec{w}_{K^*_a}))$   |
| $K_{S/L}^0 \pi^- K_{S/L}^0$ | $\frac{\sqrt{2}-1}{8\pi^2 w_\pi^2} t_p(m_{\pi^-}, m_{\pi^-}, s_1, \vec{m}_{\rho_v}, \vec{\Gamma}_{\rho_v}, \vec{w}_{\rho_v}) (t_p(m_{\pi^-}, m_{K^0}, s_2, \vec{m}_{K^*_a}, \vec{\Gamma}_{K^*_a}, \vec{w}_{K^*_a}) - t_p(m_{\pi^-}, m_{K^0}, s_4, \vec{m}_{K^*_a}, \vec{\Gamma}_{K^*_a}, \vec{w}_{K^*_a}))$  |
| $K_S^0 \pi^- K_L^0$         | $\frac{1-\sqrt{2}}{8\pi^2 w_\pi^2} t_p(m_{\pi^-}, m_{\pi^-}, s_1, \vec{m}_{\rho_v}, \vec{\Gamma}_{\rho_v}, \vec{w}_{\rho_v}) (2\sqrt{2}t(s_3, \vec{m}_\omega, \vec{\Gamma}_\omega, \vec{w}_\omega) + t_p(m_{\pi^-}, m_{K^0}, s_2, \vec{m}_{K^*_a}, \vec{\Gamma}_{K^*_a}, \vec{w}_{K^*_a}) + t_p(m_{\pi^-}, m_{K^0}, s_4, \vec{m}_{K^*_a}, \vec{\Gamma}_{K^*_a}, \vec{w}_{K^*_a}))$         |
| $K^- \pi^0 K^0$             | $\frac{1-\sqrt{2}}{8\pi^2 w_\pi^2} t_p(m_{\pi^-}, m_{\pi^-}, s_1, \vec{m}_{\rho_v}, \vec{\Gamma}_{\rho_v}, \vec{w}_{\rho_v}) (t_p(m_{\pi^-}, m_{K^0}, s_4, \vec{m}_{K^*_a}, \vec{\Gamma}_{K^*_a}, \vec{w}_{K^*_a}) - t_p(m_{\pi^-}, m_{K^0}, s_2, \vec{m}_{K^*_a}, \vec{\Gamma}_{K^*_a}, \vec{w}_{K^*_a}))$  |
| $\pi^0 \pi^0 K^-$           | $\frac{1}{8\pi^2 w_\pi^2} t_p(m_{\pi^-}, m_{K^0}, s_1, \vec{m}_{K^*_v}, \vec{\Gamma}_{K^*_v}, \vec{w}_{K^*_v}) (t_p(m_{\pi^-}, m_{K^0}, s_2, \vec{m}_{K^*_a}, \vec{\Gamma}_{K^*_a}, \vec{w}_{K^*_a}) - t_p(m_{\pi^-}, m_{K^0}, s_3, \vec{m}_{K^*_a}, \vec{\Gamma}_{K^*_a}, \vec{w}_{K^*_a}))$  |
| $K^- \pi^- \pi^+$           | $-\frac{1}{8\pi^2 w_\pi^2} t_p(m_{\pi^-}, m_{K^0}, s_1, \vec{m}_{K^*_v}, \vec{\Gamma}_{K^*_v}, \vec{w}_{K^*_v}) (t_p(m_{\pi^-}, m_{\pi^-}, s_2, \vec{m}_{\rho_a}, \vec{\Gamma}_{\rho_a}, \vec{w}_{\rho_a}) + t_p(m_{\pi^-}, m_{K^0}, s_3, \vec{m}_{K^*_a}, \vec{\Gamma}_{K^*_a}, \vec{w}_{K^*_a}))$  |
| $\pi^- \bar{K}^0 \pi^0$     | $\frac{1}{8\pi^2 w_\pi^2} t_p(m_{\pi^-}, m_{K^0}, s_1, \vec{m}_{K^*_v}, \vec{\Gamma}_{K^*_v}, \vec{w}_{K^*_v}) (2t_p(m_{\pi^-}, m_{\pi^-}, s_3, \vec{m}_{\rho_a}, \vec{\Gamma}_{\rho_a}, \vec{w}_{\rho_a}) + t_p(m_{\pi^-}, m_{K^0}, s_2, \vec{m}_{K^*_a}, \vec{\Gamma}_{K^*_a}, \vec{w}_{K^*_a}) + t_p(m_{\pi^-}, m_{K^0}, s_4, \vec{m}_{K^*_a}, \vec{\Gamma}_{K^*_a}, \vec{w}_{K^*_a}))$ |

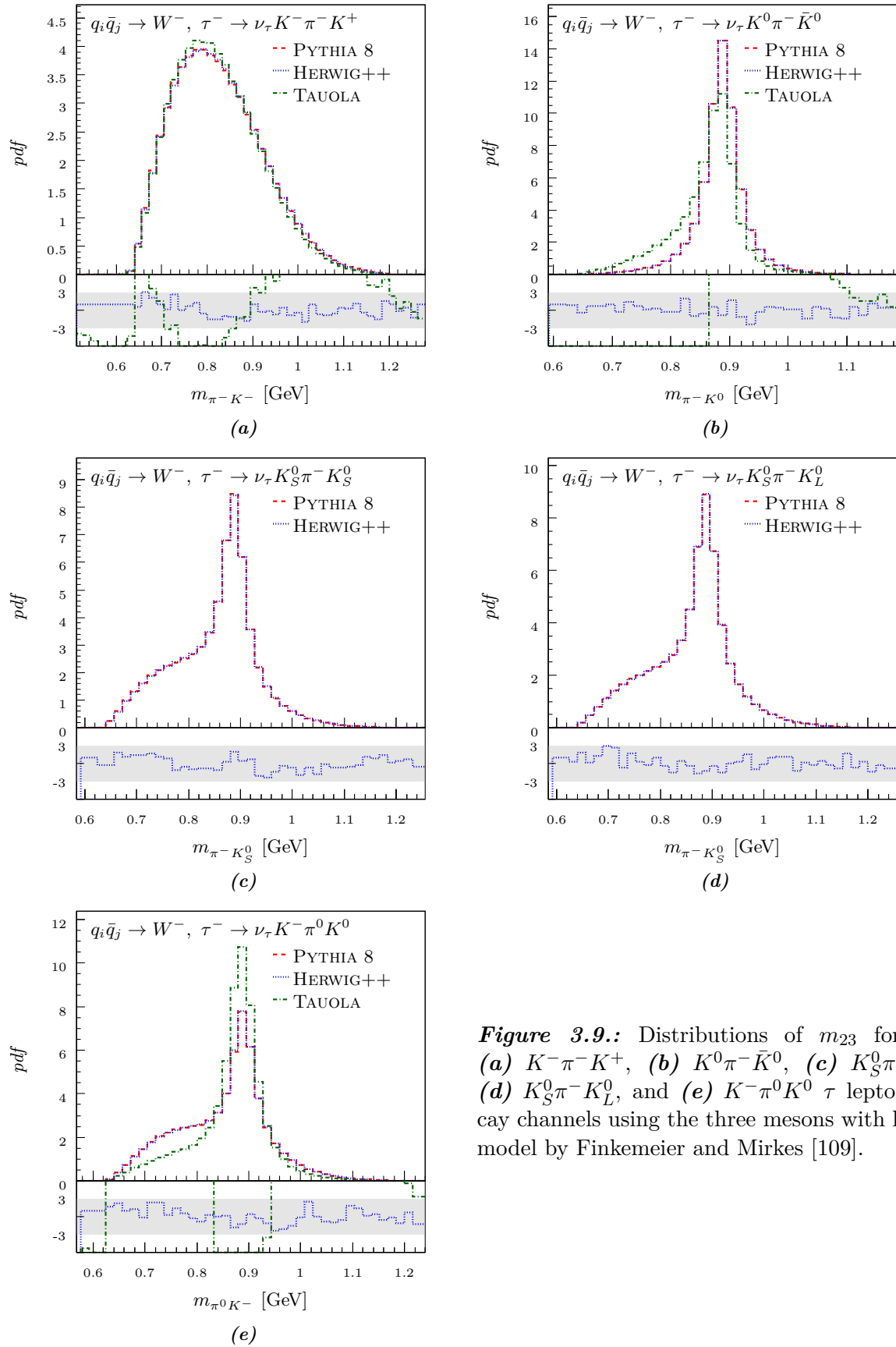


**Figure 3.9.:** Distributions of  $m_{23}$  for the (a)  $K^- \pi^- K^+$ , (b)  $K^0 \pi^- \bar{K}^0$ , (c)  $K_S^0 \pi^- K_S^0$ , (d)  $K_S^0 \pi^- K_L^0$ , and (e)  $K^- \pi^0 K^0$   $\tau$  lepton decay channels using the three mesons with kaons model by Finkemeier and Mirkes [109].



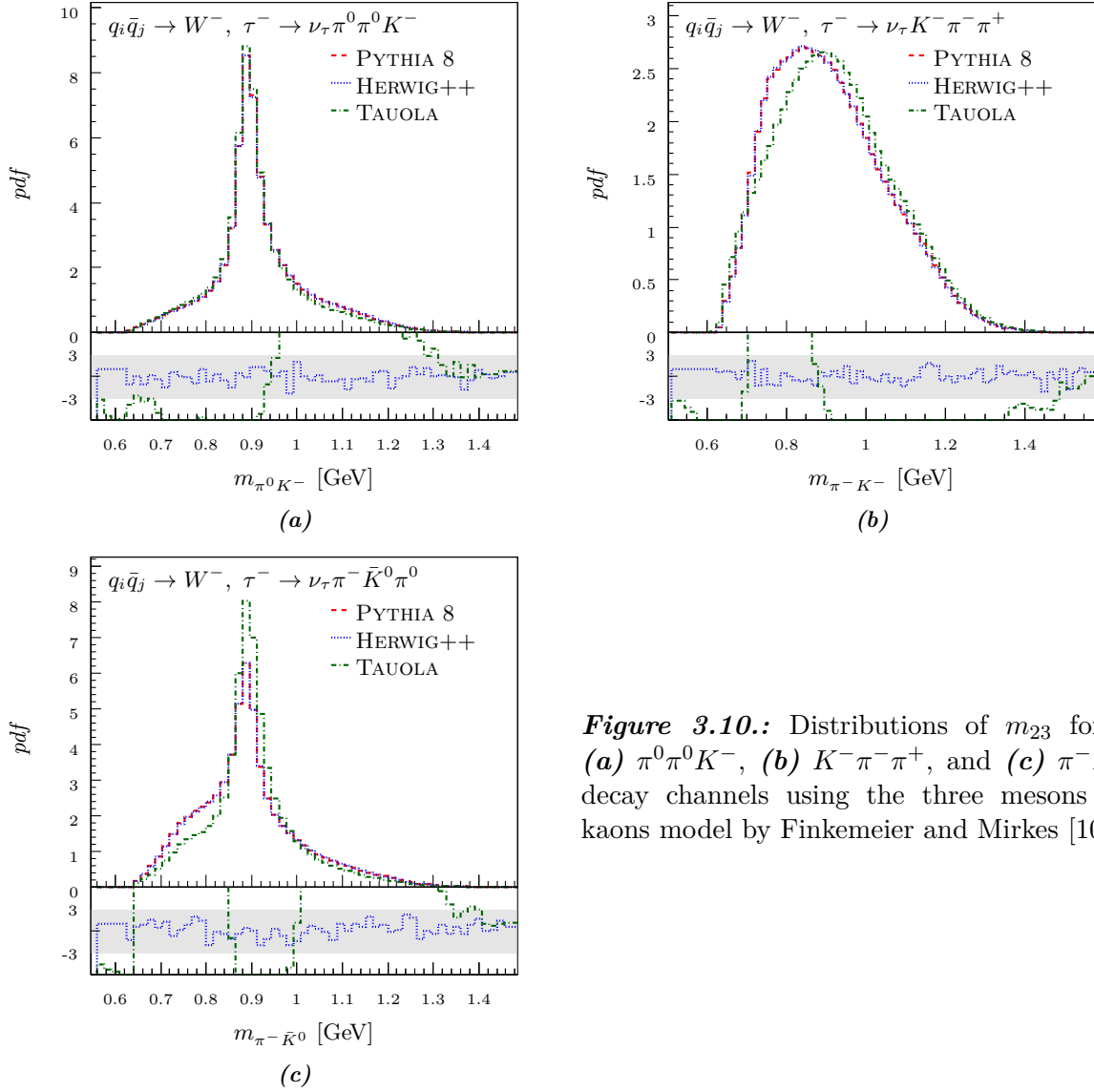


**Figure 3.10.:** Distributions of  $m_{23}$  for the (a)  $\pi^0\pi^0K^-$ , (b)  $K^-\pi^-\pi^+$ , and (c)  $\pi^-\bar{K}^0\pi^0$  decay channels using the three mesons with kaons model by Finkemeier and Mirkes [109].

### General Three Mesons

The older and more general model of Decker, *et al.* of Ref. [110] is also implemented in PYTHIA 8 and can be used to perform the  $\pi^0\pi^0\pi^+$ ,  $\pi^-\pi^-\pi^+$ ,  $K^-\pi^-K^+$ ,  $K^0\pi^-\bar{K}^0$ ,  $K^-\pi^0K^0$ ,  $\pi^0\pi^0K^-$ ,  $K^-\pi^-\pi^+$ ,  $\pi^-\bar{K}^0\pi^0$ , and  $\pi^-\pi^0\eta$  decays of the  $\tau$  lepton. However, by default, only the  $\pi^-\pi^0\eta$  decay of the  $\tau$  lepton is performed using this model. The same summation of fixed width and  $p$ -wave Breit-Wigners using  $t$  and  $t_p$  of Eq. 3.37 is used, as well as the same  $a_1$  Breit-Wigner of Eq. 3.38. However, the masses, widths, and real weights of the resonances differ from those of Table 3.8 and are given in Table 3.12. Note that no  $\omega$  resonances are introduced.

The form factors for this model are provided in Table 3.13 for  $F_1$ , Table 3.13 for  $F_2$ , and Table 3.15 for  $F_4$ . Here  $F_3$  and  $F_5$  are zero for all channels. The three pion channels decay through an initial  $a_1$  resonance followed by a decay through secondary  $\rho$  resonances. The  $K^-\pi^-K^+$  and  $K^-\pi^-\bar{K}^0$  channels can decay through an initial  $a_1$  or  $\rho$  resonance and through secondary  $K^*$  and  $\rho$  resonances. The  $K^-\pi^0K^0$  channel can proceed through an initial  $a_1$  res-

**Table 3.12.:** Vectors of masses, widths, and real weights for the resonances used in the form factors of Tables 3.13 through 3.15 for  $\tau$  lepton decays into three mesons using the general three meson model.

| resonances | $\vec{m}$ [GeV]         | $\vec{\Gamma}$ [GeV]    | $\vec{w}$                            |
|------------|-------------------------|-------------------------|--------------------------------------|
| $\rho_a$   | $(0.773, 1.370)$        | $(0.145, 0.510)$        | $(1, -\frac{29}{200})$               |
| $\rho_v$   | $(0.773, 1.500, 1.750)$ | $(0.145, 0.220, 0.120)$ | $(1, -\frac{13}{52}, -\frac{1}{26})$ |
| $K^*$      | $(0.892)$               | $(0.0513)$              | $(1)$                                |
| $K_1$      | $(1.402)$               | $(0.174)$               | $(1)$                                |

**Table 3.13.:** The  $F_1$  form factors for the general three meson model given for the relevant  $\tau$  lepton decay channels.

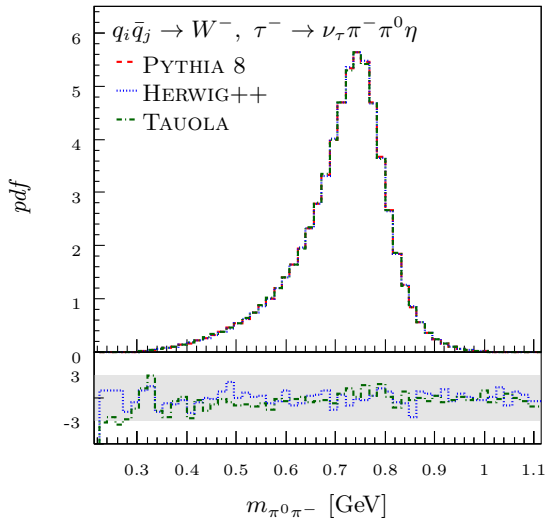
| channel                               | $F_1$   |
|---------------------------------------|---|
| $\pi^- / {}^0 \pi^- / {}^0 \pi^+ / -$ | $BW_{a_1}(s_1)t_p(m_{\pi^-}, m_{\pi^-}, s_2, \vec{m}_{\rho_a}, \vec{\Gamma}_{\rho_a}, \vec{w}_{\rho_a})$  |
| $K^- \pi^- K^+$                       | $-\frac{1}{3}BW_{a_1}(s_1)t_p(m_{\pi^-}, m_{K^0}, s_2, \vec{m}_{K^*}, \vec{\Gamma}_{K^*}, \vec{w}_{K^*})$   |
| $K^0 \pi^- \bar{K}^0$                 | $-\frac{1}{3}BW_{a_1}(s_1)t_p(m_{\pi^-}, m_{K^0}, s_2, \vec{m}_{K^*}, \vec{\Gamma}_{K^*}, \vec{w}_{K^*})$   |
| $K^- \pi^0 K^0$                       | 0   |
| $\pi^0 \pi^0 K^-$                     | $t(s_1, \vec{m}_{K_1}, \vec{\Gamma}_{K_1}, \vec{w}_{K_1})t_p(m_{\pi^-}, m_{K^0}, s_2, \vec{m}_{K^*}, \vec{\Gamma}_{K^*}, \vec{w}_{K^*})$                        |
| $K^- \pi^- \pi^+$                     | $-\frac{1}{3}t(s_1, \vec{m}_{K_1}, \vec{\Gamma}_{K_1}, \vec{w}_{K_1})t_p(m_{\pi^-}, m_{\pi^-}, s_2, \vec{m}_{\rho_a}, \vec{\Gamma}_{\rho_a}, \vec{w}_{\rho_a})$ |
| $\pi^- \bar{K}^0 \pi^0$               | 0   |
| $\pi^- \pi^0 \eta$                    | 0   |

**Table 3.14.:** The  $F_2$  form factors for the general three meson model given for the relevant  $\tau$  lepton decay channels.

| channel                               | $F_2$   |
|---------------------------------------|---|
| $\pi^- / {}^0 \pi^- / {}^0 \pi^+ / -$ | $-BW_{a_1}(s_1)t_p(m_{\pi^-}, m_{\pi^-}, s_3, \vec{m}_{\rho_a}, \vec{\Gamma}_{\rho_a}, \vec{w}_{\rho_a})$   |
| $K^- \pi^- K^+$                       | $\frac{1}{3}BW_{a_1}(s_1)t_p(m_{\pi^-}, m_{\pi^-}, s_3, \vec{m}_{\rho_a}, \vec{\Gamma}_{\rho_a}, \vec{w}_{\rho_a})$                                 |
| $K^0 \pi^- \bar{K}^0$                 | $\frac{1}{3}BW_{a_1}(s_1)t_p(m_{\pi^-}, m_{\pi^-}, s_3, \vec{m}_{\rho_a}, \vec{\Gamma}_{\rho_a}, \vec{w}_{\rho_a})$                                 |
| $K^- \pi^0 K^0$                       | $BW_{a_1}(s_1)t_p(m_{\pi^-}, m_{\pi^-}, s_3, \vec{m}_{\rho_a}, \vec{\Gamma}_{\rho_a}, \vec{w}_{\rho_a})$  |
| $\pi^0 \pi^0 K^-$                     | $-t(s_1, \vec{m}_{K_1}, \vec{\Gamma}_{K_1}, \vec{w}_{K_1})t_p(m_{\pi^-}, m_{K^0}, s_3, \vec{m}_{K^*}, \vec{\Gamma}_{K^*}, \vec{w}_{K^*})$           |
| $K^- \pi^- \pi^+$                     | $\frac{1}{3}t(s_1, \vec{m}_{K_1}, \vec{\Gamma}_{K_1}, \vec{w}_{K_1})t_p(m_{\pi^-}, m_{K^0}, s_3, \vec{m}_{K^*}, \vec{\Gamma}_{K^*}, \vec{w}_{K^*})$ |
| $\pi^- \bar{K}^0 \pi^0$               | $t(s_1, \vec{m}_{K_1}, \vec{\Gamma}_{K_1}, \vec{w}_{K_1})t_p(m_{\pi^-}, m_{\pi^-}, s_3, \vec{m}_{\rho_a}, \vec{\Gamma}_{\rho_a}, \vec{w}_{\rho_a})$ |
| $\pi^- \pi^0 \eta$                    | 0   |

**Table 3.15.:** The  $F_4$  form factors for the general three meson model given for the relevant  $\tau$  lepton decay channels.

| channel                 | $F_4$  |
|-------------------------|--|
| $\pi^-/0\pi^-/0\pi^+/-$ | 0  |
| $K^- \pi^- K^+$         | $\frac{5}{16\pi^2 w_\pi^2} t_p(m_{\pi^-}, m_{\pi^-}, s_1, \vec{m}_{\rho_v}, \vec{\Gamma}_{\rho_v}, \vec{w}_{\rho_v})(t_p(m_{\pi^-}, m_{\pi^-}, s_3, \vec{m}_{\rho_a}, \vec{\Gamma}_{\rho_a}, \vec{w}_{\rho_a}) - \frac{2}{10} t_p(m_{\pi^-}, m_{K^0}, s_2, \vec{m}_{K^*}, \vec{\Gamma}_{K^*}, \vec{w}_{K^*}))$   |
| $K^0 \pi^- \bar{K}^0$   | $-\frac{5}{16\pi^2 w_\pi^2} t_p(m_{\pi^-}, m_{\pi^-}, s_1, \vec{m}_{\rho_v}, \vec{\Gamma}_{\rho_v}, \vec{w}_{\rho_v}) (t_p(m_{\pi^-}, m_{\pi^-}, s_3, \vec{m}_{\rho_a}, \vec{\Gamma}_{\rho_a}, \vec{w}_{\rho_a}) - \frac{2}{10} t_p(m_{\pi^-}, m_{K^0}, s_2, \vec{m}_{K^*}, \vec{\Gamma}_{K^*}, \vec{w}_{K^*}))$ |
| $K^- \pi^0 K^0$         | 0  |
| $\pi^0 \pi^0 K^-$       | 0  |
| $K^- \pi^- \pi^+$       | $-\frac{5}{16\pi^2 w_\pi^2} t_p(m_{\pi^-}, m_{K^0}, s_1, \vec{m}_{K^*}, \vec{\Gamma}_{K^*}, \vec{w}_{K^*}) (t_p(m_{\pi^-}, m_{\pi^-}, s_2, \vec{m}_{\rho_a}, \vec{\Gamma}_{\rho_a}, \vec{w}_{\rho_a}) - \frac{2}{10} t_p(m_{\pi^-}, m_{K^0}, s_3, \vec{m}_{K^*}, \vec{\Gamma}_{K^*}, \vec{w}_{K^*}))$            |
| $\pi^- \bar{K}^0 \pi^0$ | $\frac{5}{8\pi^2 w_\pi^2} t_p(m_{\pi^-}, m_{K^0}, s_1, \vec{m}_{K^*}, \vec{\Gamma}_{K^*}, \vec{w}_{K^*}) (t_p(m_{\pi^-}, m_{\pi^-}, s_3, \vec{m}_{\rho_a}, \vec{\Gamma}_{\rho_a}, \vec{w}_{\rho_a}) - \frac{2}{10} t_p(m_{\pi^-}, m_{K^0}, s_2, \vec{m}_{K^*}, \vec{\Gamma}_{K^*}, \vec{w}_{K^*}))$              |
| $\pi^- \pi^0 \eta$      | $\frac{1}{4\pi^2 w_\pi^2} t_p(m_{\pi^-}, m_{\pi^-}, s_1, \vec{m}_{\rho_v}, \vec{\Gamma}_{\rho_v}, \vec{w}_{\rho_v}) t_p(m_{\pi^-}, m_{\pi^-}, s_4, \vec{m}_{\rho_a}, \vec{\Gamma}_{\rho_a}, \vec{w}_{\rho_a})$   |

**Figure 3.11.:** Distributions of  $m_{23}$  for the default  $\pi^- \pi^0 \eta$  decay channel using the general three meson model by Decker *et al.* [110].

onance followed by secondary  $K^*$  resonances. The  $\pi^0 \pi^- K^-$  channel proceeds through initial  $K_1$  resonances and secondary  $K^*$  resonances, while the  $K^- \pi^- \pi^+$  and  $\pi^- \bar{K}^0 \pi^0$  channels proceed through initial  $K_1$  or  $K^*$  resonances and secondary  $K^*$  or  $\rho$  resonances.

In Fig. 3.11 the  $m_{23}$  distribution from PYTHIA 8, HERWIG++, and TAUOLA for the  $\pi^- \pi^0 \eta$  decay channel is given. There is good agreement between all three generators. Distributions for the additional decays that can be performed with the general three meson model but are not

**Table 3.16.:** Vectors of masses, widths, and real weights for the resonances used in the form factor of Eq. 3.41 for the  $\gamma\pi^0\pi^-$  channel.

| resonances | $\vec{m}$ [GeV] | $\vec{\Gamma}$ [GeV] | $\vec{w}$            |
|------------|-----------------|----------------------|----------------------|
| $\rho$     | $(0.773, 1.7)$  | $(0.145, 0.26)$      | $(1, -\frac{1}{10})$ |
| $\omega$   | $(0.782)$       | $(0.0085)$           | $(1)$                |

used by default in PYTHIA 8 are provided in App. B for brevity, where Fig. B.1 are the  $m_{23}$  distributions for decays with only one pion and Fig. B.2 are the distributions for decays with two or more pions.

### Two Pions with a Photon

The  $\omega$  meson can decay into  $\pi^0\pi^-\pi^+$  or  $\gamma\pi^0$  final states. Consequently, the decay  $\tau^- \rightarrow \nu_\tau\omega\pi^0\pi^-$  can result in a four-body or five-body final state. The five-body final state is included in the intermediate resonances of the five-body decays in Sect. 3.2.4, but the four-body final state decay  $\tau^- \rightarrow \nu_\tau\gamma\pi^0\pi^-$  needs to be accounted for with an independent model. In PYTHIA 8 the model of Jadach *et al.* from Ref. [107] is implemented for this decay, and is given by the hadronic current,

$$\begin{aligned}
J^\mu \propto & F(s_1, \vec{m}_\rho, \vec{G}_\rho, \vec{w}_\rho) F(0, \vec{m}_\rho, \vec{G}_\rho, \vec{w}_\rho) F(s_4, \vec{m}_\omega, \vec{G}_\omega, \vec{w}_\omega) \\
& \left( \varepsilon_2^\mu \left( m_{\pi^-}^2 - q_{4\nu} q_2^\nu - q_{3\nu} q_2^\nu (q_{4\nu} q_3^\nu - q_{4\nu} q_2^\nu) \right) \right. \\
& - q_3^\mu \left( (q_{3\nu} \varepsilon_2^\nu) (q_{4\nu} q_2^\nu) - (q_{4\nu} \varepsilon_2^\nu) (q_{3\nu} q_2^\nu) \right) \\
& \left. - q_2^\mu \left( (q_{3\nu} \varepsilon_2^\nu) (q_{4\nu} q_3^\nu) - (q_{4\nu} \varepsilon_2^\nu) (m_{\pi^-}^2 + q_{3\nu} q_2^\nu) \right) \right)
\end{aligned} \tag{3.40}$$

where  $\varepsilon_2$  is the polarisation vector of the photon given by Eq. 2.38. Unlike the other hadronic currents of Sect. 3.2, this current takes on two spin states due to the photon in the final state. The form factor  $F$  is given by,

$$F(s, \vec{m}, \vec{\Gamma}, \vec{w}) = \sum_j \frac{w_j}{m_j^2 - s - im_j\Gamma_j} \tag{3.41}$$

where  $s$  is the centre-of-mass energy,  $\vec{m}$  is the vector of resonance masses,  $\vec{\Gamma}$  the vector of widths, and  $\vec{w}$  the vector of real weights. These vectors are given in Table 3.16, where the channel proceeds through initial  $\rho$  resonances followed by an  $\omega$  resonance.

In Fig. 3.12 the  $m_{23}$  distributions of the photon and neutral pion are given for PYTHIA 8, HERWIG++, and TAUOLA. All three distributions match well, although the TAUOLA distribution deviates slightly from the PYTHIA 8 and HERWIG++ distributions due to a difference in the parameters used in implementing the channel.

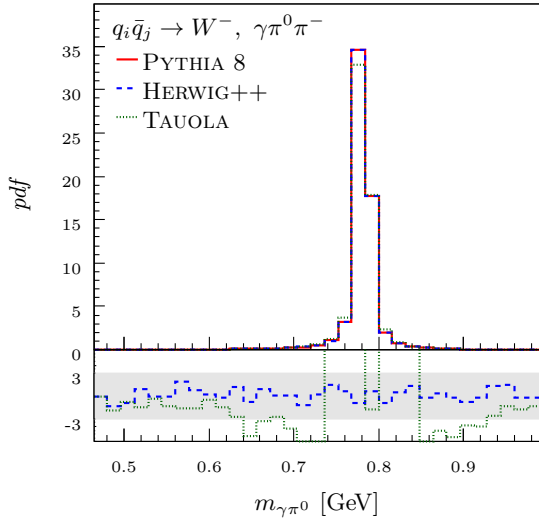


**Figure 3.12.:** Distributions of  $m_{23}$  for the default  $\gamma\pi^0\pi^-$  decay channel using the model of Eq. 3.40.

### 3.2.4. Five-Body Decays

Five-body decays of the  $\tau$  lepton into four pions and a  $\tau$  lepton neutrino have been observed experimentally, but due to the low branching ratio and complexity of the decay, experimental observations do not strongly constrain the model [111]. Consequently, the hadronic current for the  $\pi^0\pi^0\pi^0\pi^-$  and  $\pi^0\pi^-\pi^-\pi^+$  decays in PYTHIA 8 is based on the Novosibirsk model of Refs. [112] and [99], a phenomenological model fitted to four pion production from electron-positron annihilation within the energy range of 1.0 to 2.5 GeV. Within this model the hadronic decay of the  $\tau$  lepton occurs through an initial excited  $\rho$  resonance and secondary  $a_1$ ,  $\rho$ , and  $\sigma$  resonances. For the  $\pi^0\pi^-\pi^-\pi^+$  decay an additional secondary  $\omega$  resonance is also included. The four pion hadronic currents are the summation of the resonance subcurrents,

$$\begin{aligned} J_{\pi^0\pi^0\pi^0\pi^-}^\mu &\propto J_{0,a_1\rightarrow\rho\pi}^\mu + J_{0,a_1\rightarrow\sigma\pi}^\mu \\ J_{\pi^0\pi^-\pi^-\pi^+}^\mu &\propto J_{-,a_1\rightarrow\rho\pi}^\mu + J_{-,a_1\rightarrow\sigma\pi}^\mu + J_{-, \omega\rightarrow\rho\pi}^\mu \end{aligned} \quad (3.42)$$

where  $J_{0,X}$  are the subcurrents for the  $\pi^0\pi^0\pi^0\pi^-$  decay and  $J_{-,X}$  are the subcurrents for the  $\pi^0\pi^-\pi^-\pi^+$  decay.

The hadronic subcurrent for the decay of the  $a_1$  to a  $\rho\pi$  pair for the three neutral pion current is given by the combinatorics of the  $\pi^0\pi^0\pi^0\pi^-$  final state,

$$\begin{aligned} J_{0,a_1\rightarrow\rho\pi}^\mu &= G_1(s) \left( t_1^\mu(q_3, q_4, q_5, q_2) + t_1^\mu(q_3, q_2, q_5, q_4) + t_1^\mu(q_4, q_3, q_5, q_2) \right. \\ &\quad \left. + t_1^\mu(q_4, q_2, q_5, q_3) + t_1^\mu(q_2, q_3, q_5, q_4) + t_1^\mu(q_2, q_4, q_5, q_3) \right) \end{aligned} \quad (3.43)$$

where  $t_1$  is a four-vector based on the  $a_1$  and  $\rho$  resonance propagators, and  $G_1$  is a phenomenological fit of the four pion invariant mass distribution given later in Tables 3.22 through 3.24.

The Mandelstam variable  $s$  as used within this context is given by,  $q_\mu q^\mu$  where,

$$q^\mu = (q_2 + q_3 + q_4 + q_5)^\mu \quad (3.44)$$

is the four-momentum of the four pion system.

The hadronic subcurrent for the decay of the  $a_1$  into a  $\sigma\pi$  pair for the  $\pi^0\pi^0\pi^0\pi^-$  pion final state is given by,

$$J_{0,a_1 \rightarrow \sigma\pi}^\mu = G_1(s) \left( t_2^\mu(q_3, q_5, q_4, q_2) + t_2^\mu(q_4, q_5, q_3, q_2) + t_2^\mu(q_2, q_5, q_4, q_3) \right. \\ \left. - t_2^\mu(q_5, q_3, q_4, q_2) - t_2^\mu(q_5, q_4, q_3, q_2) - t_2^\mu(q_5, q_2, q_4, q_3) \right) \quad (3.45)$$

where  $t_2$  is a four-vector based on the  $a_1$  and  $\sigma$  resonance propagators.

For the  $\pi^0\pi^-\pi^-\pi^+$  decay, the hadronic subcurrent for the decay of the  $a_1$  into  $\rho\pi$  is given by,

$$J_{-,a_1 \rightarrow \rho\pi}^\mu = G_2(s) \left( t_1^\mu(q_3, q_5, q_4, q_2) + t_1^\mu(q_4, q_5, q_3, q_2) + t_1^\mu(q_3, q_4, q_5, q_2) \right. \\ \left. + t_1^\mu(q_4, q_3, q_5, q_2) + t_1^\mu(q_2, q_4, q_3, q_5) + t_1^\mu(q_2, q_3, q_4, q_5) \right) \quad (3.46)$$

where  $G_2$  is another phenomenological fit of the four pion invariant mass also given in Tables 3.22 through 3.24. The  $a_1$  to  $\sigma\pi$  subcurrent is similar,

$$J_{-,a_1 \rightarrow \sigma\pi}^\mu = G_2(s) \left( t_2^\mu(q_2, q_4, q_3, q_5) + t_2^\mu(q_2, q_3, q_4, q_5) \right. \\ \left. - t_2^\mu(q_3, q_2, q_4, q_5) - t_2^\mu(q_4, q_2, q_3, q_5) \right) \quad (3.47)$$

but the  $\sigma$  propagator is accounted for by  $t_2$ . Finally, the additional  $\omega$  to  $\rho\pi$  subcurrent for the  $\pi^0\pi^-\pi^-\pi^+$  channel is given by,

$$J_{-, \omega \rightarrow \rho\pi}^\mu = G_3(s) \left( t_3^\mu(q_3, q_5, q_4, q_2) + t_3^\mu(q_4, q_5, q_3, q_2) - t_3^\mu(q_3, q_4, q_5, q_2) \right. \\ \left. - t_3^\mu(q_4, q_3, q_5, q_2) - t_3^\mu(q_3, q_2, q_4, q_5) - t_3^\mu(q_4, q_2, q_3, q_5) \right) \quad (3.48)$$

where  $t_3$  is a four-vector based on the  $\omega$  and  $\rho$  propagators, and  $G_3$  is a phenomenological fit of the four pion invariant mass given in Tables 3.22 through 3.24.

The the four-vector  $t_1$  is given by,

$$t_1^\mu(q_i, q_j, q_k, q_l) = -F_{a_1}(s_{a_1}) \frac{m_{a_1}^2 (m_\rho^2 + m_\rho \Gamma_\rho dm(0))}{D_{a_1}(s_{a_1}) D_\rho(s_\rho)} \quad (3.49) \\ \left( (q_\nu q_{a_1}^\nu) ((q_{k\nu} q_{a_1}^\nu) q_l^\mu - (q_{l\nu} q_{a_1}^\nu) q_k^\mu) \right. \\ \left. + ((q_\nu q_l^\nu) (q_{i\nu} q_k^\nu) - (q_\nu q_k^\nu) (q_{i\nu} q_l^\nu)) q_{a_1}^\mu \right)$$

**Table 3.17.:** Parameters used by the four pion current for the  $a_1$ ,  $\rho$ ,  $\sigma$ , and  $\omega$  resonances.

| resonance     | $m$ [GeV] | $\Gamma$ [GeV] | $\phi$  | $A$     |
|---------------|-----------|----------------|---------|---------|
| $a_1(1260)$   | 1.23      | 0.45           |         |         |
| $\rho(770)$   | 0.7761    | 0.1445         |         |         |
| $\sigma$      | 0.8       | 0.88           | 0.43585 | 1.39987 |
| $\omega(782)$ | 0.782     | 0.00841        | 0       | 1       |

where  $D_{a_1}$  and  $D_\rho$  are the denominators for the  $a_1$  and  $\rho$  propagators respectively, and are given later in Eqs. 3.54 and 3.55. These propagators differ from those used by Bondar *et al.* in Ref. [112] in the numerator where the  $a_1$  and corrected  $\rho$  masses have been added such that the forms of the propagators are that of Breit-Wigners, as is done in HERWIG++. The  $\rho$  mass is corrected by a running mass correction,  $dm(s)$ , which is defined later in Eq. 3.56. The Mandelstam variables and propagator four-momenta are,

$$\begin{aligned} q_{a_1}^\mu &= (q_j + q_k + q_l)^\mu & q_\rho^\mu &= (q_k + q_l)^\mu & q_\sigma^\mu &= (q_k + q_l)^\mu & q_\omega^\mu &= (q_j + q_k + q_l)^\mu \\ s_{a_1} &= q_{a_1\mu}q_{a_1}^\mu & s_\rho &= q_{\rho\mu}q_\rho^\mu & s_\sigma &= q_{\sigma\mu}q_\sigma^\mu & s_\omega &= q_{\omega\mu}q_\omega^\mu \end{aligned} \quad (3.50)$$

for the  $a_1$ ,  $\rho$ ,  $\sigma$  and  $\omega$ . The form factor for the  $a_1$ ,  $F_{a_1}$ , is given by,

$$F_{a_1}(s) = \left( \frac{\Lambda^2 + m_{a_1}^2}{\Lambda^2 + s} \right)^2 \quad (3.51)$$

where the cutoff value  $\Lambda$  is taken as 1.2 GeV from Ref. [113].

The four-vector  $t_2$  is similar to  $t_1$  but with different combinatorics and propagators,

$$\begin{aligned} t_2^\mu(q_i, q_j, q_k, q_l) &= w_\sigma F_{a_1}(s_{a_1}) \frac{m_{a_1}^2 m_\sigma^2}{D_{a_1}(s_{a_1}) D_\sigma(s_\sigma)} \\ &\quad \left( (q^\nu q_{a_1\nu}) s_{a_1} q_j^\mu - (q^\nu q_{j\nu}) s_{a_1} q_{a_1}^\mu \right) \end{aligned} \quad (3.52)$$

where  $w_\sigma$  is a complex weight for the  $\sigma$  resonance calculated from an amplitude and phase given in Table 3.17, and  $D_\sigma$  is the denominator of the propagator for the  $\sigma$  given later in Eq. 3.59. Again, the form of  $t_2$  used in PYTHIA 8 differs from Bondar *et al.* in the propagator with the addition of  $m_{a_1}^2$  and  $m_\sigma^2$  in the numerator.

The final four-vector,  $t_3$ , is used only in the  $\pi^0\pi^-\pi^-\pi^+$  decay, where the second resonance can occur through either an  $\omega$  or  $a_1$ ,

$$\begin{aligned} t_3^\mu(q_i, q_j, q_k, q_l) &= w_\omega F_\omega(s_\omega) \frac{m_\omega^2 (m_\rho^2 + m_\rho \Gamma_\rho dm(0))}{D_\omega(s_\omega) D_\rho(s_\rho)} \\ &\quad \left( ((q_\nu q_k^\nu)(q_{i\nu} q_l^\nu) - (q_\nu q_l^\nu)(q_{i\nu} q_k^\nu)) q_j^\mu \right. \\ &\quad \left. + ((q_\nu q_l^\nu)(q_{i\nu} q_j^\nu) - (q_\nu q_j^\nu)(q_{i\nu} q_l^\nu)) q_k^\mu \right) \end{aligned} \quad (3.53)$$

**Table 3.18.:** Functions used to fit the running  $a_1$  width of Eq. 3.54 where  $s_{3\pi^-} = 0.16960 \text{ GeV}^2$  and  $s_{\rho\pi^0} = 0.83425 \text{ GeV}^2$  for the four pion current.

| limits $[\text{GeV}^2]$             | $\Gamma_{a_1}(s)$ [GeV]   |
|-------------------------------------|---|
| $0 \leq s < s_{3\pi^-}$             | 0   |
| $s_{3\pi^-} \leq s < s_{\rho\pi^0}$ | $P_0(s - s_{3\pi^-})^3 (1 - P_1(s - s_{3\pi^-}) + P_2(s - s_{3\pi^-})^2)$ |
| $s_{\rho\pi^0} \leq s$              | $P_0 + P_1s + P_2s^2 + P_3s^3 + P_4\frac{s+P_5}{s}$                       |

**Table 3.19.:** Parameters used in the  $a_1$  running width fits of Table 3.18 for the four pion current.

| limits $[\text{GeV}^2]$             | parameters                            |                                     |                                     |
|-------------------------------------|---------------------------------------|-------------------------------------|-------------------------------------|
| $s_{3\pi^-} \leq s < s_{\rho\pi^0}$ | $P_0 = 0.003052$                      | $P_1 = -151.088$                    | $P_2 = 174.495$                     |
| $s_{\rho\pi^0} \leq s$              | $P_0 = 2.60817$<br>$P_3 = -0.0678183$ | $P_1 = -2.47790$<br>$P_4 = 1.66577$ | $P_2 = 0.66539$<br>$P_5 = -1.23701$ |

$$+ ((q_\nu q_j^\nu)(q_{i\nu} q_k^\nu) - (q_\nu q_k^\nu)(q_{i\nu} q_j^\nu)) q_l^\mu$$

where  $w_\omega$  is a complex weight calculated from a phase and amplitude given in Table 3.17 using Eq. 3.25,  $F_\omega$  is the  $\omega$  form factor, and  $D_\omega$  is the denominator of the propagator for the  $\omega$ . Note that the  $\omega$  mass and corrected  $\rho$  mass have been added to the numerator of the propagator. Currently, the  $\omega$  form factor is taken as  $F_\omega = 1$ .

The energy dependent denominator of the propagator for the  $a_1$  is given by,

$$D_{a_1}(s) = s - m_{a_1}^2 + i\sqrt{s}\Gamma_{a_1}(s) \quad (3.54)$$

where the running width for the  $a_1$ ,  $\Gamma_{a_1}$ , is calculated from integrating over phase-space for the  $a_1 \rightarrow \pi^0\pi^-\pi^+$  and  $a_1 \rightarrow \pi^0\pi^0\pi^0$  decays taking into account the combinatorics of the  $\rho$  and  $\sigma$  propagators. In TAUOLA this phase-space integration is performed using Monte Carlo integration and an interpolation table is built at initialisation. In PYTHIA 8, a fit of the TAUOLA interpolation table, given in Table 3.18 with parameters in Table 3.19 and plotted in Fig. 3.13, is used for  $\Gamma_{a_1}$ .

The denominator for the  $\rho$  resonance propagator includes a running mass correction,  $dm(s)$ , similar to that of Gounaris and Sakurai from Ref. [114] which is also applied to  $m_\rho$  in the numerators of the propagators from Eqs. 3.49 to 3.53. Consequently, the denominator to the  $\rho$  propagator is,

$$D_\rho(s) = s - m_\rho^2 - m_\rho\Gamma_\rho dm(s) + im_\rho\Gamma_\rho \left( \frac{m_\rho^2(s - 4m_{\pi^-}^2)^3}{s(m_\rho^2 - 4m_{\pi^-}^2)^3} \right)^{1/2} \quad (3.55)$$



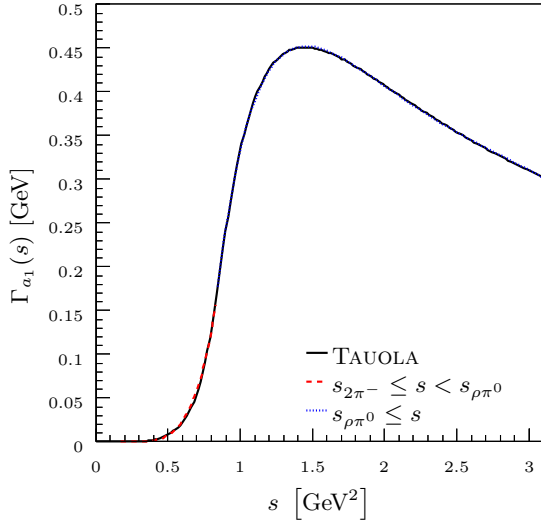


**Figure 3.13.:** Fit of the  $a_1$  running width, using Tables 3.18 and 3.19, compared to TAUOLA. This width is used in the four pion current.

where the running mass correction is given as,

$$dm(s) = \frac{m_\rho(h(s) - h(m_\rho^2) - (s - m_\rho^2)dh(m_\rho^2))}{(m_\rho^2 - 4m_{\pi^-}^2)^{3/2}} \quad (3.56)$$

and  $h(s)$  is defined by Golonka *et al.* in Ref. [99] as,

$$h(s) = \begin{cases} \frac{x}{\pi} \left( \frac{\ln(1+x)}{\ln(1-x)} \right) (s - 4m_{\pi^-}^2) & \text{if } s > 4m_{\pi^-}^2 \\ -\frac{8m_{\pi^-}^2}{\pi} & \text{if } s = 0 \\ 0 & \text{else} \end{cases} \quad (3.57)$$

where  $x = \sqrt{1 - 4m_{\pi^-}^2/s}$ . The derivative of  $h(s)$  with respect to  $s$  is given by,

$$dh(s) = \begin{cases} \frac{x}{\pi s} (sx + (2m_{\pi^-}^2 + s) \ln \left( \frac{1+x}{1-x} \right)) & \text{if } s > 4m_{\pi^-}^2 \\ 0 & \text{else} \end{cases} \quad (3.58)$$

which is used in the calculation of  $dm(s)$  in Eq. 3.56.

The denominator of the  $\sigma$  propagator,  $D_\sigma(s)$ , is given by the denominator of the  $s$ -wave Breit-Wigner of Eq. 3.16,

$$D_\sigma(s) = s - m_\sigma^2 - \left( \frac{i\Gamma_\sigma m_\sigma^2}{\sqrt{s}} \right) \left( \frac{g(m_{\pi^-}, m_{\pi^-}, s)}{g(m_{\pi^-}, m_{\pi^-}, m_\sigma^2)} \right) \quad (3.59)$$

where  $g(m_{\pi^-}, m_{\pi^-}, s)$  is given by Eq. 3.19. For the  $\omega$  resonance,

$$D_\omega(s) = s - m_\omega^2 + im_\omega\Gamma_\omega(s) \quad (3.60)$$

where the running width of the  $\omega$  is taken from Golonka *et al.* of Ref. [99] and is given by the fit of Table 3.20 with the parameters of Table 3.21.

**Table 3.20.:** Running width of the  $\omega$  from Eq. 3.60 where  $x = \sqrt{s} - m_\omega$  for the four pion current.

| limits [GeV <sup>2</sup> ]              | $\Gamma_\omega(s)$ [GeV]                                  |
|---|---|
| $\sqrt{s} < 1$                          | $P_0 + P_1x + P_2x^2 + P_3x^3 + P_4x^4 + P_5x^5 + P_6x^6$ |
| $\sqrt{s} < 1, \Gamma_\omega(s) \leq 0$ | 0   |
| $s \geq 1$                              | $P_0 + P_1s^{1/2} + P_2s + P_3s^{3/2}$                    |

**Table 3.21.:** Parameters used in the  $\omega$  running width fits of Table 3.20 for the four pion current.

| limits [GeV <sup>2</sup> ] | parameters                   |                                  |                                    |                 |
|----------------------------|------------------------------|----------------------------------|------------------------------------|-----------------|
| $\sqrt{s} < 1$             | $P_0 = 1$<br>$P_4 = 4977.35$ | $P_1 = 17.56$<br>$P_5 = 7610.66$ | $P_2 = 141.11$<br>$P_6 = -42524.4$ | $P_3 = 894.884$ |
| $s \geq 1$                 | $P_0 = -1333.26$             | $P_1 = 4860.19$                  | $P_2 = -6000.81$                   | $P_3 = 2504.97$ |

**Table 3.22.:** Fitting functions used for the phenomenological  $G$  factors where the centre-of-mass limits  $s_i$  are given in Table 3.23 and the parameters are given in Table 3.24 for the four pion current.

| limits [GeV <sup>2</sup> ] | $G(s)$                                  |
|----------------------------|---|
| $s < s_0$                  | 0                                       |
| $s_0 \leq s < s_1$         | $P_0 + P_1s$                            |
| $s_1 \leq s < s_2$         | $P_0s^{P_1} + P_2s^2 + P_3s^3 + P_4s^4$ |
| $s_2 \leq s < s_3$         | $P_0 + P_1s + P_2s^2 + P_3s^3 + P_4s^4$ |
| $s_3 \leq s < s_4$         | $P_0 + P_1s$                            |
| $s_4 \leq s < s_5$         | $P_0 + P_1s$                            |
| $s_5 \leq s$               | 0                                       |

The phenomenological  $G$  factors of the hadronic currents used in Eqs. 3.43 through 3.48 are fitted piece-wise with the functions of Table 3.22, where the limits  $s_i$  are given in Table 3.23 and the fit parameters  $P_i$  are given in Table 3.24. The fits of the three  $G$  factors are plotted in Fig. 3.14. Note that the  $G$  factors given in Ref. [112] must be corrected using the functions described in Ref. [99].

Figure 3.15 compares the invariant mass distributions of  $m_{345}$  for the four pion decays produced from PYTHIA 8, HERWIG++, and TAUOLA. The PYTHIA 8 and HERWIG++ distributions match well for both channels with four pions, with the distinct peak at 0.8 GeV in Fig. 3.15(b) due to the additional  $\omega$  resonance of the  $\pi^-\pi^-\pi^-\pi^+$  channel. The TAUOLA distributions differ slightly from the PYTHIA 8 and HERWIG++ due to differences in the implementations and the parameters used in the hadronic current.

### 3.2.5. Six-Body Decays

Three six-body decays are implemented in PYTHIA 8 with the hadronic final states  $\pi^0\pi^0\pi^-\pi^-\pi^+$ ,  $\pi^0\pi^0\pi^0\pi^0\pi^-$ , and  $\pi^-\pi^-\pi^-\pi^+\pi^+$ . These decays are modelled with the five pion current by Kühn

**Table 3.23.:** Limits used in the  $G$  factors of Table 3.22 for the four pion current.

| $G(s)$   | limits $[\text{GeV}^2]$ |                  |                 |
|----------|-------------------------|------------------|-----------------|
| $G_1(s)$ | $s_0 = 0.614403$        | $s_1 = 0.656264$ | $s_2 = 1.57896$ |
|          | $s_3 = 3.08198$         | $s_4 = 3.12825$  | $s_5 = 3.17488$ |
| $G_2(s)$ | $s_0 = 0.614403$        | $s_1 = 0.635161$ | $s_2 = 2.30794$ |
|          | $s_3 = 3.08198$         | $s_4 = 3.12825$  | $s_5 = 3.17488$ |
| $G_3(s)$ | $s_0 = 0.81364$         | $s_1 = 0.861709$ | $s_2 = 1.92621$ |
|          | $s_3 = 3.08198$         | $s_4 = 3.12825$  | $s_5 = 3.17488$ |

**Table 3.24.:** Parameters used in the  $G$  factors of Table 3.22 for the four pion current.

| $G(s)$   | limits $[\text{GeV}^2]$ | parameters       |                  |                  |                  |
|----------|-------------------------|------------------|------------------|------------------|------------------|
| $G_1(s)$ | $s_0 \leq s < s_1$      | $P_0 = -23383.7$ | $P_1 = 38059.2$  |                  |                  |
|          | $s_1 \leq s < s_2$      | $P_0 = 230.368$  | $P_1 = -4.39368$ | $P_2 = 687.002$  | $P_3 = -732.581$ |
|          | $s_2 \leq s < s_3$      | $P_0 = 1633.92$  | $P_1 = -2596.21$ | $P_2 = 1703.08$  | $P_3 = -501.407$ |
|          | $s_3 \leq s < s_4$      | $P_0 = -2982.44$ | $P_1 = 986.009$  |                  |                  |
|          | $s_4 \leq s < s_5$      | $P_0 = 6948.99$  | $P_1 = -2188.74$ |                  |                  |
| $G_2(s)$ | $s_0 \leq s < s_1$      | $P_0 = -54171.5$ | $P_1 = 88169.3$  |                  |                  |
|          | $s_1 \leq s < s_2$      | $P_0 = 454.638$  | $P_1 = -3.07152$ | $P_2 = -48.7086$ | $P_3 = 81.9702$  |
|          | $s_2 \leq s < s_3$      | $P_0 = -162.421$ | $P_1 = 308.977$  | $P_2 = -27.7887$ | $P_3 = -48.5957$ |
|          | $s_3 \leq s < s_4$      | $P_0 = -2650.29$ | $P_1 = 879.776$  |                  |                  |
|          | $s_4 \leq s < s_5$      | $P_0 = 6936.99$  | $P_1 = -2184.97$ |                  |                  |
| $G_3(s)$ | $s_0 \leq s < s_1$      | $P_0 = -84888.9$ | $P_1 = 104332$   |                  |                  |
|          | $s_1 \leq s < s_2$      | $P_0 = 2698.15$  | $P_1 = -3.08302$ | $P_2 = 1936.11$  | $P_3 = -1254.59$ |
|          | $s_2 \leq s < s_3$      | $P_0 = 7171.67$  | $P_1 = -6387.94$ | $P_2 = 3056.29$  | $P_3 = -888.635$ |
|          | $s_3 \leq s < s_4$      | $P_0 = -5607.47$ | $P_1 = 1917.27$  |                  |                  |
|          | $s_4 \leq s < s_5$      | $P_0 = 26573$    | $P_1 = -8369.76$ |                  |                  |

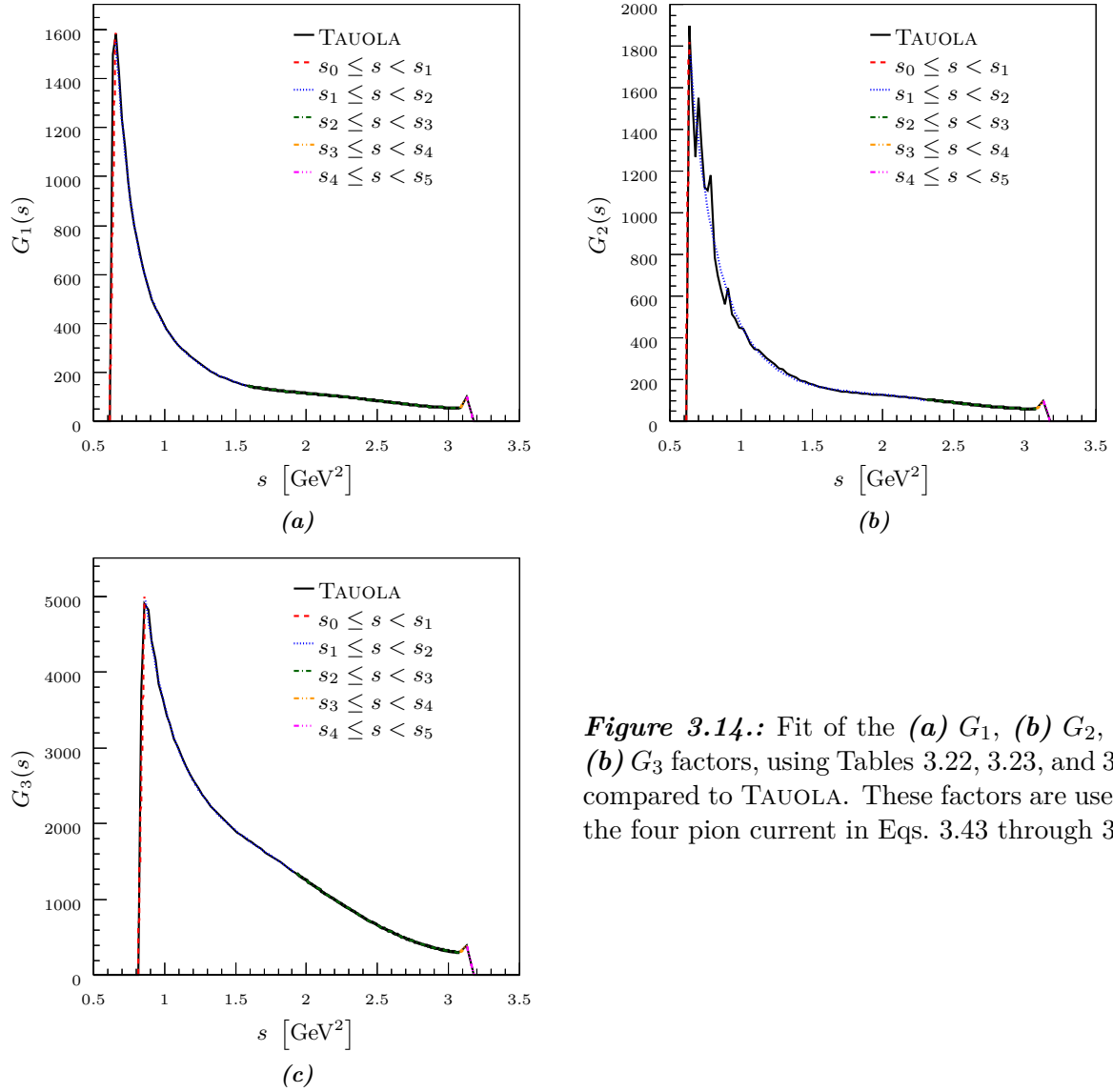


**Figure 3.14.:** Fit of the (a)  $G_1$ , (b)  $G_2$ , and (c)  $G_3$  factors, using Tables 3.22, 3.23, and 3.24, compared to TAUOLA. These factors are used in the four pion current in Eqs. 3.43 through 3.48.

and  $W_3$  of Ref. [115]. The decays can occur through  $a_1$ ,  $\rho$ ,  $\omega$ , and  $\sigma$  resonances. The hadronic currents for the three decay channels are given by,

$$\begin{aligned}
J_{\pi^0\pi^0\pi^-\pi^-\pi^+} &\propto J_a^\mu(q_6, q_4, q_2, q_5, q_3) + J_a^\mu(q_6, q_5, q_2, q_4, q_3) \\
&\quad + J_a^\mu(q_6, q_4, q_3, q_5, q_2) + J_a^\mu(q_6, q_5, q_3, q_4, q_2) \\
&\quad + J_b^\mu(q_4, q_5, q_6, q_2, q_3) + J_b^\mu(q_2, q_3, q_4, q_6, q_5) \\
&\quad + J_b^\mu(q_2, q_3, q_5, q_6, q_4) \\
J_{\pi^0\pi^0\pi^0\pi^0\pi^-} &\propto J_b^\mu(q_2, q_3, q_6, q_4, q_5) + J_b^\mu(q_5, q_3, q_6, q_4, q_2) \\
&\quad + J_b^\mu(q_3, q_4, q_6, q_2, q_5) + J_b^\mu(q_2, q_4, q_6, q_3, q_5) \\
&\quad + J_b^\mu(q_2, q_5, q_6, q_4, q_3) + J_b^\mu(q_4, q_5, q_6, q_2, q_3) \\
J_{\pi^-\pi^-\pi^-\pi^+\pi^+} &\propto J_b^\mu(q_2, q_3, q_5, q_6, q_4) + J_b^\mu(q_4, q_3, q_5, q_6, q_2) \\
&\quad + J_b^\mu(q_2, q_4, q_5, q_6, q_3) + J_b^\mu(q_2, q_3, q_6, q_5, q_4)
\end{aligned} \tag{3.61}$$

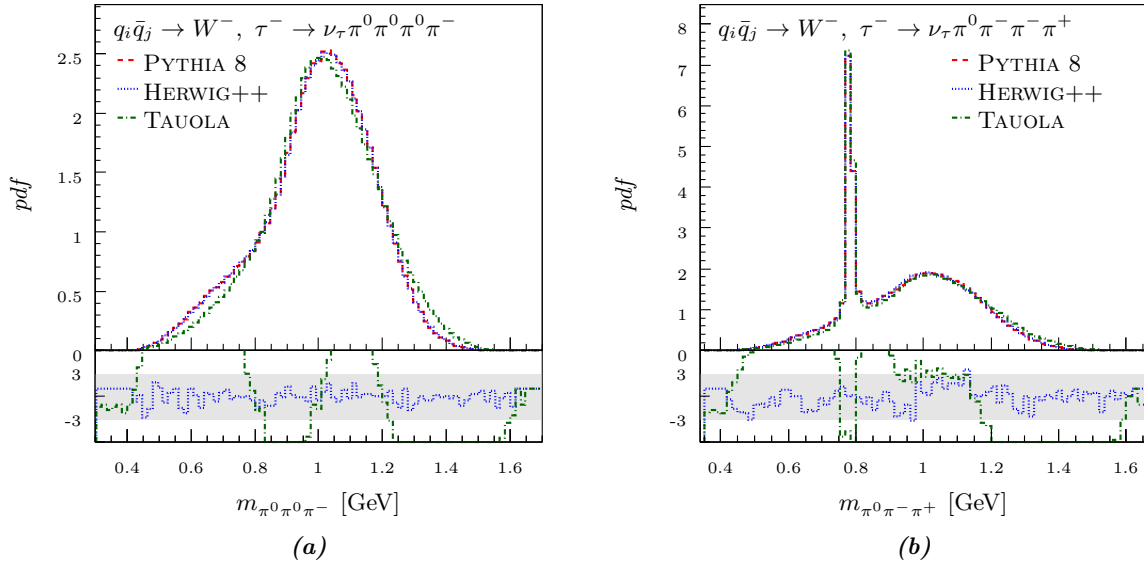


**Figure 3.15.:** Invariant mass distributions of  $m_{345}$  for the (a)  $\pi^0\pi^0\pi^0\pi^-$  and (b)  $\pi^0\pi^-\pi^-\pi^+$  decay channels of the  $\tau$  lepton using the four pion model.

$$+ J_b^\mu(q_4, q_3, q_6, q_5, q_2) + J_b^\mu(q_2, q_4, q_6, q_5, q_3)$$

where  $J_a^\mu$  and  $J_b^\mu$  are hadronic subcurrents corresponding to the decay type. A schematic of the  $a$ -type decay is given in Fig. 3.16(a) where the  $\tau$  lepton can decay through an  $a_1$  resonance. This resonance then decays into secondary  $\rho$  and  $\omega$  resonances. While the  $\omega$  resonance of the  $a$ -type decay could be modelled further with a tertiary  $\rho$  resonance decay, its decay is modelled as a contact interaction. A schematic of the  $b$ -type decay is shown in Fig. 3.16(b). Here, an  $a_1$  resonance decays into secondary  $a_1$  and  $\sigma$  resonances. This is followed with the secondary  $a_1$  decaying into a tertiary  $\rho$  resonance.

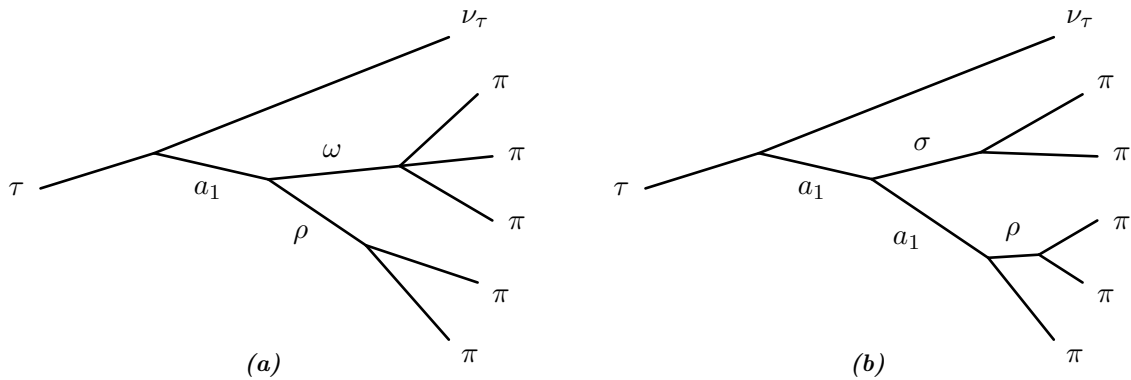


**Figure 3.16.:** Schematics of the resonance structure for (a)  $a$ -type and (b)  $b$ -type decays of the  $\tau$  lepton into a final state with five pions.

The hadronic subcurrent for the  $a$ -decay resonance structure is given by,

$$J_a^\mu(q_1, q_2, q_3, q_4, q_5) = w_\omega BW(q_\nu q^\nu, m_{a_1}, \Gamma_{a_1}) \quad (3.62)$$

| resonance     | $m$ [GeV] | $\Gamma$ [GeV] | $w$  |
|---------------|-----------|----------------|------|
| $a_1(1260)$   | 1.26      | 0.4            |      |
| $\rho(770)$   | 0.776     | 0.15           |      |
| $\sigma$      | 0.8       | 0.6            | 11.5 |
| $\omega(782)$ | 0.782     | 0.0085         | 1    |

**Table 3.25.:** Parameters used by the five pion subcurrents for the  $a_1$ ,  $\rho$ ,  $\sigma$ , and  $\omega$  resonances.

$$\begin{aligned}
& BW((q_1 + q_2 + q_3)_\nu(q_1 + q_2 + q_3)^\nu, m_\omega, \Gamma_\omega) \\
& BW((q_4 + q_5)_\nu(q_4 + q_5)^\nu, m_\rho, \Gamma_\rho) \\
& \epsilon^\mu(q_4 - q_5, \epsilon(q_1, q_2, q_3), q) (BW((q_2 + q_3)_\nu(q_2 + q_3)^\nu, m_\rho, \Gamma_\rho) \\
& + BW((q_1 + q_3)_\nu(q_1 + q_3)^\nu, m_\rho, \Gamma_\rho) \\
& + BW((q_1 + q_2)_\nu(q_1 + q_2)^\nu, m_\rho, \Gamma_\rho))
\end{aligned}$$

where  $w_\omega$  is a real weight,  $BW$  is the Breit-Wigner defined by,

$$BW(s, m, \Gamma) = \frac{m^2}{m^2 - s^2 - im\Gamma} \quad (3.63)$$

and  $\epsilon$  is the permutation operator also used in Eq. 3.27 for the three meson channel. Here,  $q$  is the sum of all five momenta,  $q_1 + q_2 + q_3 + q_4 + q_5$ . The parameters of the resonances used in PYTHIA 8 are given in Table 3.25.

The hadronic subcurrent for the  $b$ -decay resonance structure is given by,

$$\begin{aligned}
J_b^\mu(q_1, q_2, q_3, q_4, q_5) = & w_\sigma BW(q_\nu q^\nu, m_{a_1}, \Gamma_{a_1}) \\
& BW((q_1 + q_2 + q_3)_\nu(q_1 + q_2 + q_3)^\nu, m_{a_1}, \Gamma_{a_1}) \\
& BW((q_4 + q_5)_\nu(q_4 + q_5)^\nu, m_\sigma, \Gamma_\sigma) \\
& \left( \left( \frac{J_{c\nu}(q_1, q_2, q_3)q^\nu}{q_\nu q^\nu} \right) q^\mu - J_c^\mu(q_1, q_2, q_3) \right)
\end{aligned} \quad (3.64)$$

where the subcurrent  $J_c^\mu$  is,

$$\begin{aligned}
J_c^\mu(q_1, q_2, q_3) = & BW((q_1 + q_3)_\nu(q_1 + q_3)^\nu, m_\rho, \Gamma_\rho) \\
& \left( \frac{q_{2\nu}(q_1 - q_3)^\nu}{(q_1 + q_2 + q_3)_\nu(q_1 + q_2 + q_3)^\nu} (q_1 + q_2 + q_2)^\mu - q_1^\mu + q_3^\mu \right) \\
& + BW((q_2 + q_3)_\nu(q_2 + q_3)^\nu, m_\rho, \Gamma_\rho) \\
& \left( \frac{q_{1\nu}(q_2 - q_3)^\nu}{(q_1 + q_2 + q_3)_\nu(q_1 + q_2 + q_3)^\nu} (q_1 + q_2 + q_2)^\mu - q_2^\mu + q_3^\mu \right)
\end{aligned} \quad (3.65)$$

and the parameters are again given in Table 3.25. The definitions of  $q$  and  $BW$  are the same as for  $J_a^\mu$ .

In Fig. 3.17, the  $m_{234}$  invariant mass distributions are given for PYTHIA 8, HERWIG++, and TAUOLA. There is good agreement between PYTHIA 8 and HERWIG++ for the  $\pi^0\pi^0\pi^0\pi^0\pi^-$  and  $\pi^-\pi^-\pi^-\pi^+\pi^+$  channels, with a slight disagreement for the  $\pi^0\pi^0\pi^-\pi^-\pi^+$  channel. However, the

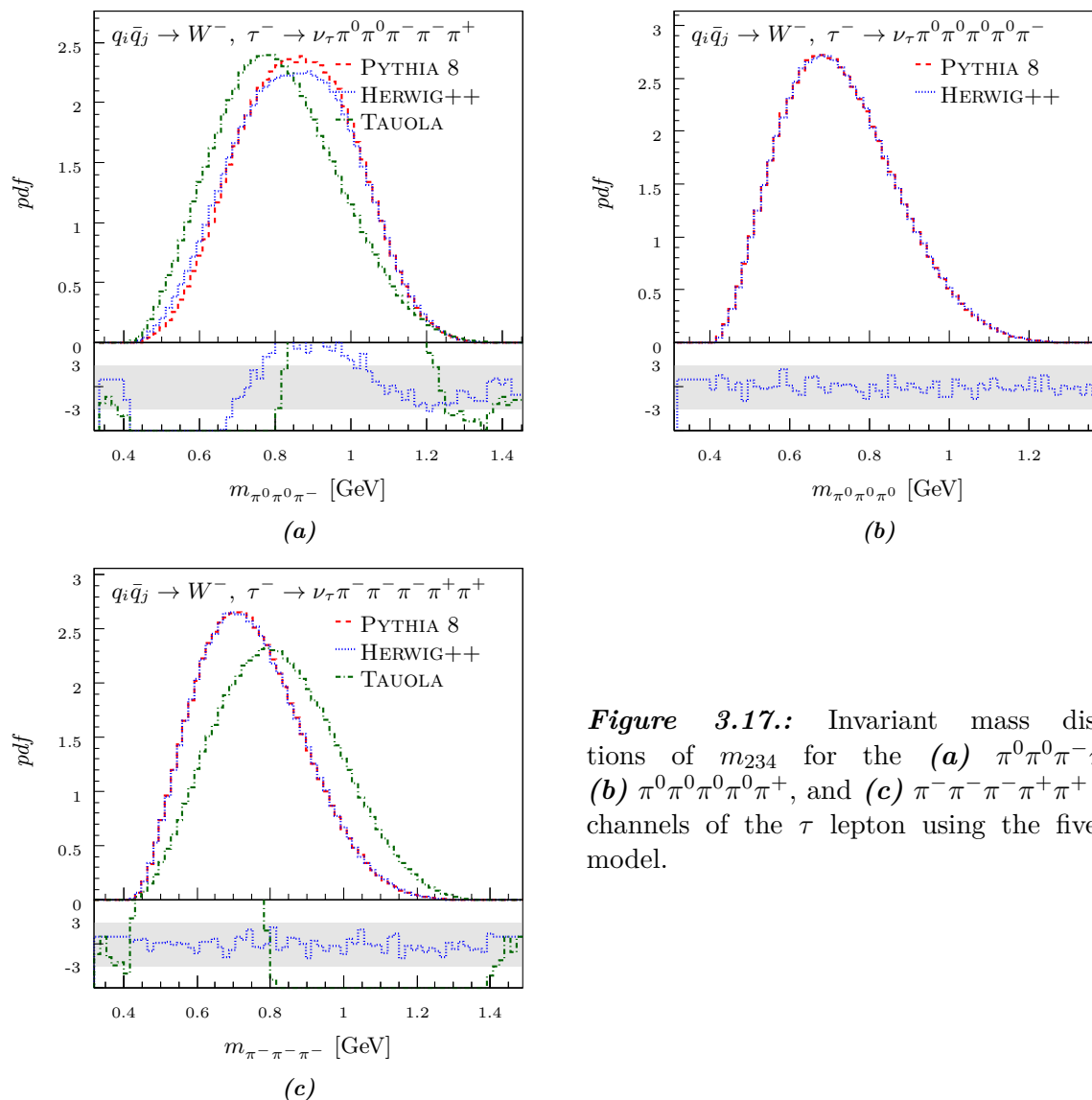


**Figure 3.17.:** Invariant mass distributions of  $m_{234}$  for the (a)  $\pi^0\pi^0\pi^-\pi^-\pi^+$ , (b)  $\pi^0\pi^0\pi^0\pi^0\pi^+$ , and (c)  $\pi^-\pi^-\pi^-\pi^+\pi^+$  decay channels of the  $\tau$  lepton using the five pion model.

TAUOLA distributions do not agree well with the PYTHIA 8 and HERWIG++ distributions.

### 3.3. Implementation

One of the goals of the  $\tau$  lepton decay implementation in PYTHIA 8 is that the production processes and decay channels of the  $\tau$  leptons are easily extensible for new physics. Additionally, the machinery used to generate helicity correlations for  $\tau$  lepton decays may also be used for helicity correlation in other processes such as  $t$ -quark decays in the future. This section outlines the  $\tau$  lepton decay machinery architecture used in PYTHIA 8 as well as the additional software developed for validation. The implementation of the  $\tau$  lepton decays with full helicity correlations is summarised in Sect. 3.3.1, while the implementation of the helicity matrix elements used in the  $\tau$  lepton decays is introduced in Sect. 3.3.2 and the validation procedure is outlined in Sect. 3.3.3. A summary of the  $\tau$  lepton production mechanisms presented in Sect. 3.1 and

**Table 3.26.:** Production mechanisms implemented in PYTHIA 8 for which full spin correlations of  $\tau$  lepton decays are calculated.

| type        | processes  |
|-------------|--|
| electroweak | $f\bar{f} \rightarrow \gamma \rightarrow f\bar{f}, f\bar{f} \rightarrow Z \rightarrow f\bar{f},$<br>$f\bar{f} \rightarrow \gamma^*/Z \rightarrow f\bar{f}, f_i\bar{f}_j \rightarrow W \rightarrow f_k\bar{f}_l,$<br>$Z \rightarrow f\bar{f}, W \rightarrow f_i\bar{f}_j$ |
| Higgs boson | $H \rightarrow f\bar{f}, h^0 \rightarrow f\bar{f}, H^0 \rightarrow f\bar{f}$<br>$A^0 \rightarrow f\bar{f}, H^\pm \rightarrow f_i\bar{f}_j$   |
| other       | $B/D \rightarrow f_i\bar{f}_j + X$   |

implemented in PYTHIA 8 is given in Table 3.26, while a summary of the default  $\tau$  lepton decays introduced in Sect. 3.2 and implemented in PYTHIA 8 is given in Table 3.27.

### 3.3.1. Tau Decays

The code for  $\tau$  lepton decays is provided in the four files (headers and source), `ParticleDecays`, `TauDecays`, `HelicityBasics`, and `HelicityMatrixElements` of the PYTHIA 8 source code. When a particle decay is requested by PYTHIA 8 the following program flow occurs, where the first step occurs within `ParticleDecays::decay` and all remaining steps occur within `TauDecays::decay`.

1. The particle is passed to `ParticleDecays::decay`.
2. If the particle is a  $\tau$  lepton, the decay is passed to `TauDecays::decay`.
3. The hard process is determined.
  - a) The correlated  $\tau$  lepton is found (if it exists).
  - b) The incoming and outgoing particles are set.
  - c) The helicity matrix element,  $\mathcal{M}$ , from `HelicityMatrixElements` is set.
4. The  $\tau$  lepton is selected (if correlated, randomly selected from the two  $\tau$  leptons).
5. The helicity density matrix,  $\rho$ , is calculated by `HelicityMatrixElement::calculateRho` using Eq. 2.108.
6. The  $\tau$  lepton children are created by `TauDecays::createChildren`.
  - a) The decay channel is selected.
  - b) The  $\tau$  lepton children are created.
  - c) The  $\tau$  lepton decay matrix element is set from `HelicityMatrixElements`.
7. The children momenta,  $q_i$ , are assigned isotropically until the condition  $x \in \mathcal{U}(0, 1) \geq \frac{\mathcal{W}}{\mathcal{W}_{\max}}$  is met.



**Table 3.27.:** Summary of default  $\tau$  lepton decay models and channels in PYTHIA 8 sorted by multiplicity. For each model the reference, internal PYTHIA 8 matrix element mode identifier `meMode`, default decay channels using the model, and branching fractions of the channels are given. The implicit  $\tau$  lepton neutrinos are omitted. Additional channels are available in PYTHIA 8 but are decayed using isotropic phase-space.

| mult. | model                                  | meMode | products   | $\mathcal{B}$ [%]  |
|-------|--|--------|--|--|
| 2     | single hadron                          | 1521   | $\pi^-$<br>$K^-$   | 10.76825<br>0.69601  |
|       | leptonic                               | 1531   | $e^- \bar{\nu}_e$<br>$\mu^- \bar{\nu}_\mu$   | 17.72832<br>17.31072   |
| 3     | two mesons via vector [103]            | 1532   | $\pi^0 \pi^-$<br>$K^0 K^-$<br>$\eta K^-$   | 25.37447<br>0.15809<br>0.01511   |
|       | two mesons via vector and scalar [104] | 1533   | $\pi^- \bar{K}^0$<br>$\pi^0 K^-$   | 0.83521<br>0.42655   |
|       | CLEO three pions [108]                 | 1541   | $\pi^0 \pi^0 \pi^-$<br>$\pi^- \pi^- \pi^+$   | 9.24697<br>9.25691   |
| 4     | three mesons with kaons [109]          | 1542   | $\pi^- \bar{K}^0 \pi^0$<br>$K^- \pi^- \pi^+$<br>$K^0 \pi^- \bar{K}^0$<br>$K^- \pi^0 K^0$<br>$K_S^0 \pi^- K_L^0$<br>$\pi^0 \pi^0 K^-$<br>$K_S^0 \pi^- K_S^0$<br>$K_L^0 \pi^- K_L^0$ | 0.39772<br>0.34701<br>0.14318<br>0.15809<br>0.11932<br>0.06463<br>0.02386<br>0.02386 |
|       | general three mesons [110]             | 1543   | $\pi^- \pi^0 \eta$   | 0.13821  |
|       | two pions with photon [107]            | 1544   | $\gamma \pi^0 \pi^-$   | 0.17520  |
| 5     | four pions [99]                        | 1551   | $\pi^0 \pi^- \pi^- \pi^+$<br>$\pi^0 \pi^0 \pi^0 \pi^-$   | 4.59365<br>1.04401   |
| 6     | five pions [115]                       | 1561   | $\pi^0 \pi^0 \pi^- \pi^- \pi^+$<br>$\pi^0 \pi^0 \pi^0 \pi^0 \pi^-$<br>$\pi^- \pi^- \pi^- \pi^+ \pi^+$  | 0.49069<br>0.09515<br>0.08342  |

**Table 3.28.:** A list of the methods implemented in the `TauDecays` class.

| method                      | description   |
|-----------------------------|---|
| <code>decay</code>          | this is the main method called by <code>ParticleDecays</code> and performs the correlated decays of the $\tau$ lepton   |
| <code>createChildren</code> | selects the $\tau$ lepton decay channel, assigns the $\tau$ lepton helicity matrix element, and returns a vector of <code>HelicityParticle</code> children with $q_i = 0$ |
| <code>isotropicDecay</code> | takes the $\tau$ lepton children and reassigns their momenta using isotropic phase-space  |
| <code>writeEvent</code>     | writes the $\tau$ lepton children to the PYTHIA 8 event record  |

- a) The variable  $x$  is a random number from a uniform distribution,  $\mathcal{U}(0, 1)$ .
  - b) The decay weight  $\mathcal{W}$  is calculated by `HelicityMatrixElements::decayWeight` using Eq. 2.109.
  - c) The maximum weight  $\mathcal{W}_{\max}$  is empirically or analytically known.
8. `TauDecays::writeEvent` writes the decay to the event record.
    - a) If there is no correlated  $\tau$  lepton, `TauDecays::decay` returns to `ParticleDecays::decay`.
  9. If the  $\tau$  lepton is correlated, the decay matrix,  $D$ , of the decayed  $\tau$  lepton is calculated by `HelicityMatrixElements::calculateD` using Eq. 2.111.
  10. The second correlated  $\tau$  lepton is selected, and steps 5 through 8 are repeated for the second  $\tau$  lepton.
  11. `TauDecays::decay` returns to `ParticleDecays::decay` which returns to the main algorithm of PYTHIA 8.

Table 3.28 outlines the methods implemented within the `TauDecays` class and provides a brief description of each method. The process of decaying a  $\tau$  lepton is very similar to the decay of a standard particle except for the use of more sophisticated helicity matrix elements and helicity correlations. As such, the `TauDecays::createChildren` method is very similar to inline code within the `ParticleDecays` class and `TauDecays::isotropicDecay` reimplements `ParticleDecays::mGenerator`, the  $m$ -generator algorithm introduced in Sect. 2.2.3.

### 3.3.2. Matrix Elements

Within the `HelicityBasics` source files, three major classes are defined: `Wave4`, `GammaMatrix`, and `HelicityParticle`. The class `Wave4` is intended to store four-momenta and spinors and is just a complex four-vector with standard vector operations defined: vector addition/subtraction, vector multiplication, and scalar multiplication/division. Additionally, the operator `Wave4::(i)` is defined, where  $i$  must be in the range  $0 \leq i \leq 3$ , and allows access to the corresponding element of the four-vector, *i.e.*  $q(0)$  returns the energy of the momentum  $q$ .

The `GammaMatrix` class is intended to be used in conjunction with the `Wave4` class such that helicity matrix elements can be easily translated from analytic expressions to code. For example, the helicity matrix element for  $\tau^- \rightarrow \nu_\tau \pi^-$ ,

$$\mathcal{M} = \bar{u}_1 \gamma_\mu (1 - \gamma_5) u_0 q_2^\mu \quad (3.66)$$

can be written in pseudo-code as,

$$\begin{aligned} \mathcal{M} = \sum_{\mu} & \text{Wave4}(\bar{u}_1) * \text{GammaMatrix}(\mu) * (1 - \text{GammaMatrix}(5)) \\ & * \text{Wave4}(u_0) * \text{GammaMatrix}(4)(\mu, \mu) * \text{Wave4}(q_2)(\mu) \end{aligned} \quad (3.67)$$

in the `HelicityMatrixElements` source code. Again, the operator `GammaMatrix::(i,j)` can be used to access the Dirac matrix element of row `i` and column `j` where  $0 \leq i, j \leq 3$ . The constructor `GammaMatrix(i)` returns  $\gamma^i$ .

The Dirac matrices are defined by Eq. 2.32, using the representation of Sect. 2.1.2, and  $\gamma^4$  is defined as  $g_{\mu\nu}$ . Because carrying out the full matrix multiplication of Eq. 3.67 is very time consuming, the special sparse properties of the Dirac matrices are exploited, as well as left to right order of operations. Accordingly, the `GammaMatrix` class is represented by four ordered `values` where the first value is the non-zero element of the first row, the second value is the non-zero element of the second row, the third is the non-zero element of the third row, and the fourth is the non-zero element of the fourth row. Corresponding to each of the `values` is an `index` which provides the column index for the non-zero value. The left to right multiplication  $w = \text{Wave4} * \text{GammaMatrix}$  is then given by,

$$w^\mu = \text{Wave4}(\text{GammaMatrix.index}[\mu]) * \text{GammaMatrix.values}[\mu] \quad (3.68)$$

which is four multiplication and four assignment operations, rather than the sixteen multiplication, sixteen addition, and four assignment operations required for full matrix multiplication.

In Eq. 3.67, the term `1 - GammaMatrix(5)` is included, where the nonsensical subtraction of a matrix from a scalar is performed. This is because the addition and subtraction of scalars with the `GammaMatrix` class is defined as the addition or subtraction of the scalar applied to the non-zero elements of the Dirac matrix. Because  $\gamma^5$  is on-diagonal in the representation used, `1 - GammaMatrix(5)` is just the subtraction of  $\gamma^5$  from the identity matrix.

The final class defined in `HelicityBasics`, `HelicityParticle`, takes the standard `Particle` class of PYTHIA 8 and extends the class to include a helicity density matrix,  $\rho$ , and a decay matrix,  $D$ . Additionally, the method `HelicityParticle::wave(h)` is defined which returns the `Wave4` spinor or polarisation vector for the particle with helicity `h`.

The actual helicity matrix elements for both the hard processes and  $\tau$  lepton decays are defined in the `HelicityMatrixElements` files which use the classes outlined above from `HelicityBasics`. The important methods of the `HelicityMatrixElement` class are outlined in Table 3.29 with brief descriptions provided for each method. The hard processes are written as classes that

**Table 3.29.:** A list of the public methods implemented in the `HelicityMatrixElement` class.

| method                      | description  |
|-----------------------------|--|
| <code>initPointers</code>   | initialise the pointers to the PYTHIA 8 SM and MSSM couplings database and particle properties database                              |
| <code>initChannel</code>    | takes as an argument a vector of <code>HelicityParticle</code> which are used to initialise any constants used in the matrix element |
| <code>decayWeight</code>    | takes a vector of <code>HelicityParticle</code> and calculates the decay weight $\mathcal{W}$ for the matrix element                 |
| <code>calculateME</code>    | calculates the helicity matrix element   |
| <code>calculateRho</code>   | calculates the helicity density matrix $\mathcal{M}$ for one of the <code>HelicityParticles</code> being used in the matrix element  |
| <code>calculateD</code>     | calculates the decay matrix $D$ for one of the <code>HelicityParticles</code> being used in the matrix element                       |
| <code>setFermionLine</code> | determines the order to assign a fermion line in the matrix element based on direction of particle or anti-particle                  |
| <code>xBreitWigner</code>   | the Breit-Wigners of Eqs. 3.15 through 3.18 where $\mathbf{x}$ is fixed, $\mathbf{s}$ , $\mathbf{p}$ , or $\mathbf{d}$               |

derive directly from the `HelicityMatrixElement` class and utilise pointer polymorphism within C++.

The  $\tau$  lepton decay matrix elements are written as classes that derive from the `HMETauDecay` class which itself derives from the `HelicityMatrixElement` class. The `HMETauDecay` class is very similar to the `HelicityMatrixElement` class except that the additional method `HMETauDecay::initHadronicCurrent` has been implemented which allows the  $\tau$  lepton decay matrix element to be calculated using the general form of Equation Eq. 3.13, so that for a new  $\tau$  lepton decay only the hadronic current needs to be defined when implementing the matrix element.

### 3.3.3. Validation

Because the matrix elements defined in Sects. 3.1 and 3.2 can be complex, it is important to validate PYTHIA 8 against the other event generators which provide similar features for  $\tau$  lepton decays. In order to facilitate validation, a series of tools were written in addition to the code implemented in PYTHIA 8 and are available by request.

Within the validation package are three sets of tools: a generation tool, an analysis tool, and a plotting tool. The generation tool provides a common ROOT  $n$ -tuple output for events generated with PYTHIA 8, HERWIG++, and PYTHIA 6 with TAUOLA. The analysis package runs over the generated  $n$ -tuples and applies a common analysis to the events from the three generators. The histograms from the analysis tool can then be plotted using the plotting tool. The tools are written in C++ and interfaced with BASH scripts. For event generation, the PYTHIA 8, HERWIG++, THEPEG, PYTHIA 6, and TAUOLA libraries are required as well as ROOT libraries. The analysis and plotting tools require only ROOT libraries.

A timing tool is provided within the validation package as a method to compare the average time per event required by the various generators to ensure that no significant timing issues

arise. Runs of various sizes, *i.e.* 2000, 6000, and 12000 events, are performed for each decay channel with each generator. The results are aggregated by the timing tool and a linear fit is performed for each decay type with each generator. The slope from the linear fit is taken as the average time per event with associated uncertainty, while the intercept of the fit is taken as the average initialisation time of the generator.

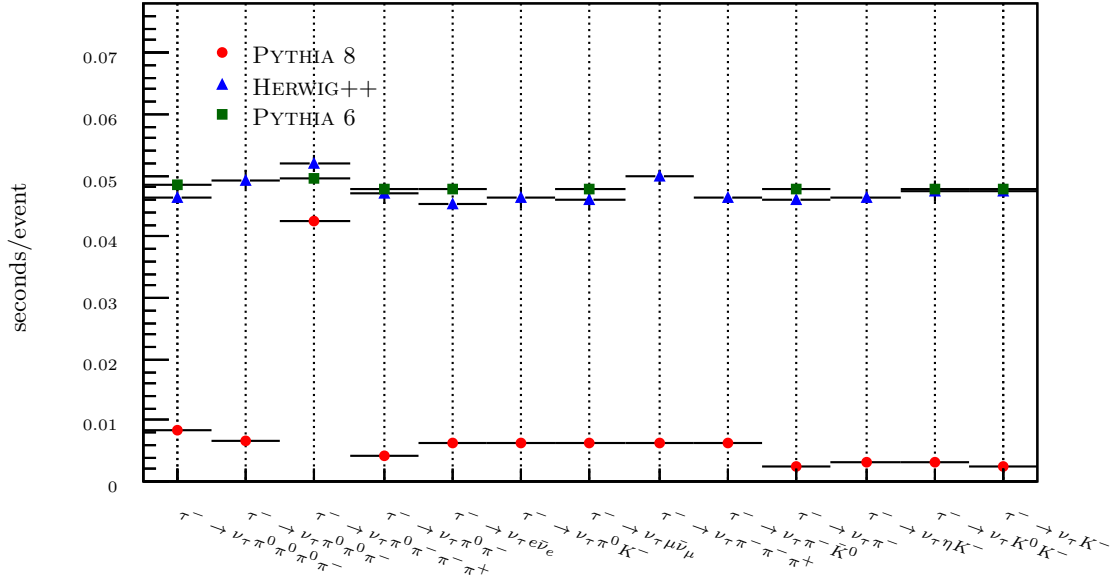


**Figure 3.18.:** A comparison of the average time per  $\tau$  lepton decay between the PYTHIA 8, HERWIG++, and TAUOLA event generators for a selection of the  $\tau$  lepton decays of Sect. 3.2.

In Fig. 3.18 the average time per event for a selection of the  $\tau$  lepton decay channels of Sect. 3.2 is given. In these tests PYTHIA 8 outperforms HERWIG++ and TAUOLA for all of the implemented  $\tau$  lepton decay channels by a factor of  $\approx 5$  except for the  $\tau^- \rightarrow \nu_\tau \pi^0 \pi^- \pi^+ \pi^+$  channel. The decrease in speed for this channel is due to the sharp resonance from the  $\omega$  which is not present in the  $\tau^- \rightarrow \nu_\tau \pi^0 \pi^0 \pi^0 \pi^-$  channel. This sharp resonance is not easily sampled using the  $m$ -generator phase-space algorithm and leads to inefficiencies for this channel. The timing information given in Fig. 3.18 is dependent upon a variety of factors other than just the  $\tau$  lepton decay algorithms used, including compile time options, machine architecture, and most importantly, the configuration used for event generation with each generator. Consequently, the results of Fig. 3.18 provide a general sense for the timing of the  $\tau$  lepton decay implementation in PYTHIA 8, but will vary from system to system.

## 4. Experimental Setup

The data used in the analyses of Chap. 5 and Chap. 6 were collected using the Large Hadron Collider Beauty detector (LHCb) on the Large Hadron Collider (LHC) at the European Organisation for Nuclear Research (CERN). CERN was founded in 1954 and is situated on the French-Swiss border near the city of Geneva, Switzerland. Currently, CERN is run by 20 European member states with 7 observer states and organisations, and 37 participating non-member states. Nearly 10,000 visiting scientists from over 600 universities and institutes and 113 countries utilise the research facilities at CERN. Fundamental advances in particle physics have been made throughout the years at CERN including the first observation of the  $W$  [116, 117] and  $Z$  bosons [118, 119] by the UA1 and UA2 detectors on the Super Proton Synchrotron (SPS), precision electroweak measurements [120] by the detectors on the Large Electron-Positron collider (LEP), the creation of anti-hydrogen [121], and most recently the discovery of a Higgs-like boson [8, 9] with the ATLAS and CMS detectors on the LHC. Within this chapter the collider is introduced in Sect. 4.1, the LHCb detector is described in Sect. 4.2, and the methods used for reconstructing events observed within the LHCb detector are outlined in Sect. 4.3.

### 4.1. Large Hadron Collider

The LHC accelerates protons in opposite directions around a 27 km ring, colliding them at four interaction points around which four detectors are built. Schematics in the vertical plane, defined by the beamline and a vector perpendicular to the LHC ring, for the general purpose ATLAS and CMS detectors are given in Figs. 4.1(a) and 4.1(b). These detectors are fully instrumented with tracking systems, calorimeters, and muon chambers. The LHCb detector, with a schematic shown in Fig. 4.1(c), is designed specifically for forward physics, in particular the physics of  $B$ -hadrons, and is a forward arm spectrometer, extending outwards on only one side of the interaction point. The data used in the analyses of Chaps. 5 and 6 were taken with this detector. Further details on the LHCb detector and LHCb event reconstruction are given in Sects. 4.2 and 4.3. The ALICE detector is a heavy ion detector, with its schematic shown in Fig. 4.1(d). During nominal LHC operations the LHCb and ALICE detectors receive reduced luminosities with respect to the ATLAS and CMS detectors.

The LHC began operation in September of 2008, but nine days after the inaugural start-up, a fault of the busbars in the interconnects between a dipole and quadrupole magnet system caused a magnet quench and delayed operations of the LHC until November of 2009 [126]. Full-scale data-taking began in March of 2010 at a centre-of-mass energy of 7 TeV, 3.5 TeV per beam, and continued until November of 2010 when lead ion beams were circulated for a month. In

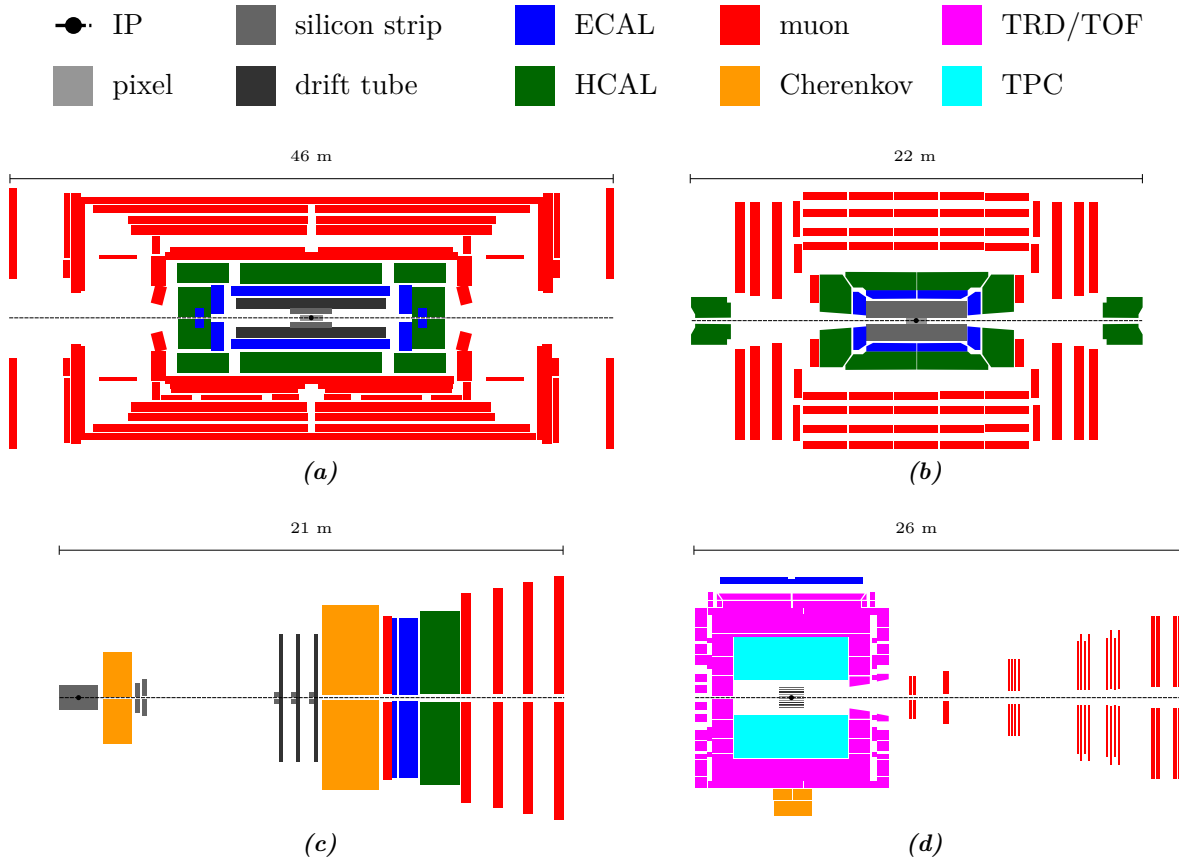


**Figure 4.1.:** Rough schematics of the (a) ATLAS, (b) CMS, (c) LHCb, and (d) ALICE detectors of the LHC. Here, ECAL are electromagnetic calorimeters, HCAL are hadronic calorimeters, TRD are transition radiation detectors, TOF are time of flight detectors, and TPC are time projection chambers. These schematics were modified from Refs. [122], [123], [124], and [125].

March of 2011 proton-proton collisions were again begun at a centre-of-mass energy of 7 TeV and continued until November of 2011. A plot of the integrated luminosity over time for the ATLAS, CMS, and LHCb detectors during 2011 data-taking is given in Fig. 4.2(a). In April of 2012, proton-proton data-taking at a centre-of-mass energy of 8 TeV began, and continued until February of 2013. The 2012 integrated luminosity is plotted in Fig. 4.2(b). Currently, the LHC has entered a long shutdown until sometime in 2014 after which operation will recommence at higher luminosities and with a centre-of-mass energy of 14 TeV [127]. The data used in Chaps. 5 and 6 were collected during the 2011 data-taking operations.

The technical design reports for the LHC can be found in the three volumes of Refs. [128], [129], and [130], corresponding to the main ring, infrastructure and general services, and injector chain for the LHC. An abridged and updated version of the technical design reports can be found in Ref. [131]. In the remainder of this section the layout of the machine is outlined in Sect. 4.1.1 and the injector chain is described in Sect. 4.1.2.

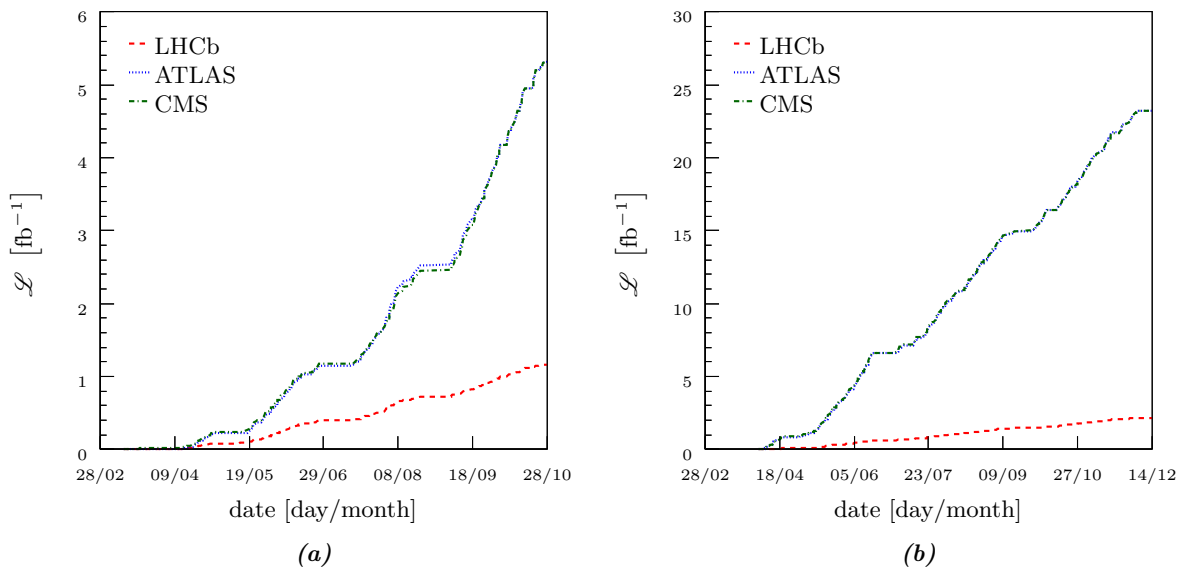


**Figure 4.2.:** Integrated luminosity as a function of time provided by the LHC to the LHCb, ATLAS, and CMS detectors for the (a) 2011 data-taking at  $\sqrt{s} = 7$  TeV and (b) 2012 data-taking at  $\sqrt{s} = 8$  TeV. The integrated luminosity data are taken from the LHC statistics web-page.

#### 4.1.1. Layout

The layout of the main LHC ring is summarised in the schematic of Fig. 4.3. The ring consists of eight long straight sections (LSS) each with a length of approximately 528 m alternating with eight arcs (ARC) each with a distance of approximately 2.8 km. The ring is also divided into octants, with each octant centred about an LSS, and each ARC divided between two octants. The collider ring is located between 45 m to 170 m below the surface, with an access point provided at every LSS. Each LSS is used for beam utilities or experiments, and the ARC segments contain the dipoles needed to bend the beam and quadrupoles used to focus the beam. Between each ARC and LSS is located a dispersion suppressor (DS) which is used to adapt the LHC reference orbit to the tunnel geometry. Additionally, the dispersion suppressors are used to match the ARC optics with the insertion optics for each LSS, as well as cancel horizontal dispersion from the dipole magnets.

The beams cross in the LSSs of the first, second, fifth, and eighth octants. The high luminosity ATLAS and CMS experiments are located at points 1 and 5 respectively. The plane of the beam crossing angle at point 1 is vertical while it is horizontal at point 5. Point 2 houses the lower luminosity ALICE experiment and point 8 contains the LHCb experiment. Beam 1, rotating clockwise from above, is injected at point 2 while beam 2, rotating anti-clockwise from above, is injected at point 8.

In the LSS of the third octant, momentum cleaning of the beams is performed while in the LSS of the seventh octant, optical cleaning of the beam is performed. The radio frequency (RF) cavities for the main ring are installed in the LSS of the fourth octant and contained in the old cavern used to house the ALEPH detector on the LEP collider. The LSS of the sixth octant



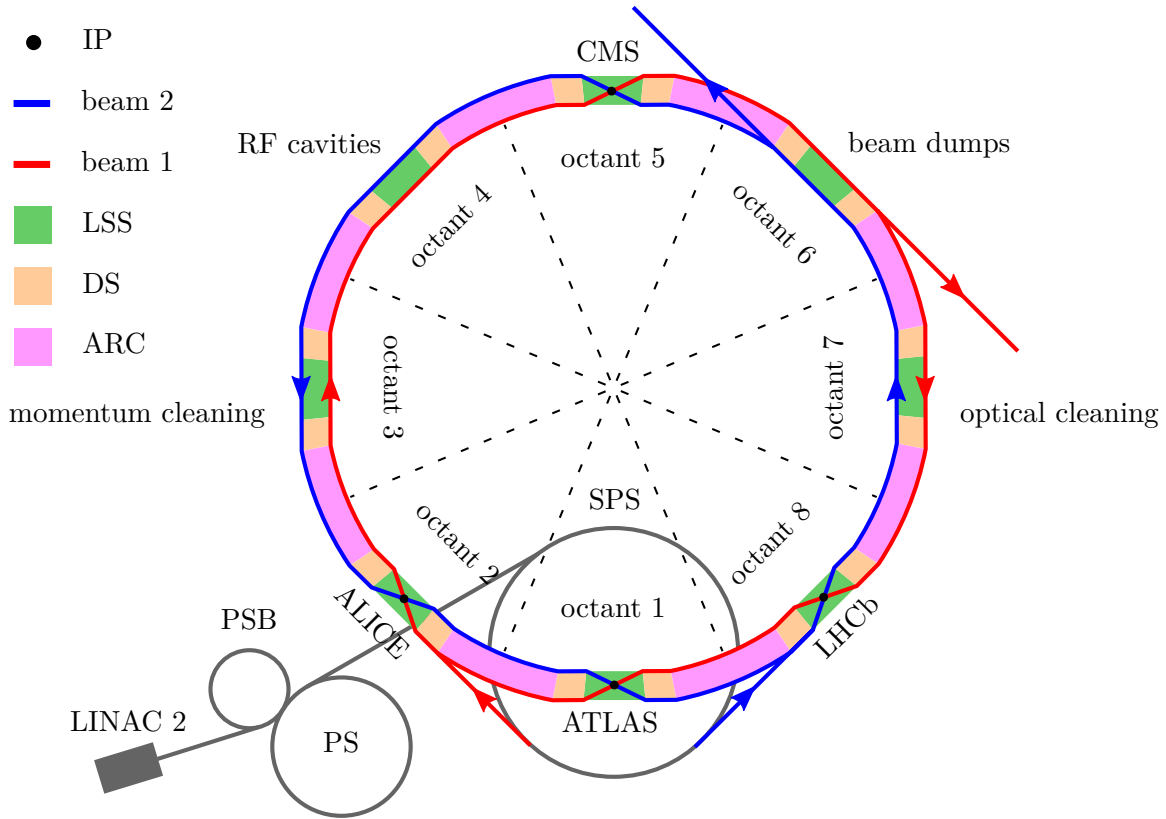


**Figure 4.3.:** Schematic of the main LHC ring and the injector chain as seen from above. The first proton beam (red) rotates clockwise while the second proton beam (blue) rotates anti-clockwise.

contains the two independent beam dump systems for both beams. These dumps abort the beams by using kicker magnets to horizontally bump the beams into septum magnets which then deflect the beams vertically into absorbers within dedicated tunnels.

#### 4.1.2. Injection Chain

The injection chain for the LHC is also shown in Fig. 4.3, and begins with LINAC 2, an Alvarez linear accelerator, where a plasma is created from an ionised gas within a duoplasmatron running at 90 kV. The plasma is formed into an ion beam within a 750 keV RF quadrupole which then passes the beam into three Alvarez tanks, consisting of in-phase drift tubes, which accelerate the beam up to an energy of 50 MeV. For nominal LHC operation, the LINAC 2 must output a proton beam with a current of 180 mA and pulse lengths of  $150 \mu\text{s}$  at a rate of 0.8 Hz into the Proton Synchrotron Booster (PSB) [132]. The PSB consists of four rings each with a radius of 25 m [133]. One proton bunch is injected into each of the rings and the four bunches are then accelerated to an energy of 1.4 GeV. These bunches are then extracted into the Proton Synchrotron (PS). The PS has a radius of 100 m and holds 84 proton bunches with a bunch spacing of  $25 \mu\text{s}$ . These bunches are accelerated to an energy of 26 GeV after which their bunch length is reduced to 4 ns for insertion into the 200 MHz RF cavities of the Super Proton Synchrotron [134]. The SPS, with a radius of 1.1 km accelerates the beam to 250 GeV using two

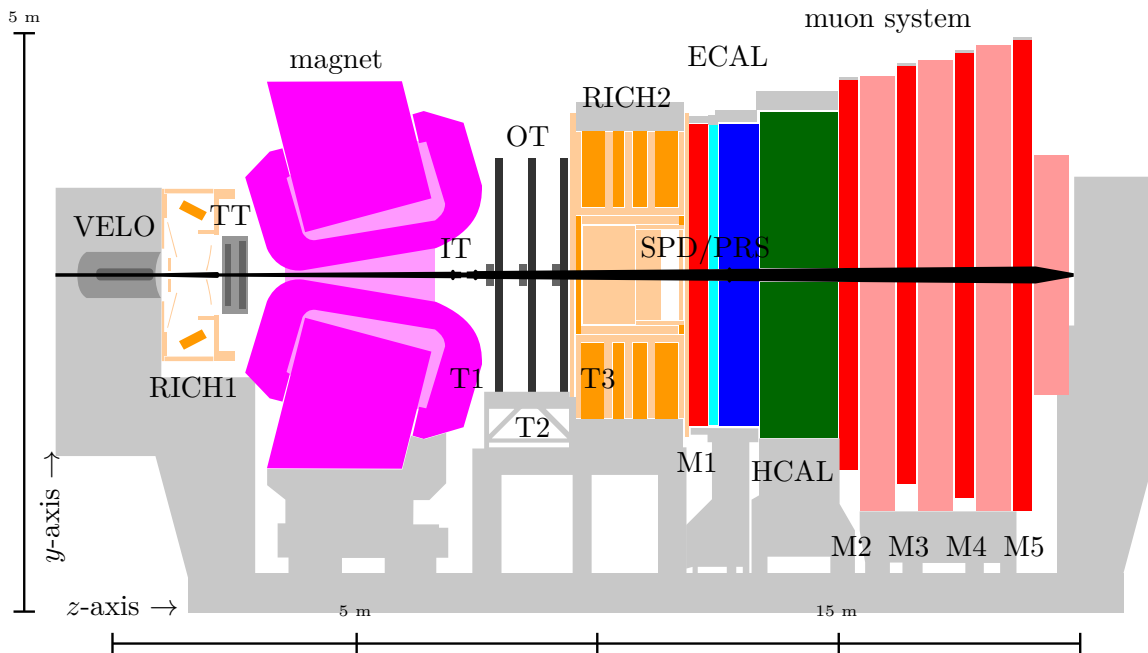


**Figure 4.4.:** Schematic of the LHCb detector in the longitudinal  $yz$ -plane.

200 MHz RF cavities and injects the beams into the main LHC ring at either point 2 or 8 [135].

## 4.2. LHC Beauty Detector

The Large Hadron Collider Beauty experiment (LHCb) is a forward arm spectrometer located in the experimental cavern of point 8 on the LHC ring. The detector is primarily designed for the identification of  $B$ -hadrons in order to further explore their decays and make precise measurements of  $\delta$ , the  $\mathcal{CP}$ -violating phase angle of the CKM matrix from the unified electroweak Lagrangian of Sect. 2.1.2, as well as to search for new physics through the deviation of rare  $B$ -hadron decays from their SM predictions, *e.g.*  $B_s \rightarrow \mu\mu$  [136]. The production of  $b$ -quark pairs within the LHC environment, which then hadronise into jets of  $B$ -hadrons, is typically close to the direction of either beam, with both  $b$ -quarks being produced in the same direction. Consequently, LHCb is designed as a forward arm spectrometer about the beamline in order to maximise the acceptance of  $B$ -hadrons while minimising construction and material costs. The reconstruction and identification of  $B$ -hadrons within the hadronic environment of the LHC requires excellent secondary vertex reconstruction, good momentum resolution, a fast and robust trigger, and hadron identification capabilities.

A detailed schematic of the LHCb detector and its sub-components in the longitudinal  $yz$ -plane is given in Fig. 4.4. The origin of the LHCb coordinate system is defined as the nominal interaction point within LHCb. The  $x$ -axis points outward from the centre of the LHC ring and is parallel to the plane of the LHC ring. The  $z$ -axis points along the beam in the direction of the detector, resulting in an angle of  $\approx 3.6$  mrad with the floor of the LHCb cavern. The  $y$ -axis points upward and is perpendicular with both the  $x$ -axis and  $z$ -axis to form a right-handed

Cartesian coordinate system. The azimuthal angle  $\phi$  is defined in the transverse  $xy$ -plane with a  $\phi$  of zero along the direction of the  $x$ -axis and ranges between values of  $-\pi$  and  $\pi$ . The polar angle  $\theta$  is defined as the opening angle with the  $z$ -axis such that a particle along the beamline has a  $\theta$  of zero. The pseudo-rapidity  $\eta$  and rapidity  $y$  are oftentimes used rather than  $\theta$  and are defined as,

$$\eta \equiv \frac{1}{2} \ln \left( \frac{|\vec{p}| + p_z}{|\vec{p}| - p_z} \right) = -\ln \left( \tan \left( \frac{\theta}{2} \right) \right), \quad y = \frac{1}{2} \ln \left( \frac{E + p_z}{E - p_z} \right) \quad (4.1)$$

where  $p_z$  is the  $z$ -component of the particle momentum. For massless particles the pseudo-rapidity and rapidity are equivalent. The transverse momentum of a particle,  $p_T$ , is also commonly used and is defined as  $\sqrt{p_x^2 + p_y^2}$ .

Surrounding the interaction point in Fig. 4.4 is a vertex locator (VELO) which is followed, in the positive  $z$ -direction, by a ring imaging Cherenkov detector (RICH1) and a tracker turicensis (TT). After the TT is a large dipole magnet which provides a bending field for the tracking systems. The remainder of the tracking system follows the magnet, consisting of an inner tracker (IT) about the beamline and an outer tracker (OT). This part of the tracking system is separated into three tracking stations, T1, T2, and T3. Another ring imaging Cherenkov detector (RICH2) is located after the IT and OT, which is larger than RICH1. After RICH2 is the first station M1 of the muon system, followed by a scintillating pad detector (SPD) and pre-shower calorimeter (PRS), an electromagnetic calorimeter (ECAL), and a hadronic calorimeter (HCAL). The remainder of the detector consists of four muon tracking stations M2 through M5. In the remainder of this section a description of the tracking system is given in Sect. 4.2.1 followed by an overview of the particle identification systems in Sect. 4.2.2. A full description of the detector can be found in Ref. [124] on which this section is based.

### 4.2.1. Tracking

The tracking system for LHCb consists of the VELO, TT, and IT which are silicon microstrip detectors, and the OT which is a straw-tube detector. The TT and IT were developed under the combined silicon tracker (ST) project and utilise similar hardware designs. Both the silicon microstrip and straw-tube technologies record the passage of charged particles, and when combined with a magnetic field, the trajectories of the charged particles built from their hits in the detectors are used to determine the momenta of the particles. The passage of a charged particle through a silicon detector ionises atoms, creating a current which is detected, while in straw-tube detectors the particle ionises the gas within the tube which then avalanches and creates a detected current. Both silicon microstrips and straw-tubes are combined in layers to provide a three-dimensional hit coordinate. During 2011 data taking the combined tracking system provided a momentum resolution,  $\delta_p/p$ , for charged particles between  $(0.4 - 0.6)\%$  [137].

A large dipole magnet located between the TT and OT provides the bending field for the tracking system. The dipole is a warm magnet consisting of two saddle-shaped coils, and is designed to meet the requirements of the tracking system while fitting within the space of the experimental cavern and minimising costs. The bending plane of the magnet is in the  $xz$ -plane

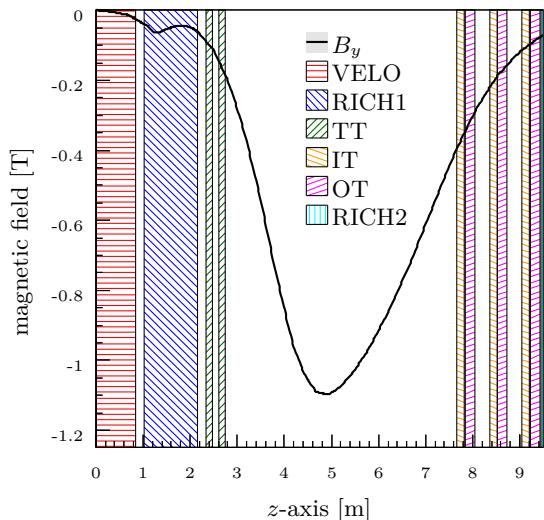


**Figure 4.5.:** Magnet-down  $y$ -component of the magnetic field within the LHCb detector along the  $z$ -axis, beginning at the VELO and moving outwards to the RICH2 detector. The uncertainty on the precision of the measurements is less than  $10^{-4}$  T. The approximate  $z$ -axis locations of the subdetectors are indicated by the shaded areas. The magnetic field data is taken from Ref. [124].

of the detector, and is designed to provide a magnetic field of less than 50 mT within the RICH systems and a maximum magnetic field between the TT and OT with an integrated magnetic field of 4 Tm for a 10 m track. The dipole can be run with a magnet-down or magnet-up configuration, corresponding to the direction of the  $y$ -component of the magnetic field. Both field configurations have been mapped between the VELO and RICH2 using an array of Hall probes within a precision of better than  $10^{-4}$  T. A report on the field map for the magnet taken during 2011 is available in Ref. [138], with the  $y$ -component of the magnetic field along the  $z$ -axis from Ref. [124] given in Fig. 4.5. The initial technical design report for the magnet system can be found in Ref. [139].

### Vertex Locator

The vertex locator is a microstrip detector located about the LHCb interaction point and is designed for high resolution reconstruction of secondary vertices from long-lived particles such as  $B$ -hadrons. The VELO is designed to have a pseudo-rapidity coverage of  $1.6 \leq \eta \leq 4.9$  for particles produced from vertices within 10.7 cm of the interaction point. A schematic of the VELO in the  $xz$ -plane is given in Fig. 4.6, consisting of 42 semi-circular detector modules and 4 pile-up veto sensors. The modules have a diameter of 9 cm and during stable beam conditions the active areas of the modules are located 8 mm from the centre of the beamline. Because the transverse beam width during injection of the LHC beams is larger than this separation, the VELO modules are retracted during beam injection so that the active areas of the module sensors are 29 mm from the centre of the beamline.

Each module consists of a back-to-back radial  $r$ -sensor and azimuthal  $\phi$ -sensor, where the  $z$ -coordinate of each module in conjunction with the  $r$  and  $\phi$ -measurements provide a full three-dimensional location for each hit in the module. The  $r$ -sensors are made up of quadrants, with each quadrant containing 512 strips, while the  $\phi$ -sensors consist of 683 inner strips and 1365 outer strips; the total number of strips per sensor for both sensor types is 2048. The strip pitch of the  $r$ -sensors increases linearly from 40  $\mu\text{m}$  to 102  $\mu\text{m}$  and the strip pitch for the  $\phi$ -sensors range

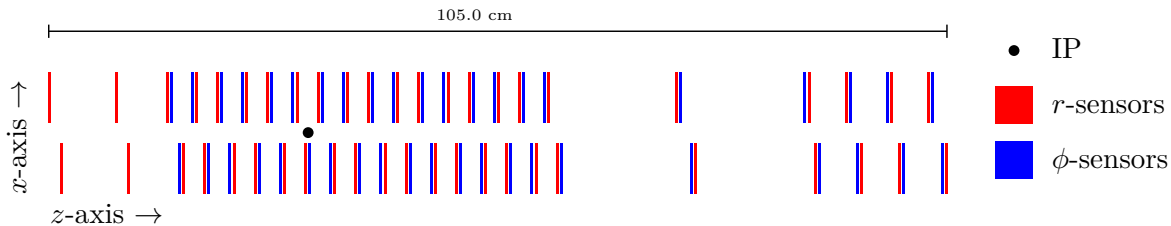


**Figure 4.6.:** Schematic of the VELO detector in the  $xz$ -plane. Each of the 42 modules consists of an  $r$ -sensor (red) and a  $\phi$ -sensor (blue). The leftmost  $r$ -sensors are pile-up veto sensors. Figure adapted from Ref. [124].

between  $38 \mu\text{m}$  and  $97 \mu\text{m}$ . The use of a cylindrical geometry for the VELO sensors, rather than a more typical rectilinear geometry, allows fast reconstruction of track impact parameters with sufficient resolution using information from the  $r$ -sensors, as is done by the high level trigger.

The pitches of the  $r$  and  $\phi$ -sensors were chosen to provide a single hit resolution of approximately  $4 \mu\text{m}$  for a track with a pseudo-rapidity of 3 passing through the inner  $\phi$ -strips. The impact parameter significance used in Sect. 5.1.2 to separate  $\tau$  lepton decays from prompt backgrounds primarily depends upon the precision which the VELO can reconstruct track positions close to the interaction region (impact parameter resolution). The impact parameter resolution is given by,

$$\delta_{\text{IP}} = \delta_{\text{HIT}} \oplus \frac{\delta_{\text{MSE}}}{p_{\text{T}}} \quad (4.2)$$

where  $\delta_{\text{HIT}}$  is the uncertainty due to the intrinsic precision of the track hits,  $\delta_{\text{MSE}}$  is the uncertainty due to multiple scattering effects, and  $p_{\text{T}}$  is the transverse momentum of the particle. From 2010 data,  $\delta_{\text{HIT}}$  was found to be 13.1 mm for the  $x$ -component and 12.1 mm for the  $y$ -component, while  $\delta_{\text{MSE}}$  was found to be 23.9 mm GeV and 23.7 mm GeV for the  $x$  and  $y$ -components of the impact parameter [1].

### Tracker Turicensis

The tracker turicensis is a microstrip silicon detector designed to be used in conjunction with the VELO, IT, and OT to measure the momenta of charged particles. This sub-detector begins approximately 2.3 m down the  $z$ -axis, ends at approximately 2.8 m along the  $z$ -axis, and covers a pseudo-rapidity range of  $2.0 \leq \eta \leq 5.0$  in the  $yz$ -plane and  $1.9 \leq \eta \leq 4.9$  in the  $xz$ -plane for particles produced from the interaction point. The TT consists of four layers, with the first two layers grouped into a single station and separated from the second station of the final two layers by a distance of 0.3 m. A schematic of the first layer in the  $xy$ -plane is given in Fig. 4.7, which includes 16 strip modules with 8 modules above the  $xz$ -plane and 8 modules below. The second TT layer is similar to the first, but the modules are rotated by an angle of  $+5^\circ$  with respect to the  $yz$ -plane. The third layer has an additional 4 modules, 2 above and 2 below the  $xz$ -plane, and is rotated by an angle of  $-5^\circ$ , while the fourth and final layer also has an additional 4 modules, but is not rotated.

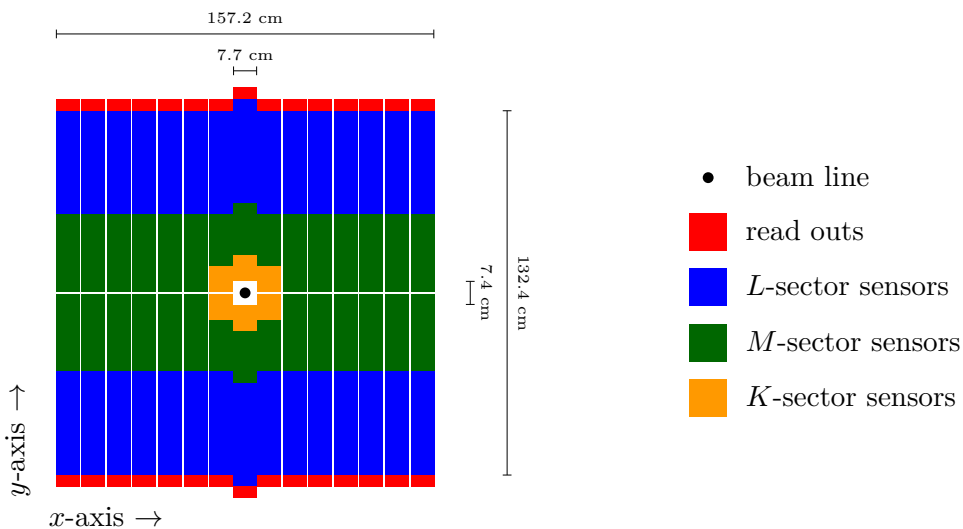


**Figure 4.7.:** Schematic of the first layer of the TT detector in the  $xy$ -plane. The layer consists of 16 strip modules, each with 7 sensors and 2 or 3 read out hybrids. Adapted from Ref. [140].

Every strip module contains 7 silicon sensors, each with 512 strips aligned vertically along the length of the module, where the pitch for each strip is  $183 \mu\text{m}$ . This vertical alignment provides maximum resolution in the bending plane of the dipole magnet. The sensors are divided into three read out sectors,  $L$ ,  $M$ , and  $K$ . The 4 outermost silicon sensors for each module read out to the  $L$ -sector, while the 3 innermost sensors read out to the  $M$ -sector. Modules with high occupancy sensors adjacent to the beamline contain an  $M$ -sector subdivided into an additional  $K$ -sector, with the two outermost sensors reading out to the  $M$ -sector, and the innermost sensor adjacent to the beamline reading out to the  $K$ -sector.

This design of the TT system provides a minimum single hit resolution of  $59 \mu\text{m}$  as found from data [137]. The TT in combination with the muon system is used to determine muon track finding efficiencies from data in Sect. 5.2.1. Further details on the TT can be found in the technical design report of Ref. [141].

### Inner Tracker

The inner tracker uses the same silicon microstrip sensors as the TT and provides high pseudo-rapidity tracking coverage along the beam line complimentary to the OT. There are three IT stations located at approximately 7.7 m, 8.4 m, and 9.0 m along the  $z$ -axis corresponding to the combined IT and OT tracking stations T1, T2, and T3 of Fig. 4.4. The three stations cover a common pseudo-rapidity range for a track produced at the interaction point of  $4.5 \leq \eta \leq 4.9$  in the  $yz$ -plane and  $3.4 \leq \eta \leq 5.0$  in the  $xz$ -plane. Despite the small acceptance of the IT, nearly 20% of all tracks produced within LHCb pass through the IT. Every IT station contains four layers, similar to the four layers of the TT. Each layer consists of 28 modules in a configuration similar to the schematic of Fig. 4.8. The strip modules of the first and fourth layers are vertical like that of Fig. 4.8, while the second layer is rotated by  $+5^\circ$  with respect to the  $yz$ -plane and the third layer is rotated by  $-5^\circ$ . This rotation configuration is the same as for the TT layers

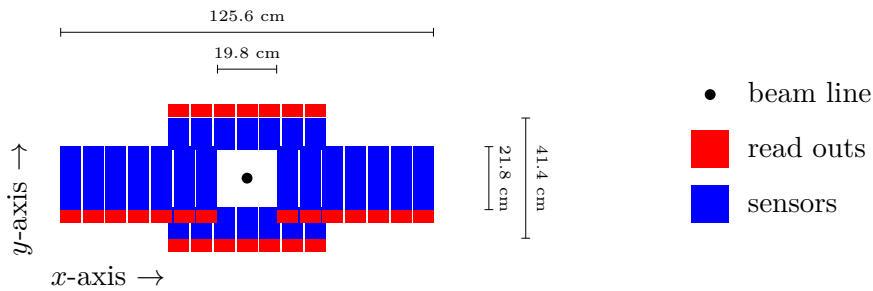


**Figure 4.8.:** Schematic of the first and fourth layer of the IT detector in the  $xy$ -plane. The layer consists of 28 strip modules, each with 1 or 2 sensors and 1 or 2 read out hybrids. Adapted from Ref. [142].

and is designed to maximise the IT resolution in the bending plane of the dipole.

The 14 outermost strip modules contain two silicon sensors each, with a dedicated read out hybrid for every sensor, while the 14 innermost strip modules only contain one sensor each. These sensors use the same technology as the TT sensors and contain 384 vertically aligned strips, each with a pitch of  $198 \mu\text{m}$ . The IT provides a single hit resolution of  $50 \mu\text{m}$  as found from data [137], and is critical for the reconstruction of the charged particle tracks used in the analysis of Chap. 5. Further details on the IT can be found in the technical design report of Ref. [142].

### Outer Tracker

The outer tracker is a large straw-tube detector which provides lower pseudo-rapidity coverage about the higher pseudo-rapidity IT stations. There are three OT stations which are contained in the combined IT and OT stations T1, T2, and T3. The three OT stations are located at 7.8 m, 8.5 m, and 9.2 m along the  $z$ -axis and cover a common pseudo-rapidity range of  $2.0 \leq \eta \leq 4.5$  in the  $yz$ -plane and  $1.8 \leq \eta \leq 3.4$  in the  $xz$ -plane. Each OT station consists of four layers, where the same rotation scheme for the TT and IT is used; the first and fourth layers are vertical, the second layer is rotated by  $+5^\circ$  with respect to the  $yz$ -plane, and the third layer is rotated by  $-5^\circ$ . A schematic of a vertical OT layer is given in Fig. 4.9, where each layer contains 14 long  $F$ -modules and 8 short  $S$ -modules.

Every  $F$ -module contains 256 straw-tubes, with the tubes divided into two monolayers in the  $xy$ -plane, each containing 128 tubes. The monolayers are divided horizontally in half, with each half containing 64 straw-tubes. Each layer half reads out at the outermost edge of the module. The  $S$ -modules also consist of two straw-tube monolayers, but these monolayers are not divided in half. Each layer contains 128 tubes, and so every  $S$ -modules contains 256 straw-tubes. Again, each layer reads out to the outermost edge of the module. The straw-tubes contain a mixture of 30% argon and 20% carbon dioxide, and with an inner diameter of 4.9 mm have a drift time of less than 50 ns. The single hit resolution of the OT is  $220 \mu\text{m}$  [143]. Hits from the OT are used in the reconstruction of the tracks used in the analysis of Chap. 5. Further details on the OT can be found in the technical design report of Ref. [144].

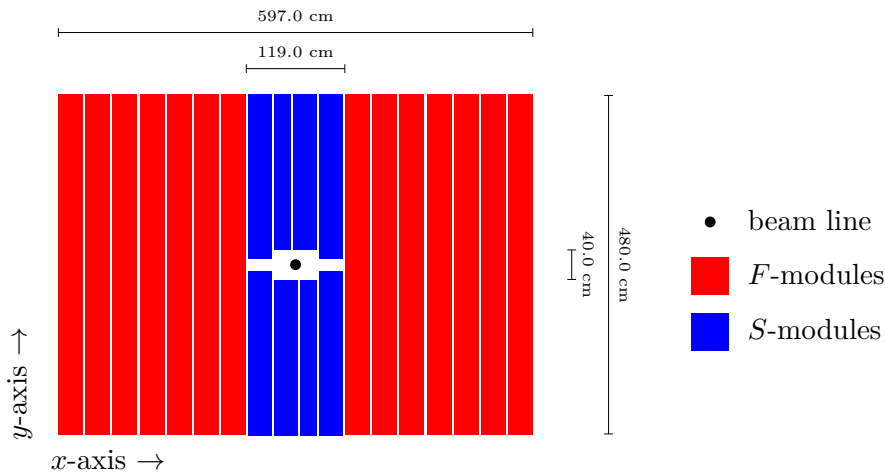


**Figure 4.9.:** Schematic of the first and fourth layer of the OT detector in the  $xy$ -plane. The layer consists of 14  $F$ -modules and 8  $S$ -modules.

#### 4.2.2. Particle Identification

The particle identification subdetectors of LHCb consist of two ring imaging Cherenkov radiation (RICH) detectors, four calorimeters, and a muon system. The RICH detectors use Cherenkov radiation from charged particles to determine the velocity of particles, and in conjunction with momentum information from the tracking system, are used to calculate the mass of charged particles. Information from the RICH detectors is used to differentiate between charged pions and kaons from  $B$ -hadron decays. The energy of charged or neutral particles are determined with the four calorimeters. Here, the particles interact with scintillating material, producing particle showers resulting in photons that are measured by photodetectors; the magnitude and intensity of the photons from the particle shower correspond to the energy of the particle passing through the calorimeter. The calorimeters are used to differentiate between hadrons and leptons, and in combination with the tracking system, between neutral and charged particles. The muon systems are designed specifically to identify muons and measure both their momentum and energy through the use of multi-wire proportional chambers.

#### Ring Imaging Cherenkov Detectors

Charged particles passing through a medium at a velocity, larger than the velocity of light propagating through that medium, radiate photons in a cone about the direction of travel of the particle. The polar angle  $\theta$  between the velocity vector of the particle and the radiated light is given by,

$$\theta = \cos^{-1} \left( \frac{1}{n\beta} \right) \quad (4.3)$$

where  $n$  is the index of refraction for the medium and  $\beta = v/c$ , where  $v$  is the velocity of the particle. RICH detectors consist of a radiating medium through which the particle passes, and



a photodetector which measures the rings produced from the radiating medium. Because RICH detectors can only resolve rings with radii within a given range, the index of refraction for the radiating material dictates the velocity range of particles observable by the detector.

The RICH1, located approximately 1.0 m along the  $z$ -axis directly after the VELO, is designed to differentiate between charged pions and kaons with low momenta within the range 1 to 60 GeV. Typically, particles produced with low momenta from  $B$ -hadron decays provide a broad spread in pseudo-rapidities, and so the RICH1 is designed to cover a pseudo-rapidity range of  $2.1 \leq \eta \leq 4.4$  in the  $yz$ -plane and  $1.9 \leq \eta \leq 4.4$  in the  $xz$ -plane for a particle originating from the interaction point. RICH1 utilises two radiating materials to achieve this momentum range, aerogel and  $C_4F_{10}$ . The photodetectors used for measuring the Cherenkov radiation are hybrid pixel photon detectors which are housed in magnetic shielding, allowing the photodetectors to operate in magnetic fields with a field strength below 50 mT. The photodetectors can detect photons with wavelengths between 200 and 600 nm, and are made up of 500 by 500  $\mu\text{m}$  pixels.

The RICH2 is located after the OT at a distance of approximately 9.5 m along the  $z$ -axis and is designed to separate charged pions and kaons with momenta in the range 15 to 100 GeV. Particles from  $B$ -hadrons with larger momenta are expected to also have larger pseudo-rapidities, and so RICH2 covers the pseudo-rapidity range  $3.0 \leq \eta \leq 4.9$  in the  $yz$ -plane and  $2.8 \leq \eta \leq 4.9$  in the  $xz$ -plane. The RICH2 uses the same photodetectors as RICH1, but uses the radiating material  $C_4F$ , with an index of refraction approximately 1.7 times smaller than  $C_4F_{10}$ , to achieve a larger momentum upper limit than RICH1. While the RICH detectors are not directly used in the analysis of Chap. 5, they provide an important component in the detection of  $B$ -hadron decays. Further details on the RICH systems can be found in the technical design report of Ref. [145].

### Scintillating Pad Detector and Preshower Calorimeter

The SPD, PRS, and ECAL are aligned along lines of pseudo-rapidity from the interaction point to provide a one-to-one mapping between calorimeter cells. The scintillating pad detector is the first calorimeter along the  $z$ -axis and is located at 12.3 m. No absorber material is placed in front of the SPD and so charged particles shower within it, providing a fast method to determine the track multiplicity of the event and differentiate between charged particles and photons. The pseudo-rapidity coverage of the SPD is designed to match the coverage of the tracking system and ranges from  $2.1 \leq \eta \leq 4.4$  in the  $yz$ -plane and from  $1.9 \leq \eta \leq 4.4$  in the  $xz$ -plane for particles produced at the interaction point. A schematic for the layout of a single quadrant of the SPD, PRS, and ECAL is given in Fig. 4.10, with the ECAL dimensions provided. The dimensions for the SPD are similar but reduced by a factor of approximately 1.0%. The SPD contains 3312 modules, with 828 modules per quadrant. The modules all have the same dimensions and are divided into outer-modules, middle-modules, and inner-modules.

Each outer-module consists of a single square scintillating tile made from polystyrene, while every middle-module houses 4 square tiles, and every inner-module contains 9 square tiles. The outer-module tiles are approximately 12 cm to a side in the  $xy$ -plane, the middle-module tiles 6 cm, and the inner-module tiles 4 cm. Each tile, which is 1.5 cm deep and 0.28 radiation

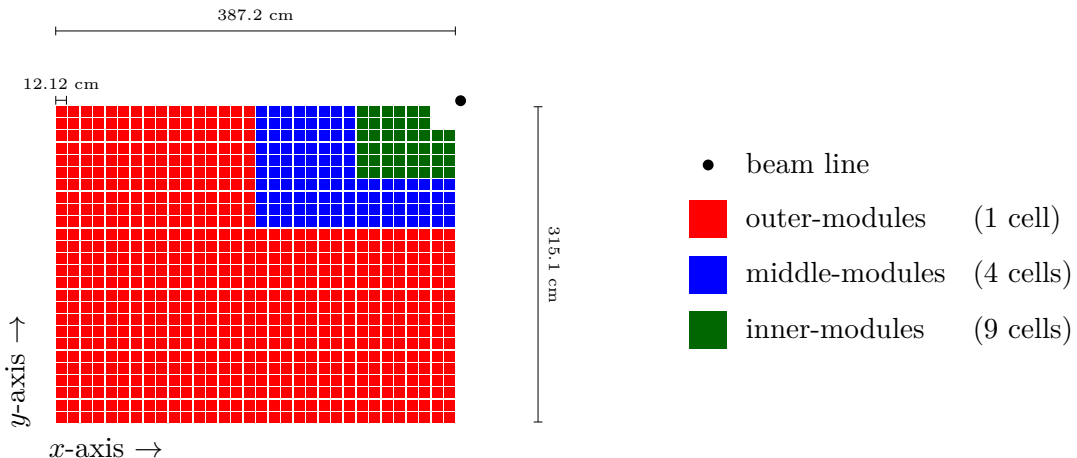


**Figure 4.10.:** Schematic of the lower left quadrant of the SPD, PRS, and ECAL in the  $xy$ -plane, along the direction of the  $z$ -axis. The quadrant consists of 672 outer-modules with 1 square cell each, 112 middle-modules with 4 square cells each, and 44 inner modules with 9 square cells each. All modules have the same dimensions, with the dimensions given here for the ECAL.

lengths, is connected via wavelength-shifting fibres to a multi-anode photomultiplier to create an SPD calorimeter cell. The segmentation of the SPD in the  $xy$ -plane ensures a roughly similar particle occupancy between all calorimeter cells. The SPD is not used in the reconstruction of electrons or hadrons in the analysis of Chap. 5, but is used to perform a fast global event cut based on the SPD multiplicity of the event which must be accounted for in Sect. 5.2.1.

Behind each SPD calorimeter cell, along the  $z$ -axis, is placed a 1.5 cm deep lead absorber of 2.5 radiation lengths, followed by another 1.5 cm deep scintillating tile of 0.28 radiation lengths. These tiles are not part of the SPD, but rather the PRS, and are slightly smaller than the ECAL cells by 0.5% in order to maintain the one-to-one correspondence between SPD, PRS, and ECAL cells along lines of pseudo-rapidity. Every PRS tile, like SPD tiles, is connected via wavelength-shifting fibres to a multi-anode photomultiplier tube to create a PRS calorimeter cell. The cells for the pre-shower calorimeter provide a segmentation in the  $yz$ -plane for the ECAL, and have the same layout and pseudo-rapidity coverage as both the SPD and ECAL. The PRS is used to identify neutral and charged particles which interact through the electromagnetic force. In the analysis of Chap. 5, the PRS is used to differentiate between the electrons and charged hadrons of Sect. 5.1.1.

### Electromagnetic Calorimeter

The electromagnetic calorimeter is used to identify photons and electrons and measure their energy. It is located 12.5 m along the  $z$ -axis, just after the SPD and PRS calorimeters. The ECAL has the same pseudo-rapidity coverage as the SPD and PRS, and is given by the schematic of Fig. 4.10, with the same module configuration and cell layout in the  $xy$ -plane as the SPD and PRS. Each module, however, contains a stack of 132 layers, alternating between lead absorbers and calorimeter tiles along the direction of the  $z$ -axis; this corresponds to 66 absorbers and 66

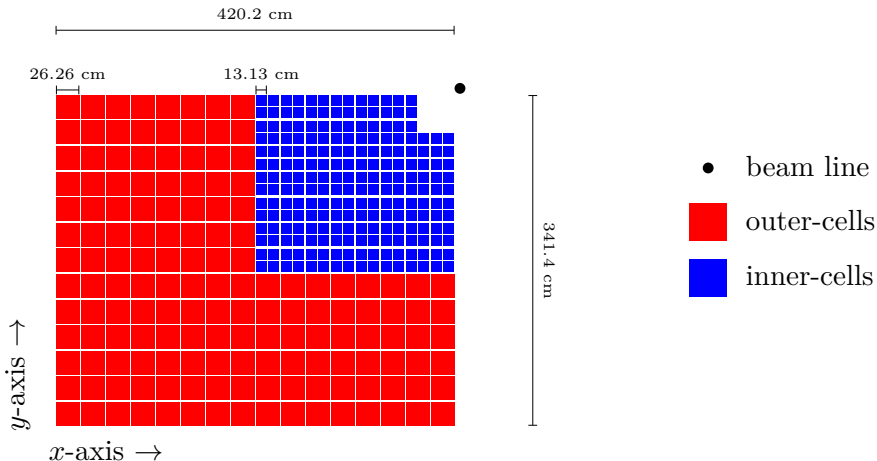


**Figure 4.11.:** Schematic of the lower left quadrant of the HCAL in the  $xy$ -plane, along the direction of the  $z$ -axis. The quadrant consists of 152 outer-cells and 215 inner-cells.

scintillating tiles. Each absorber is 0.2 cm deep and 0.33 radiation lengths, and each scintillator tile is 0.4 cm deep and 0.08 radiation lengths. The dimensions for each absorber and tile from a stack in the  $xy$ -plane are approximately the same as those for the SPD and PRS. The photons from all 66 tiles in a stack are collected via wavelength-shifting fibres into a phototube to produce a single ECAL cell. The entire ECAL covers 25 radiation lengths along the direction of the  $z$ -axis.

The energy resolution for a calorimeter can be written as,

$$\delta_E = \delta_{\text{clb}} E \oplus \delta_{\text{smp}} \sqrt{E} \oplus \delta_{\text{noi}} \quad (4.4)$$

where  $E$  is the measured energy of the particle,  $\delta_{\text{clb}}$  is the calibration uncertainty,  $\delta_{\text{smp}}$  is the uncertainty due to sampling fluctuations, and  $\delta_{\text{noi}}$  is the noise uncertainty. For high energy particles, oftentimes only the first two uncertainties are considered as the noise uncertainty is negligible. In Ref. [146] these uncertainties were measured to be  $\delta_{\text{clb}} = 8.3 \times 10^{-2}$  and  $\delta_{\text{smp}} = 9.5 \times 10^{-1} \text{ GeV}^{1/2}$  for the LHCb ECAL. The energy of particles as measured by the ECAL is used to separate electrons from hadrons in the analysis of Chap. 5.

### Hadronic Calorimeter

The hadronic calorimeter is directly after the ECAL, 13.3 m along the  $z$ -axis, and is used to identify hadrons and measure their energy. The pseudo-rapidity coverage of the HCAL is  $1.8 \leq \eta \leq 4.2$  in the  $yz$ -plane and  $2.1 \leq \eta \leq 4.2$  in the  $xz$ -plane for a particle originating from the interaction point. A schematic of the calorimeter cell layout for the HCAL is given in Fig. 4.11 for the lower left quadrant in the  $xy$ -plane along the direction of the  $z$ -axis. Each HCAL quadrant contains 152 square outer-cells with sides of 26.26 cm in the  $xy$ -plane, and 215 inner-cells with sides of 13.13 cm. The segmentation of the HCAL cells in the  $xy$ -plane is larger than the ECAL cells due to the larger size of hadronic showers.

Each outer-cell is made from a stack of 26 layers along the direction of the  $x$ -axis, opposed to

the ECAL cells which are stacked along the  $z$ -axis. The width of each layer is 1.01 cm, with a height of 26.26 cm and a depth of 128.3 cm. Every layer contains two sublayers, a 0.6 cm wide structural plate, followed by a sublayer of 3 polystyrene scintillator tiles alternating with iron absorbers along the direction of the  $z$ -axis. The scintillator tiles are 0.3 cm wide and 19.7 cm deep, while the iron absorbers are 0.4 cm wide. Each scintillator tile is separated by 20.2 cm of iron absorber along the direction of the  $z$ -axis, which is 1.0 interaction length of material. The scintillator-absorber sublayer layout is staggered between the layers so that the scintillator of one layer is followed by an absorber in the next layer of the stack. The scintillator tiles are connected to photomultiplier tubes via wavelength-shifting fibres, with one read out channel per cell.

The inner-cells have the same stack structure as the outer-cells, but each stack contains 13 layers. Additionally, each scintillator tile is split in two with the same width and depth but a height of 13.13 cm. Consequently, each inner-cell stack contains two inner-cells along the direction of the  $y$ -axis. From this configuration, each outer-cell houses 78 scintillator tiles and each inner-cell contains 39 scintillator tiles. The entire HCAL, including structure and absorbers, is 5.6 interaction lengths along the  $z$ -axis. The energy resolution of the HCAL, using the same parametrisation of Eq. 4.4, is  $\delta_{\text{clb}} = 0.9$  and  $\delta_{\text{smp}} = 6.9 \text{ GeV}^{1/2}$  from Ref. [124]. The energy of particles measured by the HCAL is used to separate hadrons from electrons in the analysis of Chap. 5. Further information on all of the calorimeter systems can be found in the technical design report of Ref. [147].

## Muon System

Because muons are two orders of magnitude more massive than electrons, the energy lost through bremsstrahlung radiation for muons is ten orders of magnitude smaller than electrons, and so muons do not shower in the ECAL. Additionally, muons interact minimally with the HCAL, as they are leptons and do not interact through the strong force. Consequently, the majority of the muon system is placed after the ECAL and HCAL. The muon system is divided into five stations, M1 through M5, located at distances of 12.1 m, 15.3 m, 16.5 m, 17.7 m, and 18.9 m along the  $z$ -axis. The five stations cover a pseudo-rapidity range of  $2.0 \leq \eta \leq 4.8$  in the  $yz$ -plane and  $1.9 \leq \eta \leq 4.6$  in the  $xz$ -plane for particles produced from the interaction point. The first three muon stations are built for high resolution transverse momentum measurements, while the final two stations are designed for primarily particle identification. To ensure only muons reach the final two stations, three iron absorbers, each with a depth of 80 cm, are placed between the final four muon stations. To reach the final station, a muon will have traversed over 20 interaction lengths of material, including the calorimeters.

The five muon stations are segmented into chambers, with the chamber layout and size designed to provide a one-to-one mapping between the chambers of each station along lines of pseudo-rapidity. A schematic of the chamber layout for a quadrant of a muon station in the  $xy$ -plane is given in Fig. 4.12. The quadrant is divided into four regions, R1 through R4, where the chamber resolution is lower for chambers in regions farther from the  $z$ -axis. Each chamber is a multi-wire proportional chamber except for the R1-chambers of the first muon station, which

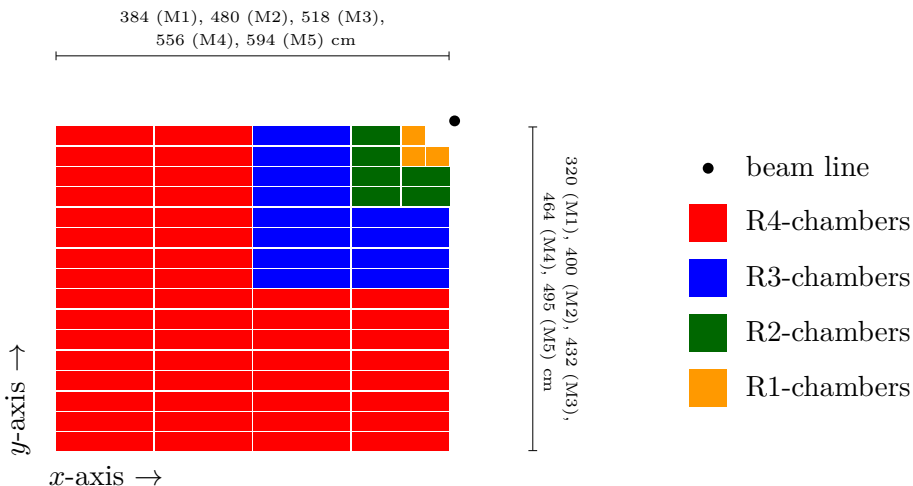


**Figure 4.12.:** Schematic of the lower left quadrant of a muon station in the  $xy$ -plane, along the direction of the  $z$ -axis. The width and height of the quadrant for each muon station is given. Adapted from Ref. [124].

are triple-gas electron multiplier chambers. The chambers are divided into rectangular pads, where each pad has a read out. For all muon stations the R1-chambers are segmented into 8 pads along the  $y$ -axis, while the R2-chambers are segmented into 4 pads, the R3-chambers into 2 pads, and the R1-chambers into only a single pad. Along the  $x$ -axis, the R1 through R3-chambers of the M1 station are divided into 24 pads, while the R4-chambers are divided into 12 pads. For M1 and M2, the number of pads along the  $x$ -axis for each chamber type are doubled with respect to the M1 segmentation. For M4 and M5, the pad segmentation of the chambers along the  $x$ -axis is halved.

The transverse momentum resolution,  $\delta_{p_T}/p_T$ , for muon tracks using only hits from the muon stations was measured to be approximately 20% in Ref. [148]. The use of the muon system in the analysis of Chap. 5 is critical. Every decay category of  $Z \rightarrow \tau\tau$  events analysed, except one, requires at least a single muon, which is identified using M2 through M5. Additionally, the track finding efficiency for muons passing through the VELO, IT, and OT is determined using combined hits from the TT and muon system in Sect. 5.2.1. Further information on the LHCb muon system can be found in the technical design report of Ref. [149].

### 4.3. LHCb Event Reconstruction

To interpret the raw output from the LHCb detector described in Sect. 4.2, the signals from the subdetectors are combined using reconstruction to produce high level physics objects that can be used in analyses. Hits from the tracking system are combined to produce tracks, particle trajectories of charged particles, while cells from the calorimeters are clustered to find deposits of energy from either charged or neutral particles. Matching algorithms between tracks and calorimeter clusters, as well as RICH information, is then run to identify particles.

Reconstruction of LHCb data is performed twice, once at the online level of the trigger system and once at the offline level. The online triggers perform a fast reconstruction that is not

complete, to quickly filter events from the detector and write them to disk for later offline reconstruction. Offline reconstruction uses the information from the entire event to create a more precise detector-wide reconstruction of the event. The offline LHCb reconstruction software is BRUNEL [150] which produces data files that can be processed by the DAVINCI [151] physics analysis software.

Full simulations of events in the detector are performed with the GAUSS [152] simulation software which utilises PYTHIA 6 [10, 153] as a general purpose Monte Carlo event generator, EVTGEN [154] as a  $B$ -hadron particle decayer, and GEANT4 as a detector simulator. The simulated events produced from GAUSS are digitised by the BOOLE [155] software, with trigger emulation applied by the MOORE [156] software.

All LHCb software is based on the GAUDI [157] framework. Large distributed processing jobs for any of the LHCb software is typically submitted through the GANGA [158] software and can be distributed to the CERN and LHCb computing grids via the DIRAC [159] software. Further information on LHCb computing and software can be found in the technical design report of Ref. [160].

The track reconstruction implemented in BRUNEL is described in Sect. 4.3.1, and the use of calorimeter information in the BRUNEL reconstruction process is outlined in Sect. 4.3.2. The trigger system, which uses similar algorithms to the tracking algorithms implemented in BRUNEL, is introduced in Sect. 4.3.3. Finally, the methods used for determining the integrated luminosity for a reconstructed data sample are described in Sect. 4.3.4.

### 4.3.1. Tracking Information

Information from the tracking system of Sect. 4.2.1 provides the foundation for LHCb event reconstruction. Hits from the VELO, TT, IT, and OT are combined into tracks which represent possible trajectories of charged particles passing through the detector. These trajectories, if passing through the dipole magnetic field of Fig. 4.5, can be used to determine the momentum of the particle. Tracks from a common origin can be used to produce vertices, *i.e.* locations in the detector where two or more particles were produced. In LHCb reconstruction, five types of tracks are considered [161].

**VELO:** Contain hits only in the VELO and consequently have no associated momenta. Because the VELO surrounds the interaction point, these tracks can have either a forward or backward direction along the  $z$ -axis. These tracks are particularly useful for vertex reconstruction.

**T (IT/OT):** Have hits from either the IT or OT, or both, but do not have any associated hits from the VELO or TT. T-tracks are combined with information from the RICH2 and used for the reconstruction of charged pions and kaons.

**upstream:** Are built from both VELO and TT hits, but do not contain VELO, IT, or OT hits. Oftentimes, these are low momentum tracks which are deflected from within the

detector by the magnetic field of the dipole. If the tracks are within RICH1 acceptance the mass of the particle producing the track can typically be determined.

downstream: Consist of hits from the TT and the IT, OT, or both. These tracks can be produced from long lived particles that may not decay within the VELO, such as the  $K_S$ .

long: Contain hits from the VELO and the IT, OT, or both. These tracks may also contain hits from the TT, but are not required to contain TT hits. This track type is the most commonly used type in LHCb analyses.

A graphical summary of the LHCb track types is given in Fig. 4.13. The tracks used in the analysis of Chap. 5 are long-tracks, and the efficiency of long-track reconstruction for muons is measured in Sect. 5.2.1.

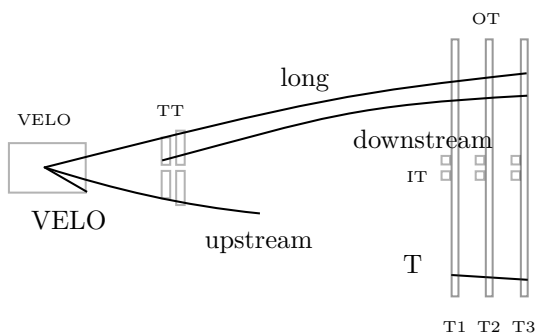


**Figure 4.13.:** Schematic of the LHCb tracking system in the bending  $xz$ -plane depicting the different types of reconstructed LHCb tracks.

Tracks are reconstructed by first track-seeding in the individual tracking system detectors, then track-finding where a search is made outside the seeding detector, and finally track-fitting where the trajectories from track-finding are refined. After this, reconstructed long-tracks are extrapolated to the muon system, and if compatible hits are found, a combined muon track is formed. The tracks produced from the reconstruction process are then used to seed possible vertices, which are then further refined through vertex fitting. Further information on LHCb track reconstruction can be found in Ref. [162].

### 4.3.2. Calorimeter Information

After the reconstruction of tracks from Sect. 4.3.1 is performed, calorimeter and RICH information is used to identify the type of particle from which the track was produced. In Chap. 5 only muon system and calorimeter information is used to identify muons, electrons, and charged hadrons, with no RICH information used. Consequently, RICH reconstruction is not introduced in this thesis, but an overview can be found in Ref. [163]. ECAL information is used to create neutral pion and photon candidates, as well as identify tracks from electrons and correct their energy. Additionally, the energies from PRS, ECAL, and HCAL cells associated with tracks extrapolated to the calorimeters are used to differentiate between muons, electrons, and charged hadrons.

Electrons within LHCb interact with the detector material, losing energy through the emission of bremsstrahlung photons, and so the recovery of these photons is important in reconstructing the full momentum of electrons. Within LHCb reconstruction, all long-tracks are considered

as electron candidates and bremsstrahlung recovery is performed by searching for compatible photon candidates and adding their momentum to the track momentum. Photon candidates are reconstructed by grouping ECAL cells into ECAL clusters, matching ECAL clusters with tracks, and generating candidates from clusters without matching tracks. Details on the LHCb calorimeter reconstruction can be found in Refs. [164], [165], and [166].

The calorimeter energy associated with a long-track is found by extrapolating the track from its last state vector to the start of the calorimeter. The track is then linearly extrapolated from the start of the calorimeter through the depth of the calorimeter and points are sampled along the line of the trajectory. A list of the calorimeter cells which contain the points is made, with any duplicate cells removed. The energies from the corresponding digits of the cells from the list are then summed to produce the associated calorimeter energy for the track.

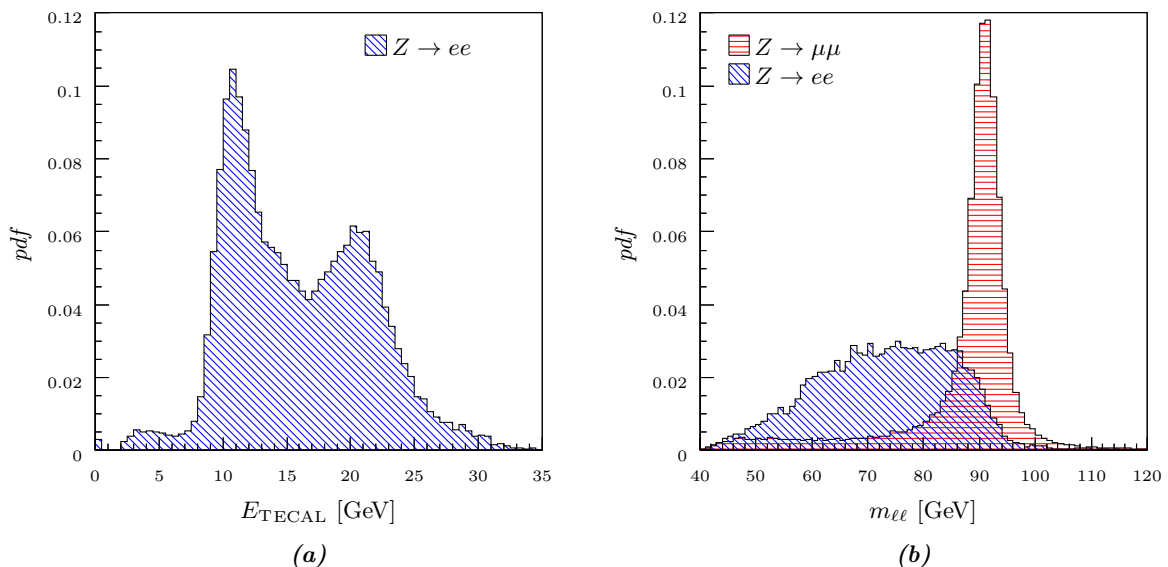


**Figure 4.14.:** (a) Distribution of transverse ECAL energy associated with electrons tracks taken from  $Z \rightarrow ee$  data events, illustrating ECAL cell saturation. (b) Invariant mass distributions for  $Z \rightarrow \mu\mu$  and  $Z \rightarrow ee$  events from data, demonstrating incomplete bremsstrahlung recovery.

The associated PRS, ECAL, and HCAL energies of tracks are used to identify high  $p_T$  electrons and charged hadrons in Chap. 5. However, the LHCb calorimeter systems were designed for lower  $p_T$   $B$ -hadron decay products, and the individual ECAL cells saturate at transverse energies,  $E_T$ , greater than 10 GeV. Consequently, many of the energies from the ECAL cells associated with an electron track are fully saturated, and so the ECAL  $E_T$  for an electron is degraded. In Fig. 4.14(a) the distribution for the  $E_T$  of electrons produced from  $Z \rightarrow ee$  events in data is plotted, where clear peaks can be seen at multiples of 10 GeV, the ECAL saturation  $E_T$ . Additionally, the energies for recovered bremsstrahlung photons are also degraded, and so the bremsstrahlung correction of the momentum for electron tracks is incomplete, resulting in a reduced momentum resolution. This can be seen in the broadened and shifted  $Z \rightarrow ee$  invariant mass distribution taken from data with respect to the  $Z \rightarrow \mu\mu$  distribution plotted in



Fig. 4.14(b).

### 4.3.3. Triggers

The rate of detectable collisions produced within the LHCb detector is approximately 10 MHz and must be reduced to a rate of 2 kHz for storage. Most of the events produced within the detector are not of interest for LHCb physics analyses, and consequently can be discarded. The LHCb trigger system provides a fast decision on whether an event should be kept or discarded and is used to reduce the rate of events from the detector to a rate that can be written to disk. The LHCb trigger system consists of both hardware and software components and is divided into a level 0 trigger (L0) and a high level trigger (HLT). A full description of the LHCb trigger system can be found in Ref. [124] and the technical design report of Ref. [167].

#### Level 0 Trigger

The level 0 trigger is a hardware trigger which must process each event within 2  $\mu$ s and reduce the event rate from 10 MHz to 1 MHz using partial detector information. At this lower event rate the entire detector can be read out for each event and passed on to the HLT for further refinement. The L0 is divided into a calorimeter trigger and a muon trigger. With these two components, the L0 attempts to reconstruct the highest  $E_T$  photon, electron, neutral pion, hadron, and the two highest  $p_T$  muons in the event. The information from each component is passed to a decision unit which then produces a combined decision on whether the event should be passed to the HLT.

The calorimeter trigger attempts to reconstruct the highest transverse energy photon, electron, and hadron in the event using 19420 read out channels from the SPD, PRS, ECAL, and HCAL. Portions of the ECAL and HCAL are read out, and the sum of the transverse energy for every two-by-two group of cells is calculated. The group of cells with the highest  $E_T$  in the HCAL is passed on as a hadron candidate. The two-by-two groups of ECAL cells are merged with the SPD and PRS cells to produce photon, electron, and neutral pion candidates. The candidate with the largest  $E_T$  of each type is passed on to the decision unit along with the total HCAL  $E_T$  and SPD multiplicity.

The muon trigger uses 25920 read out channels and searches for muon tracks in the event. The tracks are seeded from hits in the third muon station, M3, which are linearly extrapolated to the interaction point. A search for hits in a field of interest along the  $x$ -axis is made in M2 and along both the  $x$  and  $y$ -axis in M4 and M5. If hits are found in all three of these stations the line from the M3 hit to the M2 hit is extrapolated to M1 and the closest hit within a field of interest is added to the track. The momentum of the track is estimated and the two highest  $p_T$  tracks are passed on to the decision unit.

The decision unit combines the information from the two L0 triggers, and either accepts the event and passes on the information to the HLT, or discards the event. The L0 will accept an event if a hadron candidate with  $E_T > 5$  GeV is found. The L0 will also accept an event if an electron, photon, or neutral pion candidate with  $E_T > 2.5$  GeV is found or if  $p_T > 1.2$  GeV for

any muon track. Additionally, an event will be accepted if  $p_{T1} + p_{T2} > 1$  GeV for the two muon tracks. All calorimeter candidates and tracks that pass the requirements above are sent to the HLT trigger as L0 objects.

### High Level Trigger

The high level trigger is a software trigger which runs on an event filter farm consisting of 2000 computing nodes and is divided into an HLT1 and HLT2 level. The HLT1 must reduce the 1 MHz event rate from the L0 to the 30 kHz event rate required by HLT2, and begins by confirming the L0 objects. L0 calorimeter objects are confirmed by accessing tracking system information and attempting to reconstruct a track associated with the object; the L0 decision is confirmed if no track is found for neutral objects and if a track is found for charged objects.

The HLT2 takes the 30 kHz event rate from HLT1, and reduces this to a rate of 2 kHz where the raw data from the event can be written to disk for later full reconstruction and analysis. The HLT2 performs full track fitting. Because the HLT1 and HLT2 are both software based triggers, the algorithms and selections applied can be modified to accommodate improved techniques or changing physics interests. To ensure consistency between the algorithms and requirements used between data taking periods, a trigger configuration key (TCK) is assigned to each unique trigger setup which can be later accessed during analysis.

#### 4.3.4. Luminosity Determination

Many of the physics analyses performed using LHCb data require a precise measurement of the integrated beam luminosity for the dataset being analysed. The luminosity can be determined with,

$$\frac{d\mathcal{L}}{dt} = \frac{\mu N_b f}{\sigma_{\text{inelastic}}} \quad (4.5)$$

where  $\mu$  is the average number of visible proton-proton interactions per bunch crossing,  $\sigma_{\text{inelastic}}$  is the proton-proton inelastic cross-section,  $N_b$  is the number of proton bunches which is well known, and  $f$  is the revolution frequency which is also well known. Only the values of  $\mu$  and  $\sigma_{\text{inelastic}}$  are unknown;  $\mu$  must be measured per bunch crossing while  $\sigma_{\text{inelastic}}$  remains constant and need only be measured once.

The value of  $\mu$  can be measured per bunch crossing by recording observables, or luminosity counters, that are proportional to  $\mu$ . For LHCb luminosity determination, five luminosity counters are recorded: the number of VELO vertices, the number of VELO  $rz$ -tracks, the number of hits in the VELO pile-up sensors, the number of SPD hits, and the  $E_T$  deposition within the calorimeters. Of these counters, the number of VELO  $rz$ -tracks is found to be the most reliable measure of  $\mu$ . The inelastic cross-section is measured using two different methods, a Van de Meer scan and a beam-gas imaging technique. Both are described in the remainder of this section. The combination of the uncertainties from the measurements on  $\mu$  and  $\sigma_{\text{inelastic}}$  result in a 3.5% uncertainty on the integrated luminosity measurement used for any LHCb analysis

with 2011 data. Full details on the LHCb luminosity determination can be found in Ref. [168].

### Van de Meer Scan

The Van de Meer scan was first proposed by Van de Meer in Ref. [169], and is performed by scanning the two colliding beams across each other in the transverse plane. The visible inelastic cross-section is given by,

$$\sigma_{\text{inelastic}} = \frac{\int \mu(\Delta_x, \Delta_{y0}) d\Delta_x \int \mu(\Delta_{x0}, \Delta_y) d\Delta_y}{N_{p1} N_{p2} \mu(\Delta_{x0}, \Delta_{y0}) \cos \alpha_1} \quad (4.6)$$

where  $N_{p1}$  is the number of protons per bunch in the first beam,  $N_{p2}$  is the number of protons per bunch in the second beam, and  $\alpha_1$  is the polar angle of the first beam velocity with respect to the  $z$ -axis [170]. Here  $\Delta_x$  is the  $x$ -coordinate offset between the two beams with a nominal offset of  $\Delta_{x0}$ , and  $\Delta_y$  is the  $y$ -coordinate offset with a nominal value of  $\Delta_{y0}$ .

The beams are scanned over a series of approximately 15 to 30  $x$ -offset steps with a constant  $y$ -offset of  $\Delta_{y0}$ , and the average  $\mu$  per step is measured. These measurements are used to calculate the first integral of Eq. 4.6. The same process is repeated, but now with  $y$ -offsets and a constant  $x$ -offset of  $\Delta_{x0}$ . These measurements of  $\mu$  are then used to calculate the second integral. The systematic uncertainty on  $\sigma_{\text{inelastic}}$  is determined from the uncertainty from the  $\mu$  measurements of the scans, the offsets of the scans, and the uncertainty on the number of protons per bunch for both beams. The primary source of uncertainty is from the number of protons per bunch, and is on the order of 2.7%.

### Beam-Gas Imaging

The beam-gas imaging method, first proposed in Ref. [171], uses the vertices reconstructed within the VELO from the interactions of the beams with residual gas in the beam pipes to measure the profile of the beams and determine  $\sigma_{\text{inelastic}}$ . The distribution of vertices provide a transverse image of the beams from which their angles, profiles, and positions can be extracted. While the rate of interactions is much smaller than for a Van de Meer scan, the beams do not need to be moved, and so many uncertainties of the Van de Meer scan method are mitigated. However, the beam-gas imaging method requires a vertex resolution smaller than the transverse beam width and a well understood uncertainty, as this contributes to the overall systematic uncertainty.

Beam-gas interaction measurements are made both when the bunches collide and do not collide. Only the measurements from colliding bunches can be used to make luminosity measurements, but the measurements from non-colliding bunches can be used to further understand the beams and perform cross-checks with the measurements from the colliding bunches. The transverse beams widths are determined with beam-gas interactions from colliding bunches, but must be measured away from the interaction point so beam-gas interactions can be separated from proton-proton interactions. The same beam width measurement can be made from non-colliding bunches, but the measurement can also be made at the interaction point. These two

widths from non-colliding bunches are compared to ensure the offset width does not differ within uncertainty from the interaction point width. The beam crossing angles are also measured using beam-gas interactions from non-colliding beams.

The systematic uncertainty on the luminosity determination using the beam-gas imaging method depends upon the vertex resolution, time stability, beam sizes and offsets, gas pressure gradient, and crossing-angle effects as well as the number of protons per bunch. The luminosity measurements made with the beam-gas imaging method for 2011 data are consistent with the Van de Meer measurements, and also have a systematic uncertainty dominated by the number of protons per bunch.

## 5. Z Boson Cross-Section

Within this chapter, a measurement of the cross-section for  $Z$  bosons decaying into a  $\tau$  lepton pair using data from LHCb with  $\sqrt{s} = 7$  TeV is presented. The analysis is described in Sect. 5.1, while the cross-section measurement is performed in Sect. 5.2 and the results are presented in Sect. 5.3. In this introduction, the  $pp \rightarrow Z \rightarrow \tau\tau$  cross-section measurement is motivated by describing how it can be used to test lepton universality, search for new physics, and further constrain the proton PDF.

In the standard model of particle physics (SM), the  $Z$  boson couples to fermions with a vertex given by Fig. 2.4(b) which is a factor of  $\frac{-ig_w}{2\cos\theta_w}\gamma^\mu(v_f - a_f\gamma^5)$  where the vector and axial couplings,  $v_f$  and  $a_f$ , are for neutral leptons, charged leptons,  $u$ -type quarks, or  $d$ -type quarks, and are given in Table 2.2. The charged leptons,  $e$ ,  $\mu$ , and  $\tau$ , all have the same factors, and so the  $Z$  boson couples with an identical strength to each charged lepton. This property of the SM, lepton universality, can be experimentally tested by comparing the ratios of  $Z \rightarrow ee$ ,  $Z \rightarrow \mu\mu$ , and  $Z \rightarrow \tau\tau$  production. Previous measurements by LEP [120] have been made,

$$\frac{\sigma_{ee \rightarrow Z \rightarrow \mu\mu}}{\sigma_{ee \rightarrow Z \rightarrow ee}} = 1.0009 \pm 0.0028, \quad \frac{\sigma_{ee \rightarrow Z \rightarrow \tau\tau}}{\sigma_{ee \rightarrow Z \rightarrow ee}} = 1.0019 \pm 0.0032 \quad (5.1)$$

which verify lepton universality in  $Z$  boson decays to a precision of better than 1%. The measurement of  $\sigma_{pp \rightarrow Z \rightarrow \tau\tau}$  within this chapter, when compared to the LHCb measurements of  $\sigma_{pp \rightarrow Z \rightarrow ee}$  [172] and  $\sigma_{pp \rightarrow Z \rightarrow \mu\mu}$  [173], can test lepton universality to the level of 4% at best, assuming the precision of  $\sigma_{pp \rightarrow Z \rightarrow \tau\tau}$  is similar to the precisions of the  $\sigma_{pp \rightarrow Z \rightarrow ee}$  and  $\sigma_{pp \rightarrow Z \rightarrow \mu\mu}$  measurements. However, the LHCb tests of lepton universality are unique; the  $Z$  bosons are produced from proton-proton collisions, unlike the electron-positron collisions at LEP, and the leptons produced from the  $Z$  bosons are observed in the forward pseudo-rapidity range of  $2.0 \leq \eta \leq 4.5$ .

Measuring a ratio different from unity might be indicative of new physics, rather than a failure of lepton universality. In most models with Higgs bosons, described in Sect. 2.1.2 for the SM and Sect. 2.1.4 for the minimal supersymmetric model (MSSM), the Higgs bosons are expected to couple to fermions with a strength proportional to the mass of the fermion. This can be seen by the factor of the fermion mass,  $m_f$ , in the vertices of Fig. 2.6(g) for the SM and Figs. 2.10(a) through 2.10(f) for the MSSM. The Higgs bosons can also couple to the electroweak vector bosons with strengths proportional to the mass of the electroweak bosons. The relevant vertices are given in Figs. 2.6(b) and 2.6(c) for the SM and Figs. 2.10(i) through 2.10(l) for the MSSM.

Consequently, for a neutral Higgs boson with a mass less than  $2m_W$ , the dominant decays of the Higgs boson at leading order are into  $\tau$  lepton and  $b$ -quark pairs. For the case of neutral

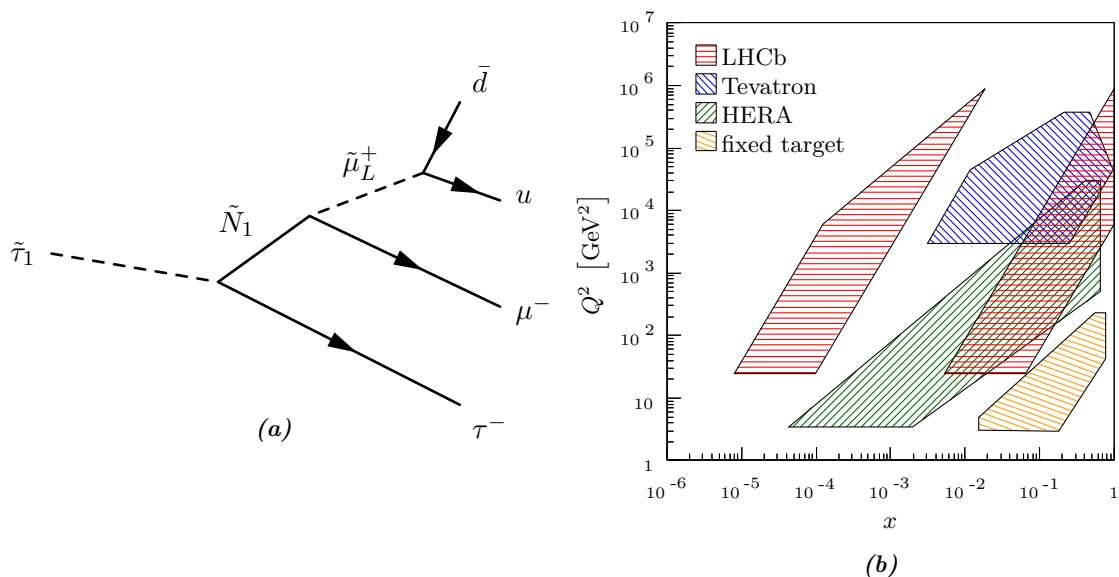


**Figure 5.1.:** (a) An example SUSY decay chain from a stau LSP, producing a  $\tau$  lepton in the final state. Dashed lines indicate bosons and solid line fermions. (b) Rough outline in momentum fraction and momentum transfer space of the measurements currently used to constrain the proton PDF. The  $x$  and  $Q^2$  limits on the data available from Tevatron (blue), HERA (green), and fixed target experiment (yellow) are taken from Ref. [174].

Higgs bosons decaying into  $\tau$  lepton pairs, this process will be similar to the  $Z \rightarrow \tau\tau$  signal, except for the invariant mass and spin correlations of the  $\tau$  lepton pair, and will provide an unaccounted background to the  $Z \rightarrow \tau\tau$  signal, resulting in an excess of observed events. Using the measured  $pp \rightarrow Z \rightarrow \tau\tau$  cross-section, Higgs boson searches are performed in Chap. 6 by looking for an unexpected excess of events.

In addition to excesses from Higgs boson decays, many SUSY models, described in Sect. 2.1.4, predict a lightest supersymmetric partner (LSP) such as the stau. The decay of the stau depends upon the SUSY parameter space, but oftentimes the stau will decay via chains containing  $\tau$  leptons, such as the decay of Fig. 5.1(a) [175]. Here, the stau decays into a virtual lightest neutralino,  $\tilde{N}_1$ , and a  $\tau$  lepton. The neutralino then decays into a muon and left-handed smuon,  $\tilde{\mu}_L$ , which further decays into a  $u$ -quark and  $d$ -quark pair. The dashed lines in this diagram indicate bosons, while the solid lines indicate fermions and the arrows indicate the flow of electromagnetic charge. These types of events can also produce unaccounted backgrounds to the  $Z \rightarrow \tau\tau$  signal, resulting in an excess in the ratio of the measured  $\sigma_{pp \rightarrow Z \rightarrow \tau\tau}$  to  $\sigma_{pp \rightarrow Z \rightarrow \mu\mu}$  and  $\sigma_{pp \rightarrow Z \rightarrow ee}$ .

Unlike at LEP,  $Z$  bosons at LHCb are produced from composite particles; typically a valence quark and sea anti-quark from two protons annihilate, producing a  $Z$  boson. Consequently, the measurement of the  $Z$  cross-section at LHC can be used to refine the structure of the proton PDF, described in Sect. 2.1.3. The proton PDF is constrained by previous results from Tevatron, HERA, and fixed target experiments at values of the parton momentum fraction,  $x$ , and momentum transfer,  $Q^2$ , in the regions of parameters space shown in Fig. 5.1(b). The 7 TeV centre-of-mass energy of the LHC combined with the forward coverage of LHCb provides

$Z$  boson data, which can be used to further constrain the proton PDF. The region in which LHCb data can be used is also shown in Fig. 5.1(b). This estimated coverage for LHCb  $Z$  boson data is bounded by,

$$Q^2(x) = \begin{cases} xs & \text{upper bound} \\ e^{\pm 2|\eta|} x^2 \sqrt{s} & \text{left-right bounds} \\ m_{\min}^2 & \text{lower bound} \end{cases} \quad (5.2)$$

where  $\sqrt{s}$  is the centre-of-mass energy of the two colliding beams,  $\eta$  is defined in Eq. 4.1 and is the minimum or maximum pseudo-rapidity of the detector, and  $m_{\min}$  is the minimum measured invariant mass of the two leptons produced from the  $Z$  boson. The relations of the upper and left-right bounds from Eq. 5.2 are determined by setting the momentum of one colliding parton as  $x\sqrt{s}/2$ , the momentum of the other parton as  $Q^2/(2x/\sqrt{s})$ , and assuming both partons have only longitudinal momentum.

## 5.1. Analysis

Within this section the methods used for selecting the  $Z \rightarrow \tau\tau$  events used in the cross-section calculation of Sect. 5.2 are described. First the final states of the  $Z \rightarrow \tau\tau$  signal events and possible backgrounds are outlined. In Sect. 5.1.1 the details of the particle identification criteria used to obtain  $\tau$  lepton decay product candidates are given. The event selection which uses these candidates is then described in Sect. 5.1.2. Finally, in Sect. 5.1.3 the methods used to estimate the backgrounds to the  $Z \rightarrow \tau\tau$  signal are introduced.

The cross-section for producing a  $\tau$  lepton pair from the partons of two protons can be perturbatively expanded into terms represented by diagrams mediated by an excited photon or  $Z$  boson with their leading order matrix elements given by Eqs. 3.1 and 3.2 respectively. Experimentally, these terms and their interference, given by Eq. 3.3, cannot be separated. Consequently, for the remainder of this chapter, the symbol  $Z$  is used to indicate contributions from an excited photon or  $Z$  boson with an invariant mass about the on-shell mass of the  $Z$  boson. Additionally, the symbol  $\ell$  for a charged lepton is used to indicate only an electron or muon, and not a  $\tau$  lepton.

Most  $\tau$  leptons produced within LHCb decay before reaching the VELO which is described in Sect. 4.2.1, and so the experimental selection of  $Z \rightarrow \tau\tau$  events must use  $\tau$  lepton decay products rather than the  $\tau$  leptons themselves, contrary to  $Z \rightarrow \mu\mu$  and  $Z \rightarrow ee$  analyses where lepton pairs can be directly selected. Because the  $\tau$  lepton is heavier than the lightest mesons and all other leptons, it can decay into a variety of final states with multiplicities of up to seven particles, as detailed in Sect. 3.2 and summarised in Table 3.27. However, the experimental reconstruction of high multiplicity  $\tau$  lepton final states can have large backgrounds from QCD induced processes at hadron colliders which introduce undesirable systematic uncertainties. Consequently, this analysis only utilises leptonic  $\tau$  lepton decays into a  $\tau$  lepton neutrino with a lepton and lepton neutrino, or semi-leptonic  $\tau$  lepton decays into a  $\tau$  lepton neutrino and single charged hadron; only a single muon, electron, or charged hadron is selected as a  $\tau$  lepton decay product, as

neutrinos are not reconstructed. The matrix elements for these decays are given by Eqs. 3.20 and 3.22 of Sect. 3.2.

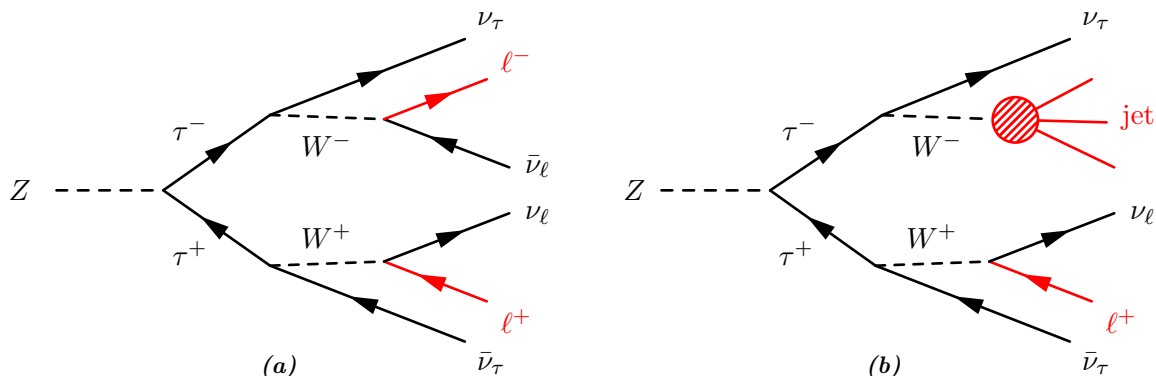


**Figure 5.2.:** The signal  $Z \rightarrow \tau\tau$  final states considered with (a) two leptonic  $\tau$  lepton decays and (b) one leptonic decay and one semi-leptonic decay. The experimentally selected final state is highlighted in red.

A lepton is required to experimentally trigger  $Z \rightarrow \tau\tau$  events, and so only final states where both  $\tau$  lepton decays are leptonic, or where one  $\tau$  lepton decay is leptonic and one  $\tau$  lepton decay is semi-leptonic, are selected. Feynman diagrams for these two final states are given in Fig. 5.2. A variety of processes, with examples diagrammed in Fig. 5.3, contribute experimental backgrounds to the  $Z \rightarrow \tau\tau$  final states of Fig. 5.2. For this analysis the SM Higgs boson provides a negligible contribution, as demonstrated in Chap. 6, and consequently is not considered as a background. In both Fig. 5.2 and Fig. 5.3 the possibly selected  $\tau$  lepton decay product candidates are highlighted in red.

A  $Z \rightarrow \ell\ell$  background is shown in Fig. 5.3(a) where an electron or muon pair is produced from a  $Z$  boson. This acts as a background to  $Z \rightarrow \tau\tau$  signal events consisting of an electron or muon pair where both  $\tau$  leptons decay leptonically. If one of the leptons from the event type of Fig. 5.3(a) is mis-identified as a hadron, then these events can also act as a background to the  $Z \rightarrow \tau\tau$  signal events of Fig. 5.2(b) where only one of the  $\tau$  leptons decays leptonically and the other decays semi-leptonically. For signal events where one  $\tau$  lepton decays leptonically into an electron and the other into a muon, the  $Z \rightarrow \ell\ell$  background is not considered, as the probability of mis-identifying a muon as an electron, or conversely an electron as a muon, is negligible.

In Figs. 5.3(c) and 5.3(b) a single charged lepton from a  $Z$  or  $W$  boson decay falls within LHCb acceptance and an associated jet provides either an additional charged lepton or hadron. Alternatively, this jet could be produced from jet activity not associated with the vector boson. These two backgrounds are grouped together as an electroweak background, EWK, and are considered for both  $Z \rightarrow \tau\tau$  signal event types. Backgrounds consisting of particles produced from jet activity, Fig. 5.3(d), are grouped into a general QCD background where a hard lepton is typically produced from the decay of a heavy flavour meson and either an additional lepton or a charged hadron is produced within the event. This background, like the EWK background, is considered for both  $Z \rightarrow \tau\tau$  signal event types.

Pairs of  $W$  bosons can be produced within LHCb, resulting in the background shown in



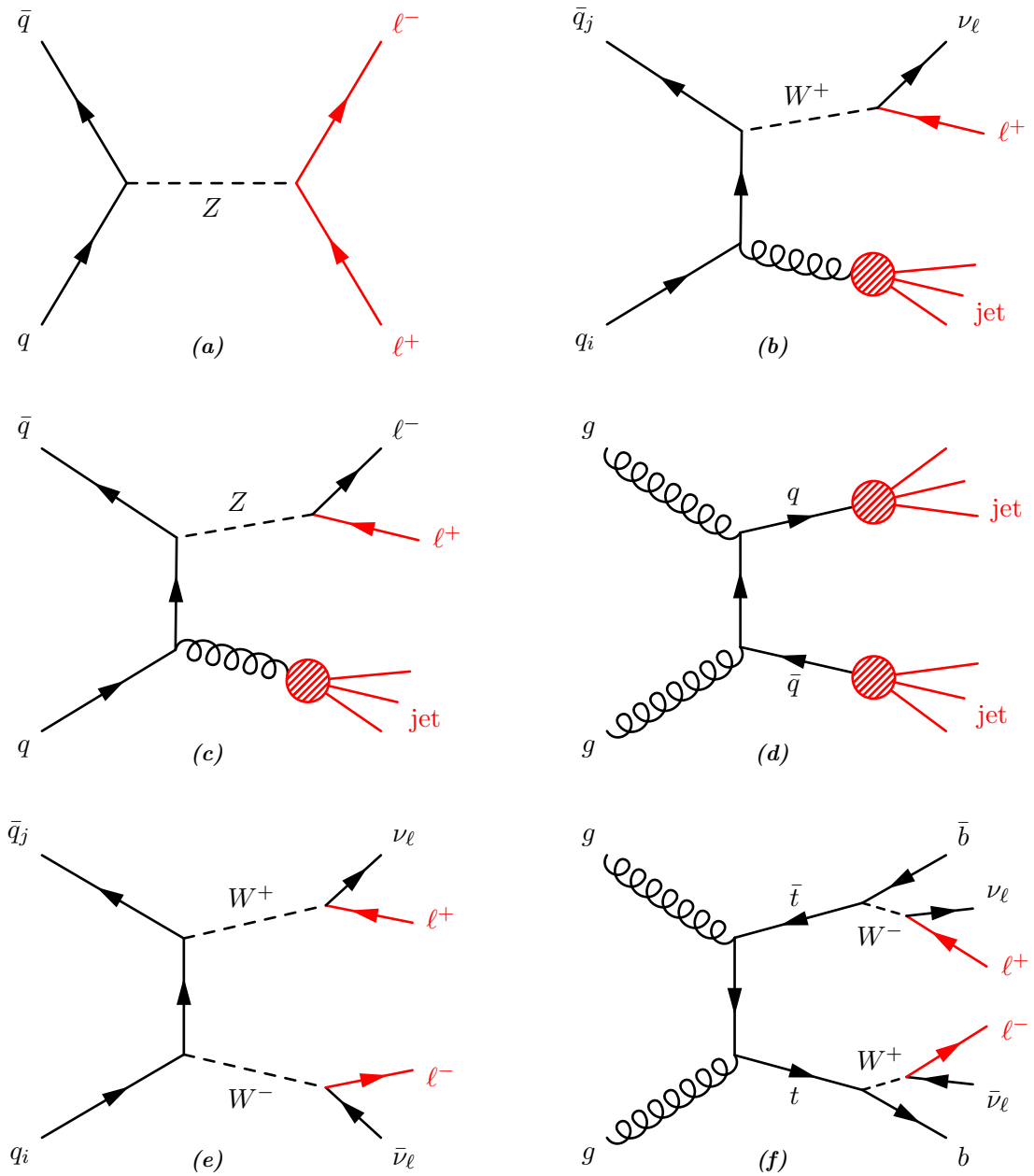


**Figure 5.3.:** Examples of the (a)  $Z \rightarrow \ell\ell$ , (b)–(c) EWK, (d) QCD, (e)  $WW$ , and (f)  $t\bar{t}$  backgrounds are given, with the experimentally selected final state highlighted in red.

Fig. 5.3(e). Here, both the  $W$  bosons decay leptonically, providing a background to signal events where both  $\tau$  leptons decay leptonically. One of the  $W$  bosons can also decay into quarks, providing a background to signal events with a leptonic and semi-leptonic  $\tau$  lepton decay. In Fig. 5.3(f) a background to signal events where both  $\tau$  leptons decay leptonically is produced from a pair of  $t$ -quarks decaying leptonically. One of the  $t$ -quarks can also decay hadronically, producing a background to signal events with a leptonic and semi-leptonic  $\tau$  lepton decay.

### 5.1.1. Particle Identification

In order to select  $Z \rightarrow \tau\tau$  signal events, the muons, electrons, and charged hadrons within an event must first be reconstructed and identified. All reconstructed particles considered as  $\tau$  lepton decay product candidates are long tracks, described in Sect. 4.3.1, which are required to have a  $\chi^2$  probability greater than 0.1% and a pseudo-rapidity within the range  $2.0 \leq \eta \leq 4.5$ . Hits associated with the long tracks from the muon system are used to identify muons, while associated calorimeter energy, described in Sect. 4.3.2, from the PRS, ECAL, and HCAL is used to differentiate between electrons and charged hadrons. Additionally, the momenta for electron candidates is corrected for bremsstrahlung radiation losses using the method of Sect. 4.3.2.

Four variables associated with long tracks are used for particle identification: the number of muon stations with hits, the PRS energy, the ECAL energy over the momentum of the track, and the HCAL energy over the momentum of the track. Distributions of these variables, normalised to an integral of one, for muons, electrons, and hadrons are shown in Fig. 5.4. The muon distributions are taken from data events consistent with a  $Z \rightarrow \mu\mu$  signal, which are selected by requiring an isolated muon and an isolated opposite-sign track. Both the muon and track must have  $p_T > 20$  GeV, a combined invariant mass within the range  $60 \leq m \leq 120$  GeV, and an azimuthal angle separation of greater than 2.7 radians. The distributions are then produced from the variables of the isolated track. The same method is used to obtain the electron distributions, but a  $Z \rightarrow ee$  signal is selected by requiring isolated electrons rather than muons. The charged hadron distributions are obtained from long tracks in minimum bias data with  $p_T > 5$  GeV.

The distributions of Fig. 5.4 are intended to illustrate the particle identification requirements and will be similar to, but not the same, as the muon, electron, and charged hadron distributions from  $Z \rightarrow \tau\tau$  signal events which are unavailable directly from data. Primarily, the  $p_T$  spectrum of the electrons and muons used to produce these distributions will be harder than the spectrum for electrons and muons from  $Z \rightarrow \tau\tau$  events. The vertical black lines of Fig. 5.4 indicate the particle identification requirements used for selecting  $\tau$  lepton decay product candidates and are summarised in Table 5.1. A more detailed motivation of the selection criteria for each particle type is given in the remainder of this section.

#### Muon Identification

Muons are reconstructed as described in Sect. 4.3.1, where tracks are extrapolated to the four muon stations downstream of the calorimeters and matched to compatible hits. Muon candidates must have an associated hit in each of the four muon stations, requiring the candidate to

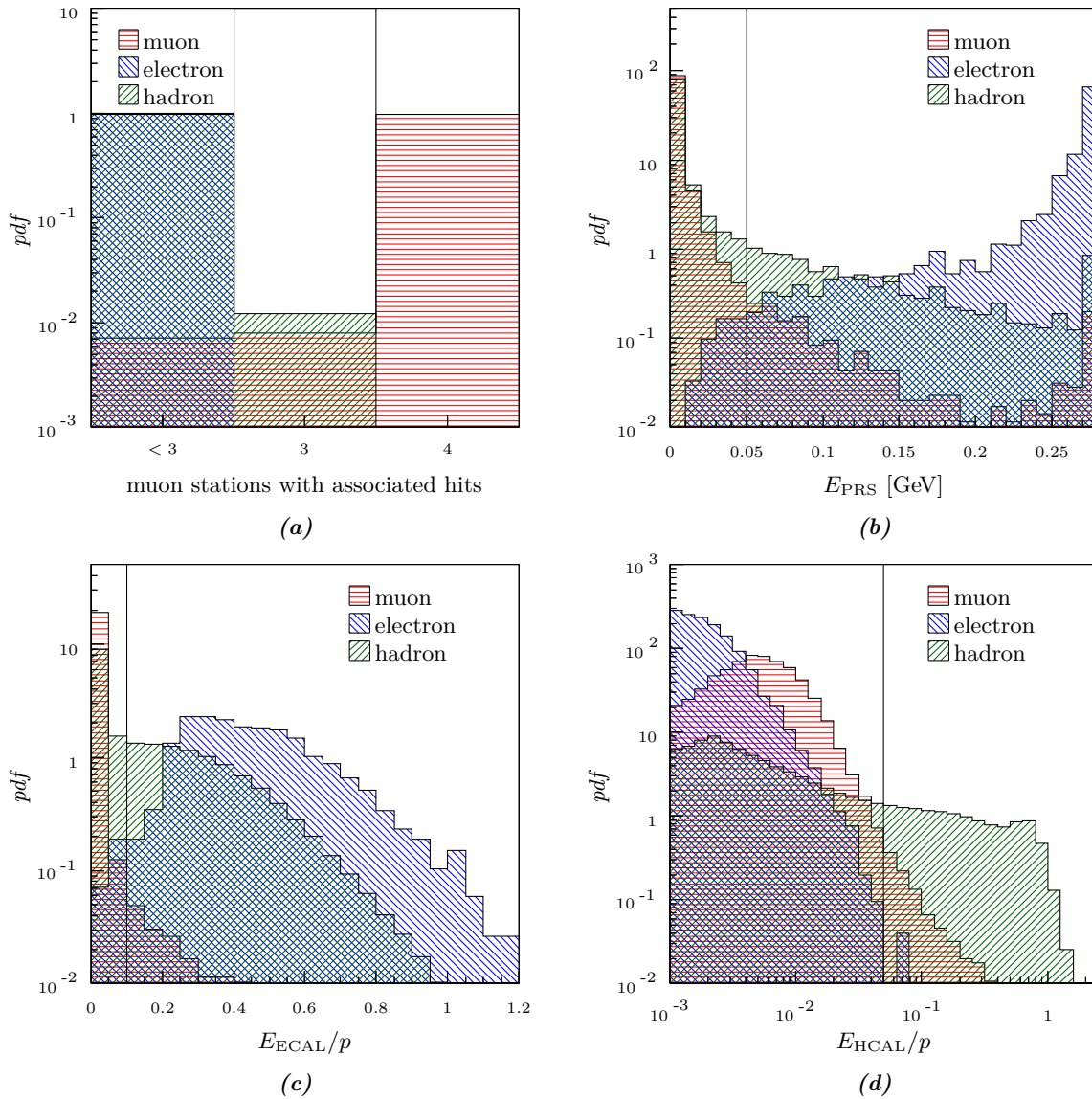


**Figure 5.4.:** The (a) number of muon stations with associated hits, (b) PRS energy, (c) fractional ECAL energy over track momentum, and (d) fractional HCAL energy over track momentum distributions for muons (red), electrons (blue), and pions (green) from data. The particle identification requirements, as described in the text, are indicated by the black lines.

traverse approximately twenty hadronic interaction lengths of material. The high efficiency of this requirement can be seen in the distribution of muon stations with associated hits for muons in Fig. 5.4(a), where nearly all muons have associated hits in all four muon stations. Charged hadrons and electrons typically have less than three stations with associated hits. Because the muons from  $\tau$  lepton decays have a lower  $p_T$  spectrum than the muons from the  $Z \rightarrow \mu\mu$  events of Fig. 5.4(a), the muon identification efficiency for  $Z \rightarrow \tau\tau$  events is slightly reduced.

**Table 5.1.:** A summary of the particle identification requirements for muons, electrons, and charged hadrons.

|                        | muons                    | electrons                | hadrons                    |
|------------------------|--------------------------|--------------------------|----------------------------|
| track $P(\chi^2)$ [%]  | $> 0.01$                 | $> 0.01$                 | $> 0.01$                   |
| track $\eta$           | $2.0 \leq \eta \leq 4.5$ | $2.0 \leq \eta \leq 4.5$ | $2.25 \leq \eta \leq 3.75$ |
| muon stations          | 4                        | $< 3$                    | $< 3$                      |
| $E_{\text{PRS}}$ [GeV] | –                        | $> 0.05$                 | –                          |
| $E_{\text{ECAL}}/p$    | –                        | $> 0.1$                  | –                          |
| $E_{\text{HCAL}}/p$    | –                        | $< 0.05$                 | $> 0.05$                   |

### Electron Identification

Electrons are reconstructed by extrapolating tracks into the ECAL, matching ECAL clusters with the track, and then performing bremsstrahlung recovery, as described in Sect. 4.3.2. The ECAL cells saturate at transverse energies above 10 GeV, also described in Sect. 4.3.2, and so bremsstrahlung recovery for high  $p_T$  electrons from  $Z$  bosons is incomplete. The standard LHCb electron identification requirements were designed for low  $p_T$  electrons from  $B$ -hadron decays, relying upon RICH information, and so different requirements suited for high momentum electrons are used instead.

High momentum electrons begin showering within the PRS, but deposit most of their energy within the ECAL. Conversely, most hadrons do not shower until the HCAL, and muons typically do not shower. The  $E_{\text{PRS}}$  distributions for muons and electrons with  $p_T > 20$  GeV and charged hadrons with  $p_T > 5$  GeV are shown in Fig. 5.4(b). An associated PRS energy,  $E_{\text{PRS}}$ , greater than 0.05 GeV is required for electron identification, as most electrons from  $Z$  boson decays will have energies well above this requirement.

The ECAL and HCAL energies are dependent upon the energy and momentum of the electron and so the fractional ECAL and HCAL energy with respect to the electron momentum are used as electron identification variables. The ECAL energy over momentum distribution is shown in Fig. 5.4(c) and the HCAL energy over momentum distribution is shown in Fig. 5.4(d) for muons, electrons, and pions. Electrons are expected to deposit a large fraction of their momentum within the ECAL, as can be seen in Fig. 5.4(c), and so electron candidates must satisfy  $E_{\text{ECAL}}/p > 0.1$ . Conversely, electrons are not expected to reach the HCAL and are required to have  $E_{\text{HCAL}}/p < 0.05$ , as shown in Fig. 5.4(d). By requiring less than three muon stations with associated hits, electron candidates by definition are mutually exclusive to muon candidates.

### Charged Hadron Identification

Charged hadrons are identified using a mutually exclusive selection to both muons and electrons. They are expected to shower within the HCAL, as described in Sect. 4.2.2, and so all charged hadron candidates must satisfy  $E_{\text{HCAL}}/p > 0.05$ , in addition to the requirement of less than three muon stations with associated hits. To ensure coverage of the HCAL, charged hadron

candidates must also fall within the reduced pseudo-rapidity range of  $2.25 \leq \eta \leq 3.75$ .

### 5.1.2. Event Selection

Once reconstructed particles are identified using the criteria of Sect. 5.1.1,  $Z \rightarrow \tau\tau$  events from data can be selected. The data used have been collected via a single muon trigger requiring  $p_T > 10$  GeV and a single electron trigger requiring  $p_T > 15$  GeV. Further details on the trigger can be found in Sect. 4.3.3. The selection of  $Z \rightarrow \tau\tau$  events is divided into five mutually exclusive categories:  $\tau_\mu\tau_\mu$ ,  $\tau_\mu\tau_e$ ,  $\tau_e\tau_\mu$ ,  $\tau_\mu\tau_h$ ,  $\tau_e\tau_h$ . The first  $\tau$  lepton decay product candidate is labelled by the first  $\tau$  lepton subscript, while the second candidate is labelled by the second subscript; here  $\mu$ ,  $e$ , and  $h$  indicate muons, electrons, and charged hadrons respectively. The first three categories select signal events where both  $\tau$  leptons decay leptonically, while the last two categories select signal events where the first  $\tau$  lepton decays leptonically and the second  $\tau$  lepton decays semi-leptonically into a  $\tau$  lepton neutrino and single charged hadron. No di-electron category is considered due to the ECAL saturation described in Sect. 4.3 which results in poor separation of this signal from large backgrounds.

To eliminate large QCD backgrounds with soft  $p_T$  spectra, the first  $\tau$  lepton decay product candidate is required to have  $p_T > 20$  GeV while the second candidate must have  $p_T > 5$  GeV. The following additional trigger and particle identification requirements are applied for each category.

$\tau_\mu\tau_\mu$ : Requires two oppositely-charged muons, where the muon with the larger  $p_T$  is considered the first  $\tau$  lepton decay product candidate. Either or both muons can trigger the event.

$\tau_\mu\tau_e$ : Requires a muon and an oppositely-charged electron. Only the muon can trigger the event.

$\tau_e\tau_\mu$ : Requires an electron and an oppositely-charged muon with  $p_T < 20$  GeV. Either or both the electron and muon can trigger the event.

$\tau_\mu\tau_h$ : Requires a muon and an oppositely-charged hadron. Only the muon can trigger the event.

$\tau_e\tau_h$ : Requires an electron and an oppositely-charged hadron. Only the electron can trigger the event.

Additional selection requirements, dependent upon the category, are also applied to further separate the  $Z \rightarrow \tau\tau$  signal from its backgrounds. These variables, as well as the requirements placed on them, are described in the remainder of this section. The selection requirements are not optimised using multivariate techniques, but are manually selected to adequately separate signal and background without severely limiting signal statistics. For each variable, its distributions for  $Z \rightarrow \mu\mu$  events from simulation and data are compared to validate simulation. The  $Z \rightarrow \mu\mu$  data events are selected by requiring two opposite-sign muons with  $p_T > 20$  GeV and a combined

invariant mass within the range  $80 \leq m \leq 100$  GeV. If the simulation does not match well with data, it is corrected to data and the distribution for this calibrated simulation is also provided.

Distributions for the  $Z \rightarrow \tau\tau$  signal and its backgrounds, described in the introduction of Sect. 5.1, are also given for each variable. The  $Z \rightarrow \tau\tau$ , EWK,  $WW$ , and  $t\bar{t}$  distributions are taken from calibrated simulation, while the QCD and  $Z \rightarrow \ell\ell$  background distributions are estimated from data using the methods described in Sect. 5.1.3. All distributions are normalised to an integral of one for comparison purposes and are provided for only the  $\tau_\mu\tau_\mu$  event category.

### Invariant Mass

The invariant mass of the two  $\tau$  lepton decay product candidates is defined as,

$$m \equiv \sqrt{(E_1 + E_2)^2 - (\vec{p}_1 + \vec{p}_2)^2} \quad (5.3)$$

where  $E_1$  and  $E_2$  are the energies of the two  $\tau$  lepton decay product candidates and  $\vec{p}_1$  and  $\vec{p}_2$  are their three-momenta. The momentum resolution observed in data is underestimated in simulation, resulting in narrower mass distributions from simulation. This effect can be seen by comparing the invariant mass distribution from  $Z \rightarrow \mu\mu$  data to the distribution from simulation, as shown in Fig. 5.5(a). The momentum components,  $p_i$ , for a reconstructed particle in simulation are calibrated using,

$$p_i = f_{\text{shift}} \left( p_{i\text{gen}} + f_{\text{width}}(p_{i\text{rec}} - p_{i\text{gen}}) \right) \quad (5.4)$$

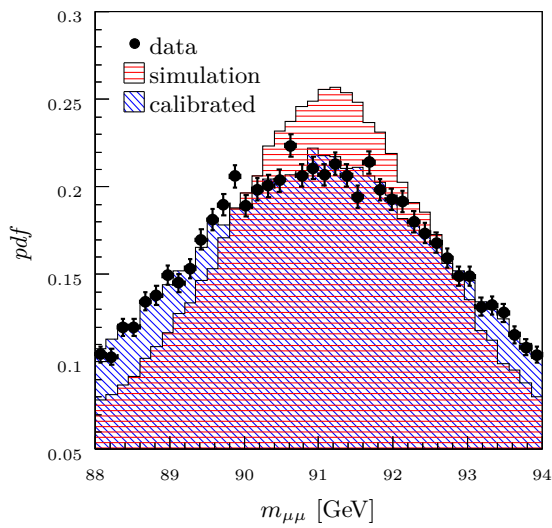
where  $p_{\text{gen}}$  is the generated momentum of the particle and  $p_{\text{rec}}$  is the reconstructed momentum of the particle. The parameter  $f_{\text{shift}}$  shifts the distribution, while  $f_{\text{width}}$  adjusts the width of the distribution. Values of  $f_{\text{shift}} = 0.998 \pm 0.001$  and  $f_{\text{width}} = 2.0 \pm 0.1$  were obtained by fitting the simulated invariant mass distribution to the data distribution, resulting in the calibrated distribution of Fig. 5.5(a). This calibration is used for all mass distributions taken from simulation and is assumed to remain constant for the lower momentum range of the  $Z \rightarrow \tau\tau$  signals and backgrounds.

The invariant mass for a  $Z$  boson decay into a back-to-back  $\tau$  lepton pair in the transverse plane is,

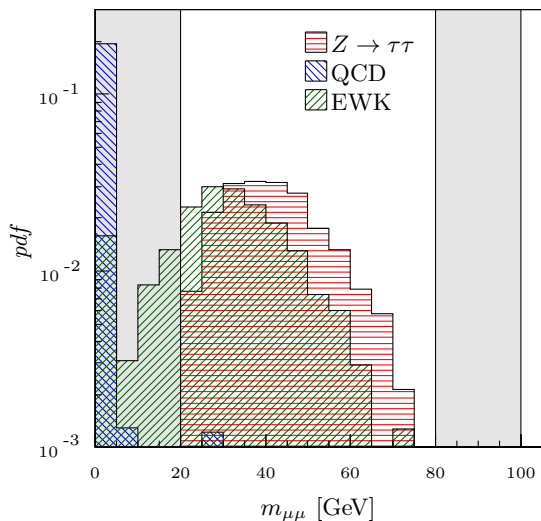
$$m^2 \geq \left( \sqrt{p_{T1}^2 + m_1^2} + \sqrt{p_{T2}^2 + m_2^2} \right)^2 - (p_{T1} - p_{T2})^2 \geq 4p_{T1}p_{T2} \quad (5.5)$$

where  $p_{T1}$  and  $p_{T2}$  are the transverse momenta of the two  $\tau$  leptons, and  $m_1$  and  $m_2$  are their masses. As  $m_Z \gg m_\tau$ , the single charged visible decay products of the  $\tau$  leptons are approximately collinear with their parent  $\tau$  leptons. Consequently, the inequality of Eq. 5.5 also holds for the invariant mass of the decay products from the  $\tau$  leptons.

Since  $\tau$  lepton pairs produced from  $Z$  bosons within LHCb fulfil the assumptions of Eq. 5.5 and  $p_{T1} > 20$  GeV and  $p_{T2} > 5$  GeV are required for the  $\tau$  lepton decay product candidates, the invariant mass of the two  $\tau$  lepton decay products must be greater than 20 GeV. Figure 5.5(b)

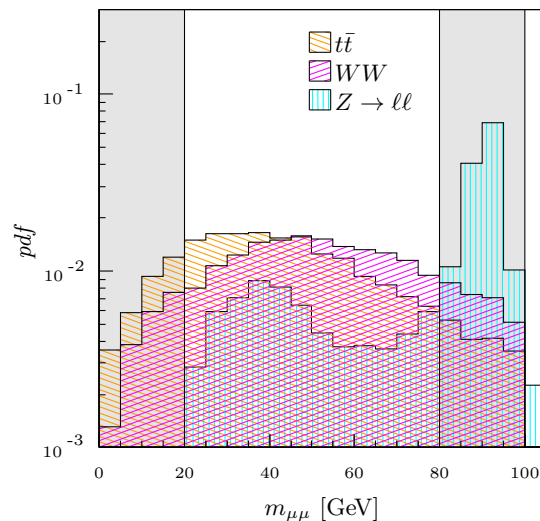


(a)



(b)

**Figure 5.5.:** (a) A comparison of the invariant mass distributions between data (points), simulation (red), and calibrated simulation (blue) for  $Z \rightarrow \mu\mu$  events. Invariant mass distributions for (b)  $Z \rightarrow \tau\tau$  (red), QCD (blue), and EWK (green) events and (c)  $t\bar{t}$  (orange),  $WW$  (magenta), and  $Z \rightarrow \ell\ell$  (cyan) events. The distributions from simulation are corrected with the momentum calibration of Eq. 5.4 and the mass ranges excluded by the  $\tau_\mu\tau_\mu$  selection requirement are shaded in grey.



(c)

shows the  $Z \rightarrow \tau\tau$  invariant mass distribution for the  $\tau_\mu\tau_\mu$  category of events.

Of the five backgrounds, only the  $Z \rightarrow \ell\ell$  background fulfils the assumptions of Eq. 5.5 and consequently has no events below 20 GeV. The  $Z \rightarrow \mu\mu$  background distribution is shown in Fig. 5.5(c) and has a sharp peak at 90 GeV, corresponding to the on-shell mass of the  $Z$  boson. The  $Z \rightarrow \mu\mu$  background dominates the signal for the  $\tau_\mu\tau_\mu$  category, and so the mass window of  $80 < m < 100$  GeV is excluded for the  $\tau_\mu\tau_\mu$  category only.

The invariant mass distribution for the QCD background is given in Fig. 5.5(b) and shows that QCD background events have a significantly lower invariant mass than signal  $Z \rightarrow \tau\tau$  events. For EWK events, a single lepton with hard  $p_T$  from a  $W$  or  $Z$  boson is combined with a candidate from the underlying event to produce an invariant mass distribution harder than the QCD background, yet softer than the signal, see Fig. 5.5(b). In Fig. 5.5(c) the  $\tau_\mu\tau_\mu$  invariant mass distributions are given for the  $t\bar{t}$  and  $WW$  backgrounds. The  $\tau$  lepton decay product candidates from these events are produced from massive parents and produce distributions with

higher mass tails than either the QCD or EWK backgrounds.

### Track Isolation

The track isolation associated to a candidate track,  $I_{p_T}$ , is defined as,

$$I_{p_T} \equiv \sum_i^{\text{tracks}} p_{x_i} \oplus \sum_i^{\text{tracks}} p_{y_i} \quad (5.6)$$

where the  $x$  and  $y$ -momenta of all tracks within a cone of  $\Delta R \equiv \Delta\phi \oplus \Delta\eta < 0.5$  around the candidate track are summed and then added in quadrature. Here,  $\Delta\phi$  and  $\Delta\eta$  are the differences in  $\phi$  and  $\eta$ , defined in Sect. 4.2, between the candidate and the track. The track of the candidate itself is excluded from the sum. Physically,  $I_{p_T}$  is the  $p_T$  of the vectorial sum of all tracks in a cone surrounding the candidate and quantifies the charged isolation of the candidate. Note that a large  $I_{p_T}$  corresponds to a poorly isolated track.

In Fig. 5.6(a), the distributions of the maximum  $I_{p_T}$  of the two muons from  $Z \rightarrow \mu\mu$  data and simulation are compared. The isolation of the two muon candidates is dependent primarily upon the underlying event activity, which is underestimated in simulation. Consequently, the  $I_{p_T}$  distribution produced from simulation is softer than that from data. The soft underlying event cannot be calculated perturbatively, and must be modelled phenomenologically in simulation, as described in Chap. 2. As there is no simple relation between data and simulation, calibration of the  $I_{p_T}$  distribution from simulation is not possible. However, the efficiency of the  $I_{p_T}$  selection is calculated from data, as described in Sect. 5.2.2, and so the cross-section determination of Sect. 5.2 does not depend upon the accuracy of the simulated  $I_{p_T}$  distribution.

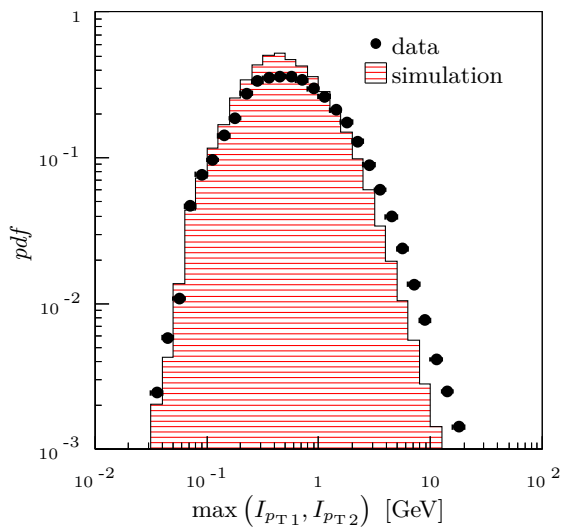
Figures 5.6(b) and 5.6(c) show the distribution of the maximum  $I_{p_T}$  of the two  $\tau$  lepton decay product candidates for signal and background events. The  $\tau$  lepton decay product candidates produced from  $Z \rightarrow \tau\tau$ ,  $WW$ , and  $Z \rightarrow \ell\ell$  events are expected to be relatively isolated, as the candidates are produced from the decays of massive electroweak bosons, and the jets from the underlying event will be uncorrelated with the candidate direction. For  $t\bar{t}$  events, the associated  $b$ -jets from the decay of the  $t$ -quark slightly contaminate the isolation of the  $\tau$  lepton decay product candidates.

For the QCD backgrounds the candidates are produced from jet activity, resulting in tracks that are not isolated, as can be seen Fig. 5.6(b). Similarly, for the EWK backgrounds, one of the  $\tau$  lepton decay product candidates typically is produced from a jet and is not isolated. The QCD and EWK backgrounds are separated from  $\tau_\mu\tau_\mu$ ,  $\tau_\mu\tau_e$ , and  $\tau_e\tau_\mu$  signal events by requiring the  $I_{p_T}$  for both  $\tau$  lepton decay product candidates to be less than 2 GeV. For the  $\tau_\mu\tau_h$  and  $\tau_e\tau_h$  signals a harsher criteria of  $I_{p_T} < 1$  GeV is necessary as the initial QCD and EWK backgrounds are larger.

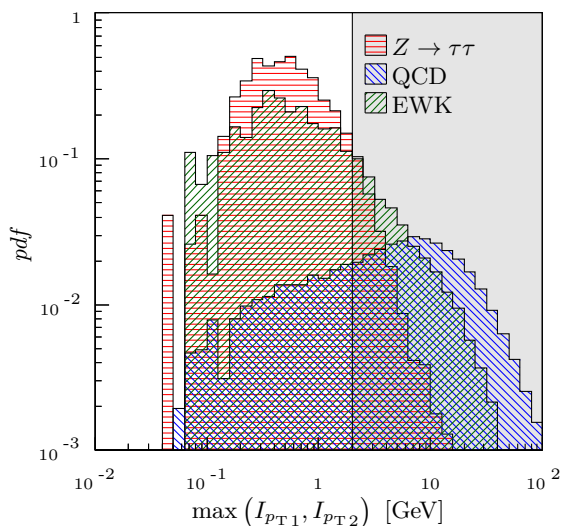
### Azimuthal Separation

For  $Z$  bosons produced at the LHC, their  $p_T$  is typically small. In the subsequent decay of the  $Z$  boson, transverse momentum must be conserved, and so the two  $Z$  boson decay products are



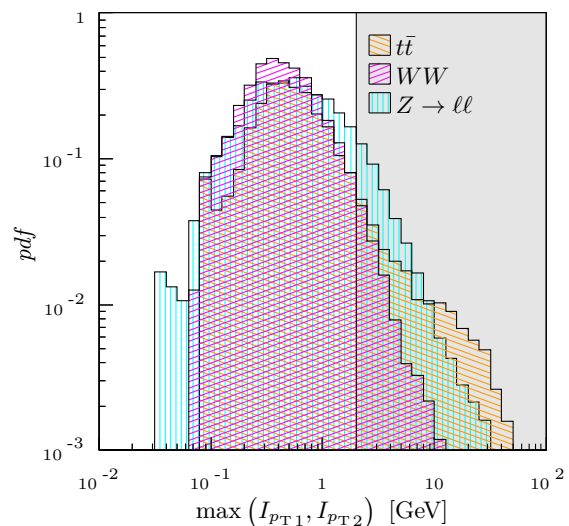


(a)



(b)

**Figure 5.6.:** (a) A comparison of the maximum track isolation distributions between data (points) and simulation (red) for  $Z \rightarrow \mu\mu$  events. Distributions of the maximum track isolation between the two  $\tau$  lepton decay product candidates for (b)  $Z \rightarrow \tau\tau$  (red), QCD (blue), and EWK (green) events and (c)  $t\bar{t}$  (orange),  $WW$  (magenta), and  $Z \rightarrow \ell\ell$  (cyan) events. The isolation range excluded by the  $\tau_\mu\tau_\mu$  selection requirement is shaded in grey.



(c)

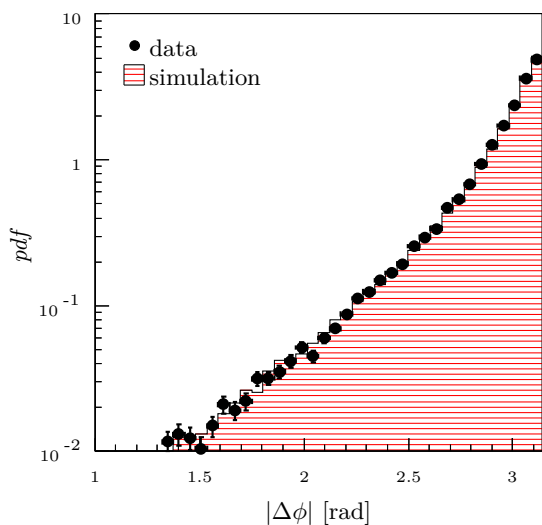
approximately back-to-back in the transverse plane. For  $Z \rightarrow \tau\tau$  decays  $m_\tau \ll m_Z$ , resulting in the decay products of the  $\tau$  leptons produced in a collinear direction with their parent  $\tau$  lepton, and so the decay products of the two  $\tau$  leptons will also be back-to-back.

The azimuthal separation of the observed  $\tau$  lepton decay product candidates,  $|\Delta\phi|$ , is defined as,

$$|\Delta\phi| \equiv \begin{cases} |\phi_1 - \phi_2| & \text{if } |\phi_1 - \phi_2| \leq \pi \\ 2\pi - |\phi_1 - \phi_2| & \text{else} \end{cases} \quad (5.7)$$

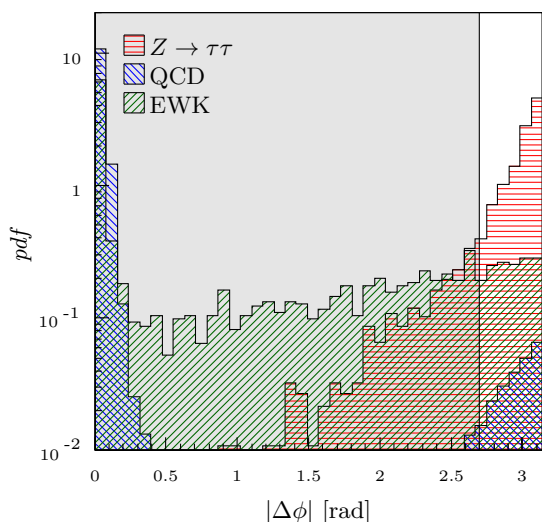
where values near  $\pi$  radians indicate events where the two  $\tau$  lepton decay product candidates are back-to-back. Here  $\phi_1$  and  $\phi_2$  are the azimuthal angles of the first and second  $\tau$  lepton decay product candidates. Given the definition of Eq. 5.7,  $|\Delta\phi|$  must range between 0 and  $\pi$  radians.

A comparison between the  $Z \rightarrow \mu\mu$   $|\Delta\phi|$  distributions from data and simulation is given in

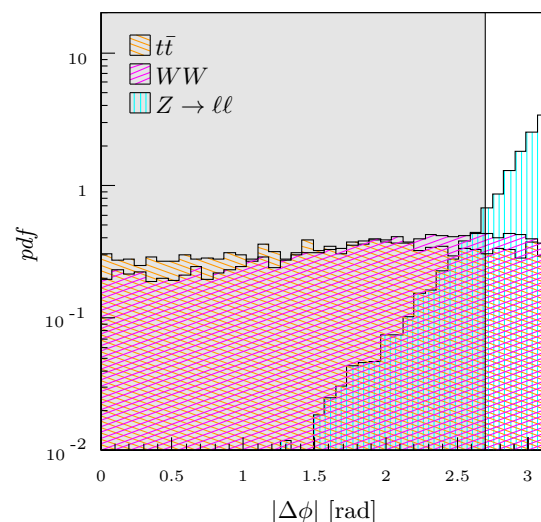


(a)

**Figure 5.7.:** (a) A comparison of the azimuthal separation distributions between data (points) and simulation (red) for  $Z \rightarrow \mu\mu$  events. Distributions of the azimuthal separation between the two  $\tau$  lepton decay product candidates for (b)  $Z \rightarrow \tau\tau$  (red), QCD (blue), and EWK (green) events and (c)  $t\bar{t}$  (orange),  $WW$  (magenta), and  $Z \rightarrow \ell\ell$  (cyan) events. The range excluded by the azimuthal separation selection requirement is shaded in grey.



(b)



(c)

Fig. 5.7(a). The distribution is described by the decay kinematics of the  $Z$  boson which are well modelled in simulation, and so there is good agreement between data and simulation.

The distributions of  $|\Delta\phi|$  are shown in Figs. 5.7(b) and 5.7(c) for  $\tau_\mu\tau_\mu$  signal and background events. The back-to-back nature of  $Z \rightarrow \tau\tau$  and  $Z \rightarrow \ell\ell$  events is apparent and these distributions are nearly identical, validating the collinear approximation of the  $\tau$  lepton decays. The  $\tau$  lepton decay product candidates from the QCD background are primarily produced from the same jet, and travel approximately in the same direction, producing events with small  $|\Delta\phi|$ . However, the candidates can also be produced from di-jet events, contributing to the high  $|\Delta\phi|$  tail of the QCD distribution. The  $|\Delta\phi|$  distributions of the EWK,  $t\bar{t}$ , and  $WW$  backgrounds are relatively flat, as expected due to the small correlations between the production of the two candidates. For all five event categories,  $|\Delta\phi| > 2.7$  radians is required.

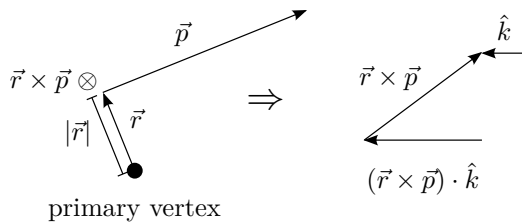


**Figure 5.8.:** Schematic of the components used to build the signed impact parameter,  $r$ , of Eq. 5.8. The diagram on the left-hand side is in the plane of the particle momentum and impact parameter. The diagram on the right-hand side is in the plane of  $\vec{r} \times \vec{p}$  and the  $z$ -axis.

### Impact Parameter Significance

The mean lifetime of the  $\tau$  lepton is experimentally known to be  $0.2906 \pm 0.0010$  ps [15] and so  $\tau$  leptons produced from  $Z$  boson decays are expected to travel on the order of a centimetre within LHCb before decaying. While the decay vertex position for a  $\tau$  lepton decaying into a single visible track cannot be directly measured within LHCb, the impact parameter of the  $\tau$  lepton decay product candidate can be measured. Here, the impact parameter,  $\vec{r}$ , is defined as the vector of closest approach between the  $\tau$  lepton decay product candidate track and the associated primary vertex. The associated primary vertex is refitted, as described in Sect. 4.3.1, without including the candidate track in the fit.

The uncertainty on the impact parameter resolution is dependent upon the uncertainty of not only the track fit but also the primary vertex location. However, by summing the signed impact parameters of the two  $\tau$  lepton decay product candidates, the associated primary vertex uncertainties can be effectively cancelled [176, 177], yielding a variable more sensitive to the lifetime of the  $\tau$  lepton. The signed impact parameter,  $r$ , is defined as,

$$r \equiv |\vec{r}| \left( \frac{(\vec{r} \times \vec{p}) \cdot \hat{k}}{|(\vec{r} \times \vec{p}) \cdot \hat{k}|} \right) \quad (5.8)$$

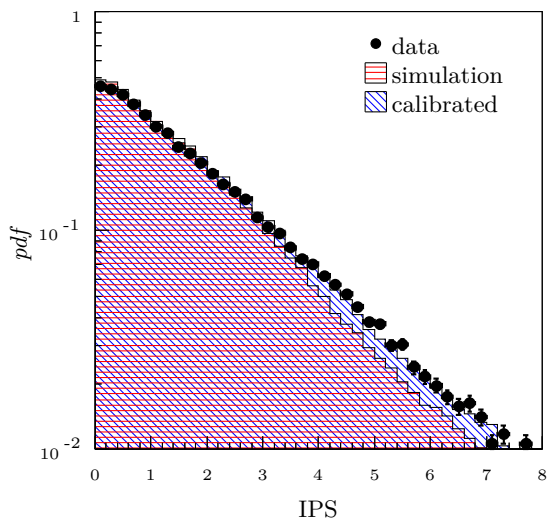
where  $\vec{p}$  is the momentum of the track and  $\hat{k}$  is the  $z$ -direction unit vector. A diagram of the signed impact parameter is shown in Fig. 5.8.

The summed impact parameter significance, IPS, can then be written as,

$$\text{IPS} \equiv \frac{|r_1 + r_2|}{\delta_1 \oplus \delta_2} \quad (5.9)$$

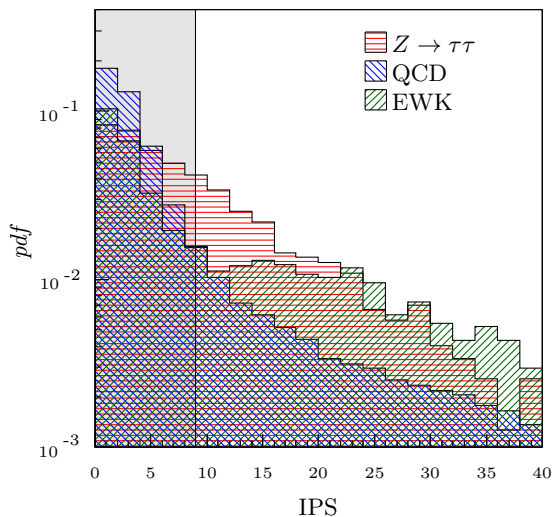
where  $r_1$  and  $r_2$  are the signed impact parameters for the first and second  $\tau$  lepton decay product candidates and  $\delta_1$  and  $\delta_2$  are their associated uncertainties calculated from the track fit covariance matrices.

For accurate simulation of the IPS, correct modelling of the track fit and its associated uncertainty is critical. The IPS is underestimated in simulation as demonstrated in Fig. 5.9(a) which plots the IPS distributions for  $Z \rightarrow \mu\mu$  events from data and simulation. The IPS distribution from simulation can be corrected to match the distribution from data by multiplying the IPS for each simulated event by a factor  $f_{\text{scale}}$ . An  $f_{\text{scale}}$  of  $1.12 \pm 0.01$  is found to minimise the  $\chi^2$  between the data distribution and the corrected simulated distribution, and is used to calibrate all simulated samples. This calibration is assumed to propagate from the lower IPS values of

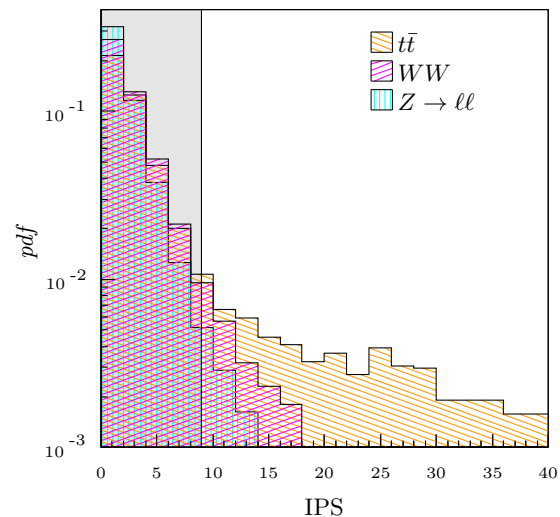


(a)

**Figure 5.9.:** (a) A comparison of the impact parameter significance distributions between data (points), uncalibrated simulation (red), and calibrated (blue) simulation for  $Z \rightarrow \mu\mu$  events. Distributions of the impact parameter significance for (b)  $Z \rightarrow \tau\tau$  (red), QCD (blue), and EWK (green) events and (c)  $t\bar{t}$  (orange),  $WW$  (magenta), and  $Z \rightarrow \ell\ell$  (cyan) events. The distributions from simulation are corrected with the  $f_{\text{scale}}$  factor described in the text and the range excluded by the impact parameter significance selection requirement is shaded in grey.



(b)



(c)

$Z \rightarrow \mu\mu$  events to the higher IPS values of  $Z \rightarrow \tau\tau$  events.

In Figure 5.9(b) the IPS distribution for  $Z \rightarrow \tau\tau$  signal events of the  $\tau_\mu\tau_\mu$  category is shown, as well as the distributions for the QCD and EWK backgrounds. The signal distribution has a longer tail than the QCD distribution as most particles produced within a jet are either stable or have a shorter lifetime than the  $\tau$  lepton. However, heavy-flavour mesons can have longer lifetimes than the  $\tau$  lepton and produce the harder tail of the QCD distribution. The EWK background has a much harder IPS spectrum than either the signal or QCD distributions, which could be a result of the two candidates being produced from a separate electroweak boson and jet in the event.

The IPS distributions for the  $t\bar{t}$ ,  $WW$ , and  $Z \rightarrow \mu\mu$  backgrounds are provided in Fig. 5.9(c). The  $t\bar{t}$  background distribution has a much harder tail than both the signal distribution and all other background distributions. This is most probably caused by one of the candidates being produced by a heavy-flavour meson decay from one of the  $b$ -jets. The  $WW$  and  $Z \rightarrow \mu\mu$  distri-

**Table 5.2.:** A summary of the event selection requirements: invariant mass ( $m$ ), charged track isolation ( $I_{p_T}$ ), azimuthal separation ( $|\Delta\phi|$ ), impact parameter significance (IPS), and  $p_T$  asymmetry ( $A_{p_T}$ ). The requirements applied to each of the five event categories is given.

|                      | $\tau_\mu\tau_\mu$       | $\tau_\mu\tau_e$ | $\tau_e\tau_\mu$ | $\tau_\mu\tau_h$ | $\tau_e\tau_h$ |
|----------------------|--------------------------|------------------|------------------|------------------|----------------|
| $m$ [GeV]            | $> 100$ or $20 < m < 80$ | $> 20$           | $> 20$           | $> 20$           | $> 20$         |
| $I_{p_T}$ [GeV]      | $< 2$                    | $< 2$            | $< 2$            | $< 1$            | $< 1$          |
| $ \Delta\phi $ [rad] | $> 2.7$                  | $> 2.7$          | $> 2.7$          | $> 2.7$          | $> 2.7$        |
| IPS                  | $> 9$                    | –                | –                | $> 9$            | $> 9$          |
| $A_{p_T}$            | $> 0.3$                  | –                | –                | –                | –              |

butions, however, are both softer than the  $Z \rightarrow \tau\tau$  signal distribution. The  $Z \rightarrow \mu\mu$  distribution is softer because both  $\tau$  lepton decay product candidates are produced directly from the same  $Z$  boson, while the  $WW$  distribution is softer because the lifetime of  $W$  bosons is approximately twelve orders of magnitude smaller than the  $\tau$  lepton.

For the  $\tau_\mu\tau_\mu$ ,  $\tau_\mu\tau_h$ , and  $\tau_e\tau_h$  categories a requirement of  $\text{IPS} > 9$  is applied, as indicated by the shaded grey areas of Figs. 5.9(b) and 5.9(c). For the  $\tau_\mu\tau_\mu$  category this reduces the dominant  $Z \rightarrow \ell\ell$  background, while for the  $\tau_\mu\tau_h$  and  $\tau_e\tau_h$  categories this requirement reduces the QCD backgrounds. The IPS requirement is not necessary for the cleaner  $\tau_\mu\tau_e$  and  $\tau_e\tau_\mu$  categories.

### Transverse Momentum Asymmetry

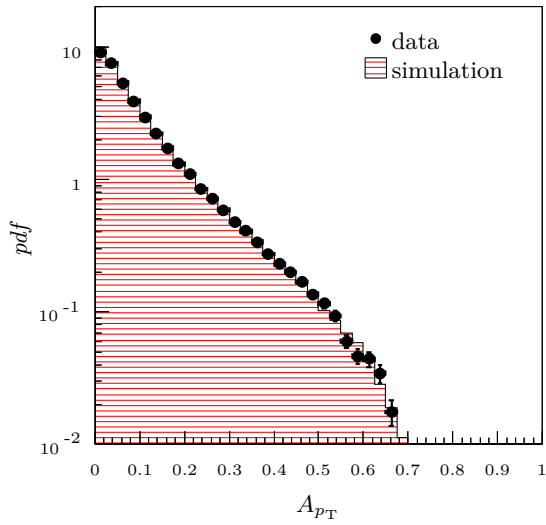
While the selection requirements detailed above are sufficient for separating signal from background for the  $\tau_\mu\tau_e$ ,  $\tau_e\tau_\mu$ ,  $\tau_\mu\tau_h$ , and  $\tau_e\tau_h$  event categories, these requirements are inadequate in eliminating the  $Z \rightarrow \mu\mu$  background from  $\tau_\mu\tau_\mu$  signal events. The transverse momentum asymmetry is defined as,

$$A_{p_T} \equiv \frac{|p_{T1} - p_{T2}|}{p_{T1} + p_{T2}} \quad (5.10)$$

where  $p_{T1}$  and  $p_{T2}$  are the transverse momenta of the first and second  $\tau$  lepton decay product candidates respectively. The muons from background  $Z \rightarrow \mu\mu$  events will have balanced  $p_T$ , resulting in a low  $A_{p_T}$  while  $Z \rightarrow \tau\tau$  signal events have missing neutrinos, oftentimes resulting in a larger  $A_{p_T}$ .

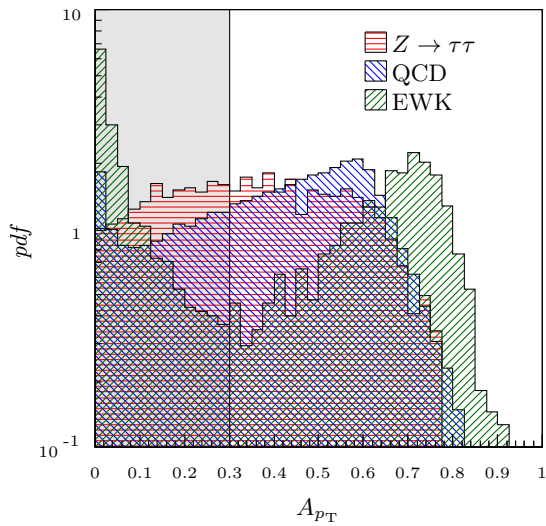
The  $A_{p_T}$  is primarily dependent upon the decays of the parent particle, and for the case of  $Z \rightarrow \tau\tau$ , the decays of the  $\tau$  leptons. These decays are well modelled in simulation, and so no calibration of the simulation is necessary, as can be seen in the  $A_{p_T}$  distributions for  $Z \rightarrow \mu\mu$  events from data and simulation of Fig. 5.10(a). The  $A_{p_T}$  distributions for  $Z \rightarrow \tau\tau$ , QCD, and EWK events for the  $\tau_\mu\tau_\mu$  category are shown in Fig. 5.10(b), while the  $A_{p_T}$  distributions for the  $t\bar{t}$ ,  $WW$ , and  $Z \rightarrow \mu\mu$  backgrounds are shown in Fig. 5.10(c). As can be seen, the  $A_{p_T}$  for  $Z \rightarrow \tau\tau$  events can be large, while the  $A_{p_T}$  for  $Z \rightarrow \mu\mu$  background events is much smaller. For the  $\tau_\mu\tau_\mu$  event category, the criteria  $A_{p_T} > 0.3$  is required, as shown by the grey exclusions. No  $A_{p_T}$  minimum is required for the  $\tau_\mu\tau_e$ ,  $\tau_e\tau_\mu$ ,  $\tau_\mu\tau_h$ , and  $\tau_e\tau_h$  event categories.

A summary of the event selection requirements placed on the five variables of this section for

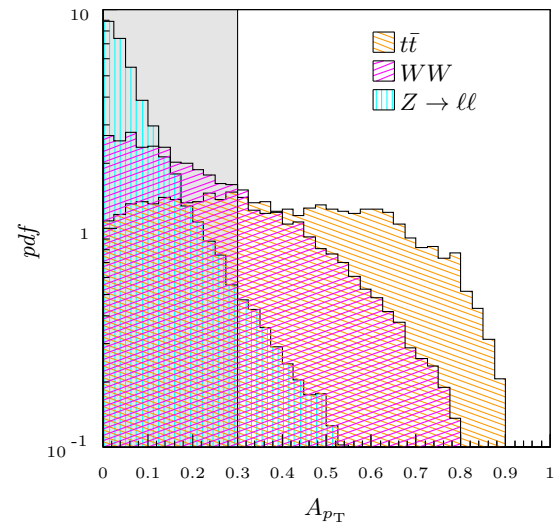


(a)

**Figure 5.10.:** (a) A comparison of the  $p_T$  asymmetry distributions between data (points) and simulation (red) for  $Z \rightarrow \mu\mu$  events. Distributions of the  $p_T$  asymmetry between the two  $\tau$  lepton decay product candidates for (b)  $Z \rightarrow \tau\tau$  (red), EWK (blue), and QCD (green) events and (c)  $t\bar{t}$  (orange),  $WW$  (magenta), and  $Z \rightarrow \ell\ell$  (cyan) events. The range excluded by the  $p_T$  asymmetry selection requirement is shaded in grey.



(b)



(c)

each event category is given in Table 5.2. Only the  $\tau_\mu\tau_\mu$  category places requirements on all five variables, with the IPS and  $A_{p_T}$  requirements designed to remove  $Z \rightarrow \mu\mu$  background. The IPS requirement is also kept for the  $\tau_\mu\tau_h$  and  $\tau_e\tau_h$  categories to help reduce QCD background. The  $\tau_\mu\tau_e$  and  $\tau_e\tau_\mu$  categories have much less QCD background than the  $\tau_\mu\tau_h$  and  $\tau_e\tau_h$  categories and do not utilise the IPS requirement.

### 5.1.3. Background Estimation

The selection criteria developed in Sect. 5.1.2 are applied to data to select  $Z \rightarrow \tau\tau$  signal events. In order to calculate the  $pp \rightarrow Z \rightarrow \tau\tau$  cross-section in Sect. 5.2 the number of background events in the selected data must be estimated. The methods used to estimate the number of events from the backgrounds categorised in the beginning of Sect. 5.1 and shown in Fig. 5.3 are now described.

The invariant mass distributions for  $Z \rightarrow \tau\tau$  candidates from data for all five event categories,

**Table 5.3.:** Estimated number of events for each background component and their sum, together with the observed number of candidates for each of the five event categories.

|                          | $\tau_\mu\tau_\mu$ | $\tau_\mu\tau_e$ | $\tau_e\tau_\mu$ | $\tau_\mu\tau_h$ | $\tau_e\tau_h$  |
|--------------------------|--------------------|------------------|------------------|------------------|-----------------|
| QCD                      | $11.7 \pm 3.4$     | $72.4 \pm 2.2$   | $54.0 \pm 3.0$   | $41.9 \pm 0.5$   | $24.5 \pm 0.6$  |
| EWK                      | $0.0 \pm 3.5$      | $40.3 \pm 4.3$   | $0.0 \pm 1.3$    | $10.8 \pm 0.5$   | $9.3 \pm 0.5$   |
| $t\bar{t}$               | $< 0.1 \pm 0.1$    | $3.6 \pm 0.4$    | $1.0 \pm 0.1$    | $< 0.1 \pm 0.1$  | $0.7 \pm 0.4$   |
| $WW$                     | $< 0.1 \pm 0.1$    | $13.3 \pm 1.2$   | $1.6 \pm 0.2$    | $0.2 \pm 0.1$    | $< 0.1 \pm 0.1$ |
| $Z \rightarrow \ell\ell$ | $29.8 \pm 7.0$     | –                | –                | $0.4 \pm 0.1$    | $2.0 \pm 0.2$   |
| Background               | $41.6 \pm 8.5$     | $129.7 \pm 4.9$  | $56.6 \pm 3.3$   | $53.3 \pm 0.8$   | $36.6 \pm 0.9$  |
| Observed                 | 124                | 421              | 155              | 189              | 101             |

together with the estimated backgrounds which are described in the remainder of this section, are given in Fig. 5.11. No events were observed in data above an invariant mass of 120 GeV. The simulated signal is normalised to the difference between the number of observed and estimated background events. A summary of these values is given in Table 5.3. Further validation plots are provided in Figs. C.1 through C.6 of App. C for the  $p_T$  and  $\eta$  distributions of the combined  $\tau$  lepton decay product candidates, as well as the  $p_T$  and  $\eta$  distributions of the individual candidates and the number of primary vertices for the event.

### QCD and EWK Backgrounds

The number of QCD and EWK background events given in Table 5.3 are estimated from data. A signal-depleted data sample is produced by applying the selection criteria of Sect. 5.1.2 to data, but requiring the two  $\tau$  lepton decay product candidates have the same-sign charge. The distributions from the same-sign sample of the  $p_T$  difference between the first and second  $\tau$  lepton decay product candidates,  $p_{T1} - p_{T2}$ , are fitted with QCD and EWK templates to determine the number of same-sign charge QCD and EWK events,  $S_{\text{QCD}}$  and  $S_{\text{EWK}}$ . The same-sign QCD template is taken from data fulfilling the selection requirements of Sect. 5.1.2, but requiring  $I_{p_T} > 10$  GeV for both  $\tau$  lepton decay product candidates. The EWK template is taken from simulation without the  $I_{p_T}$  selection applied.

The  $p_{T1} - p_{T2}$  distributions from same-sign data, with their respective QCD and EWK template fits, are given in Fig. 5.12 for the five event categories. In QCD events both  $\tau$  lepton decay product candidates are typically produced from the same jet, resulting in a similar  $p_T$  for the two candidates and a small  $p_T$  difference. For EWK events the first candidate produced is generally from an electroweak boson and will have a hard  $p_T$ , while the second candidate will have a softer  $p_T$  from jet activity, and so the  $p_T$  difference distribution is shifted upwards to larger  $p_T$  differences than the QCD distribution.

The number of same-sign background events  $S_{\text{QCD}}$  and  $S_{\text{EWK}}$  are extrapolated to the number of opposite-sign events,  $N_{\text{QCD}}$  and  $N_{\text{EWK}}$ , using,

$$N_{\text{QCD}} = r_{\text{QCD}} S_{\text{QCD}}, \quad N_{\text{EWK}} = r_{\text{EWK}} S_{\text{EWK}} \quad (5.11)$$

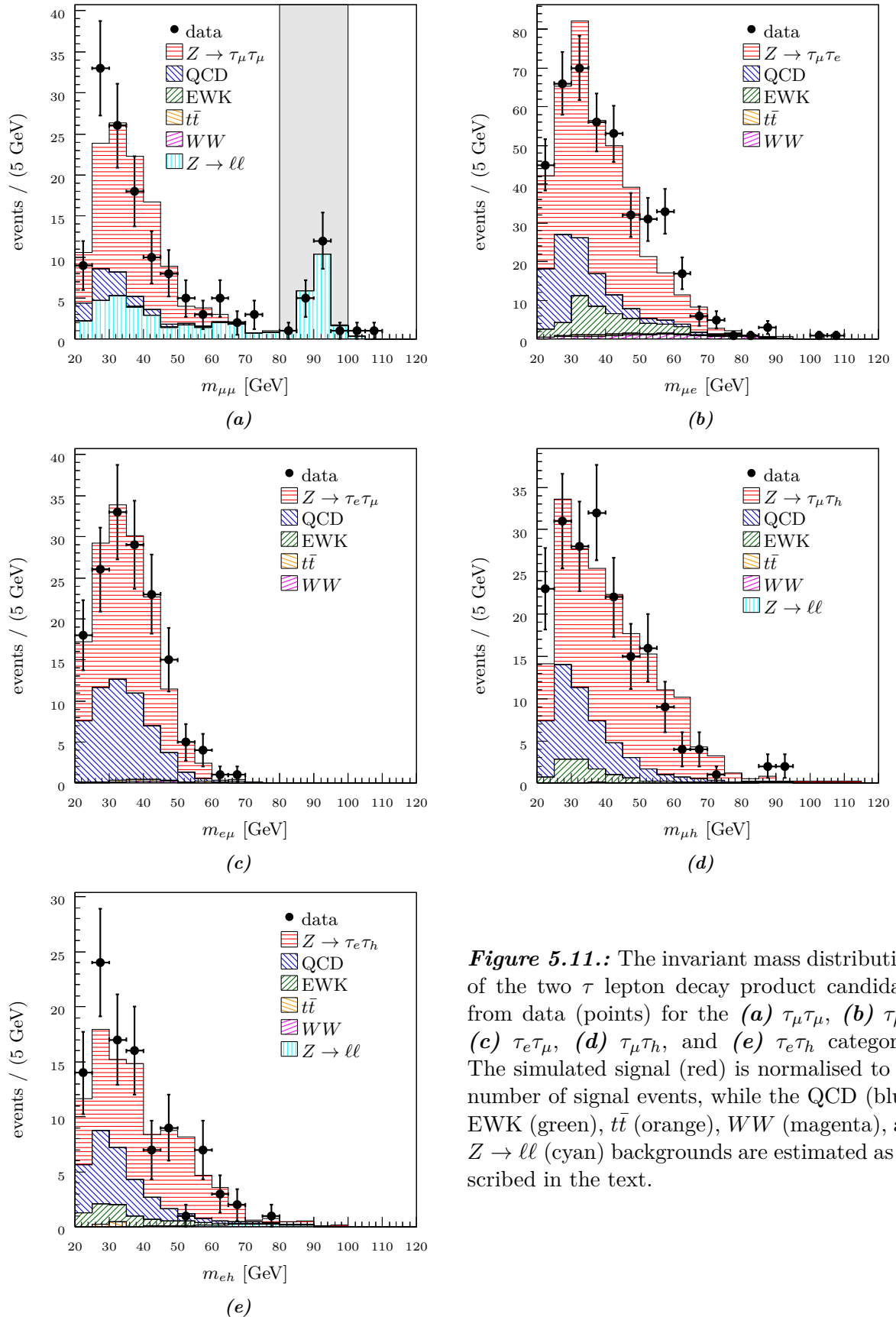


**Figure 5.11.:** The invariant mass distributions of the two  $\tau$  lepton decay product candidates from data (points) for the (a)  $\tau_\mu\tau_\mu$ , (b)  $\tau_\mu\tau_e$ , (c)  $\tau_e\tau_\mu$ , (d)  $\tau_\mu\tau_h$ , and (e)  $\tau_e\tau_h$  categories. The simulated signal (red) is normalised to the number of signal events, while the QCD (blue), EWK (green),  $t\bar{t}$  (orange),  $WW$  (magenta), and  $Z \rightarrow \ell\ell$  (cyan) backgrounds are estimated as described in the text.



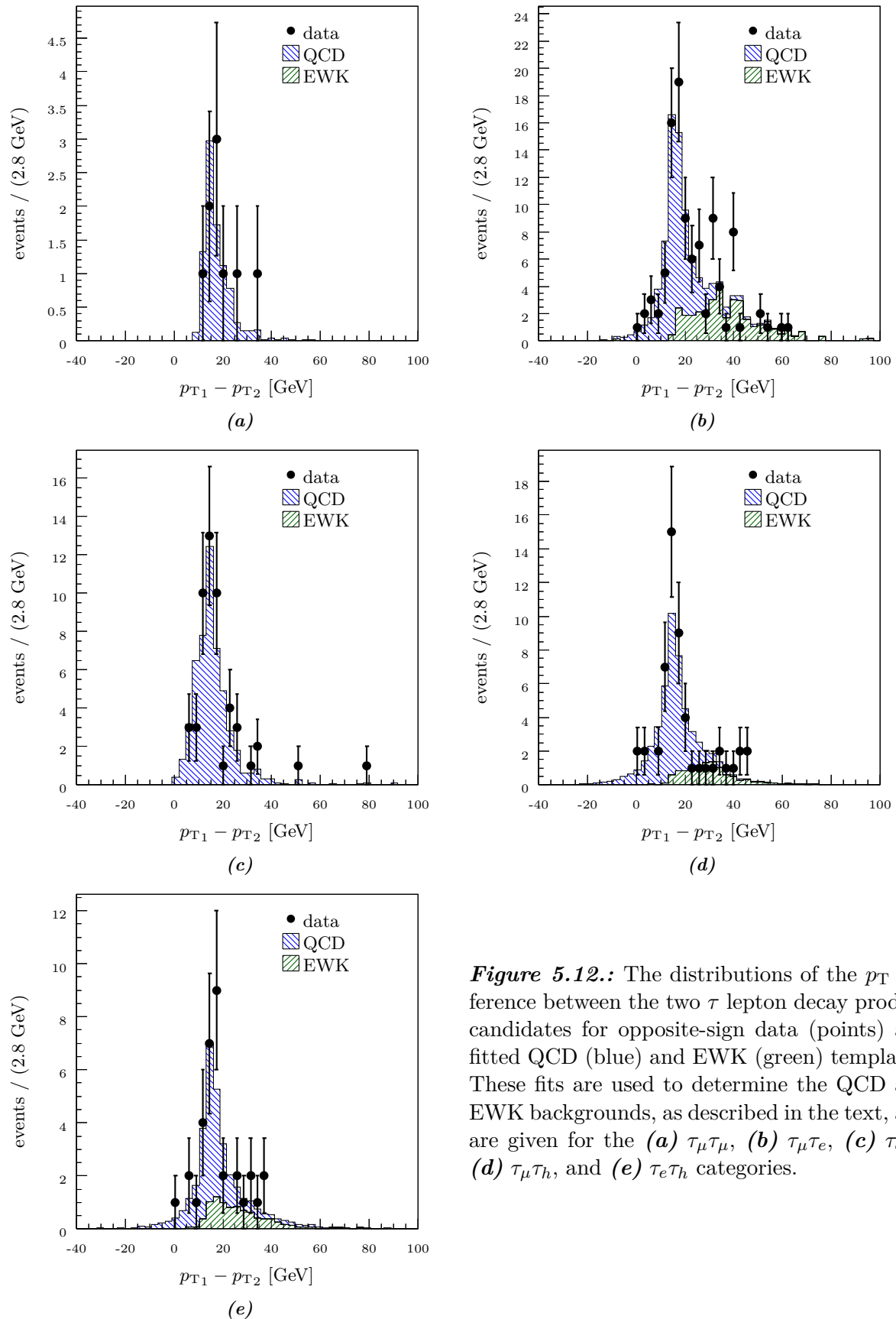


**Figure 5.12.:** The distributions of the  $p_T$  difference between the two  $\tau$  lepton decay product candidates for opposite-sign data (points) and fitted QCD (blue) and EWK (green) templates. These fits are used to determine the QCD and EWK backgrounds, as described in the text, and are given for the (a)  $\tau_\mu\tau_\mu$ , (b)  $\tau_\mu\tau_e$ , (c)  $\tau_e\tau_\mu$ , (d)  $\tau_\mu\tau_h$ , and (e)  $\tau_e\tau_h$  categories.

where  $r$  is the ratio of opposite-sign to same-sign events evaluated from data for the QCD background and from simulation for the EWK background. These  $r$  are calculated from the ratio of opposite-sign to same-sign events satisfying the QCD and EWK sample requirements. The value of  $r_{\text{QCD}}$  was found to remain consistent, within statistical uncertainty, when varying the QCD sample  $I_{p_T}$  requirement between 5 and 20 GeV, and consequently is assumed to remain valid for the  $Z \rightarrow \tau\tau$   $I_{p_T}$  selection requirements. A cross-check with data was made for  $r_{\text{EWK}}$  by selecting an EWK sample from data using  $I_{p_T} < 1$  GeV for the first  $\tau$  lepton decay product candidate and  $I_{p_T} > 10$  GeV for the second candidate.

The uncertainties on the QCD and EWK backgrounds are taken from the uncertainties of the same-sign template fit,  $r_{\text{QCD}}$ , and  $r_{\text{EWK}}$ . The uncertainties on  $r_{\text{QCD}}$  and  $r_{\text{EWK}}$  are statistical and uncorrelated between the two backgrounds. The same-sign template fit requires the sum of the QCD and EWK events,  $S_{\text{QCD}} + S_{\text{EWK}}$ , to equal the total number of same-sign data events,  $S$ , and so the fit uncertainty is fully correlated between the two backgrounds. The combined number of QCD and EWK background events, using Eq. 5.11 is,

$$N_{\text{QCD+EWK}} = r_{\text{QCD}}S_{\text{QCD}} + r_{\text{EWK}}S_{\text{EWK}} = r_{\text{QCD}}f_{\text{fit}}S + r_{\text{EWK}}(1 - f_{\text{fit}})S \quad (5.12)$$

where  $f_{\text{fit}}$  is defined as  $S_{\text{QCD}}/S$ . Assuming the uncertainties on  $f_{\text{fit}}$ ,  $r_{\text{QCD}}$ , and  $r_{\text{EWK}}$  are uncorrelated and normally distributed, the uncertainty on  $N_{\text{QCD+EWK}}$  is,

$$\delta_{N_{\text{QCD+EWK}}}^2 = (r_{\text{QCD}}S - r_{\text{EWK}}S)^2 \delta_{f_{\text{fit}}}^2 + (f_{\text{fit}}S)^2 \delta_{r_{\text{QCD}}}^2 + (S - f_{\text{fit}}S)^2 \delta_{r_{\text{EWK}}}^2 \quad (5.13)$$

where  $\delta_{f_{\text{fit}}}$ ,  $\delta_{r_{\text{QCD}}}$ , and  $\delta_{r_{\text{EWK}}}$  are the uncertainties on  $f_{\text{fit}}$ ,  $r_{\text{QCD}}$ , and  $r_{\text{EWK}}$  respectively.

In Table 5.3, the number of QCD and EWK backgrounds, with associated uncertainty, have been presented separately for clarity. Here, the uncertainty for the two backgrounds from Eq. 5.13 is split between the two backgrounds using the arbitrary convention,

$$\delta_{N_{\text{QCD}}}^2 = \frac{1}{2} (r_{\text{QCD}}S - r_{\text{EWK}}S)^2 \delta_{f_{\text{fit}}}^2 + (f_{\text{fit}}S)^2 \delta_{r_{\text{QCD}}}^2 \quad (5.14a)$$

$$\delta_{N_{\text{EWK}}}^2 = \frac{1}{2} (r_{\text{QCD}}S - r_{\text{EWK}}S)^2 \delta_{f_{\text{fit}}}^2 + (S - f_{\text{fit}}S)^2 \delta_{r_{\text{EWK}}}^2 \quad (5.14b)$$

where the template fit uncertainty term is evenly divided between the QCD and EWK background uncertainties.

### $Z \rightarrow \ell\ell$ Background

The number of  $Z \rightarrow \ell\ell$  background events, given in Table 5.3 are evaluated only for the  $\tau_\mu\tau_\mu$ ,  $\tau_\mu\tau_h$ , and  $\tau_e\tau_h$  categories and not for the  $\tau_\mu\tau_e$  and  $\tau_e\tau_\mu$  categories, as the background for these categories is negligible. For the  $\tau_\mu\tau_\mu$  and  $\tau_\mu\tau_h$  categories the  $Z \rightarrow \ell\ell$  background consists of  $Z \rightarrow \mu\mu$  events, while for the  $\tau_\mu\tau_e$  category the  $Z \rightarrow \ell\ell$  background is from  $Z \rightarrow ee$  events.

In the  $\tau_\mu\tau_\mu$  invariant mass distribution from data of Fig. 5.11(a), the  $Z \rightarrow \mu\mu$  events from an on-shell  $Z$  boson are clearly visible in the excluded mass range of  $80 < m < 100$  GeV. The shape for the  $Z \rightarrow \mu\mu$  background is obtained from data by applying the  $\tau_\mu\tau_\mu$  selection of

Sect. 5.1.2, but requiring  $\text{IPS} < 1$  to eliminate  $Z \rightarrow \tau\tau$  events. This shape is then normalised to the number of  $\tau_\mu\tau_\mu$  events within the excluded mass range  $80 < m < 100$  GeV. The uncertainty on the number of  $Z \rightarrow \mu\mu$  background events is estimated from the statistical uncertainty on the normalisation of the background sample and is the primary systematic uncertainty for the  $\tau_\mu\tau_\mu$  category.

Events from the  $Z \rightarrow \mu\mu$  process contribute a small background to the  $\tau_\mu\tau_h$  category when one of the muons is mis-identified as a hadron. The data sample for this background is found by applying the  $\tau_\mu\tau_h$  requirements of Sect. 5.1.2, but requiring that the second  $\tau$  lepton decay product candidate fulfil the muon identification criteria of Sect. 5.1.1. The sample is scaled by the probability of mis-identifying a muon as a hadron. The muon mis-identification probability is determined from data where  $Z \rightarrow \mu\mu$  events are selected by requiring a single well defined muon and a second isolated track with a combined invariant mass within the range  $80 < m < 100$  GeV. Only  $(0.06 \pm 0.01)\%$  of the isolated tracks pass the hadron identification requirement. The uncertainty on the  $\tau_\mu\tau_h$   $Z \rightarrow \ell\ell$  background is estimated from the statistical uncertainty of the background sample and the muon mis-identification.

For  $\tau_e\tau_h$  events, a small  $Z \rightarrow ee$  background can contribute when one of the two electrons is mis-identified as a hadron. The background sample is found by applying the  $\tau_e\tau_h$  selection of Sect. 5.1.2 to data, but requiring the second  $\tau$  lepton decay product candidate to fulfil the electron identification criteria of Sect. 5.1.1. The background sample is scaled by the probability for an electron to be misidentified as a hadron, which is determined from simulation to be  $(0.63 \pm 0.02)\%$ . The uncertainty on the background is estimated as the statistical uncertainty of the background sample and the electron mis-identification.

### ***WW* and *t $\bar{t}$* Backgrounds**

Both the  $WW$  and  $t\bar{t}$  samples are estimated to be small for all event categories as shown in Table 5.3. These backgrounds are estimated from simulation which has been calibrated for the variables described in Sect. 5.1.2 and normalised to theoretical cross-sections. Additionally, the simulation samples are corrected on an event-by-event basis for the differences observed in the reconstruction efficiencies between data and simulation. Details on the reconstruction efficiencies are provided in Sect. 5.2.1.

## **5.2. Cross-Section**

For consistency with the  $pp \rightarrow Z \rightarrow \mu\mu$  and  $pp \rightarrow Z \rightarrow ee$  cross-section measurements published by the LHCb collaboration in Refs. [173] and [172], the  $pp \rightarrow Z \rightarrow \tau\tau$  cross-section is evaluated in the kinematic region  $60 < m_{\tau\tau} < 120$  GeV,  $p_{T\tau} > 20$  GeV, and  $2.0 \leq \eta_\tau \leq 4.5$ , where  $\tau$  indicates the  $\tau$  lepton before decaying. The cross-section is calculated with,

$$\sigma_{pp \rightarrow Z \rightarrow \tau\tau} = \frac{\sum_i^{N_{\text{obs}}} (\varepsilon_{\text{rec}i}^{-1}) - \sum_j (N_{\text{bkg}j} \langle \varepsilon_{\text{rec}j}^{-1} \rangle)}{\varepsilon_{\text{sel}} \mathcal{L} \mathcal{A}_{\tau_1\tau_2} \mathcal{B}_{\tau_1\tau_2}} \quad (5.15)$$

where  $N_{\text{obs}}$  is the number of candidate events observed in data,  $N_{\text{bkg}_j}$  is the number of estimated background events for each background source  $j$ , and  $\langle \varepsilon_{\text{rec}_j}^{-1} \rangle$  is the average  $\varepsilon_{\text{rec}}^{-1}$  for each background source  $j$ . The reconstruction efficiency,  $\varepsilon_{\text{rec}}$ , is calculated from data or simulation and is dependent upon the momentum and pseudo-rapidity of the  $\tau$  lepton decay product candidates for each event, while the event selection efficiency,  $\varepsilon_{\text{sel}}$ , is an average efficiency for all events. The integrated luminosity is given by  $\mathcal{L}$ , while  $\mathcal{A}_{\tau_1\tau_2}$  is an acceptance and final state radiation factor and  $\mathcal{B}_{\tau_1\tau_2}$  is the branching fraction for the event category.

The first summation with index  $i$  over all observed events, corrects each event by the reconstruction efficiency,  $\varepsilon_{\text{rec}_i}$ , evaluated for the  $\tau$  lepton decay product candidates of that event. The second summation with index  $j$  over all background sources, is the addition of the estimated number of events for each background source, weighted by the average event reconstruction efficiency for the data or simulation sample used to evaluate that background.

In Sect. 5.2.1, the methods used to calculate the reconstruction efficiency are described, while in Sect. 5.2.2 the selection efficiency is calculated and in Sect. 5.2.3, the acceptance and branching fractions are determined. The reconstruction efficiencies are tabulated in Table 5.4 of Sect. 5.2.1, while the selection efficiencies are provided in Table 5.5 of Sect. 5.2.2. The acceptance and branching fractions are given in Table 5.6 of Sect. 5.2.3.

The integrated luminosity was determined using the Van de Meer scan [169] and beam-gas imaging [171] methods described in Sect. 4.3.4. These methods provide similar results and so the integrated luminosity is taken as the average of the two with an estimated uncertainty of 3.5% [138]. For the  $\tau_\mu\tau_\mu$ ,  $\tau_\mu\tau_e$ , and  $\tau_\mu\tau_h$  categories the integrated luminosity is  $1028 \pm 28 \text{ pb}^{-1}$ , while the integrated luminosity for the  $\tau_e\tau_\mu$  and  $\tau_e\tau_h$  channels is  $955 \pm 33 \text{ pb}^{-1}$ . The reduction in integrated luminosity for the  $\tau_e\tau_\mu$  and  $\tau_e\tau_h$  categories is due to a change in the electron triggers during the 2011 data-taking period.

### 5.2.1. Reconstruction Efficiency

The reconstruction efficiency,  $\varepsilon_{\text{rec}}$ , used in the cross-section determination of Eq. 5.15, is defined as,

$$\varepsilon_{\text{rec}} \equiv \varepsilon_{\text{GEC}} \varepsilon_{\text{trg}} \varepsilon_{\text{trk1}} \varepsilon_{\text{trk2}} \varepsilon_{\text{id1}} \varepsilon_{\text{id2}} \quad (5.16)$$

where  $\varepsilon_{\text{GEC}}$  is the global event cut (GEC) efficiency,  $\varepsilon_{\text{trg}}$  the trigger efficiency,  $\varepsilon_{\text{trk}}$  the track finding efficiency, and  $\varepsilon_{\text{id}}$  the particle identification efficiency. The numerical subscripts indicate whether the efficiency is evaluated for the first or second  $\tau$  lepton decay product candidate. A summary of these component reconstruction efficiencies for muons, electrons, and charged hadrons is given in Table 5.4. The component efficiencies are calculated in the order indicated in Eq. 5.16, *e.g.* the muon identification efficiency is determined for muons with reconstructed tracks from events passing the GEC and single-muon trigger requirement.

The trigger efficiencies are evaluated individually for muons and electrons and combined to determine the trigger efficiency for the given event category. For the  $\tau_\mu\tau_\mu$  and  $\tau_e\tau_\mu$  categories

**Table 5.4.:** The individual reconstruction efficiencies for muons, electrons, and charged hadrons. The track and identification requirements are given in Sect. 5.1.1 and the trigger requirements for each category in Sect. 5.1.2.

|                            | muons             | electrons         | hadrons       |
|----------------------------|-------------------|-------------------|---------------|
| $\varepsilon_{\text{GEC}}$ | $0.955 \pm 0.001$ | $0.951 \pm 0.001$ | —             |
| $\varepsilon_{\text{trg}}$ | $0.76 - 0.79$     | $0.65 - 0.72$     | —             |
| $\varepsilon_{\text{trk}}$ | $0.87 - 0.93$     | $0.83 \pm 0.03$   | $0.73 - 0.79$ |
| $\varepsilon_{\text{id}}$  | $0.93 - 0.99$     | $0.79 - 0.93$     | $0.92 - 0.96$ |

either the first or second  $\tau$  lepton decay product candidate can trigger the event, and so  $\varepsilon_{\text{trg}}$  is,

$$\varepsilon_{\text{trg}} = \varepsilon_{\text{trg1}} + \varepsilon_{\text{trg2}} - \varepsilon_{\text{trg1}} \varepsilon_{\text{trg2}} \quad (5.17)$$

where the numerical subscripts indicate the first or second candidate. For the  $\tau_\mu\tau_e$ ,  $\tau_\mu\tau_h$ , and  $\tau_e\tau_h$  categories the first  $\tau$  lepton decay product is required to trigger the event, and so the corresponding trigger efficiency for the candidate type is used.

The lepton trigger, track finding, and identification efficiencies are evaluated using tag-and-probe methods on  $Z \rightarrow \ell\ell$  events from data. The  $Z \rightarrow \ell\ell$  events are selected by requiring a tag lepton passing the full trigger, track, and identification reconstruction requirements and a probe lepton passing looser reconstruction requirements, where the requirement being tested is omitted; oftentimes further event requirements are necessary to ensure a pure  $Z \rightarrow \ell\ell$  sample. The efficiency is then calculated as the percentage of probes passing the test requirement. The event topologies for  $Z \rightarrow \ell\ell$  and  $Z \rightarrow \tau\tau$  are nearly identical except for the momenta of the final state candidates, due to the decays of the  $\tau$  leptons, and so the lepton reconstruction efficiencies from  $Z \rightarrow \ell\ell$  samples are evaluated only as a function of lepton momentum, when practicable.

In the remainder of this section the methods used to determine the reconstruction efficiencies are detailed. Plots of the trigger, track finding, and identification efficiencies for muons, electrons, and charged hadrons are also provided. In these plots the efficiency determined from data is compared to the biased and unbiased efficiencies from simulation. The biased efficiency is found by applying the tag-and-probe method to the reconstructed level of simulated events, while the unbiased efficiency is found directly from the generator level of simulated events.

### Global Event Cut

The global event cut is applied at the L0 trigger, described in Sect. 4.3.3, to eliminate high multiplicity events which require significant processing time, and the GEC efficiency,  $\varepsilon_{\text{GEC}}$ , is the probability for an event to pass the GEC requirement. For the single-muon and single-electron triggers, the SPD multiplicity for an event is required to be less than 600 hits, while for the di-muon trigger, the SPD multiplicity must be less than 900 hits.

In Fig. 5.13(a) the SPD distribution for  $Z \rightarrow \mu\mu$  events from data requiring a di-muon trigger is given. The  $Z \rightarrow \mu\mu$  data is selected by requiring two opposite-sign muons with  $p_T > 20$  GeV and an invariant mass within the range  $60 \leq m \leq 120$  GeV. The distribution for  $Z \rightarrow \mu\mu$  events

from data requiring a single-muon trigger is also given in Fig. 5.13(a), but normalised so the integral of the distribution equals the integral for the di-muon trigger distribution below 600 hits.

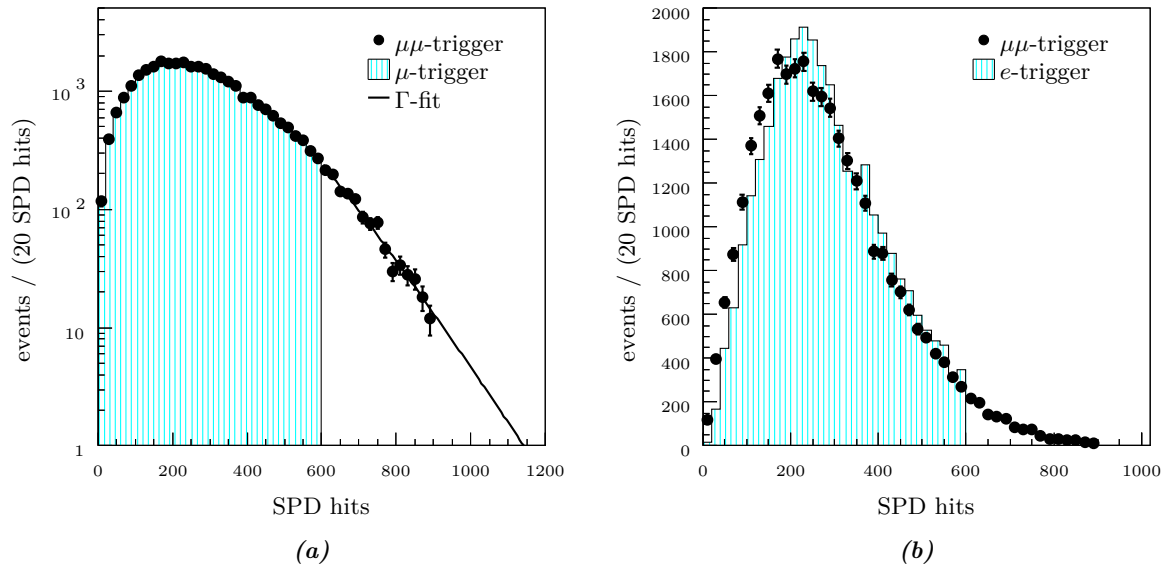


**Figure 5.13.:** (a) The SPD hit distributions from  $Z \rightarrow \mu\mu$  data events passing the di-muon (points) and single-muon (cyan) triggers, where the single-muon distribution is normalised to the di-muon distribution below 600 SPD hits. Between 600 and 900 SPD hits the di-muon distribution is fit with the  $\Gamma$ -function of Eq. 5.18 (line). (b) The SPD hit distribution from  $Z \rightarrow ee$  events passing the single-electron trigger (cyan) normalised to the  $Z \rightarrow \mu\mu$  di-muon distribution (points), where the shift upwards of 20 SPD hits is apparent in the  $Z \rightarrow ee$  distribution.

The tail of the di-muon trigger distribution of Fig. 5.13(a) is fit over the range 600 to 900 hits with a  $\Gamma$ -function,

$$\Gamma(x) \equiv P_0 x^{P_1} e^{-\frac{x}{P_2}} \quad (5.18)$$

where  $P_0$ ,  $P_1$ , and  $P_2$  are free parameters. This function is chosen as the SPD multiplicity should be roughly Poisson in shape. The single-muon trigger GEC efficiency,  $\varepsilon_{\text{GEC}}$ , is then evaluated as the number of events in the di-muon trigger distribution with less than 600 hits over the total number of events in the distribution plus the integrated tail of Eq. 5.18. The uncertainty on the efficiency is determined from the statistical uncertainty of the di-muon distribution and the uncertainty on the integral of the tail from the fit of the  $\Gamma$ -function.

The SPD multiplicity distribution for  $Z \rightarrow ee$  events from data requiring a single-electron trigger is given in Fig. 5.13(b), where the distribution has been normalised to the integral below 600 hits of the di-muon trigger distribution of Fig. 5.13(a). The  $Z \rightarrow ee$  events from data are selected by requiring opposite-sign electrons with  $p_T > 20$  GeV and an invariant mass within the range  $60 \leq m \leq 120$  GeV. The di-muon trigger distribution from  $Z \rightarrow \mu\mu$  events of Fig. 5.13(a) is also plotted in Fig. 5.13(b) to provide a comparison.

As can be seen in Fig. 5.13(b), the  $Z \rightarrow ee$  single-electron trigger distribution is shifted upwards

by 20 SPD hist with respect to the di-muon trigger distribution, due to additional SPD activity in the event from early showering of the electrons. The single-electron trigger GEC efficiency is evaluated with the same method used for the single-muon GEC efficiency, but with the di-muon distribution shifted upwards by 20 hits. The  $\varepsilon_{\text{GEC}}$  for both muons and electrons is found to be approximately 95%. The muon  $\varepsilon_{\text{GEC}}$  is used for the  $\tau_\mu\tau_\mu$ ,  $\tau_\mu\tau_e$ , and  $\tau_\mu\tau_h$  categories, while the electron  $\varepsilon_{\text{GEC}}$  is used for the  $\tau_e\tau_\mu$  and  $\tau_e\tau_h$  categories.

### Muon and Electron Trigger

The muon trigger efficiency,  $\varepsilon_{\text{trg}\mu}$ , is evaluated using a tag-and-probe method on  $Z \rightarrow \mu\mu$  events from data and is the probability for a muon to pass the triggers of Sect. 4.3.3. The tag is a muon passing trigger, track, and identification requirements, while the probe is a muon passing only the track and identification requirements. The tag and probe are required to have  $p_T > 10$  GeV, opposite charge, and a combined invariant mass within the range  $60 < m < 120$  GeV. The efficiency is calculated as the number of probes passing the muon trigger requirement over the total number of probes, and is evaluated as a function of the probe muon momentum in bins of 50 GeV within the range 0 to 500 GeV.

In Fig. 5.14(a) the efficiency is plotted for data, biased simulation, and unbiased simulation, and ranges from 87% to 93% for the data determined efficiency. The uncertainty on the efficiencies is determined from the statistical uncertainty on the number of events used to determine the efficiency for each bin. The biased and unbiased efficiencies match within uncertainty, indicating no bias is introduced via the event requirements.

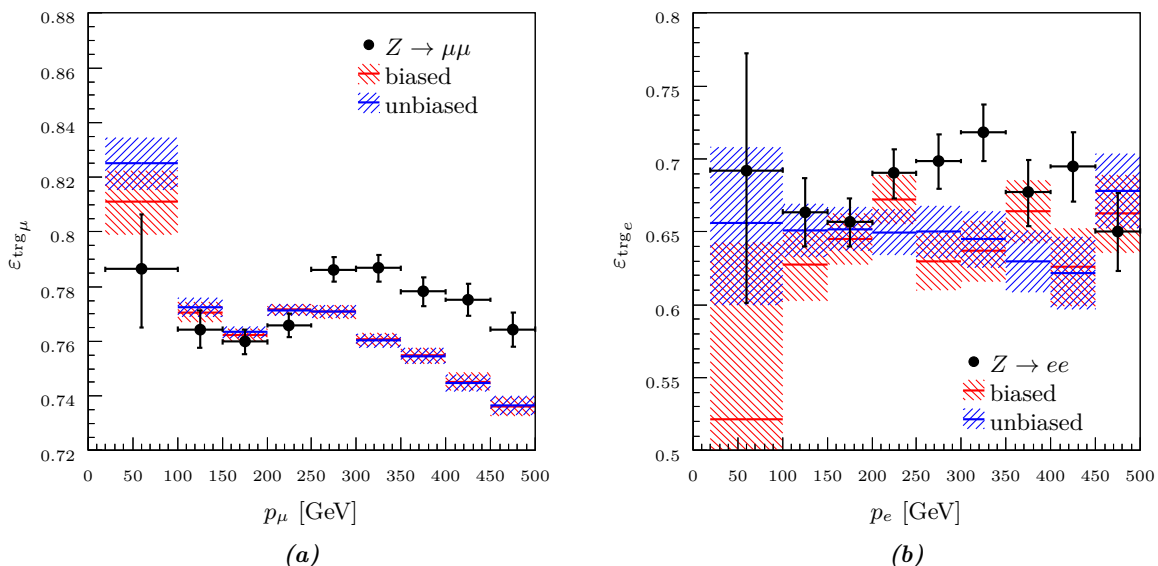


**Figure 5.14.:** (a) The muon trigger efficiency as a function of muon momentum from  $Z \rightarrow \mu\mu$  data (points), biased simulation (red), and unbiased simulation (blue). The  $\varepsilon_{\text{trg}\mu}$  is taken from the data-driven efficiency. (b) The electron trigger efficiency as a function of electron momentum from  $Z \rightarrow ee$  data (points), biased simulation (red), and unbiased simulation (blue). The  $\varepsilon_{\text{trg}e}$  is taken from the data-driven efficiency.

The electron trigger efficiency,  $\varepsilon_{\text{trg}_e}$ , is the probability for an electron to pass the triggers of Sect. 4.3.3 and is evaluated using a tag-and-probe method similar to the method for muons, but now on  $Z \rightarrow ee$  events from data. The  $Z \rightarrow ee$  sample, if selected using the same requirements as the  $Z \rightarrow \mu\mu$  trigger efficiency sample, is contaminated by a background on the order of 5%. This lowers  $\varepsilon_{\text{trg}_e}$  on the percent level and so stricter requirements on the tag and probe of  $p_T > 20$  GeV and a combined invariant mass within the range  $70 < m < 120$  GeV are required. Additionally, the tag electrons must be isolated with  $I_{p_T} < 2$  GeV.

Again, the efficiency is evaluated as a function of probe momentum in bins of 50 GeV within the range 0 to 500 GeV and is given in Fig. 5.14(b). The efficiency is found to vary from 65% to 72%. No bias is observed between the simulated samples. The uncertainty for each bin is evaluated from the statistical uncertainties of the data sample and is the primary systematic uncertainty for the  $\tau_e\tau_h$  category cross-section measurement.

### Muon Track Finding

The muon track finding efficiency,  $\varepsilon_{\text{trk}\mu}$ , is the probability for a muon to have a reconstructed track fulfilling the requirements of Sect. 5.1.1. The efficiency is determined from  $Z \rightarrow \mu\mu$  data using the tag-and-probe method diagrammed in Fig. 5.15(b), first proposed in Ref. [178]. The tag is a muon passing the trigger, track finding, and identification requirements. The probe is a track reconstructed from hits within the TT and muon system, as neither set of hits is used in the initial reconstruction of the muon track. The tag and probe are required to have  $p_T > 20$  GeV and opposite charge with a separation of  $|\Delta\phi| > 1$  radians to ensure the tag and probe are not produced from the same muon. The tag and probe are also required to be produced from the same vertex with a  $\chi^2$  less than 5.

The probe is matched with tracks fulfilling the requirements of Sect. 5.1.1. If more than 40% of the TT and muon system hits from the probe match the hits from the track, the probe is considered to have an associated reconstructed track. The tracking efficiency is evaluated as the number of probes with a reconstructed track over the total number of probes, and is given as a function of probe momentum in Fig. 5.15(a) with bins of 50 GeV from 0 to 500 GeV. The large difference between the efficiencies from data and simulation is primarily due to poor modeling of the probability  $\chi^2$  variable in simulation. A slight bias between the biased and unbiased efficiencies from simulation is introduced by the selection used to obtain the tag-and-probe sample, but is less than the uncertainty on the efficiency evaluated from data. The uncertainty is estimated as the statistical uncertainty on the sample used to calculate each bin.

The  $p_T$  requirement eliminates low momentum probes, and no efficiencies from  $Z \rightarrow \mu\mu$  data events are available for the probe momentum range of 0 to 100 GeV in Fig. 5.15(a). To access this low momentum range, the same tag-and-probe method is applied to low mass  $J/\psi \rightarrow \mu\mu$  events. Now, the tag is required to have  $p_T > 1.3$  GeV and the combined tag and probe are required to have  $p_T > 1$  GeV with an invariant mass within the range  $3.0 < m < 3.2$  GeV and vertex  $\chi^2 < 5$ . The  $J/\psi \rightarrow \mu\mu$  sample is not pure, and so the  $J/\psi$  mass peak must be fit to determine the number of signal events. Two different fit methods are used, and the difference between the tracking efficiencies determined from the two fits is estimated as the systematic



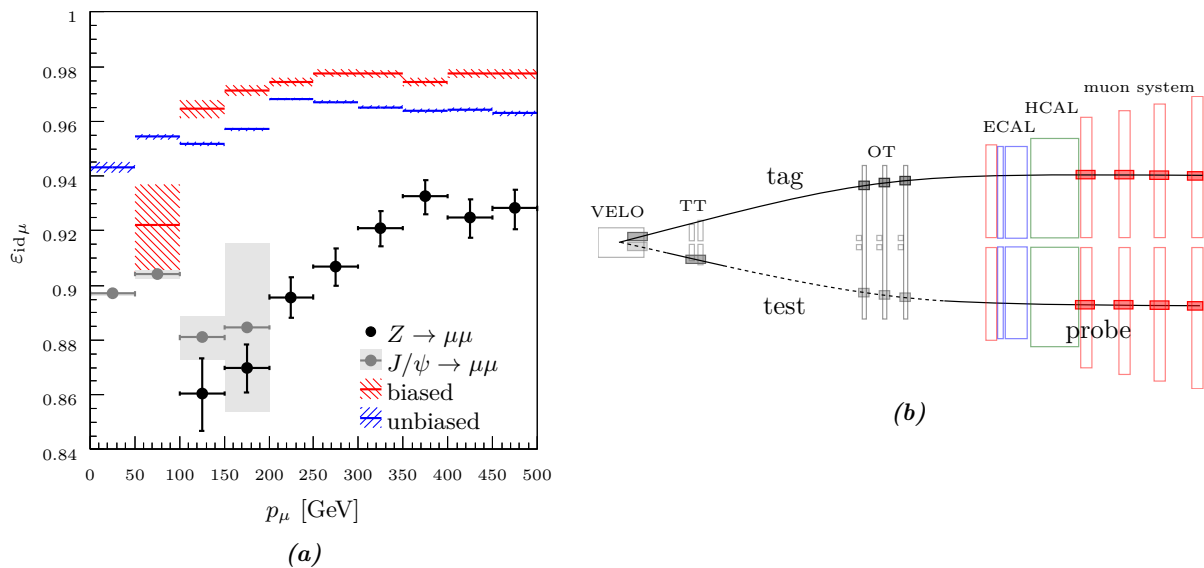


**Figure 5.15.:** (a) The muon track finding efficiency as a function of muon momentum from  $Z \rightarrow \mu\mu$  data (points),  $J/\psi \rightarrow \mu\mu$  data (grey points with uncertainty given by fill), biased simulation (red), and unbiased simulation (blue). The first three  $J/\psi$  bins and the remaining  $Z$  bins are used for  $\epsilon_{\text{trk}\mu}$ . (b) A schematic, in the bending  $xz$ -plane of the detector, for the tag-and-probe method used to determine the  $\epsilon_{\text{trk}\mu}$  from data.

uncertainty. Further details can be found in App. C.2.

The pseudo-rapidity distribution of  $J/\psi \rightarrow \mu\mu$  events differs from  $Z \rightarrow \mu\mu$  events due to the mass difference between the on-shell  $Z$  boson and  $J/\psi$  masses. Consequently, the muon tracking efficiency from  $J/\psi \rightarrow \mu\mu$  events is evaluated as a function of both probe  $\eta$  and  $p$ . The efficiency is reduced to only a function of  $p$  by taking the weighted average of the  $\eta$  bins for a given  $p$ , where the weight for each  $\eta$  bin is taken from the  $Z \rightarrow \mu\mu$  pseudo-rapidity distribution. The resultant efficiency from  $J/\psi \rightarrow \mu\mu$  events is given in Fig. 5.15(a) and matches the overlapping  $Z \rightarrow \mu\mu$  efficiencies, within uncertainty. The uncertainty on this efficiency is the combination of the systematic uncertainty from fitting the  $J/\psi$  peak and the statistical uncertainty of the sample. This uncertainty is indicated by the grey error bands of Fig. 5.15(a).

The  $\epsilon_{\text{trk}\mu}$  used in Eq. 5.16 and given in Table 5.4 is evaluated from the  $J/\psi \rightarrow \mu\mu$  efficiency for muon momenta between 0 to 150 GeV and from the  $Z \rightarrow \mu\mu$  efficiency for momenta between 150 and 500 GeV. The efficiency is found to range from 87% to 93%.

### Electron Track Finding

The electron track finding efficiency,  $\epsilon_{\text{trk}e}$ , is the probability that an electron produces a reconstructable track, and is determined using the tag-and-probe method diagrammed in Fig. 5.16(b) on  $Z \rightarrow ee$  events from data. The tag is an electron passing the trigger, track finding, and identification requirements of Sect. 5.1.1 with a  $p_T > 20$  GeV, while the probe is an ECAL cluster with an  $E_T > 5$  GeV. The tag is required to be isolated with  $I_{p_T} < 2$  GeV and the HCAL energy in a cone of  $\Delta R < 5$  about the probe must be less than 50% of the ECAL energy in the

same cone. The tag and probe are required to be back-to-back in the azimuthal plane with  $|\Delta\phi| > 3$  radians and the difference in ECAL  $E_T$  between the probe and tag must be less than 20% of the ECAL  $E_T$  of the probe.

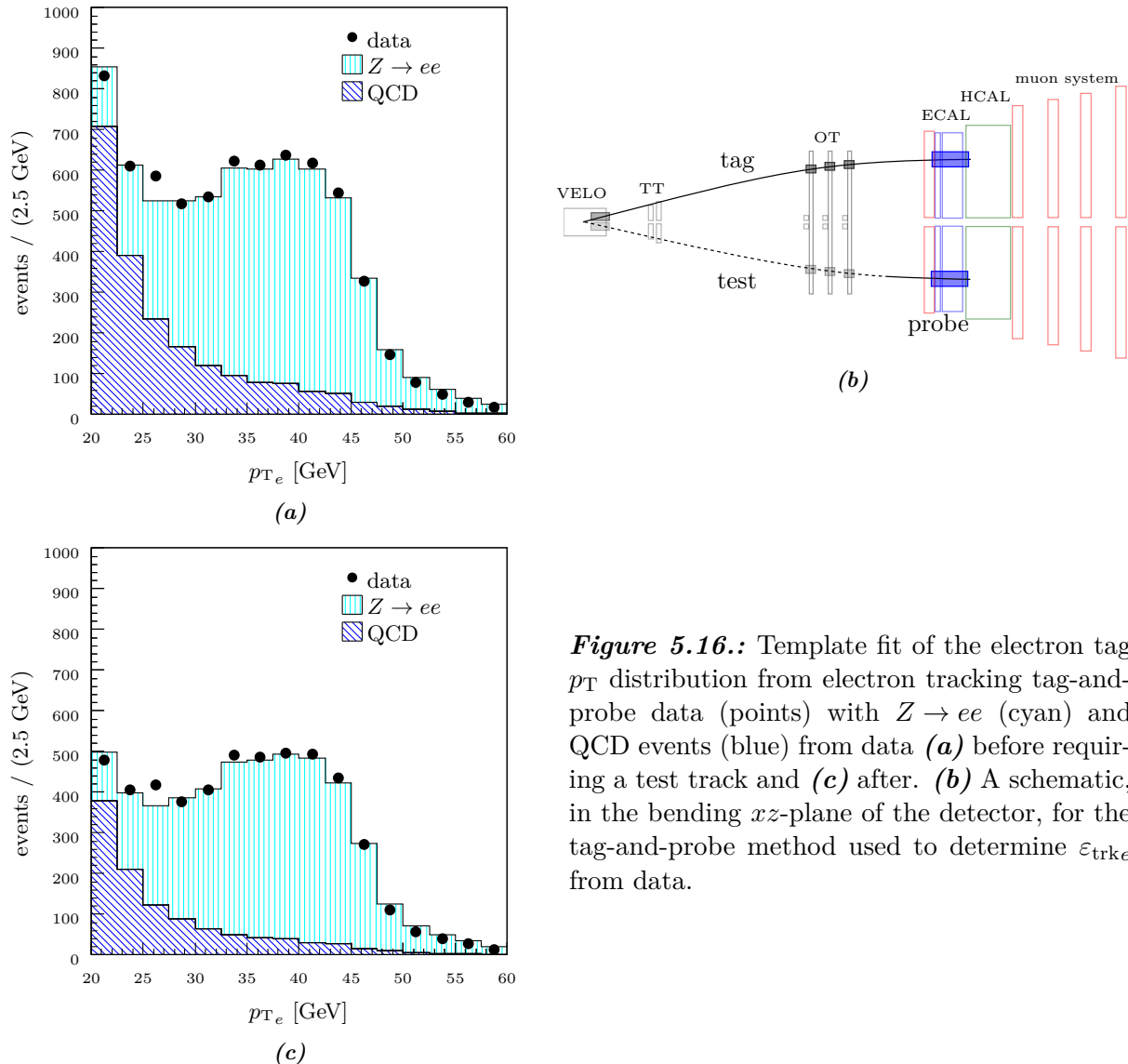


**Figure 5.16.:** Template fit of the electron tag  $p_T$  distribution from electron tracking tag-and-probe data (points) with  $Z \rightarrow ee$  (cyan) and QCD events (blue) from data (a) before requiring a test track and (c) after. (b) A schematic, in the bending  $xz$ -plane of the detector, for the tag-and-probe method used to determine  $\varepsilon_{\text{tr}ke}$  from data.

This selection results in a sample of  $Z \rightarrow ee$  events contaminated with a small QCD background. The purity of the sample is determined by fitting the  $p_T$  distribution of the tag with  $Z \rightarrow ee$  and QCD templates. For  $Z \rightarrow ee$  events a peak is expected in the tag  $p_T$  distribution at half the on-shell mass of the  $Z$  boson, while a much softer distribution is expected from QCD events. The  $Z \rightarrow ee$  template is constructed by selecting events from data with two identified electrons with opposite charge and a combined invariant mass in the range  $60 < m < 120$  GeV. The QCD template is taken from data using the same requirements as the tag-and-probe sample, but omitting the tag isolation, azimuthal separation, and  $E_T$  balance requirements. Additionally, the sub-leading  $p_T$  track in the event must have the same charge as the leading  $p_T$  tag.

The fit of the  $Z \rightarrow ee$  tag-and-probe  $p_T$  distribution with the  $Z \rightarrow ee$  and QCD templates,

is given in Fig. 5.16(a), resulting in a signal purity of approximately 70%. The tag-and-probe sample is tested for electron track finding by requiring a track, fulfilling the requirements of Sect. 5.1.1, with opposite charge and an azimuthal separation of  $|\Delta\phi| > 2.5$  radians with the tag. The fit of this distribution is given in Fig. 5.16(c) and is estimated to have a signal purity of approximately 80%. As expected, both the total number of events and the QCD background in this distribution are reduced.

The electron track finding efficiency is calculated as the number of  $Z \rightarrow ee$  signal events from Fig. 5.16(c), after requiring a track, over the number of signal events from Fig. 5.16(a), prior to requiring a track, and is found to be  $(83.0 \pm 0.3)\%$ . The uncertainty is estimated from the fit uncertainty combined in quadrature with the statistical uncertainty of the efficiency. While no momentum information is available, the electron track finding efficiencies from simulated  $Z \rightarrow ee$  and  $Z \rightarrow \tau\tau$  events are found to be in statistical agreement with values of  $(85.2 \pm 0.2)\%$  and  $(85.7 \pm 4.9)\%$ , respectively. These two efficiencies demonstrate that while the electron tracking efficiency is estimated from generator level simulation to have a momentum dependence, the net effect is small. No additional systematic uncertainty is included in the  $\varepsilon_{\text{re}ce}$  uncertainty for this effect. The  $\varepsilon_{\text{re}ce}$  uncertainty is the dominant systematic uncertainty for the cross-section measurements of the  $\tau_\mu\tau_e$  and  $\tau_e\tau_\mu$  categories, as well as a large systematic uncertainty for the  $\tau_e\tau_h$  category cross-section measurement.

### Charged Hadron Track Finding

The charged hadron track finding efficiency,  $\varepsilon_{\text{tr}kh}$ , is the probability for a charged hadron to produce a reconstructable track. Prior to the final tracking station, particles pass through approximately 20% of a hadronic interaction length of material, resulting in the early showering of charged hadrons caused by their nuclear interactions with the detector material. Consequently, the muon track finding efficiency is used as the charged hadron track finding efficiency, but with a correction for additional material interactions which is estimated from  $Z \rightarrow \tau\tau$  simulation to be  $(84.3 \pm 1.5)\%$ . The uncertainty on this correction factor is from the uncertainty of the LHCb material budget of 10% [179].

The grey points in Fig. 5.17 are the muon track finding efficiency from Fig. 5.15(a) as a function of momentum, corrected for material interactions, and are used as the hadron track finding efficiency. The grey bands indicate the uncertainty on the efficiency which is the combination of the muon track finding efficiency uncertainty and the correction uncertainty. The uncorrected muon track finding efficiency from data is also plotted in Fig. 5.17, as well as the unbiased muon and charged hadron track finding efficiencies from simulation. The hadron track finding efficiency ranges from values of 73% to 79%.

### Muon Identification

The muon identification efficiency is the probability for a muon with a track to pass the muon identification requirements of Sect. 5.1.1. Here, the muon is already required to have a reconstructed track from hits within the VELO and TT stations and a search for hits from the

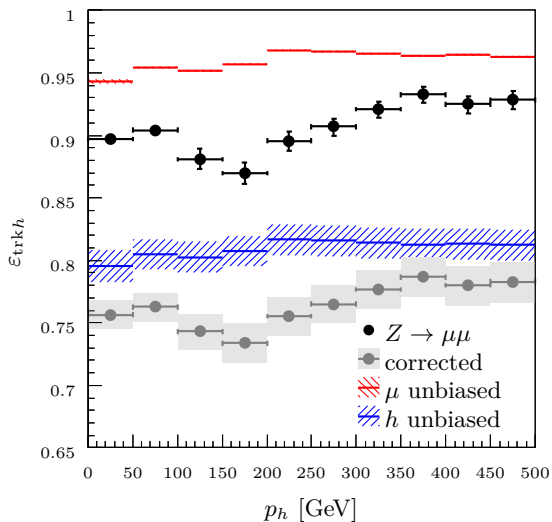


**Figure 5.17.:** The charged hadron track finding efficiency (points with fill) determined from the  $Z \rightarrow \mu\mu$  data-driven muon track finding efficiency (points) corrected for hadronic nuclear interactions. The associated uncertainty is the LHCb material budget uncertainty combined in quadrature with the muon track finding uncertainty. The unbiased muon (red) and charged hadron (blue) track finding efficiencies from simulation are shown for comparison.

muon system is performed, in contrast to the muon track finding efficiency where a track is not required *a priori* and hits from the muon system are not required. The muon identification efficiency is evaluated from data using a tag-and-probe method on  $Z \rightarrow \mu\mu$  data, diagrammed in Fig. 5.18(b), where the tag is a muon passing the trigger, track, and identification requirements and the probe is a muon passing the track requirements. Additionally, the tag and probe are required to have  $p_T > 20$  GeV, an isolation of  $I_{p_T} < 2$  GeV, opposite charge, and a combined invariant mass within the range  $60 < m < 120$  GeV. The efficiency is then taken as the number of probes with associated hits in each of the four outermost muon stations over the total number of probes.

The muon identification efficiency from  $Z \rightarrow \mu\mu$  events is determined with respect to the probe momentum, and is plotted in Fig. 5.18(a). Due to the  $p_T$  requirements on the tag and probe, the low momentum bins between 0 and 150 GeV must be supplemented using efficiencies from  $J/\psi \rightarrow \mu\mu$  events. For the  $J/\psi \rightarrow \mu\mu$  sample, the probe must have  $p_T > 1.5$  GeV and  $p > 6$  GeV while the tag must have  $p_T > 0.8$  GeV and  $p > 3$  GeV. The combined invariant mass of the  $J/\psi \rightarrow \mu\mu$  tag and probe is required to be within the range  $3.0 < m < 3.2$  and the vertex  $\chi^2$  for the event must be less than 8.

Just as for the muon track finding efficiency, the pseudo-rapidity distributions between the  $J/\psi \rightarrow \mu\mu$  and  $Z \rightarrow \mu\mu$  samples differ. Consequently, the muon identification efficiency from  $J/\psi \rightarrow \mu\mu$  events is evaluated as a function of probe  $\eta$  and  $p$ . This efficiency is reduced to a function of only  $p$  using the same weighted average method as the muon track finding efficiency and is given in Fig. 5.18(a). The uncertainty on this efficiency is the combination of the statistical uncertainty for the sample and the uncertainty from the fit of the  $J/\psi$  peak.

The two overlapping bins between the  $J/\psi \rightarrow \mu\mu$  and  $Z \rightarrow \mu\mu$  tag-and-probe efficiencies match within uncertainty, although the uncertainty for the final  $J/\psi \rightarrow \mu\mu$  bin is large due to poor fits from low statistics. Additionally, the decrease in efficiency at low momentum for the  $Z \rightarrow \mu\mu$  tag-and-probe efficiency arises from minor background contamination in the data sample. There is good agreement between the biased and unbiased efficiencies from simulation, verifying no

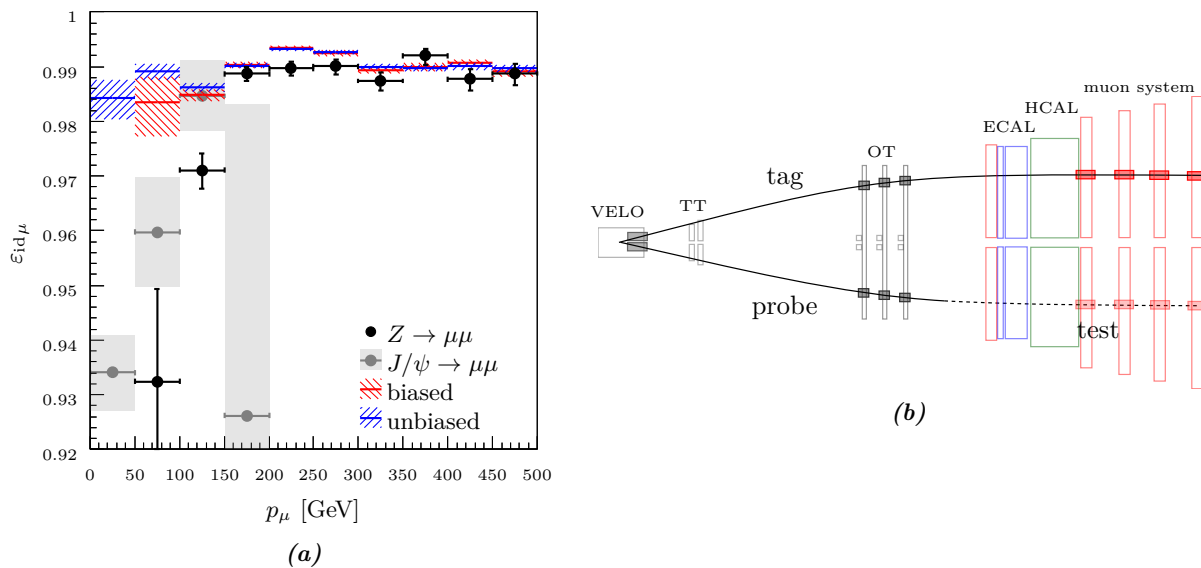


**Figure 5.18.:** (a) The muon identification efficiency as a function of muon momentum from  $Z \rightarrow \mu\mu$  data (points),  $J/\psi \rightarrow \mu\mu$  data (points with fill), biased simulation (red), and unbiased simulation (blue). The first three  $J/\psi$  bins and the remaining  $Z$  bins are used for  $\epsilon_{id\mu}$ . (b) A schematic, in the bending  $xz$ -plane of the detector, for the tag-and-probe method used to determine  $\epsilon_{id\mu}$  from data.

bias has been introduced by the  $Z \rightarrow \mu\mu$  selection requirements. The biased efficiency is determined from applying the  $Z \rightarrow \mu\mu$  tag-and-probe method to simulation, while the unbiased efficiency is taken directly from the generator level information in simulation. The muon identification efficiency, used in Eq. 5.16 and given in Table 5.4, is taken from the  $J/\psi \rightarrow \mu\mu$  data for  $0 < p < 150$  GeV and from the  $Z \rightarrow \mu\mu$  data for  $150 < p < 500$  GeV, with values ranging from 93% to 99%.

### Electron Identification

The probability for an electron with a track fulfilling the requirements of Sect. 5.1.1 to pass the electron identification requirements is given by the electron identification efficiency,  $\epsilon_{ide}$ . This efficiency is determined using the tag-and-probe method of Fig. 5.19(b) on  $Z \rightarrow ee$  events from data. The tag is an electron passing the trigger, track, and identification requirements with  $p_T > 20$  GeV, while the probe is a track, also with  $p_T > 20$  GeV. Both the tag and probe are required to be isolated with  $I_{p_T} < 2$  GeV, have a combined invariant mass within the range  $60 < m < 120$  GeV, and an azimuthal separation of  $|\Delta\phi| > 3.0$  radians.

The efficiency is then calculated as the number of probes passing the electron identification requirements over the total number of probes, and is plotted as a function of probe momentum in Fig. 5.19(a). A large bias is introduced by the tag-and-probe selection requirements, as can be seen by the disagreement between the biased and unbiased efficiencies from simulation. Relaxing the selection requirements reduces the bias, but introduces background contamination to the  $Z \rightarrow ee$  signal.

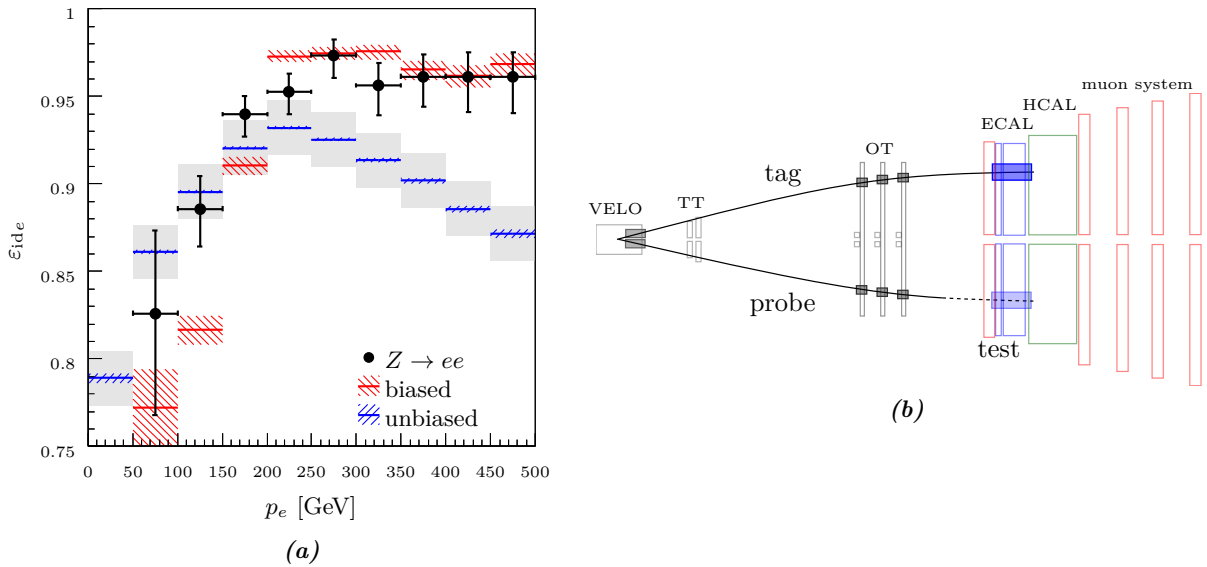


**Figure 5.19.:** (a) The electron identification efficiency as a function of electron momentum from  $Z \rightarrow ee$  data (points), biased simulation (red), and unbiased simulation (blue). The  $\varepsilon_{ide}$  is taken as the unbiased efficiency with the total efficiency difference between data and biased simulation estimated as the associated uncertainty (grey fill). (b) A schematic, in the bending  $xz$ -plane of the detector, for the tag-and-probe method used to determine  $\varepsilon_{ide}$  from data.

However, the efficiency from data matches the efficiency from biased simulation, and so the unbiased efficiency from simulation is taken to describe the inaccessible unbiased efficiency from data. Consequently, the electron identification efficiency used in Eq. 5.16 and given in Table 5.4 is evaluated as the unbiased efficiency from simulation, and ranges between values of 79% to 93%. The uncertainty is estimated as the difference between the total biased efficiencies from simulation and data, combined in quadrature with the statistical uncertainty from simulation. This uncertainty is shown in Fig. 5.19(a) as the grey band about the unbiased efficiency.

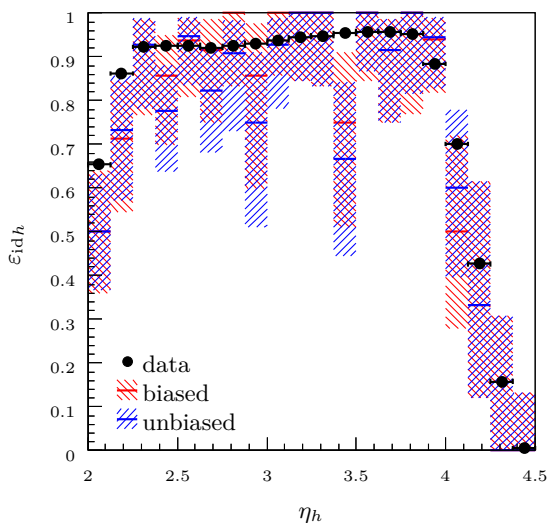


**Figure 5.20.:** Hadron identification efficiency as a function of hadron pseudo-rapidity from minimum bias data (points), biased simulation (red), and unbiased simulation (blue). The drop-off in efficiency at low and high pseudo-rapidity is due to HCAL geometrical acceptance.

**Table 5.5.:** The total selection efficiency and component selection efficiencies corresponding to the selection requirements of Sect. 5.1.2.

|                              | $\tau_\mu\tau_\mu$ | $\tau_\mu\tau_e$  | $\tau_e\tau_\mu$  | $\tau_\mu\tau_h$  | $\tau_e\tau_h$    |
|------------------------------|--------------------|-------------------|-------------------|-------------------|-------------------|
| $\varepsilon_{\text{sel}}$   | $0.138 \pm 0.006$  | $0.517 \pm 0.012$ | $0.344 \pm 0.016$ | $0.135 \pm 0.004$ | $0.082 \pm 0.004$ |
| $\varepsilon_{\text{kin}}$   | —                  | $0.993 \pm 0.010$ | $0.668 \pm 0.019$ | —                 | $0.670 \pm 0.013$ |
| $\varepsilon_{I_{p_T}}$      | $0.660 \pm 0.012$  | $0.613 \pm 0.012$ | $0.623 \pm 0.020$ | $0.413 \pm 0.007$ | $0.386 \pm 0.011$ |
| $\varepsilon_{ \Delta\phi }$ | $0.848 \pm 0.009$  | $0.850 \pm 0.009$ | $0.827 \pm 0.015$ | $0.845 \pm 0.005$ | $0.838 \pm 0.008$ |
| $\varepsilon_{\text{IPS}}$   | $0.414 \pm 0.011$  | —                 | —                 | $0.387 \pm 0.007$ | $0.379 \pm 0.011$ |
| $\varepsilon_{A_{p_T}}$      | $0.597 \pm 0.012$  | —                 | —                 | —                 | —                 |

### Hadron Identification

The charged hadron identification,  $\varepsilon_{\text{id}_h}$ , is the probability for a hadron with a reconstructed track fulfilling the requirements of Sect. 5.1.1 to pass the charged hadron particle identification requirements. Events selected using a minimum bias trigger from data are assumed to consist primarily of charged hadrons, validated with simulation, and so this efficiency is taken as the percentage of events where the highest  $p_T$  track in the event, with a minimum  $p_T$  of 5 GeV passes the charged hadron identification requirements. The efficiency as a function of hadron momentum is flat, but is highly dependent upon  $\eta$  due to the acceptance of the HCAL, as can be seen in Fig. 5.20. Consequently,  $\varepsilon_{\text{id}_h}$  is evaluated from minimum bias data in pseudo-rapidity bins of 0.125 and found to range from 92% to 96%.

### 5.2.2. Selection Efficiency

The event selection efficiency,  $\varepsilon_{\text{sel}}$ , is the probability for an event with two reconstructed  $\tau$  lepton decay product candidates to pass the selection requirements of Sect. 5.1.2 summarised in Table 5.2. The event selection efficiency is defined as,

$$\varepsilon_{\text{sel}} \equiv \varepsilon_{\text{kin}} \varepsilon_{I_{p_T}} \varepsilon_{|\Delta\phi|} \varepsilon_{\text{IPS}} \varepsilon_{A_{p_T}} \quad (5.19)$$

where each component is the efficiency for a reconstructed event to pass the corresponding selection of Table 5.2. The invariant mass selection efficiency is excluded, as this efficiency is by definition one. However, a kinematic efficiency,  $\varepsilon_{\text{kin}}$ , is included which is the probability for a true reconstructable event passing the kinematic requirements of Sect. 5.1.2 to have its reconstruction also fulfil the same kinematic requirements. Each component efficiency from Eq. 5.19 is determined from either data or simulation calibrated to data, with the component values for each event category tabulated in Table 5.5. More details on the determination for each component efficiency are provided in the remainder of this section.

### Kinematic

The kinematic efficiency is found by applying the pseudo-rapidity,  $p_T$ , and invariant mass requirements of Sect. 5.1.2 to simulated  $Z \rightarrow \tau\tau$  events. The efficiency is defined as the number

of events fulfilling these requirements at the reconstructed level of simulation divided by the number of events fulfilling the requirements at the generated level of simulation. For the  $\tau_\mu\tau_\mu$  and  $\tau_\mu\tau_h$  categories  $\varepsilon_{\text{rec}}$  is found to be consistent with unity, as these variables are well reconstructed for both muons and hadrons. Because of ECAL saturation, described in Sect. 4.3.2, the brehmsstrahlung recovery for high  $p_T$  electrons is incomplete, and their reconstructed momenta is lower than their generated momenta. This leads to low kinematic efficiencies for the  $\tau_e\tau_\mu$  and  $\tau_e\tau_h$  categories, on the order of 70%, and an efficiency near one for the  $\tau_\mu\tau_e$  category, as given in Table 5.5.

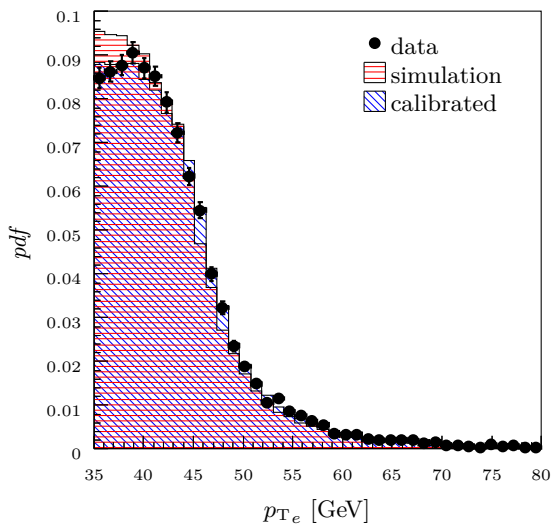


**Figure 5.21.:** The  $p_T$  distribution of  $Z \rightarrow ee$  events from data (points), uncalibrated simulation (red), and calibrated simulation (blue). The calibrated distribution of the electron  $p_T$  is scaled by a factor of  $1.02 \pm 0.01$  and is applied when evaluating  $\varepsilon_{\text{kin}}$  for the  $\tau_\mu\tau_e$ ,  $\tau_e\tau_\mu$ , and  $\tau_e\tau_h$  categories.

When calculating  $\varepsilon_{\text{kin}}$  for the categories containing an electron, the  $p_T$  distribution of the electrons is scaled by a factor of  $1.02 \pm 0.01$ . The scale is determined from a fit between the electron  $p_T$  distributions of  $Z \rightarrow ee$  events from simulation and data, where the procedure for the fit is similar to the invariant mass fit of Sect. 5.1.2; the result of the fit is given in Fig. 5.21. The associated uncertainties for the  $\varepsilon_{\text{kin}}$  values are estimated as the propagated electron  $p_T$  scale uncertainty combined in quadrature with the statistical uncertainty from simulation.

### Track Isolation

The track isolation variable of Eq. 5.6,  $I_{p_T}$ , is not well described by simulation, as previously shown in Fig. 5.6(a), due to an underestimation of the underlying event. However, the  $I_{p_T}$  distributions for  $Z \rightarrow \mu\mu$  and  $Z \rightarrow \tau_\mu\tau_\mu$  events from simulation match, as the underlying event topologies are identical. Consequently, the track isolation selection efficiency,  $\varepsilon_{I_{p_T}}$ , for each category is calculated from  $Z \rightarrow \tau\tau$  simulation and calibrated to data by the ratio of the  $I_{p_T}$  selection efficiencies from  $Z \rightarrow \mu\mu$  data to  $Z \rightarrow \tau\tau$  simulation. The uncertainty for  $\varepsilon_{I_{p_T}}$  is estimated as the difference between the  $I_{p_T}$  selection efficiencies evaluated using events from  $Z \rightarrow \mu\mu$  and  $Z \rightarrow \tau_\mu\tau_\mu$  simulation.

The  $I_{p_T}$  selection efficiencies for the  $\tau_\mu\tau_\mu$ ,  $\tau_\mu\tau_e$ , and  $\tau_e\tau_\mu$  categories are given in Table 5.5 and range from approximately (60 – 70)%. For the  $\tau_\mu\tau_\mu$  and  $\tau_e\tau_\mu$  categories, both with an electron in the final state, the efficiency is slightly lower than the  $\tau_\mu\tau_\mu$  category due to contamination of



the electron candidate isolation by pair production from brehmstrahlung photons. The harsher isolation requirement for the semi-leptonic  $\tau_\mu\tau_h$  and  $\tau_e\tau_h$  categories,  $I_{p_T} < 1$  GeV, results in an efficiency of approximately 40% which is slightly lower for the  $\tau_e\tau_h$  category, again as a result of brehmstrahlung radiation from the electron.

### Azimuthal Angle and Transverse Momentum Asymmetry

Both the variables of azimuthal angle separation and transverse momentum asymmetry are well described by simulation, as previously shown in Figs. 5.7(a) and 5.10(a). The two selection efficiencies,  $\varepsilon_{|\Delta\phi|}$  and  $\varepsilon_{A_{p_T}}$  are determined from simulation and are given for each category in Table 5.2. The  $\varepsilon_{|\Delta\phi|}$  is found to be approximately 85% for all categories, while the  $\varepsilon_{A_{p_T}}$  is found to be approximately 60% for  $\tau_\mu\tau_\mu$  events. The associated uncertainty for each category is estimated as the difference between these efficiencies evaluated in  $Z \rightarrow \mu\mu$  data and simulation, combined in quadrature with the statistical uncertainty on the efficiency from  $Z \rightarrow \tau\tau$  simulation.

### Impact Parameter Significance

The impact parameter significance requirement efficiency,  $\varepsilon_{\text{IPS}}$ , is calculated from  $Z \rightarrow \tau\tau$  simulation using the IPS calibration of Sect. 5.1.2, with the agreement between data and calibrated simulation previously shown in Fig. 5.9(a). The uncertainty on  $\varepsilon_{\text{IPS}}$  is determined by re-calculating the efficiency in simulated  $Z \rightarrow \tau\tau$  events, where the calibration factor has been varied within uncertainty. This uncertainty is the dominant systematic uncertainty for the cross-section measurement of the  $\tau_\mu\tau_h$  category. For the  $\tau_\mu\tau_\mu$ ,  $\tau_\mu\tau_h$ , and  $\tau_e\tau_h$  categories the  $\varepsilon_{\text{IPS}}$  is on the order of 40%, as given in Table 5.5.

### 5.2.3. Acceptance and Branching Fractions

Without an acceptance factor,  $\mathcal{A}_{\tau_1\tau_2}$ , the cross-section calculation of Eq. 5.15 would yield a measurement dependent upon the the kinematic requirements of Sect. 5.1.2 on the pseudo-rapidities, transverse momenta, and combined invariant mass of the  $\tau$  lepton decay products for each category. Consequently, to allow comparison between these cross-section measurements and the  $pp \rightarrow Z \rightarrow \mu\mu$  and  $pp \rightarrow Z \rightarrow ee$  cross-sections of Refs. [173] and [172], the acceptance factor corrects the kinematics for each category to  $60 < m_{\tau\tau} < 120$  GeV,  $p_{T\tau} > 20$  GeV, and  $2.0 \leq \eta_\tau \leq 4.5$  with no  $\tau$  lepton final state radiation. The acceptance factor is taken from  $Z \rightarrow \tau\tau$  simulation and is defined for each category as the number of events, after electroweak final state radiation, passing the  $\eta$ ,  $p_T$ , and  $m$  requirements of Sect. 5.1.2 over the number of events, before electroweak final state radiation, passing the requirements  $60 < m_{\tau\tau} < 120$  GeV,  $p_{T\tau} > 20$  GeV, and  $2.0 \leq \eta_\tau \leq 4.5$ .

Simulation samples are generated for each category using PYTHIA 8 [10, 11, 12] at leading order, HERWIG++ [72, 73] at leading order, and HERWIG++ at next-to-leading order using the POWHEG method [180]. The  $\tau$  lepton decays in PYTHIA 8 are simulated using the methods of Chap. 3 with full spin correlations, while the  $\tau$  lepton decays in HERWIG++ are also decayed

**Table 5.6.:** The acceptances  $\mathcal{A}_{\tau_1\tau_2}$ , and branching fractions  $\mathcal{B}_{\tau_1\tau_2}$ , as a percent, for each of the five categories.

|                              | $\tau_\mu\tau_\mu$ | $\tau_\mu\tau_e$  | $\tau_e\tau_\mu$  | $\tau_\mu\tau_h$   | $\tau_e\tau_h$     |
|------------------------------|--------------------|-------------------|-------------------|--------------------|--------------------|
| $\mathcal{A}_{\tau_1\tau_2}$ | $0.405 \pm 0.006$  | $0.248 \pm 0.004$ | $0.152 \pm 0.002$ | $0.182 \pm 0.002$  | $0.180 \pm 0.002$  |
| $\mathcal{B}_{\tau_1\tau_2}$ | $3.031 \pm 0.014$  | $6.208 \pm 0.020$ | $6.208 \pm 0.020$ | $16.933 \pm 0.056$ | $17.341 \pm 0.057$ |

with full spin correlations and decay models as outlined in Ref. [97]. The CTEQ6L1 leading-order PDF set [181] was used with PYTHIA 8 while the MSTW08 PDF sets [57] were used with HERWIG++. A sufficient number of events were generated to ensure the statistical uncertainties for each sample are much less than the associated systematic uncertainties.

The acceptance factors for each category are given in Table 5.6 and are calculated as the mean of the maximum and minimum acceptances from the three samples. The uncertainty is taken as half the difference between the maximum and minimum values. Because the three samples encompass different PDF sets,  $\tau$  lepton decay and correlation mechanisms, hard matrix elements, initial state radiation, and final state radiation, this uncertainty determination is expected to provide a conservative estimate.

The  $\tau_\mu\tau_\mu$  acceptance of Table 5.6 is the largest of the five categories, as both muons can fulfill either of the two  $p_T$  requirements. The remaining acceptances are smaller than the  $\tau_\mu\tau_\mu$  acceptance as the two  $\tau$  lepton decay product candidates are not the same particle type. The  $\tau_e\tau_\mu$  acceptance is smaller than the  $\tau_\mu\tau_e$  acceptance because of the additional  $p_{T\mu} < 20$  GeV requirement. The  $\tau_\mu\tau_h$  and  $\tau_e\tau_h$  acceptances are also smaller than the  $\tau_\mu\tau_e$  acceptance, primarily from the additional  $2.25 \leq \eta_h \leq 3.75$  requirement.

The branching fractions for each category, given in Table 5.6, are calculated using the world averaged  $\tau$  lepton decay branching fractions of Ref. [15],

$$\begin{aligned}
\mathcal{B}_{\tau_\mu\tau_\mu} &= \mathcal{B}_{\tau^- \rightarrow \nu_\tau \mu^- \bar{\nu}_\mu} \mathcal{B}_{\tau^- \rightarrow \nu_\tau \mu^- \bar{\nu}_\mu}, & \mathcal{B}_{\tau_\mu\tau_e, \tau_e\tau_\mu} &= 2\mathcal{B}_{\tau^- \rightarrow \nu_\tau \mu^- \bar{\nu}_\mu} \mathcal{B}_{\tau^- \rightarrow \nu_\tau e^- \bar{\nu}_e} \\
\mathcal{B}_{\tau_\mu\tau_h} &= 2\mathcal{B}_{\tau^- \rightarrow \nu_\tau \mu^- \bar{\nu}_\mu} \mathcal{B}_{\tau^- \rightarrow \nu_\tau h^- \geq 0h^0}, & \mathcal{B}_{\tau_e\tau_h} &= 2\mathcal{B}_{\tau^- \rightarrow \nu_\tau e^- \bar{\nu}_e} \mathcal{B}_{\tau^- \rightarrow \nu_\tau h^- \geq 0h^0}
\end{aligned}
\tag{5.20}$$

where  $\mathcal{B}_{\tau^- \rightarrow \nu_\tau h^- \geq 0h^0}$  is the branching fraction of a  $\tau$  lepton to a single charged hadron with zero or more neutral hadrons. The uncertainty on the branching fraction for each category is propagated from the uncertainties on the  $\tau$  lepton branching fractions, assuming the uncertainty for each unique channel is uncorrelated and normally distributed.

### 5.3. Results

The cross-sections for each category are determined using Eq. 5.15 and the values presented in Tables 5.3, 5.4, 5.5, and 5.6. These cross-sections are calculated for the production of  $Z$  bosons, with photon interference, from proton-proton collisions at  $\sqrt{s} = 7$  TeV where the  $Z$  boson mass is between 60 and 120 GeV and the  $Z$  boson decays into a  $\tau$  lepton pair, both within the pseudo-rapidity range  $2.0 \leq \eta \leq 4.5$  and with transverse momenta greater than 20 GeV. A summary of the systematic uncertainties for these values propagated to percentage uncertainties on the

cross-section is given in Table 5.7. The results for each event category are,

$$\begin{aligned}
\sigma_{pp \rightarrow Z \rightarrow \tau\tau} (\tau_\mu\tau_\mu) &= 77.4 \pm 10.4 \pm 8.6 \pm 2.7 \text{ pb} \\
\sigma_{pp \rightarrow Z \rightarrow \tau\tau} (\tau_\mu\tau_e) &= 75.2 \pm 5.4 \pm 4.1 \pm 2.6 \text{ pb} \\
\sigma_{pp \rightarrow Z \rightarrow \tau\tau} (\tau_e\tau_\mu) &= 64.2 \pm 8.2 \pm 4.9 \pm 2.2 \text{ pb} \\
\sigma_{pp \rightarrow Z \rightarrow \tau\tau} (\tau_\mu\tau_h) &= 68.3 \pm 7.0 \pm 2.6 \pm 2.4 \text{ pb} \\
\sigma_{pp \rightarrow Z \rightarrow \tau\tau} (\tau_e\tau_h) &= 77.9 \pm 12.2 \pm 6.1 \pm 2.7 \text{ pb}
\end{aligned} \tag{5.21}$$

where the first uncertainty is statistical, the second is systematic, and the third is due to the uncertainty on the integrated luminosity.

A fit of the five cross-sections is performed using the method of the best linear unbiased estimator [182] with further details given in App. C.3. A combined result of,

$$\sigma_{pp \rightarrow Z \rightarrow \tau\tau} = 72.3 \pm 3.5 \pm 2.9 \pm 2.5 \tag{5.22}$$

with a  $\chi^2$  per degrees of freedom of 0.40 is obtained. Each category is a mutually exclusive dataset, and so the statistical uncertainties were assumed to be uncorrelated, while the luminosity and shared reconstruction and selection efficiencies are assumed to be fully correlated. The theoretical cross-section for  $\sigma_{pp \rightarrow Z \rightarrow \tau\tau}$  is  $74.3^{+1.9}_{-2.1}$  pb, and was calculated at next-to-next-to-leading order using DYNLO [183, 184, 185] with the MSTW08 NNLO PDF set [57].

A graphical comparison between the combined result of Eq. 5.22 and the individual results of Eq. 5.21 is given in Fig. 5.22 where the values are expressed as the ratio of experiment to theory. The theoretical uncertainty is given by the blue band centered about unity, while the statistical uncertainty is given by the dark inner error bars and the systematic and luminosity uncertainty are given by the light outer error bars for each point. Each decay channel of the  $Z$  boson is highlighted in red, while the  $\tau$  lepton decay categories for the  $Z \rightarrow \tau\tau$  channels are given in black. Comparisons to the  $pp \rightarrow Z \rightarrow \mu\mu$  [173] and  $pp \rightarrow Z \rightarrow ee$  [172] cross-sections from LHCb are made, as well as the  $pp \rightarrow Z \rightarrow \tau\tau$  cross-section measurements from ATLAS [187, 186] and CMS [188].

All measurements, within uncertainty, are consistent with their corresponding SM theory predictions. Of the three combined  $pp \rightarrow Z \rightarrow \tau\tau$  measurements, the LHCb measurement of this chapter is the most precise, primarily due to a much lower systematic uncertainty than either the ATLAS or CMS measurements, specifically in the semi-hadronic final states. Both ATLAS and CMS reconstruct hadronic final states of the  $\tau$  lepton decay using jet reconstruction algorithms, resulting in large uncertainties on the jet energy scale and identification efficiency. The combined cross-section uncertainty for the LHCb measurement is 7.2% while the ATLAS uncertainty is 9.5% and the CMS uncertainty is 10.2%.

The efficacy of the VELO subdetector in separating  $Z \rightarrow \tau\tau$  events in the  $\tau_\mu\tau_\mu$  category from  $Z \rightarrow \mu\mu$  events is clear, in comparison to the  $\tau_\mu\tau_\mu$  results from ATLAS and CMS. In this category, LHCb achieves a signal purity of approximately 70% while ATLAS attains a purity of 50% and CMS a purity of 60%. The purity of the LHCb  $\tau_\mu\tau_e$  category is slightly reduced to

**Table 5.7.:** Systematic uncertainties expressed as a percentage of the cross-section for each  $Z \rightarrow \tau\tau$  category. The acceptance  $\mathcal{A}_{\tau_1\tau_2}$ , branching fractions  $\mathcal{B}_{\tau_1\tau_2}$ , number of background events  $N_{\text{bkg}}$ , reconstruction efficiency  $\varepsilon_{\text{rec}}$ , and selection efficiency  $\varepsilon_{\text{sel}}$  contributions are listed, where the numerical subscripts indicate the first or second  $\tau$  lepton decay product candidate. The percentage uncertainties on the cross-section for  $N_{\text{bkg}}$  are given for each background and the total background. A similar splitting of the efficiency uncertainties is also provided.

|                                  |                          | $\delta\sigma_{pp \rightarrow Z \rightarrow \tau\tau}$ [%] |                  |                  |                  |                |
|----------------------------------|--------------------------|--|------------------|------------------|------------------|----------------|
|                                  |                          | $\tau_\mu\tau_\mu$   | $\tau_\mu\tau_e$ | $\tau_e\tau_\mu$ | $\tau_\mu\tau_h$ | $\tau_e\tau_h$ |
| $\mathcal{A}_{\tau_1\tau_2}$     |                          | 1.48   | 1.61             | 1.32             | 1.10             | 1.11           |
| $\mathcal{B}_{\tau_1\tau_2}$     |                          | 0.46   | 0.32             | 0.32             | 0.32             | 0.33           |
| $N_{\text{bkg}}$                 | QCD                      | 4.33   | 0.80             | 3.08             | 0.40             | 0.92           |
|                                  | EWK                      | 4.22   | 1.54             | 1.52             | 0.40             | 0.72           |
|                                  | $t\bar{t}$               | 0.02   | 0.08             | 0.12             | 0.00             | 0.58           |
|                                  | $WW$                     | 0.02   | 0.14             | 0.13             | 0.09             | 0.08           |
|                                  | $Z \rightarrow \ell\ell$ | 8.00   | –                | –                | 0.22             | 0.23           |
| Total $N_{\text{bkg}}$           |                          | 10.03  | 1.75             | 3.44             | 0.61             | 1.32           |
| $\varepsilon_{\text{rec}}$       | GEC                      | 0.10   | 0.10             | 0.10             | 0.10             | 0.10           |
|                                  | trg                      | 0.88   | 0.71             | 2.29             | 0.72             | 4.30           |
|                                  | trk <sub>1</sub>         | 0.71   | 0.74             | 3.67             | 0.79             | 3.67           |
|                                  | trk <sub>2</sub>         | 0.34   | 3.67             | 0.61             | 1.76             | 1.68           |
|                                  | id <sub>1</sub>          | 0.38   | 0.28             | 1.72             | 0.29             | 1.73           |
|                                  | id <sub>2</sub>          | 0.78   | 0.18             | 0.56             | 0.03             | 0.09           |
| Total $\varepsilon_{\text{rec}}$ |                          | 1.47   | 4.21             | 4.73             | 2.08             | 6.15           |
| $\varepsilon_{\text{sel}}$       | kin                      | –  | 1.04             | 2.89             | –                | 1.91           |
|                                  | $I_{p_T}$                | 1.79   | 1.91             | 3.19             | 1.65             | 2.75           |
|                                  | $ \Delta\phi $           | 1.08   | 1.03             | 1.86             | 0.60             | 0.97           |
|                                  | IPS                      | 2.70   | –                | –                | 1.92             | 2.85           |
|                                  | $A_{p_T}$                | 2.03   | –                | –                | –                | –              |
| Total $\varepsilon_{\text{sel}}$ |                          | 3.97   | 2.41             | 4.69             | 2.60             | 4.50           |
| Total systematic                 |                          | 11.13  | 5.41             | 7.56             | 3.88             | 7.88           |

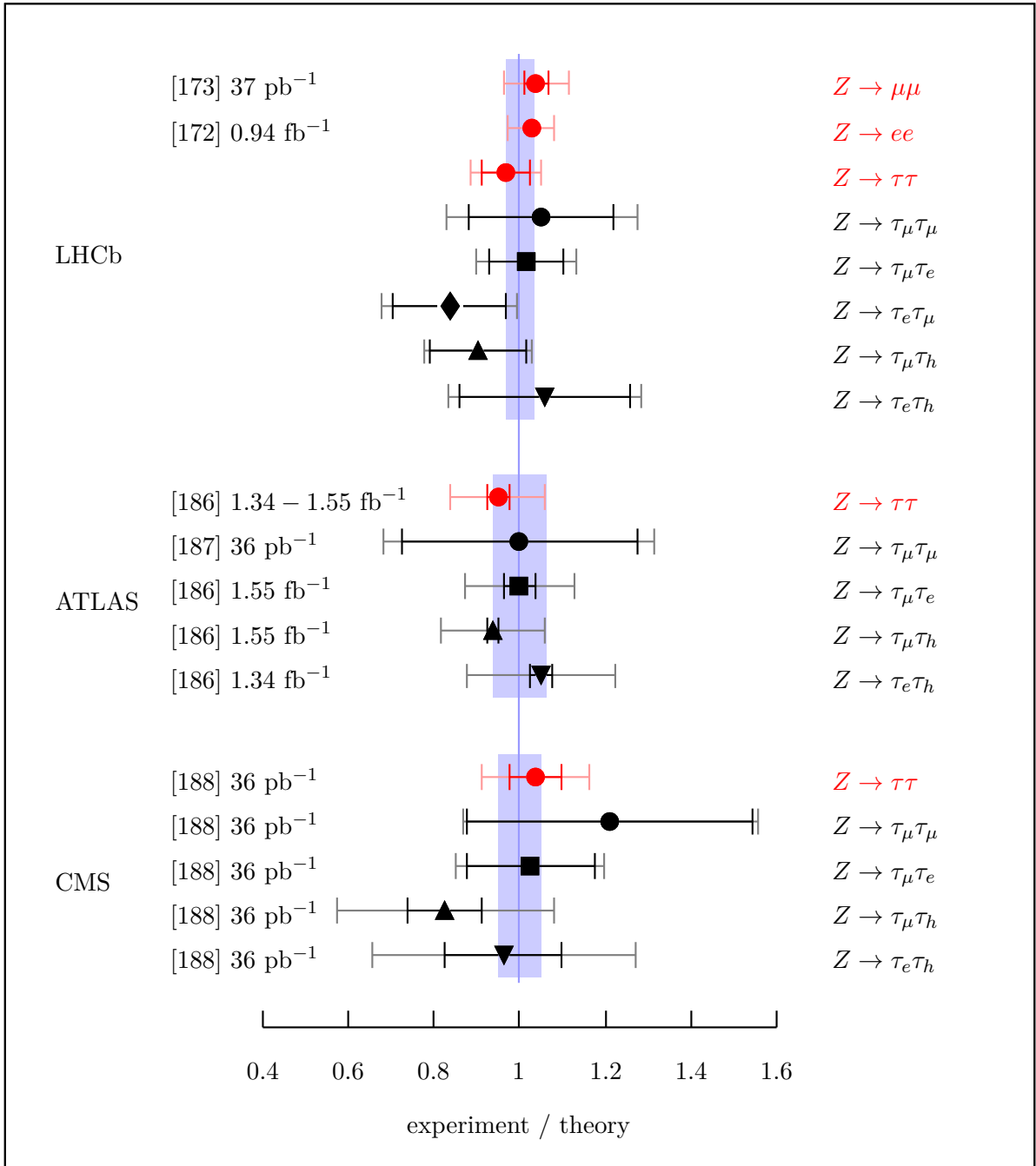


**Figure 5.22.:** A comparison between the LHCb  $pp \rightarrow Z \rightarrow \mu\mu$ ,  $pp \rightarrow Z \rightarrow ee$ , and  $pp \rightarrow Z \rightarrow \tau\tau$  cross-section measurements divided by their expected SM theoretical values. The equivalent  $pp \rightarrow Z \rightarrow \tau\tau$  measurements from ATLAS and CMS are also provided. The red points indicate the muon, electron, or combined  $\tau$  lepton decay channels of the  $Z$  boson while the black points represent the individual  $\tau$  lepton categories. The blue bar provides the theoretical uncertainty, centred about unity. The dark inner error bars correspond to the statistical uncertainty for the individual measurements, while the light outer error bars are the combined systematic and luminosity uncertainties.

the ATLAS and CMS measurements as  $\cancel{E}_T$  cannot be reconstructed within LHCb and used to further reduce the QCD and EWK backgrounds. The purities for the semi-leptonic  $\tau_\mu\tau_h$  and  $\tau_e\tau_h$  categories are approximately equivalent between the three experiments.

The lepton universality test of Eq. 5.1 can be performed,

$$\frac{\sigma_{pp \rightarrow Z \rightarrow \mu\mu}}{\sigma_{pp \rightarrow Z \rightarrow ee}} = 1.01 \pm 0.08, \quad \frac{\sigma_{pp \rightarrow Z \rightarrow \tau\tau}}{\sigma_{pp \rightarrow Z \rightarrow ee}} = 0.95 \pm 0.07 \quad (5.23)$$

using the combined result of this chapter and the  $pp \rightarrow Z \rightarrow \mu\mu$  and  $pp \rightarrow Z \rightarrow ee$  cross-section measurements of LHCb. Here, the luminosity uncertainty is assumed to be fully correlated as the  $Z \rightarrow \tau\tau$  and  $Z \rightarrow ee$  analyses were both performed using the same luminosity measurement. Additionally the ratio,

$$\frac{\sigma_{pp \rightarrow Z \rightarrow \tau\tau}}{\sigma_{pp \rightarrow Z \rightarrow \mu\mu}} = 0.94 \pm 0.09 \quad (5.24)$$

can be calculated where all uncertainties between the two cross-sections are assumed to be uncorrelated as the  $Z \rightarrow \mu\mu$  LHCb analysis uses the 2010 dataset and not the 2011 dataset of the  $Z \rightarrow \tau\tau$  analysis. All three ratios from Eqs. 5.23 and 5.24 verify lepton universality under the unique conditions observed by LHCb.

## 6. Higgs Boson Limits

The upper limits on the production of neutral Higgs bosons decaying into  $\tau$  lepton pairs using the data from the analysis of Chap. 5 are presented within this chapter. The Higgs boson phenomenology needed to determine the event model is introduced in Sect. 6.1 while the event model itself is described in Sect. 6.2, the statistical methods used to calculate the limits are outlined in Sect. 6.3, and the limits are presented in Sect. 6.4.

Further investigation of the boson with a mass of approximately 125 GeV, discovered by ATLAS [8] and CMS [9] is required to determine whether the properties of the boson match those of a Higgs boson from the standard model (SM), supersymmetry (SUSY), or other models beyond the SM. Within both the SM and the minimal supersymmetric model (MSSM), the Higgs boson is predicted to couple to fermions with a strength proportional to the mass of the fermion, as previously shown by the vertices of Fig. 2.6(g), and Figs. 2.10(a) through 2.10(h). Consequently, the neutral Higgs bosons, whether SM or MSSM, are expected to decay into  $\tau$  lepton pairs over two orders of magnitude more often than into muon pairs, and seven orders of magnitude more often than into electron pairs.

Within this chapter the neutral SM Higgs boson is denoted by  $H$ , while for the MSSM Higgs bosons the light  $\mathcal{CP}$ -even Higgs boson is denoted by  $h^0$ , the heavy  $\mathcal{CP}$ -even Higgs boson by  $H^0$ , the  $\mathcal{CP}$ -odd Higgs boson by  $A^0$ , and the charged Higgs bosons by  $H^\pm$ . Any neutral Higgs boson, whether SM, MSSM, or otherwise, is indicated by  $\phi^0$ , while any neutral MSSM Higgs boson is indicated by  $\Phi^0$ . Model independent upper limits on the production for a neutral Higgs boson decaying into a  $\tau$  lepton pair,  $\sigma_{pp \rightarrow \phi^0 \rightarrow \tau\tau}$ , within the LHCb acceptance,  $2.0 \leq \eta_\tau \leq 4.5$ , as a function of the mass of the Higgs boson are set using both the individual event categories of Chap. 5 and their combination. The combined limit is compared to the expected cross-section from the SM Higgs boson. Model dependent limits on  $\tan \beta$  are set for the three neutral MSSM Higgs bosons decaying into  $\tau$  lepton pairs as a function of the mass of the  $\mathcal{CP}$ -odd Higgs boson. These limits are also set using the individual categories and their combination.

The MSSM limits are set using the  $m_{h^0}^{\max}$  scenario of Ref. [189] where the parameter space is selected to maximise the mass of the light  $\mathcal{CP}$ -even Higgs boson. This benchmark provides the most conservative limits on  $\tan \beta$  for a given mass of the  $\mathcal{CP}$ -odd Higgs boson and is commonly used amongst experiments when reporting MSSM limits. This allows the limits of this chapter to be compared to results from ATLAS, CMS, and LEP. The SM parameters for this scenario are set at 172.5 GeV for the  $t$ -quark mass  $m_t$ , 4.213 GeV for the bottom quark mass  $m_b$  using the  $\overline{\text{MS}}$  scheme, and 0.119 for the strong coupling  $\alpha_s(m_Z)$ . The SUSY parameters are set at 1 TeV for the soft SUSY-breaking mass  $m_{\text{SUSY}}$ , 2 TeV for the stop mixing parameter  $X_t$ , 200 GeV for the  $SU(2)$  gaugino mass parameter  $m_2$ , 200 GeV for the Higgs mixing parameter  $\mu$ , and 800 GeV

for the gluino mass parameter  $m_3$ .

## 6.1. Higgs Phenomenology

To set limits on the production of Higgs bosons, both the production and decay of the Higgs bosons must be known. Within this section the branching fractions are given in Sect. 6.1.1 and the cross-sections in Sect. 6.1.2 for both the SM Higgs boson and the neutral MSSM Higgs bosons. The branching fractions and cross-sections depend upon the mass of the Higgs boson, and for the MSSM, also depend upon  $\tan\beta$ . However, the masses of the light and heavy  $\mathcal{CP}$ -even Higgs bosons of the MSSM can be written in terms of the  $\mathcal{CP}$ -odd Higgs boson mass,  $m_{A^0}$ , and  $\tan\beta$ . Consequently, the branching fractions and cross-sections for the SM are given as a function of only  $m_H$ , while the MSSM branching fractions and cross-sections are given as a function of  $m_{A^0}$  and  $\tan\beta$ .

In Fig. 6.1 the light and heavy  $\mathcal{CP}$ -even Higgs boson masses are plotted as a function of the  $\mathcal{CP}$ -odd Higgs boson mass and  $\tan\beta$ . The masses are calculated using the program FEYNHIGGS [190, 191, 192, 193, 194] which performs the calculations up to the order  $\alpha_e\alpha_s$ . The features of these mass functions can be understood at tree-level using the relations,

$$\begin{aligned} m_{h^0}^2 &= \frac{1}{2} \left( m_{A^0}^2 + m_Z^2 - \left( (m_{A^0}^2 - m_Z^2)^2 + 4m_Z^2 m_{A^0}^2 \sin^2 2\beta \right)^{\frac{1}{2}} \right) \\ m_{H^0}^2 &= \frac{1}{2} \left( m_{A^0}^2 + m_Z^2 + \left( (m_{A^0}^2 - m_Z^2)^2 + 4m_Z^2 m_{A^0}^2 \sin^2 2\beta \right)^{\frac{1}{2}} \right) \\ m_{H^\pm}^2 &= m_{A^0}^2 + m_W^2 \end{aligned} \tag{6.1}$$

which are determined from the MSSM Higgs boson mass eigenstate matrix of Eq. 2.86. Here,  $\mu$  is the Higgs mixing parameter as described in Sect. 2.1.4.

The relations of Eq. 6.1 result in a light  $\mathcal{CP}$ -even Higgs boson mass that must be less than or equal to  $m_Z |\cos 2\beta|$ , a heavy  $\mathcal{CP}$ -even Higgs boson mass that must be greater than or equal to  $m_Z$ , and a charged Higgs boson mass that must be greater than  $m_W$ . The mass of the  $\mathcal{CP}$ -odd Higgs boson is bounded by the light and heavy  $\mathcal{CP}$ -even masses,  $m_{h^0} \leq m_{A^0} \leq m_{H^0}$ , and for large  $m_{A^0}$  the mass of the heavy  $\mathcal{CP}$ -even Higgs boson approaches that of the  $\mathcal{CP}$ -odd Higgs boson.

In Fig. 6.1 the light  $\mathcal{CP}$ -even Higgs boson mass plateaus at 130 GeV for larger  $m_{A^0}$  rather than  $m_Z$ , as heavy quark and squark loops provide sizable corrections at the one-loop level. The heavy  $\mathcal{CP}$ -even Higgs boson mass approaches the maximum  $m_{h^0}$  at low  $m_{A^0}$  as expected, and for  $m_{A^0} > 140$  GeV is nearly degenerate with the  $\mathcal{CP}$ -odd Higgs boson at  $\tan\beta$  values greater than 20. However, for a given  $m_{A^0}$ , the heavy  $\mathcal{CP}$ -even Higgs boson mass increases asymptotically as  $\tan\beta$  approaches zero.



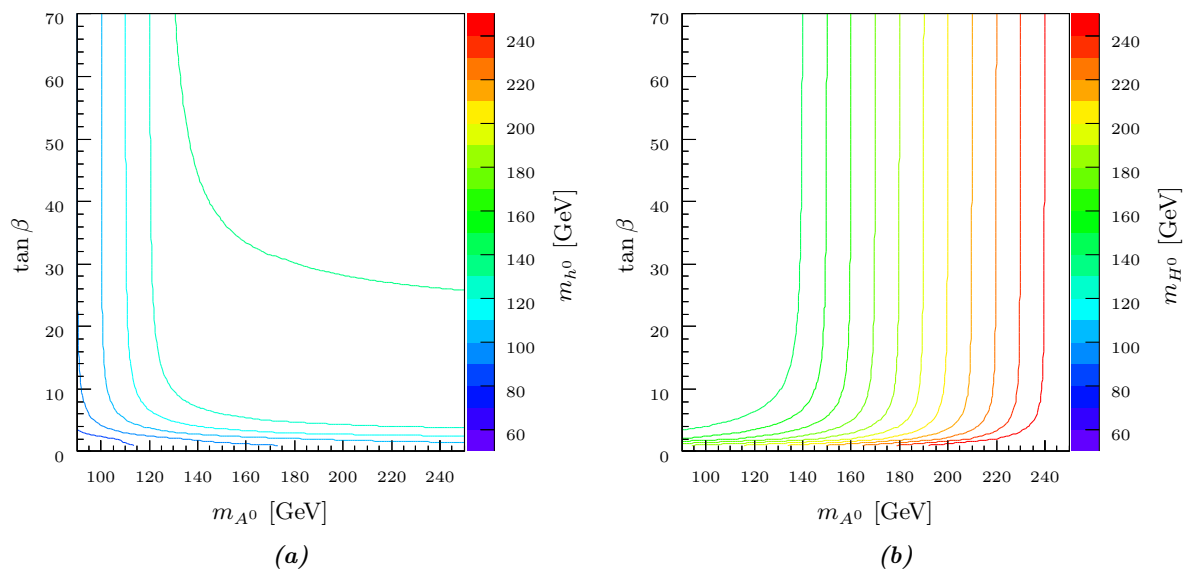


**Figure 6.1.:** Masses of the (a) light  $\mathcal{CP}$ -even and (b) heavy  $\mathcal{CP}$ -even MSSM Higgs bosons as a function of the  $\mathcal{CP}$ -odd Higgs boson mass and  $\tan\beta$ , calculated using FEYNHIGGS [190, 191, 192, 193, 194].

### 6.1.1. Branching Fractions

The decay width for the SM or MSSM Higgs bosons is calculated as the sum of the partial decay widths,

$$\Gamma_{\phi^0} = \sum_i \Gamma_{\phi^0 \rightarrow f_i \bar{f}_i} + \Gamma_{\phi^0 \rightarrow gg} + \Gamma_{\phi^0 \rightarrow \gamma\gamma} + \Gamma_{\phi^0 \rightarrow Z\gamma} + \Gamma_{\phi^0 \rightarrow ZZ} + \Gamma_{\phi^0 \rightarrow WW} \quad (6.2)$$

where the summation is over muon,  $\tau$  lepton,  $s$ -quark,  $c$ -quark,  $b$ -quark, and  $t$ -quark pairs, and the remaining terms are the possible gauge boson combinations. The branching fraction for a given channel is then,

$$\mathcal{B}_{\phi^0 \rightarrow X} = \frac{\Gamma_{\phi^0 \rightarrow X}}{\Gamma_{\phi^0}} \quad (6.3)$$

where  $\Gamma_{\phi^0 \rightarrow X}$  is the partial decay width for the channel. First the SM Higgs boson branching fractions are described, followed by a description of the MSSM Higgs bosons branching fractions.

#### SM Branching Fractions

Over the SM Higgs boson mass range considered in this chapter,  $90 < m_{\phi^0} < 250$  GeV, the  $\tau$  lepton,  $b$ -quark, gluon,  $W$  boson, and  $Z$  boson pair partial widths dominate the total width of the SM Higgs boson. The branching fractions for these channels as a function of the SM Higgs boson mass are plotted in Fig. 6.2. These branching fractions, with uncertainties, are calculated following the prescription of Ref. [195] which uses the programs HDECAY [96, 196, 197, 198] and PROPHECY4F [199, 200, 201, 202]. Further details on these calculations are given in App. D.1.2, as well as tabulated values for the  $H \rightarrow \tau\tau$  branching fraction. The features of the branching

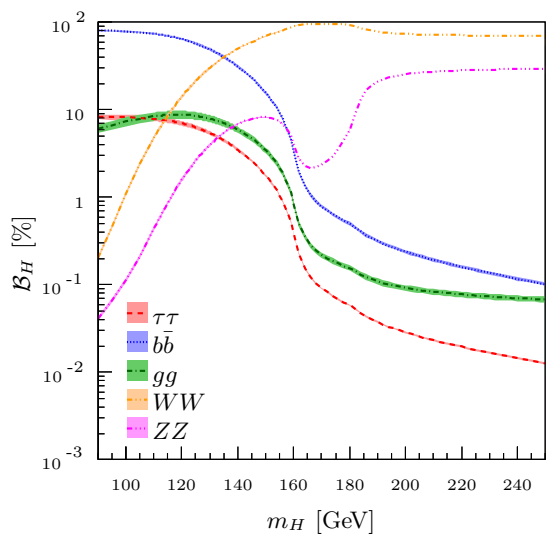


**Figure 6.2.:** Branching fractions, as a percentage, for the five leading decay channels of the SM Higgs boson in the relevant mass range:  $\tau\tau$  (red),  $b\bar{b}$  (blue),  $gg$  (green),  $WW$  (orange), and  $ZZ$  (magenta). The branching fractions and uncertainties, indicated by the coloured bands, are calculated using the results of Ref. [195] and plotted as a function of the Higgs boson mass.

fractions plotted in Fig. 6.2 can be understood from the simpler tree-level calculations of the partial widths which can be determined using the vertices of Fig. 2.6, Eq. 2.68, and the methods outlined in Chap. 2.

For fermions above the threshold  $m_H > 2m_f$  the relevant vertex is Fig. 2.6(g) and the tree-level decay width from Ref. [203] is,

$$\Gamma_{H \rightarrow f\bar{f}} = \frac{N_c g_w^2 m_f^2}{32\pi m_W^2} \left(1 - \frac{4m_f^2}{m_H^2}\right)^{\frac{3}{2}} m_H \quad (6.4)$$

where  $N_c$  is the number of colours, 1 for leptons and 3 for quarks, and  $g_w$  is the  $SU(2)$  gauge coupling. For the Higgs boson masses considered, the  $\tau$  lepton and  $b$ -quark channels dominate the fermion partial width, and the  $b$ -quark pair partial width is expected to be a factor of  $3m_b^2/m_\tau^2 \approx 15$  times larger than the  $\tau$  lepton pair width as can be seen in Fig. 6.2. Electron,  $u$ -quark, and  $d$ -quark pairs are not considered in the calculation of the total decay width, as their partial widths are less than six orders of magnitude smaller than the  $H \rightarrow b\bar{b}$  width resulting in a maximum branching fraction of less than  $10^{-4}\%$ .

For on-shell vector bosons,  $W$  and  $Z$ , the corresponding vertices are Figs. 2.6(b) and 2.6(c) and the tree-level decay width from Ref. [204] is,

$$\Gamma_{H \rightarrow VV} = \frac{N_m g_w^2}{64\pi m_W^2} \left(1 - \frac{4m_V^2}{m_H^2}\right)^{\frac{1}{2}} \left(1 - \frac{4m_V^2}{m_H^2} + \frac{3}{4} \left(\frac{4m_V^2}{m_H^2}\right)^2\right) m_H^3 \quad (6.5)$$

for a Higgs boson mass above threshold,  $m_H > 2m_V$ , where  $N_m$  is a multiplicity factor of 1/2 for the  $Z$  boson and 1 for the  $W$  boson. This factor results in a  $W$  boson pair partial width approximately double that of the  $Z$  boson pair width for  $m_H > 2m_Z$ , as can be seen in Fig. 6.2. Additionally, the  $m_H^3$  term ensures that the partial widths of Eq. 6.5 are on the order of  $m_H^2$  times larger than the fermionic partial widths for large  $m_H$ .

However, the on-shell decay width of Eq. 6.5 is not sufficient to describe the full  $W$  and  $Z$

boson branching fractions. It is also necessary to include decays where one or both of the vector bosons are off-shell. From Ref. [205], this partial width can be written as,

$$\begin{aligned} \Gamma_{H \rightarrow VV^*} = & \frac{F_V g_w^4}{\pi^3} \left( \frac{3(1 - 8x^2 + 20x^4)}{\sqrt{4x^2 - 1}} \cos^{-1} \left( \frac{3x^2 - 1}{2x^3} \right) \right. \\ & - 3(1 - 6x^2 + 4x^4) \ln(x) \\ & \left. - (1 - x^2) \left( \frac{47}{2}x^2 - \frac{13}{2} + x^{-2} \right) \right) m_H \end{aligned} \quad (6.6)$$

where  $x$  is  $m_V/m_H$  and the pre-factors  $F_V$  are,

$$F_W = \frac{3}{512}, \quad F_Z = \frac{7 - \frac{40}{20}\sin^2 \theta_w + \frac{160}{9}\sin^4 \theta_w}{2048 \cos^4 \theta_w} \quad (6.7)$$

for the  $W$  boson and  $Z$  boson respectively; here,  $\theta_w$  is the weak-mixing angle. Over the mass range  $2m_W < m_H < 2m_Z$  the partial width for the  $W$  boson pair channel is given by Eq. 6.5 while the width for the  $Z$  boson pair channel is given by Eq. 6.6 resulting in a dip in the  $H \rightarrow ZZ$  branching fraction, which is clearly visible in Fig. 6.2. Over this range the  $W$  boson pair partial width is anywhere between ten to fifty times larger than the  $Z$  boson pair width. For Higgs boson masses below the mass of the  $W$  and  $Z$  bosons, the double off-shell width is necessary, which is not discussed here, but can be found in Ref. [196].

The decay widths for the additional gauge boson combinations, gluon pairs, photon pairs, and  $Z$  bosons with photons, do not have tree-level diagrams due to the massless gluon and photon. Of these three channels, only the gluon pair channel provides a considerable contribution to the total decay width for the Higgs boson masses considered here. From Ref. [48], the width for Higgs boson decays into gluon pairs can be written as,

$$\Gamma_{H \rightarrow gg} = \frac{g_s^4 g_w^2}{2048 \pi^5 m_W^2} \left( \sum_i (x_i + (x_i - x_i^2)F(x_i)) \right) \left( \sum_i (x_i + (x_i - x_i^2)F(x_i)) \right)^\dagger m_H^3 \quad (6.8)$$

where  $g_s$  is the  $SU(3)$  gauge coupling and  $x_i$  is  $4m_i^2/m_H^2$  for fermion  $i$ . The summations are over all contributing fermion loops where,

$$F(x) = \begin{cases} \left( \sin^{-1} x^{-\frac{1}{2}} \right)^2 & \text{if } x \geq 1 \\ \frac{1}{4} \left( \pi + i \ln \left( \frac{2+2\sqrt{1-x-x}}{x} \right) \right)^2 & \text{else} \end{cases} \quad (6.9)$$

and only massive quarks are considered, with the  $t$ -quark loop dominating the decay width. From the ratio of Eq. 6.8 to Eq. 6.4 for both  $\tau$  lepton and  $b$ -quark pairs, one can see that for the mass range considered in Fig. 6.2, the gluon pair width will remain above the  $\tau$  lepton pair width, but below the  $b$ -quark pair width.

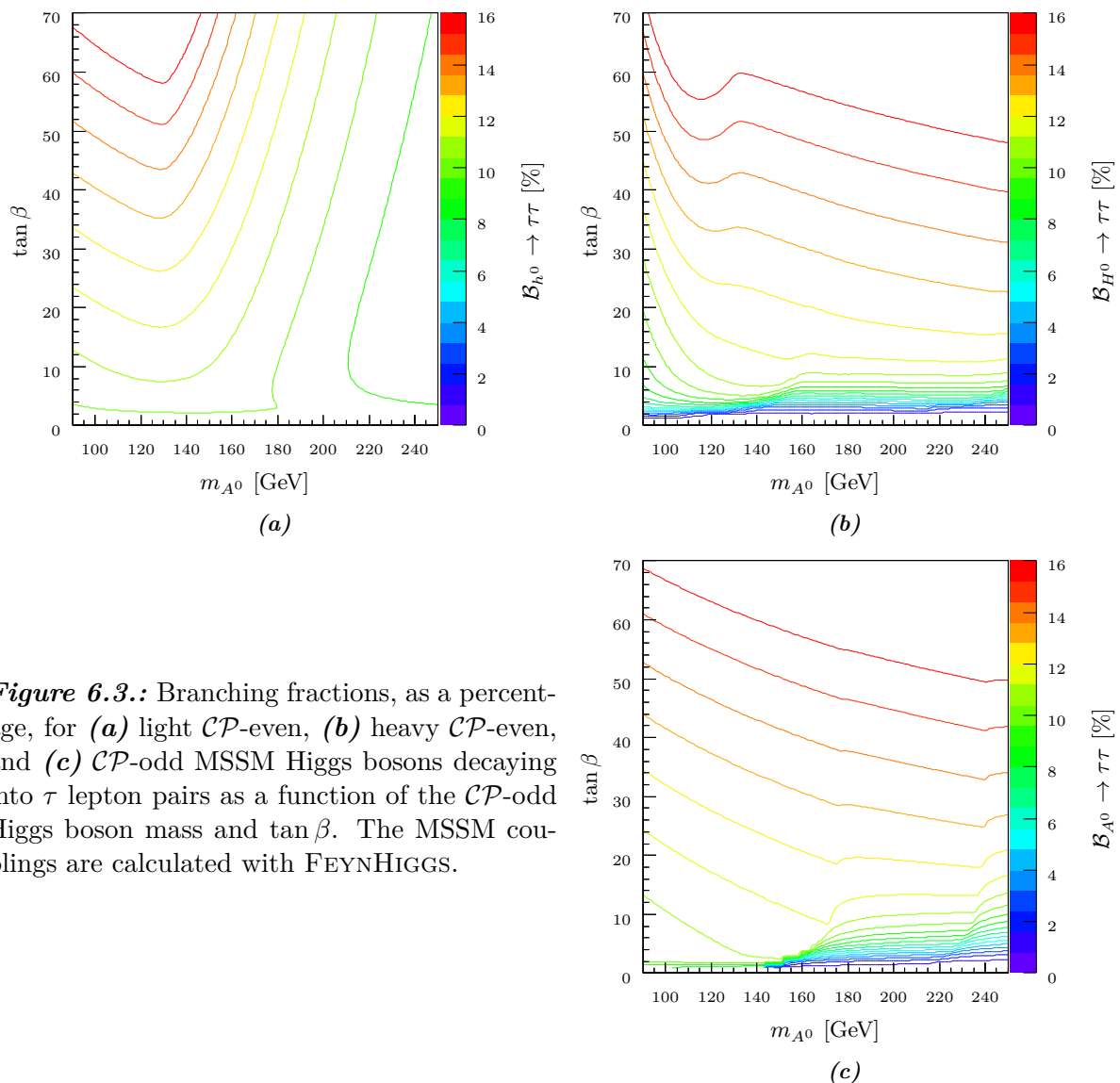


**Figure 6.3.:** Branching fractions, as a percentage, for (a) light  $\mathcal{CP}$ -even, (b) heavy  $\mathcal{CP}$ -even, and (c)  $\mathcal{CP}$ -odd MSSM Higgs bosons decaying into  $\tau$  lepton pairs as a function of the  $\mathcal{CP}$ -odd Higgs boson mass and  $\tan\beta$ . The MSSM couplings are calculated with FEYNHIGGS.

### MSSM Branching Fractions

The branching fractions for the  $h^0$ ,  $H^0$ , and  $A^0$  Higgs bosons decaying into a  $\tau$  lepton pair as a function of the  $\mathcal{CP}$ -odd Higgs boson mass,  $m_{A^0}$ , and  $\tan\beta$  are plotted in Fig. 6.3. These branching fractions are calculated using the programs HDECAY and PROPHECY4F, and dressed with MSSM couplings from FEYNHIGGS following the recommendations of Ref. [195]. Details on the calculation, as well as plots with numerical values of these branching fractions, are provided in App. D.1.3. Just as for the SM Higgs boson, the features of Fig. 6.3 can be understood using tree-level calculations of the partial widths.

Comparing the couplings of the neutral MSSM Higgs bosons with fermions from the vertex factors of Figs. 2.10(a) through 2.10(f) with the SM Higgs boson coupling given in Fig. 2.6(g), the partial decay width for all three neutral Higgs bosons can be written as,

$$\Gamma_{\Phi^0 \rightarrow f\bar{f}} = F_{\Phi^0} \Gamma_{H \rightarrow f\bar{f}} \quad (6.10)$$

where  $\Gamma_{\Phi^0 \rightarrow f\bar{f}}$  is given by Eq. 6.4. For the  $\mathcal{CP}$ -odd Higgs boson the exponent of 3/2 in Eq. 6.4 is reduced to an exponent of 1/2 due to the additional  $\gamma^5$  factor in the couplings of Figs. 2.10(c) and 2.10(f). The pre-factors  $F_{\Phi^0}$  are given by,

$$F_{h^0} = \begin{cases} \frac{\cos^2 \alpha}{\sin^2 \beta} & \text{for } \nu, u \\ \frac{\sin^2 \alpha}{\cos^2 \beta} & \text{for } \ell, d \end{cases}, \quad F_{H^0} = \begin{cases} \frac{\sin^2 \alpha}{\sin^2 \beta} & \text{for } \nu, u \\ \frac{\cos^2 \alpha}{\cos^2 \beta} & \text{for } \ell, d \end{cases}, \quad (6.11)$$

$$F_{A^0} = \begin{cases} \tan^{-2} \beta & \text{for } \nu, u \\ \tan^2 \beta & \text{for } \ell, d \end{cases}$$

for the three neutral Higgs bosons where  $u$  is a  $u$ -type quark,  $\nu$  is a neutrino,  $d$  is a  $d$ -type quark, and  $\ell$  is a charged lepton. The parameter  $\alpha$  is the Higgs boson mass mixing angle.

A similar procedure for calculating the vector boson pair partial width is possible by comparing the SM Higgs boson vertices from Figs. 2.6(b) and 2.6(c) with the MSSM Higgs bosons vertices from Figs. 2.10(i) through 2.10(l). Notice that here, the  $\mathcal{CP}$ -odd Higgs boson does not couple with  $W$  or  $Z$  bosons. The vector boson partial decay width can then be written as,

$$\Gamma_{\Phi^0 \rightarrow VV} = F_{\Phi^0} \Gamma_{H \rightarrow VV} \quad (6.12)$$

where the pre-factors are given by,

$$F_{h^0} = \sin^2(\beta - \alpha), \quad F_{H^0} = \cos^2(\beta - \alpha), \quad F_{A^0} = 0 \quad (6.13)$$

for the light and heavy  $\mathcal{CP}$ -even Higgs bosons and the  $\mathcal{CP}$ -odd Higgs boson. The factor  $\cos^2(\beta - \alpha)$  can be rewritten in terms of,

$$\cos^2(\beta - \alpha) = \frac{1}{2} - \frac{m_{A^0}^2 - m_Z^2 \cos 4\beta}{2(m_{A^0}^4 + m_Z^4 - 2m_{A^0}^2 m_Z^2 \cos 4\beta)^{\frac{1}{2}}} \quad (6.14)$$

for a given  $m_{A^0}$  and  $\tan \beta$ . In the limit of large  $m_{A^0}$  the term  $\cos^2(\beta - \alpha)$  approaches zero and so the vector boson pair partial widths are suppressed at large  $m_{A^0}$  for the heavy  $\mathcal{CP}$ -even Higgs boson, while they approach the SM widths for the light  $\mathcal{CP}$ -even Higgs boson.

The branching fractions for the light  $\mathcal{CP}$ -even Higgs boson, given in Fig. 6.3(a), range from 8% at large  $m_{A^0}$  up to values of 16% for large  $\tan \beta$  and low  $m_{A^0}$ . The upper limit on the branching fraction is governed by the ratio of the  $\tau$  lepton and  $b$ -quark pair partial widths from Eq. 6.10, which are enhanced by a factor of  $1 + \tan^2 \beta$ . However, for large  $m_{A^0}$  the vector boson pair widths increase, just as in the SM, and so the  $\tau$  lepton branching fraction is reduced.

For the heavy  $\mathcal{CP}$ -even Higgs boson, the vector boson pair partial widths of Eq. 6.12 are suppressed by a factor of  $\cos^2(\beta - \alpha)$ , and so the  $\tau$  lepton and  $b$ -quark pair partial widths dominate the total width at large  $m_{A^0}$ , as can be seen in Fig. 6.3(b), resulting in the maximum  $\tau$  lepton pair branching fraction of 16%. Similar behaviour can be seen in Fig. 6.3(c) at large  $m_{A^0}$  for the  $\mathcal{CP}$ -odd Higgs boson due to the lack of couplings with vector bosons. The  $\tau$  lepton

and  $b$ -quark partial widths for the heavy  $\mathcal{CP}$ -even Higgs boson are enhanced by a factor of  $1 + \tan^2 \beta$ , while the  $\mathcal{CP}$ -odd widths are enhanced by a factor of  $\tan^2 \beta$ .

### 6.1.2. Cross-Sections

The cross-section for incoming particles  $p_1$  and  $p_2$  producing a Higgs boson can be related to the decay widths of Sect. 6.1.1 using a result of Ref. [206],

$$\sigma_{p_1 p_2 \rightarrow \phi^0}(s) \approx \frac{16\pi}{(2N_{s_{p_1}} + 1)(2N_{s_{p_2}} + 1)N_{c_{p_1}}N_{c_{p_2}}} \frac{\Gamma_{\phi^0 \rightarrow p_1 p_2} \Gamma_{\phi^0}}{(s - m_Z^2)^2 + m_{\phi^0}^2 \Gamma_{\phi^0}} \quad (6.15)$$

where  $s$  is the centre-of-mass energy, and  $N_c$  and  $N_s$  are the colour and spin multiplicities for  $p_1$  and  $p_2$ . At the LHC,  $p_1$  and  $p_2$  are two partons from the colliding protons, and so the observable cross-section  $\sigma_{pp \rightarrow \phi^0}$  is calculated using the partonic cross-section  $\sigma_{p_1 p_2 \rightarrow \phi^0}$  and the factorisation theorem of Eq. 2.78. Thus, the cross-section for Higgs boson production at the LHC depends upon the knowledge of the proton PDF, which introduces an uncertainty within the range of (2 – 14)%.

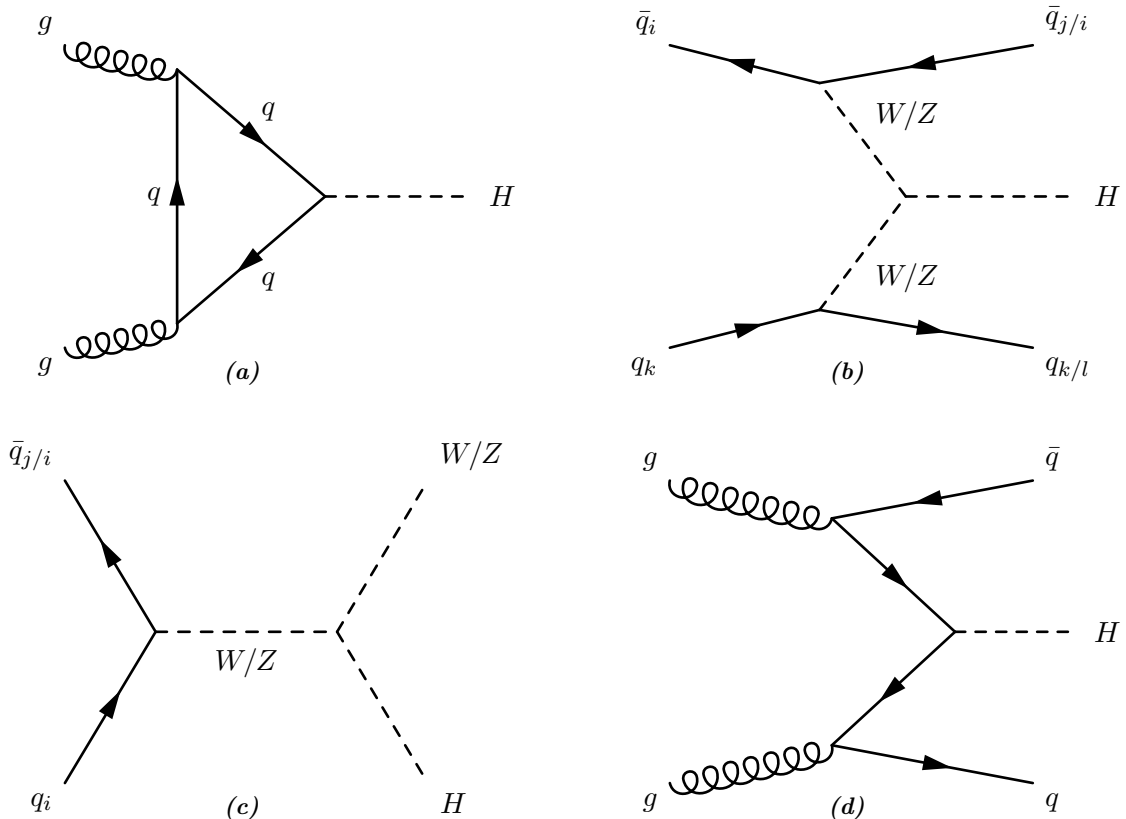


**Figure 6.4.:** Example diagrams of SM Higgs boson production at the LHC from (a) gluon-gluon fusion, (b) vector-boson fusion, (c) associated vector boson production, and (d) associated heavy quark production.

Production of Higgs bosons at the LHC in proton-proton collisions occurs primarily through four partonic processes, outlined in the example diagrams of Fig. 6.4. Gluon-gluon fusion is

shown in Fig. 6.4(a), vector-boson fusion in Fig. 6.4(b), associated vector boson production in Fig. 6.4(c), and associated heavy quark production in Fig. 6.4(d). The cross-sections for each of these mechanisms is dependent upon the mass and type of the Higgs boson, as well as  $\tan\beta$  for the MSSM Higgs bosons. The cross-sections for SM and MSSM Higgs bosons produced in proton-proton collisions at a centre-of-mass energy of 7 TeV through these production mechanisms are given in this section.

### SM Cross-Sections

The SM Higgs boson cross-sections, as a function of mass, are shown in Fig. 6.5. These cross-sections are calculated using the programs HIGLU [207, 208, 209, 210], DFG [211, 212, 213], and VBF@NNLO [214, 215, 216] following the methods of Ref. [217]. Further details on these calculations can be found in App. D.1.4.

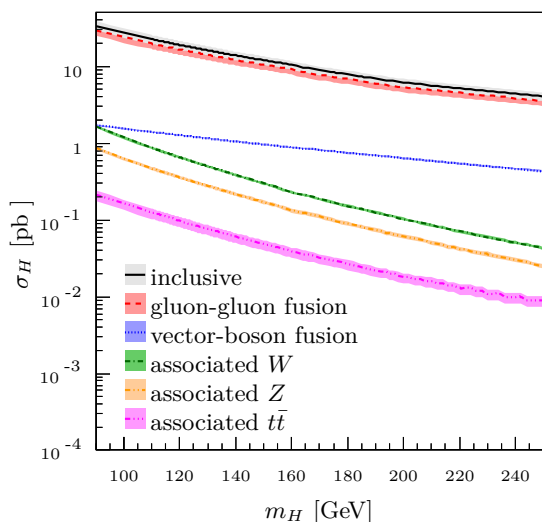


**Figure 6.5.:** Cross-sections for  $pp \rightarrow H$  production at the LHC with a centre-of-mass energy of 7 TeV. The inclusive cross-section (black) is the sum of gluon-gluon fusion (red), vector-boson fusion (blue), associated  $W$  boson production (green), associated  $Z$  boson production (orange), and associated heavy quark production (magenta). The coloured bands provide the linearly combined QCD scale,  $\alpha_s$ , and PDF uncertainties for the cross-sections.

The leading SM Higgs boson production mechanism is gluon-gluon fusion which, just like the Higgs boson decay into a gluon pair of Eq. 6.8, must proceed through a fermion loop, as the massless gluon does not couple directly with the Higgs boson. At lower masses this loop is dominated by  $b$ -quarks, but for  $m_H > 2m_t$  the  $t$ -quark loop contributes. While the gluon pair partial decay width of Eq. 6.8 is not the largest width for the Higgs boson, the gluon contribution to the proton at low momentum transfer is much larger than the other partons, as shown in Fig. 2.9(a), resulting in a large cross-section from gluon-gluon fusion.

The vector-boson fusion contribution to the inclusive SM Higgs boson cross-section is nearly an order of magnitude smaller than the gluon-gluon fusion contribution, as the partons for this process are quarks and not gluons. The cross-section for associated vector boson production is even smaller with respect to gluon-gluon fusion, but at lower Higgs boson masses is comparable to the vector-boson fusion contribution, as can be seen in Fig. 6.5. The associated heavy quark production cross-section is calculated for associated  $t$ -quarks and is nearly two orders of magnitude smaller than the gluon-gluon fusion cross-section.

### MSSM Cross-Sections

Two cross-sections are included in the inclusive cross-sections for the MSSM Higgs bosons, gluon-gluon fusion and associated  $b$ -quark production, and are given for the three neutral Higgs bosons as a function of the  $\mathcal{CP}$ -odd Higgs boson mass and  $\tan\beta$  in Fig. 6.6. These cross-sections are calculated following the recommendations of Ref. [217] using the programs HIGLU and GGH@NNLO [218, 219, 220] for the gluon-gluon fusion cross-section and the program BBH@NNLO [221, 222] for the associated  $b$ -quark production cross-section. Both of these calculations are modified with MSSM couplings from FEYNHIGGS. Further details on the calculations, including additional plots, can be found in App. D.1.5.

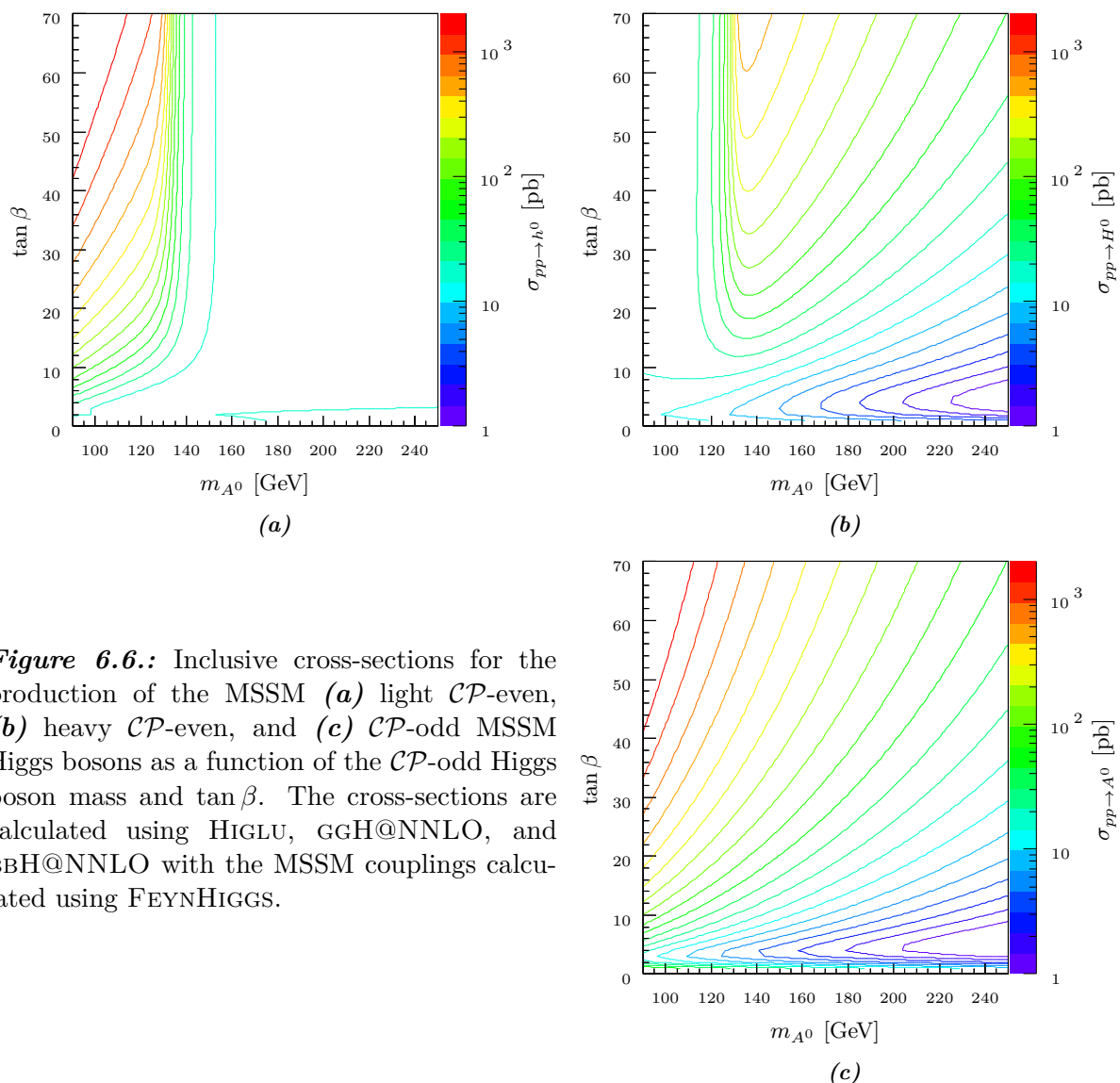


**Figure 6.6.:** Inclusive cross-sections for the production of the MSSM (a) light  $\mathcal{CP}$ -even, (b) heavy  $\mathcal{CP}$ -even, and (c)  $\mathcal{CP}$ -odd MSSM Higgs bosons as a function of the  $\mathcal{CP}$ -odd Higgs boson mass and  $\tan\beta$ . The cross-sections are calculated using HIGLU, GGH@NNLO, and BBH@NNLO with the MSSM couplings calculated using FEYNHIGGS.

At large  $\tan\beta$  the inclusive MSSM Higgs boson cross-sections can be enhanced by nearly two orders of magnitude with respect to the SM Higgs boson cross-section, due to the additional  $\tan\beta$  dependence in the couplings of Fig. 2.10. The light  $\mathcal{CP}$ -even Higgs boson approaches a maximum mass of 130 GeV for large  $m_{A^0}$  resulting in an inclusive cross-section similar to the SM



Higgs boson for all  $\tan\beta$ . As can be seen in Fig. 6.6(a), this maximum inclusive cross-section is on the order of 10 pb which is comparable to the inclusive cross-section for the SM Higgs boson given in Fig. 6.5.

## 6.2. Event Model

The decay of a neutral Higgs boson into a  $\tau$  lepton pair produces an experimental signature similar to  $Z \rightarrow \tau\tau$  events, and so the analysis of Chap. 5 can also be used to determine the cross-section for neutral Higgs boson production. However, the  $pp \rightarrow Z \rightarrow \tau\tau$  cross-sections measured in Chap. 5 match well with the theoretical prediction, and so if  $\phi^0 \rightarrow \tau\tau$  events are present within the data, their contribution is too small to measure a cross-section. Instead, this data can be used to set upper limits on neutral Higgs boson production.

To set these limits, the expected number of background and Higgs boson signal events is required, as well as the observed number of events. Here, the  $Z \rightarrow \tau\tau$  signal of Chap. 5 is now considered a background. In Sect. 6.2.1 the simulation samples used to determine the number of expected Higgs boson signal events is described, and in Sect. 6.2.2 both the expected number of background and signal events are estimated. However, using just the number of expected and observed events to set upper limits does not utilise differences between the signal  $\phi^0 \rightarrow \tau\tau$  events and the dominant  $Z \rightarrow \tau\tau$  background events. The primary difference between these two event types is the invariant mass of the  $\tau$  lepton decay products, and so the invariant mass distributions of Fig. 5.11, normalised to the number of expected events, can be used to increase the information used to set the limits. In Sect. 6.2.3 the signal and background mass distributions are given, using both the simulation samples of Sect. 6.2.1 and the normalisation of Sect. 6.2.2.

### 6.2.1. Simulation

The  $\phi^0 \rightarrow \tau\tau$  simulation samples are used to determine the efficiency and acceptance corrections necessary to calculate the number of expected signal events in Sect. 6.2.2, as well as determine the invariant mass distributions of Sect. 6.2.3. The samples are generated, simulated, digitised, and reconstructed following the process described in Sect. 4.3. All samples are generated with PYTHIA 6 [10, 153] and simulated with GAUSS using the LHCb simulation configuration MC11a. Over the Higgs boson mass range considered in this chapter the leading order treatment of PYTHIA 6 is sufficient, as effects from higher order corrections, off-shell effects, and signal and background interference are small [223].

The Higgs boson signals are generated for seventeen mass steps between 90 GeV and 250 GeV in steps of 10 GeV. For each mass step five samples are generated, one for each event category of Sect. 5.1.2. Only events with generator level  $\tau$  lepton decay products matching the  $\eta$ ,  $p_T$ , and particle type requirements of Sect. 5.1.2 are selected for full simulation and reconstruction. A total of  $10^4$  events are fully reconstructed and simulated for each mass step and event category.

The primary production mechanism for the SM Higgs boson, as described in Sect. 6.1.2, is gluon-gluon fusion and so the  $H \rightarrow \tau\tau$  samples are generated for gluon-gluon fusion production.

In the MSSM, the dominant Higgs boson production mechanisms are both gluon-gluon fusion and associated  $b$ -quark production. However, the expected number of signal events and invariant mass distribution when determined from samples produced with either mechanism are found to be consistent within uncertainty. Additionally, the  $\mathcal{CP}$  of the Higgs boson affects neither the expected number of signal events nor the mass distribution, within uncertainty, and so the same simulation samples used for the SM Higgs boson are also used for all three neutral MSSM Higgs bosons.

### 6.2.2. Event Yields

The expected number of background events for the QCD, EWK,  $t\bar{t}$ ,  $WW$ , and  $Z \rightarrow \ell\ell$  backgrounds have already been estimated in Sect. 5.1.3, and so only the expected number of  $Z \rightarrow \tau\tau$  background events and  $\phi^0 \rightarrow \tau\tau$  signal events need to be estimated. In this section these expected number of events are calculated using the results of Sect. 5.2, the theoretical branching fractions and cross-sections of Sect. 6.1, and the simulation of Sect. 6.2.1.

#### Expected $Z \rightarrow \tau\tau$ Background

Given a simulated  $Z \rightarrow \tau\tau$  sample, the expected number of  $Z \rightarrow \tau\tau$  events in data is given by,

$$N_{Z \rightarrow \tau\tau} = \frac{\sigma_{pp \rightarrow Z \rightarrow \tau\tau} \varepsilon_{\text{sel}} \mathcal{L} \mathcal{A}_{\tau_1 \tau_2} \mathcal{B}_{\tau_1 \tau_2}}{\frac{1}{N_{\text{sim}}} \sum_i^{N_{\text{sim}}} \left( \varepsilon_{\text{rec}i}^{-1} \right)} \quad (6.16)$$

where  $\sigma_{pp \rightarrow Z \rightarrow \tau\tau}$  is  $74.3_{-2.1}^{+1.9}$  pb,  $N_{\text{sim}}$  is the number of events in the simulation sample, and all remaining variables are the same as for the cross-section formula of Eq. 5.15. In the summation,  $\varepsilon_{\text{rec}i}$  is the reconstruction efficiency evaluated for event  $i$  in the simulated  $Z \rightarrow \tau\tau$  sample. The theoretical cross-section for  $\sigma_{pp \rightarrow Z \rightarrow \tau\tau}$  from Sect. 5.3 is used as this cross-section has a higher precision than either of the experimental  $pp \rightarrow Z \rightarrow \ell\ell$  cross-sections,  $\sigma_{pp \rightarrow Z \rightarrow \tau\tau}$  and  $\sigma_{pp \rightarrow Z \rightarrow \tau\tau}$ , measured with LHCb.

In Table 6.1 the number of expected  $Z \rightarrow \tau\tau$  background events in data, calculated using Eq. 6.16, is given. The remaining backgrounds from Table 5.3 have been summed and are also provided, as well as the sum of these backgrounds and the  $Z \rightarrow \tau\tau$  background. The number of events observed in data from Table 5.3 is given for comparison. As can be seen, the expected number of total background events and the number of events observed in data are compatible within uncertainty.

#### Expected Higgs Boson Signal

For the Higgs boson signal, the expected number of events is,

$$N_{\phi^0 \rightarrow \tau\tau}(m_{\phi^0}) = \frac{\sigma_{pp \rightarrow \phi^0}(m_{\phi^0}) \mathcal{B}_{\phi^0 \rightarrow \tau\tau}(m_{\phi^0}) \varepsilon_{\text{sel}}(m_{\phi^0}) \mathcal{L} \mathcal{A}_{\tau_1 \tau_2}(m_{\phi^0}) \mathcal{B}_{\tau_1 \tau_2}}{\frac{1}{N_{\text{sim}}} \sum_i^{N_{\text{sim}}} \left( \varepsilon_{\text{rec}i}^{-1} \right)} \quad (6.17)$$

**Table 6.1.:** Expected number of events for the  $Z \rightarrow \tau\tau$  background, remaining backgrounds summed from Table 5.3, and total background for each event category. The number of events observed in data, from Table 5.3, as well as the expected number of SM Higgs boson events multiplied by a factor of 100 for  $m_{\phi^0} = 125$ , are also given.

|                                     | $\tau_\mu\tau_\mu$ | $\tau_\mu\tau_e$ | $\tau_e\tau_\mu$ | $\tau_\mu\tau_h$ | $\tau_e\tau_h$ |
|-------------------------------------|--------------------|------------------|------------------|------------------|----------------|
| $Z \rightarrow \tau\tau$            | $79.8 \pm 5.6$     | $288.2 \pm 26.2$ | $115.8 \pm 12.7$ | $146.1 \pm 9.7$  | $62.1 \pm 8.0$ |
| other bkg.                          | $41.6 \pm 8.5$     | $129.7 \pm 4.9$  | $56.6 \pm 3.3$   | $53.3 \pm 0.8$   | $36.6 \pm 0.9$ |
| total bkg.                          | $121.4 \pm 10.2$   | $417.9 \pm 26.7$ | $172.4 \pm 13.1$ | $199.3 \pm 9.7$  | $98.7 \pm 8.0$ |
| observed                            | 124                | 421              | 155              | 189              | 101            |
| $H \rightarrow \tau\tau \times 100$ | $3.9 \pm 0.5$      | $11.9 \pm 1.6$   | $3.8 \pm 0.5$    | $9.7 \pm 1.3$    | $4.2 \pm 0.6$  |

where  $m_{\phi^0}$  indicates the term is dependent upon the Higgs boson mass and  $N_{\text{sim}}$  is the number of events in the simulated  $\phi^0 \rightarrow \tau\tau$  sample. The term  $\mathcal{B}_{\phi^0 \rightarrow \tau\tau}$  is the branching fraction of the Higgs boson into a  $\tau$  lepton pair and  $\sigma_{pp \rightarrow \phi^0}$  is the Higgs boson inclusive cross-section. Both terms are mass dependent and are provided by the calculations of Sects. 6.1.1 and 6.1.2 for SM and MSSM Higgs bosons. For the MSSM these terms also depend upon  $\tan\beta$ .

The cross-section  $\sigma_{pp \rightarrow \phi^0}$  is calculated with no kinematic requirements, unlike  $\sigma_{pp \rightarrow Z \rightarrow \tau\tau}$  of Eq. 6.16, and so the mass dependent acceptance is defined as the fraction of generator level events from  $\phi^0 \rightarrow \tau\tau$  simulation passing the  $p_T$  and  $\eta$  requirements of Sect. 5.1.2. Because the same simulation samples are used for all Higgs boson types and production mechanisms, the acceptance can be plotted as a function of the Higgs boson mass, as is done for the five event categories in Fig. 6.7(a). As  $m_{\phi^0}$  increases, the longitudinal boost of the Higgs boson is reduced, resulting in less events where both  $\tau$  leptons from the Higgs boson fall within LHCb. Consequently, the acceptance decreases for increasing  $m_{\phi^0}$ . Numerical values for these acceptances are provided in Fig. D.8 of App. D.2.

The selection efficiency  $\varepsilon_{\text{sel}}$  is mass dependent and is calculated using the same methods as Sect. 5.2.2 but with  $\phi^0 \rightarrow \tau\tau$  simulation samples. The combined selection and reconstruction efficiency correction from Eq. 6.17 is,

$$\varepsilon_{\tau_1\tau_2}(m_{\phi^0}) \equiv \frac{\varepsilon_{\text{sel}}(m_{\phi^0})}{\frac{1}{N_{\text{sim}}} \sum_i^{N_{\text{sim}}} (\varepsilon_{\text{rec}i}^{-1})} \quad (6.18)$$

and is plotted in Fig. 6.7(b) for all five event categories. Again, the same Higgs boson simulation samples are used for all Higgs boson types, and so  $\varepsilon_{\tau_1\tau_2}$  is only a function of the Higgs boson mass. As  $m_{\phi^0}$  increases, the boosts of the  $\tau$  leptons from the Higgs boson increase, producing more collinear  $\tau$  lepton decays and subsequent decay products with larger momenta. Consequently, both the  $|\Delta\phi|$  selection efficiency is expected to increase, as well as the reconstruction efficiencies, resulting in  $\varepsilon_{\tau_1\tau_2}$  rising for increasing  $m_{\phi^0}$ . Numerical values of the efficiency for each event category are given in Fig. D.9 of App. D.2.

In Table 6.1, the expected number of SM Higgs boson events multiplied by a factor of 100 and assuming  $m_H = 125$  GeV is given for each event category. The number of expected SM

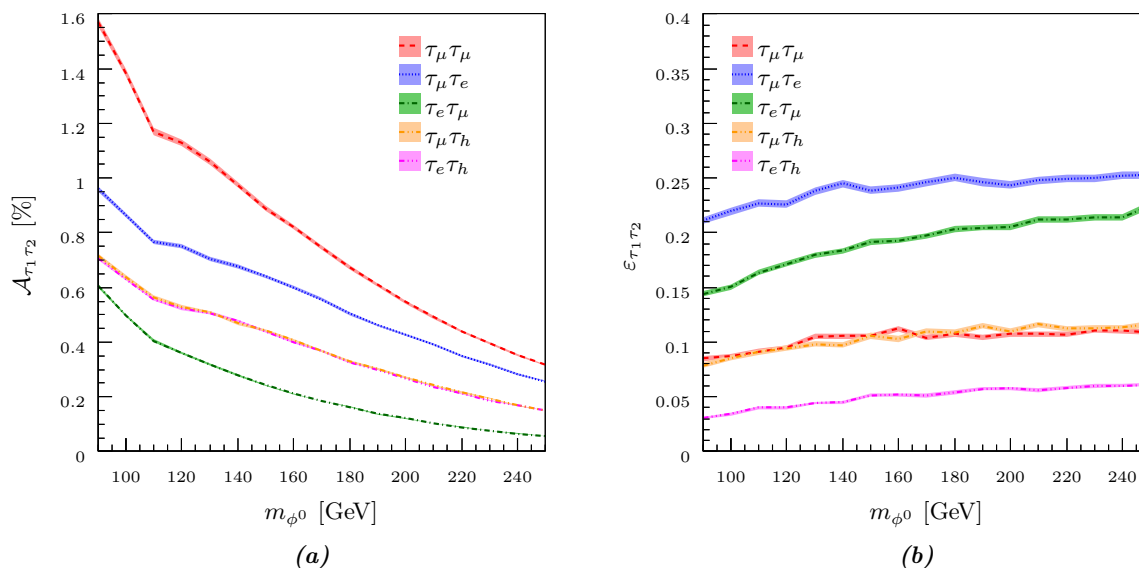


**Figure 6.7.:** (a) Acceptances and (b) efficiencies for the Higgs boson signal as a function of the Higgs boson mass for the five event categories. The uncertainties for the  $\tau_\mu\tau_\mu$  (red),  $\tau_\mu\tau_e$  (blue),  $\tau_e\tau_\mu$  (green),  $\tau_\mu\tau_h$  (orange), and  $\tau_e\tau_h$  (magenta) event categories are provided by their corresponding coloured bands.

Higgs boson events, without uncertainty included, is tabulated as a function of  $m_{\phi^0}$  in Fig. 6.8 for all five event categories, as well as the sum of all five categories. The expected number of neutral MSSM Higgs boson events for each category is tabulated in Fig. 6.9 and for the sum of all categories in Fig. 6.10 as a function of  $m_{A^0}$  and  $\tan\beta$ . As can be seen, the expected number of SM Higgs boson signal events is less than 1 for all event categories, while for the MSSM as many as 120 events are expected.

### 6.2.3. Mass Distributions

The invariant mass distributions for the QCD and  $Z \rightarrow \ell\ell$  backgrounds are determined from data as described in Sect. 5.1.3. The distributions for the EWK,  $t\bar{t}$ ,  $WW$ , and  $Z \rightarrow \tau\tau$  backgrounds as well as the  $\phi^0 \rightarrow \tau\tau$  signal, are taken from simulation which has been calibrated as described in Sect. 5.1.2. Additionally, the events used to produce the distributions are weighted on an event-by-event basis for the differences between the efficiencies evaluated from simulation and data as determined in Sects. 5.2.1 and 5.2.2. This correction is negligible in comparison to the momentum resolution calibration.

The invariant mass distributions for the expected backgrounds and an example MSSM signal, with  $m_{A^0} = 125$  GeV and  $\tan\beta = 60$ , is given for the combination of the five event categories in Fig. 6.11(a) and separated into the five individual categories in Fig. 6.12. The individual background distributions are normalised to the expected number of events from Tables 6.1 for the  $Z \rightarrow \tau\tau$  backgrounds and Table 5.3 for all other backgrounds. The signal distribution is normalised to the number of events calculated with Eq. 6.17. Additionally, an example model independent neutral Higgs boson signal which can be excluded, using the invariant mass distri-

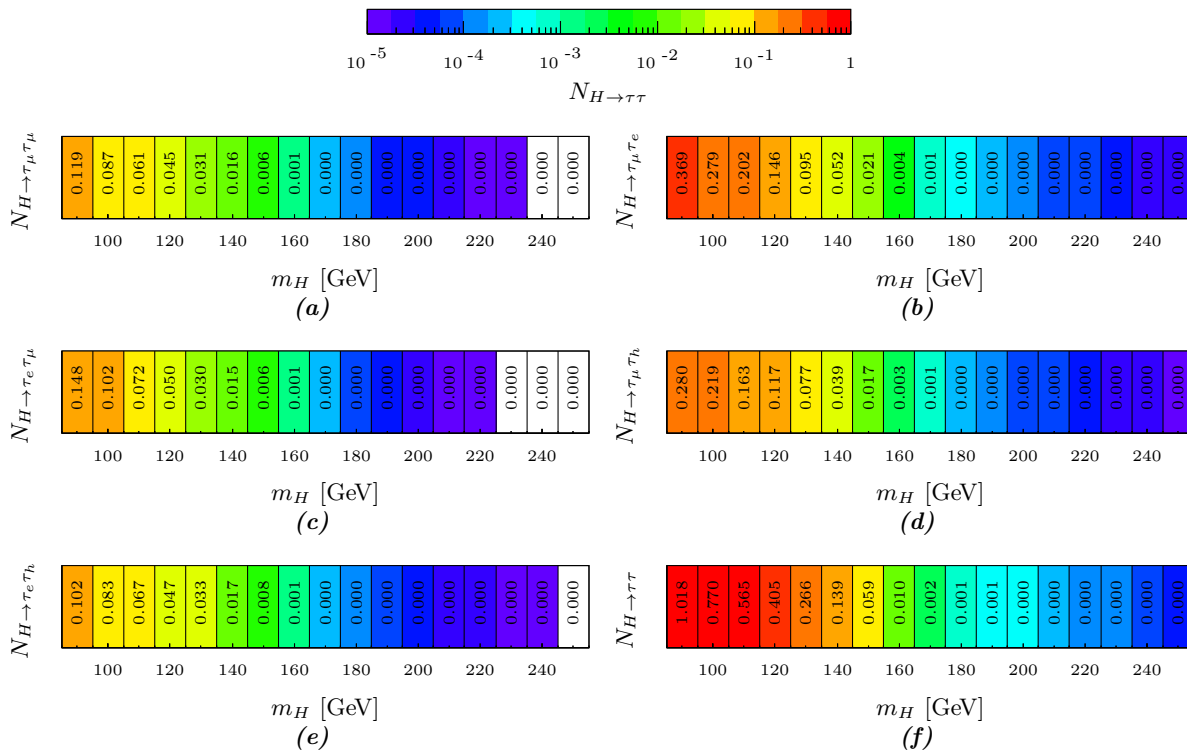


**Figure 6.8.:** Values of the expected number of signal events from the SM Higgs boson for the (a)  $\tau_\mu\tau_\mu$ , (b)  $\tau_\mu\tau_e$ , (c)  $\tau_e\tau_\mu$ , (d)  $\tau_\mu\tau_h$ , (e)  $\tau_e\tau_h$  categories as a function of mass. (f) The sum of all five event categories. Uncertainty is excluded for clarity.

bution information, is provided in Fig. 6.11(b) for the combination of the five event categories.

### 6.3. Statistical Methods

The tool-set used to set model independent and dependent limits on Higgs boson production within the forward region of LHCb is now presented. The primary background can be found in the general statistics textbooks of Refs. [224] and [225], and the more particle physics oriented textbooks of Refs. [226] and [227], as well as the Particle Data Group review of statistics in Ref. [15]. This analysis also relies heavily upon asymptotic approximations of test statistics, for which a comprehensive guide is given in Ref. [228].

Two hypothesis are considered: a background only hypothesis,  $\mathcal{H}_0$ , and a signal plus background hypothesis,  $\mathcal{H}_1$ . The hypotheses can be parametrised as  $\mathcal{H}_\mu$  by a fractional signal strength factor  $\mu$ , where  $\mu = 0$  is the background only hypothesis and  $\mu = 1$  is the signal plus background hypothesis. If a hypothesis is fully specified with no unknown parameters, the hypothesis is simple, while if the hypothesis depends upon one or more unknown parameters, *e.g* reconstruction efficiencies, the hypothesis is complex.

A set of random variables  $\vec{x}$  observed in data is compared with the hypotheses. The agreement between the set of random variables and the proposed hypothesis can be expressed via a test statistic,  $\vec{t}(\vec{x})$ . Ideally the test statistic can be expressed as a single random variable,  $t(\vec{x})$ , without a loss of discrimination between the hypotheses.

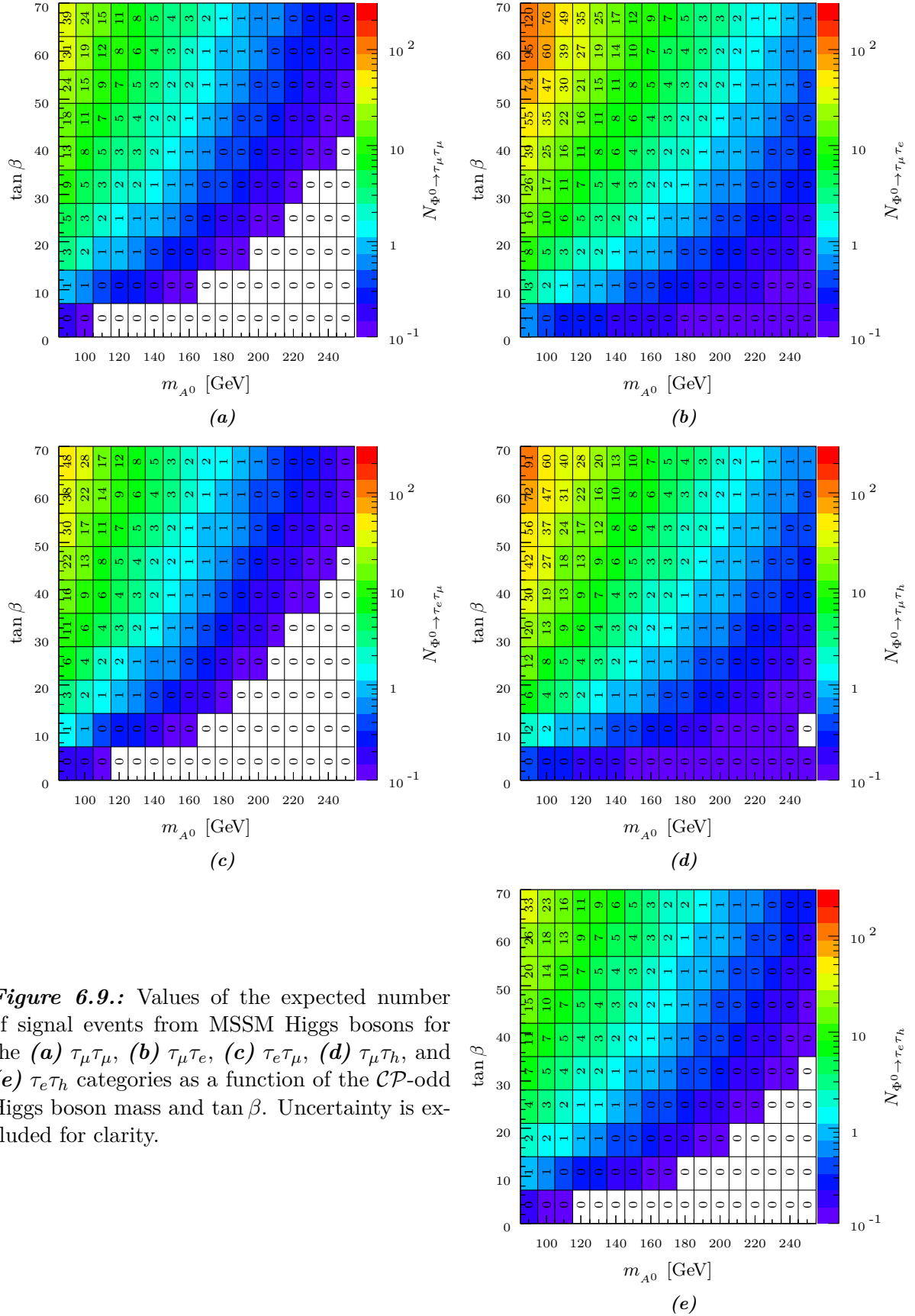
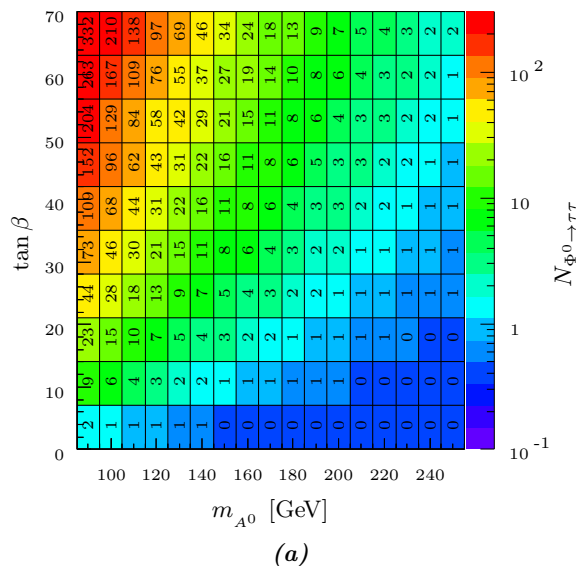


**Figure 6.9.:** Values of the expected number of signal events from MSSM Higgs bosons for the (a)  $\tau_\mu\tau_\mu$ , (b)  $\tau_\mu\tau_e$ , (c)  $\tau_e\tau_\mu$ , (d)  $\tau_\mu\tau_h$ , and (e)  $\tau_e\tau_h$  categories as a function of the  $CP$ -odd Higgs boson mass and  $\tan \beta$ . Uncertainty is excluded for clarity.

**Figure 6.10.:** Values of the expected number of signal events from MSSM Higgs bosons, summed for all event categories, as a function of the  $\mathcal{CP}$ -odd Higgs boson mass and  $\tan\beta$ . Uncertainty is excluded for clarity.



### 6.3.1. Hypothesis Testing

The probability density function for a test statistic is dependent upon the hypothesis considered,  $pdf(t|\mu)$ , where  $\mu$  is the fractional signal strength parameter of the hypothesis  $\mathcal{H}_\mu$ . In Fig. 6.13 an example of the  $pdf$ s for a test statistic is given. The dashed red curve gives the test statistic probability density function for the background only hypothesis,  $pdf(t|0)$ , while the dotted blue curve gives  $pdf(t|1)$  for the signal plus background hypothesis. An example experimental measurement is made with a result of  $\vec{x}_{\text{obs}}$  and the corresponding test statistic is  $t_{\text{obs}}$ , given by the vertical black line of Fig. 6.13.

A hypothesis  $\mathcal{H}_\mu$  is always tested via rejection, not acceptance, by defining a critical region,  $\mathcal{C}$ , within the space of possible test statistics, such that the probability of observing  $\vec{t}$  in  $\mathcal{C}$ , assuming  $\mathcal{H}_\mu$ , is  $p$ . An experimental measurement is then made, and if  $\vec{t}_{\text{obs}}$  falls within the critical region the hypothesis is rejected with a significance level  $p$ . For a test statistic of dimension one like that of Fig. 6.13, the critical region can be defined by,

$$p \equiv \int_{c_1}^{c_2} pdf(t|\mu) dt \quad (6.19)$$

where  $c_1$  and  $c_2$  are the limits of the critical region. The critical region is determined by which hypothesis is being tested and at what confidence level the test is being performed.

### Confidence Levels

If looking for evidence of a new signal, the background only hypothesis must be rejected. For an observed test statistic  $t_{\text{obs}}$ , the background only hypothesis can be rejected at a maximum significance of,

$$p_0 \equiv \int_{t_{\text{obs}}}^{\infty} pdf(t|0) dt \quad (6.20)$$

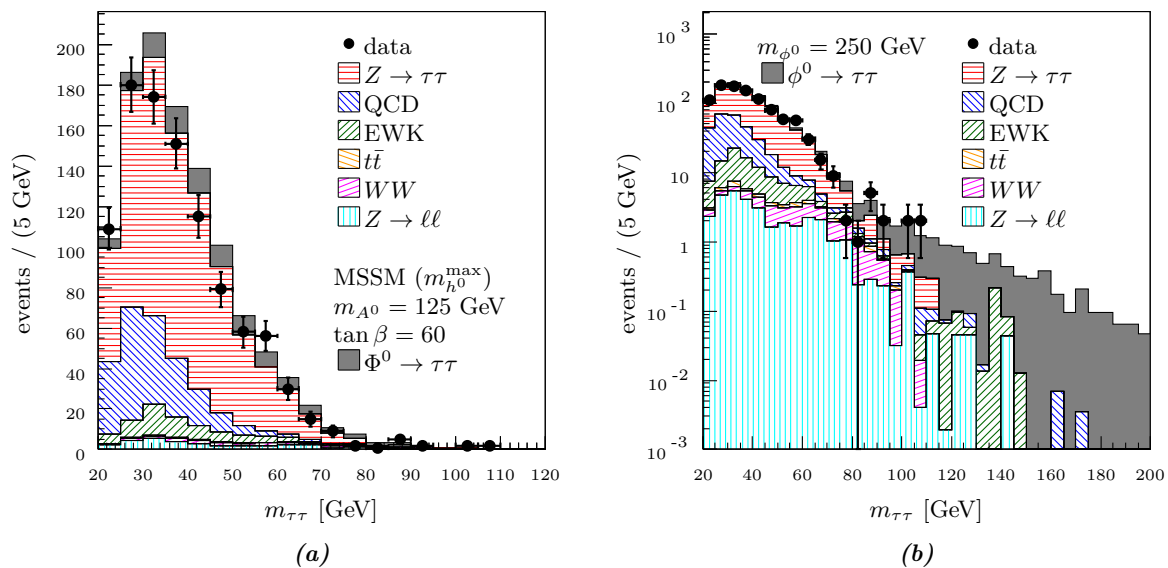


**Figure 6.11.:** (a) Invariant mass distributions for the five combined event categories of the backgrounds and an example expected MSSM Higgs boson signal (grey) with  $m_{A^0} = 125$  GeV and  $\tan \beta = 60$ . The backgrounds from the five event categories are grouped into  $Z \rightarrow \tau\tau$  (red), QCD (blue), EWK (green),  $t\bar{t}$  (orange),  $WW$  (magenta), and  $Z \rightarrow \ell\ell$  (cyan). The  $Z \rightarrow \tau\tau$  and Higgs boson signal distributions are normalised following the prescriptions of Eqs. 6.16 and 6.17. (b) The same invariant mass distribution, but with an example model independent neutral Higgs boson signal (grey) with  $m_{\phi^0} = 250$  GeV which can be excluded is shown.

where  $p_0$  is the background only  $p$ -value, given by the red fill in the example of Fig. 6.13. The background only  $p$ -value is then the probability of observing a  $t$  larger than  $t_{\text{obs}}$  for an ensemble of repeated experiments, assuming  $\mathcal{H}_0$ . Alternatively, the background only hypothesis confidence level is oftentimes defined as,

$$\text{CL}_b \equiv 1 - p_0 \quad (6.21)$$

for which a large value indicates a low level of confidence in the hypothesis. Typically to claim the discovery of a new signal in particle physics, the background only hypothesis must be rejected with a  $p_0$  of  $(2.9 \times 10^{-5})\%$  or less. Further discussion of this convention can be found in Ref. [229].

When testing the signal plus background hypothesis  $\mathcal{H}_1$  the  $p$ -value,

$$p_1 \equiv \int_{-\infty}^{t_{\text{obs}}} pdf(t|1) dt \quad (6.22)$$

is used, which in the example of Fig. 6.13 is given by the blue fill. Assuming  $\mathcal{H}_1$  is true,  $p_1$  is the probability of observing a  $t$  lower than  $t_{\text{obs}}$  for an ensemble of repeated experiments. The signal plus background confidence level is defined as,

$$\text{CL}_{s+b} \equiv p_1 \quad (6.23)$$



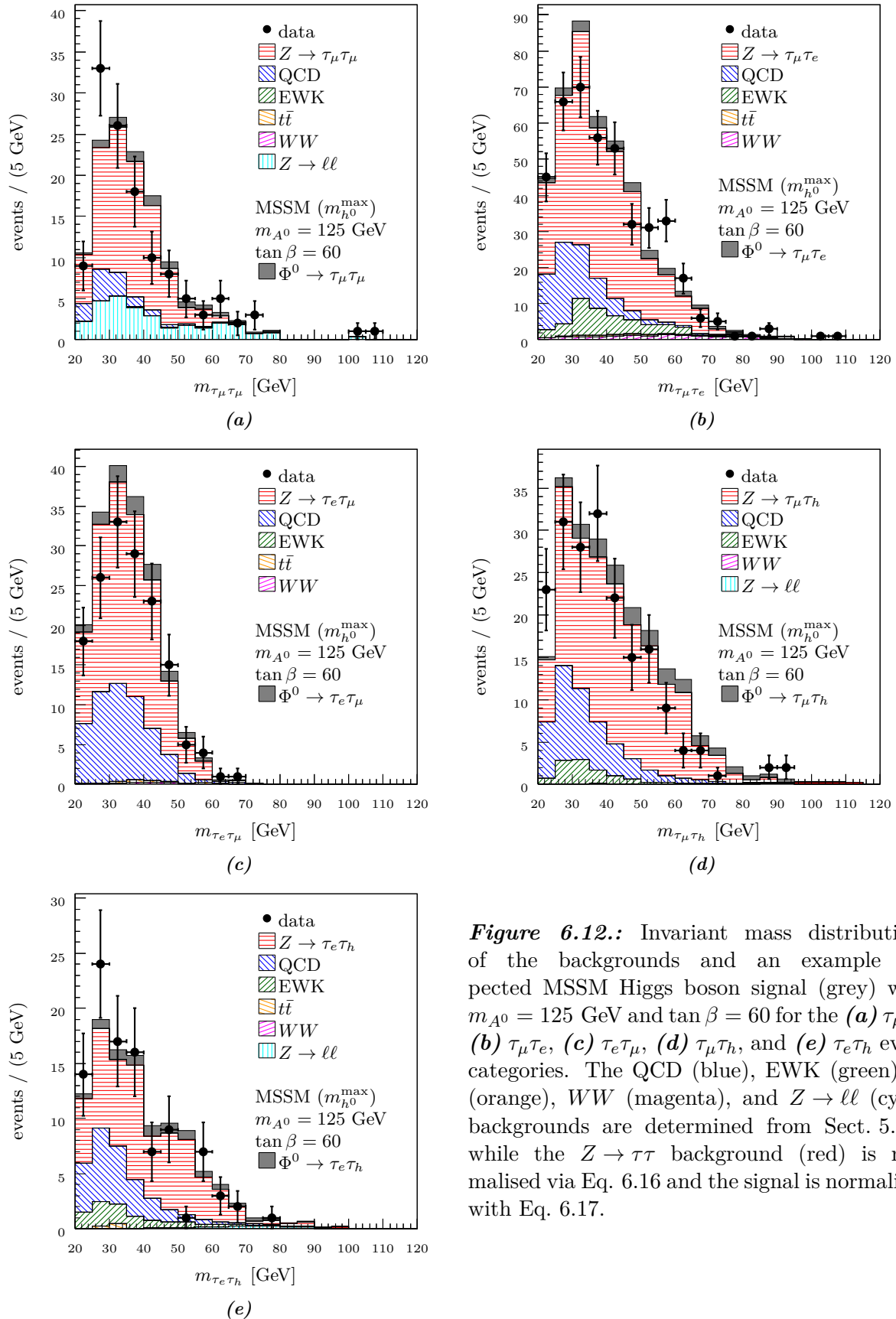


**Figure 6.12.:** Invariant mass distributions of the backgrounds and an example expected MSSM Higgs boson signal (grey) with  $m_{A^0} = 125$  GeV and  $\tan \beta = 60$  for the (a)  $\tau_\mu\tau_\mu$ , (b)  $\tau_\mu\tau_e$ , (c)  $\tau_e\tau_\mu$ , (d)  $\tau_\mu\tau_h$ , and (e)  $\tau_e\tau_h$  event categories. The QCD (blue), EWK (green),  $t\bar{t}$  (orange),  $WW$  (magenta), and  $Z \rightarrow \ell\ell$  (cyan) backgrounds are determined from Sect. 5.1.3, while the  $Z \rightarrow \tau\tau$  background (red) is normalised via Eq. 6.16 and the signal is normalised with Eq. 6.17.

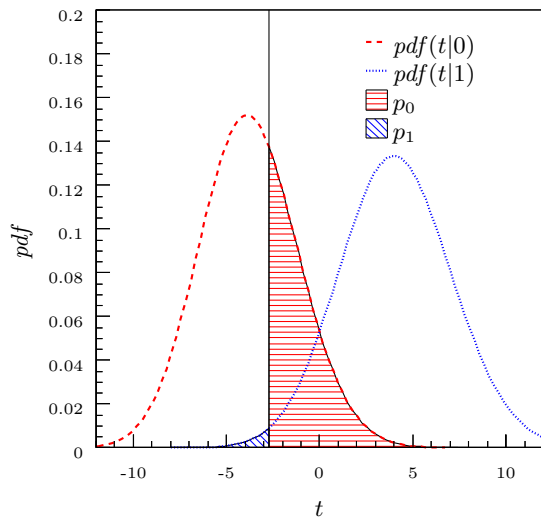


**Figure 6.13.:** Probability density functions for the test statistic  $t$ , using the test statistic of Eq. 6.25 with the likelihood function of Eq. 6.38, assuming the background only hypothesis (red) and the signal plus background hypothesis (blue). The  $p$ -values are given by the fills for  $p_0$  (red) and  $p_1$  (blue).

where now a small value indicates a low level of confidence in the hypothesis. In particle physics, a signal plus background hypothesis is oftentimes considered to be excluded at a 95% confidence level if  $\text{CL}_{\text{s+b}}$  is found to be less than 5%. Here, the confidence level is defined as  $1 - \text{CL}_{\text{s+b}}$ . At this confidence level, assuming the signal plus background hypothesis, 95% of repeated experiments will produce a  $t$  greater than  $t_{\text{obs}}$ .

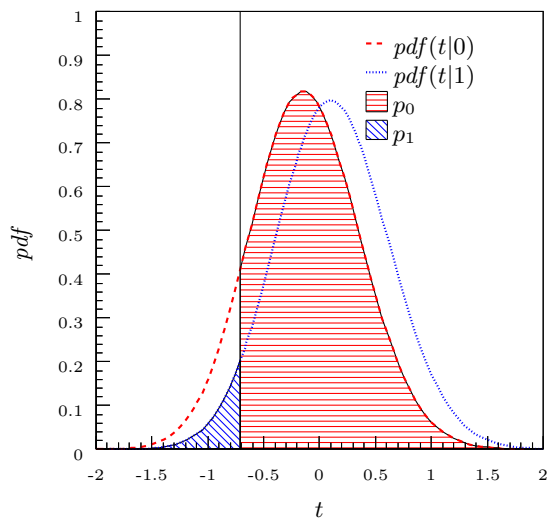


**Figure 6.14.:** The test statistic  $pdf$ s for an example experiment resulting in a mis-leading exclusion at 95%  $\text{CL}_{\text{s+b}}$ . The black line indicates the observed test statistic  $t_{\text{obs}}$ .

Using  $\text{CL}_{\text{s+b}}$  for an experiment with a small signal and large background can result in mis-leading exclusions of the signal plus background hypothesis when there is a large downward fluctuation in the observed number of events. The  $pdf$ s for the test statistic assuming  $\mathcal{H}_0$  and  $\mathcal{H}_1$  for such an example are given in Fig. 6.14. Here, the signal plus background hypothesis can be rejected at a confidence level of 95% using the  $\text{CL}_{\text{s+b}}$  method, despite poor agreement of the observed test statistic with the background only hypothesis. One method to combat mis-leading exclusions like this is to report both  $p_0$  and  $p_1$  so the agreement with not only the signal plus background hypothesis but also the background hypothesis is known.

However, this method does not allow for a simple comparison between different experimental results. In particle physics the  $CL_s$  method,

$$CL_s \equiv \frac{CL_{s+b}}{CL_b} = \frac{p_1}{1 - p_0} \quad (6.24)$$

from Refs. [230] and [231] is oftentimes used instead of the  $CL_{s+b}$  method. Using this method for the example of Fig. 6.14 does not result in a mis-leading exclusion at the 95% confidence level, because while  $p_1$  is less than 5%,  $p_0$  is also large, resulting in a larger  $CL_{s+b}$ .

Particle physics lends itself towards a frequentist interpretation of probability, where probability is defined as the relative frequency for an event to occur. The  $CL_s$  method, like the  $CL_{s+b}$  method, also has a frequentist interpretation as shown in Ref. [232], and when the expected number of signal events is large with respect to the expected background the limits produced from the  $CL_{s+b}$  and  $CL_s$  methods converge. Alternatives to  $CL_s$  have been proposed, *e.g.* Ref. [233], but for comparison purposes with other experiments the  $CL_s$  method is used in this analysis.

### Test Statistics

The above discussion relies upon the test statistic  $t$ , which is defined here. From the result of Neyman and Pearson [234] the most powerful test statistic, assuming simple hypotheses, is

$$t \equiv LL(\vec{x}|1) - LL(\vec{x}|0) = \ln \left( \frac{pdf(\vec{x}|1)}{pdf(\vec{x}|0)} \right) \quad (6.25)$$

when using the background only hypothesis test of Eq. 6.20 and the signal plus background hypothesis test of Eq. 6.22. Here,  $LL(\vec{x}|\mu)$  is the natural logarithm of the likelihood function,

$$L(\vec{x}|\mu) \equiv \prod_i pdf(x_i|\mu) \quad (6.26)$$

given the random variables  $x_i$  of  $\vec{x}$  are independent. The log-likelihood function is used for numerical stability.

The *pdf* of  $t$  can be determined analytically when the *pdfs* of  $LL(t|0)$  and  $LL(t|1)$  are known and Eq. 6.25 is an invertible function. However, this is oftentimes not the case, and so the *pdf* of  $t$  must be built using a Monte Carlo technique: a large number of pseudo-experiments are generated, the test statistic for each experiment is built, and the *pdf* is taken as the normalised distribution of  $t$ . This process can be computationally expensive, particularly for complicated likelihood functions, and so a numerically simpler alternative which provides a similar separation power is preferable to  $t$  of Eq. 6.25.

Consider maximising  $LL(\vec{x}|\nu)$  with respect to a signal strength parameter  $\nu$  such that  $LL(\vec{x}|\hat{\nu})$  is the maximum log-likelihood for a given  $\vec{x}$  and  $\hat{\nu}$  is the maximum likelihood estimator. The first derivative of  $LL(\vec{x}|\nu)$  can be expanded about the point  $\hat{\nu}$ ,

$$\frac{\partial LL(\vec{x}|\nu)}{\partial \nu} = \left. \frac{\partial LL(\vec{x}|\nu)}{\partial \nu} \right|_{\hat{\nu}} + (\nu - \hat{\nu}) \left. \frac{\partial^2 LL(\vec{x}|\nu)}{\partial \nu^2} \right|_{\hat{\nu}} + \dots \quad (6.27)$$

where the first term vanishes since  $LL(\vec{x}|\nu)$  is at a maximum for  $\hat{\nu}$ . In the limit for a large number of repeated experiments  $N$ , the second derivative approaches the expectation value of the set of experiments and can be written as  $-1/\sigma^2$  where  $\sigma^2$  is the variance. Additionally, the maximum likelihood estimator  $\hat{\nu}$  becomes normally distributed,

$$pdf(\hat{\nu}|\mu) = \frac{1}{\sigma\sqrt{2\pi}} e^{-\frac{(\hat{\nu}-\mu)^2}{2\sigma^2}} \quad (6.28)$$

with the same variance  $\sigma^2$  and a mean of  $\mu$ ; see Ref. [225] for further details.

Equation 6.27 can then be written as,

$$\frac{\partial LL(\vec{x}|\nu)}{\partial \nu} = -\frac{\nu - \hat{\nu}}{\sigma^2} \quad (6.29)$$

where the higher orders terms have been neglected. Integrating yields,

$$LL(\vec{x}|\nu) = -\frac{(\nu - \hat{\nu})^2}{2\sigma^2} + LL(\vec{x}|\hat{\nu}) \quad (6.30)$$

where the initial condition  $\nu = \hat{\nu}$  is used to determine the constant of integration  $LL(\vec{x}|\hat{\nu})$ . Using Eq. 6.30 the profile likelihood ratio test statistic,

$$t_\nu \equiv -2(LL(\vec{x}|\nu) - LL(\vec{x}|\hat{\nu})) = \frac{(\nu - \hat{\nu})^2}{\sigma^2} \quad (6.31)$$

is defined. This provides a test statistic that can be written without likelihood functions but also provides a discrimination close to the most powerful test statistic of Eq. 6.25. The only random variable of  $t_\nu$  is  $\hat{\nu}$  and so the *pdf* of  $t_\nu$  can be found by,

$$pdf(t_\nu|\mu) = pdf(\hat{\nu}(t_\nu)|\mu) \left| \frac{\partial \hat{\nu}(t_\nu)}{\partial t_\nu} \right| \quad (6.32)$$

where the *pdf* of  $\hat{\nu}$  is transformed to the variable  $t_\nu$ . The inverse of  $t_\nu$ ,  $\hat{\nu}(t_\nu)$ , is  $\nu \pm \sigma\sqrt{t_\nu}$  and so Eq. 6.32 becomes,

$$pdf(t_\nu|\mu) = \frac{1}{\sqrt{8\pi t_\nu}} e^{-\frac{1}{2}\left(\frac{\nu-\mu}{\sigma} + \sqrt{t_\nu}\right)^2} + \frac{1}{\sqrt{8\pi t_\nu}} e^{-\frac{1}{2}\left(\frac{\nu-\mu}{\sigma} - \sqrt{t_\nu}\right)^2} \quad (6.33)$$

where  $pdf(\hat{\nu}|\mu)$  is given by Eq. 6.28, the first term is from the  $\nu + \sigma\sqrt{t_\nu}$  solution, and the second term is from the  $\nu - \sigma\sqrt{t_\nu}$  solution of  $\hat{\nu}(t_\nu)$ . This *pdf*, further discussed in Ref. [228], is a non-central chi-squared distribution for one degree of freedom. From a result of Ref. [235] the remaining terms of Eq. 6.27, which have not been explicitly written, can be shown to contribute to  $t_\nu$  on the order of  $1/\sqrt{n}$  where  $n$  is the size of  $\vec{x}$ .

For the case when  $\nu = \mu$ , Eq. 6.33 is a chi-squared distribution of one degree of freedom, a result first shown by Wilks in Ref. [236]. The distributions necessary for background and signal plus background hypothesis testing,  $pdf(t_0|0)$  and  $pdf(t_1|1)$ , are then fully defined by Eq. 6.33 as  $\nu$  and  $\mu$  cancel and the terms with  $\sigma$  are zero.

In Fig. 6.15 the same example of Fig. 6.13 is used and the distributions for  $pdf(t_0|0)$  and

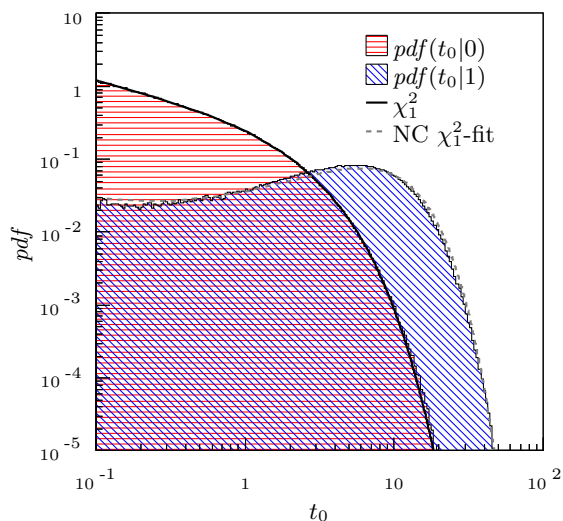


**Figure 6.15.:** Probability density functions from  $10^6$  pseudo-experiments for the two-sided test statistic  $t_0$ , using the test statistic of Eq. 6.31 with the likelihood function of Eq. 6.38, assuming the background hypothesis (red) and the signal plus background hypothesis (blue). The two  $pdfs$  are compared to Eq. 6.33, a chi-squared distribution with one degree of freedom for  $\mathcal{H}_0$  (solid black) and a fitted non-central chi-squared distribution with one degree of freedom for  $\mathcal{H}_1$  (dashed grey).

$pdf(t_0|1)$ , the two-sided test statistic of Eq. 6.31, are generated using the Monte Carlo technique from  $10^6$  pseudo-experiments. These distributions are shown in Eq. 6.33, where  $pdf(t_0|0)$  approaches a chi-squared distribution of one degree of freedom and  $pdf(t_0|1)$  approaches a non-central chi-squared distribution. The two  $pdfs$  are also compared to the chi-squared functions of Eq. 6.33 which they approach.

In Ref. [228] a test statistic for performing an upper limit test on the signal plus background hypothesis is proposed,

$$q_\nu \equiv \begin{cases} -2(LL(\vec{x}|\nu) - LL(\vec{x}|\hat{\nu})) & \text{if } \hat{\nu} \leq \nu \\ 0 & \text{else} \end{cases} \quad (6.34)$$

which, following the same transformation procedure of Eq. 6.32, results in the  $pdf$ ,

$$pdf(q_\nu|\mu) = \Phi\left(-\frac{\nu - \mu}{\sigma}\right) \delta(q_\nu) + \frac{1}{\sqrt{8\pi q_\nu}} e^{-\frac{1}{2}\left(\frac{\nu - \mu}{\sigma} - \sqrt{q_\nu}\right)^2} \quad (6.35)$$

for the limit of large  $N$  where  $\Phi$  is the standard normal cumulative distribution function. The cumulative distribution function is then given by,

$$cdf(q_\nu|\mu) = \int_{-\infty}^{q_\nu} pdf(q'_\nu|\mu) dq'_\nu = \Phi\left(\sqrt{q_\nu} - \frac{\nu - \mu}{\sigma}\right) \quad (6.36)$$

and so for the special case of  $\nu = \mu$  the  $cdf$  is given by  $\Phi(\sqrt{q_\nu})$ . Consequently,  $p_0$  and  $p_1$  can be calculated quickly by,

$$p_0 = \Phi(q_{0\text{obs}}), \quad p_1 = 1 - \Phi(q_{1\text{obs}}) \quad (6.37)$$

without the need to employ Monte Carlo techniques. In the example of Figs. 6.13 and 6.15 the  $p$ -values, assuming the signal plus background hypothesis, are found to be  $p_1 = 1.07 \times 10^{-2}$  using  $t$  of Eq. 6.25, and  $p_1 = 0.91 \times 10^{-2}$  using  $q_\nu$  of Eq. 6.34.

### 6.3.2. Likelihoods, Medians, and Uncertainties

The test statistics of Sect. 6.3.1 are built from likelihood functions, which have not yet been defined. In this analysis two likelihood functions are used, a simple likelihood function for consistency checks and an extended likelihood function which utilises the mass distributions of Sect. 6.2.3 for producing the final upper limits of Sect. 6.4. In this section these likelihoods are described. Additionally, a method for building the median test statistic with these likelihood functions as well as how uncertainty can be incorporated into a likelihood function is outlined.

#### Likelihood Functions

The simple likelihood function is a Poisson *pdf*,

$$L_s(x|\mu) = pdf_p(x|N_{\text{bkg}} + \mu N_{\text{sig}}) = \frac{(N_{\text{bkg}} + \mu N_{\text{sig}})^x e^{-N_{\text{bkg}} - \mu N_{\text{sig}}}}{x!} \quad (6.38)$$

where  $x$  is the number of observed events,  $N_{\text{bkg}}$  is the expected number of background events,  $N_{\text{sig}}$  is the number of expected signal events, and  $\mu$  is the signal strength parameter of Sect. 6.3.1. In the test statistics of Eqs. 6.25, 6.31, and 6.34 the ratio of two likelihoods is always taken for a given  $x$  and so the discrete  $x$  factorial terms cancel. Consequently, while the observed  $x$  from an experiment must be an integer, the defined test statistics can still be calculated for any real-valued  $x$ . Additionally, the  $e^{N_{\text{bkg}}}$  terms cancel and can be omitted when calculating the test statistics with this likelihood function.

The simple likelihood only utilises the number of expected and observed events, without considering any additional information from the events. The extended likelihood function utilises not only the number of events, but also any other observables which are measured for each event. The extended likelihood function is defined as,

$$L_e(\vec{x}|\mu) = e^{-N_{\text{bkg}} - \mu N_{\text{sig}}} \prod_i ((N_{\text{bkg}} + \mu N_{\text{sig}}) pdf(\vec{o}_i|\mu)) \quad (6.39)$$

where  $\vec{x}$  consists of a set of observables  $\vec{o}_i$  for each event  $i$ , and the product is over all events. The probability density function for the set of observables  $\vec{o}_i$ , assuming a signal strength  $\mu$ , is given by  $pdf(\vec{o}_i|\mu)$ . For this analysis, only the invariant mass of the  $\tau$  lepton decay products is measured per event, and so  $\vec{o}_i$  is just the invariant mass for event  $i$ . The extended likelihood function of Eq. 6.39 is the limit of the binned likelihood function, which is the product of the simple likelihood function for every bin, as the widths of the bins approach zero. For further details on the properties of the extended likelihood function, refer to Ref. [237].

An example demonstrating the additional separation power between the background only and signal plus background hypotheses when using the extended likelihood function is given in Fig. 6.16. This is the same example as Fig. 6.13, but now the extended likelihood is used to calculate the test statistic of Eq. 6.25 rather than the simple likelihood function. The invariant mass distributions used in this example are given in Fig. 6.16(b). As can be seen, the additional information from the mass for each event produces a more significant exclusion of the signal

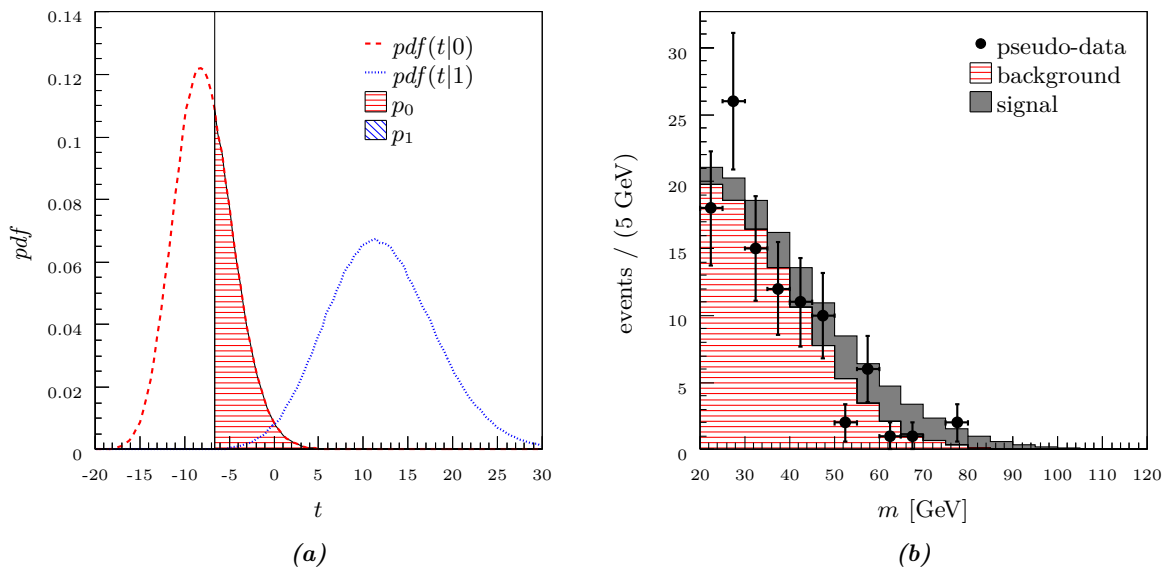


**Figure 6.16.:** (a) The example of Fig. 6.13 but now using the extended likelihood function of Eq. 6.39 rather than the simple likelihood function to calculate the test statistic. (b) Invariant mass distribution for pseudo-data (points), expected background (red), and expected signal (grey) used when calculating the extended likelihood for this example.

plus background hypothesis.

### Median Values

The sensitivity of an experiment in rejecting a given hypothesis is quantified by the  $p$ -values for the median test statistics when testing the null hypothesis, assuming the alternative hypothesis. When rejecting  $\mathcal{H}_0$ ,  $p_0$  for the median test statistic assuming  $\mathcal{H}_1$ ,  $M[t|1]$ , characterises the experimental sensitivity. Conversely, when rejecting  $\mathcal{H}_1$ ,  $p_1$  for  $M[t|0]$  characterises the sensitivity. The  $p$ -values from the median test statistics can also be used to perform consistency checks.

The median test statistic is determined from,

$$cdf(M[t|\mu]|\mu) = \int_{-\infty}^{M[t|\mu]} pdf(t'|\mu) dt' = \frac{1}{2} \quad (6.40)$$

where the test statistics for half of all repeated experiments are expected to fall below  $M[t|\mu]$  and half above, assuming the signal strength parameter  $\mu$  is the true signal strength.

For the Neyman-Pearson ratio test statistic of Eq. 6.25, the median test statistic can be determined by integrating the test statistic  $pdf$ s. When using the simple likelihood function of Eq. 6.38 the  $pdf$  of the test statistic is,

$$pdf(t|\mu) = \frac{pdf_p \left( \frac{t+N_{\text{sig}}}{\ln(N_{\text{bkg}}+N_{\text{sig}})-\ln(N_{\text{bkg}})} \middle| N_{\text{bkg}} + \mu N_{\text{sig}} \right)}{\ln(N_{\text{bkg}} + N_{\text{sig}}) - \ln(N_{\text{bkg}})} \quad (6.41)$$

which is a modified Poisson distribution. The mean of this distribution is  $t$  evaluated for an  $x$  of  $N_{\text{bkg}} + \mu N_{\text{sig}}$ . If the expected background plus signal is large, the  $pdf(t|\mu)$  approaches a normal

distribution and,

$$M[t|\mu] = t(N_{\text{sig}} + \mu N_{\text{bkg}}) \quad (6.42)$$

since the mean of the test statistic *pdf* approaches the median.

For the test statistic  $q_\nu$  of Eq. 6.34, the median test statistic can be found using the Asimov dataset proposed in Ref. [228] and inspired by Ref. [238]. The extended log-likelihood function evaluated with the Asimov data set is,

$$LL_e(\vec{a}(\mu)|\nu) = \int \ln \left( (N_{\text{bkg}} + \nu N_{\text{sig}}) pdf(\vec{o}|\nu) \right) (N_{\text{bkg}} + \mu N_{\text{sig}}) pdf(\vec{o}|\mu) d\vec{o} - N_{\text{bkg}} - \nu N_{\text{sig}} \quad (6.43)$$

as shown in App. D.3.1. Here, the integral is over the joint *pdf* of the observables  $\vec{o}$ , where the first instance of the *pdf* is evaluated with signal strength  $\nu$  of the test statistic  $q_\nu$  and the second instance of the *pdf* is evaluated with signal strength  $\mu$ , the signal strength of the Asimov dataset. In this analysis, the integral is only over the invariant mass *pdf*. As an example, the median value for the  $q_1$  test statistic of Eq. 6.35 can be evaluated as,

$$M[q_1|0] = LL_e(\vec{a}(0)|1) - LL_e(\vec{a}(0)|0) \quad (6.44)$$

when using the extended likelihood function and assuming the background only hypothesis is true.

### Uncertainties

The test statistics of Eqs. 6.25, 6.31, and 6.34 as well as the likelihood functions of Eqs. 6.38 and 6.39 do not incorporate any experimental systematic uncertainties. While there is no standardised method for incorporating uncertainties, a variety of methods can be used. For the frequentist hypothesis testing of Sect. 6.3.1 the systematic uncertainties are introduced into the likelihood function and the method of maximum likelihood from Eq. 6.27 is used. The alternative methods of marginalisation and hybrid marginalisation are described in App. D.3.2, but are not used here.

If the uncertainties factorise, the likelihood function becomes,

$$L(\vec{x}|\mu, \vec{\theta}) = \prod_i pdf(x_i|\mu, \vec{\theta}) \prod_j pdf(\theta_j) \quad (6.45)$$

where the first product is over all  $x_i$  of  $\vec{x}$  and the second product is over all  $\theta_j$  of  $\vec{\theta}$ . The probability density function for each nuisance parameter is given by  $pdf(\theta_j)$ . This likelihood function is then introduced into the profiled likelihood ratios which become,

$$t_\nu = -2(LL(\vec{x}|\nu, \hat{\hat{\theta}}) - LL(\vec{x}, \hat{\nu}, \hat{\theta})) \quad (6.46)$$



and,

$$q_\nu = \begin{cases} -2 \left( LL(\vec{x}|\nu, \hat{\theta}) - LL(\vec{x}|\hat{\nu}, \hat{\theta}) \right) & \text{if } \hat{\nu} \leq \nu \\ 0 & \text{else} \end{cases} \quad (6.47)$$

where  $\hat{\theta}$  is the maximum likelihood estimator for a given  $\vec{x}$  and  $\nu$ , and  $\hat{\theta}$  is the maximum likelihood estimator for a given  $\vec{x}$  and  $\hat{\nu}$ . The *pdfs* for  $t_\nu$  and  $q_\nu$  of Eqs. 6.33 and 6.35 still hold, as does the method of obtaining the median test statistic using the Asimov dataset.

In this analysis, each systematic uncertainty is introduced as a normally distributed nuisance parameter with a mean of  $\epsilon$  and a deviation of  $\delta$ . The likelihood functions of Eqs. 6.38 and 6.39 then become,

$$L(\vec{x}|\mu, \vec{\theta}) = L(\vec{x}|\mu) \prod_i \left( \frac{1}{\delta_i \sqrt{2\pi}} e^{-\frac{(\theta_i - \epsilon_i)^2}{2\delta_i^2}} \right) \quad (6.48)$$

where  $L(\vec{x}|\mu)$  is determined using  $pdf(\vec{x}|\mu, \theta)$  evaluated at  $\vec{\theta}$  rather than the central values  $\vec{\epsilon}$ , and the product is over all nuisance parameters  $\theta_i$ .

## 6.4. Results

Because no excess is seen in the number of observed events shown in Fig. 6.12 and tabulated in Table 6.1 when compared to the background only hypothesis, upper limits are set on neutral Higgs boson production. Limits on model independent production of neutral Higgs bosons decaying into  $\tau$  lepton pairs,  $\sigma_{pp \rightarrow \Phi^0 \rightarrow \tau\tau}$ , within the LHCb acceptance  $2.0 \leq \eta_\tau \leq 4.5$ , using the Higgs boson phenomenology of Sect. 6.1, the event model of Sect. 6.2, and the statistical methods of Sect. 6.3, are calculated for the individual event categories. The limits are set at a 95% confidence level, using  $CL_s$  with the profiled likelihood method and are determined as a function of the neutral Higgs boson mass,  $m_{\phi^0}$ . Similarly, upper limits on  $\tan\beta$  from the production of the three neutral MSSM Higgs bosons decaying into  $\tau$  lepton pairs, assuming the  $m_{h^0}^{\max}$  scenario, are calculated for the five event categories as a function of the  $\mathcal{CP}$ -odd Higgs boson mass,  $m_{A^0}$ .

The observed limits are calculated using the test statistic  $q_\nu$  of Eq. 6.47 and the extended likelihood function of Eq. 6.39. The likelihood function is determined using the invariant mass distributions of Fig. 6.12. The systematic uncertainty on each background component, given in Table 6.1 for the  $Z \rightarrow \tau\tau$  background and Table 5.3 for the remaining backgrounds, is introduced into the extended likelihood function as a nuisance parameter using Eq. 6.48. Each uncertainty affects the shape of the expected invariant mass distribution,  $pdf(m|\mu, \vec{\theta})$ , by scaling the individual background distribution component associated with the uncertainty. The expected number of background events is also affected by each nuisance parameter such that  $N_{\text{bkg}_i} = \theta_i$ . The uncertainty on the simulated mass shape, determined in Sect. 5.1.2 using the

calibration of Fig. 5.5(a), is also introduced as a nuisance parameter, where the parameter only affects the component mass distributions from simulation, *e.g.* the  $Z \rightarrow \tau\tau$  background mass shape.

These limits are given as the solid black lines in Figs. 6.17 through 6.22 for each of the five event categories, and in Fig. 6.23 for the combination of the five categories. In Sect. 6.4.1, the observed limits for each event category are checked for consistency against additional validation limits in Fig. 6.17 for the SM and Fig. 6.18 for the MSSM. In Sect. 6.4.2 the final observed limits are compared with the expected limits in Fig. 6.21 for the SM and Fig. 6.22 for the MSSM, as well as limits from previous results in Fig. 6.23.

### 6.4.1. Validation

The final observed limit is compared against three validation limits for each of the five event categories in Fig. 6.17 for the model independent limits and Fig. 6.18 for the MSSM limits. The dashed green line is the observed limit, using the same statistical methods, but without uncertainties introduced. The dash-dotted orange line is the observed limit using the  $q_\nu$  test statistic with a simple likelihood and with uncertainties. For this limit, because no mass distribution information is utilised, the mass shape uncertainty is not included. Finally, the dash-dotted magenta line is the observed limit using the  $q_\nu$  test statistic with a simple likelihood and no uncertainties. These validation limits can be compared using either Fig. 6.17 or Fig. 6.18, but the results are more easily interpreted for the model independent limits, as the MSSM limits are presented in  $m_{A^0}$  and  $\tan\beta$  space. Consequently, only the model independent limits are discussed here.

The effect of including systematic uncertainties in the limits is seen for the extended likelihood function by comparing the green and black lines of Fig. 6.17. As expected, the limit calculated without uncertainties is lower than the limit with uncertainties. Additionally, for larger  $m_{\phi^0}$  the difference between the two limits decreases, as the limit becomes more influenced by the shape of the mass distribution which has a smaller uncertainty than the relative scaling of the background components. The introduction of the systematic uncertainties can also be seen in the magenta and orange lines, calculated with the simple likelihood function, but now the difference between the two limits is not dependent upon  $m_{\phi^0}$ . The pulls of the nuisance parameters,  $(\theta - \epsilon)/\delta$ , where  $\theta$  is the nuisance parameter,  $\epsilon$  is its mean, and  $\delta$  is its deviation, are given in Fig. 6.19 for  $m_{\phi^0} = 90$  GeV and  $\mu = \hat{\mu}$  when calculated using the extended likelihood function. Here the nuisance parameters for each of the five event categories as well as the combined result are given.

The effect of using the extended likelihood function, rather than the simple likelihood function can be seen by comparing the black line with the orange line or green line with the magenta line in Fig. 6.17. The limits calculated using the extended likelihood function are consistently lower than the limits calculated using the simple likelihood function, demonstrating the additional exclusion power gained from utilising the mass shape information. The difference between these two sets of limits is particularly pronounced at large  $m_{\phi^0}$  where the mass distribution expected for the signal differs significantly from the background mass distribution.

However, in Fig. 6.17(b), the extended likelihood function limits are consistently worse than

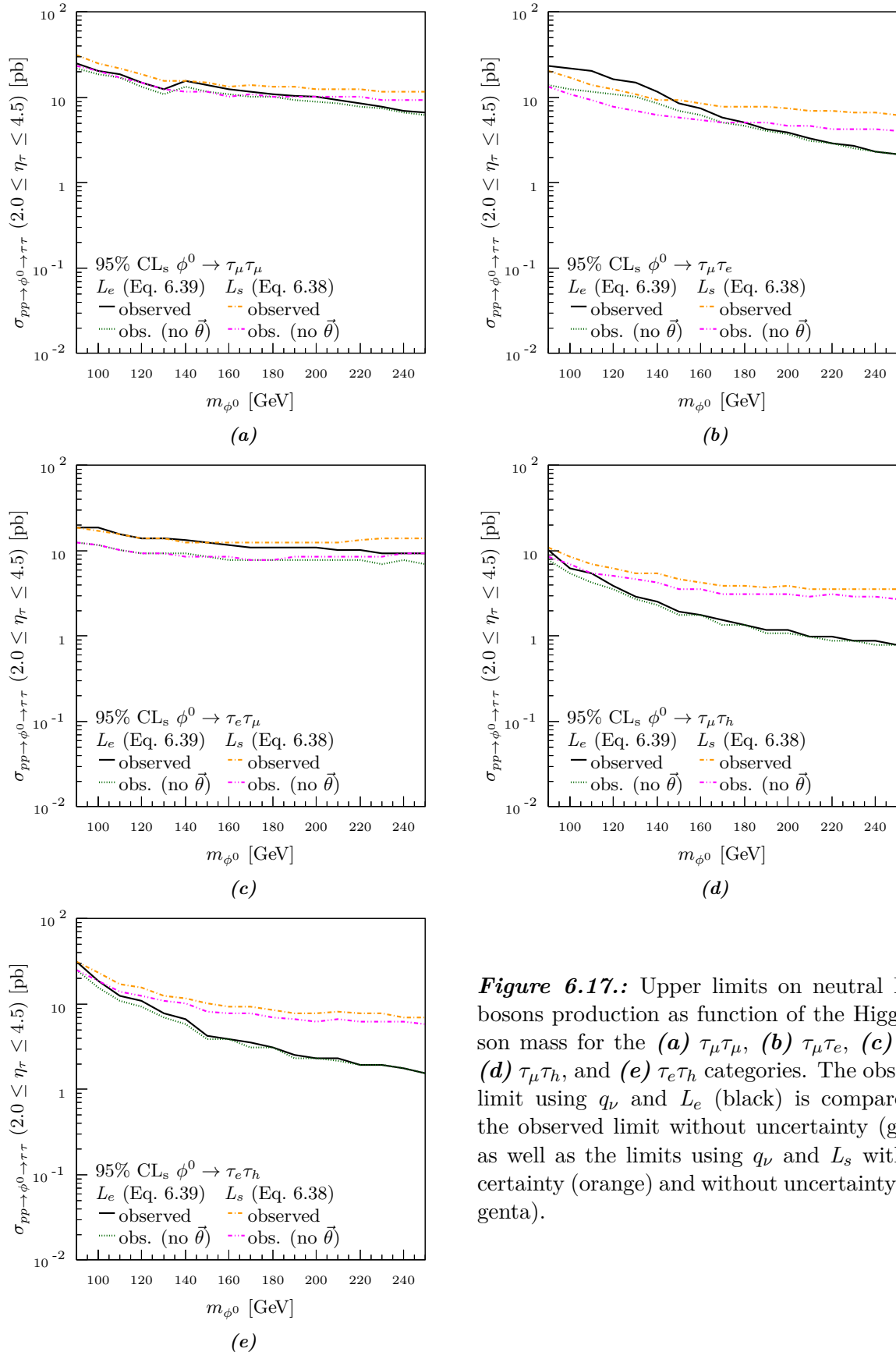


**Figure 6.17.:** Upper limits on neutral Higgs bosons production as function of the Higgs boson mass for the (a)  $\tau_\mu \tau_\mu$ , (b)  $\tau_\mu \tau_e$ , (c)  $\tau_e \tau_\mu$ , (d)  $\tau_\mu \tau_h$ , and (e)  $\tau_e \tau_h$  categories. The observed limit using  $q_\nu$  and  $L_e$  (black) is compared to the observed limit without uncertainty (green) as well as the limits using  $q_\nu$  and  $L_s$  with uncertainty (orange) and without uncertainty (magenta).

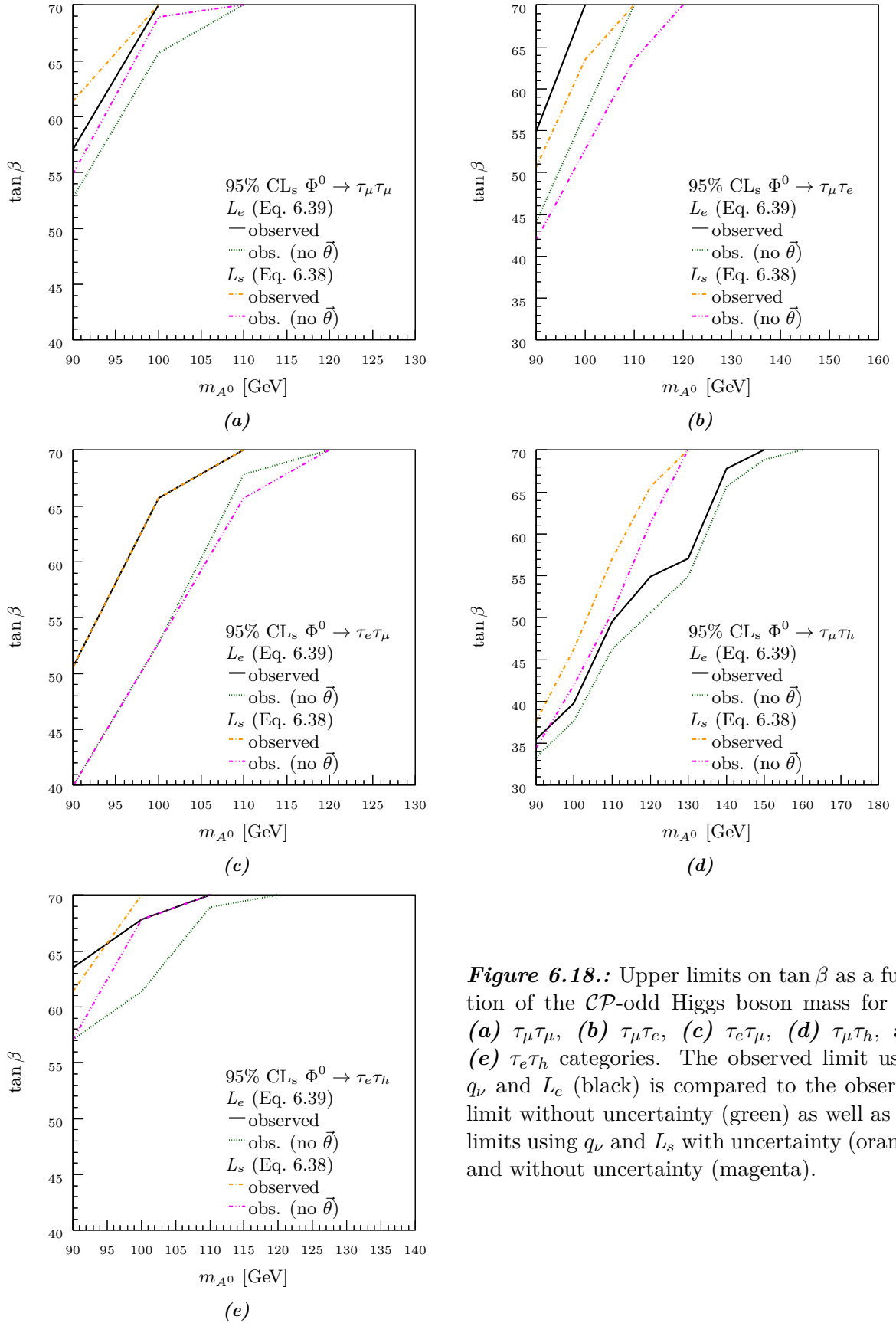


**Figure 6.18.:** Upper limits on  $\tan \beta$  as a function of the  $\mathcal{CP}$ -odd Higgs boson mass for the (a)  $\tau_\mu \tau_\mu$ , (b)  $\tau_\mu \tau_e$ , (c)  $\tau_e \tau_\mu$ , (d)  $\tau_\mu \tau_h$ , and (e)  $\tau_e \tau_h$  categories. The observed limit using  $q_\nu$  and  $L_e$  (black) is compared to the observed limit without uncertainty (green) as well as the limits using  $q_\nu$  and  $L_s$  with uncertainty (orange) and without uncertainty (magenta).

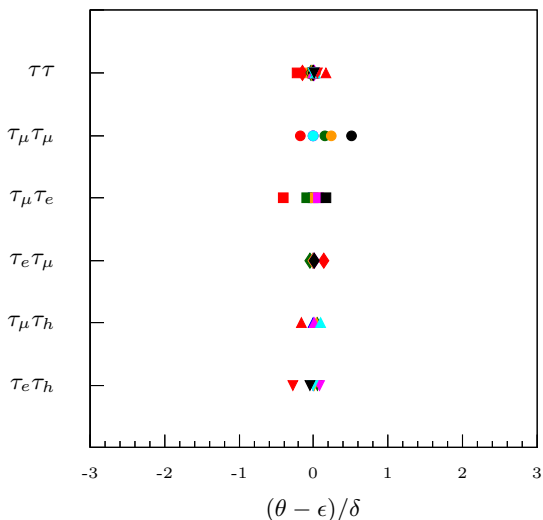


**Figure 6.19.:** Pulls of the nuisance parameters for  $m_h = 90$  GeV and  $\mu = \hat{\mu}$  calculated using the extended likelihood for the five event categories  $\tau_\mu\tau_\mu$  (circles),  $\tau_\mu\tau_e$  (square),  $\tau_e\tau_\mu$  (diamond),  $\tau_\mu\tau_h$  (up triangle), and  $\tau_e\tau_h$  (down triangle), as well as the combined results. The colours of the points correspond to the colour of the associated background as given in Fig. 6.12 for which the nuisance parameter is assigned. The black points are for mass shape uncertainty nuisance parameters.

the simple likelihood function limits for the Higgs boson mass range of  $90 \leq m_{\phi^0} \leq 145$  GeV. This behaviour can be attributed to an observed invariant mass shape, given in Fig. 6.12(b), that is more consistent with the signal than with the background within this  $m_{\phi^0}$  range. To check this, the data has been modified to be more consistent with the expected background in Fig. 6.20(a) which results in the limits of Fig. 6.20(b), where the limits calculated using the extended likelihood function are now found to outperform the limits calculated using the simple likelihood function.

The asymptotic approximation made in calculating  $q_\nu$  can be checked by using the Monte Carlo technique, where a large number of pseudo-experiments are randomly generated and a *pdf* for  $q_\nu$  is built. Because this process is time consuming, checks were made for only a few limit points. The limits calculated at these points using the Monte Carlo technique are consistent with the limits calculated assuming the asymptotic approximation.

### 6.4.2. Final Limits

In Figs. 6.21 and 6.22, the final limit is plotted with the expected limits for a median experiment, assuming the background only hypothesis. The dashed red line provides the central expected limit. The dark blue band is the  $\pm 1\sigma$  range for the median experiment, *i.e.* 68% of experiments, assuming the background only hypothesis, are expected to produce a limit within this band. Similarly, the light blue band provides the  $\pm 2\sigma$  range about the limits expected from a median experiment. The expected limit is calculated using  $q_\nu$  evaluated with the Asimov dataset of Sect. 6.3.2, which for the extended likelihood function is given by Eq. 6.43.

The expected limits can be compared to the observed limits in either Fig. 6.21 or Fig. 6.22, but just as for the validation limits, the results are most easily interpreted for the model independent limits. However, for both Figs. 6.21 and 6.22 the observed limits are consistent with the expected limits for the background only hypothesis and fall within the expected  $\pm 2\sigma$  band for most of the five categories.

In the  $\tau_\mu\tau_e$  category, given by Fig. 6.21(b), a slight excess of events with respect to the

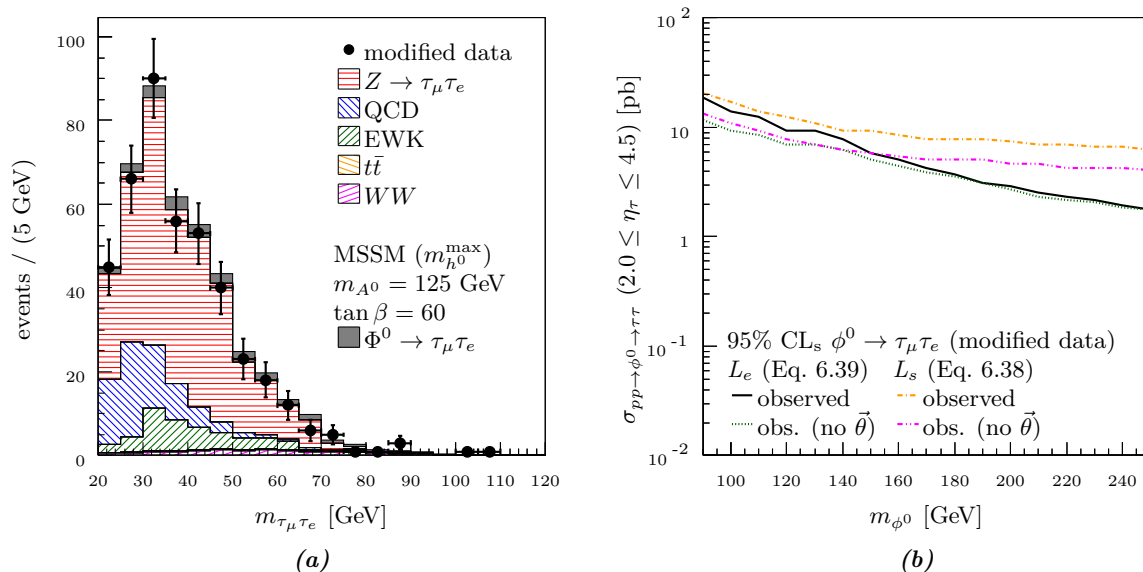


**Figure 6.20.:** (a) Invariant mass distribution of Fig. 6.12(b) modified to produce an observed distribution more consistent with the background only hypothesis. (b) Validation limits for this modified data, equivalent to Fig. 6.20(b), where the limits calculated using the extended likelihood function now outperform the limits calculated using the simple likelihood function.

background only hypothesis is observed, resulting in a higher than expected upper limit, slightly above the  $\pm 2\sigma$  band at large  $m_{\phi^0}$ . The excess of events is particularly visible in the 55 – 60 GeV invariant mass bin of Fig. 6.12(b), resulting in the difference between the expected limits and the observed limits increasing for larger values of  $m_{\phi^0}$ , as the mass distribution for large  $m_{\phi^0}$  becomes more consistent with this excess.

The  $\tau_\mu\tau_\mu$  category of Fig. 6.21(a) also has an observed number of events larger than the background only hypothesis. This excess is more evenly spread across the mass distribution of Fig. 6.12(a) than for the  $\tau_\mu\tau_e$  category, although a small excess is observed in the two invariant mass bins from 100 – 110 GeV resulting in the difference between the observed and expected limits increasing slightly for large  $m_{\phi^0}$ . The  $\tau_e\tau_h$  category has an overall excess of observed events, but a slight deficiency in events for large invariant masses, resulting in an observed limit above the expected limit for small  $m_{\phi^0}$  and below the expected limit for large  $m_{\phi^0}$ . The  $\tau_e\tau_\mu$  and  $\tau_\mu\tau_h$  categories both have a deficiency in the observed number of events with respect to the background only hypothesis, yielding observed limits slightly lower than the expected limits.

The five event categories are combined to produce the model independent limits and the MSSM limits of Fig. 6.23. The limits are calculated using the same methods described for the individual limits of Figs. 6.21 and 6.22. In Fig. 6.23(a) the expected cross-section  $\sigma_{pp \rightarrow H \rightarrow \tau\tau}$  from the SM Higgs boson is given by the dotted black line, with the theoretical uncertainty given by the grey band. A neutral Higgs boson mass of 125 GeV is indicated by the vertical black line. The ratio of this limit to the SM expectation is given in Fig. 6.23(b) for further comparison. As can be seen, the limit from data is nearly two orders of magnitude larger than the expected SM cross-section at lower Higgs boson masses. In Fig. 6.23(c) the LHCb limit

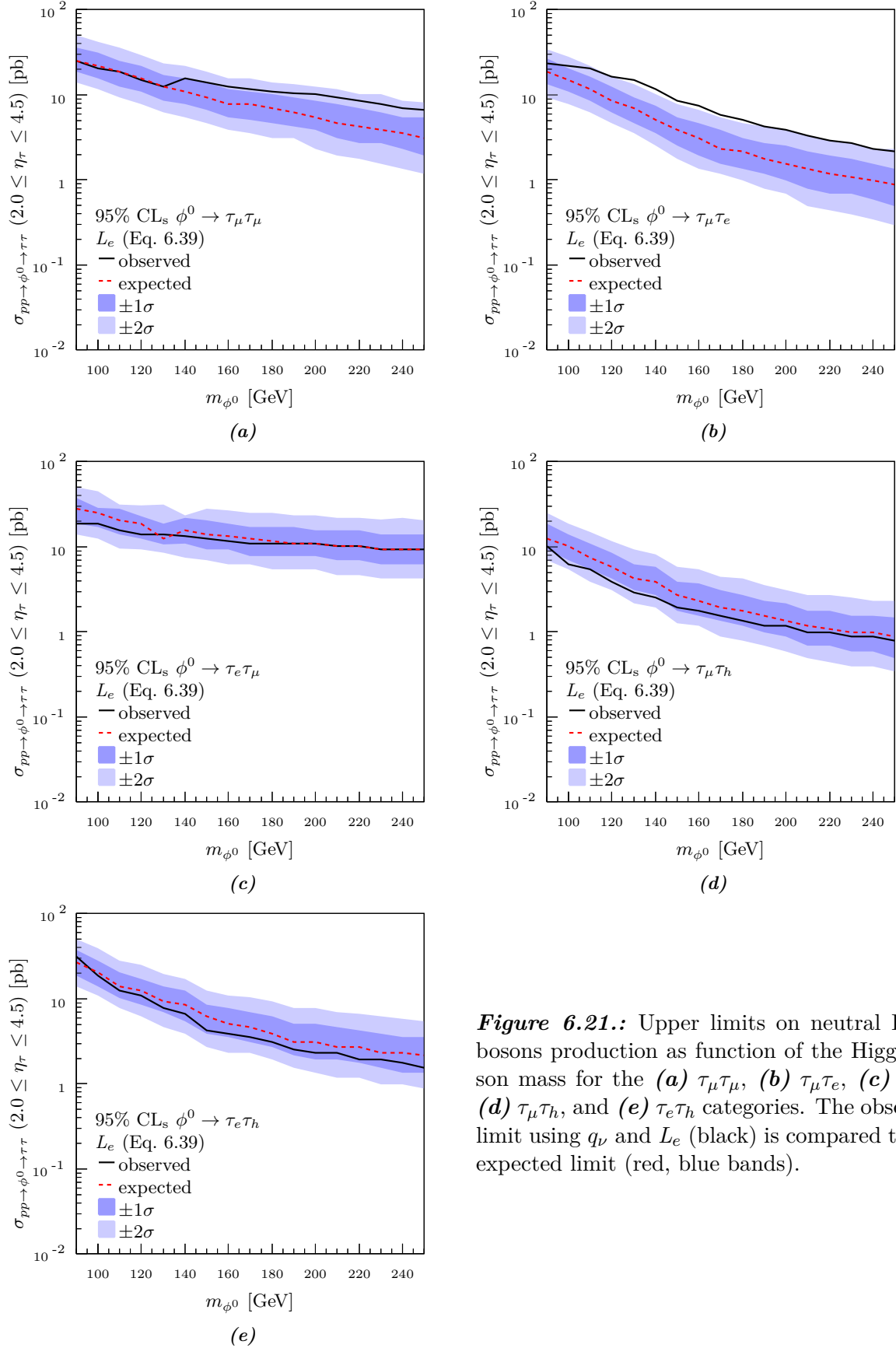


**Figure 6.21.:** Upper limits on neutral Higgs bosons production as function of the Higgs boson mass for the (a)  $\tau_\mu\tau_\mu$ , (b)  $\tau_\mu\tau_e$ , (c)  $\tau_e\tau_\mu$ , (d)  $\tau_\mu\tau_h$ , and (e)  $\tau_e\tau_h$  categories. The observed limit using  $q_\nu$  and  $L_e$  (black) is compared to the expected limit (red, blue bands).

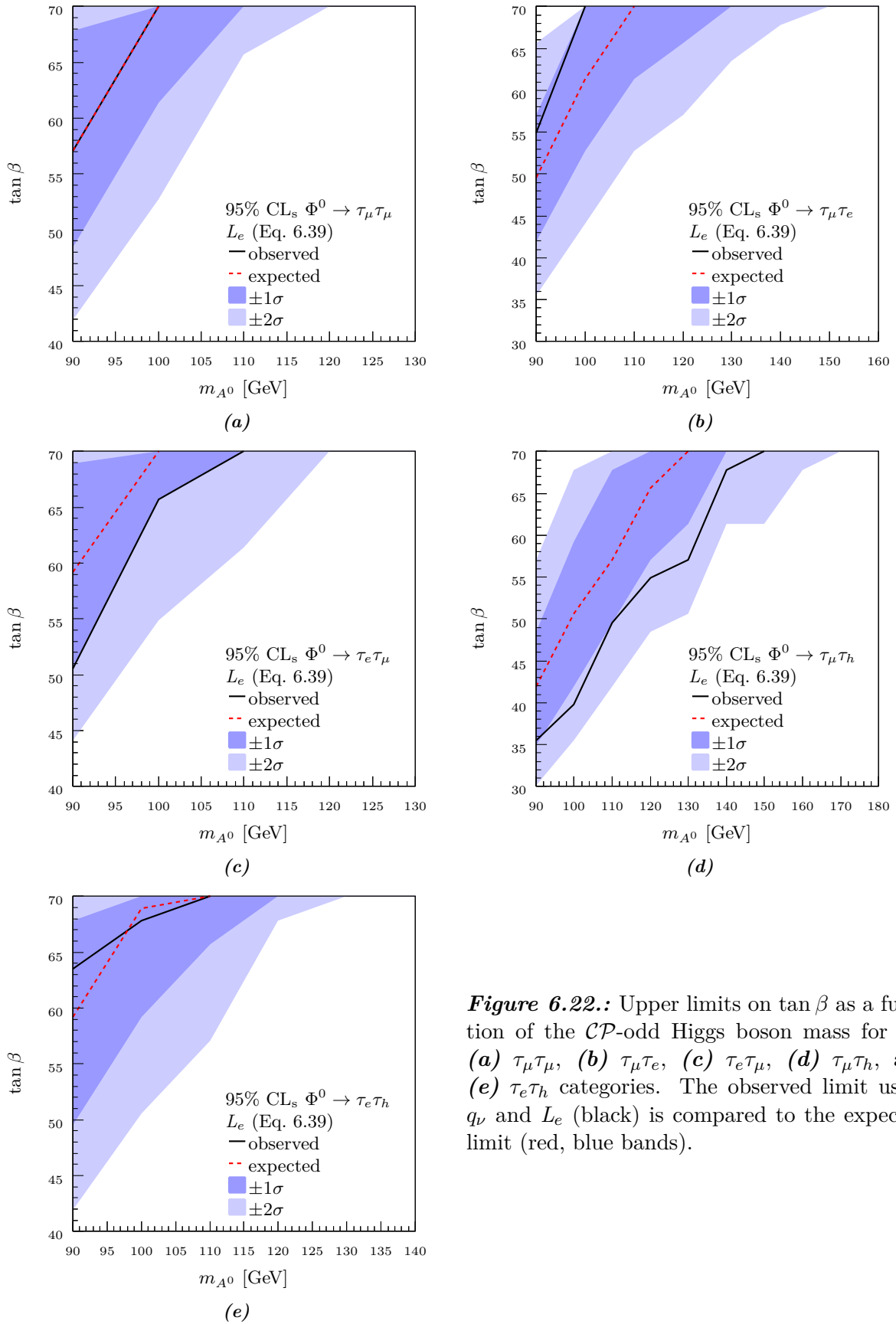


**Figure 6.22.:** Upper limits on  $\tan \beta$  as a function of the  $\mathcal{CP}$ -odd Higgs boson mass for the (a)  $\tau_\mu \tau_\mu$ , (b)  $\tau_\mu \tau_e$ , (c)  $\tau_e \tau_\mu$ , (d)  $\tau_\mu \tau_h$ , and (e)  $\tau_e \tau_h$  categories. The observed limit using  $q_\nu$  and  $L_e$  (black) is compared to the expected limit (red, blue bands).



from this analysis is compared with limits from ATLAS, CMS, and LEP. The  $36 \text{ pb}^{-1}$  and  $4.7 \text{ fb}^{-1}$  ATLAS limits from Refs. [239] and [240] correspond to analyses performed using the 2010 and 2011 ATLAS datasets respectively. Similarly the  $36 \text{ pb}^{-1}$  and  $4.6 \text{ fb}^{-1}$  CMS limits from Refs. [241] and [242] correspond to the 2010 and 2011 CMS datasets. The LEP limit is a combined lower limit for all LEP data from Ref. [243]. The LHCb limit of this analysis is competitive with the ATLAS and CMS limits using 2010 datasets, but not with the ATLAS and CMS limits using 2011 datasets. While ATLAS and CMS maintain or even gain sensitivity for large  $m_{A^0}$ , the results of this chapter lose sensitivity due to the decreased acceptance of  $A^0/H^0 \rightarrow \tau\tau$  events where both  $\tau$  leptons are produced within LHCb.

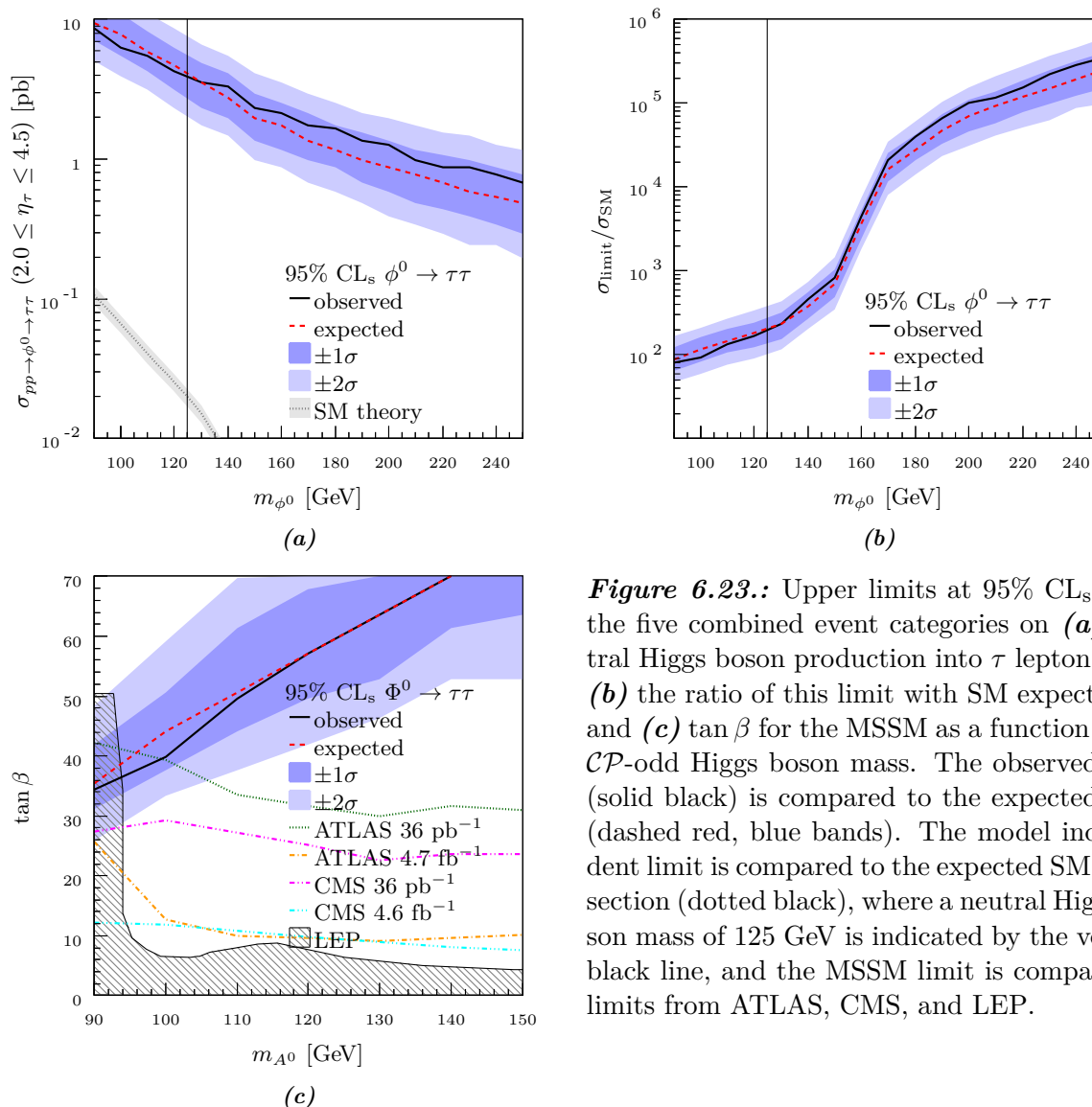


**Figure 6.23.:** Upper limits at 95%  $\text{CL}_s$  using the five combined event categories on (a) neutral Higgs boson production into  $\tau$  lepton pairs, (b) the ratio of this limit with SM expectation, and (c)  $\tan \beta$  for the MSSM as a function of the  $\mathcal{CP}$ -odd Higgs boson mass. The observed limit (solid black) is compared to the expected limit (dashed red, blue bands). The model independent limit is compared to the expected SM cross-section (dotted black), where a neutral Higgs boson mass of 125 GeV is indicated by the vertical black line, and the MSSM limit is compared to limits from ATLAS, CMS, and LEP.

## 7. Conclusion

Within this thesis a full analysis, from theory to experimental result, has been presented. The results of Chap. 3 demonstrate how  $\tau$  lepton decays may be used to differentiate between their production mechanisms. Future measurements of the Higgs boson, in conjunction with  $\tau$  lepton decays from PYTHIA 8, could verify both the spin and  $\mathcal{CP}$  of the Higgs boson. A similar analysis can be applied to  $W \rightarrow \nu_\tau \tau$  measurements to search for charged Higgs bosons, supersymmetric particle decays, and other new physics which produce unique helicity correlations in the decays of  $\tau$  leptons. The results of Chap. 3 can also be used in lower energy particle physics. The models implemented in PYTHIA 8 can be tuned to data from  $\tau$  lepton factories such as BaBar and provide insights into QCD at energies where perturbative calculations fail. These tunes could also be used to improve meson resonance decay models.

The work of Chap. 3 can be expanded with the addition of a variety of features to PYTHIA 8. Currently the decay widths for the  $\tau$  lepton decay channels are not calculated, as constants of proportionality have been omitted from the implemented hadronic currents. Including these constants of proportionality, as well as an extension of the code to perform the decay width integration, can be implemented so that PYTHIA 8 could be used to calculate  $\tau$  lepton decay widths in a fashion similar to its cross-section calculations. Additionally, the parameters for the hadronic currents should be migrated to user settings so they can easily be modified by the user without the need to recompile source code. With added decay width calculations and modifiable parameters, the PYTHIA 8  $\tau$  lepton decay machinery could more easily be used to perform phenomenological tunes of  $\tau$  lepton decays similar to the three pion CLEO fit. Common preset fits could also be included in the PYTHIA 8 user settings, allowing users to quickly and simply switch between parameter sets for a  $\tau$  lepton decay channel.

The forward cross-section for the production of  $Z$  bosons decaying into  $\tau$  leptons was measured to a precision of 7% in Chap. 5. This measurement, as well as the individual measurements for each final state category, are consistent with the expected cross-section from the SM. The final cross-section can be used in PDF fits to constrain the proton PDF at both high and low momentum fractions. The ratios of the  $Z \rightarrow \tau\tau$  cross-section with the  $Z \rightarrow ee$  and  $Z \rightarrow \mu\mu$  cross-sections from LHCb, test lepton universality in the forward region to a precision of 7% and 9% respectively. No excess was observed in either of these ratios, testing the absence of additional heavy particles decaying into  $\tau$  leptons, as predicted by the SM.

The cross-section measurement of Chap. 5 should be extended to both 2012 and future data from LHCb. In the process, improvements can be made to the analysis. One of the more confusing aspects of the analysis is the difference between the  $\tau_\mu\tau_e$  and  $\tau_e\tau_\mu$  categories. The reason for this differentiation is purely historical, and in an updated version of this analysis,

the two categories should be simplified into a single  $\tau_\mu\tau_e$  category. A similar change could also be made in the handling of the efficiencies. Here, the efficiencies are split into a reconstruction efficiency and a selection efficiency but this division is somewhat artificial, and is not necessary.

Currently, the  $Z \rightarrow \tau\tau$  cross-section measurement is dominated by statistical uncertainties, but in the future the systematic uncertainties will need to be reduced. One of the largest sources of uncertainty for the event categories containing an electron is due to the electron track finding efficiency which is determined from data using a tag-and-probe method. Currently, the probe is a high energy ECAL cluster. However, a two part approach could be taken where a probe of a VELO track and ECAL cluster is used, followed by a probe of a downstream track and an ECAL cluster. These two probes could then be used to calculate the VELO and downstream electron track finding efficiencies separately, potentially resulting in a reduced systematic uncertainty on the electron track finding efficiency.

The selection requirements for the  $Z \rightarrow \tau\tau$  cross-section measurement of Chap. 5 were optimised manually, rather than with multivariate techniques. Further gains in reducing the background with respect to the signal could be accomplished by optimising the selection requirements using multivariate techniques such as boosted decision trees or artificial neural nets. Additionally, final state signals with multi-pronged  $\tau$  lepton decays, rather than just the single-pronged  $\tau$  lepton decays of this analysis, could be included.

The limits of Chap. 6 exclude the production of neutral Higgs bosons decaying into  $\tau$  leptons within the forward region with cross-sections larger than 8.6 to 0.7 pb over the Higgs boson mass range 90 to 250 GeV. This result is two orders of magnitude larger than the expected cross-section from the SM, and so no conclusions can be drawn about the SM Higgs boson. The limits for the MSSM exclude a  $\tan\beta$  greater than 34 for a  $\mathcal{CP}$ -odd Higgs boson mass of 90 GeV to a  $\tan\beta$  greater than 70 for a  $\mathcal{CP}$ -odd Higgs boson mass of 140 GeV. These limits, in conjunction with the limits from ATLAS and CMS, are rapidly reducing the remaining parameter space for the MSSM which has not yet been excluded.

Unique forward measurements of the Higgs boson in the future, using the LHCb detector, will need to combine a variety of Higgs boson decay channels and cannot rely solely upon  $\tau$  lepton pair decays of the Higgs boson. Within the analysis of Chap. 6 the simulated Higgs boson signal samples were generated using PYTHIA 6. The simulation framework of LHCb, GAUSS, needs to be expanded to allow the simulation of samples generated with higher-order hard matrix elements, such as those produced using the POWHEG method. Particularly, this simulation will be critical for associated vector boson analyses where well modelled  $W$  and  $Z$  boson simulation samples with associated hard jets will be needed.

The statistical analysis of Chap. 6 could also be improved with a refinement of the nuisance parameters, specifically with the addition of correlated systematic uncertainties. Currently there is no dedicated statistics group for Higgs boson analyses within the LHCb collaboration. Upcoming Higgs boson analyses could benefit from such a group, which would provide a consistent statistical treatment for all Higgs boson analyses produced by LHCb.

Future analyses at LHCb, based on results from this thesis, should provide complementary measurements of the properties for the Higgs-like boson discovered by ATLAS and CMS. The

forward capabilities of LHCb will allow models such as the diffractive production of Higgs bosons from intrinsic heavy flavours within the proton [244] to be tested. The selection for  $\tau$  leptons developed in this thesis could also be used to select  $W$  bosons decaying into  $\tau$  leptons and search for heavy charged particles such as the charged MSSM Higgs boson.

# Bibliography

- [1] S. Farry, *A measurement of Z production using tau final states with the LHCb detector*, PhD thesis, University College Dublin, August, 2012.
- [2] LHCb collaboration, *A study of the Z production cross-section in pp collisions at  $\sqrt{s} = 7$  TeV using tau final states*, JHEP **01** (2013) 111, [arXiv:1210.6289](#).
- [3] P. Ilten, *Z  $\rightarrow \tau\tau$  and W  $\rightarrow \tau\nu$  Cross-Sections at the LHC*, 12th International Workshop on Tau Physics, Nagoya University, 2012; P. Ilten, *Z  $\rightarrow \tau\tau$  and W  $\rightarrow \tau\nu_\tau$  Cross-Sections at the LHC*, Nucl. Phys. Proc. Suppl. (2012) [arXiv:1211.7229](#).
- [4] LHCb collaboration, *Limits on neutral Higgs boson production in the forward region in pp collisions at  $\sqrt{s} = 7$  TeV*, JHEP **05** (2013) 132, [arXiv:1304.2591](#).
- [5] P. Ilten, *Limits on neutral Higgs boson production in the forward region in pp collisions at  $\sqrt{s} = 7$  TeV*, XXI International Workshop on Deep-Inelastic Scattering and Related Subjects, National Institute of Nuclear and Particle Physics, 2013; P. Ilten, *Limits on neutral Higgs production in the forward region in pp collisions at  $\sqrt{s} = 7$  TeV*, PoS (2013).
- [6] P. Ilten, *Tau Decays in Pythia 8*, 12th International Workshop on Tau Physics, Nagoya University, 2012.
- [7] P. Ilten, *Tau Decays in Pythia 8*, Nucl. Phys. Proc. Suppl. (2012) [arXiv:1211.6730](#).
- [8] ATLAS collaboration, *Observation of a new particle in the search for the Standard Model Higgs boson with the ATLAS detector at the LHC*, Phys. Lett. **B716** (2012) 1, [arXiv:1207.7214](#).
- [9] CMS collaboration, *Observation of a new boson at a mass of 125 GeV with the CMS experiment at the LHC*, Phys. Lett. **B716** (2012) 30, [arXiv:1207.7235](#).
- [10] T. Sjöstrand, S. Mrenna, and P. Skands, *PYTHIA 6.4 physics and manual*, JHEP **05** (2006) 026, [arXiv:hep-ph/0603175](#).
- [11] T. Sjöstrand, S. Mrenna, and P. Skands, *A brief introduction to PYTHIA 8.1*, Comput. Phys. Commun. **178** (2008) 852, [arXiv:0710.3820](#).
- [12] PYTHIA 8, *Present program version: PYTHIA 8.1*, <http://home.thep.lu.se/~torbjorn/Pythia.html>, 2013.
- [13] S. Weinberg, *A Model of Leptons*, Phys. Rev. Lett. **19** (1967) 1264.

- [14] A. Salam, *Weak and Electromagnetic Interactions*, Conf. Proc. **C680519** (1968) 367.
- [15] Particle Data Group, J. Beringer *et al.*, *Review of Particle Physics*, Phys. Rev. **D86** (2012) .
- [16] D. D. Bjorken and S. D. Drell, *Relativistic Quantum Fields*, International Series in Pure and Applied Physics, McGraw-Hill Book Company, 1965.
- [17] M. Veltman, *Diagrammatica: The Path to Feynman Rules*, Cambridge University Press, 1994.
- [18] M. E. Peskin and D. V. Schroeder, *An Introduction To Quantum Field Theory*, The Advanced Book Program, Wetview Press, 1994.
- [19] S. Weinberg, *The Quantum Theory of Fields: Volume I Foundations*, Cambridge University Press, 1995.
- [20] P. A. M. Dirac, *A new notation for quantum mechanics*, Mathematical Proceedings of the Cambridge Philosophical Society **35** (1939) 416.
- [21] E. Schrödinger, *An Undulatory Theory of the Mechanics of Atoms and Molecules*, Phys. Rev. **28** (1926) 1049.
- [22] S. Tomonaga, *On a relativistically invariant formulation of the quantum theory of wave fields*, Prog. Theor. Phys. **1** (1946) 27.
- [23] J. S. Schwinger, *Quantum electrodynamics. I A covariant formulation*, Phys. Rev. **74** (1948) 1439.
- [24] G. Frobenius, *Über die Integration der linearen Differentialgleichungen durch Reihen*, Journal für die reine und angewandte Mathematik **76** (1873) 214.
- [25] F. Dyson, *The S matrix in quantum electrodynamics*, Phys. Rev. **75** (1949) 1736.
- [26] G. Wick, *The Evaluation of the Collision Matrix*, Phys. Rev. **80** (1950) 268.
- [27] P. A. Dirac, *The Lagrangian in quantum mechanics*, Phys. Z. Sowjetunion **3** (1933) 64.
- [28] R. Feynman, *Space-time approach to nonrelativistic quantum mechanics*, Rev. Mod. Phys. **20** (1948) 367.
- [29] P. A. Dirac, *The Quantum theory of electron*, Proc. Roy. Soc. Lond. **A117** (1928) 610.
- [30] K. Hagiwara and D. Zeppenfeld, *Helicity Amplitudes for Heavy Lepton Production in  $e^+e^-$  Annihilation*, Nucl. Phys. **B274** (1986) 1.
- [31] K. Hagiwara and D. Zeppenfeld, *Amplitudes for Multiparton Processes Involving a Current at  $e^+e^-$ ,  $e^+p$ , and Hadron Colliders*, Nucl. Phys. **B313** (1989) 560.

- [32] V. Bargmann and E. P. Wigner, *Group Theoretical Discussion of Relativistic Wave Equations*, Proc. Nat. Acad. Sci. **34** (1948) 211.
- [33] C.-N. Yang and R. L. Mills, *Conservation of Isotopic Spin and Isotopic Gauge Invariance*, Phys. Rev. **96** (1954) 191.
- [34] M. Han and Y. Nambu, *Three Triplet Model with Double  $SU(3)$  Symmetry*, Phys. Rev. **139** (1965) B1006.
- [35] V. Ezhela, S. Lugovsky, and O. Zenin, *Hadronic part of the muon  $g - 2$  estimated on the  $\sigma_{\text{total}}^{2003}(e^+e^- \rightarrow \text{hadrons})$  evaluated data compilation*, arXiv:hep-ph/0312114.
- [36] G. Dissertori, *Measurements of the QCD color factors at LEP*, Nucl. Phys. Proc. Suppl. **65** (1998) 43, arXiv:hep-ex/9705016.
- [37] D. Griffiths, *Introduction to Elementary Particles*, Wiley-VCH, 2008.
- [38] D. Gross and F. Wilczek, *Asymptotically Free Gauge Theories. 1*, Phys. Rev. **D8** (1973) 3633.
- [39] H. D. Politzer, *Reliable Perturbative Results for Strong Interactions?*, Phys. Rev. Lett. **30** (1973) 1346.
- [40] R. W. Haymaker, *Confinement studies in lattice QCD*, Phys. Rept. **315** (1999) 153, arXiv:hep-lat/9809094.
- [41] S. Glashow, *Partial Symmetries of Weak Interactions*, Nucl. Phys. **22** (1961) 579.
- [42] M. Kobayashi and T. Maskawa, *CP Violation in the Renormalizable Theory of Weak Interaction*, Prog. Theor. Phys. **49** (1973) 652.
- [43] B. Cleveland *et al.*, *Measurement of the solar electron neutrino flux with the Homestake chlorine detector*, Astrophys. J. **496** (1998) 505.
- [44] S. M. Bilenky, J. Hosek, and S. Petcov, *On Oscillations of Neutrinos with Dirac and Majorana Masses*, Phys. Lett. **B94** (1980) 495.
- [45] F. Englert and R. Brout, *Broken Symmetry and the Mass of Gauge Vector Mesons*, Phys. Rev. Lett. **13** (1964) 321.
- [46] P. W. Higgs, *Broken Symmetries and the Masses of Gauge Bosons*, Phys. Rev. Lett. **13** (1964) 508.
- [47] G. Guralnik, C. Hagen, and T. Kibble, *Global Conservation Laws and Massless Particles*, Phys. Rev. Lett. **13** (1964) 585.
- [48] J. F. Gunion, H. E. Haber, G. L. Kane, and S. Dawson, *The Higgs Hunter's Guide*, no. 80 in Frontiers in Physics, Perseus Publishing, 1990.

- [49] H. Casimir, *The intensity of scattered radiation from bound electrons*, *Helv. Phys. Act.* **6** (1933) 287.
- [50] G. 't Hooft and M. Veltman, *Regularization and Renormalization of Gauge Fields*, *Nucl. Phys.* **B44** (1972) 189.
- [51] G. 't Hooft, *Dimensional regularization and the renormalization group*, *Nucl. Phys.* **B61** (1973) 455.
- [52] S. Weinberg, *New approach to the renormalization group*, *Phys. Rev.* **D8** (1973) 3497.
- [53] U. Amaldi, W. de Boer, and H. Furstenau, *Comparison of grand unified theories with electroweak and strong coupling constants measured at LEP*, *Phys. Lett.* **B260** (1991) 447.
- [54] H. Georgi and S. Glashow, *Unity of All Elementary Particle Forces*, *Phys. Rev. Lett.* **32** (1974) 438.
- [55] H.-B. Kim and J. E. Kim, *Coupling constant unification and LEP data*, *J. Korean Phys. Soc.* **27** (1994) 129, [arXiv:hep-ph/9302260](#).
- [56] S. P. Martin, *A Supersymmetry primer*, [arXiv:hep-ph/9709356](#).
- [57] A. Martin, W. Stirling, R. Thorne, and G. Watt, *Parton distributions for the LHC*, *Eur. Phys. J.* **C63** (2009) 189, [arXiv:0901.0002](#).
- [58] Y. L. Dokshitzer, *Calculation of the Structure Functions for Deep Inelastic Scattering and  $e^+ e^-$  Annihilation by Perturbation Theory in Quantum Chromodynamics.*, *Sov. Phys. JETP* **46** (1977) 641.
- [59] V. Gribov and L. Lipatov, *Deep inelastic  $e p$  scattering in perturbation theory*, *Sov. J. Nucl. Phys.* **15** (1972) 438.
- [60] G. Altarelli and G. Parisi, *Asymptotic Freedom in Parton Language*, *Nucl. Phys.* **B126** (1977) 298.
- [61] R. K. Ellis, W. J. Stirling, and B. Webber, *QCD and collider physics*, vol. 8 of *Cambridge Monographs on Particle Physics, Nuclear Physics, and Cosmology*, Cambridge University Press, 1996.
- [62] V. Trimble, *Existence and Nature of Dark Matter in the Universe*, *Ann. Rev. Astron. Astrophys.* **25** (1987) 425.
- [63] G. Lemaitre, *A homogeneous Universe of constant mass and growing radius accounting for the radial velocity of extragalactic nebulae*, *Annales Soc. Sci. Brux. Ser. I Sci. Math. Astron. Phys.* **A47** (1927) 49.
- [64] WMAP collaboration, *Nine-Year Wilkinson Microwave Anisotropy Probe (WMAP) Observations: Final Maps and Results*, [arXiv:1212.5225](#).



- [65] AMS collaboration, *First Result from the Alpha Magnetic Spectrometer on the International Space Station: Precision Measurement of the Positron Fraction in Primary Cosmic Rays of 0.5 to 350 GeV*, Phys. Rev. Lett. **110** (2013), no. 14 141102.
- [66] G. Drexlin, V. Hannen, S. Mertens, and C. Weinheimer, *Current direct neutrino mass experiments*, Adv. High Energy Phys. **2013** (2013) 293986, [arXiv:1307.0101](https://arxiv.org/abs/1307.0101).
- [67] H. Fritzsch and P. Minkowski, *Unified Interactions of Leptons and Hadrons*, Annals Phys. **93** (1975) 193.
- [68] L. Susskind, *Dynamics of Spontaneous Symmetry Breaking in the Weinberg-Salam Theory*, Phys. Rev. **D20** (1979) 2619.
- [69] L. Susskind, *Harmonic-oscillator analogy for the veneziano model*, Phys. Rev. Lett. **23** (1969) 545.
- [70] J. Wess and B. Zumino, *A Lagrangian Model Invariant Under Supergauge Transformations*, Phys. Lett. **B49** (1974) 52.
- [71] W. H. Press, S. A. Teukolsky, W. T. Vetterling, and B. P. Flannery, *Numerical Recipes: The Art of Scientific Computing*, Cambridge University Press, 3 ed., 2007.
- [72] M. Bähr *et al.*, *Herwig++ physics and manual*, Eur. Phys. J. **C58** (2008) 639, [arXiv:0803.0883](https://arxiv.org/abs/0803.0883).
- [73] HERWIG++, *The Herwig++ Event Generator*, <https://herwig.hepforge.org/>, 2013.
- [74] T. Gleisberg *et al.*, *Event generation with SHERPA 1.1*, JHEP **0902** (2009) 007, [arXiv:0811.4622](https://arxiv.org/abs/0811.4622).
- [75] SHERPA, *HEPForge: Sherpa*, <https://sherpa.hepforge.org/>, 2013.
- [76] A. Buckley *et al.*, *General-purpose event generators for LHC physics*, Phys. Rept. **504** (2011) 145, [arXiv:1101.2599](https://arxiv.org/abs/1101.2599).
- [77] T. Sjostrand, *A Model for Initial State Parton Showers*, Phys. Lett. **B157** (1985) 321.
- [78] G. Marchesini and B. Webber, *Monte Carlo Simulation of General Hard Processes with Coherent QCD Radiation*, Nucl. Phys. **B310** (1988) 461.
- [79] B. Andersson, G. Gustafson, G. Ingelman, and T. Sjostrand, *Parton Fragmentation and String Dynamics*, Phys. Rept. **97** (1983) 31.
- [80] G. C. Fox and S. Wolfram, *A Model for Parton Showers in QCD*, Nucl. Phys. **B168** (1980) 285.
- [81] X. Artru and G. Mennessier, *String model and multiproduction*, Nucl. Phys. **B70** (1974) 93.

- [82] R. Field and R. Feynman, *A Parametrization of the Properties of Quark Jets*, Nucl. Phys. **B136** (1978) 1.
- [83] H. Suganuma *et al.*, *Lattice QCD Study for Confinement in Hadrons*, AIP Conf. Proc. **1388** (2011) 195, [arXiv:1103.4015](#).
- [84] B. Andersson, G. Gustafson, and T. Sjostrand, *Baryon Production in Jet Fragmentation and Upsilon Decay*, Phys. Scripta **32** (1985) 574.
- [85] P. Eden and G. Gustafson, *Baryon production in the string fragmentation picture*, Z. Phys. **C75** (1997) 41, [arXiv:hep-ph/9606454](#).
- [86] JADE collaboration, *Experimental Study of Jets in electron - Positron Annihilation*, Phys. Lett. **B101** (1981) 129.
- [87] D. Amati and G. Veneziano, *Preconfinement as a Property of Perturbative QCD*, Phys. Lett. **B83** (1979) 87.
- [88] M. Dasgupta, L. Magnea, and G. P. Salam, *Non-perturbative QCD effects in jets at hadron colliders*, JHEP **0802** (2008) 055, [arXiv:0712.3014](#).
- [89] R. Kleiss, W. J. Stirling, and S. Ellis, *A New Monte Carlo Treatment Of Multiparticle Phase Space at High-Energies*, Comput. Phys. Commun. **40** (1986) 359.
- [90] F. James, *Monte-Carlo phase space*, CERN-68-15 (1968).
- [91] P. Richardson, *Spin correlations in Monte Carlo simulations*, JHEP **0111** (2001) 029, [arXiv:hep-ph/0110108](#).
- [92] J. C. Collins, *Spin Correlations in Monte Carlo Event Generators*, Nucl. Phys. **B304** (1988) 794.
- [93] I. Knowles, *A Linear Algorithm for Calculating Spin Correlations in Hadronic Collisions*, Comput. Phys. Commun. **58** (1990) 271.
- [94] M. Wingate, T. A. DeGrand, S. Collins, and U. M. Heller, *Properties of the  $a_1$  meson from lattice QCD*, Phys. Rev. Lett. **74** (1995) 4596, [arXiv:hep-ph/9502274](#).
- [95] G. Colangelo, M. Finkemeier, and R. Urech, *Tau decays and chiral perturbation theory*, Phys. Rev. **D54** (1996) 4403, [arXiv:hep-ph/9604279](#).
- [96] A. Djouadi, J. Kalinowski, and M. Spira, *HDECAY: A Program for Higgs boson decays in the standard model and its supersymmetric extension*, Comput. Phys. Commun. **108** (1998) 56, [arXiv:hep-ph/9704448](#).
- [97] D. Grellscheid and P. Richardson, *Simulation of Tau Decays in the Herwig++ Event Generator*, [arXiv:0710.1951](#).

- [98] T. Laubrich, *Implementation of  $\tau$ -lepton Decays into the Event-Generator Sherpa*, Master's thesis, Technische Universität Dresden, March, 2006.
- [99] P. Golonka *et al.*, *The Tauola photos F environment for the TAUOLA and PHOTOS packages: Release. 2.*, Comput. Phys. Commun. **174** (2006) 818, [arXiv:hep-ph/0312240](#).
- [100] M. Kramer, J. H. Kuhn, M. Stong, and P. Zerwas, *Prospects of measuring the parity of Higgs particles*, Z. Phys. **C64** (1994) 21, [arXiv:hep-ph/9404280](#).
- [101] Z. Was and M. Worek, *Transverse spin effects in  $H/A \rightarrow \tau^+\tau^-$ ;  $\tau^\pm \rightarrow \nu X^pm$ , Monte Carlo approach*, Acta Phys. Polon. **B33** (2002) 1875, [arXiv:hep-ph/0202007](#).
- [102] S. Jadach, J. H. Kuhn, and Z. Was, *TAUOLA: A Library of Monte Carlo programs to simulate decays of polarized tau leptons*, Comput. Phys. Commun. **64** (1990) 275.
- [103] J. H. Kuhn and A. Santamaria, *Tau decays to pions*, Z. Phys. **C48** (1990) 445.
- [104] M. Finkemeier and E. Mirkes, *The Scalar contribution to  $\tau \rightarrow K\pi\nu_\tau$* , Z. Phys. **C72** (1996) 619, [arXiv:hep-ph/9601275](#).
- [105] CLEO collaboration, *Hadronic structure in the decay  $\tau^- \rightarrow \pi^-\pi^0\bar{\nu}_\tau$* , Phys. Rev. **D61** (2000) 112002, [arXiv:hep-ex/9910046](#).
- [106] Belle collaboration, *Study of  $\tau \rightarrow K_S\pi^-\nu_\tau$  decay at Belle*, Phys. Lett. **B654** (2007) 65, [arXiv:0706.2231](#).
- [107] S. Jadach, Z. Was, R. Decker, and J. H. Kuhn, *The tau decay library TAUOLA: Version 2.4*, Comput. Phys. Commun. **76** (1993) 361.
- [108] CLEO collaboration, *Hadronic structure in the decay  $\tau^- \rightarrow \nu_\tau\pi^-\pi^0\pi^0$  and the sign of the tau-neutrino helicity*, Phys. Rev. **D61** (2000) 012002, [arXiv:hep-ex/9902022](#).
- [109] M. Finkemeier and E. Mirkes, *Tau decays into kaons*, Z. Phys. **C69** (1996) 243, [arXiv:hep-ph/9503474](#).
- [110] R. Decker, E. Mirkes, R. Sauer, and Z. Was, *Tau decays into three pseudoscalar mesons*, Z. Phys. **C58** (1993) 445.
- [111] A. J. Weinstein, *Semihadronic tau decays at CLEO*, Nucl. Phys. Proc. Suppl. **98** (2001) 261, [arXiv:hep-ex/0012064](#).
- [112] A. Bondar *et al.*, *Novosibirsk hadronic currents for  $\tau \rightarrow 4\pi$  channels of tau decay library TAUOLA*, Comput. Phys. Commun. **146** (2002) 139, [arXiv:hep-ph/0201149](#).
- [113] A. Bondar, S. Eidelman, A. Milstein, and N. Root, *On the role of  $a_1(1260)$  meson in the  $\tau \rightarrow 4\pi\nu_\tau$  decay*, Phys. Lett. **B466** (1999) 403, [arXiv:hep-ph/9907283](#).
- [114] G. Gounaris and J. Sakurai, *Finite width corrections to the vector meson dominance prediction for  $\rho \rightarrow e^+e^-$* , Phys. Rev. Lett. **21** (1968) 244.

- [115] J. H. Kuhn and Z. Was, *Tau decays to five mesons in TAUOLA*, Acta Phys. Polon. **B39** (2008) 147, [arXiv:hep-ph/0602162](#).
- [116] UA1 collaboration, *Experimental Observation of Isolated Large Transverse Energy Electrons with Associated Missing Energy at  $\sqrt{s} = 540$  GeV*, Phys. Lett. **B122** (1983) 103.
- [117] UA2 collaboration, *Observation of Single Isolated Electrons of High Transverse Momentum in Events with Missing Transverse Energy at the CERN anti-p p Collider*, Phys. Lett. **B122** (1983) 476.
- [118] UA1 collaboration, G. Arnison *et al.*, *Experimental Observation of Lepton Pairs of Invariant Mass Around 95-GeV/c\*\*2 at the CERN SPS Collider*, Phys. Lett. **B126** (1983) 398.
- [119] UA2 collaboration, *Evidence for  $Z^0 \rightarrow e^+e^-$  at the CERN anti-p p Collider*, Phys. Lett. **B129** (1983) 130.
- [120] ALEPH collaboration, DELPHI collaboration, L3 collaboration, OPAL collaboration, SLD collaboration, LEP electroweak working group, SLD electroweak group, SLD heavy flavour group, *Precision electroweak measurements on the Z resonance*, Phys. Rept. **427** (2006) 257, [arXiv:hep-ex/0509008](#).
- [121] PS210 collaboration, *Production of anti-hydrogen*, Phys. Lett. **B368** (1996) 251.
- [122] ATLAS collaboration, *The ATLAS Experiment at the CERN Large Hadron Collider*, JINST **3** (2008) S08003.
- [123] CMS collaboration, *The CMS experiment at the CERN LHC*, JINST **3** (2008) S08004.
- [124] LHCb collaboration, J. Alves, A. Augusto *et al.*, *The LHCb Detector at the LHC*, JINST **3** (2008) S08005.
- [125] ALICE collaboration, *The ALICE experiment at the CERN LHC*, JINST **3** (2008) S08002.
- [126] M. Bajko *et al.*, *Report of the task force on the incident of 19th September 2008 at the LHC*, CERN-LHC-PROJECT-REPORT-1168 (2009).
- [127] R.-D. Heuer, *News from CERN, LHC Status and Strategy for Linear Colliders*, [arXiv:1202.5860](#).
- [128] O. S. Bruning *et al.*, *LHC Design Report. 1. The LHC Main Ring*, CERN-2004-003-V-1 (2004).
- [129] O. Bruning *et al.*, *LHC Design Report. 2. The LHC infrastructure and general services*, CERN-2004-003-V-2 (2004).
- [130] M. Benedikt *et al.*, *LHC Design Report. 3. The LHC injector chain*, CERN-2004-003-V-3 (2004).

- [131] L. Evans and P. Bryant, *LHC Machine*, JINST **3** (2008) S08001.
- [132] C. Hill *et al.*, *Tests of the CERN proton linac performance for LHC - type beams*, eConf **C000821** (2000) TUD17, [arXiv:physics/0008102](https://arxiv.org/abs/physics/0008102).
- [133] K. Reich, *The CERN Proton Synchrotron Booster*, IEEE Trans. Nucl. Sci. **16** (1969) 959.
- [134] M. Benedikt *et al.*, *The PS complex as proton pre-injector for the LHC: Design and implementation report*, CERN-2000-003 (2000).
- [135] K. Schindl, *The injector chain for the LHC*, CERN-PS-99-018-DI (1999) 47.
- [136] LHCb collaboration and CMS collaboration, *Combination of results on the rare decays  $B_{(s)}^0 \rightarrow \mu^+ \mu^-$  from the CMS and LHCb experiments*, LHCb-CONF-2013-012.
- [137] LHCb collaboration, M. Tobin, *Performance of the LHCb Tracking Detectors*, LHCb-PROC-2013-015.
- [138] LHCb collaboration, *Absolute luminosity measurements with the LHCb detector at the LHC*, JINST **7** (2012) P01010, [arXiv:1110.2866](https://arxiv.org/abs/1110.2866).
- [139] LHCb collaboration, *LHCb magnet: Technical Design Report*, LHCb-TDR-1.
- [140] LHCb collaboration, *Layout and Expected Performance of the LHCb TT Station*, LHCb-2003-140.
- [141] LHCb collaboration, *Reoptimized Detector Design and Performance*, LHCb-TDR-9.
- [142] LHCb collaboration, *Inner Tracker Technical Design Report*, LHCb-TDR-8.
- [143] LHCb collaboration, B. Storaci, *The Performance of the Outer Tracker Detector at LHCb*, LHCb-PROC-2011-058.
- [144] LHCb collaboration, *Outer Tracker Technical Design Report*, LHCb-TDR-6.
- [145] LHCb collaboration, *RICH Technical Design Report*, LHCb-TDR-3.
- [146] LHCb collaboration, *Beam Test Results of the LHCb Electromagnetic Calorimeter*, LHCb-2007-149.
- [147] LHCb collaboration, *LHCb Calorimeters*, LHCb-TDR-2.
- [148] LHCb collaboration, *Performance of the LHCb muon system with cosmic rays*, JINST **5** (2010) P10003, [arXiv:1009.1963](https://arxiv.org/abs/1009.1963).
- [149] LHCb collaboration, *Muon System Technical Design Report*, LHCb-TDR-4.
- [150] BRUNEL, *The BRUNEL Project*, <http://lhcb-release-area.web.cern.ch/LHCb-release-area/DOC/brunel/>, 2013.

- [151] DAVINCI, *The DAVINCI Project*, <http://lhcb-release-area.web.cern.ch/LHcb-release-area/DOC/davinci/>, 2013.
- [152] GAUSS, *The GAUSS Project*, <http://lhcb-release-area.web.cern.ch/LHcb-release-area/DOC/gauss/>, 2013.
- [153] PYTHIA 6, *HEPForge: Pythia 6.4*, <https://pythia6.hepforge.org/>, 2013.
- [154] EVTGEN, *EvtGen Project*, <http://evtgen.warwick.ac.uk/docs/>, 2013.
- [155] BOOLE, *The BOOLE Project*, <http://lhcb-release-area.web.cern.ch/LHcb-release-area/DOC/boole/>, 2013.
- [156] MOORE, *The MOORE Project*, <http://lhcb-release-area.web.cern.ch/LHcb-release-area/DOC/moore/>, 2013.
- [157] GAUDI, *The GAUDI Project*, <http://proj-gaudi.web.cern.ch/proj-gaudi/>, 2013.
- [158] GANGA, *Ganga: Configure once - run anywhere*, <http://ganga.web.cern.ch/ganga/>, 2013.
- [159] DIRAC, *The DIRAC Project*, <http://lhcb-release-area.web.cern.ch/LHcb-release-area/DOC/dirac/>, 2013.
- [160] LHCb collaboration, *LHCb Computing*, LHCb-TDR-11.
- [161] LHCb collaboration, *Tracking Definitions*, LHCb-2007-006.
- [162] LHCb collaboration, *Online Pattern Recognition*, LHCb-2004-094; LHCb collaboration, *Dealing with Clones in the Tracking*, LHCb-2006-057; LHCb collaboration, *VELO Pattern Recognition*, LHCb-2007-013; LHCb collaboration, *Standalone Track Reconstruction in the T-stations*, LHCb-2007-022; LHCb collaboration, *The Forward Tracking: Algorithm and Performance Studies*, LHCb-2007-015; LHCb collaboration, *Performance of the track matching*, LHCb-2007-020; LHCb collaboration, *VELO-TT track reconstruction*, LHCb-2007-010; LHCb collaboration, *Downstream Pattern Recognition*, LHCb-2007-026; LHCb collaboration, *Primary vertex reconstruction*, LHCb-2007-011.
- [163] LHCb collaboration, *Isolated Cherenkov rings and refractive index monitoring in the LHCb RICH detectors*, LHCb-2008-039.
- [164] LHCb collaboration, *A clustering algorithm for the LHCb electromagnetic calorimeter using a cellular automaton*, LHCb-2001-123.
- [165] LHCb collaboration, *Photon and Neutral Pion reconstruction*, LHCb-2003-091.
- [166] LHCb collaboration, *Particle identification with LHCb Calorimeters*, LHCb-2003-092.
- [167] LHCb collaboration, *Trigger System Technical Design Report*, LHCb-TDR-10.

- [168] LHCb collaboration, *Absolute luminosity measurements with the LHCb detector at the LHC*, JINST **7** (2012) P01010, [arXiv:1110.2866](#).
- [169] S. van der Meer, *Calibration of the effective beam height in the ISR*, CERN-ISR-PO **68-31** (1968).
- [170] V. Balagura, *Notes on van der Meer Scan for Absolute Luminosity Measurement*, Nucl. Instrum. Meth. **A654** (2011) 634, [arXiv:1103.1129](#).
- [171] M. Ferro-Luzzi, *Proposal for an absolute luminosity determination in colliding beam experiments using vertex detection of beam-gas interactions*, Nucl. Instrum. Meth. **A553** (2005) 388.
- [172] LHCb collaboration, *Measurement of the cross-section for  $Z \rightarrow e^+e^-$  production in pp collisions at  $\sqrt{s} = 7$  TeV*, JHEP **1302** (2013) 106, [arXiv:1212.4620](#).
- [173] LHCb collaboration, *Inclusive W and Z production in the forward region at  $\sqrt{s} = 7$  TeV*, JHEP **06** (2012) 058, [arXiv:1204.1620](#).
- [174] NNPDF collaboration, R. D. Ball *et al.*, *On the Impact of NMC Data on NLO and NNLO Parton Distributions and Higgs Production at the Tevatron and the LHC*, Phys. Lett. **B704** (2011) 36, [arXiv:1102.3182](#).
- [175] H. Dreiner, S. Grab, and M. Trenkel,  *$S\tau$  LSP Phenomenology: Two versus Four-Body Decay Modes. Example: Resonant Single Slepton Production at the LHC*, Phys. Rev. **D79** (2009) 016002, [arXiv:0808.3079](#).
- [176] ALEPH collaboration, *A Precise measurement of the tau lepton lifetime*, Phys. Lett. **B297** (1992) 432.
- [177] I. Ferrante, *Tau lifetime measurements with impact parameters sum method in 1-1 events*, Nucl. Phys. Proc. Suppl. **40** (1995) 299.
- [178] LHCb collaboration, *A Measurement of the Tracking Efficiency for High- $p_T$  Tracks in Reco06-Stripping10 Collision Data*, LHCb-INT-2010-058.
- [179] LHCb collaboration, *Measurement of the track finding efficiency*, LHCb-PUB-2011-025.
- [180] S. Frixione, P. Nason, and C. Oleari, *Matching NLO QCD computations with parton shower simulations: the POWHEG method*, JHEP **11** (2007) 070, [arXiv:0709.2092](#).
- [181] CTEQ collaboration, H. Lai *et al.*, *Global QCD analysis of parton structure of the nucleon: CTEQ5 parton distributions*, Eur. Phys. J. **C12** (2000) 375, [arXiv:hep-ph/9903282](#).
- [182] L. Lyons, D. Gibaut, and P. Clifford, *How to combine correlated estimates of a single physical quantity*, Nucl. Instrum. Meth. **A270** (1988) 110.

- [183] S. Catani and M. Grazzini, *An NNLO subtraction formalism in hadron collisions and its application to Higgs boson production at the LHC*, Phys. Rev. Lett. **98** (2007) 222002, [arXiv:hep-ph/0703012](#).
- [184] S. Catani *et al.*, *Vector boson production at hadron colliders: A Fully exclusive QCD calculation at NNLO*, Phys. Rev. Lett. **103** (2009) 082001, [arXiv:0903.2120](#).
- [185] DYNLO, *Vector boson production at hadron colliders*, <http://theory.fi.infn.it/grazzini/dy.html>, 2013.
- [186] ATLAS collaboration, *Z  $\rightarrow$   $\tau\tau$  cross section measurement in proton-proton collisions at 7 TeV with the ATLAS experiment*, ATLAS-CONF-2012-006.
- [187] ATLAS collaboration, *Measurement of the Z  $\rightarrow$   $\tau\tau$  Cross Section with the ATLAS Detector*, Phys. Rev. **D84** (2011) 112006, [arXiv:1108.2016](#).
- [188] CMS collaboration, *Measurement of the Inclusive Z Cross Section via Decays to Tau Pairs in pp Collisions at  $\sqrt{s} = 7$  TeV*, JHEP **1108** (2011) 117, [arXiv:1104.1617](#).
- [189] M. Carena, S. Heinemeyer, C. Wagner, and G. Weiglein, *Suggestions for benchmark scenarios for MSSM Higgs boson searches at hadron colliders*, Eur. Phys. J. **C26** (2003) 601, [arXiv:hep-ph/0202167](#).
- [190] S. Heinemeyer, W. Hollik, and G. Weiglein, *FeynHiggs: A Program for the calculation of the masses of the neutral CP even Higgs bosons in the MSSM*, Comput. Phys. Commun. **124** (2000) 76, [arXiv:hep-ph/9812320](#).
- [191] S. Heinemeyer, W. Hollik, and G. Weiglein, *The Masses of the neutral CP - even Higgs bosons in the MSSM: Accurate analysis at the two loop level*, Eur. Phys. J. **C9** (1999) 343, [arXiv:hep-ph/9812472](#).
- [192] G. Degrossi *et al.*, *Towards high precision predictions for the MSSM Higgs sector*, Eur. Phys. J. **C28** (2003) 133, [arXiv:hep-ph/0212020](#).
- [193] M. Frank *et al.*, *The Higgs Boson Masses and Mixings of the Complex MSSM in the Feynman-Diagrammatic Approach*, JHEP **0702** (2007) 047, [arXiv:hep-ph/0611326](#).
- [194] FEYNHIGGS, *FeynHiggs: overview*, <http://www.feynhiggs.de/>, 2013.
- [195] A. Denner *et al.*, *Standard Model Higgs-Boson Branching Ratios with Uncertainties*, Eur. Phys. J. **C71** (2011) 1753, [arXiv:1107.5909](#).
- [196] M. Spira, *QCD effects in Higgs physics*, Fortsch. Phys. **46** (1998) 203, [arXiv:hep-ph/9705337](#).
- [197] J. Butterworth *et al.*, *The Tools and Monte Carlo working group Summary Report*, [arXiv:1003.1643](#).



- [198] HDECAY, *Index of /spira/hdecay*, <http://people.web.psi.ch/spira/hdecay/>, 2013.
- [199] A. Bredenstein, A. Denner, S. Dittmaier, and M. Weber, *Precise predictions for the Higgs-boson decay  $H \rightarrow WW/ZZ \rightarrow 4$  leptons*, Phys. Rev. **D74** (2006) 013004, [arXiv:hep-ph/0604011](https://arxiv.org/abs/hep-ph/0604011).
- [200] A. Bredenstein, A. Denner, S. Dittmaier, and M. Weber, *Precision calculations for the Higgs decays  $H \rightarrow ZZ/WW \rightarrow 4$  leptons*, Nucl. Phys. Proc. Suppl. **160** (2006) 131, [arXiv:hep-ph/0607060](https://arxiv.org/abs/hep-ph/0607060).
- [201] A. Bredenstein, A. Denner, S. Dittmaier, and M. Weber, *Radiative corrections to the semileptonic and hadronic Higgs-boson decays  $H \rightarrow WW/ZZ \rightarrow 4$  fermions*, JHEP **0702** (2007) 080, [arXiv:hep-ph/0611234](https://arxiv.org/abs/hep-ph/0611234).
- [202] PROPHECY4F, *A Monte Carlo generator for a Proper description of the Higgs decay into 4 fermions*, <http://omnibus.uni-freiburg.de/~sd565/programs/prophecy4f/prophecy4f.html>, 2013.
- [203] L. Resnick, M. Sundaresan, and P. Watson, *Is there a light scalar boson?*, Phys. Rev. **D8** (1973) 172.
- [204] B. W. Lee, C. Quigg, and H. Thacker, *The Strength of Weak Interactions at Very High-Energies and the Higgs Boson Mass*, Phys. Rev. Lett. **38** (1977) 883.
- [205] W.-Y. Keung and W. J. Marciano, *Higgs Scalar Decays:  $H \rightarrow W^\pm X$* , Phys. Rev. **D30** (1984) 248.
- [206] J. Bijnens, L. Lönnblad, and T. Sjöstrand, *Cross sections, Decay width and Lifetimes*, vol. HT06 of *FYS230 Theoretical Particle Physics*, Lund University, 1995.
- [207] D. Graudenz, M. Spira, and P. Zerwas, *QCD corrections to Higgs boson production at proton proton colliders*, Phys. Rev. Lett. **70** (1993) 1372.
- [208] M. Spira, A. Djouadi, D. Graudenz, and P. Zerwas, *Higgs boson production at the LHC*, Nucl. Phys. **B453** (1995) 17, [arXiv:hep-ph/9504378](https://arxiv.org/abs/hep-ph/9504378).
- [209] M. Spira, *HIGLU: A program for the calculation of the total Higgs production cross-section at hadron colliders via gluon fusion including QCD corrections*, [arXiv:hep-ph/9510347](https://arxiv.org/abs/hep-ph/9510347).
- [210] HIGLU, *Index of /spira/higlu*, <http://people.web.psi.ch/spira/higlu/>, 2013.
- [211] S. Catani, D. de Florian, M. Grazzini, and P. Nason, *Soft gluon resummation for Higgs boson production at hadron colliders*, JHEP **0307** (2003) 028, [arXiv:hep-ph/0306211](https://arxiv.org/abs/hep-ph/0306211).
- [212] D. de Florian and M. Grazzini, *Higgs production through gluon fusion: Updated cross sections at the Tevatron and the LHC*, Phys. Lett. **B674** (2009) 291, [arXiv:0901.2427](https://arxiv.org/abs/0901.2427).
- [213] DFG, *Higgs production at hadron colliders: online calculators*, <http://theory.fi.infn.it/grazzini/hcalculators.html>, 2013.

- [214] P. Bolzoni, F. Maltoni, S.-O. Moch, and M. Zaro, *Higgs production via vector-boson fusion at NNLO in QCD*, Phys. Rev. Lett. **105** (2010) 011801, arXiv:1003.4451.
- [215] P. Bolzoni, F. Maltoni, S.-O. Moch, and M. Zaro, *Vector boson fusion at NNLO in QCD: SM Higgs and beyond*, Phys. Rev. **D85** (2012) 035002, arXiv:1109.3717.
- [216] VBF@NNLO, *VBF@NNLO: Cross-Section Calculator*, <http://vbf-nnlo.phys.ucl.ac.be/vbf.html>, 2013.
- [217] LHC Higgs Cross Section Working Group, *Handbook of LHC Higgs Cross Sections: 1. Inclusive Observables*, arXiv:1101.0593.
- [218] R. V. Harlander and W. B. Kilgore, *Next-to-next-to-leading order Higgs production at hadron colliders*, Phys. Rev. Lett. **88** (2002) 201801, arXiv:hep-ph/0201206.
- [219] R. V. Harlander and W. B. Kilgore, *Production of a pseudoscalar Higgs boson at hadron colliders at next-to-next-to leading order*, JHEP **0210** (2002) 017, arXiv:hep-ph/0208096.
- [220] GGH@NNLO, *Robert Harlander: ggh@nnlo*, <http://particle.uni-wuppertal.de/harlander/software/ggh@nnlo/>, 2013.
- [221] R. V. Harlander and W. B. Kilgore, *Higgs boson production in bottom quark fusion at next-to-next-to leading order*, Phys. Rev. **D68** (2003) 013001, arXiv:hep-ph/0304035.
- [222] BBH@NNLO, *Robert Harlander: bbh@nnlo*, <http://particle.uni-wuppertal.de/harlander/software/bbh@nnlo/>, 2013.
- [223] LHC Higgs Cross Section Working Group, *Handbook of LHC Higgs Cross Sections: 2. Differential Distributions*, arXiv:1201.3084.
- [224] M. G. Kendall, *The Advanced Theory of Statistics*, vol. 1, Charles Griffin & Company Ltd., 2 ed., 1945; M. G. Kendall, *The Advanced Theory of Statistics*, vol. 2, Charles Griffin & Company Ltd., 1 ed., 1946.
- [225] S. Brandt, *Data Analysis: Statistical and Computational Method for Scientists and Engineers*, Springer-Verlag New York Inc., 1999.
- [226] G. Cowan, *Statistical Data Analysis*, Oxford University Press, 1998.
- [227] R. J. Barlow, *Statistics: A Guide to the Use of Statistical Methods in the Physical Sciences*, John Wiley & Sons Ltd., 1989.
- [228] G. Cowan, K. Cranmer, E. Gross, and O. Vitells, *Asymptotic formulae for likelihood-based tests of new physics*, Eur. Phys. J. **C71** (2011) 1554, arXiv:1007.1727.
- [229] G. J. Feldman, *Concluding Talk: Physics*, PHYSTAT 05, p. 283, Imperial College Press, 2005.

- [230] T. Junk, *Confidence level computation for combining searches with small statistics*, Nucl. Instrum. Meth. **A434** (1999) 435, [arXiv:hep-ex/9902006](#).
- [231] A. L. Read, *Presentation of search results: the  $CL(s)$  technique*, J. Phys. **G28** (2002) 2693.
- [232] A. Birnbaum, *On the Foundations of Statistical Inference*, J. Am. Statist. Assoc. **57** (1962) 269.
- [233] G. Cowan, K. Cranmer, E. Gross, and O. Vitells, *Power-Constrained Limits*, [arXiv:1105.3166](#).
- [234] J. Neyman and E. S. Pearson, *On the problem of the most efficient tests of statistical hypotheses*, Philosophical Transactions of the Royal Society of London. Series A, Containing Papers of a Mathematical or Physical Character **231** (1933) 289.
- [235] A. Wald, *Tests of statistical hypotheses concerning several parameters when the number of observations is large*, Transactions of the American Mathematical Society **54** (1943), no. 3 426.
- [236] S. S. Wilks, *The large-sample distribution of the likelihood ratio for testing composite hypotheses*, The Annals of Mathematical Statistics **9** (1938), no. 1 60.
- [237] R. J. Barlow, *Extended maximum likelihood*, Nucl. Instrum. Meth. **A297** (1990) 496.
- [238] I. Asomiv, *Franchise, If: Worlds of Science Fiction* **5** (1955).
- [239] ATLAS collaboration, *Search for neutral MSSM Higgs bosons decaying to  $\tau^+\tau^-$  pairs in proton-proton collisions at  $\sqrt{s} = 7$  TeV with the ATLAS detector*, Phys. Lett. **B705** (2011) 174, [arXiv:1107.5003](#).
- [240] ATLAS collaboration, *Search for the neutral Higgs bosons of the Minimal Supersymmetric Standard Model in  $pp$  collisions at  $\sqrt{s} = 7$  TeV with the ATLAS detector*, JHEP **02** (2013) 095, [arXiv:1211.6956](#).
- [241] CMS collaboration, *Search for neutral MSSM Higgs bosons decaying to tau pairs in  $pp$  collisions at  $\sqrt{s} = 7$  TeV*, Phys. Rev. Lett. **106** (2011) 231801, [arXiv:1104.1619](#).
- [242] CMS collaboration, *Search for neutral Higgs bosons decaying to  $\tau$  pairs in  $pp$  collisions at  $\sqrt{s} = 7$  TeV*, Phys. Lett. **B713** (2012) 68, [arXiv:1202.4083](#).
- [243] ALEPH collaboration, DELPHI collaboration, L3 collaboration, OPAL collaboration, LEP Working Group for Higgs Boson Searches, *Search for neutral MSSM Higgs bosons at LEP*, Eur. Phys. J. **C47** (2006) 547, [arXiv:hep-ex/0602042](#).
- [244] S. J. Brodsky, B. Kopeliovich, I. Schmidt, and J. Soffer, *Diffraction Higgs production from intrinsic heavy flavors in the proton*, Phys. Rev. **D73** (2006) 113005, [arXiv:hep-ph/0603238](#).

- [245] T. Skwarnicki, *A study of the radiative cascade transitions between the Upsilon-prime and Upsilon resonances*, PhD thesis, Institute of Nuclear Physics, Krakow, 1986, DESY-F31-86-02.
- [246] S. Actis, G. Passarino, C. Sturm, and S. Uccirati, *NLO Electroweak Corrections to Higgs Boson Production at Hadron Colliders*, Phys. Lett. **B670** (2008) 12, [arXiv:0809.1301](#).
- [247] S. Actis, G. Passarino, C. Sturm, and S. Uccirati, *NNLO Computational Techniques: The Cases  $H \rightarrow \gamma\gamma$  and  $H \rightarrow gg$* , Nucl. Phys. **B811** (2009) 182, [arXiv:0809.3667](#).
- [248] O. Brein, R. V. Harlander, and T. J. Zirke, *vh@nnlo - Higgs Strahlung at hadron colliders*, Comput. Phys. Commun. **184** (2013) 998, [arXiv:1210.5347](#).
- [249] vH@NNLO, *Robert Harlander: vh@nnlo*, <http://particle.uni-wuppertal.de/harlander/software/vh@nnlo/>, 2013.
- [250] M. Ciccolini, S. Dittmaier, and M. Kramer, *Electroweak radiative corrections to associated WH and ZH production at hadron colliders*, Phys. Rev. **D68** (2003) 073003, [arXiv:hep-ph/0306234](#).
- [251] O. Brein, A. Djouadi, and R. Harlander, *NNLO QCD corrections to the Higgs-strahlung processes at hadron colliders*, Phys. Lett. **B579** (2004) 149, [arXiv:hep-ph/0307206](#).
- [252] S. Dawson, L. Orr, L. Reina, and D. Wackerroth, *Associated top quark Higgs boson production at the LHC*, Phys. Rev. **D67** (2003) 071503, [arXiv:hep-ph/0211438](#).
- [253] T. Bayes, *An essay toward solving a problem in the doctrine of chances*, Phil. Trans. Roy. Soc. Lond. **53** (1764) 370.
- [254] O. Helene, *Errors in Experiments with Small Numbers of Events*, Nucl. Instrum. Meth. **A228** (1984) 120.
- [255] R. D. Cousins and V. L. Highland, *Incorporating systematic uncertainties into an upper limit*, Nucl. Instrum. Meth. **A320** (1992) 331.

# A. Theory

In this appendix, additional material for the theoretical review of Chap. 2 is provided. In App. A.1 the notational conventions used are outlined. In App. A.2 the electroweak Lagrangian is given and in App. A.3 the minimal Higgs mechanism Lagrangian is given.

## A.1. Notation

The momentum four-vector is given by  $q = (E, q_x, q_y, q_z)$  and the spatial component by  $\vec{q} = (q_x, q_y, q_z)$ . The Einstein notation  $q^\mu$  and  $q_\mu$  indicate the four-vectors,

$$q^\mu = \begin{pmatrix} E \\ q_x \\ q_y \\ q_z \end{pmatrix}, \quad q_\mu = (E, -q_x, -q_y, -q_z), \quad (\text{A.1})$$

where the metric,

$$g_{\mu\nu} = g^{\mu\nu} = \begin{pmatrix} 1 & 0 & 0 & 0 \\ 0 & -1 & 0 & 0 \\ 0 & 0 & -1 & 0 \\ 0 & 0 & 0 & -1 \end{pmatrix} \quad (\text{A.2})$$

is used to raise and lower indices, *i.e.*  $q_\mu = g_{\mu\nu}q^\nu$ . Furthermore, Greek indices indicate summation over the four components and Latin indices indicate summation over the three spatial components where the conventions,

$$\begin{aligned} q^2 &= qq = q_\mu q^\mu = E^2 - q_x^2 - q_y^2 - q_z^2, & \vec{q}^2 &= q_i q^i = q_x^2 + q_y^2 + q_z^2, \\ |\vec{q}| &= \sqrt{q_x^2 + q_y^2 + q_z^2}, & q_T &= \sqrt{q_x^2 + q_y^2} \end{aligned} \quad (\text{A.3})$$

are used. The notation  $q_a$  where  $a \neq x, y, z$ , indicates the momentum four-vector for particle  $a$  and subsequently the notation  $q_{x_a}$  indicates the  $x$ -component of the momentum for particle  $a$ .

The units throughout this thesis follow the convention of Ref. [18] where  $\hbar$ , the reduced Planck constant, and  $c$ , the speed of light, are taken as unity. However, the value of  $c = 3.0 \times 10^8$  m/s is sometimes needed, particularly in Chap. 4. The explicit use of  $c$  in an equation indicates this value of  $c$  should be used rather than unity.

## A.2. Electroweak Lagrangian

Following the discussion of Sect. 2.1.2 the Lagrangian for unified electroweak theory can be written as,

$$\begin{aligned}
\mathcal{L}_{\text{EWK}} = & \underbrace{i\bar{\psi}_f\gamma^\mu\partial_\mu\psi_f}_{\text{Eqs. 2.27, 2.31}} - \underbrace{\frac{1}{2}(\partial^\mu A^\nu - \partial^\nu A^\mu)(\partial_\mu A_\nu - \partial_\nu A_\mu)}_{\text{Eqs. 2.37, 2.38}} & (\text{A.4}) \\
& - \underbrace{\frac{1}{2}(\partial^\mu Z^\nu - \partial^\nu Z^\mu)(\partial_\mu Z_\nu - \partial_\nu Z_\mu)}_{\text{Eqs. 2.35, 2.38}} \\
& - \underbrace{(\partial^\mu W^{+\nu} - \partial^\nu W^{+\mu})(\partial_\mu W_\nu^- - \partial_\nu W_\mu^-)}_{\text{Eqs. 2.35, 2.38}} \\
& + \underbrace{iQ_f g_e A_\mu \bar{\psi}_f \gamma^\mu \psi_f}_{\text{Fig. 2.4(a)}} - \underbrace{\frac{ig_w}{2\cos\theta_w} Z_\mu \bar{\psi}_f \gamma^\mu (v_f - a_f \gamma^5) \psi_f}_{\text{Fig. 2.4(b)}} \\
& - \underbrace{\frac{ig_w}{2\sqrt{2}} (W_\mu^- \bar{\ell}_f \gamma^\mu (1 - \gamma^5) \nu_f + W_\mu^+ \bar{\nu}_f \gamma^\mu (1 - \gamma^5) \ell_f)}_{\text{Fig. 2.4(c)}} \\
& - \underbrace{\frac{ig_w V_{ij}}{2\sqrt{2}} (W_\mu^- \bar{q}_f^j \gamma^\mu (1 - \gamma^5) q_f^i + W_\mu^+ \bar{q}_f^i \gamma^\mu (1 - \gamma^5) q_f^j)}_{\text{Fig. 2.4(d)}} \\
& - \underbrace{ig_e (\partial_\nu A_\mu (W_\mu^+ W_\nu^- - W_\nu^+ W_\mu^-) - A_\nu (W_\mu^+ \partial_\nu W_\mu^- - W_\mu^- \partial_\nu W_\mu^+) + A_\mu (W_\nu^+ \partial_\nu W_\mu^- - W_\nu^- \partial_\nu W_\mu^+))}_{\text{Fig. 2.4(e)}} \\
& - \underbrace{ig_w \cos\theta_w (\partial_\nu Z_\mu (W_\mu^+ W_\nu^- - W_\nu^+ W_\mu^-) - Z_\nu (W_\mu^+ \partial_\nu W_\mu^- - W_\mu^- \partial_\nu W_\mu^+) + Z_\mu (W_\nu^+ \partial_\nu W_\mu^- - W_\nu^- \partial_\nu W_\mu^+))}_{\text{Fig. 2.4(f)}} \\
& - \underbrace{ig_w^2 (W_\mu^+ W_\mu^- W_\nu^+ W_\nu^- - W_\mu^+ W_\nu^- W_\mu^+ W_\nu^-)}_{\text{Fig. 2.4(g)}} \\
& + \underbrace{ig_w^2 \cos^2\theta_w (Z_\mu W_\mu^+ Z_\nu W_\nu^- - Z_\mu Z_\mu W_\nu^+ W_\nu^-)}_{\text{Fig. 2.4(h)}}
\end{aligned}$$

$$\begin{aligned}
& \underbrace{+ig_e^2 \left( A_\mu W_\mu^+ A_\nu W_\nu^- - A_\mu A_\mu W_\nu^+ W_\nu^- \right)}_{\text{Fig. 2.4(i)}} \\
& \underbrace{+ig_e g_w \cos \theta_w \left( A_\mu Z_\nu (W_\mu^+ W_\nu^- - W_\nu^+ W_\nu^-) - 2A_\mu Z_\mu W_\nu^+ W_\nu^- \right)}_{\text{Fig. 2.4(j)}}
\end{aligned}$$

where the covariant derivatives of Eq. 2.51 have been introduced into the free Lagrangians for  $y_f$  of Eq. 2.46 and  $t_f$  of Eq. 2.48, as well as free Lagrangians, using Eq. 2.33, for the photon,  $W$  bosons, and  $Z$  boson. Here,  $\psi_f$  indicates any fermion field of flavour  $f$ . Note that mass terms for the fermions and bosons have not been introduced, as these terms are introduced via the Higgs mechanism and are included in  $\mathcal{L}_{\text{MHM}}$  of Eq. A.5.

### A.3. Higgs Lagrangian

The Lagrangian for the minimal Higgs mechanism of the SM can be written as,

$$\begin{aligned}
\mathcal{L}_{\text{MHM}} = & \underbrace{-m_f^2 \bar{\psi}_f \psi_f}_{m_f} \underbrace{-m_W^2 W_\mu^+ W^{-\mu}}_{m_W} \underbrace{-\frac{m_Z^2}{2} Z_\mu Z^\mu}_{m_Z} \underbrace{-\frac{1}{2} \partial_\mu H \partial^\mu H - \frac{m_H^2}{2} H H}_{\text{Eq. 2.24}} \tag{A.5} \\
& \underbrace{-\frac{3ig_w m_H^2}{2m_W} H H H}_{\text{Fig. 2.6(a)}} \underbrace{+ig_w m_W W_\mu^+ W^{-\mu} H}_{\text{Fig. 2.6(b)}} \underbrace{+\frac{ig_w m_z}{\cos \theta_w} Z_\mu Z^\mu H}_{\text{Fig. 2.6(c)}} \\
& \underbrace{-\frac{3ig_w^2 m_H^2}{4m_W^2} H H H H}_{\text{Fig. 2.6(d)}} \underbrace{+\frac{ig_w^2}{4} W_\mu^+ W^{-\mu} H H}_{\text{Fig. 2.6(e)}} \underbrace{+\frac{ig_w^2}{8\cos^2 \theta_w} Z_\mu Z^\mu H H}_{\text{Fig. 2.6(f)}} \\
& \underbrace{-\frac{ig_w m_f}{2m_W} H \bar{\psi}_f \psi_f}_{\text{Fig. 2.6(g)}}
\end{aligned}$$

where the terms follow the conventions of Sect. 2.1.2.

## B. Tau Leptons

Distributions of  $m_{23}$ , the invariant mass of the second and third  $\tau$  lepton decay products, for the general three meson current of Sect. 3.2.3 by Decker *et al.* [110] are given for the channels which do not use this model by default. In Fig. B.1 the distributions for  $\tau$  lepton decays with one pion and two kaons are given, while in Fig. B.2 the distributions for decays with two or more pions are given.

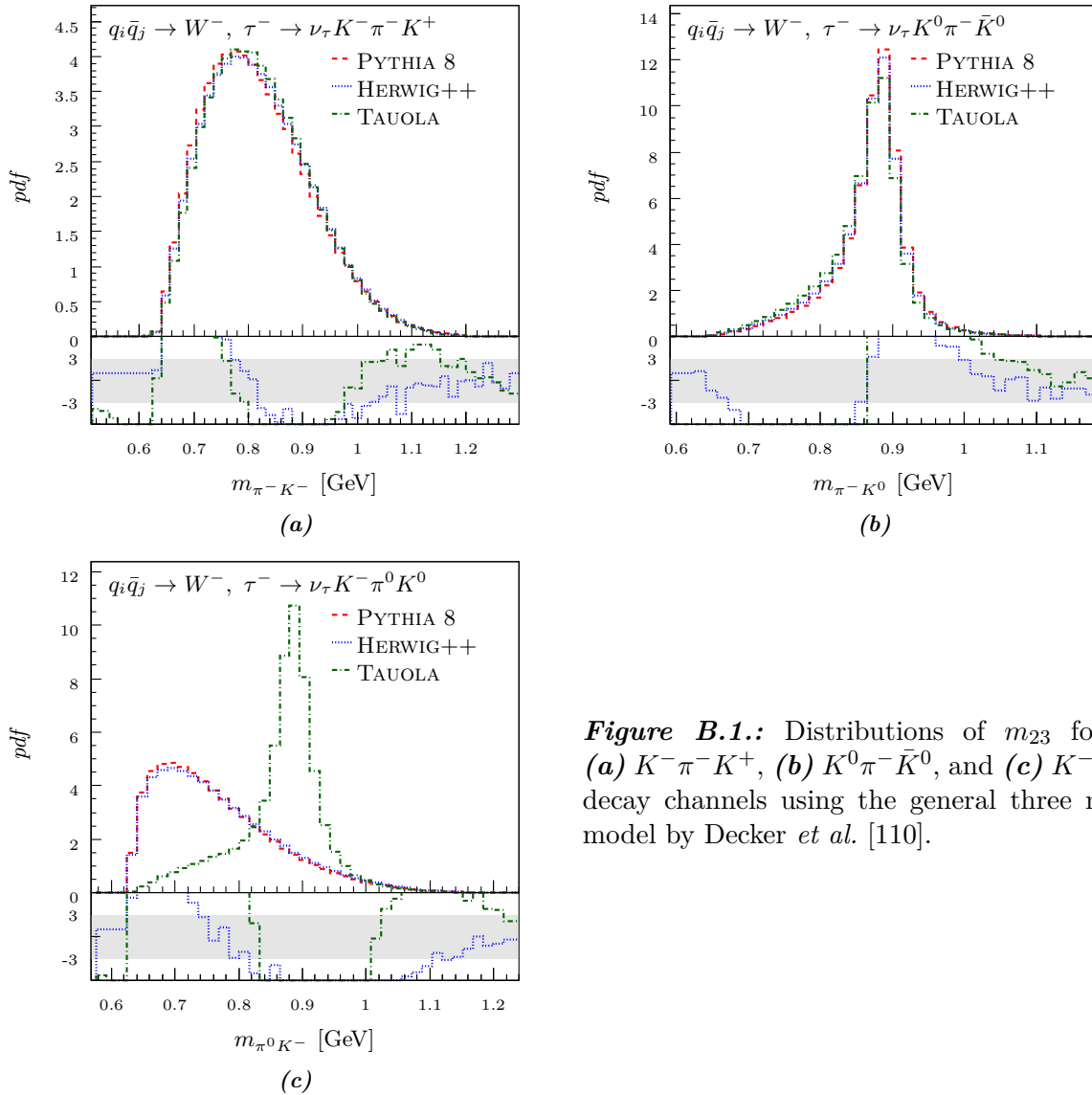


**Figure B.1.:** Distributions of  $m_{23}$  for the (a)  $K^- \pi^- K^+$ , (b)  $K^0 \pi^- \bar{K}^0$ , and (c)  $K^- \pi^0 K^0$  decay channels using the general three meson model by Decker *et al.* [110].



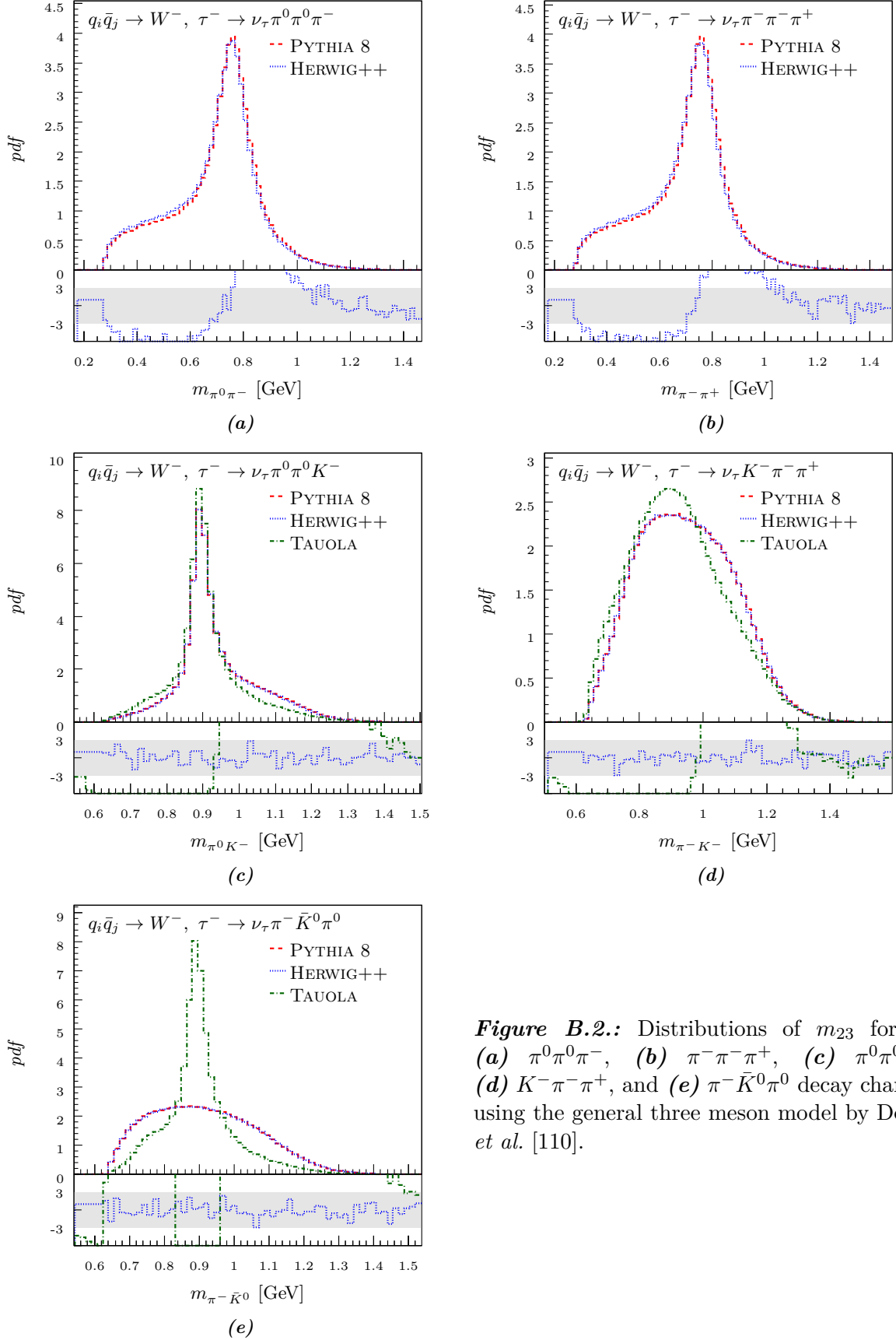


**Figure B.2.:** Distributions of  $m_{23}$  for the (a)  $\pi^0 \pi^0 \pi^-$ , (b)  $\pi^- \pi^- \pi^+$ , (c)  $\pi^0 \pi^0 K^-$ , (d)  $K^- \pi^- \pi^+$ , and (e)  $\pi^- \bar{K}^0 \pi^0$  decay channels using the general three meson model by Decker *et al.* [110].

## C. $Z$ Boson

Additional information for the  $Z \rightarrow \tau\tau$  cross-section measurement of Chap. 5 is given in this appendix. Additional distributions for the data, estimated signal, and estimated backgrounds are given in App. C.1. The method for determining low momentum muon track finding and identification efficiencies using the tag-and-probe method on  $J/\psi \rightarrow \mu\mu$  events from data is outlined in App. C.2. Finally, the combined cross-section fit of the cross-sections from each event category is detailed in App. C.3.

### C.1. Distributions

The pseudo-rapidity distributions for the combination of the two  $\tau$  lepton decay product candidates are given in Fig. C.1 for each event category, while the distributions for the number of primary vertices in the event are given in Fig. C.2. The transverse momentum distributions for the first and second  $\tau$  lepton decay products are given in Figs. C.3 and C.4 respectively. Similarly, their pseudo-rapidity distributions are given in Figs. C.5 and C.6. All these distributions were determined using the selection of Sect. 5.1.2 and the background estimation of Sect. 5.1.3.

### C.2. Efficiencies

The low momentum, 0 to 150 GeV, muon track finding and identification efficiencies are determined using a tag-and-probe method on  $J/\psi \rightarrow \mu\mu$  events selected from data, as described in Sect. 5.2.1. These events, unlike the  $Z \rightarrow \mu\mu$  events used for the high momentum muon efficiencies, are contaminated with a significant background contribution. Additionally, because these events do not have the same pseudo-rapidity distribution as  $Z \rightarrow \tau\tau$  signal events, the efficiencies from  $J/\psi \rightarrow \mu\mu$  events must be determined as a function of both the momentum and pseudo-rapidity of the probe muon candidate,  $\eta_\mu$  and  $p_\mu$ .

The  $J/\psi \rightarrow \mu\mu$  tag-and-probe events are separated into twelve bins, three bins in pseudo-rapidity for each of the four bins in momentum. The pseudo-rapidity bin widths are  $5/6$  of  $\eta$  and range from 2.0 to 4.5, while the momentum bin widths are 50 GeV and range from 0 to 200 GeV. The last momentum bin,  $150 < p_\mu < 200$  GeV, is only used as a consistency check and is not used for final efficiencies. The distributions of the di-muon invariant mass for each of the twelve bins are shown in Fig. C.7 for the muon track finding efficiency before the track selection criteria is applied to the probe. The  $J/\psi$  resonance is clearly visible, with its width increasing for larger momenta due to a decrease in momentum resolution. This is particularly visible in the final pseudo-rapidity column,  $3.67 < \eta_\mu < 4.50$ .

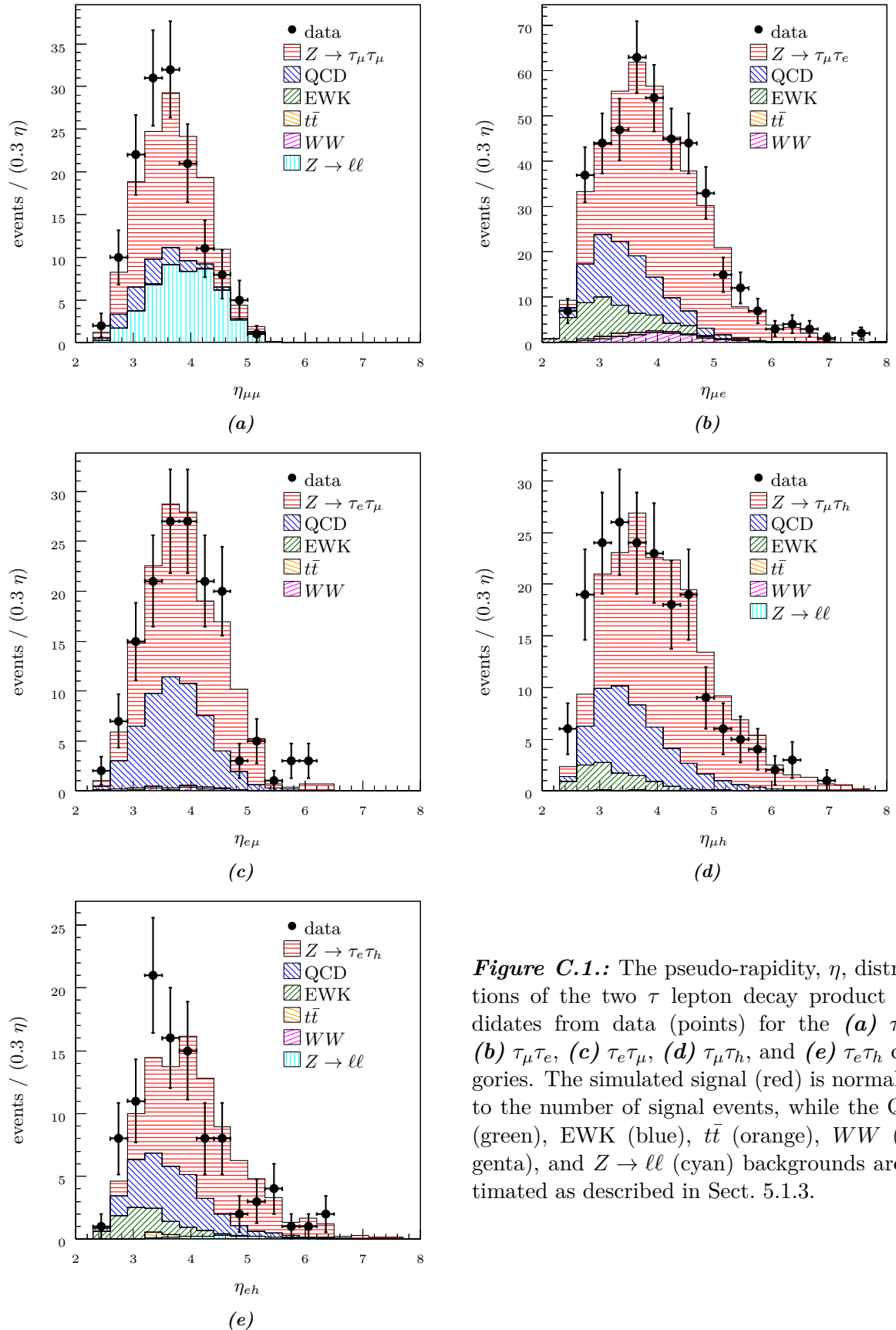


**Figure C.1.:** The pseudo-rapidity,  $\eta$ , distributions of the two  $\tau$  lepton decay product candidates from data (points) for the (a)  $\tau_\mu\tau_\mu$ , (b)  $\tau_\mu\tau_e$ , (c)  $\tau_e\tau_\mu$ , (d)  $\tau_\mu\tau_h$ , and (e)  $\tau_e\tau_h$  categories. The simulated signal (red) is normalised to the number of signal events, while the QCD (green), EWK (blue),  $t\bar{t}$  (orange),  $WW$  (magenta), and  $Z \rightarrow \ell\ell$  (cyan) backgrounds are estimated as described in Sect. 5.1.3.

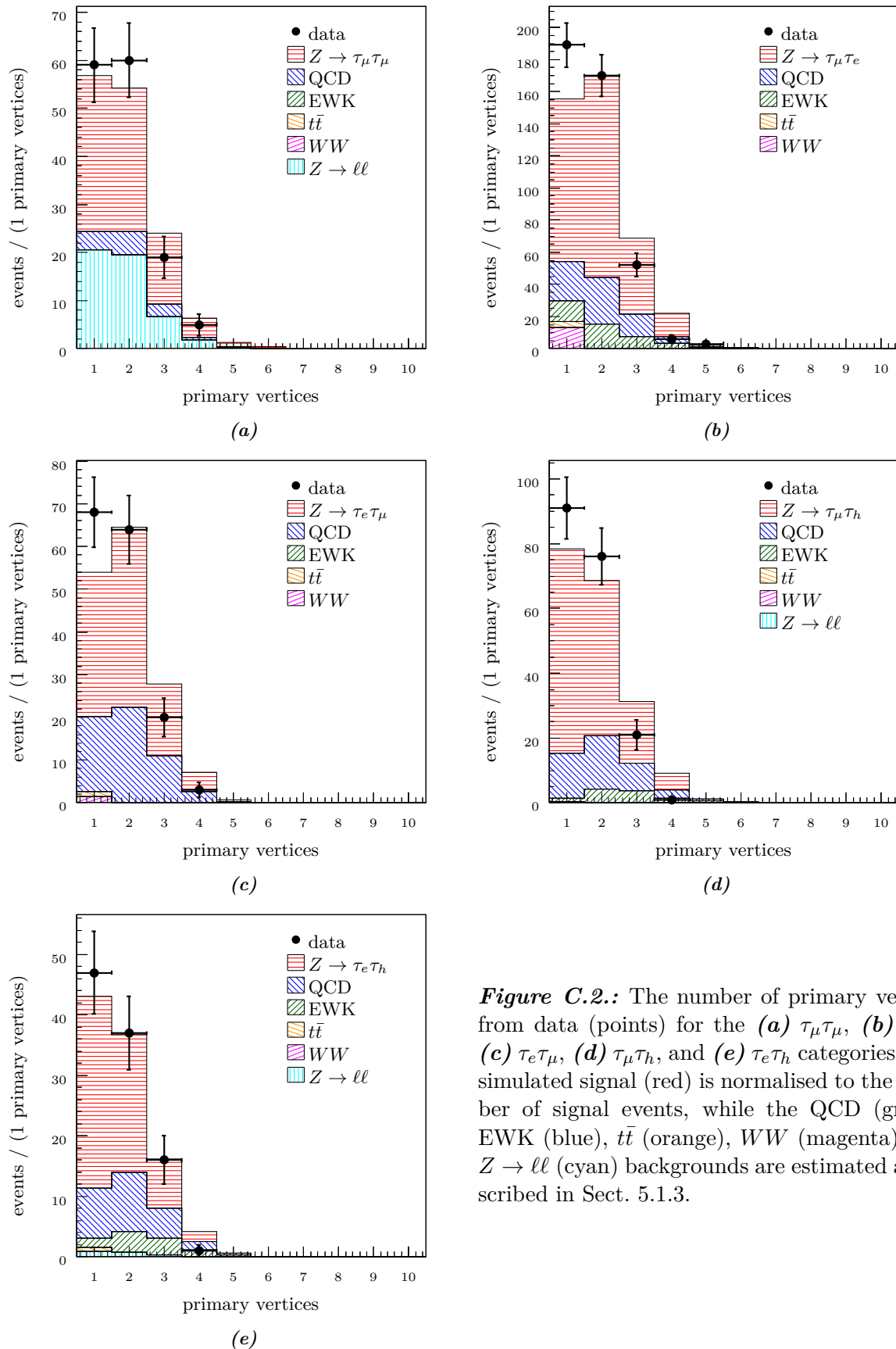


**Figure C.2.:** The number of primary vertices from data (points) for the (a)  $\tau_\mu\tau_\mu$ , (b)  $\tau_\mu\tau_e$ , (c)  $\tau_e\tau_\mu$ , (d)  $\tau_\mu\tau_h$ , and (e)  $\tau_e\tau_h$  categories. The simulated signal (red) is normalised to the number of signal events, while the QCD (green), EWK (blue),  $t\bar{t}$  (orange), WW (magenta), and  $Z \rightarrow \ell\ell$  (cyan) backgrounds are estimated as described in Sect. 5.1.3.

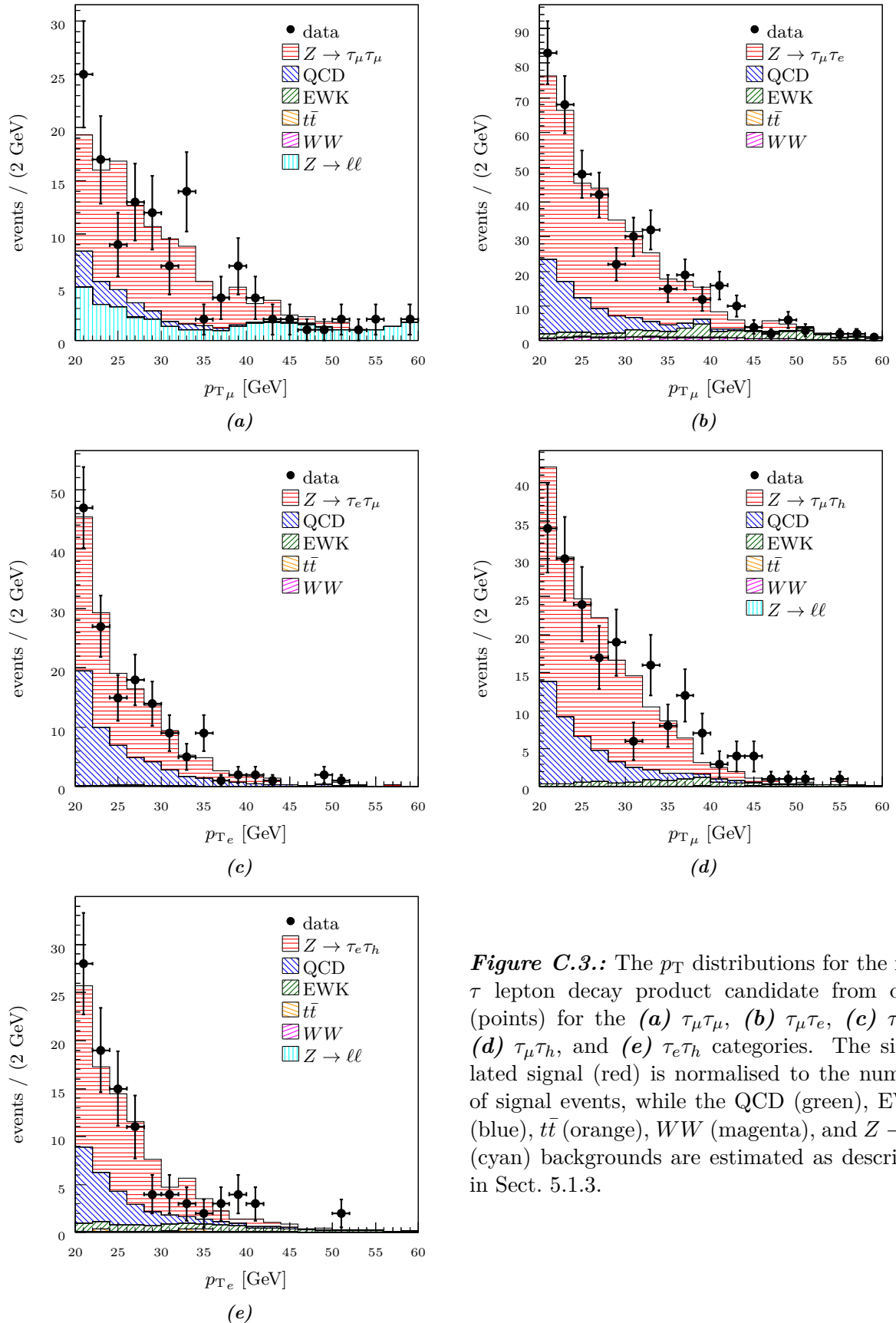


**Figure C.3.:** The  $p_T$  distributions for the first  $\tau$  lepton decay product candidate from data (points) for the (a)  $\tau_\mu \tau_\mu$ , (b)  $\tau_\mu \tau_e$ , (c)  $\tau_e \tau_\mu$ , (d)  $\tau_\mu \tau_h$ , and (e)  $\tau_e \tau_h$  categories. The simulated signal (red) is normalised to the number of signal events, while the QCD (green), EWK (blue),  $t\bar{t}$  (orange),  $WW$  (magenta), and  $Z \rightarrow \ell\ell$  (cyan) backgrounds are estimated as described in Sect. 5.1.3.

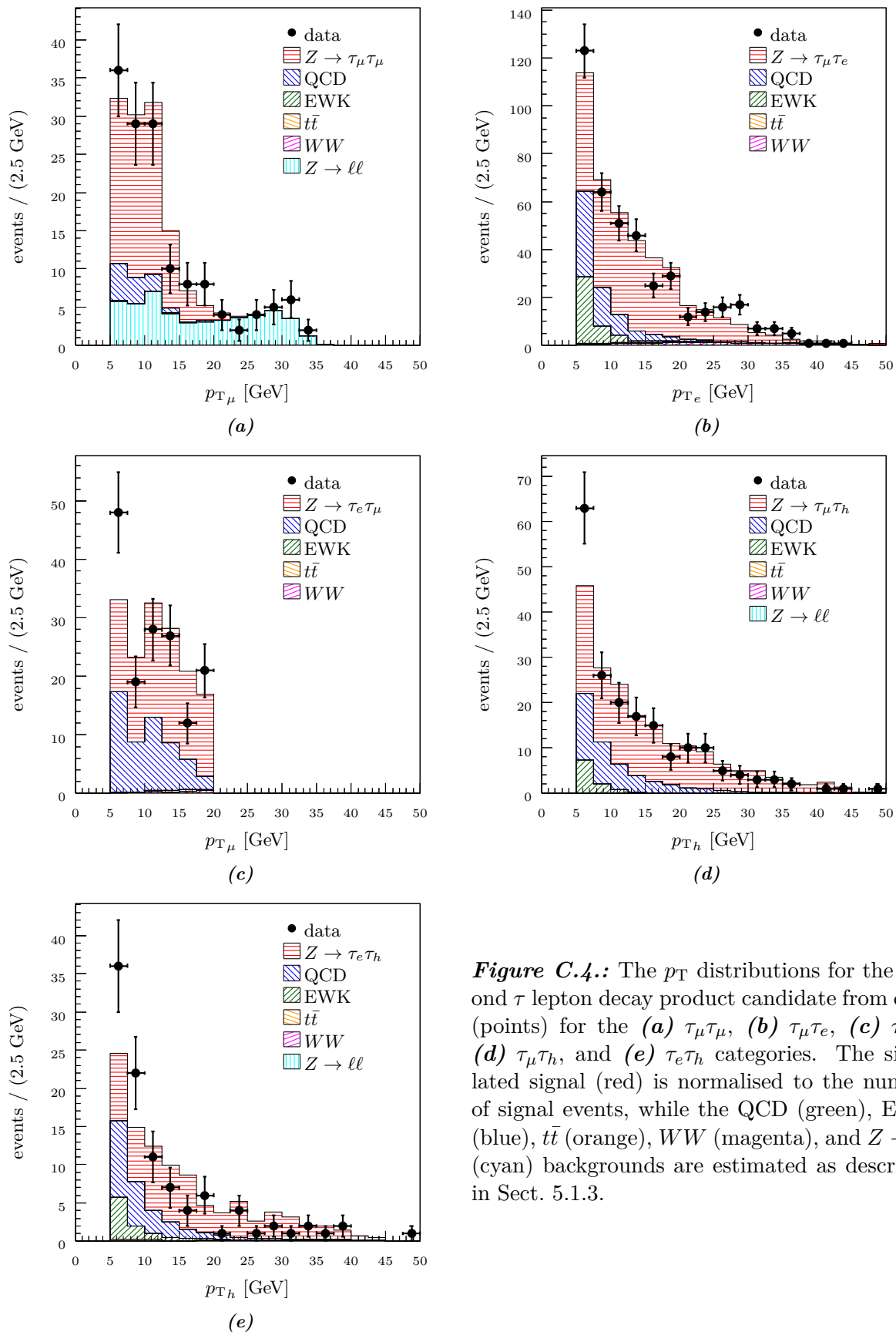


**Figure C.4.:** The  $p_T$  distributions for the second  $\tau$  lepton decay product candidate from data (points) for the (a)  $\tau_\mu \tau_\mu$ , (b)  $\tau_\mu \tau_e$ , (c)  $\tau_e \tau_\mu$ , (d)  $\tau_\mu \tau_h$ , and (e)  $\tau_e \tau_h$  categories. The simulated signal (red) is normalised to the number of signal events, while the QCD (green), EWK (blue),  $t\bar{t}$  (orange),  $WW$  (magenta), and  $Z \rightarrow \ell\ell$  (cyan) backgrounds are estimated as described in Sect. 5.1.3.

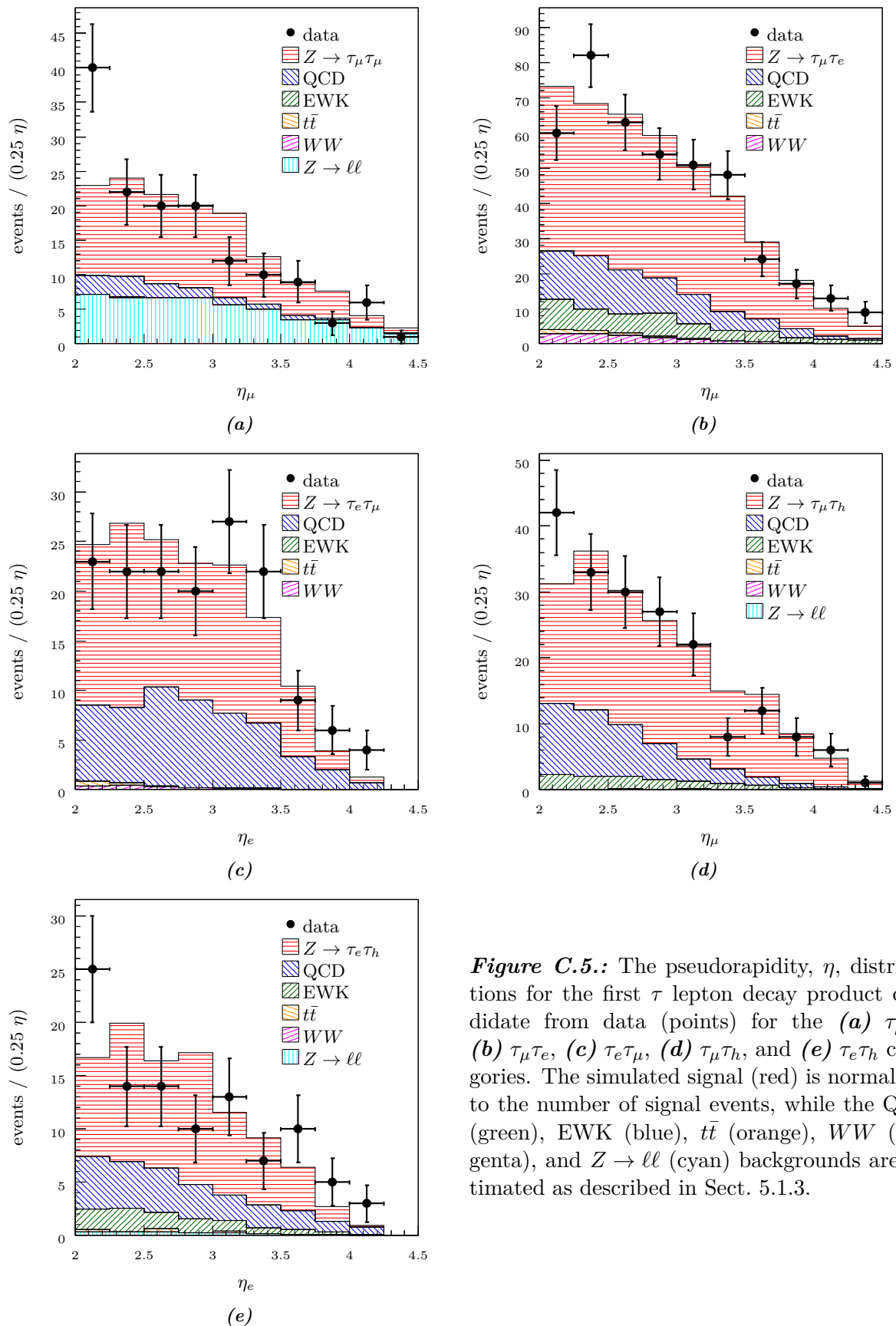


**Figure C.5.:** The pseudorapidity,  $\eta$ , distributions for the first  $\tau$  lepton decay product candidate from data (points) for the (a)  $\tau\mu\tau\mu$ , (b)  $\tau\mu\tau e$ , (c)  $\tau e\tau\mu$ , (d)  $\tau\mu\tau h$ , and (e)  $\tau e\tau h$  categories. The simulated signal (red) is normalised to the number of signal events, while the QCD (green), EWK (blue),  $t\bar{t}$  (orange),  $WW$  (magenta), and  $Z \rightarrow \ell\ell$  (cyan) backgrounds are estimated as described in Sect. 5.1.3.

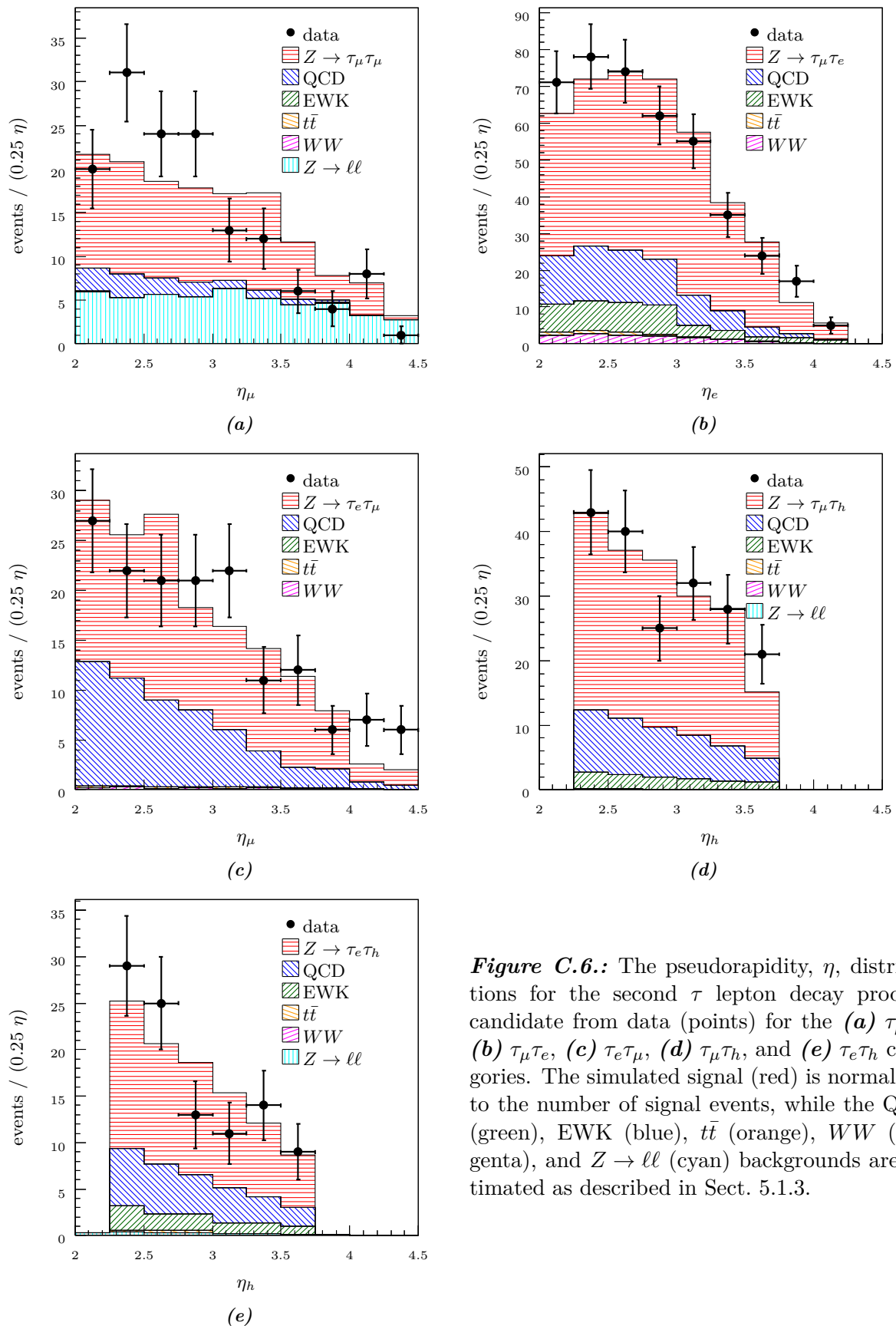


**Figure C.6.:** The pseudorapidity,  $\eta$ , distributions for the second  $\tau$  lepton decay product candidate from data (points) for the (a)  $\tau\mu\tau\mu$ , (b)  $\tau\mu\tau_e$ , (c)  $\tau_e\tau\mu$ , (d)  $\tau\mu\tau_h$ , and (e)  $\tau_e\tau_h$  categories. The simulated signal (red) is normalised to the number of signal events, while the QCD (green), EWK (blue),  $t\bar{t}$  (orange),  $WW$  (magenta), and  $Z \rightarrow \ell\ell$  (cyan) backgrounds are estimated as described in Sect. 5.1.3.



The same distributions are given in Fig. C.8, but now for events where the probe muon candidate passes the track selection requirement. As expected, there are fewer events in these distributions than the distributions of Fig. C.7. The same plots, but for muon identification, are given in Fig. C.10 before requiring the probe muon candidate pass the muon identification of Sect. 5.1.1, and after, in Fig. C.9. The  $J/\psi$  resonances in these distributions are much narrower as the probe track has a much better resolution than the probe muon-track for the track finding efficiency. The widening of the  $J/\psi$  resonance due to a decrease in momentum resolution can also be seen in both of these plots.

The number of signal events in Figs. C.7 through C.9 are extracted using two different fitting methods. The efficiency for each bin in momentum and pseudo-rapidity is the number of extracted signal events after applying the selection criteria to the probe, over the number of extracted signal events before applying the selection criteria. The first method is performed by fitting a first degree polynomial,

$$f_1(x) = P_0 + P_1x \quad (\text{C.1})$$

to the background on either side of the  $J/\psi$  resonance with initial values of  $P_0 = 0$  and  $P_1 = 0$ . For the muon track finding efficiency, the ranges  $2.70 < m_{\mu\mu} < 2.95$  GeV and  $3.30 < m_{\mu\mu} < 3.70$  GeV are fit while the ranges  $2.95 < m_{\mu\mu} < 3.03$  GeV and  $3.20 < m_{\mu\mu} < 3.25$  GeV are fit for the muon identification efficiency. The number of extracted signal events is the number of events within the distribution, less the integral of the polynomial divided by the bin width.

The second fitting method uses four fits to converge to a final fit of the distributions. The method begins by fitting the distributions with Eq. C.1 and using the initial parameters  $P_0 = 0$  and  $P_1 = 0$ . Next, the distributions are fit with a first degree polynomial plus a Gaussian distribution,

$$f_2(x) = f_1(x) + P_2 e^{-\frac{(x-P_3)^2}{2P_4^2}} \quad (\text{C.2})$$

where the initial values for  $P_0$  and  $P_1$  are taken from the first fit,  $P_2 = 0$ ,  $P_3 = 3.1$ , and  $P_4 = 0.05$ . Following this, the distributions are fit with a crystal ball function [245],

$$f_3(x) = f_1(x) + P_2 \begin{cases} \left(\frac{P_6}{|P_5|}\right)^{P_6} e^{-\frac{P_5^2}{2}} \left(\frac{P_6}{|P_5|} - |P_5| - \frac{x-P_3}{P_4}\right)^{-P_6} & \text{if } \frac{x-P_3}{4} \leq -P_5 \\ e^{-\frac{(x-P_3)^2}{2P_4^2}} & \text{if } \frac{x-P_3}{4} > -P_5 \end{cases} \quad (\text{C.3})$$

where the initial values for  $P_0$  through  $P_4$  are taken from the fit with Eq. C.2,  $P_5 = 1$ , and the value for  $P_6$  is fixed at 1.

The distributions from before applying the selection criteria and after are then fit simultaneously for each bin in momentum and pseudo-rapidity using Eq. C.3, where the background and normalisation parameters  $P_0$  through  $P_2$  are independent between the two distributions, but the shape parameters  $P_3$  through  $P_6$  are shared, with  $P_6$  being allowed to vary. The number of signal events is estimated as the integral of the final simultaneous fits when setting the linear

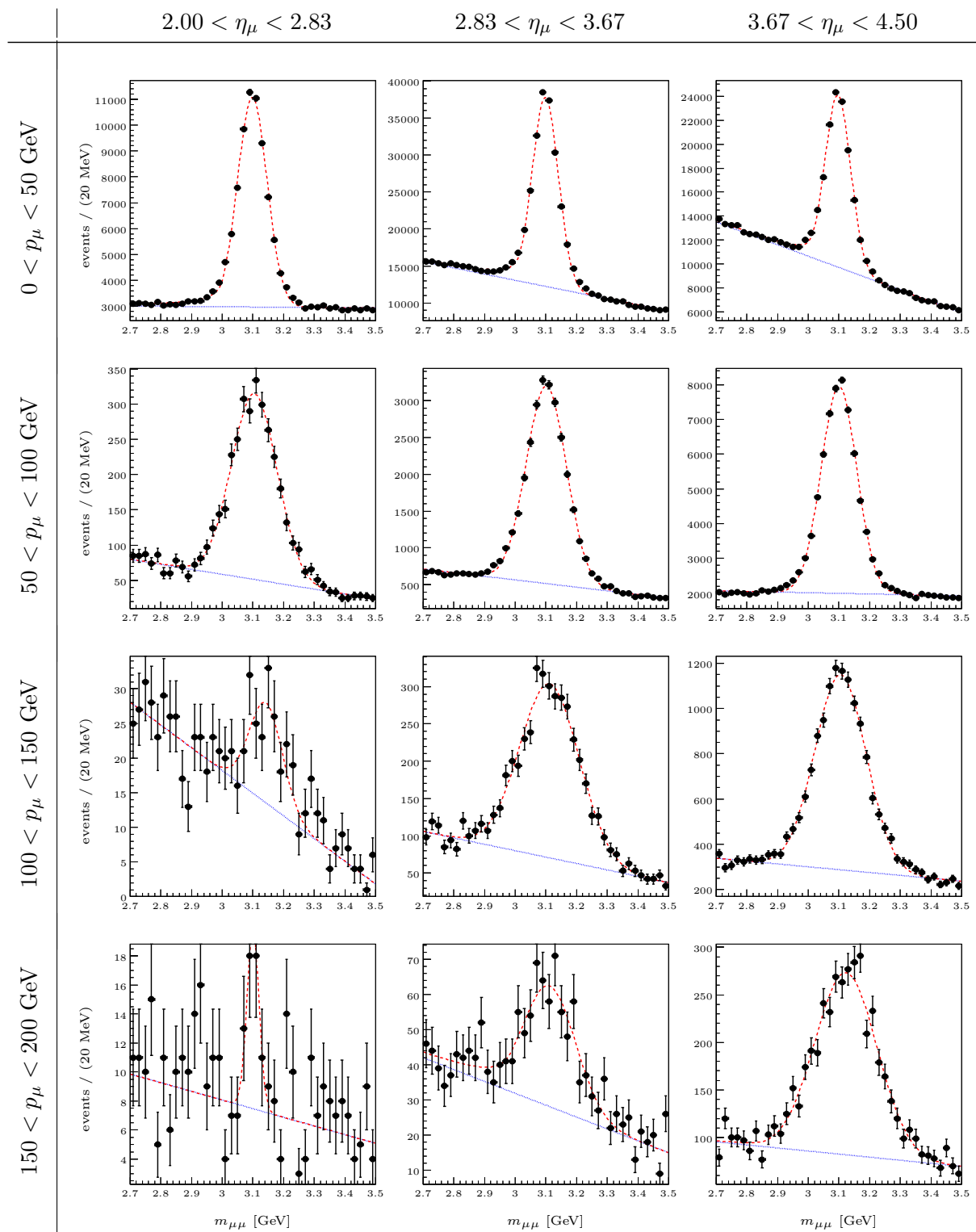


**Figure C.7.:** Crystal ball fits (dashed red) with a linear background (dotted blue) of the  $J/\psi \rightarrow \mu\mu$  data (points) used to determine the muon track finding efficiency, before requiring a reconstructed track. The fits are given in three bins of pseudo-rapidity between 2.0 and 4.5 and four bins of momentum between 0 and 200 GeV.

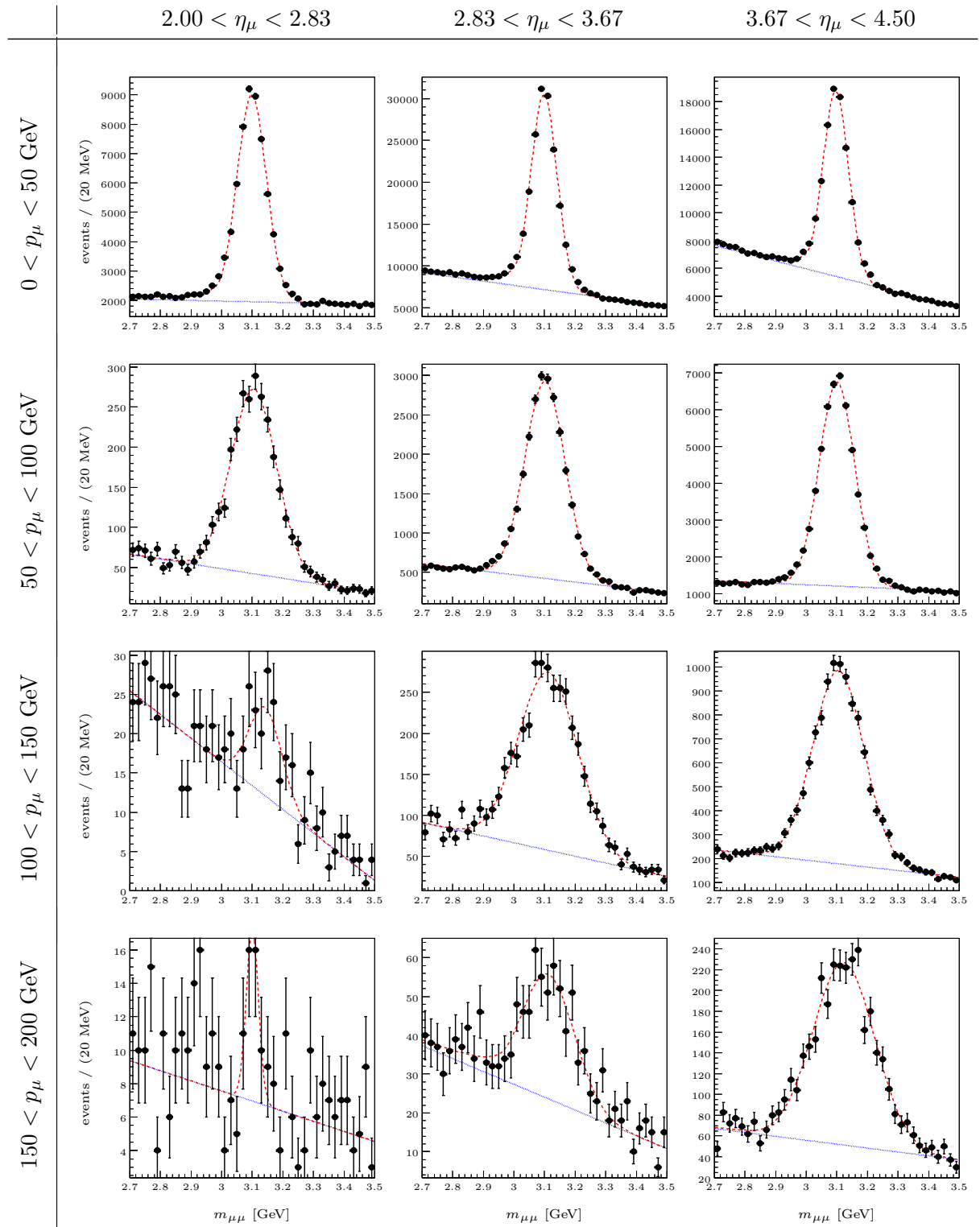


**Figure C.8.:** Crystal ball fits (dashed red) with a linear background (dotted blue) of the  $J/\psi \rightarrow \mu\mu$  data (points) used to determine the muon track finding efficiency, after requiring a reconstructed track. The fits are given in three bins of pseudo-rapidity between 2.0 and 4.5 and four bins of momentum between 0 and 200 GeV.

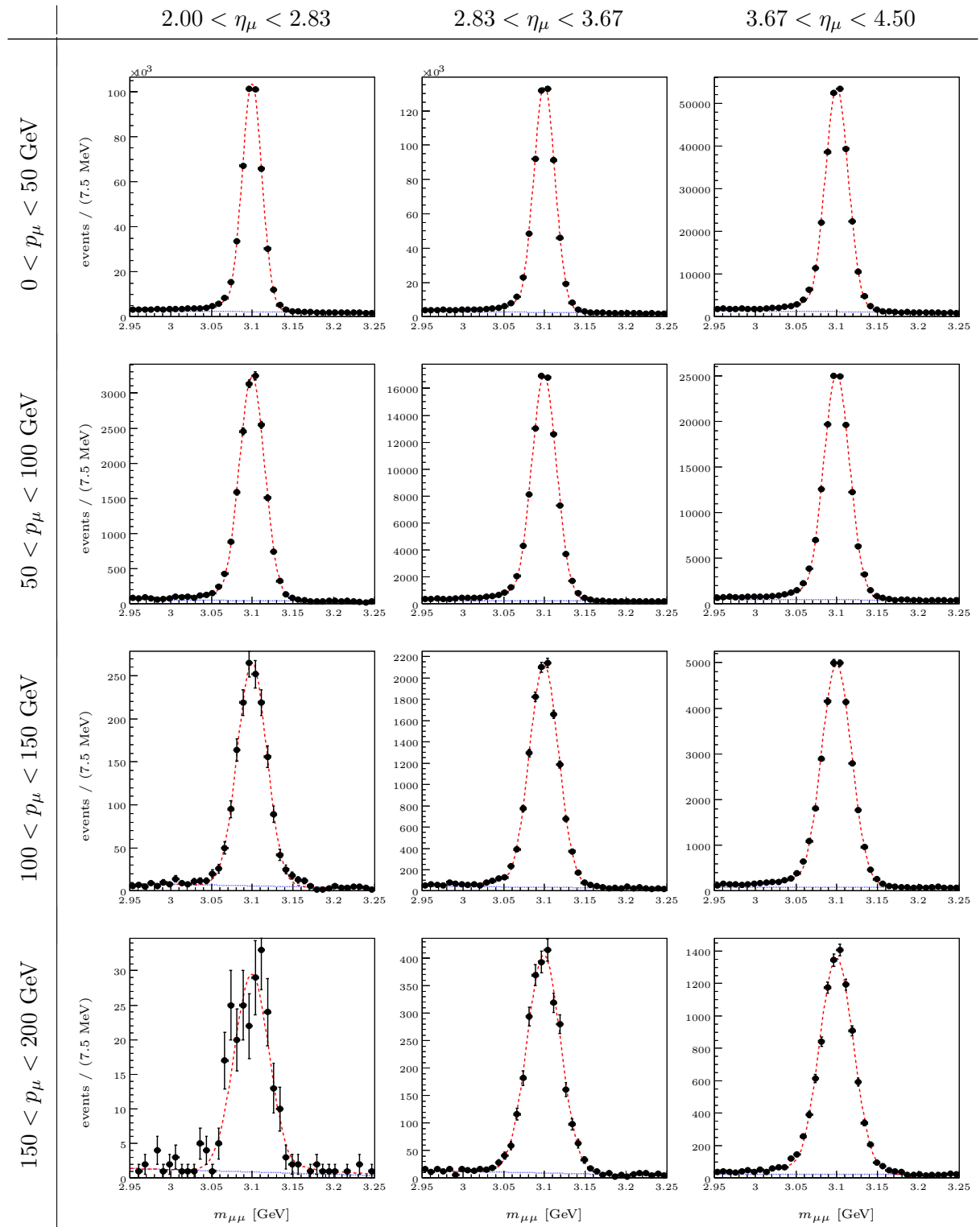


**Figure C.9.:** Crystal ball fits (dashed red) with a linear background (dotted blue) of the  $J/\psi \rightarrow \mu\mu$  data (points) used to determine the muon track identification efficiency, after requiring an identified muon. The fits are given in three bins of pseudo-rapidity between 2.0 and 4.5 and four bins of momentum between 0 and 200 GeV.

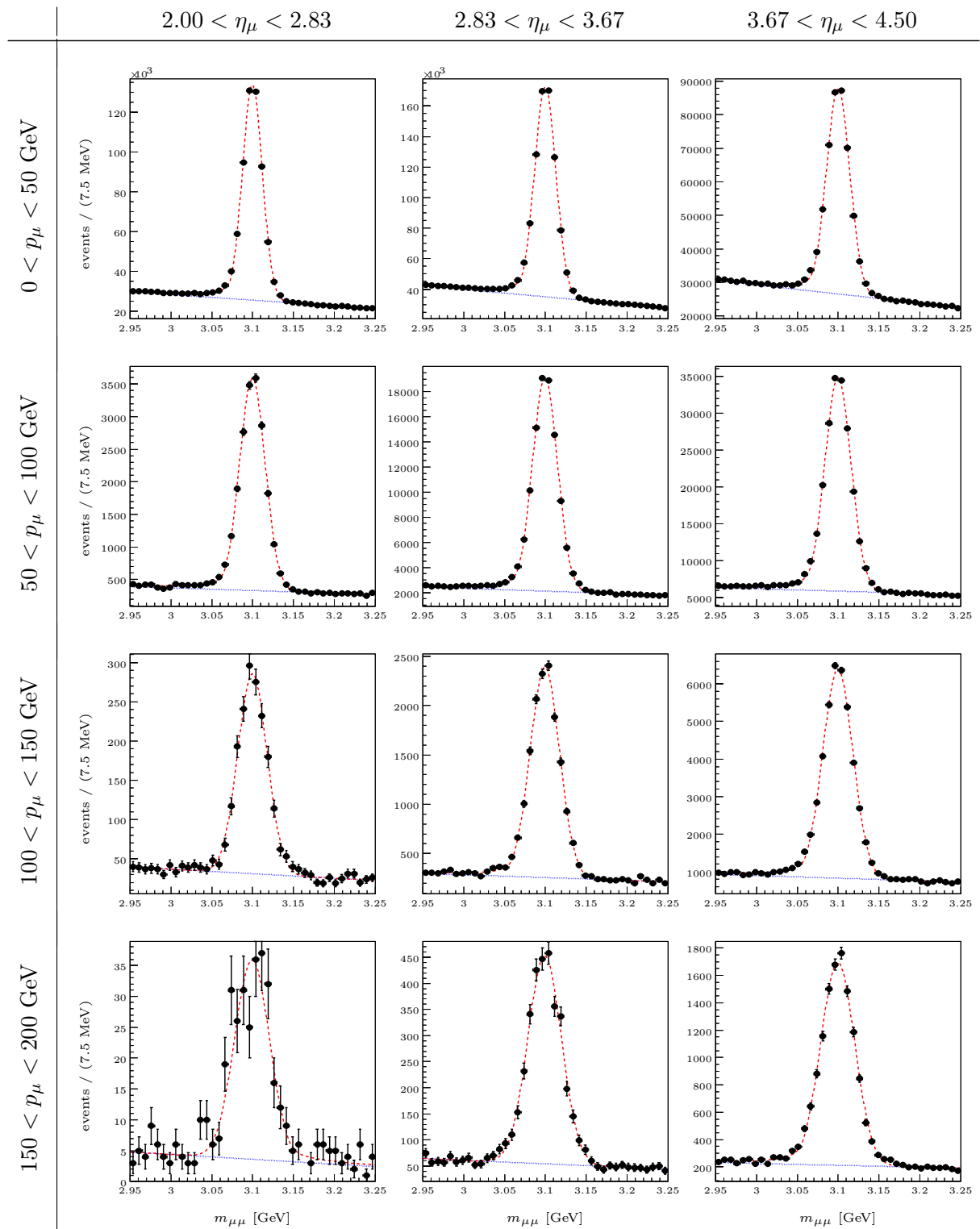


**Figure C.10.:** Crystal ball fits (dashed red) with a linear background (dotted blue) of the  $J/\psi \rightarrow \mu\mu$  data (points) used to determine the muon track identification efficiency, before requiring an identified muon. The fits are given in three bins of pseudo-rapidity between 2.0 and 4.5 and four bins of momentum between 0 and 200 GeV.

background to zero,  $P_1 = P_1 = 0$ , and dividing by the bin width of the distribution.

### C.3. Combined Fit

The combined fit of the five cross-sections in Sect. 5.3 is performed using the method of the best linear unbiased estimator from Ref. [182]. The best linear unbiased estimator  $\hat{x}$  is,

$$\hat{x} = \vec{w}\vec{x}^\dagger \quad (\text{C.4})$$

where  $\vec{x}$  is a row vector of the  $n$  independent measurements being combined, and  $\vec{w}$  is a row vector of weights, required to sum to unity, with an element for each measurement. The uncertainty for  $\hat{x}$  is,

$$\delta_{\hat{x}}^2 = \vec{w}\mathcal{V}\vec{w}^\dagger \quad (\text{C.5})$$

where  $\mathcal{V}$  is the  $n$ -by- $n$  symmetric covariance matrix for  $\vec{x}$ . The weights  $\vec{w}$  are found by minimising  $\delta_{\hat{x}}$  which is given by,

$$\vec{w} = \left( \frac{\mathcal{V}^{-1}\vec{u}^\dagger}{\vec{u}\mathcal{V}^{-1}\vec{u}^\dagger} \right)^\dagger \quad (\text{C.6})$$

using the method of Lagrange multipliers [71] where  $\vec{u}$  is a row matrix of dimension  $n$  with all entries unity and  $\mathcal{V}^{-1}$  is the inverse of the covariance matrix. The  $\chi^2$  for the estimator is given by,

$$\chi^2 = (\hat{x}\vec{u} - \vec{x})\mathcal{V}^{-1}(\hat{x}\vec{u} - \vec{x})^\dagger \quad (\text{C.7})$$

where the number of degrees of freedom is  $n - 1$ .

For the combined measurement of Eq. 5.22 the  $\hat{x}$  and  $\vec{x}$  are given by,

$$\hat{x} = \sigma_{pp \rightarrow Z \rightarrow \tau\tau}, \quad \vec{x} = \sigma_{pp \rightarrow Z \rightarrow \tau\tau} \left( (\tau_\mu\tau_\mu), (\tau_\mu\tau_e), (\tau_e\tau_\mu), (\tau_\mu\tau_h), (\tau_e\tau_h) \right) \quad (\text{C.8})$$

where the values for the five cross-sections,  $\sigma_{pp \rightarrow Z \rightarrow \tau\tau}$  ( $\tau_1\tau_2$ ), are given by Eq. 5.21. The components of the covariance matrix  $\mathcal{V}$  are given by,

$$\mathcal{V} = \sum_i \vec{\delta}_{\text{sys}_i} \mathcal{C}_{\text{sys}_i} \vec{\delta}_{\text{sys}_i}^\dagger + \vec{\delta}_{\mathcal{L}} \mathcal{U} \vec{\delta}_{\mathcal{L}}^\dagger + \vec{\delta}_N \mathcal{I} \vec{\delta}_N^\dagger \quad (\text{C.9})$$

where numerical values for the first term are tabulated in Table C.1(a), while the second term is tabulated in Table C.1(b) and the third term is tabulated in Table C.1(c). The matrix  $\mathcal{C}_{\text{sys}_i}$  is the correlation coefficient matrix for the row vector  $\vec{\delta}_{\text{sys}_i}$  of each systematic uncertainty  $i$ . The components of these matrices for the eleven reconstruction and selection efficiency uncertainties are given in Table C.2. All background uncertainties are assumed to be uncorrelated and so their correlation coefficient matrix is the identity matrix. The row vector  $\vec{\delta}_{\mathcal{L}}$  consists of the luminosity

uncertainty for each event category, and  $\vec{\delta}_N$  is a row vector of the statistical uncertainties for the five category. The matrix  $\mathcal{U}$  is a five-by-five matrix of ones and  $\mathcal{I}$  is the five-by-five identity matrix. The covariance matrix  $\mathcal{V}$  is initially estimated for the first iteration of the fit using the relative uncertainties of Table 5.7 and the cross-sections of Eq. 5.21. A second iteration of the fit is then performed using a covariance matrix determined from the relative uncertainties of Table 5.7 and the prior best fit value. No further iterations are required as convergence within numerical precision is reached after this second fit.

|                    |                    | $\sum_i \vec{\delta}_{\text{sys}_i} \mathcal{C}_{\text{sys}_i} \vec{\delta}_{\text{sys}_i}^\dagger \text{ [pb}^2\text{]}$ |                  |                  |                  |                |
|--------------------|--------------------|---|------------------|------------------|------------------|----------------|
|                    |                    | $\tau_\mu\tau_\mu$  | $\tau_\mu\tau_e$ | $\tau_e\tau_\mu$ | $\tau_\mu\tau_h$ | $\tau_e\tau_h$ |
| $\tau_\mu\tau_\mu$ | $\tau_\mu\tau_\mu$ | 63.3  | 4.9              | 5.6              | 6.1              | 8.0            |
|                    | $\tau_\mu\tau_e$   |   | 15.3             | 6.9              | 3.5              | 5.5            |
|                    | $\tau_e\tau_\mu$   |   |                  | 30.4             | 4.4              | 21.4           |
|                    | $\tau_\mu\tau_h$   |   |                  |                  | 6.7              | 7.7            |
|                    | $\tau_e\tau_h$     |   |                  |                  |                  | 32.0           |

(a)

|                    |                    | $\vec{\delta}_\mathcal{L} \mathcal{U} \vec{\delta}_\mathcal{L}^\dagger \text{ [pb}^2\text{]}$ |                  |                  |                  |                |
|--------------------|--------------------|---|------------------|------------------|------------------|----------------|
|                    |                    | $\tau_\mu\tau_\mu$  | $\tau_\mu\tau_e$ | $\tau_e\tau_\mu$ | $\tau_\mu\tau_h$ | $\tau_e\tau_h$ |
| $\tau_\mu\tau_\mu$ | $\tau_\mu\tau_\mu$ | 6.4   | 6.4              | 6.4              | 6.4              | 6.4            |
|                    | $\tau_\mu\tau_e$   |   | 6.4              | 6.4              | 6.4              | 6.4            |
|                    | $\tau_e\tau_\mu$   |   |                  | 6.4              | 6.4              | 6.4            |
|                    | $\tau_\mu\tau_h$   |   |                  |                  | 6.4              | 6.4            |
|                    | $\tau_e\tau_h$     |   |                  |                  |                  | 6.4            |

(b)

|                    |                    | $\vec{\delta}_N \mathcal{I} \vec{\delta}_N^\dagger \text{ [pb}^2\text{]}$ |                  |                  |                  |                |
|--------------------|--------------------|---|------------------|------------------|------------------|----------------|
|                    |                    | $\tau_\mu\tau_\mu$  | $\tau_\mu\tau_e$ | $\tau_e\tau_\mu$ | $\tau_\mu\tau_h$ | $\tau_e\tau_h$ |
| $\tau_\mu\tau_\mu$ | $\tau_\mu\tau_\mu$ | 93.8  | 0.0              | 0.0              | 0.0              | 0.0            |
|                    | $\tau_\mu\tau_e$   |   | 26.6             | 0.0              | 0.0              | 0.0            |
|                    | $\tau_e\tau_\mu$   |   |                  | 85.0             | 0.0              | 0.0            |
|                    | $\tau_\mu\tau_h$   |   |                  |                  | 54.9             | 0.0            |
|                    | $\tau_e\tau_h$     |   |                  |                  |                  | 127.4          |

(c)

**Table C.1.:** The covariance matrices used in the best linear unbiased estimate decomposed into **(a)** the systematic uncertainty, **(b)** the fully correlated luminosity uncertainty, and **(c)** the fully uncorrelated statistical uncertainty.

**Table C.2.:** Table of systematic uncertainty correlations used in the global fit.

|                     | $\tau_\mu \tau_e$   | $\tau_e \tau_\mu$   | $\tau_\mu \tau_h$   | $\tau_e \tau_h$   |
|---------------------|---|---|---|---|
| $C_{\text{rec}}$    | $C_{\text{GEC}} C_{\text{trg}} C_{\text{trk1}} C_{\text{trk2}} C_{\text{id1}} C_{\text{id2}}$ | $C_{\text{GEC}} C_{\text{trg}} C_{\text{trk1}} C_{\text{trk2}} C_{\text{id1}} C_{\text{id2}}$ | $C_{\text{GEC}} C_{\text{trg}} C_{\text{trk1}} C_{\text{trk2}} C_{\text{id1}} C_{\text{id2}}$ | $C_{\text{GEC}} C_{\text{trg}} C_{\text{trk1}} C_{\text{trk2}} C_{\text{id1}} C_{\text{id2}}$ |
| $C_{\text{sel}}$    | $C_{\text{kin}} C_{I_{\text{PT}}} C_{ \Delta\phi } C_{\text{IPS}} C_{A_{\text{PT}}}$          | $C_{\text{kin}} C_{I_{\text{PT}}} C_{ \Delta\phi } C_{\text{IPS}} C_{A_{\text{PT}}}$          | $C_{\text{kin}} C_{I_{\text{PT}}} C_{ \Delta\phi } C_{\text{IPS}} C_{A_{\text{PT}}}$          | $C_{\text{kin}} C_{I_{\text{PT}}} C_{ \Delta\phi } C_{\text{IPS}} C_{A_{\text{PT}}}$          |
| $\tau_\mu \tau_\mu$ | 1 1 1 0 1 0<br>0 1 1 0 0 0  | 0 0 0 1 0 1<br>0 1 1 0 0 0  | 1 1 1 1 1 0<br>0 1 1 1 1 0  | 0 0 0 1 0 0<br>0 1 1 1 1 0  |
| $\tau_\mu \tau_e$   | 0 0 0 0 0 0<br>0 1 1 0 0 0  | 0 0 0 0 0 0<br>0 1 1 0 0 0  | 1 1 1 0 1 0<br>0 1 1 0 0 0  | 0 0 0 0 0 0<br>0 1 1 0 0 0  |
| $\tau_e \tau_\mu$   | $\tau_e \tau_\mu$   |   |   |   |
|                     | 0 0 0 1 0 0<br>0 1 1 0 0 0  | 0 0 0 1 0 0<br>0 1 1 0 0 0  | 1 1 1 0 1 0<br>0 1 1 0 0 0  | 1 1 1 1 1 0<br>0 1 1 1 0 0  |
|                     | $\tau_\mu \tau_h$   |   |   | 0 0 0 1 0 1<br>0 1 1 1 1 0  |



## D. Higgs Boson

This appendix provides supplemental material for Chap. 6. Additional information and plots for the Higgs boson phenomenology of Sect. 6.1 are given in App. D.1. In App. D.2 numerical values for the acceptances and efficiencies of Sect. 6.2.2 are tabulated. Further information on the statistical methods of Sect. 6.3 is provided in App. D.3.

### D.1. Higgs Phenomenology

Details on the masses of the  $\mathcal{CP}$ -even MSSM Higgs bosons are given in App. D.1.1. The methods used for calculating the branching fractions of Sect. 6.1.1 are given in App. D.1.2 for the SM Higgs boson and in App. D.1.3 for the MSSM Higgs bosons. The cross-section calculations of Sect. 6.1.2 are detailed in App. D.1.4 for the SM Higgs boson and App. D.1.5 for the MSSM Higgs bosons.

#### D.1.1. MSSM Higgs Boson Masses

The masses of the light and heavy  $\mathcal{CP}$ -even Higgs bosons from Fig. 6.1 are given in Fig. D.1, but with overlaid numerical values. These values are given in 17 bins of 10 GeV for the  $\mathcal{CP}$ -odd Higgs boson mass and 20 bins of 7 for  $\tan\beta$ .

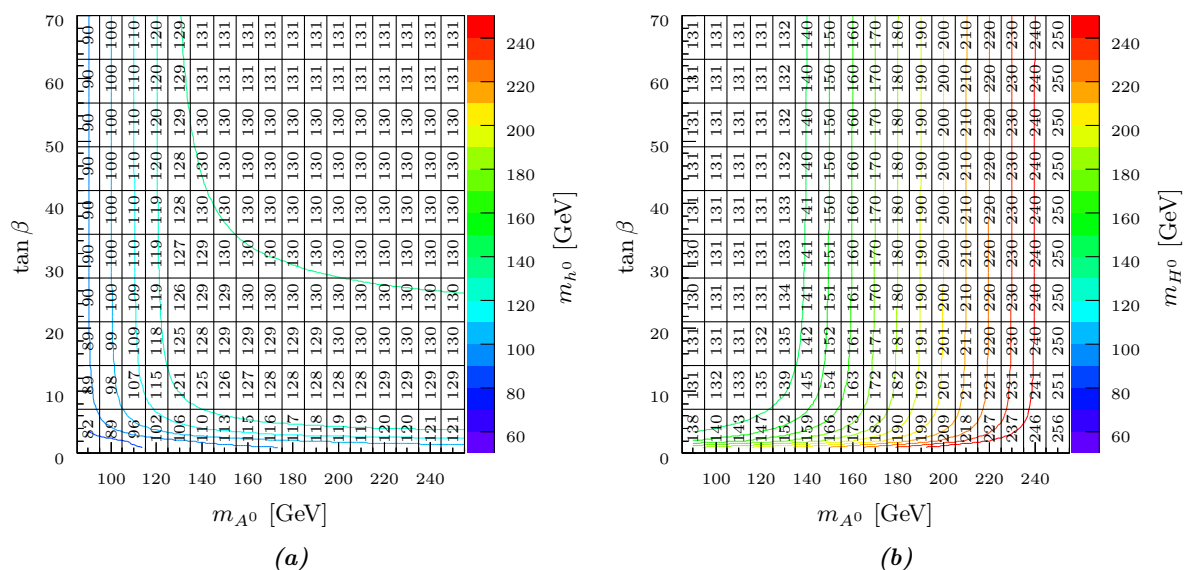


**Figure D.1.:** Numerical values for the mass of the (a) light  $\mathcal{CP}$ -even and (b) heavy  $\mathcal{CP}$ -even MSSM Higgs bosons as a function of the  $\mathcal{CP}$ -odd Higgs boson mass and  $\tan\beta$ .

### D.1.2. SM Branching Fraction Calculations

The SM Higgs boson branching fractions are calculated using the results of Ref. [195] and the Higgs boson decay calculators HDECAY [96, 196, 197, 198] and PROPHECY4F [199, 200, 201, 202]. The Higgs boson width is calculated as,

$$\begin{aligned} \Gamma_H = & \Gamma_H^{\text{HDECAY}} - \Gamma_{H \rightarrow ZZ}^{\text{HDECAY}} - \Gamma_{H \rightarrow WW}^{\text{HDECAY}} \\ & + \Gamma_{H \rightarrow Z^*Z^*}^{\text{PROPHECY4F}} + \Gamma_{H \rightarrow W^*W^*}^{\text{PROPHECY4F}} + \Gamma_{H \rightarrow Z^*Z^*/W^*W^*}^{\text{PROPHECY4F}} \end{aligned} \quad (\text{D.1})$$

where the superscript indicates the program used to calculate the width.

The program HDECAY calculates partial widths for all channels that are kinematically allowed with branching fractions greater than  $10^{-4}\%$  resulting in the Higgs boson decay width of Eq. 6.2 with the electron,  $u$ -quark, and  $d$ -quark pair widths excluded. For Higgs boson masses well above the quark pair threshold the quark pair partial widths are calculated up to order  $\alpha_s^3$ , while the near threshold widths are calculated up to order  $\alpha_s^2$ . Electroweak corrections are included at order  $\alpha_e^2$  but are small in the considered Higgs boson mass range. For  $t$ -quark pair decays, radiative corrections at order  $\alpha_s$  are included and below threshold, the partial width for an on-shell and off-shell pair is calculated as a three-body decay,  $H \rightarrow t\bar{t}^* \rightarrow t\bar{b}W$ .

For the gauge boson combinations, the gluon pair width is calculated up to order  $\alpha_s^2$  including splittings of the gluons into heavy quark flavours. The photon pair and  $Z$  boson and photon partial widths are calculated including heavy fermion and  $Z$  boson loops, where no radiative QCD corrections are made to the quark loops as they are small. Next-to-leading order electroweak corrections for both the gluon and photon pair widths are applied using calculations from Refs. [246] and [247]. The vector boson pair widths are calculated in three regimes: both bosons are off-shell, one boson is off-shell, and both bosons are on-shell. Neither interference between the four fermion final states  $\nu\nu\ell\ell$  and  $q_iq_iq_jq_j$ , nor electroweak corrections are included when calculating the vector boson pair partial widths.

Because the vector boson branching fractions are critical in the Higgs boson mass region considered, a more complete calculation is performed using the decay width calculator PROPHECY4F. Here, the vector boson partial width is calculated explicitly for the four fermion final states by consistently using a complex-mass scheme over the full range of masses for the Higgs boson at next-to-leading order. Radiative electroweak corrections are applied on the order  $\alpha_e$  and interference between the four fermion states from virtual  $W$  and  $Z$  bosons is included. In Eq. D.1 the full width from HDECAY is corrected by subtracting the HDECAY vector boson partial widths and adding the PROPHECY4F partial width including the interference term,  $\Gamma_{H \rightarrow Z^*Z^*/W^*W^*}^{\text{PROPHECY4F}}$ .

The uncertainty for the partial widths and branching fractions, given by the coloured bands of Fig. 6.2 are calculated from both parametric and theoretical uncertainty. The parametric uncertainty incorporates the experimental uncertainty on the measurement of  $\alpha_s$  and the masses of the  $c$ -quark,  $b$ -quark, and  $t$ -quark masses. The theoretical uncertainties are due to missing higher orders, and are estimated from explicitly known electroweak and QCD higher order calculations.

Numerical values for the SM Higgs boson decaying into a  $\tau$  lepton pair are tabulated as a

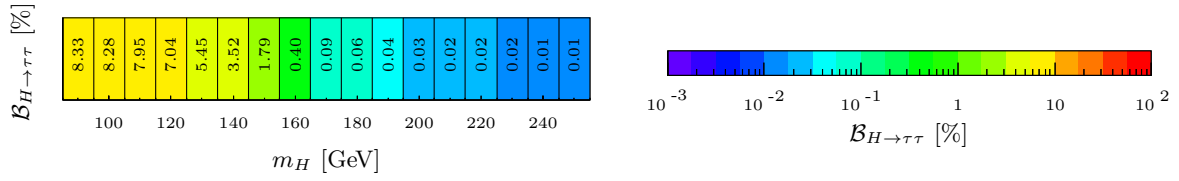


**Figure D.2.:** Numerical values for the SM Higgs boson branching fraction into  $\tau$  lepton pairs as a function of the SM Higgs boson mass.

function of the SM Higgs boson mass in Fig. D.2.

### D.1.3. MSSM Branching Fraction Calculations

The  $\tau$  lepton branching fractions of Fig. 6.3 are calculated following the recommendations of Ref. [223]. The total decay width is calculated as,

$$\begin{aligned} \Gamma_{\Phi^0} = & \Gamma_{\Phi^0 \rightarrow \mu\mu}^{\text{FEYNHIGGS}} + \Gamma_{\Phi^0 \rightarrow \tau\tau}^{\text{FEYNHIGGS}} + \Gamma_{\Phi^0 \rightarrow c\bar{c}}^{\text{HDECAY}} + \Gamma_{\Phi^0 \rightarrow b\bar{b}}^{\text{HDECAY}} + \Gamma_{\Phi^0 \rightarrow t\bar{t}}^{\text{HDECAY}} \\ & + \Gamma_{\Phi^0 \rightarrow gg}^{\text{HDECAY}} + \Gamma_{\Phi^0 \rightarrow \gamma\gamma}^{\text{HDECAY}} + \Gamma_{\Phi^0 \rightarrow Z\gamma}^{\text{HDECAY}} + \Gamma_{\Phi^0 \rightarrow Z^*Z^*}^{\text{PROPHECY4F}} + \Gamma_{\Phi^0 \rightarrow W^*W^*}^{\text{PROPHECY4F}} \end{aligned} \quad (\text{D.2})$$

where the superscripts indicate the decay width calculator used. The two leptonic partial widths are calculated using FEYNHIGGS [190, 191, 192, 193, 194] with a full one-loop calculation. The vector boson pair partial widths are calculated using PROPHECY4F, just as for the SM, but excluding the interference terms and with the couplings between the Higgs bosons and the vector bosons modified using the couplings calculated from FEYNHIGGS. The remaining partial widths are calculated using HDECAY where the Higgs boson masses and couplings are passed to HDECAY from FEYNHIGGS. No uncertainties have been calculated for the MSSM branching fractions.

Numerical values for the branching fractions of the MSSM Higgs bosons into  $\tau$  lepton pairs are tabulated as a function of the  $\mathcal{CP}$ -odd Higgs boson and  $\tan\beta$  in Fig. D.3.

### D.1.4. SM Cross-Section Calculations

The gluon-gluon fusion cross-section is determined using the HIGLU [207, 208, 209, 210] and DFG [211, 212, 213] cross-section calculators. At next-to-leading order HIGLU calculates,

$$\sigma_{gg \rightarrow H} = \sigma_{gg \rightarrow H}^{\text{LO}} + \Delta\sigma_{\text{virt}} + \Delta\sigma_{gg \rightarrow Hg} + \Delta\sigma_{gq \rightarrow Hq} + \Delta\sigma_{qq \rightarrow Hg} \quad (\text{D.3})$$

where the first term is the leading order one-loop gluon-gluon fusion cross-section, the second term parametrises the infrared regularised virtual two-loop corrections, and the three remaining terms correct for the one-leg sub-processes, calculated with one loop. Resummation of soft gluon contributions at next-to-leading log are then included by DFG. Contributions from the  $t$ -quark loop are calculated using the large- $m_t$  limit and added at next-to-next-to-leading log and next-to-next-to-leading order. The result is then corrected for electroweak contributions. The next-to-leading order corrections increase the cross-section by approximately 80% while the

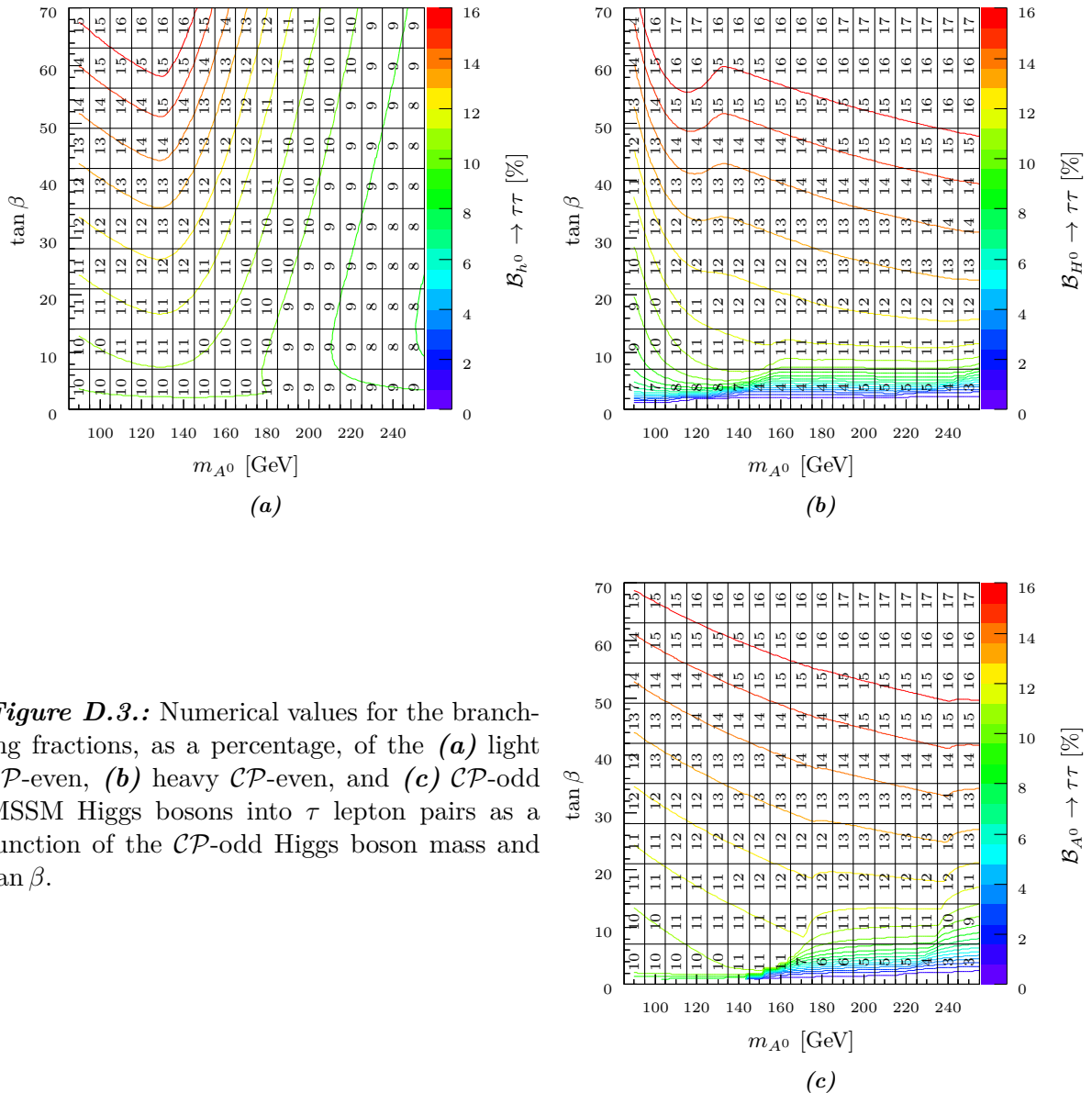


**Figure D.3.:** Numerical values for the branching fractions, as a percentage, of the (a) light  $\mathcal{CP}$ -even, (b) heavy  $\mathcal{CP}$ -even, and (c)  $\mathcal{CP}$ -odd MSSM Higgs bosons into  $\tau$  lepton pairs as a function of the  $\mathcal{CP}$ -odd Higgs boson mass and  $\tan \beta$ .

next-to-next-to-leading order corrections increase the cross-section by approximately 25%.

The uncertainty for the gluon-gluon fusion cross-section in Fig. 6.5 is indicated by the red band and is calculated from five sources. The higher-order radiative QCD corrections provide the largest uncertainty and are determined by varying the factorisation and renormalisation scales. The electroweak corrections introduce another perturbative uncertainty, while the large- $m_t$  approximation yields a small uncertainty. The input masses for the  $b$ -quark and  $t$ -quark cause a scheme dependence which is found to be small. The final source of uncertainty is from the proton PDF and is determined using the MSTW08 PDF sets.

The vector-boson fusion cross-section given is determined at next-to-next-to-leading order using the VBF@NNLO [214, 215, 216] cross-section calculator. Here the process is treated as a double deep-inelastic scattering process where the two quark lines are assumed not to interfere and the structure functions can be factorised. This assumption holds at not only leading-order,

but also next-to-leading order where contributions from a single connecting colour line must conserve colour. At next-to-next-to-leading order this assumption no longer remains valid, but the dominant contributions can be included in the structure functions.

At leading-order the vector-boson fusion final states can interfere with both associated vector boson production and associated heavy quark production final states, for which the structure function factorisation does not hold. These interference contributions, however, can be directly calculated and are accounted for in the final cross-section result. By kinematic arguments, this interference at next-to-leading order and higher orders can be shown to contribute at below the percent level, and consequently are not included. Finally, electroweak contributions have also been included under the assumption that the QCD and electroweak contributions factorise.

The associated vector boson production cross-section is calculated using `vH@NNLO` [248, 249] where electroweak corrections are calculated at next-to-leading order and QCD corrections are calculated at next-to-next-to-leading order. These two sets of corrections are assumed to factorise and were originally calculated independently in Refs. [250] and [251], respectively.

The predominant channel for associated heavy quark production is in association with a  $t$ -quark pair. Currently, only leading order cross-section calculators are publicly available, although full next-to-leading order cross-sections have been calculated in Ref. [252], and are found to increase the cross-section by approximately 20% at most. The results provided in Fig. 6.5 are from Ref. [217] and are calculated at next-to-leading order. Numerical values for the inclusive cross-section of Fig. 6.5 are tabulated in Fig. D.4.

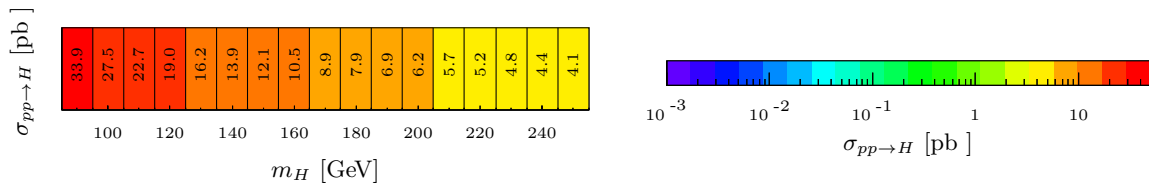


**Figure D.4.:** Numerical values for the inclusive SM Higgs boson cross-section as a function of the SM Higgs boson mass.

### D.1.5. MSSM Cross-Section Calculations

The MSSM Higgs boson cross-sections for gluon-gluon fusion are determined using the cross-section calculators `HIGLU` and `GGH@NNLO` [218, 219, 220] with the MSSM couplings calculated using `FEYNHIGGS`. The cross-section is calculated as,

$$\begin{aligned} \sigma_{gg \rightarrow \Phi^0} = & \left( \frac{F_{\Phi^0 b\bar{b}}}{F_{H b\bar{b}}} \right)^2 \sigma_{gg \rightarrow b\bar{b} \rightarrow H}^{\text{NLO}} + \left( \frac{F_{\Phi^0 t\bar{t}}}{F_{H t\bar{t}}} \right)^2 \left( \sigma_{gg \rightarrow t\bar{t} \rightarrow H}^{\text{NLO}} + \Delta\sigma_{gg \rightarrow t\bar{t} \rightarrow H}^{\text{NNLO}} \right) \\ & + \left( \frac{F_{\Phi^0 t\bar{t}} F_{\Phi^0 b\bar{b}}}{F_{H t\bar{t}} F_{H b\bar{b}}} \right) \sigma_{gg \rightarrow b\bar{b}/t\bar{t} \rightarrow H}^{\text{NLO}} \end{aligned} \quad (\text{D.4})$$

where the pre-factors  $F_{\Phi^0 q\bar{q}}$  and  $F_{H q\bar{q}}$  are the MSSM and SM couplings of the Higgs bosons with the specified quark pair, calculated via `FEYNHIGGS`. At tree-level these couplings are given by Figs. 2.10(a) through 2.10(f) for the MSSM Higgs bosons and Fig. 2.6(g) for the SM Higgs

boson. The next-to-leading order terms  $\sigma_{gg \rightarrow t\bar{t} \rightarrow H}^{\text{NLO}}$ ,  $\sigma_{gg \rightarrow b\bar{b} \rightarrow H}^{\text{NLO}}$ , and  $\sigma_{gg \rightarrow b\bar{b}/t\bar{t} \rightarrow H}^{\text{NLO}}$  are calculated with HIGLU for the SM Higgs boson using Eq. D.3 where the cross-section has been split into the individual  $t$ -quark,  $b$ -quark, and interference contributions respectively.

The next-to-next-to-leading order  $t$ -quark correction term,  $\Delta\sigma_{gg \rightarrow t\bar{t} \rightarrow H}^{\text{NNLO}}$ , is given by,

$$\Delta\sigma_{b\bar{b} \rightarrow t\bar{t} \rightarrow H}^{\text{NNLO}} = \left( \frac{\sigma_{gg \rightarrow t\bar{t} \rightarrow H}^{\text{NNLO}} - \sigma_{gg \rightarrow t\bar{t} \rightarrow H}^{\text{NLO}}}{\sigma_{gg \rightarrow t\bar{t} \rightarrow H}^{\text{LO}}} \right) \sigma_{gg \rightarrow t\bar{t} \rightarrow H}^{\text{LO}} \quad (\text{D.5})$$

where all the terms are evaluated from GGH@NNLO. No electroweak corrections are applied to the cross-sections from either Eq. D.4 or Eq. D.5 as the SM couplings cannot be easily corrected to MSSM couplings. Additionally, in Eq. D.5 next-to-next-to-leading log resummation is not performed as this has not been calculated for the  $\mathcal{CP}$ -odd Higgs boson and next-to-next-to-leading log PDFs are not available.

The associated  $b$ -quark production cross-section is calculated by,

$$\sigma_{b\bar{b} \rightarrow \Phi^0} = \left( \frac{F_{\Phi^0 b\bar{b}}}{F_{H b\bar{b}}} \right)^2 \sigma_{b\bar{b} \rightarrow H}^{\text{NNLO}} \quad (\text{D.6})$$

at next-to-next-to-leading order using the cross-section calculator BBH@NNLO [221, 222] dressed with the MSSM and SM couplings of the Higgs bosons with  $b$ -quarks,  $F_{\Phi^0 b\bar{b}}$  and  $F_{H b\bar{b}}$ , from FEYNHIGGS. The tree-level couplings are given for the MSSM Higgs bosons in Figs. 2.10(d) through 2.10(f) and the SM Higgs boson in Fig. 2.6(g). The following sub-processes for  $\sigma_{b\bar{b} \rightarrow H}^{\text{NNLO}}$  are evaluated by BBH@NNLO,

$$\left. \begin{array}{l} b\bar{b} \rightarrow Hgg, \quad b\bar{b} \rightarrow Hq\bar{q}, \quad b\bar{b} \rightarrow Hb\bar{b} \\ gb \rightarrow Hgb, \quad bb \rightarrow Hbb, \quad bq \rightarrow Hbq \\ gg \rightarrow Hb\bar{b}, \quad q\bar{q} \rightarrow Hb\bar{b} \end{array} \right\} \text{tree level} \quad \left. \begin{array}{l} b\bar{b} \rightarrow Hq \\ gb \rightarrow Hb \\ b\bar{b} \rightarrow H \end{array} \right\} \begin{array}{l} \text{one loop} \\ \text{two loop} \end{array} \quad (\text{D.7})$$

where  $q$  indicates a  $u$ -quark,  $d$ -quark,  $c$ -quark, or  $s$ -quark. There is no overlap between the one-leg sub-processes of Eq. D.3 and Eq. D.7 and so the MSSM gluon-gluon fusion cross-sections from Eq. D.4 and the associated  $b$ -quark production cross-sections from Eq. D.6 can be summed to determine the inclusive cross-section without introducing double-counting.

In Fig. D.5 the inclusive cross-sections for the MSSM Higgs bosons, given in Fig. 6.6, are provided with numerical values as a function of the  $\mathcal{CP}$ -odd Higgs boson mass and  $\tan\beta$ . The inclusive cross-sections are separated into the gluon-gluon fusion component in Fig. D.6 and the associated  $b$ -quark production component in Fig. D.7.

## D.2. Acceptances and Efficiencies

The numerical values for the acceptances used to calculate the number of expected Higgs boson events in Sect. 6.2.2 are given in Fig. D.8 for the five event categories as a function of the Higgs boson mass,  $m_{\phi^0}$ . In Fig. D.9, numerical values for the efficiencies given by Eq. 6.18 for the five event categories are tabulated as a function of the Higgs boson mass.

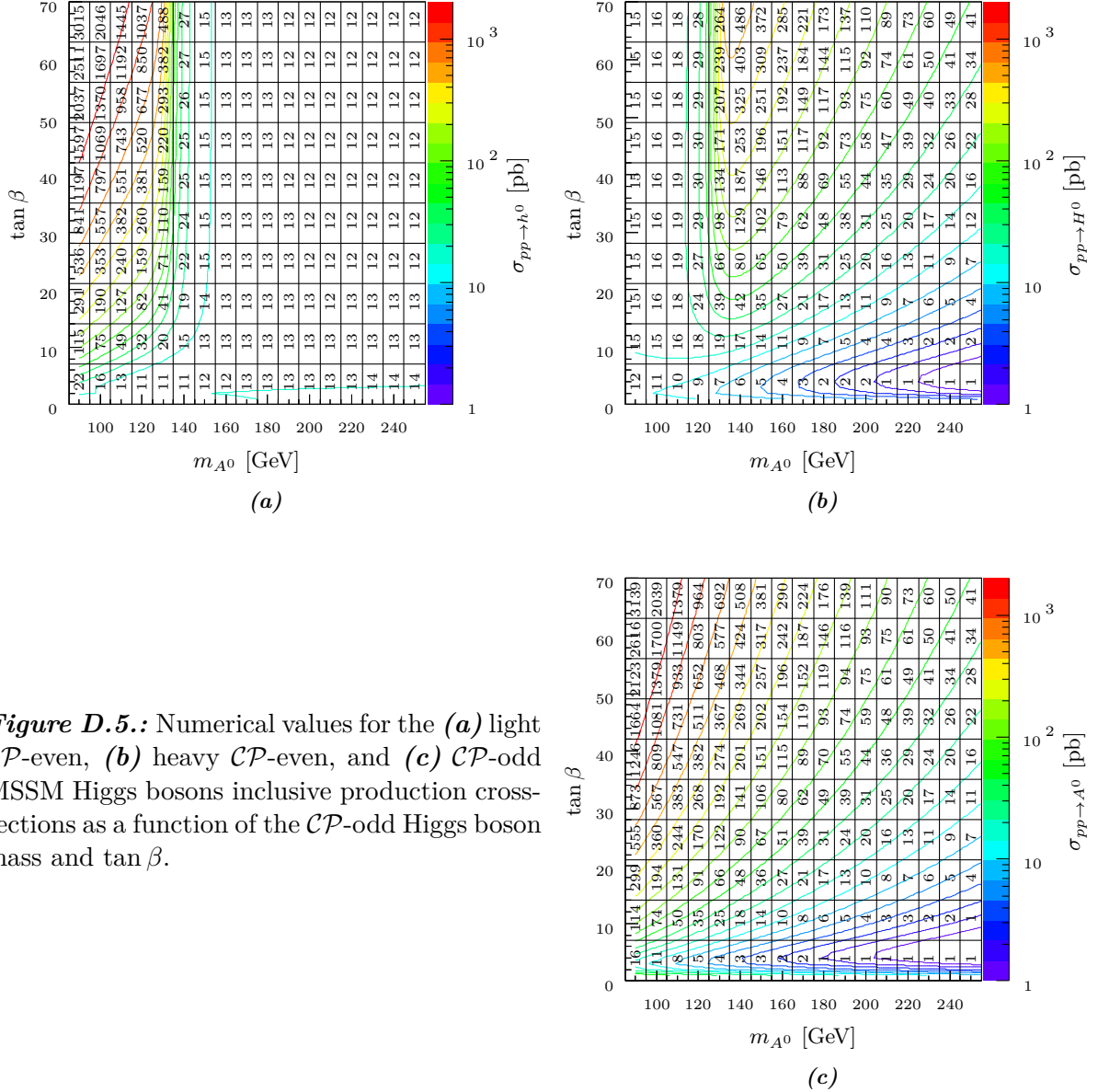


**Figure D.5.:** Numerical values for the (a) light  $CP$ -even, (b) heavy  $CP$ -even, and (c)  $CP$ -odd MSSM Higgs bosons inclusive production cross-sections as a function of the  $CP$ -odd Higgs boson mass and  $\tan \beta$ .





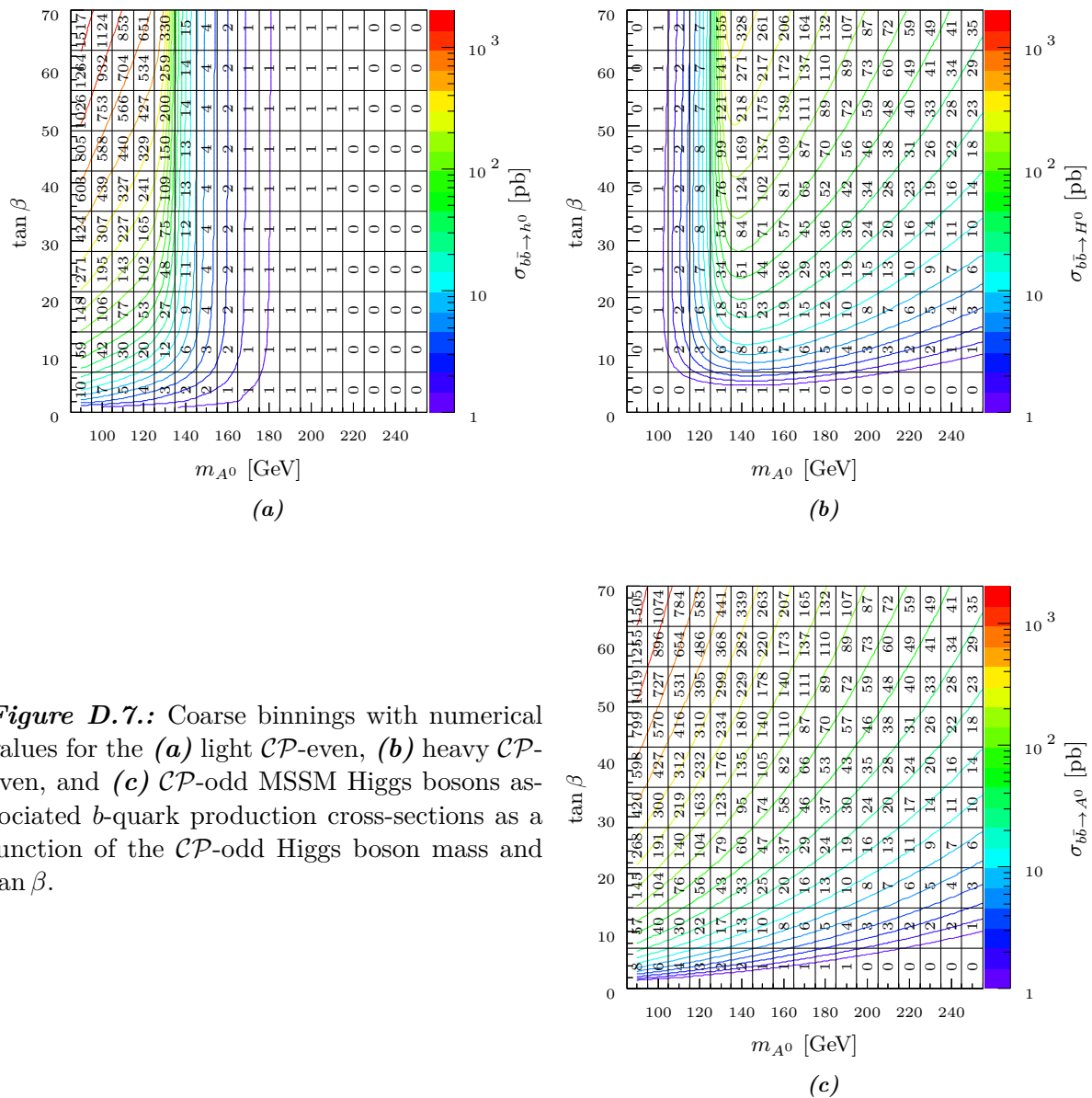


**Figure D.7.:** Coarse binnings with numerical values for the (a) light  $\mathcal{CP}$ -even, (b) heavy  $\mathcal{CP}$ -even, and (c)  $\mathcal{CP}$ -odd MSSM Higgs bosons associated  $b$ -quark production cross-sections as a function of the  $\mathcal{CP}$ -odd Higgs boson mass and  $\tan \beta$ .

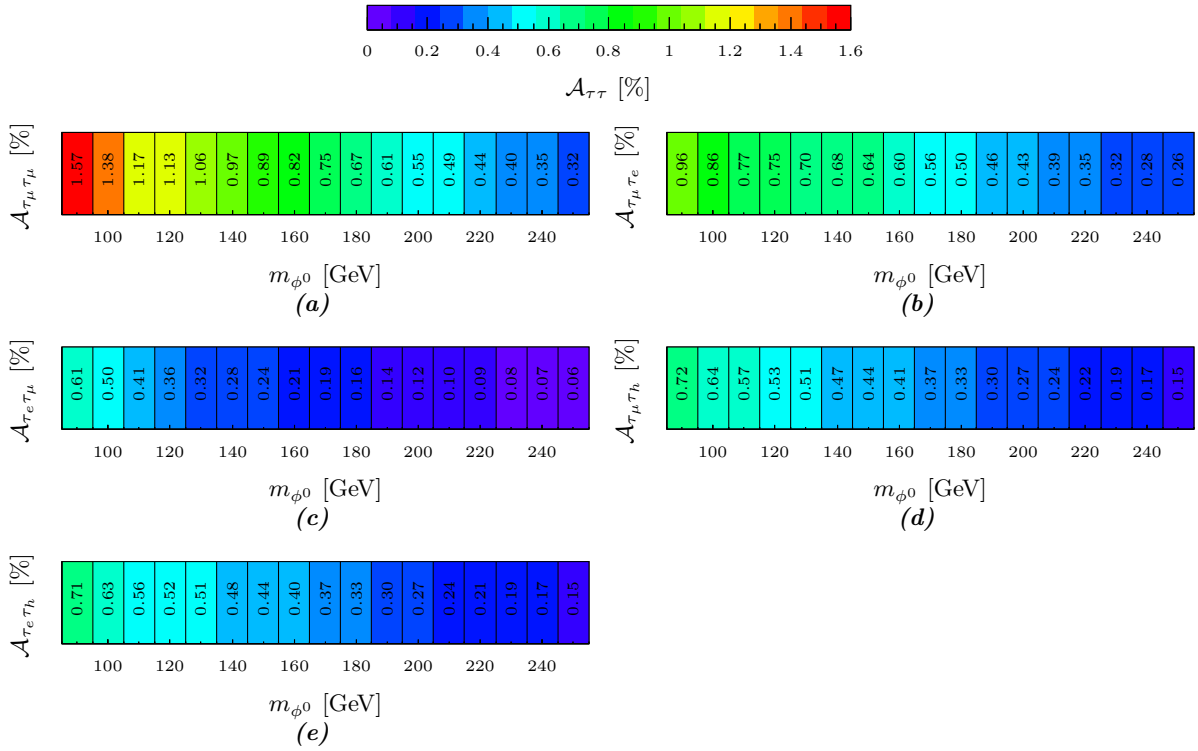


**Figure D.8.:** Acceptances, with numerical values, for Higgs bosons decaying into the (a)  $\tau_\mu\tau_\mu$ , (b)  $\tau_\mu\tau_e$ , (c)  $\tau_e\tau_\mu$ , (d)  $\tau_\mu\tau_h$ , and (e)  $\tau_e\tau_h$  categories to pass the  $\eta$  and  $p_T$  requirements of Sect. 5.1.1 as a function of the Higgs boson mass.

### D.3. Statistical Methods

Details on the Asimov dataset of Ref. [228], as well as a derivation for Eq. 6.43, the extended likelihood evaluated with an Asimov dataset, from the results Ref. [228] is given in App. D.3.1. Further information on incorporating systematic uncertainties into hypothesis testing using marginalisation techniques is given in App. D.3.2.

#### D.3.1. Asimov Dataset

Consider binning the  $N$  events into  $N_{\text{bins}}$  using one or more observables for each event, *e.g.* the invariant mass of the event. The probability density function for each bin is then described by the Poisson distribution, and so the binned likelihood function is,

$$\begin{aligned}
 L_b(\vec{x}|\mu) &= \prod_i L_s(x_i|\mu) = \prod_i \frac{(N_{\text{bkg}_i} + \mu N_{\text{sig}_i})^{x_i} e^{-N_{\text{bkg}_i} - \mu N_{\text{sig}_i}}}{x_i!} \\
 &= \prod_i \frac{\left( (N_{\text{bkg}} + \mu N_{\text{sig}}) \text{pdf}(\vec{b}_i|\mu) d\vec{b}_i \right)^{x_i} e^{-(N_{\text{bkg}} + \mu N_{\text{sig}}) \text{pdf}(\vec{b}_i|\mu) d\vec{b}_i}}{x_i!}
 \end{aligned} \tag{D.8}$$

where the product of the likelihoods for each bin is taken over all  $N_{\text{bins}}$ . The number of events in each bin is  $x_i$  and the number of expected background and signal events for each bin  $i$  is given by  $N_{\text{bkg}_i}$  and  $N_{\text{sig}_i}$ . In the second line, the number of expected background and signal events

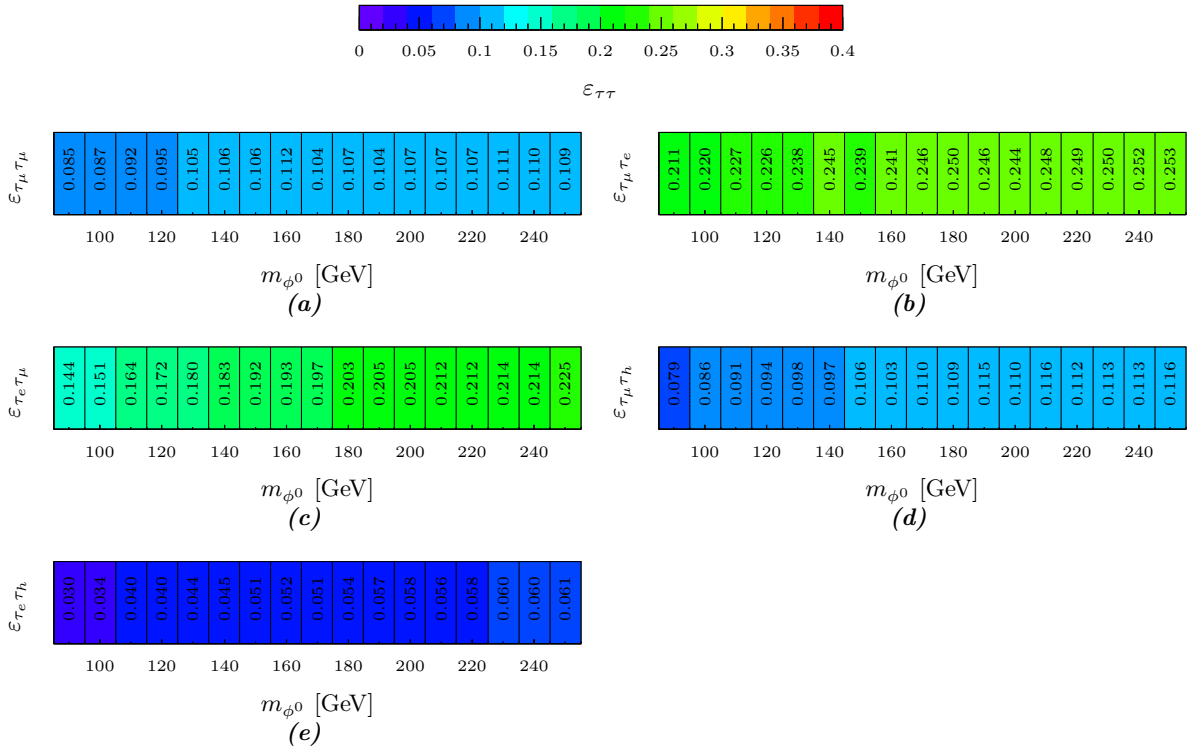


**Figure D.9.:** Efficiency corrections, with numerical values, for Higgs bosons decaying into the (a)  $\tau_\mu\tau_\mu$ , (b)  $\tau_\mu\tau_e$ , (c)  $\tau_e\tau_\mu$ , (d)  $\tau_\mu\tau_h$ , and (e)  $\tau_e\tau_h$  categories as a function of the Higgs boson mass. The efficiency determination is described in Sects. 5.2.1 and 5.2.2.

for a given bin are written in terms of the joint *pdf* for the set of observables for the bin,  $\vec{b}_i$ , and the width of the bin,  $d\vec{b}_i$ . The binned likelihood function is dependent upon not only the number of observed events, but also the observables of the events.

For the test statistic  $q_\nu$  of Eq. 6.34 calculated with any likelihood function, the median is found using the definition of the median from Eq. 6.40 and the *cdf* of  $q_\nu$  from Eq. 6.36,

$$M[q_\nu|\mu] = \left( \Phi^{-1} \left( \frac{1}{2} \right) + \frac{\nu - \mu}{\sigma} \right)^2 = \frac{(\nu - \mu)^2}{\sigma^2} \quad (\text{D.9})$$

where  $\sigma^2$  is the variance of the maximum likelihood estimator  $\hat{\nu}$ . The binned log-likelihood function can be written as,

$$LL_b(\vec{x}|\mu) = \ln L_b(\vec{x}|\mu) = \sum_i (x_i \ln u_i - u_i - x_i!) \quad (\text{D.10})$$

where the summation is over all bins, the binned likelihood function of Eq. D.8 has been used, and the change of variable  $u_i = N_{\text{bkg}_i} + \mu N_{\text{sig}_i}$  has been made. The derivative of the binned log-likelihood function with respect to the signal strength parameter  $\mu$  is then,

$$\frac{\partial LL_b(\vec{x}|\mu)}{\partial \mu} = \sum_i \left( \left( \frac{x_i}{u_i} - 1 \right) \frac{\partial u_i}{\partial \mu} \right) \quad (\text{D.11})$$

where again the summation is over all bins. If this derivative for a given  $\vec{x}$  is zero, then

the maximum likelihood estimator  $\hat{\nu}$  for  $\vec{x}$  is  $\mu$ . The dataset  $\vec{a}(\mu)$  fulfils this condition if  $a_i(\mu) = u_i = N_{\text{bkg}_i} + \mu N_{\text{sig}_i}$ . This representative dataset first proposed in Ref. [228] is named the Asimov dataset as it was inspired by the short story of Ref. [238] written by Isaac Asimov.

Calculating the test statistic  $q_\nu$  using  $\vec{a}(\mu)$  results in,

$$\begin{aligned} q_\nu(\vec{a}(\mu)) &= -2(LL(\vec{a}(\mu)|\nu) - LL(\vec{a}(\mu)|\mu)) \\ &= \frac{(\nu - \mu)^2}{\sigma^2} \\ &= M[q_\nu|\mu] \end{aligned} \tag{D.12}$$

for  $\mu \leq \nu$  where Eq. 6.34 has been used in the first line, Eq. 6.31 in the second line, and Eq. D.9 in the third line. Consequently, the median test statistics parameter  $q_\nu$ , assuming  $\mu$ , can be found by evaluating  $q_\nu$  with the Asimov dataset of  $\mu$ . This also provides the non-centrality parameter of  $pdf(t_\nu|\mu)$  and  $pdf(q_\nu|\mu)$  from Eqs. 6.33 and 6.35. In the example of Fig. 6.15 the non-centrality parameter for  $pdf(t_1|0)$  is determined from the fit to be  $8.1 \pm 1.4$  and found to be 7.5 using the Asimov dataset  $\vec{a}(0)$ .

Using  $a_i(\mu) = N_{\text{bkg}_i} + \mu N_{\text{sig}_i}$  defines the Asimov dataset for the simple and binned likelihood functions, but must be taken to the continuous limit for the extended likelihood function. The extended likelihood function can be obtained by taking the limit of the binned likelihood function as the widths of the bins approach zero. Each bin will contain either no events or a single event. The simple likelihood function for bin  $i$  with zero events is,

$$L_s(0|\mu) = e^{-N_{\text{bkg}_i} - \mu N_{\text{sig}_i}} = e^{-(N_{\text{bkg}} + \mu N_{\text{sig}}) pdf(\vec{b}_i|\mu) d\vec{b}_i} \tag{D.13}$$

where the bin centre is given by the set of observables  $\vec{b}_i$  and the width of the bin is given by  $d\vec{b}_i$ . Similarly,

$$\begin{aligned} L_s(1|\mu) &= (N_{\text{bkg}_i} + \mu N_{\text{sig}_i}) e^{-N_{\text{bkg}_i} - \mu N_{\text{sig}_i}} \\ &= \left( (N_{\text{bkg}} + \mu N_{\text{sig}}) pdf(\vec{b}_i|\mu) d\vec{b}_i \right) e^{-(N_{\text{bkg}} + \mu N_{\text{sig}}) pdf(\vec{b}_i|\mu) d\vec{b}_i} \end{aligned} \tag{D.14}$$

is the simple likelihood for a bin with one event. From these two likelihood functions, the likelihood function for all the bins becomes,

$$\begin{aligned} L_e(\vec{x}|\mu) &= \prod_j \left( e^{-(N_{\text{bkg}} + \mu N_{\text{sig}}) pdf(\vec{b}_i|\mu) d\vec{b}_i} \right) \prod_i \left( (N_{\text{bkg}} + \mu N_{\text{sig}}) pdf(\vec{b}_i|\mu) d\vec{b}_i \right) \\ &= e^{-N_{\text{bkg}} - \mu N_{\text{sig}}} \prod_i \left( (N_{\text{bkg}} + \mu N_{\text{sig}}) pdf(\vec{o}_i|\mu) \right) \end{aligned} \tag{D.15}$$

where the first product is over all bins and the second product is only over the  $N$  bins with a single event. In the second line, the first product has been integrated in the limit  $d\vec{b}_i \rightarrow 0$  and the second product is expressed in terms of the joint  $pdf$  for the set of observables  $\vec{o}_i$  for an event  $i$ . The extended likelihood function becomes the simple likelihood function, without the factorial denominator, when the set of observables  $\vec{o}_i$  for each event is 1.

Evaluating the extended likelihood function for a binned Asimov data set yields,

$$L_e(\vec{a}(\mu)|\nu) = e^{-N_{\text{bkg}} - \nu N_{\text{sig}}} \prod_i ((N_{\text{bkg}} + \nu N_{\text{sig}}) pdf(\vec{b}_i|\nu))^{(N_{\text{bkg}} + \mu N_{\text{sig}}) pdf(\vec{b}_i|\mu)} d\vec{b}_i \quad (\text{D.16})$$

where  $\vec{b}_i$  is the set of observables for each bin of  $\vec{a}$  and  $d\vec{b}_i$  is the width of each bin. The product is over all bins of the Asimov dataset. However, as each bin no longer contains a single event like the second product of Eq. D.15, but rather  $(N_{\text{bkg}} + \mu N_{\text{sig}}) pdf(\vec{b}_i|\mu) d\vec{b}_i$  events, each argument of the product is exponentiated by this non-integer number of events. The extended log-likelihood function can then be written as,

$$\begin{aligned} LL_e(\vec{a}(\mu)|\nu) &= \sum_i \ln \left( (N_{\text{bkg}} + \nu N_{\text{sig}}) pdf(\vec{b}_i|\nu) \right) (N_{\text{bkg}} + \mu N_{\text{sig}}) pdf(\vec{b}_i|\mu) d\vec{b}_i \\ &\quad - N_{\text{bkg}} - \nu N_{\text{sig}} \\ &= \int \ln \left( (N_{\text{bkg}} + \nu N_{\text{sig}}) pdf(\vec{\sigma}|\nu) \right) (N_{\text{bkg}} + \mu N_{\text{sig}}) pdf(\vec{\sigma}|\mu) d\vec{\sigma} \\ &\quad - N_{\text{bkg}} - \nu N_{\text{sig}} \end{aligned} \quad (\text{D.17})$$

where in the first step the summation is over all bins of the Asimov dataset and in the second step the limit has been taken as the bin width for the Asimov dataset approaches zero. This result can then be used to determine the Asimov test statistic for a test statistic calculated using the extended likelihood function. When the test statistic, Asimov or otherwise, is evaluated using a binned likelihood function or an extended likelihood function using a *pdf* from a histogram with identical binning to the binned likelihood function, the results from the two different likelihood function methods are equivalent.

### D.3.2. Marginalisation

An alternative to the frequentist hypothesis testing of Sect. 6.3.1 using *p*-values is a Bayesian approach where hypotheses are treated as random variables. From Bayes' theorem of Ref. [253], the probability density function for the signal strength parameter  $\mu$  as a function of the observed data  $\vec{x}$  can be written as,

$$pdf(\mu|\vec{x}) = \frac{L(\vec{x}|\mu) pdf(\mu)}{\int L(\vec{x}|\mu') pdf(\mu') d\mu'} \quad (\text{D.18})$$

where *pdf*( $\mu$ ) is the prior probability density function for the signal strength and  $L(\vec{x}|\mu)$  is the likelihood function for  $\vec{x}$ . The choice of *pdf*( $\mu$ ) is highly dependent upon the analysis, although oftentimes *pdf*( $\mu$ ) is chosen as a divergent uniform prior. The probability for the signal strength to be greater than  $\mu$  is then just the integral of *pdf*( $\mu|\vec{x}$ ) from  $\mu$  upwards, while the probability for the signal strength to be less than  $\mu$  is the integral from  $\mu$  downwards.

Systematic uncertainties can be introduced into Eq. D.18 using a method similar to Ref. [254]

by incorporating them into the *pdfs* via nuisance parameters,  $\vec{\theta}$ ,

$$pdf(\mu, \vec{\theta}|\vec{x}) = \frac{L(\vec{x}|\mu, \vec{\theta})pdf(\mu, \vec{\theta})}{\int L(\vec{x}|\mu', \vec{\theta}')pdf(\mu') d\mu' d\vec{\theta}'} \quad (\text{D.19})$$

where each  $\theta$  represents a systematic uncertainty. The dependence upon the hypothesis *pdf* on the nuisance parameters can be eliminated by,

$$pdf(\mu|\vec{x}) = \int pdf(\mu, \vec{\theta}|\vec{x}) d\vec{\theta} \quad (\text{D.20})$$

where the nuisance parameters have been marginalised via integration. If the nuisance parameters are independent of the hypothesis, then the likelihood function can be marginalised with respect to  $\vec{\theta}$ ,

$$L(\vec{x}|\mu) = \int L(\vec{x}|\mu, \vec{\theta})pdf(\vec{\theta}) d\vec{\theta} \quad (\text{D.21})$$

and used directly in Eq. D.18. The marginalised likelihood function can also be used in the test statistics of Eqs. 6.25, 6.31, and 6.34, resulting in the hybrid approach proposed in Ref. [255]. The integration of the *pdf* of the observables is oftentimes not trivial and cannot be done analytically, requiring the use of numerical methods such as Monte Carlo integration instead.